The Thermal, Metamorphic and Magmatic Evolution of a Rapidly Exhuming Terrane: the Nanga Parbat Massif, Northern Pakistan.

Thesis

UNRESTRICTED

The thermal, metamorphic and magmatic evolution of a rapidly exhuming terrane: the Nanga Parbat Massif, northern Pakistan.

A thesis accepted for the degree of
Doctor of Philosophy

by

Alan Geoffrey Whittington,
M.A. (Cantab.)

Department of Earth Sciences,
The Open University

August 1997

Date of submission: 5th June 1997
Date of award: 20th November 1997

ProQuest LLC.
789 East Eisenhower Parkway
P.O. Box 1346
Ann Arbor, MI 48106 – 1346

ABSTRACT

The Nanga Parbat-Haramosh Massif (NPHM) is the most northerly outcrop of Indian Plate rocks in the Himalayan orogen, exposed by rapid recent exhumation through the structurally overlying Kohistan Island Arc in northern Pakistan. Exhumation has been achieved by erosion in the apparent absence of extensional tectonics. Metabasaltic dykes intruded into polymetamorphic basement rocks provide time markers that distinguish early from late fabrics that probably correlated with Precambrian and Himalayan deformation respectively. Nanga Parbat is anomalous within the Himalayan orogen for both the timing and nature of metamorphism and anatexis. A multidisciplinary approach allows the thermal history to be tightly constrained.

Metamorphism is characterised by cordierite growth during near-isothermal decompression. Garnet inclusion assemblages record P-T conditions of 720 ± 50°C and 7.5 ± 1.5 kbar, while spinel-cordierite intergrowths unique to the massif interior formed at 710 ± 60°C and 5.0 ± 1.1 kbar. Lower grade assemblages are exposed towards the massif margins. Tourmaline leucogranite plutons and sheets are characterised by similar trace element geochemistry to Miocene High Himalayan granites, indicative of vapour-absent crustal melting as would result from rapid decompression, but were emplaced more than 10 million years later. More recently, fluid infiltration into conjugate shear zones accommodating vertical stretching in the core of the massif resulted in anatexis and the formation of restitic cordierite-bearing pods. ^{40}Ar-^{39}Ar studies indicate regional cooling below 400°C as recently as 1 Ma, and the distribution of excess ^{40}Ar in basement samples is indicative of magmatic/metamorphic fluids at depths > 10 km.

One-dimensional thermal modelling indicates that increasing cooling rates through time do not require increasing exhumation rates because advection of heat results in a steepened near-surface geotherm. These models predict both the style and timing of metamorphism and anatexis in this rapidly exhuming terrane, and are consistent with petrological and geochemical constraints determined from the NPHM basement.

FOREWORD

Bonsai Mountains. .... Just any old piece of rock won't do. The trick is to spot the mountains while they are young. In a sense the expert is selecting that piece of rock which, after the normal processes of continental collision and upheaval, will be at the very peak - i.e., from one pont of view, the rock with the correct morphic field which will cause the rest of the mountain to form underneath it ....

(from "The Discworld Companion", by Terry Pratchett and Stephen Briggs, 1994, Cassell, London)

JIM AND ELRIC
LOOKING ETHNIC IN FRONT OF NANGA PARBAT.

JIM DAVIS

Acknowledgements

I am very grateful to many people who have contributed directly and indirectly to the completion of this thesis. My supervisors, Nigel Harris and Rob Butler, provided support and two amusingly different approaches to fieldwork. I must thank Nigel in particular for his fearless perusal of various manuscripts and chapters over the last 3 (and a bit) years.

Drs. Mubarik Ali and Azam Khwaja in Islamabad are thanked for their hospitality, and assistance in exporting rocks. Jim Davis was a superb field assistant, showing restraint in the face of militant incompetence, and stoicism in the face of jiardia. Judy Baker, Dave Mattey, Martin Hand, Karen and Phil also provided interesting diversions during fieldwork. Ghulam Nabi, and extended family, provided diversions from fieldwork, and are thanked for providing traditional remedies for our various ailments. Abdullah Baig, expert in most aspects (cultural, scientific, culinary and pecuniary) of the Northern Areas, was an excellent host at the Hunza Inn, and never complained at our unusual night-time antics. The involvement of various drivers, porters, guides, cooks and hangers-on is gratefully acknowledged (where appropriate!).

I owe thanks also to numerous people who assisted me with various machines and labs, including Eric Condliffe (Leeds), Stephen Reed and Mike N. (Cambridge), Andy Tindle and Phil Potts, Nick Rogers, John Watson and Pete Webb, Holly Holbrook, Mike, Brian and Kay, while PVC and Mabs (just) tolerated my obscenely radiogenic samples in the isotope lab, and Simon Kelley and Jo Wartho made the argon work possible. Other work-related help came from Jessica Bartlett, Anthony Cohen, Janet Dryden, Mark George, Dave Peate, Rita Quill, Steve Reddy, Simon Turner, Derek Vance, and numerous Himalayan types at conferences. My best wishes to the next generation, Christophe, Sarah and Gavin.

Well done to various housemates and office mates who have survived the Elric experience (and some who still talk to me) including Mike, Rhino, Orange, John, Johnny, Zelkjo, Arlene, Pete, Rob, and Yiming. Also to Linda, Rick, Ed, Alex, Fiona, Jugs, Ben and Fran, Mike, Bill, Treez, Paul and Jane, Sephs, Ant, and others who I never officially lived with but have fallen over my prostrate form on their floor at various times. Farewell to Beatrice, who didn't survive the Elric experience and cost me my no claims bonus. Love to all the departmental babes, especially Butty "not a thug", Claire "not a bimbo", Linda "Hello young man", Liz and Johnny, Lou, Phil "Blando", Rob "Kula Shaker", Russ "5 years" and Yvette. Thanks also to members of the OU Club and PGSS committees, all the bar staff, and anyone I've missed. "Aloha" to H, co-worker in the "Warp Toilet" aural adventure, and respect to Mike Bullivant for asking me to play my records at other people, to Madcap Gordon for wearing mustard cords, Skaz/Slunk and Camilla, Simon, Manna Maya, and the more famous ones...

The Mad Kows have been a source of misplaced pride for a couple for years now, so large moos and big ups to the Mad Kow posse: Ed (the enforcer), Carolyn, "end zone" Andy, Sarah and Thomas, Babs, John B, John D, Trevor, Tim, Mandy, Loz, Speds, Teri, Sara, Leroi, Johnny, American Martin, Martian Martin, Fred, Aaron, Linda, Cads, various Australian internationals and anyone else who has ever chased the plastic disc.

Thanks also to my parents and Richard who provided encouragement during writing, and constant reminders of the clean-cut and besuited fate awaiting me should I falter in the last stages. At last I can dedicate an obscure academic work to them, for a change.

Finally, huge hugs to Angela (aka DJ Boss) for providing much needed relief from work, liking the Sisters, putting up with plastic discs and other foibles, not (quite) biting my finger off, and moving to London just so I wouldn't get distracted from writing....

TABLE OF CONTENTS

LIST OF FIGURES

LIST OF TABLES

CHAPTER 1 - INTRODUCTION

1.1 Aims of the project

This thesis investigates the thermal, magmatic and metamorphic history of an anomalous part of the Himalayan orogen, the Nanga Parbat-Haramosh Massif (NPHM). This chapter will describe the aims of the project and the contents of this thesis, and then introduce the reader to the geo-tectonic framework of the Himalaya. Specific points of interest concerning the NPHM are then discussed.

With the advent of plate tectonic theory in the late 1960's, mountain belts assumed a new importance in science. They are one of the first order features of physical maps of the world, and their uplift and erosion histories have major implications for climate (e.g. Ruddiman and Kutzbach, 1989; Raymo and Ruddiman, 1992) and ocean chemistry (e.g. Palmer and Elderfield, 1985; Raymo et al., 1988; Harris, 1995), yet their behaviour during continental collision is poorly understood. Two fundamental controls on the style of deformation, uplift and erosion, are lithology and thermal structure. While the former is quite well known for many mountain belts through geological mapping, thermal structure must be modelled, and the results compared with geological evidence.

The Himalayan orogen is one of the best places in the world to study the geodynamics of continent-continent collisions. This thesis focusses the north-west corner of the Himalayan orogen, the Nanga Parbat Massif in northern Pakistan. This was the first part of the northern edge of India to be involved in the collision between India and Asia, about 55 million years ago, and is anomalous within the Himalaya for both the nature and timing of its geological events. It has recently

undergone very rapid uplift and erosion, making it ideal for studying the thermal consequences of such events. Features normally concealed for millions of years have been exposed very rapidly at Nanga Parbat, for example granite plutons emplaced as recently as 1 Ma. My thesis investigates the link between geologically recent melting, metamorphism and exhumation at Nanga Parbat, and synthesises data from all three strands into a thermo-tectonic model.

Previous workers have placed time constraints on growth of metamorphic accessory minerals, pluton emplacement, and regional cooling, and this thesis concentrates on processes, utilising previously published geochronological data where appropriate. The project consists of two approaches, forward and inverse modelling. Forward modelling was conducted prior to field work, and involved one-dimensional thermal modelling of collision and rapid exhumation, with the aim of investigating the evolution of thermal structure during these processes. In particular, predictions were made about the pattern of cooling ages to be expected from different systems in such a terrain, and the P-T-t paths of rocks currently exposed, rocks already eroded, and rocks remaining at depth. The preferred model from a range of scenarios was constrained by a small geochronological dataset, but did not rely on P-T information from metamorphic or igneous rocks.

The inverse approach consisted of field mapping and sample collecting, conducted in the early summers of 1994 and 1995, followed by geochemical analysis. Interpretation of igneous and metamorphic rocks has placed pressure-temperature (P-T) and time (t) constraints on the paths followed by Nanga Parbat crust, using similar techniques to those applied in previous studies of orogenic belts. The combination of forward modelling (prediction) and inverse modelling (deduction), which happily led to similar conclusions, enables some confidence to be placed in the findings of this thesis.

1.2 Thesis structure

During the course of this project, several pieces of work have been accepted for publication. These manuscripts are included in their entirety in this thesis, since each is a self-contained piece of work which would not benefit from re-organisation. Each chapter deals with a different piece of the P-T-t puzzle, starting with regional and local geology, then focussing on metamorphic rocks, igneous rocks, cooling history, and thermal modelling. Previous work on each of these subjects is discussed at the start of each chapter.

Section 1.3 describes the broad tectonic framework of the Himalaya, since many of the anomalous features described from Nanga Parbat are contrasted with "typical" Himalayan features in this thesis. The unusual geotectonic setting and neotectonic activity of the Nanga Parbat-Haramosh Massif are described in Section 1.4.

Chapter 2 describes the field relations and petrography of lithologies studied in the field area, and combines these observations with previous structural and geochronological work to produce a basement stratigraphy for the NPHM. This will serve as a reference point in later chapters, and the importance of distinguishing Himalayan and pre-Himalayan features in this polymetamorphic terrain is emphasised.

Chapter 3 investigates metamorphic lithologies at Nanga Parbat, and uses thermobarometric techniques to attempt to constrain the high-grade part of the P-T-t path. Patterns of garnet zoning are described and interpreted to constrain the T-t history of metamorphic events. Section 3.4 investigates the petrogenesis of spinel-bearing lithologies from the interior of the NPHM, and combines thermobarometry and petrogenetic grid calculations.

Chapter 4 is concerned with recent igneous events at Nanga Parbat, and includes geochemical description and petrogenetic interpretation of major, trace and isotopic geochemical analysis from leucogranites and cordierite-bearing leucosomes. The results yield information on both fluid activity and P-T conditions of melting.

Chapter 5 describes the geochemistry of amphibolite dykes found within the massif, and compares them with similar sheets from nearby parts of the Himalayan orogen. The timing of early basement isotopic homogenisation is discussed.

Chapter 6 contains ^{40}Ar-^{39}Ar data and the interpretation of these data in terms of cooling ages, igneous or metamorphic crystallisation ages, and the effects of excess argon. The use of argon as a tracer to constrain fluid evolution within the NPHM is discussed.

Chapter 7 is concerned with thermal modelling of the Nanga Parbat Massif. After an introduction to thermal modelling and some of the problems associated with such modelling in a region of extreme topography and cooling rates, a one-dimensional model of the evolution of the massif core is constructed and then tested.

Chapter 8 summarises the findings of the preceding chapters into a synthesis of current knowledge of the tectonothermal evolution of the NPHM, and the broader implications of the findings of this thesis for other orogenic belts.

1.3 Geology of the Himalaya

1.3.1 Introduction

The large-scale tectonic features of Central Asia are dominated by the Himalayan mountains and the Tibetan plateau (Figure 1.1). The Asian Plate is comprised of a series of blocks which gradually accreted from the south during the Mesozoic (Allègre et al., 1984), until the closure of Tethys and collision of India in the Tertiary. At the southern margin of the Asian Plate, the Indus-Tsangpo suture zone (ITSZ) marks the boundary with the Indian Plate. This zone is comprised of ophiolites, flysch and mélange, the remnants of the Tethyan Ocean which separated the two continents prior to collision (Gansser, 1964, 1980; Dewey et al., 1988). The suture zone is further complicated in the west where the Kohistan-Ladakh island arc terrain was sutured to Asia in the Cretaceous (Treloar et al., 1989a), prior to Indian collision. The suture between Kohistan-Ladakh and Asia is termed the Shyok Suture (SS); previous names such as the Northern Suture (Coward et al., 1986) are misleading because there are older suture zones further north. The boundary between the Indian Plate and Kohistan-Ladakh is locally termed the Main Mantle Thrust (MMT). This suture zone is a 150m to 4 km wide belt containing a mélange of volcanic, sedimentary and serpentinite blocks, with no blueschist facies assemblages (Coward et al., 1982; Pudsey, 1986).

The subduction of Tethys resulted in the formation of the Transhimalayan Batholith, also called the Gangdese belt, an Andean-type batholith intruded between 110 and 40 Ma (Maluski et al., 1982; Schärer et al., 1984a). This belt consists of sub-alkaline to calc-alkaline intrusive and volcanic rocks, with Sm-Nd and U-Pb systematics indicative of crustal contamination of original mantle melts during intrusion into a continental margin (Allegre et al., 1984; Schärer et al., 1984b; Xu et al., 1985; Harris et al., 1988). The close proximity between the ITSZ

and the Trans-Himalayan batholith led Molnar and Taponnier (1975) to infer that subduction occurred at a relatively steep angle, but it is more likely that most of the forearc was underthrust beneath the southern margin of the Lhasa Block following collision (Harrison et al., 1992). The youngest subduction-related granodiorite ages of about 41 Ma (Schärer et al., 1984a) have been cited as evidence for collision at or shortly before this time, but a large body of evidence now suggests collision occurred much earlier, at between 50 and 65 Ma. This important topic is the subject of the next section.

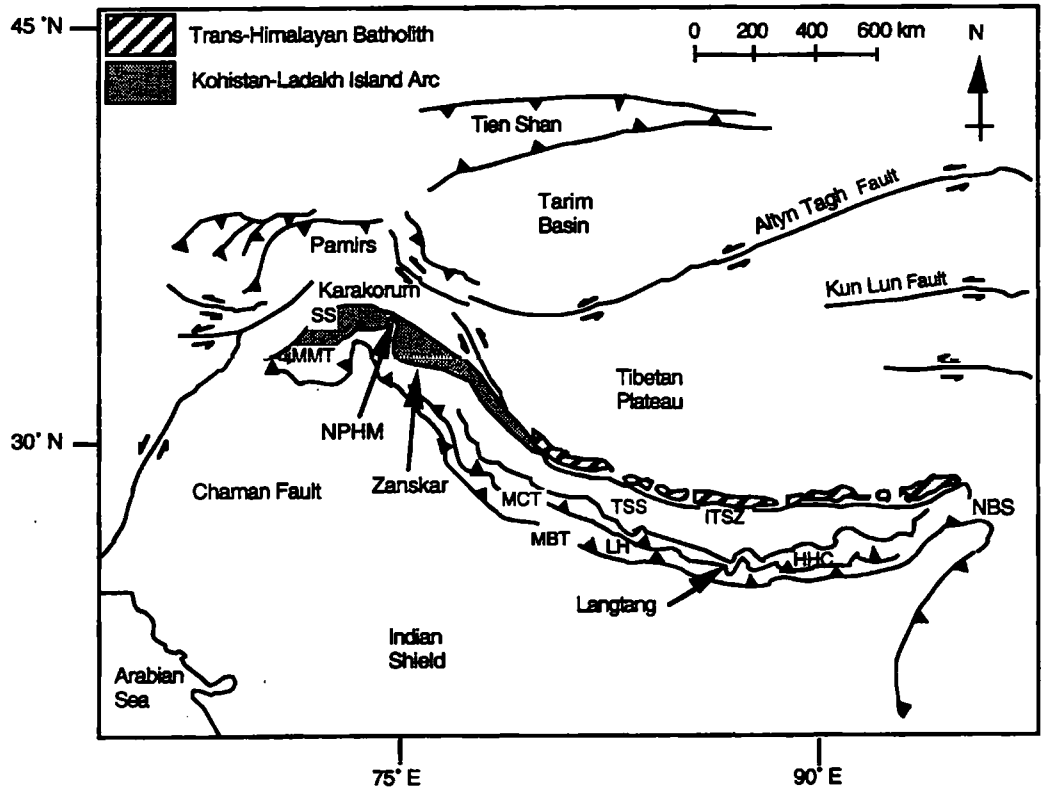

Fig. 1.1. Simplified tectonic map of southern Asia and the Himalayan orogen, after Massey (1994). MMT = Main Mantle Thrust, SS = Shyok Suture, ITSZ = Indus-Tsangpo Suture Zone, TSS = Tethyan Sedimentary Series, HHC - High Himalayan Crystallines, MCT = Main Central Thrust, LH = Lesser Himalayas, MBT = Main Boundary Thrust, NP = Nanga Parbat, NBS = Namche Barwa Syntaxis.

1.3.2 Timing and nature of collision

The timing of collision between the Indian and Asian plates has been a matter of considerable research and debate over the past two decades and more. Different researchers employing different methods in different field areas frequently suggest different times (Butler, 1995). Collision occurred somewhere between 65 Ma (Beck et al., 1995) and 40 Ma (Patriat and Achache, 1984), but this general statement deserves further discussion, because the timing of this major tectonic event has far-reaching consequences not only for the evolution of the Himalaya, but also for the different geological techniques which have been used to constrain the timing of collision.

The terms "collision" and "suturing" are often used interchangeably, but in the author's opinion the two imply different stages of the same process. For the main Himalayan chain, "collision" may used to describe the change between normal northward subduction of the Tethys ocean beneath the southern margin of Asia, to the more unusual subduction of continental crust. "Suturing" may be considered complete when large scale movement has ceased across the suture zone itself, and deformation is transferred to nappe emplacement in the external zones. The northern margin of India was a passive margin, so that a transitional period would be expected between Andean-style subduction and intracontinental thrusting, and care must be taken when interpreting which part of the collision process will be recorded.

Early estimates of the timing of collision relied on ocean floor magnetic "stripes" which are used to calculate spreading rates and plate motions. Molnar and Taponnier (1975) suggested that a slowing in the northward motion of India occurred at anomaly 22 (about 50 Ma), dating collision with Asia (Fig. 1.2). Johnson et al. (1976) correlated collision with a decrease in the spreading rate of the East India Ridge at about 50 Ma. Patriat and Achache (1984) estimated the

total shortening since collision to be 2600 ± 900 km, and interpreted the irregularity in India's motion between anomalies 22 and 21 (about 50 and 48 Ma) as representing the timing of collision (Fig. 1.2). Both Dewey et al. (1989) and Le Pichon et al. (1992) suggested that initial collision was as late as 45 Ma, on the grounds of pre-collisional plate shapes and rates of plate movement.

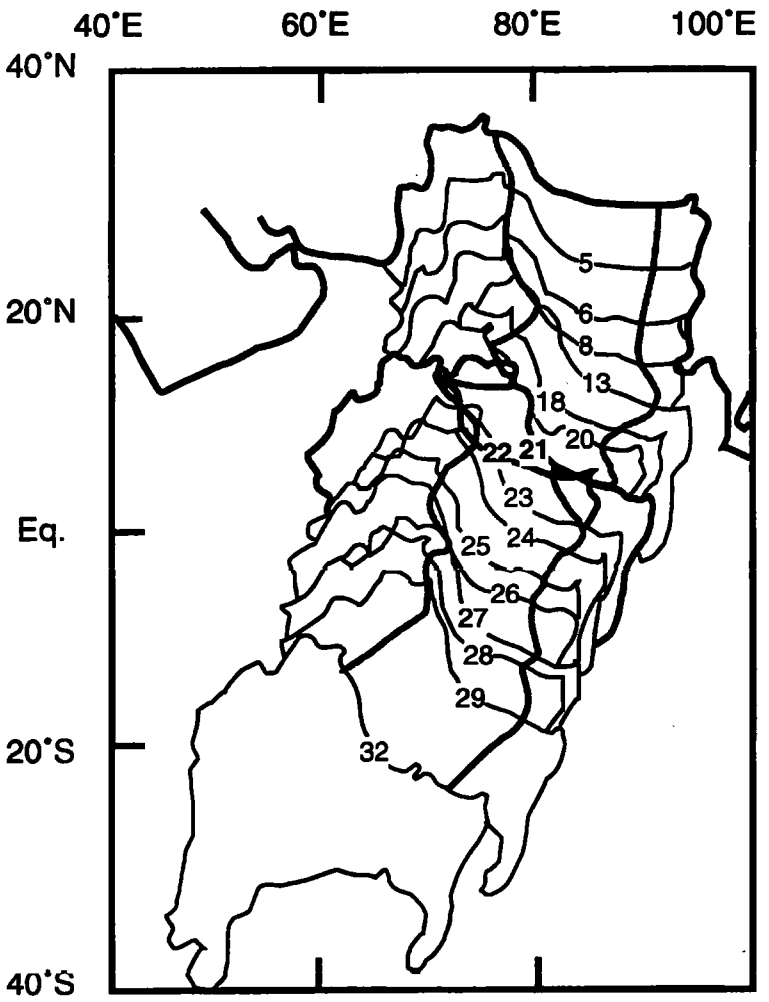

Anomaly number	Age (Ma)
5	10
6	21
8	29
13	36
18	42
20	44
21	48
22	50
23	52
24	53
25	55
26	57
27	59
28	61
29	62
32	70

Fig. 1.2. Relative Cenozoic northward drift of India relative to Eurasia, arbitrarily fixed in its present position, from Patriat and Achache (1984). Note the distinct wobble between anomalies 22 and 21 (50 and 48 Ma).

The different estimates of collision timing from this one method demonstrate the problems of using an indirect approach. India's relative direction and rate of motion may not have been affected by initial contact, and may have changed significantly only upon more complete suturing. Hence these estimates are minimum ages for the timing of initial collision, but may date the initiation of significant continental deformation.

Another method is to extrapolate apparent polar wander paths (APWPs) from palaeomagnetic measurements, which can give both absolute movements and relative movements between different locations. Klootwijk et al. (1984) suggested that collision could have occurred as early as 60 Ma, at equatorial to low northern latitudes (0° to 10°N). Klootwijk (1984) found two groups of magnetic overprints in Himalayan rocks, between 50 and 60 Ma in the internal zones both north and south of the ITSZ, and between 20 and 40 Ma in the external thrust zones. These were interpreted to reflect a late phase of relaxation following early Tertiary collision, followed by relaxation following intracontinental deformation.

Klootwijk et al. (1985) considered the tectonic implications of the palaeomagnetic dataset, and suggested that collision was diachronous along the Himalayan chain, initiating in the north-west during the Palaeocene and concluding at the eastern end of the orogen in the Early Eocene. Klootwijk et al. (1985) proposed a two-stage model for the collision, with shortening of about 2000 km until the early Miocene resulting in south-eastwards extrusion of Indochina along the Red River Fault (Taponnier et al., 1982), followed by anticlockwise rotational underthrusting of Greater India along the MCT throughout the Neogene, accompanied by oroclinal bending of the Himalayan Arc from the Pliocene onwards.

Klootwijk et al. (1992) presented palaeomagnetic data from ODP Leg 121, again supporting initial contact prior to the K/T boundary. Patzelt et al. (1996) applied palaeomagnetic techniques to Cretaceous-Tertiary sediments from southern Tibet,

and by comparison with palaeolatitudes for the Lhasa Block calculated that initial contact was established by 65-60 Ma, with suturing completed by 55-50 Ma. Additional evidence for a K/T boundary age of collision includes plate re-organisation within the western Indian Ocean at about 65 Ma (Courtillot et al., 1986), zircon fission track ages from northern Pakistan of 68 to 55 Ma (Zeitler, 1985), and regional hiatuses in the sedimentary record in both Zanskar (Gaetani and Garzanti, 1991) and the Himalayan foothills of northern Pakistan (Yeats and Hussain, 1987) at about this time. One major consequence of such an early collision would be that about 4000 km of continental shortening must have occurred following collision, compared with previous estimates of 2500 km, which assumed a collision age of about 50 Ma.

A third method of dating collision relies on biostratigraphy, either dating sediments unconformably overlying the suture zone, or investigating faunal exchange between India and Asia. Jaeger et al. (1989) proposed an early date of collision based on intercalated sediments within the Deccan Traps. Palaeontological evidence placed the sediments in chron 29R, and the Eurasian character of K/T boundary terrestrial faunas in India suggests that collision occurred prior to this time. Ar-Ar ages for the Deccan Traps suggest eruption over a short interval at 65.7 ± 2.0 Ma which led Jaeger et al. (1989) to speculate on a causal link between collision and flood basalt extrusion.

Beck et al. (1995) presented biostratigraphic evidence from Waziristan in north-west Pakistan, which showed that accretionary-prism and trench strata were first thrust onto the north-west Indian passive margin after 66 Ma but before 55.5 Ma. Both the suture zone and the Indian craton were overlapped by Lower Eocene strata, indicating that suturing was complete by 49 Ma. In a review of available stratigraphic data, Rowley (1996) suggests that the collision constrained by the work of Beck et al. (1995) may be between the northern margin of India and a microplate, rather than with the Transhimalayan margin of Asia. Treloar and Izatt

(1993) noted the complicated nature of collision at the western margin of the Indian Plate, where collision with the Kabul block of eastern Afghanistan may only have occurred in the Pliocene. Based on stratigraphic data from the main Himalayan range, and the emplacement of Ladakh and the Spontang ophiolite onto the northern Himalayan margin at about 51 Ma (Gaetani and Garzanti, 1991; Garzanti et al., 1987), Rowley suggests collision in Zanskar occurred at about 52 Ma, whereas further east collision occurred later.

In summary, a range of methods have led to a range in estimates for the age of collision, although many of these methods constrain only the time of significant reduction in plate motion, or the oldest preserved post-collisional sediments. Collision was diachronous along the Himalaya, with first contact in the west between 65 and 50 Ma, although final suturing may have occurred later. Subsequent anticlockwise (widdershins) rotation of India and oroclinal bending has led to the large scale morphology observed today, and indirectly to the evolution of the syntaxial regions of the western Himalaya (section 1.4).

1.3.3 Post-collisional evolution of the Himalaya

Subsequent to collision, palaeomagnetic data indicate that continental India has moved northwards relative to Asia by about 1800 km in the west and 2700 km in the east (Dewey et al., 1988, 1989), although these estimates are affected by the assumed timing of collision, discussed above. The mode of accommodation of this shortening has been the subject of much discussion, with three main mechanisms.

Underthrusting of Indian continental crust beneath Eurasia has been suggested as a mechanism for the rise of the Tibetan plateau (Powell and Conaghan, 1973; Klootwijk et al., 1985; Powell, 1986), although since then it has been shown that the rise of Tibet was a more recent occurrence, possibly caused by delamination of the

underlying mantle lithosphere (England and Houseman, 1988). Large scale strike-slip faults have accommodated at least some northward motion of India subsequent to collision, resulting in the eastward lateral extrusion of Indochina along the Red River Fault (Taponnier et al., 1982, 1986; Peltzer and Taponnier, 1988), and strike-slip faulting in Tibet (Molnar and Taponnier, 1975; Taponnier and Molnar, 1976; Taponnier et al., 1982).

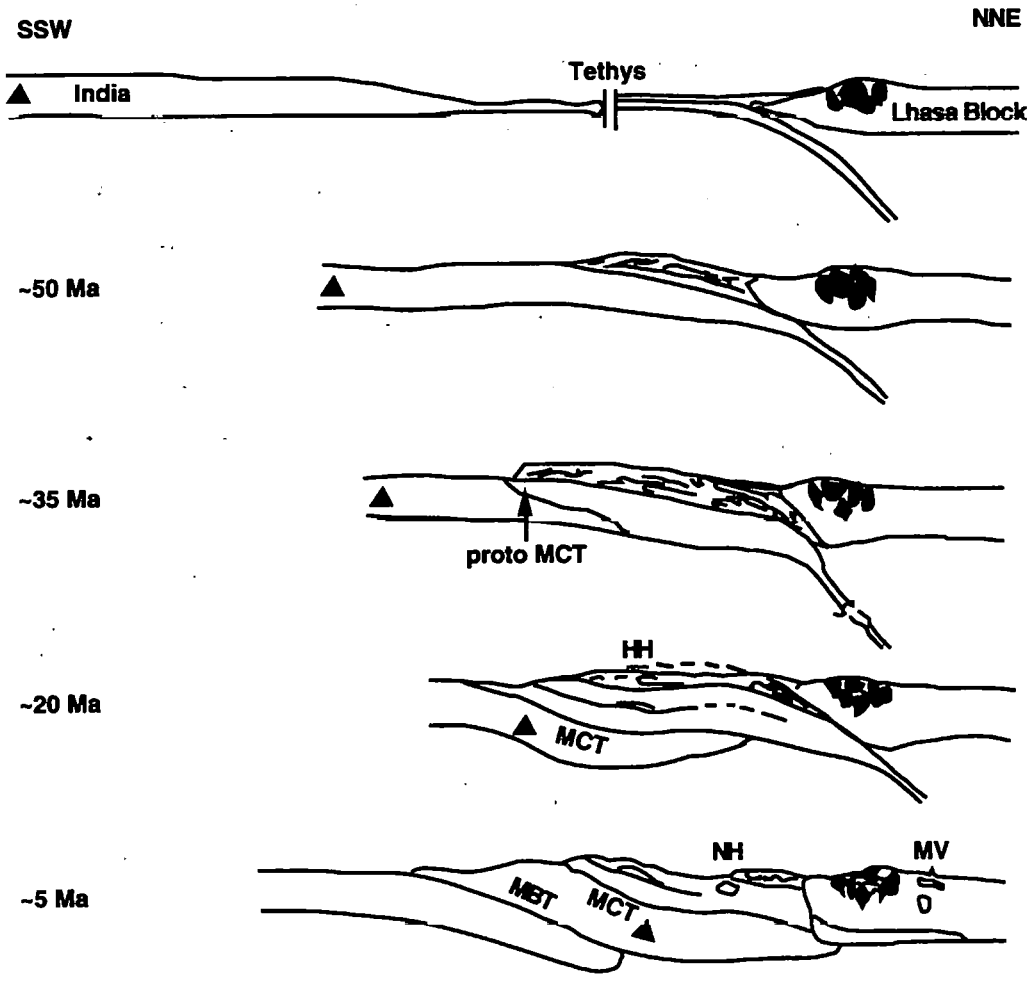

Fig. 1.3. Schematic evolution of the Himalaya from the Mesozoic to the Recent, from Le Fort (1988). HH = High Himalayan leucogranites, NH = North Himalayan leucogranites, MV = Maqiang volcanics of Tibet (Neogene), other abbreviations as for Fig. 1.1.

Within the Indian Plate, many south-verging thrust faults have also accommodated shortening (Fig. 1.3). Coward and Butler (1985) used palinspastic reconstruction to calculate about 450 km of shortening, while Besse et al. (1984) used palaeomagnetic data to estimate 400 ± 400 km of shortening by intracontinental thrusting within the Indian plate, and 550 ± 650 km convergence across the suture zone. Patzelt et al. (1996) have calculated 1500 km of shortening between the Tethyan Himalaya (at ~89°E and ~28°N) and the Indian Shield, based on palaeomagnetic data.

Thrusting within the Indian Plate has progressed southwards over time, beginning at the ITSZ in the late Eocene-Oligocene, moving to the Main Central Thrust (MCT) 150 km south of the ITSZ in the early Miocene (Le Fort, 1975; Maluski and Matte, 1984). Movement occurred on the Main Boundary Thrust (MBT) from the Pliocene to Recent, with additional thrusts developing further south in the late Pliocene-Pleistocene (Le Fort, 1989; Ni and Rawazangi, 1984).

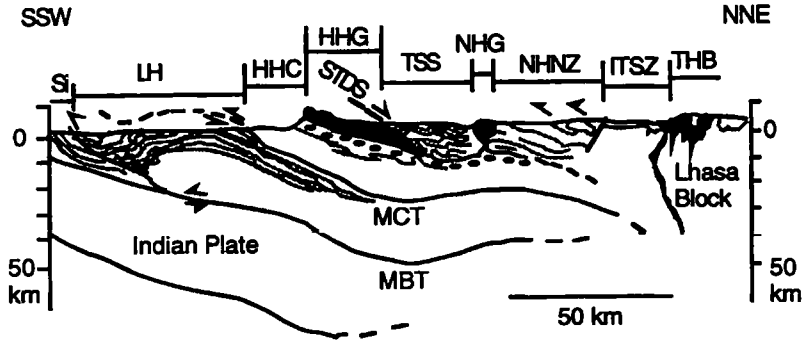

Fig. 1.4. Generalised cross-section of a typical Himalayan transect, from Le Fort et al. (1987). THB = Transhimalayan Batholith, NHNZ = north Himalayan Nappe Zone, NHG = North Himalayan Granites, HHG = High Himalayan Granites, Si = Siwaliks, STDS = South Tibetan Detachment System, other abbreviations as for Fig. 1.1.

Along the central part of its 2500 km length, the main features of the Himalayan orogen are fairly constant, and can be described in a single generalised traverse across strike (Fig. 1.4). Simultaneous with reverse movement on the MCT in the early Miocene, the extensional South Tibetan Detachment System (STDS) carried the Tethyan Sedimentary Series (TSS) at least 35 km northwards (Burg et al., 1984; Herren, 1987; Burchfiel et al., 1992), leading to rapid decompression of the underlying High Himalayan Crystalline series (HHC). The High Himalayan Leucogranites (HHL) were generated coevally with both movement on both faults, and emplaced between 24 and 18 Ma (Schärer et al., 1984a, 1986; Copeland et al., 1988; Harrison et al., 1995; Noble and Searle, 1995). These granites form a discontinuous chain of sheet-like intrusions and dykes which are now exposed on either side of the STDS.

Early models for generation of the HHL invoked a combination of devolatilisation of the Midlands Formations (Lesser Himalaya) below the MCT, and shear heating on the MCT, leading to anatexis of the migmatitic HHC (Le Fort, 1975, 1981, 1986). This elegant solution has had to be revised somewhat since subsequent studies have shown that the isotopic signature of the HHL rules out the exposed migmatitic zone of the HHC as a source (Harris et al., 1993), and that trace element modelling rules out vapour-saturated conditions during melting (Harris and Inger, 1992; Harris et al., 1993, 1995). Recent studies have also suggested that sillimanite-grade metamorphism within the HHC predates movement on the MCT (Brouand et al., 1990; Inger and Harris, 1993; Massey, 1994).

Other models to explain melting in the hangingwall of the MCT, while the subduction of Indian crust refrigerates the system, have suggested different heat sources, including rapid denudation coupled with accretion of high heat-producing crust (Royden, 1993), mantle delamination (Bird, 1978), and very high frictional stresses (≥100 MPa) leading to significant shear heating (Molnar and England, 1990).

Accessory phase modelling of the HHL have suggested melting temperatures of about 680 to 710 °C (Montel, 1993), above the vapour-present solidus. Suitable melt-producing reactions at these temperatures involve dehydration melting of micas, and have positive slopes in P-T space, so that a combination of heating and/or decompression will cross the solidus. Fluid-absent dehydration melting, also called "decompression melting", has been suggested as a mechanism for leucogranite generation both in the western Himalaya (Zeitler and Chamberlain, 1991) and in the central Himalayan orogen (Harris et al., 1993). The tectonic removal of the TSS provides the explanation for rapid decompression, although the involvement of the MCT in melt production remains a topic of considerable interest and debate .

The North Himalayan Granites (NHG) run parallel to, and 100 km north of, the HHL (Le Fort, 1988). The NHG belt is comprised of several elliptical shaped plutons which intrude into the TSS, and differ from the HHL in their diapiric emplacement style, younger ages (17-9 Ma), and higher melting temperatures up to 760 °C (Schärer et al., 1986; Montel, 1993; Debon et al., 1986). Generation of the NHG has also been linked with movement on the MCT (Harrison et al., 1997).

Following a change in location of thrusting from the MCT to the MBT, Cenozoic to Quaternary molasse deposits have been thrust over each other in the foreland, so that deposition is followed by uplift and erosion, and re-sedimentation in a new locality further south (Johnson et al., 1982). In addition, the molasse sediments preserve the climatic and denudation histories of their sources, as shown by ^{40}Ar-^{39}Ar and $\partial^{13}C$ isotopic studies of the Siwaliks (Harrison et al., 1993). The most recent thrust system to emerge is the Main Boundary Thrust, carrying the Salt Ranges in its hangingwall, recognised only in Pakistan (Fig. 1.6). The progressive southerly change of thrust movement has not been uniform, since it has been shown that while the MBT was active at 4-5 Ma, the MCT was partially reactivated, although with little displacement (Copeland et al., 1991; Macfarlane,

1993). Field observations and numerical modelling suggest that the order of succession of thrusts within the sub-Himalaya depends on a number of parameters, including the geometry of the wedge, erosion and sedimentation (Chalaron and Mugnier, 1993; Chalaron et al., 1995).

The most exciting recent developments in the Himalayan orogen have occurred at the eastern and western extremities, the Namche Barwa and Nanga Parbat syntaxes respectively (Fig. 1.1). The Namche Barwa syntaxis is a deeply eroded crustal antiform, and exposes Indian Plate rocks in the core which are structurally overlain by plutonic rocks of the Transhimalaya (Burg et al., 1997). Migmatitic orthogneisses show cauliflower structures indicating a subhorizontal orientation during anatexis, but have since been tilted to a steep attitude, probably coeval with syntaxial development. U-Pb and Th-Pb ages of xenotime and thorite range between 2.9 and 3.9 Ma, with zircon and apatite fission track ages of 2.6 and 1.,1 Ma respectively indicating very rapid cooling and exhumation over the last 4 Ma (Burg et al., 1997). Young post-deformation granites have not been observed at Namche Barwa, although these are widespread at Nanga Parbat. The next section introduces the western Himalaya, and the Nanga Parbat syntaxis.

1.4 The western Himalaya

The western end of the Himalaya terminates at the NPHM, also called the Nanga Parbat syntaxis. There are three tectonic plates of relevance to this study, the Indian Plate, the Kohistan-Ladakh island arc, and the Asian Plate (Fig. 1.5). The southern margin of the Asian Plate is itself an amalgam of terranes and microplates which sutured together prior to 100 Ma, these earlier suture zones

being identified from field studies in Afghanistan, the western Pamirs and western Tibet (Taponnier et al., 1981).

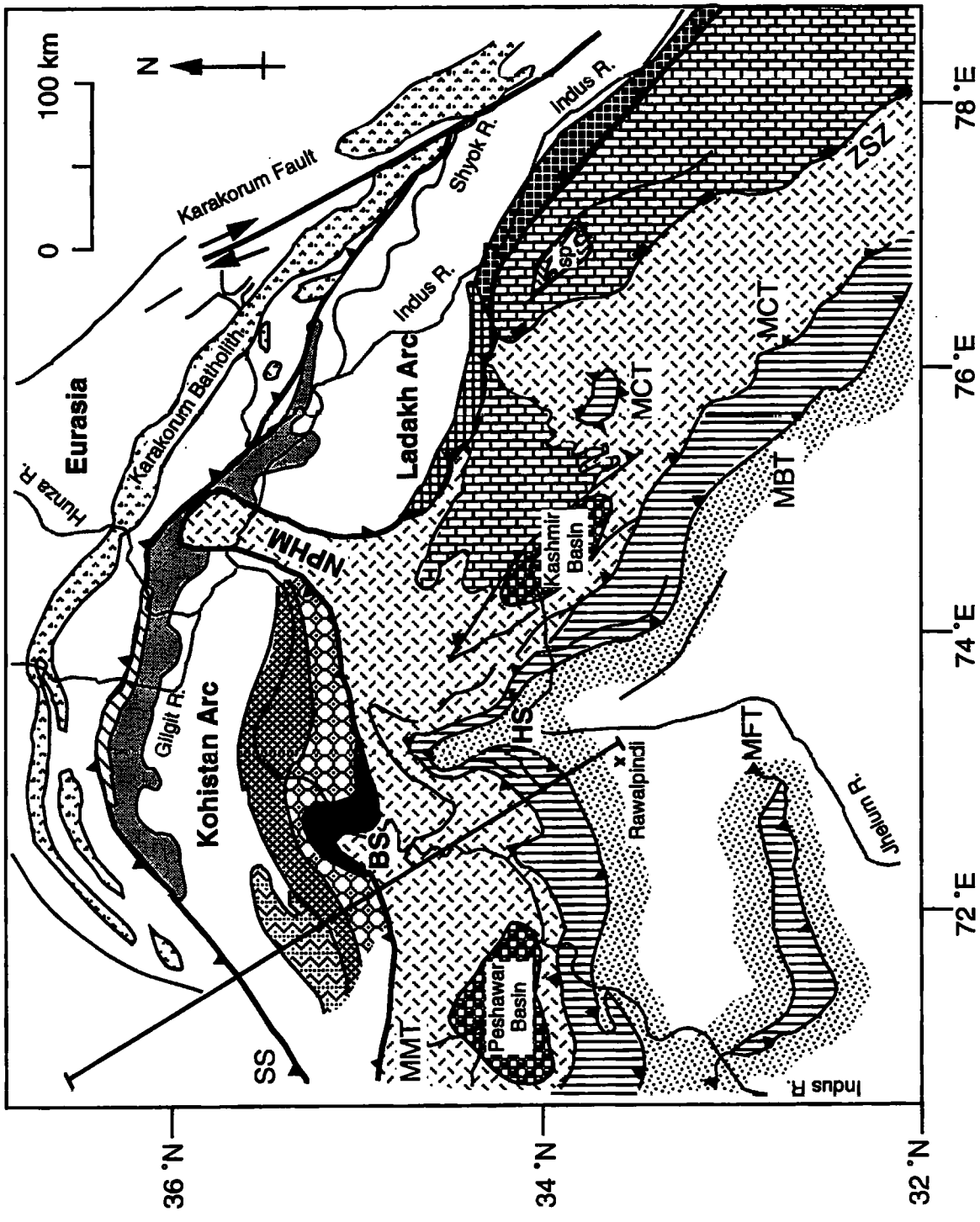

Fig. 1.5. Geological map of the western Himalaya and Karakorum , after Coward et al. (1986) and Searle et al. (1989), showing the line of section for Fig. 1.6. HS = Hazara syntaxis, BS = Besham (proto)syntaxis, MFT = Main Frontal Thrust, sp = Spontang ophiolite, other abbreviations as for Fig. 1.1.

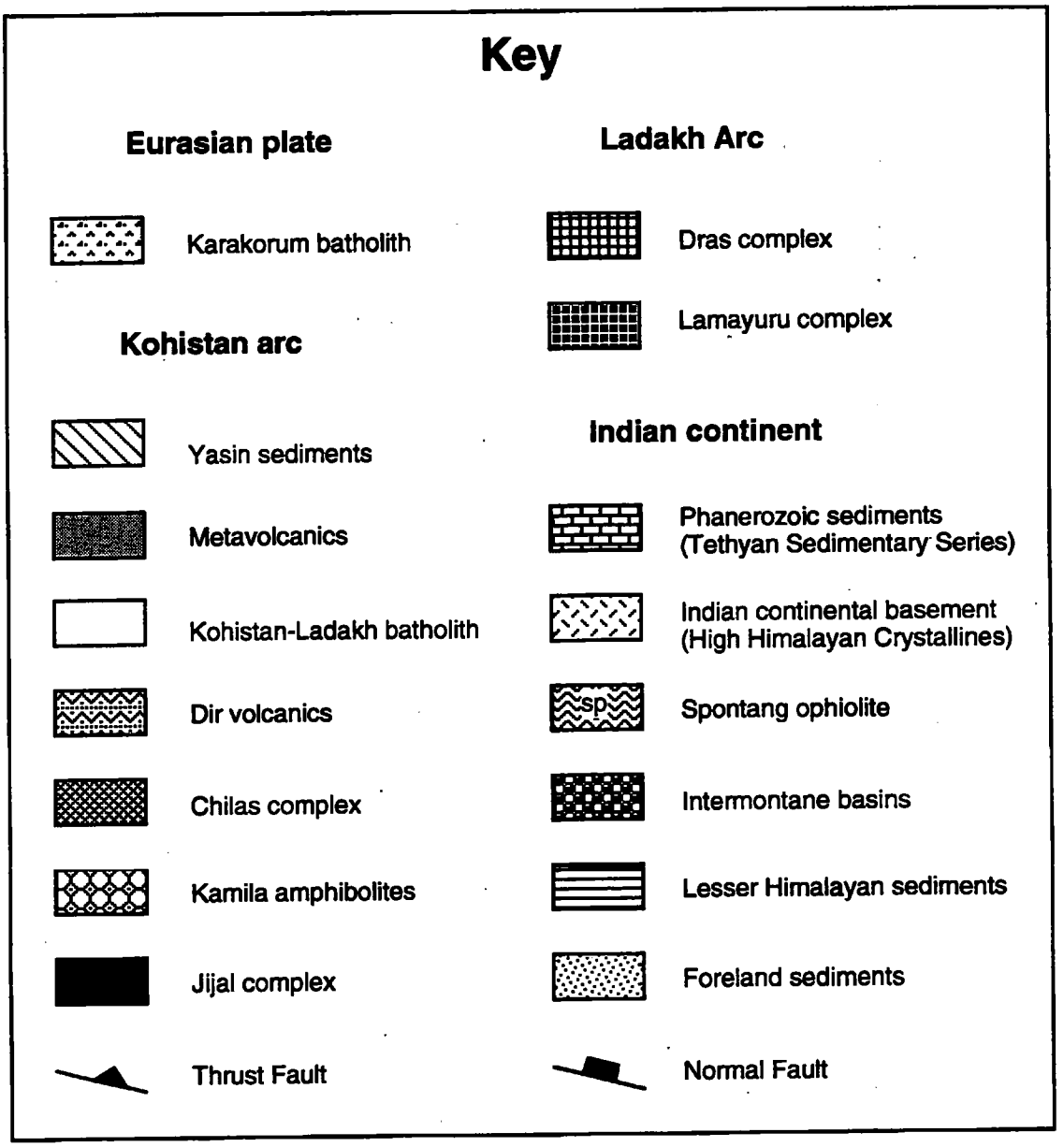

1.4.1 Kohistan

The southern branch of the ITSZ is called the Main Mantle Thrust in northern Pakistan, where it separates basement rocks of the Indian Plate from the Kohistan island arc terrain, because ultramafic rocks and high pressure granulites occur

sporadically in the hanging wall (Tahirkheli et al., 1979). In the Indus valley, the MMT is a 10-15 km wide north-dipping shear zone, but further west in the Swat valley, it is amore complex zone containing blueschists and melange (Shams, 1972; Coward et al., 1982; Kazmi et al., 1984). In the Hazara area, the MMT has had a protracted deformation history, indicated by rapid changes in the ductility and temperature of deformation fabrics across the shear zone, and the truncation of young SSE-directed shears in the footwall by MMT fabrics (Lawrence and Ghauri, 1983; Treloar et al., 1989c). The youngest movements on the MMT accommodated top-to-the-north extension during the Miocene (Vince and Treloar, 1996), coeval with extension within the main Himalayan orogen on the STDS (Burg et al., 1984; Burchfiel and Royden, 1985; Hodges et al., 1992).

The arc developed above a north-dipping subduction zone (Tahirkheli et al., 1977, 1979; Bard et al., 1980; Coward et al., 1982), and was accreted to the Asian Plate along the Shyok suture between 75 and 102 Ma (Petterson and Windley, 1985; Treloar et al., 1989a). The arc underwent metamorphism from greenschist to granulite facies, the grade possibly controlled by magmatic heat sources (Bard, 1983). Continued subduction led to closure of the back-arc basin and generated an Andean-type margin which led to formation of the Kohistan-Ladakh batholith at about 95 Ma (Petterson and Windley, 1985). Subduction halted with collision with India, and a Barrovian metamorphic overprint was associated with obduction onto the northern margin of India (Bard, 1983), although post-collisional plutonism continued to 40 Ma (Petterson and Windley, 1985) and late granite sheets with little crustal involvement were emplaced until 26 Ma (George et al., 1993).

The Kohistan arc has been subdivided into seven different lithological units, which show increasing metamorphic grade and reveal deeper parts of the arc in the south (Tahirkheli et al., 1979; Bard, 1980). Although previously interpreted to be a complete vertical section (Bard, 1983), more recent studies have suggested that the present structure has been extensively modified both by deformation

associated with obduction, and later imbrication associated with post-metamorphic crustal stacking (e.g. Coward et al., 1987, 1988).

Starting in the south of Kohistan, the Jijal complex consists of high pressure garnet granulites, intruded in the south by a slab of ultramafics (Jan and Howie, 1981). The garnet granulites are meta-igneous in origin, followed an anticlockwise P-T path reaching maximum pressures of about 17 kbar at 950 °C (Yamamoto, 1993), and record an Sm-Nd age of 91 ± 6.3 Ma (Yamamoto and Nakamura, 1996). Coward et al. (1982) obtained an Sm-Nd age for granulite facies metamorphism of 104 Ma, and these ages may reflect either crustal thickening by magmatic underplating during arc growth, or tectonic thickening during collision between Kohistan and Asia (Yamamoto, 1993). The ultramafics were metamorphosed at temperatures of 800 to 850 °C, and pressures of 8 to 12 kbar (Jan and Howie, 1981). These pressures of metamorphism indicate that the arc had thickened to at least 35 km prior to the Indian collision.

The Kamila amphibolite belt is separated from the Jijal complex by a shear zone (Coward et al., 1982), and incorporates a range of highly deformed amphibolites, clinopyroxenites, anorthosites, and tonalites. Rare garnet granulites within the Kamila belt record metamorphic conditions of 600 to 720 °C at 6 to 8 kbar (Yamamoto, 1993). The Kamila belt was initially interpreted to be relict oceanic crust (Tahirkheli, 1979a, b; Bard et al., 1980), but has since been variably interpreted as a deformed sequence of arc volcanics, possibly equivalent to the Dras volcanics of Ladakh (Coward et al., 1986), or the retrograde equivalent of the granulites of the Chilas complex (Treloar et al., 1990). The southern part of the Kamila amphibolites is a high strain zone (Kamila shear zone), which may be a relict suture associated with southward thrusting of the Kohistan arc over a forearc region (Coward et al., 1987; Treloar et al., 1990).

To the north of the Kamila amphibolite complex is the Chilas complex, a large basic-ultrabasic intrusive body comprised of layered norites and pyroxene gabbros, interpreted to result from intra-arc rifting (Khan et al., 1993). The Chilas complex underwent granulite facies metamorphism during the early Cretaceous, shortly after its emplacement (Jan and Howie, 1980; Bard, 1983). Subsequent retrogression to amphibolite facies has been dated at about 80 Ma (Treloar et al., 1989a).

Both the Chilas complex and Kamila amphibolites are cut by numerous shear zones showing both thrust and normal fault geometry. Some of these shears are cross-cut by pegmatites emplaced at about 80 Ma, and may reflect thickening and collapse during and after collision along the Shyok suture. Other shears deform these pegmatites, and may relate to the later uplift history of the arc (Coward et al., 1987).

The Dir volcanics are exposed in western Kohistan, and consist of calc-alkaline volcanics, including andesites, rhyolites, agglomerates and ignimbrite tuffs, interbedded with sediments containing lower Eocene marine microfossils (Bard et al., 1980). A basaltic andesite has yielded a ^{40}Ar-^{39}Ar age of 55 ± 2 Ma (Sullivan et al., 1993). These volcanics unconformably overlie some plutons of the batholith.

The Kohistan-Ladakh batholith intrudes the northern part of the arc, and was emplaced into the arc sequence both prior and subsequent to suturing of the arc with Asia (Petterson and Windley, 1985). Early magmatism is characterised by deformed gabbro, diorite and tonalite plutons, metamorphosed at greenschist to lower amphibolite facies, and dated at 110 to 90 Ma (Petterson, 1984; Petterson and Windley, 1991). Younger post-kinematic plutons were intruded between 85 and 30 Ma, and range from gabbros to leucogranites, becoming predominantly less basic over time. Bard (1983) suggested that these magmas were derived by crustal anatexis associated with intracontinental thrusting, but geochemical studies have

shown that they were generated at a more Andean-type margin, although there is no involvement of mature continental crust (Petterson and Windley, 1985; Debon et al., 1987).

Northern Kohistan is comprised largely of low-grade metavolcanics with volcaniclastics and metasediments (Chalt volcanics of Coward et al., 1982 and Petterson and Windley, 1985, 1991). Tahirkheli (1979b) correlated this group with similar volcanics exposed in the Shigar valley of Baltistan (NW Ladakh), where they are interbedded with limestones containing Cretaceous fossils. The volcanics are high-Mg tholeiites and calc-alkaline andesites, thought to have been generated by melting of a depleted mantle source and a metasomatised mentle wedge respectively (Petterson and Windley, 1991). The Yasin group is a thin sequence of sediments containing Aptian and Albian fossils, probably deposited in a back-arc environment (Pudsey, 1986). It occurs sporadically along the Shyok suture zone in northern Kohistan, and has no equivalent in Ladakh.

Gravity modelling suggests a present thickness for the arc of between 7 and 9 km, with thicker sections occurring closer to the southern margin (Malinconico, 1986), although structural mapping suggests an original stratigraphic thickness of about 30 to 40 km (Bard et al., 1980). Coward et al. (1988) interpreted the structure of Kohistan to have been significantly modified after obduction onto the northern margin of India, with imbrication and deformation of the arc by Himalayan age thrusting (Fig. 1.6). The Nanga Parbat Massif may be visualised on this diagram as Indian Plate basement exhumed through the Kohistan arc by a combination of large scale folding and reverse faulting.

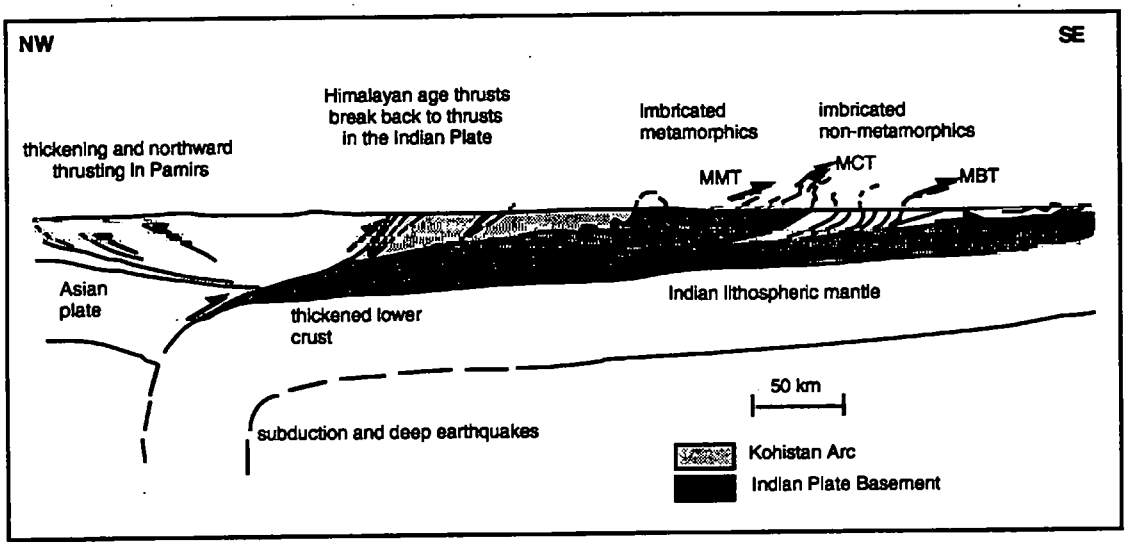

Fig. 1.6. Sketch cross-section through the western Himalaya, from the foreland basin to the Pamirs, from Coward et al. (1988).

East of the NPHM, the Ladakh terrain contains similar lithologies to Kohistan, and the two are now interpreted to have been contiguous prior to collision. The southern margin of the Ladakh arc is the ITSZ, a structurally complex melange zone containing blueschists, Mesozoic flysch, basaltic relicts of Jurassic-Cretaceous ocean floor and rare eclogites at Tso Morari (Frank et al., 1977; Honegger et al., 1982, 1985; Guillot et al., 1995). The present day tectonic contacts in this zone are predominantly north-directed backthrusts (Searle, 1986). Fossiliferous sediments are preserved in this suture zone, in contrast to the MMT further west. Alkaline volcanics, interpreted to be formed at a Triassic rifted continental margin, are associated with the flysch (Honegger et al., 1982). The Shyok suture at the northern margin of Ladakh consists of a steep belt of volcanics, melange and flysch containing Upper Cretaceous to Eocene fossils, cross-cutting amphibolite grade metamorphic isograds (Hanson, 1989). Thrust contacts often repeat the lithological sequence (Srimal, 1986).

The Dras volcanics of southern Ladakh are a belt of weakly metamorphosed deformed island arc tholeiites, bounded by tectonic contacts (Dietrich et al., 1983;

Searle, 1983). The volcanics occur as irregular flows, with occasional pillows and dykes, and contain imbricates of ophiolitic melange, intercalated radiolarian cherts and Upper Cretaceous orbitulina limestones, suggesting an Upper Jurassic-mid Cretaceous age (Honegger et al., 1982; Dietrich et al., 1983). The Dras volcanics are locally underlain by cumulate gabbros, norites and anorthosites, which have similar geochemical compositions to the volcanics and have been interpreted as relict magma chambers (Honegger et al., 1982; Dietrich et al., 1983), possibly comparable with the Chilas complex of Kohistan (Searle, 1983).

The Lamayuru Complex is exposed in the ITSZ in southern Ladakh. It is comprised of deep-water sedimentary rocks, remnants of the Mesozoic north-facing Triassic to Upper Cretaceous Indian passive margin, which experienced several extensional pulses over this time (Robertson and Degnan, 1993). The sedimentary succession consists of sandstones, shales, limestones and basic volcanic rocks, and is pervasively sheared, folded and bounded by thrusts.

Northern Ladakh is dominated by the eastern part of the Kohistan-Ladakh batholith, which here consists of a suite of calc-alkaline diorites, granodiorites and granites (Honegger et al., 1982). Some have experienced low grade metamorphism, while others are post-kinematic (Schärer et al., 1984a; Hanson, 1989). Locally, plutons intrude and thermally metamorphose parts of the Dras unit, whilst other plutons are transgressed by the Indus molasse which contains a non-marine fauna of Eocene-Miocene age (Shah et al., 1976). Clasts derived from these plutons are found within the Indus molasse, suggesting uplift and erosion of the batholith prior to the Eocene (Frank et al., 1977). Granitoids from the Ladakh batholith have yielded U-Pb zircon and Rb-Sr whole-rock ages in the range 60 to 100 Ma (Honegger et al., 1982; Schärer et al., 1984a), while mica cooling ages lie in the range 36-78 Ma (Desio et al., 1964; Saxene and Miller, 1972; Brookfield and Reynolds, 1981; Honegger et al., 1982).

In brief, the Kohistan-Ladakh island arc terrain was sutured to the southern margin of Asia prior to 80 Ma, and was obducted onto the northern margin of India at about 60 Ma. Higher metamorphic grades and deeper arc assemblages are found in the south of Kohistan, and the arc has been imbricated, uplifted and eroded with the underlying Indian Plate, so that its present thickness represents only a fraction of its original size.

1.4.2 The Karakorum Block

The Karakorum block lies to the north of the Kohistan-Ladakh island arc, extending northwards to the Pamirs and Kun Lun, westwards into theHindu Kush, and eastwards into western Tibet (the Lhasa block). Upper Palaeozoic sediments in the southern Karakorum contain Eurasian-type faunas, suggesting that the Karakorum was never a part of Gondwanaland, in contrast to the Lhasa Block (Pudsey et al., 1985).

The Karakorum block is divided into three zones, the Karakorum metamorphic complex, the Karakorum batholith, and the northern Karakorum zone, from south to north (Desio, 1979; Searle and Tirrul, 1991). The northern Karakorum zone consists of weakly metamorphosed Palaeozoic to Late Cretaceous platform sediments (Desio, 1979; Searle et al., 1986, 1989), which may be unmetamorphosed equivalents of the high-grade metamorphic complex to the south (Rex et al., 1988).

The Karakorum axial batholith occurs as a 600 km long, discontinuous belt of plutons, recording magmatism on the southern margin of Eurasia from the Jurassic through to the Miocene. Early subduction-related plutons are penetratively deformed, while younger undeformed bodies are related to crustal thickening (Reynolds et al., 1983; Debon et al., 1987; Searle et al., 1989, 1990; Crawford and Searle, 1992). These plutons are characterised by heterogeneous Sr

and Nd systematics (Le Fort et al., 1983; Debon et al., 1987; Crawford and Searle, 1992), and zircons show crustal inheritance, which led Crawford and Searle (1992) to suggest a petrogenesis involving crustal contamination of mantle-derived melts.

Scattered undeformed leucogranites, intruding the axial batholith and cross-cutting the metamorphic complex, have yielded U-Pb zircon and Rb-Sr whole-rock ages of 43 to 14 Ma (Debon et al., 1987; Searle and Tirrul, 1991). The Baltoro Plutonic Unit (BPU) forms a massive plutonic unit within the Karakorum batholith, composed of comagmatic monzogranites and leucogranites. U-Pb ages in the range 21 to 25 Ma have been obtained from zircons from the BPU (Parrish and Tirrul, 1989; Schärer et al., 1990). Initial strontium isotopic ratios in the range 0.7070 to 0.7183, $\varepsilon_{Nd}(T)$ in the range -6.6 to -11.0, trace element abundances and inherited components in zircons all suggest a crustal source for the BPU (Rex et al., 1988; Schärer et al., 1990, Searle et al., 1989, 1992a). Searle et al. (1992a) suggested that the source may have been immature metapelites present in the thickened Karakorum crust, and melting may have been induced by fluids or material derived from a dehydrating mantle wedge being displaced downwards by crustal thickening. The latter theory is supported by scattered occurrences of mantle-derived lamprophyres adjacent to the BPU (Crawford and Windley, 1990).

Geochronological data shows that the BPU was intruded into warm country rocks, and stayed at relatively high temperatures for some time (Parrish and Tirrul, 1989; Schärer et al., 1990). Initial cooling may have been retarded by the northward downfaulting of a slab of low conductivity sediments which were subsequently thermally metamorphosed (Rex et al., 1988), and such an extensional regime would have accommodated rising magma (Searle et al., 1992a). Field relations to the south of the BPU are complex, with further evidence of thermal overprinting of high grade gneisses by the BPU.

The metamorphic complex to the south of the batholith consists of meta-sedimentary, -volcanic and -plutonic rocks (Desio et al., 1964), displaying a polymetamorphic history (Bertrand et al., 1988; Hanson, 1989; Searle et al., 1989; Allen and Chamberlain, 1991; Searle and Tirrul, 1991). In the central Karakorum these lithologies have been deformed by south-vergent isoclinal folds and metamorphosed at about 700 °C and 7.5 to 11 kbar (M1), followed by a lower pressure metamorphism characterised by sillimanite growth at 630 to 700 °C and 7.5 to 4 kbar (M2, Lemennicier et al., 1996).

A U-Pb zircon date of 37 ± 0.8 Ma from the Mango Gusor granite (Parrish and Tirrul, 1989) has not cleared up the disagreements about the timing of the two main episodes of metamorphism, since both Allen and Chamberlain (1991) and Searle and Tirrul (1991) consider the main tectonometamorphic evolution of the area to have taken place prior to this intrusion. Lemennicier et al. (1996) propose a short gap between M1 and M2, and suggest that both events are Miocene-Pliocene in age, with dome structures generated by vertical and dextral extrusion of the mid crust. Regional cooling ages for the Karakorum basement are less than 10 Ma for the ^{40}Ar-^{39}Ar system, and two muscovites from a foliated intrusion emplaced on the MMT between Ladakh and the NPHM date thrust movement at just before 9 Ma (Villa et al., 1996). Coeval metamorphism, thrusting, uplift and denudation are thought to have occurred in this area in the Miocene-Pliocene, and Lemennicier et al. (1996) and Villa et al. (1996) both tentatively suggest that the subsequent evolution of the Karakorum metamorphic complex is strongly related to that of the NPHM, with no extensional activity in the last 10 Ma.

1.4.3 The Indian Plate in Pakistan

Peak metamorphism in northern Pakistan was attained at about 50 Ma (Treloar and Rex, 1990; Chamberlain et al., 1991; Smith et al., 1994), while ages of peak

metamorphism in the main orogen are constrained by the timing of garnet growth to be much younger at about 39 to 29 Ma (Prince et al., 1997; Vance et al., 1997), consistent with an earlier age of collision in the western Himalaya. Diachronous suturing along the Himalaya has been proposed by Klootwijk et al. (1985), Dewey et al. (1989) and Searle et al. (1987) among others, all suggesting that collision initially took place at the western end of the orogen. It is therefore reasonable to suppose that the first contact in Pakistan occurred at higher velocities than further east, and this may explain why the occurrence of eclogites is apparently restricted to the western end of the Himalaya.

Eclogites have been found along the MMT in the upper Kaghan valley (Pognante and Spencer, 1991; Spencer et al., 1995), in the ITSZ between the NPHM and Ladakh (Le Fort et al., 1997), and at Tso Morari in eastern Ladakh (Guillot et al., 1995). Eclogites from the Upper Kaghan nappe were metamorphosed at 650 ± 50 °C and 14.5 ± 2.5 kbar (Pognante and Spencer, 1991), at about 49 ± 6 Ma (Tonarini et al., 1993) while other assemblages reached 7.2 ± 0.7 kbar and at least 540 °C (Smith et al., 1994).

Pognante (1992) and Pognante et al. (1993) proposed that formation of eclogites and the lack of a heating stage during rapid exhumation, which are features unique to the western Himalaya, are linked to initial collision occurring in the west. High convergence rates in this region caused higher rates of subduction and exhumation, with lower thermal gradients, relative to those seen in the High Himalayan Crystallines of the main orogen further east. Slower subduction in the east allowed more time for thermal relaxation, enabling the formation of the High Himalayan Leucogranites.

Post-collisional granites from Naran, between the Kaghan valley and Nanga Parbat, have been dated at between 49 and 47 Ma (Zeitler and Chamberlain, 1991; Chamberlain et al., 1991). Granites from the Upper Kaghan valley have been

dated at 47 ± 3 Ma by U-Pb on zircon (Smith et al., 1994), and the Malakand granite in Swat, 200 km to the west, has yielded the same age (Smith et al., 1994).

Biotite granite sheets (Confluence granites) were emplaced into the Kohistan batholith at 50 to 30 Ma, followed by muscovite granite sheets (Parri granites) at circa 26 Ma (George, 1993). The two groups are chemically distinct, but both probably originate from juvenile arc sources. These sheets post-date initial collision with the Indian Plate, but are pre- or syn-tectonic with respect to continued underthrusting of Indian continental crust below the Kohistan Arc, suggesting that significant underthrusting by Precambrian basement could not have occurred before 26 Ma (George et al., 1993).

In general, temperatures of metamorphism in Indian Plate metasediments are lower in the western Himalaya than those recorded from the main orogen, where rocks had longer to heat up by thermal relaxation following collision. For example, peak metamorphic conditions from the Babusar Pass, just west of Nanga Parbat, were about 8.5 kbar and 550 °C, whereas rocks from the calc-schist melange of the MMT zone record lower P-T conditions of 400 °C and 7 kbar (Chamberlain et al., 1991). Treloar et al. (1989b) obtained conditions of between 500 and 650 °C from different zones within the Hazara nappe, and conditions of 8 to 12 kbar at 550 to 650 °C from the Alpurai schists further west. Treloar (1995) proposed a model combining conductive cooling and dissipative shear heating to explain both the inverted metamorphic sequence observed below the MMT in the Hazara region, and the rapid achievement of peak metamorphic conditions by 50 Ma, in a maximum of 15 Ma since initial collision.

Imbrication of the Indian basement occurred subsequent to peak metamorphism over the interval 40 to 25 Ma, as deformation progressed southwards (Treloar et al., 1989a, 1989b; Treloar and Rex, 1990). Rapid post-metamorphism cooling has been well documented using fission tracks in zircon and apatite, and Ar-Ar on

micas and hornblendes (Zeitler, 1985; Treloar and Rex, 1990). Nappe stacking was completed in the Miocene, and erosion of the uplifted regions is recorded in the Miocene molasse sediments of the foreland basin. Later reactivation of the MMT in an extensional sense (Vince and Treloar, 1996) is constrained to have occurred between about 20 and 16 Ma, because zircon fission track ages differ across the MMT, while apatite fission track ages show no change (Zeitler, 1985).

In the last 10 Ma, singular tectonic activity in the western Himalaya has led to formation of the Nanga Parbat and Hazara syntaxes (Desio, 1976, 1979; Sarwar and DeJong, 1979). Growth of these regions is discussed in the next section, and details of the metamorphic, magmatic and thermal history of the NPHM are contained in other chapters. Away from the syntaxial regions, the most recent structure in the western Himalaya is the Main Frontal Thrust, which carries the Salt Ranges in its hangingwall (Fig. 1.5).

To summarise, deformation in northern Pakistan has been accommodated by active thrust faulting propagating southwards over time and imbricating rocks which had already obtained their peak metamorphic grades during crustal thickening, which occurred at about 50 Ma in northern Pakistan and later further east. Thin-skinned tectonics have dominated post-collisional deformation in Pakistan, whereas the main orogen has been dominated by thick-skinned tectonics (c.f. Figs. 1.4 and 1.6). The difference in timing of metamorphism between the two areas reflects initial collision in the west, where initial convergence and subduction rates were also higher. This enabled subducted rocks to achieve depths of 60 km in 1 to 2.5 Ma for slab dips of between 15 and 30° (Rowley, 1996), which were subsequently rapidly exhumed along the MMT zone. Slower convergence and subduction in the east has prevented the exhumation of any rocks that preserve eclogite facies assemblages.

1.4.4 Growth of the NPHM

Growth of the NPHM and the Hazara syntaxis are thought to be linked by interference of the southwest-verging thrusts of the main Himalayan chain, and the south-south-east-verging thrusts of north Pakistan (Treloar et al., 1991; Fig. 1.7). Fault plane solutions of seismic first motions on intermediate depth events (Seeber et al., 1981) show compression parallel to stretching lineations and perpendicular to strike as the belt curves around in a radial pattern. Klootwijk et al. (1985) have shown a decrease in thrust displacement, and an increase in Tertiary clockwise rotation, towards the western end of the orogen.

The NPHM may be broadly described as a NNE-plunging crustal-scale antiformal structure (Coward et al., 1986; Treloar et al., 1991), although the youngest structures form shear zones which lie along the western margin of the NPHM (Chapter 2). Structural studies of the NPHM have suggested that it grew above the pinned lateral termination of a major Himalayan thrust, possibly (but not necessarily) the MCT (Coward et al., 1986; Butler et al., 1989; Madin et al., 1989). The observed pattern of rotation and displacement is consistent with this theory (Fig. 1.8).

Early thrusts at Nanga Parbat should have a westerly vergence as a result of local rotation, and the eastward increase in displacement will generate a dextral shear couple near the pinning point. This will result in gradual overprinting of the marginal thrusts by dextral strike-slip movements, as observed by Butler et al. (1989). If strain became distributed throughout the hangingwall rather than concentrated along a thrust, large scale antiformal folds would be generated, for example the NPHM itself.

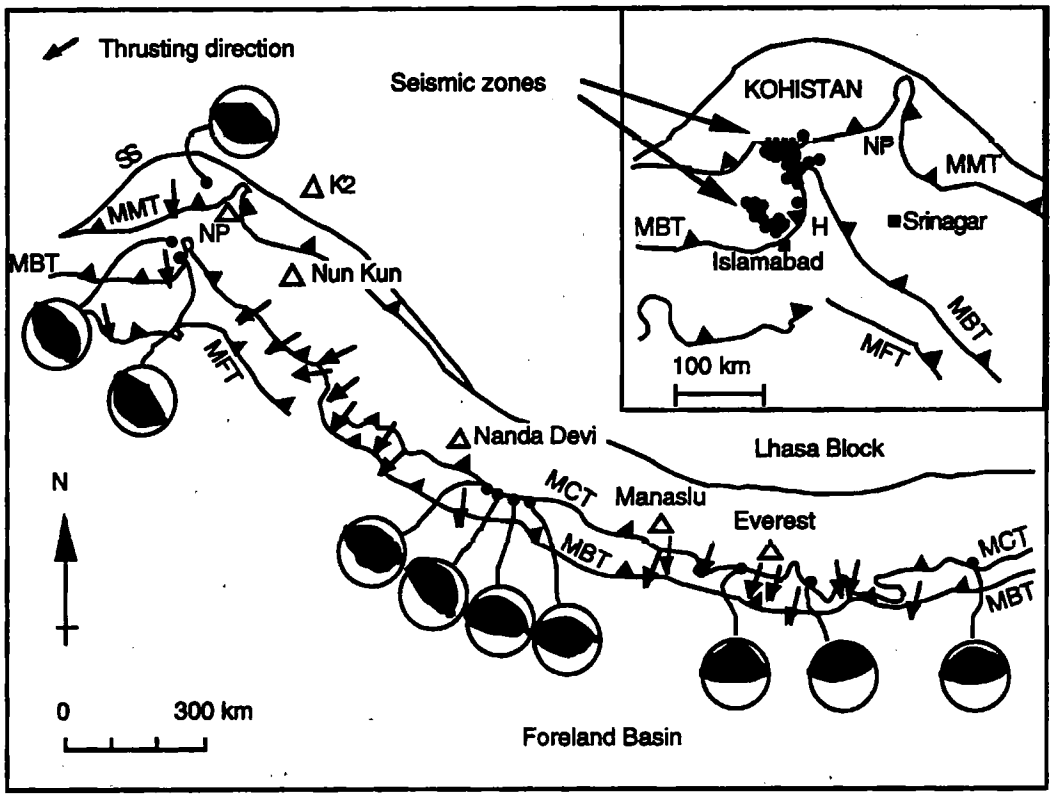

Fig. 1.7. Simplified tectonic map of the Himalayan orogen, after Butler et al. (1989). Thrusting directions are from stretching lineations reported by Brunel (1985), with selected fault plane solutions of earthquakes from Armbruster et al. (1978), Seeber and Armbruster (1979), Jackson and Yielding (1983), Seeber et al. (1983), and Ni and Barazangi (1984). Abbreviations as for Fig. 1.1. Inset: detail of the north-western termination of the Himalayan range, filled circles indicate seismic zones associated with the Hazara and Nanga Parbat syntaxes from Armbruster et al. (1978).

Hence the growth of the NPHM is controlled by early structures, developed within the southeast-verging Pakistani thrust system, being reworked by structures related the main southwest-verging Himalayan thrusts (Coward et al., 1986, 1988; Treloar et al., 1991). In contrast, the Hazara syntaxis results from an anticlockwise rotation of thrusting direction (Bossart et al., 1988; Fig. 1.9), and the relationship between the two thrust systems is opposite to that seen at Nanga Parbat.

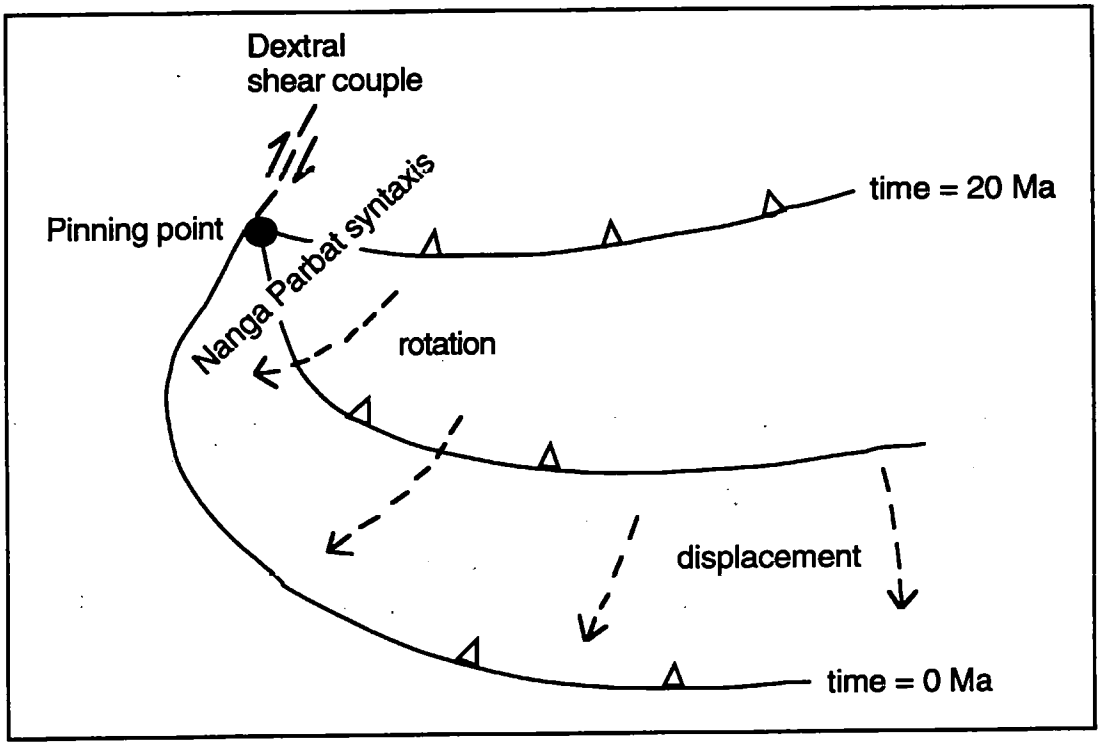

Fig. 1.8. Diagram showing the expected relationships between displacement amounts, rotations of movement direction, dextral shearing and crustal scale folding at the lateral terminations of the main Himalayan thrusts, from Treloar et al. (1991).

Southwest-verging thrusting is stepping south-westward, as indicated by earthquake fault plane solutions in the active Indus Kohistan Seismic Zone (Seeber and Armbruster, 1979; Jackson and Yielding, 1983; Fig. 1.7). The Besham antiform, north-west of the Hazara syntaxis (Fig. 1.5), shows younger apatite fission-track ages than surrounding regions (Zeitler, 1985), and has been interpreted to be a proto-syntaxis developing in the hangingwall of the IKSZ (Treloar et al., 1989c).

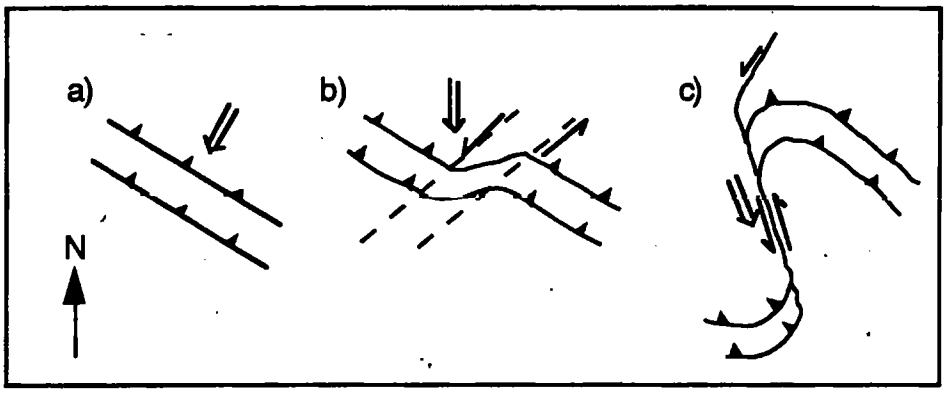

Fig. 1.9. Model for the formation of the Hazara syntaxis, from Bossart et al. (1988), showing an anticlockwise rotation of the thrust stacking direction. a) An early set of nappe units is developed by southwest-verging thrusting. b) Rotation of movement direction to south-verging results in formation of a major sinistral shear zone. c) Further rotation results in south-south-east-verging thrusting, a large offset on the sinistral shear zone, and syntaxial formation.

The growth of the syntaxial regions of northern Pakistan thus represents interference between two thrust systems, generated by rotation of the main Himalayan thrusts around a pinning point. This behaviour is clearly anomalous, both within the main Himalayan orogen and the internal zones of northern Pakistan, but it affords an ideal natural laboratory for the study of active compressional tectonics and may offer a view of the future of younger syntaxes (Hazara) and proto-syntaxes (Besham).

1.4.5 Recent events

The NPHM provides abundant evidence of Neogene activity, exposing both intrusive granite plutons dated as young as 1.0 Ma (Zeitler et al., 1993), and high-grade assemblages thought to result from the most recent episode of metamorphism, only a few million years after monazite growth (Smith et al., 1992). Long-term exhumation rates, over the scale of several Ma, are discussed at

length in Chapter 7, and this section will briefly discuss evidence for neotectonic activity and rapid Recent denudation.

The most obvious evidence for neotectonic activity around the NPHM is the Liachar Thrust, which has placed Indian Plate basement over Quaternary fluvial sediments on the western margin (Butler and Prior, 1988a, 1988b; Owen, 1989). This fault is marked by a cataclastic gouge zone, which is overlain by a ductile shear zone several km in extent, indicating a prolonged history at a range of depths. Cronin et al. (1993) conducted a Landsat lineament analysis of the NPHM, and identified several strong lineaments defined by sets of collinear drainage segments and aligned linear grey tone boundaries. Some of these correspond to known faults, for example the Liachar Thrust, while others have not been mapped. Structure of the margins is discussed further in Chapter 2.

Burbank et al. (1996) used cosmogenic ^{10}Be and ^{26}Al to calculate exposure ages for abandoned river terraces above the Indus river across the NPHM and into Ladakh, and found bedrock incision rates of between 2 and 12 mm/y, with the highest rates in and adjacent to the NPHM. Reconstruction of longitudinal profiles along the Indus suggests that incision and bedrock uplift are approximately balanced, while denudation rates are sufficiently high that rapid mass transfer through landsliding is the predominant mechanism for hillslopes to adjust to river incision at their toes (Burbank et al., 1996). An example of such landsliding is the 1841 event just south of Liachar, which resulted in several cubic kilometres of material damming the Indus. When the dam was breached a year later, the catastrophic flood destroyed an army camped several km downstream (Butler et al., 1988). Several other slides occurred in the same year (Shroder, 1993), probably all triggered by seismic activity.

In a seismic survey conducted over one month in 1980, Yielding et al. (1984) monitored a large amount of activity, predominantly deep earthquakes in the

Pamirs. Several earthquakes were located within the NPHM, and one deep event was recorded below Nanga Parbat itself, possibly related to deep movement on the Liachar Thrust.

Nanga Parbat is thus a prime example of an active mountain belt, with rapid denudation and well documented neotectonic activity. Chapter 2 describes the structure of the NPHM and its margins, and constructs a basement stratigraphy for the massif.

CHAPTER 2 - FIELD RELATIONS AND PETROGRAPHY

2.1 Introduction

The NPHM is comprised of upper amphibolite grade orthogneisses and paragneisses, often intensely deformed. These are intruded by amphibolite dykes, discordant to some gneissic fabrics and deformed by others. A suite of leucogranite dykes and small plutons have been emplaced more recently. Some dykes are deformed by marginal shear zones but other dykes and plutons are undeformed away from massif margins. Quaternary fluvioglacial sediments are widespread, and cover most valley floors. These are overthrust by orthogneisses at the Liachar thrust, on the western margin of the massif (Butler and Prior, 1988a).

This chapter summarises field relations within the NPHM and at its margins, with brief descriptions of the petrography of the main lithologies. The main objective of this chapter is to establish a basement stratigraphy for reference in subsequent chapters. Mineral chemistry and metamorphic textures are described in more detail in chapter 3, and more detailed description of igneous rocks can be found in chapter 4. This section describes previous work on the basement stratigraphy of the NPHM, and subsequent sections describe microstructural and lithological variations in a traverse from the Kohistan Arc into the high-grade interior of the southern NPHM. The findings of this chapter are synthesised into a basement stratigraphy in section 2.4.

2.2 Previous work and structural geology

The rocks of the NPHM were first described in detail by Wadia (1932), who observed that the margins of the massif were dominated by biotite gneisses with subordinate metasediments, and correlated these with the Precambrian Salkhala series, which outcrop north of the Hazara syntaxis. Towards the core of the massif, Wadia (1932) noted an increase in both metamorphic grade and the proportion of orthogneiss, which was correlated with the Central Gneiss of the High Himalaya (now termed the High Himalayan Crystalline Unit). Wadia (1932) described the frequent interbedding of orthogneisses and paragneisses, which he attributed to lit-par-lit injection.

Misch (1949) suggested that these migmatites were generated by sub-solidus lit-par-lit granitisation of metasediments by metasomatism. According to Misch (1949) an influx of hot granitising fluids in the core of the massif resulted in higher temperature assemblages in this region, and caused "metasomatic granitisation of batholithic dimensions". Field relations do not support this theory, and deformed megacrystic granitic bodies from the NPHM (e.g. Butler et al., 1997) are more likely to be related to Cambro-Ordovician granites similar to those seen in the Lesser Himalaya, such as the Mansehra pluton (Le Fort et al., 1980). Misch (1949) mapped lower grade muscovite-kyanite schists around the margin of the NPHM, and related the increase in grade towards the core of the massif to increasing temperature.

Madin et al. (1989) divided the basement rocks of the NPHM into three units, the Shengus gneiss, Iskere gneiss, and Haramosh schist, from structurally lowest to highest (Fig. 2.1). The Shengus gneisses outcrop in the southern and eastern NPHM, and were mapped in the Astor gorge and the eastern Indus gorge (Madin et al., 1989). The Shengus gneiss is predominantly pelitic or psammitic biotite

gneiss, with common migmatitic horizons and rare calc-silicate horizons. Zircon cores from the Shengus gneiss have yielded U-Pb ages of about 400 to 500 Ma, with some evidence of an older component of about 2500 Ma (Zeitler et al., 1989). Treloar et al. (1991) correlated the Shengus gneiss with the Tanawal formation and Mansehra Granite series of the Hazara region (Treloar et al., 1989c), and interpreted the Shengus gneiss to be a supracrustal cover to the structurally higher Iskere gneiss.

The Iskere gneiss has its type area in the north-western part of the NPHM, and consists mainly of coarse-grained biotite orthogneiss (Madin et al., 1989). The presence of streaky, deformed and concordant segregations of leucosome often confers a migmatitic appearance (George, 1993). Wedges of metasediments are found within the Iskere gneiss in the Indus valley section, but they are often intercalated with orthogneisses or show transitional contacts (George, 1993). Zircon cores from the Iskere orthogneiss have yielded U-Pb ages of about 1850 Ma (Zeitler et al., 1989; Zeitler et al., 1993).

The Haramosh schist is the structurally highest unit within the NPHM (Madin et al., 1989), and corresponds to the "layered unit" of Butler et al. (1992) which was mapped around the northern antiformal termination of the NPHM. George (1993) correlated this unit with the intercalated sequence of metasediments present at Sassi, which are thought to be derived from both the Kohistan Arc and the Indian continent (Butler and Prior, 1988b). Treloar et al. (1991) mapped a narrow zone of metasediments on the western margin of the massif at Raikhot Bridge, and correlated these with the Alpurai schists exposed in the footwall to the MMT to the south-west in Swat (Kazmi et al., 1984).

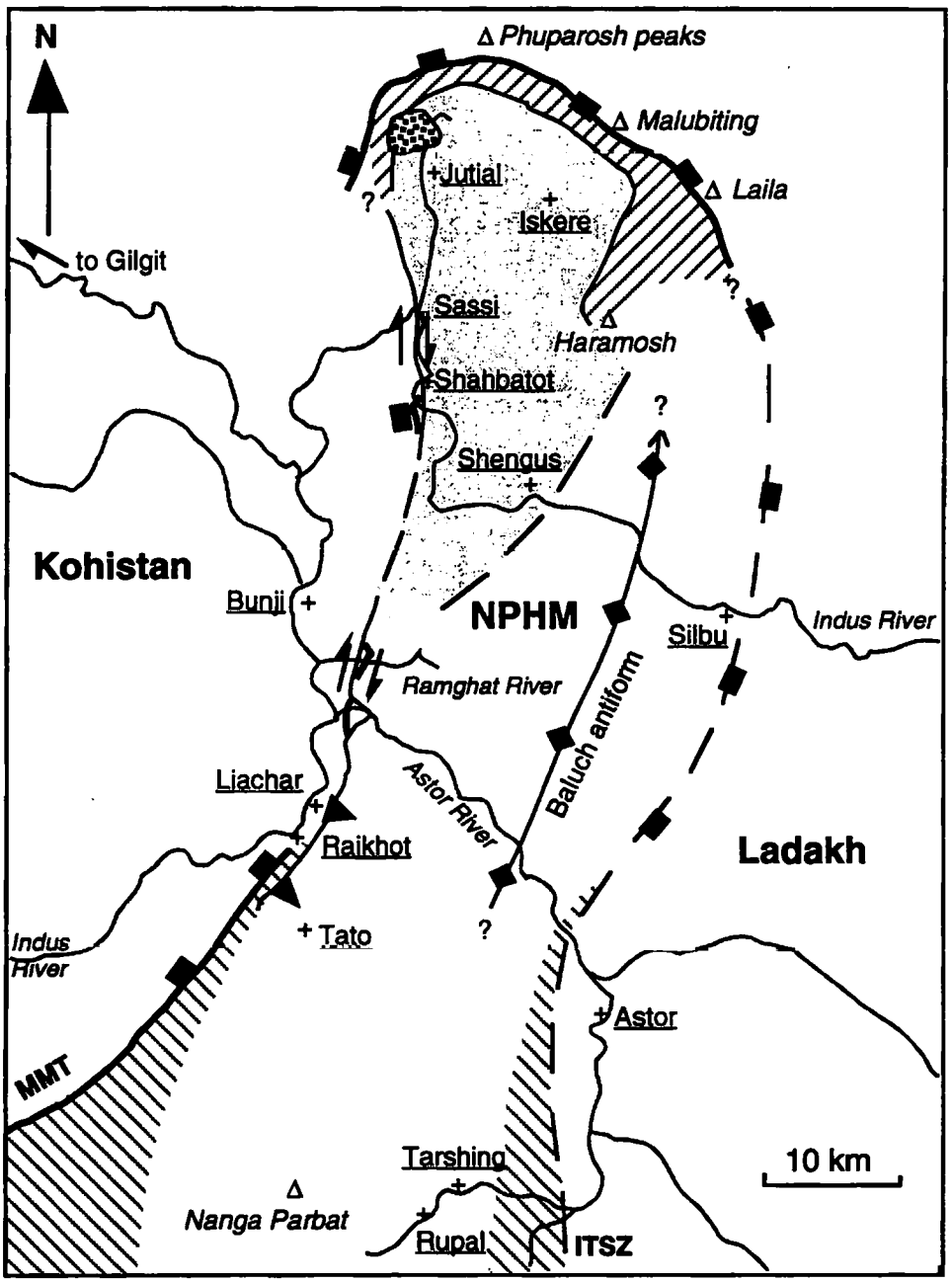

Fig. 2.1. Geological map of the NPHM, with main structural elements and lithological boundaries compiled from Butler et al. (1989), Butler et al. (1992), George (1993), Madin et al. (1989), and Treloar et al. (1991). The MMT is shown in bold with a brick ornament, dashed where inferred, and the outcrop of the Liachar Thrust is ornamented with teeth. Hatched shading indicates metasedimentary cover in the south, and the "Layered Unit" (Butler et al., 1992) or "Haramosh schists" (Madin et al., 1989) in the north. Heavy stipple indicates the Jutial leucogranite, light stipple indicates Iskere orthogneiss, and the Shengus gneiss is not ornamented.

Treloar et al. (1991) suggested that significant post-metamorphic imbrication has occurred within the NPHM, as was previously demonstrated for Indian Plate rocks to the south-west of Nanga Parbat (Treloar et al., 1989c). A high strain zone between Shengus and Iskere gneisses was interpreted to be a reverse shear zone which had placed Iskere gneiss over the Shengus gneiss.

Wheeler et al. (1995) mapped a traverse along the Indus valley in some detail, and found that corresponding rock types do not appear on either side of the main antiformal closure (the Bulache antiform of Madin et al., 1989). Rocks on the western limb of the antiform are predominantly orthogneiss (Iskere gneiss), and rocks on the eastern limb of the antiform are predominantly paragneiss (Shengus gneiss), while the apparently high strain zones near the contact between the two were interpreted to be due to contrasting rheologies, rather than a major shear zone (Fig. 2.2).

Both Shengus and Iskere gneisses were found by Wheeler et al. (1995) to be cross-cut by basic dykes, often strongly deformed and metamorphosed to amphibolite grade. These dykes post-dated early migmatisation and granulite facies metamorphism, which is therefore constrained to be pre-Himalayan since no basic magmatism is known from the Himalayan orogen. These dykes are discussed further in chapter 5.

The relation between the Shengus and Iskere gneisses is still not clear, since the oldest zircon ages are found in the Shengus gneiss. These may be inherited grains incorporated into a supracrustal sedimentary sequence, with later zircon growth recording the Cambro-Ordovician orogenic event which also led to the emplacement of the Mansehra granite, dated at 516 ± 16 Ma by a whole-rock Rb-Sr isochron (Le Fort et al., 1980). In this case, the ~1850 Ma zircon ages from the Iskere gneiss may represent the early basement migmatisation event prior to emplacement of the amphibolite sheets, and the structurally lower Shengus unit

must have been tectonically emplaced into its present position (Treloar et al., 1991). The timing of Precambrian events is discussed further in Chapter 5.

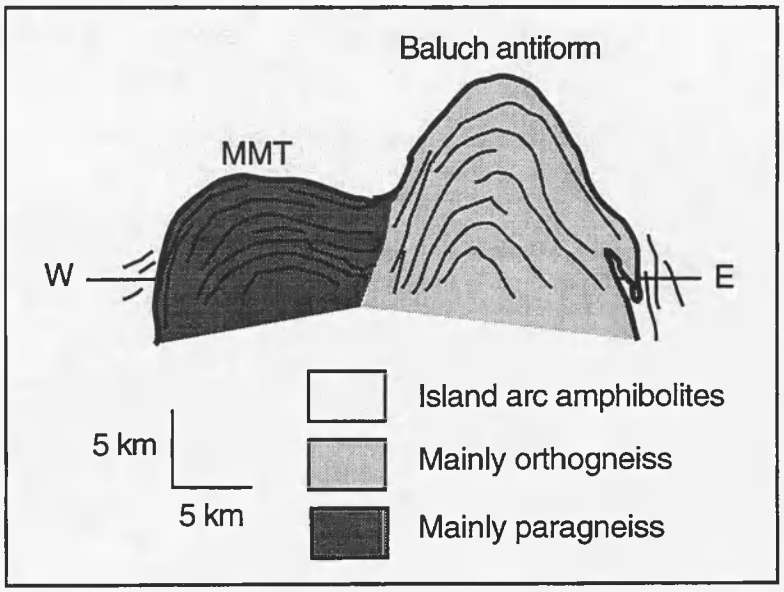

Fig. 2.2. Sketch cross-section across the Indus traverse of the NPHM (Fig. 2.1), from Wheeler et al. (1995). The Iskere gneiss and Shengus gneiss of Madin et al. (1989) correspond to mainly orthogneiss and mainly paragneiss units respectively.

Although there is no conclusive evidence for post-metamorphic imbrication of the NPHM, the area has been extremely tectonically active following collision. At the western margin of the NPHM, at Raikhot (Fig. 2.1), the MMT is a distinct mappable zone of amphibolite-grade shear involving rocks of the Kohistan arc, Nanga Parbat basement gneisses, and a thin layer of sedimentary cover (Butler and Prior, 1988a, b; Treloar et al., 1991). Examination of the MMT further north at Sassi (Fig. 2.1) reveals that this shear zone was subhorizontal during displacement (Butler and Prior, 1988b; Coward et al., 1986), with small-scale linear structures and shear sense criteria indicating SSE-NNW subduction of the Indian continent

under Kohistan (sinistral transpression). At the present time, foliation within both Kohistan and Nanga Parbat gneisses is generally subvertical, parallel to the MMT foliation.

Further southeast into the syntaxis, the foliation within the Nanga Parbat gneisses dips more gently southeast and develops a prominent SE-plunging stretching lineation. Shear criteria, from rotated feldspar augen (Passchier and Simpson, 1986), foliation fish, deformed granite sheets and rotated blocks of more rigid material all show top-to-the-west reverse faulting (Figs. 2.3 to 2.7). This ductile zone, the Liachar Shear Zone (LSZ), was initiated at amphibolite facies but was active through biotite and chlorite grades, and is carried on a brittle zone of cataclastic faulting with prominent gouges and penetrative fracturing (Butler and Prior, 1988a, b). This zone is termed the Liachar Thrust, after its type locality (Fig. 2.1), which places basement gneiss over Quaternary gravels deposited by the Indus river (Butler and Prior, 1988a). A cross-section across the western margin at Raikhot Bridge (Fig. 2.8) emphasises the discrete nature of the MMT zone and Liachar Thrust at this point. Butler et al. (1989) noted steep north-south trending zones of penetrative fracturing and shatter which do not show significant offset, which may represent tips to strike-slip faults.

A few kilometres further north, between the Ramghat and Astor river valleys, there are two shear zones developed in the Nanga Parbat gneisses, and the MMT zone has been cut out of the section by the continuation of the Liachar Thrust (Fig. 2.9). Here there is a combination of top-to-the-north-west thrusting and steep dextral strike-slip faulting, determined by riedel shear orientations (Butler et al., 1989).

Fig. 2.3. Macroscopically boudinaged leucogranite sheets from the Liachar Shear Zone. The granite has an undeformed internal texture indicating deformation occurred pre-complete crystallisation. This feature probably represents a collapsed feeder for tension gashes elsewhere in the shear zone. Looking southwest, shear sense is top to the north-west.

Fig. 2.4. Metapelitic and calc-silicate lithologies deformed in the Liachar Shear Zone, looking south-west. Note isoclinal fold closure (arrowed) and top to the north-west shear sense deduced from deformed banding in calc-silicate lithology at top of pen. The pen is 15 cm long.

Fig. 2.5. Photograph of boudinaged calc-silicate band in the Liachar Shear Zone, looking west, showing top to the north shear sense. The lens cap is 5.5 cm in diameter.

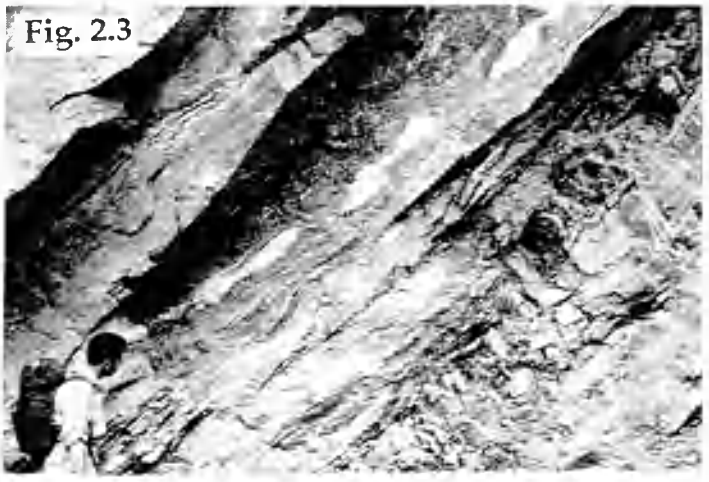
Fig. 2.3

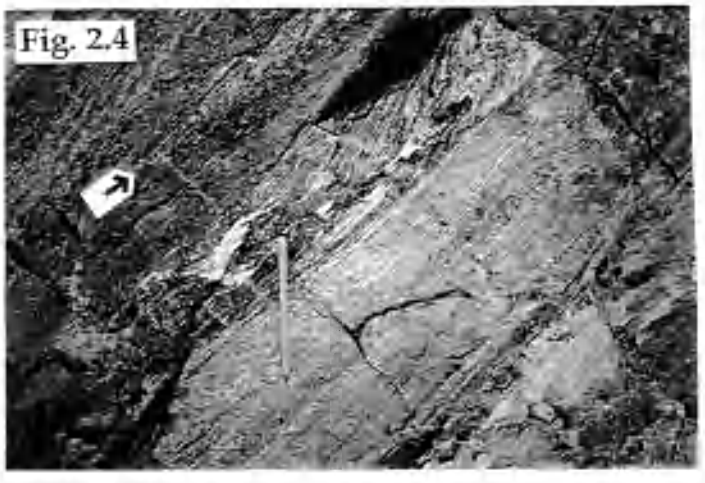
Fig. 2.4

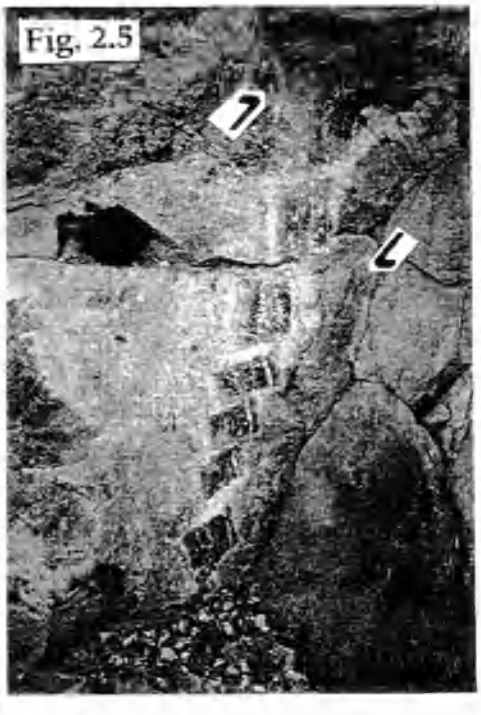
Fig. 2.5

Fig. 2.6. Cliff section through the Liachar Shear Zone, looking south-west. Note deformed leucogranite sheets, boudinaged amphibolite dyke (arrowed) and large scale (~50 m length) foliation fish, all indicating top to the north-west shear sense. The cliffs are c. 200m high above the road.

Fig. 2.7. Fault in augen gneiss within the Liachar Shear Zone showing evidence for ductile and brittle deformation. Ductile shear zone defined by bending-in of feldspar augen, brittle deformation has resulted in a fine-grained fault gouge (above the hammer). Note foliation fish (arrowed). Looking southwest, shear sense is top to the north-west. The hammer is ~40 cm long.

Fig. 2.6

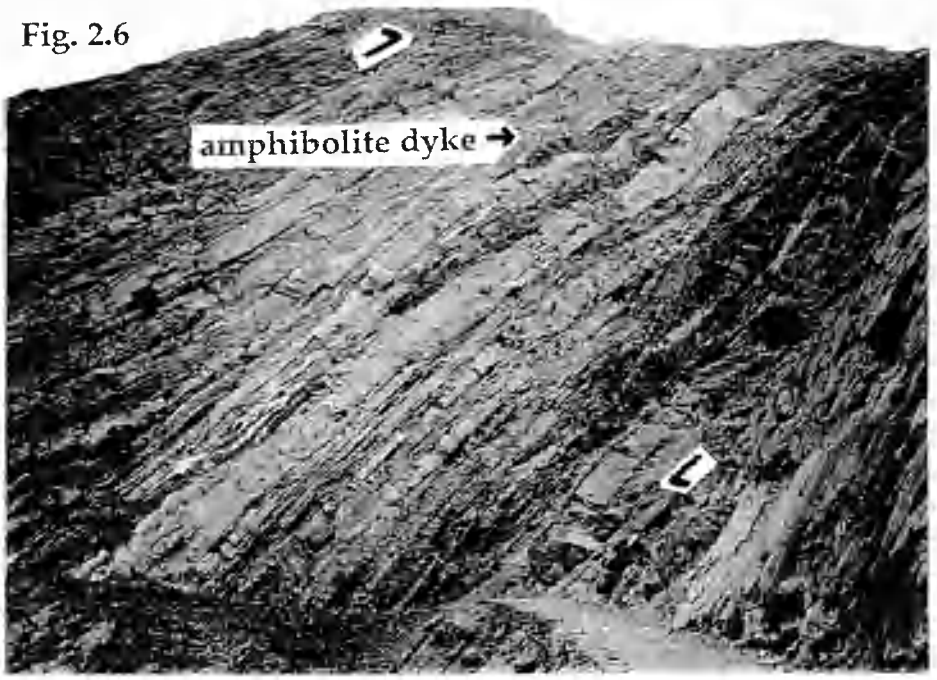

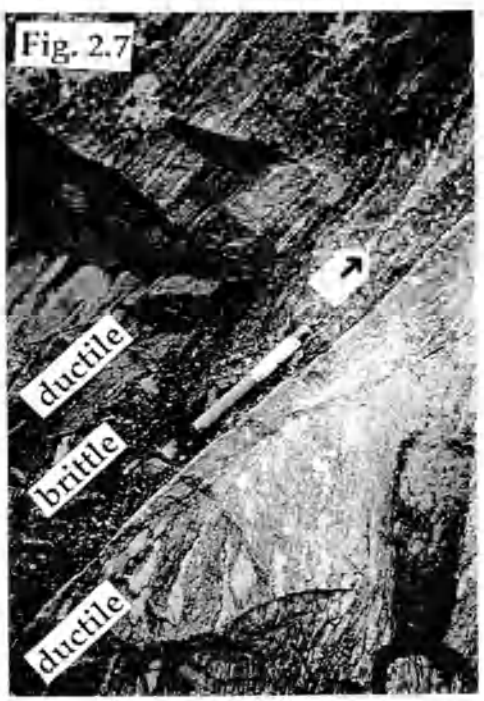

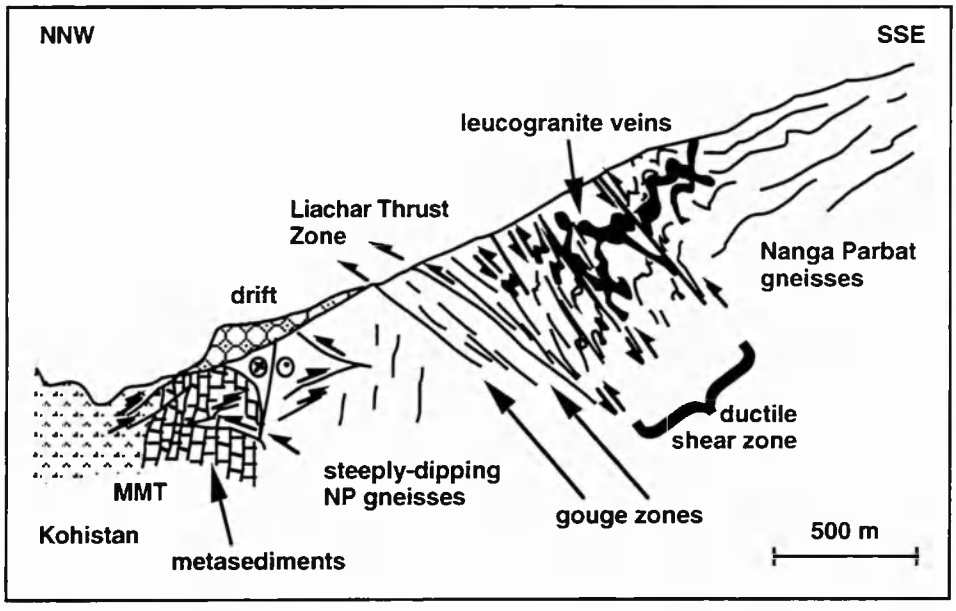

Fig. 2.8. Sketch cross-section through the western margin of the NPHM at Raikhot (Fig. 2.1), from Butler et al. (1989).

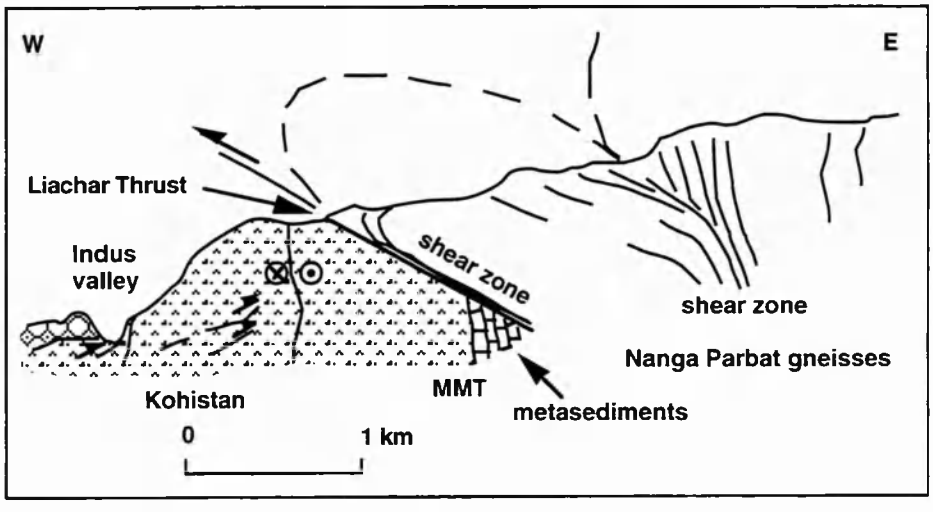

Fig. 2.9. Sketch cross-section through the western margin of the NPHM, exposed along the ridge between the Ramghat and Astor river valleys (Fig. 2.1), from Butler et al. (1989).

Further north, the MMT is cut out by a steep fault zone which separates gently dipping Kohistan rocks from steeply dipping Nanga Parbat gneisses containing slices of the MMT and Kohistan. The western edge of this fault zone is a dextral strike-slip fault, termed the Shabhatot Fault by Butler et al. (1989), which accommodated the most recent deformation at this point. Earlier brittle reverse faults form conjugate sets which show east-west compression.

Butler et al. (1992) conducted a detailed study of the geology of the northern NPHM, and found that the northern margin was a concordant ductile shear zone separating Kohistan Arc material from the "layered unit" of interbanded ortho- and para-gneiss, with intercalations of deformed granitoids, equivalent to the Haramosh schist of Madin et al. (1989). This marginal zone was correlated with the MMT, and showed stretching lineations defining a NNW-SSE transport direction, although these were folded around the north-plunging antiformal closure of the NPHM.

The eastern margin was first interpreted to be a major reverse fault, called the Stak Fault (Verplanck et al., 1985), so that the NPHM appeared to be a crustal scale pop-up structure. Pognante et al. (1993) investigated the contact in the upper Stak and Turmik valleys, 15 km north of the Indus. The contact was a mylonitic zone dipping gently ESE, recording dextral strike-slip, relating to underthrusting of Nanga Parbat gneisses below the Kohistan-Ladakh arc. Other studies have also concluded that the eastern margin was passively folded, and affected only by small-scale brittle faulting (Butler and Prior, 1988b; Butler et al., 1992; Coward et al., 1988, Treloar et al., 1991; Wheeler et al., 1995).

Briefly, the NPHM is a polymetamorphic terrain comprised of two different gneisses which have experienced granulite facies metamorphism in the past, and since been intruded by basic sheets which have subsequently also been metamorphosed. A third unit which outcrops around the massif margins may

have been a Phanerozoic sedimentary cover to the older gneisses. The western margin of the massif is dominated by dextral strike-slip faulting, which is migrating southwards to overprint northwest-verging reverse shear, often cutting out the MMT. In contrast, the northern and eastern margins appear to have been passively folded, with minor brittle faulting. These observations are consistent with the interference model for syntaxial formation outlined in Chapter 1 (Butler et al., 1989; Treloar et al., 1991), and set the structural framework for the basement stratigraphy outlined below.

2.3 Lithologies of the southern NPHM

This section contains a detailed description of lithologies and field relations in the Tato and Rupal Valleys, starting in Kohistan and traversing southwards through the core of the massif in this area. The outcrops studied were restricted by time and accessibility, so that north of Tato only the road section was mapped (Fig. 2.10). South of Tato, where the Raikhot valley ceases to be a narrow gorge, both sides of the valley were investigated to an altitude of over 4000m, and the highest sample comes from the ridge to the west of Fairy Meadows, at 4950m. One outcrop at the foot of the Raikhot Face was visited, and several samples were collected from the moraine at this point, restricting their origin to over 4500m on this face. Some samples were also collected from the glacier at the level of Fairy Meadows, with a less restricted origin from south of this point, at an altitude of at least 3300m. Collecting of boulders was a necessary evil in order to investigate lithologies exposed in inaccessible locations, although every outcrop visited was also sampled.

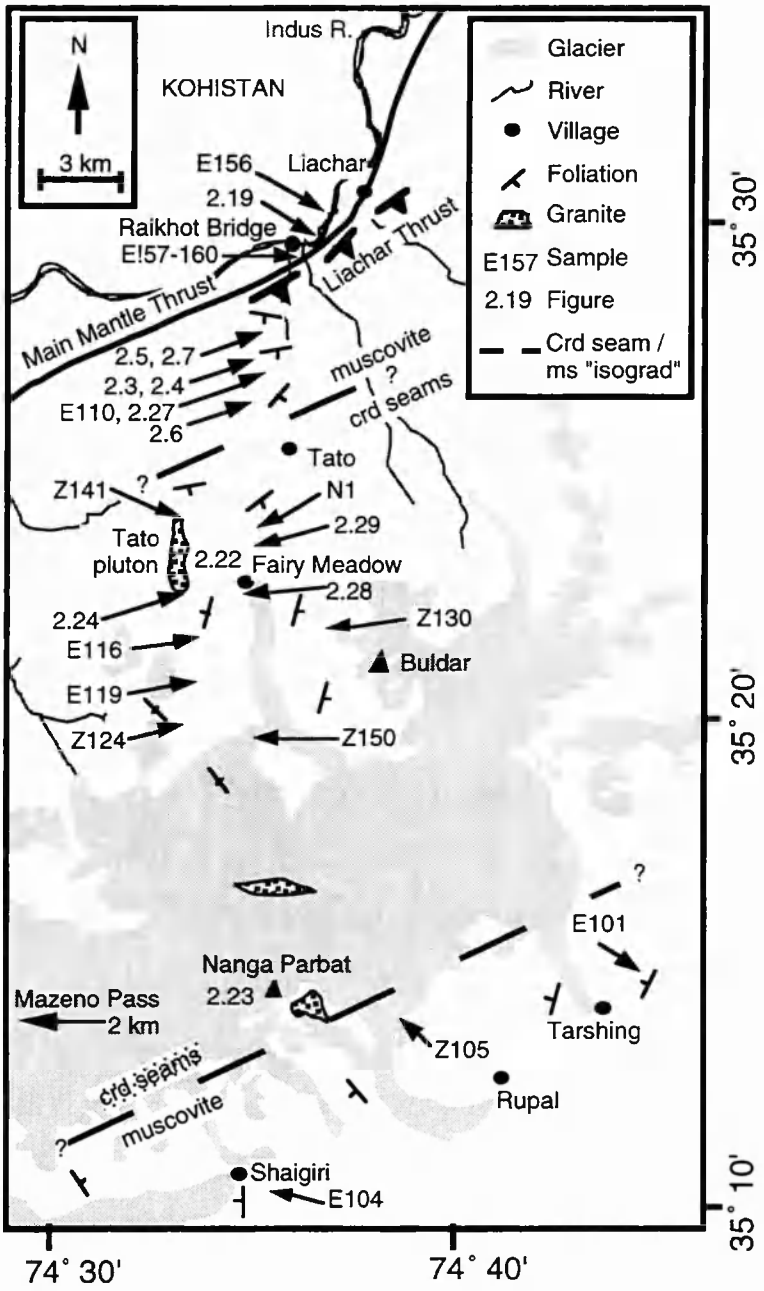

Fig. 2.10. Location map of the southern NPHM, showing locations of photographs and samples discussed in the text, with approximate "isograds" delimiting the extent of in situ cordierite and muscovite.

In the field area covered by the present study, orthogneiss of granitic to tonalitic composition forms the majority of visible outcrop. On the northern side of Nanga

Parbat, biotite augen gneisses contain intercalations of pelitic, psammitic and calc-silicate lithologies with either concordant or gradational margins. There is no apparent preferential distribution of pelitic, calcareous or meta-igneous gneisses within the basement, but mineral assemblages vary systematically across the field area. Muscovite occurs only in the Liachar Shear Zone, and kyanite is also restricted to the massif margins (Fig. 2.10). Metamorphic grade increases as the interior of the massif is approached. In the "core" of the massif, that is south of Tato and north of the Rupal Valley, cordierite-bearing leucosomes are found in shear zones (Chapter 4), and cordierite-spinel assemblages are found in pelitic gneisses (Chapter 3). Amphibolitic sheets are found throughout the massif, as are leucogranitic sheets and small plutons (Chapter 4). Other leucogranite bodies are visible in both the north and south faces of Nanga Parbat itself (the Raikhot and Rupal faces respectively) but they were not sampled directly.

On the south side of Nanga Parbat, in the Rupal Valley, the main lithology is a locally migmatitic biotite gneiss. Muscovite is often a stable fabric-forming phase, and fibrolitic sillimanite is the stable aluminosilicate polymorph. In the Rupal Valley, from Tarshing westwards to the Mazeno Pass Base Camp, kyanite was not observed, although Misch (1949) mapped kyanite-bearing rocks to the east of Tarshing. Pelitic lithologies to the east of Tarshing contain garnet porphyroblasts with sinuous inclusion trails of opaque oxides and quartz, with ilmenite and rutile sometimes present, interpreted to indicate strong shearing deformation during garnet growth (George, 1993). One sample of such a lithology was collected 2 km east of Tarshing (E100), but the matrix was completely retrogressed to chlorite. Garnet in this sample showed two phases of growth, with an inclusion-free core and the rim crowded with spiral inclusions of rutile and ilmenite. Garnet chronometry applied to this area may provide significant information on the timing of prograde metamorphism within the NPHM (Gavin Foster, pers. comm.).

2.3.1 Kohistan

Only two samples were collected from Kohistan, both at Raikhot Bridge, where the "Kohistan granulite belt" of Bard (1983), or the "Kamila amphibolite" of Coward et al. (1982) is exposed. E160 is a metadiorite collected from the MMT zone on the eastern side of the river, and will be discussed in the next section. E156 is a diorite collected from a road cutting on the western side of the Indus River. The outcrop shows a weak foliation, and is cross-cut by thin undeformed quartz veins. The rock is medium-grained, with hornblende visible in hand specimen, as well as quartz, plagioclase and biotite. Grain size varies from about 0.2 to 2 mm, with no phase occurring as phenocrysts.

In thin section, the rock is seen to be comprised of 40 to 50 % plagioclase, 20 to 25% amphibole and clinopyroxene, 10 to 15% biotite and 15 to 20% quartz. Relict clinopyroxene crystals containing numerous small rounded quartz inclusions are rimmed first by opaque oxides and quartz, and then by pleochroic amphibole, containing quartz and plagioclase inclusions. Amphiboles display twinning and subhedral to euhedral crystal habit, but usually overgrow pyroxene. This suggests replacement of clinopyroxene by hornblende, and in places the core of the pyroxene is also replaced by hornblende. This replacement does not appear to have been accompanied by significant deformation, since there is no preferred elongation of the amphibole porphyroblasts. Biotite is in textural equilibrium with amphibole, and does not form a foliation.

Oscillatory zoned plagioclase confirms an igneous origin for this rock, with a seriate igneous texture in some parts of the matrix. Quartz is often dusty, and has an undulose extinction with subgrain formation, although crystal shapes are often euhedral. Plagioclase twins are also often strained or bent, indicating brittle deformation, with minor sericitisation which may have been coeval with emplacement of quartz veins. This rock records only weak deformation and fluid

infiltration, in marked contrast to NPHM lithologies less than a km to the south. This and related plutons have been interpreted as Lower- to Middle- Cretaceous layered calc-alkaline plutons, emplaced during arc building prior to obduction onto the Asian plate at c. 85 Ma (Bard, 1983).

2.3.2 Massif Margins

The eastern margin was not investigated in the present study due to time constraints, but several samples were collected from the MMT zone at Raikhot Bridge, just below the outcrop of the Liachar Shear Zone (Fig. 2.10). E157, E158 and E159 are pelitic gneisses of Indian Plate origin, and E160 is a meta-diorite of Kohistan origin. All four were collected from a zone of about 100m in width, on the eastern side of the Indus.

E160 contains hornblende, zoisite, quartz, K-feldspar and plagioclase, with secondary calcite and epidote in veins. Hornblende (45 - 50%) shows slightly inclined extinction, and occurs as relict porphyroblasts up to 2 mm across, with inclusions of quartz and zoisite. K-feldspar (30%) is often dusty due to fine inclusions, and forms porphyroblasts with similar relict appearance to hornblende. It also occurs as a finer-grained matrix phase, indicating recrystallisation and grain-size reduction during deformation. Quartz (~15%) occurs as small rounded grains in the matrix, while plagioclase (~5%) shows some zoning and lamellar twinning. Zoisite (~5%) is the only euhedral phase present, with an elongate habit, sometimes occurring as inclusions within hornblende or K-feldspar. Zoisite does not appear to show any preferred orientation.

The rock shows evidence for two or more episodes of fluid infiltration. On one side of the thin section, epidote has partially replaced hornblende along cleavage

planes, and also forms part of the matrix. It is brown in plane-polarised light, and shows high birefringence under crossed polars. It also occurs as acicular euhedral crystals, and comprises up to 50% of the rock in the zone where it occurs. Chlorite is associated with this zone, which is interpreted as resulting from pervasive fluid infiltration and metasomatic replacement. There are also two different types of vein: a coarse-grained quartz vein shows undulose extinction sand sub-grain formation, indicating post-crystallisation deformation. Very fine-grained calcite occurs in narrow smooth-sided cracks in several orientations, clearly cross-cutting the zone of epidote metasomatism, and does not show any evidence for deformation. The veins are interpreted as being emplaced relatively recently at shallow depths in the brittle regime, while the epidote metasomatism is more pervasive and is interpreted to have occurred at greater depth.

E158 and E159 are strongly altered by fluids, an orange stain in hand specimen suggesting oxidation of iron. Garnet porphyroblasts were visible in hand specimen, wrapped by a strong foliation. One oriented sample, E157, was sectioned parallel to lineation and perpendicular to foliation, and reveals a mylonitic fabric. The rock consists of quartz (40%), K-feldspar (30%), plagioclase (<5%) biotite (10%), muscovite (15%) and garnet (5%), proportions estimated by eye. Garnet porphyroblasts of a few mm diameter are wrapped by strained quartz ribbons, and a fabric defined by muscovite and biotite. Since the muscovite is fabric-forming in this rock, it is not due to late alteration, although it may be a product of a retrograde reaction during deformation. Biotite is altered to chlorite in parts, particularly where biotite is seen to fill cracks in garnet porphyroblasts.

Strained feldspar augen are also seen wrapped by quartz ribbons, and show pressure shadows containing finer grained feldspar. Subgrains forming in the strained augen are of a similar size to the finer grained crystals surrounding the augen, and so recrystallisation by subgrain formation and rotation may be inferred. Parallel with the foliation, myrmekite has formed along the margins of

K-feldspar augen. Myrmekite is an intergrowth of branching rods of quartz set in a single crystal of plagioclase (Shelley, 1993), and is interpreted by Becke (1908) as resulting from the interaction of Ca- and Na- bearing fluids with K-feldspar. In E157, myrmekite grows into K-feldspar perpendicular to the shape fabric. Simpson and Wintsch (1989) show that myrmekite may form only on the sides of K-feldspar facing the shortening direction, because of the volume decrease associated with myrmekite formation.

Garnet porphyroblasts display cracks running perpendicular to the fabric, mostly filled with chlorite, and shears which have moved and rotated small parts of the porphyroblast (Fig. 2.11). These features indicate brittle extension parallel to the main fabric.

The above-mentioned features of samples from the MMT zone lead to the conclusion that the fabric is extensional. In a major shear zone such as the Main Mantle Thrust, a component of non-coaxial deformation would be expected, and relative shear sense in this rock may be determined by rotations in porphyroclast systems (Passchier and Simpson, 1986; Mawer, 1987). Mica foliations deformed around garnet porphyroblasts predominantly show top to the north shear sense, although these are by no means conclusive. The cracks in garnet occasionally show a component of rotation, and where garnet is displaced by a shear zone, the sense is also top to the north. The direction of deformation bands in quartz ribbons may also be used to determine shear sense, but in E157 these are equivocal, with both directions of shear being indicated.

Fig. 2.11. Photomicrograph of mylonite E157, showing brittle deformation of garnet porphyroblast, breaking down to chlorite in extensional cracks. Plane polarised light, long dimension of the photograph is ~ 3 mm.

Fig. 2.12. Photomicrograph of E101, a muscovite-biotite gneiss from the Rupal Valley. Note stable muscovite and biotite, with deformed quartz showing undulose extinction and minor sericitisation of plagioclase. Crossed polars, the long dimension of the photograph is ~ 3 mm.

Fig. 2.13. Photomicrograph of banded gneiss E116 from Bayal Camp. Note relict appearance of garnet, and presence of chlorite replacing biotite. Plane polarised light, long dimension of the photograph is ~ 3 mm.

Fig. 2.14. Photomicrograph of pelitic gneiss X67, showing the GASP reaction (Chapter 3) frozen due to sillimanite exhaustion. Inclusion-rich poikiloblastic garnet is in extinction under crossed polars, long dimension of the photograph is ~ 1 mm.

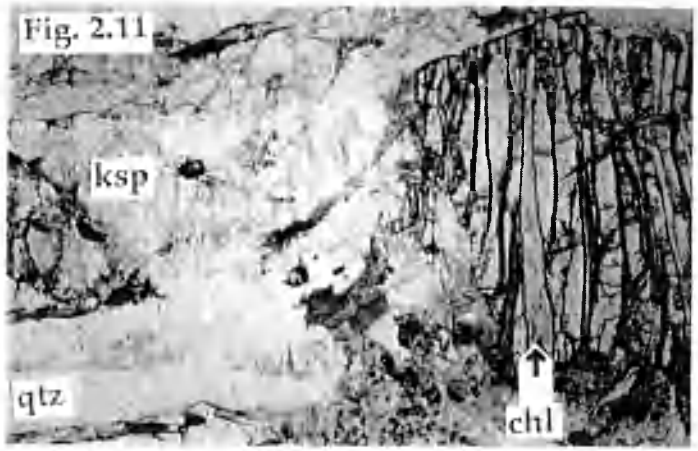
Fig. 2.11
ksp
qtz
chl

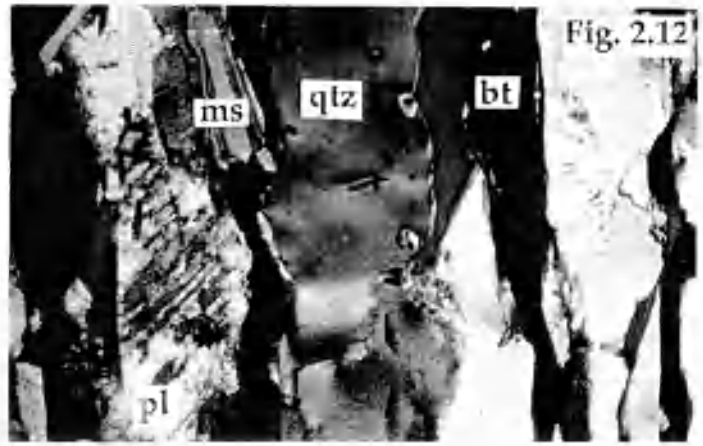
Fig. 2.12
ms
qtz
bt
pl

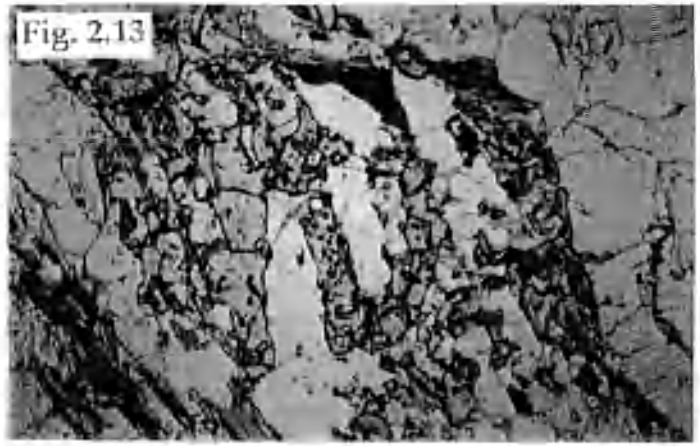
Fig. 2.13

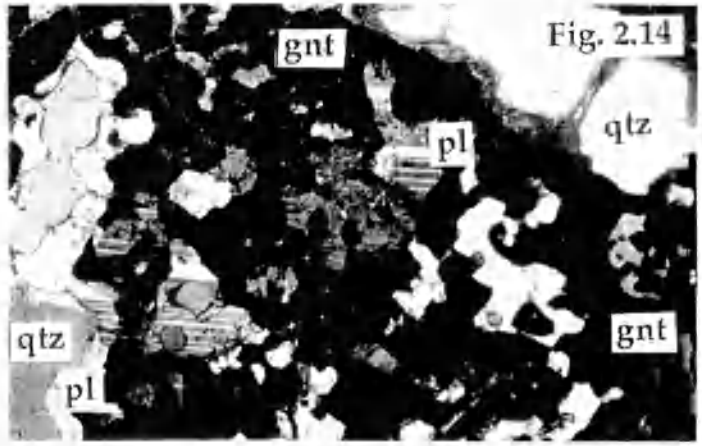
Fig. 2.14
gnt
pl
qtz
qtz
pl
gnt

2.3.3 Basement gneisses

The basement of the Nanga Parbat Massif is comprised of Indian plate gneisses metamorphosed under upper-amphibolite facies conditions. Compositions range from metapelites and metagreywackes with occasional calc-silicate layers, to orthogneisses of granitic composition. Contacts between these different lithologies appear to be conformable, and there is no evidence for faulted contacts between them (Madin et al., 1989). Several generations of leucocratic material occur, from lit-par-lit migmatites, to leucogranite sheets and cordierite-bearing leucosomes. The last two will be described separately, since they are clearly cross-cutting many fabrics and are related to recent events within the massif.

Since metapelites are the most likely source material for crustally derived granitic melts (Wyllie, 1977), these lithologies will be described in more detail in Chapter 3. Lit-par-lit migmatites found in some locations are unlikely to represent the source of the leucogranites, since migmatitic fabrics are cross-cut by metabasaltic sheets of probable pre-Himalayan age (Wheeler et al., 1995).

2.3.3.1 Orthogneisses

Much of the exposure within the NPHM is comprised of coarse-grained biotite-quartz-plagioclase-K-feldspar gneiss of probable metagranitic origin. In the Liachar Shear Zone and for several kilometres into the massif, this assemblage occurs as augen gneiss, with biotite defining an S-C fabric wrapping coarse K-feldspar porphyroblasts, or augen.

E110 is a typical coarse-grained augen gneiss from the Liachar Shear Zone, containing biotite (10 - 15%), K-feldspar (50%), plagioclase (15 - 20%) and quartz (25%) with occasional traces of garnet and no sillimanite. In thin section, biotite

has a ragged appearance, with occasional crystals oriented perpendicular to the main fabric. These may be un-recrystallised remnants of an earlier fabric. Large anhedral K-feldspar porphyroblasts, up to 2 cm across, often contain rounded quartz inclusions. K-feldspar shows myrmekite growth perpendicular to foliation, indicative of high strain (Simpson and Wintsch, 1989), and is commonly altered to sericite along cleavage planes. Unzoned plagioclase occurs as a finer-grained matrix phase, appears to be undeformed, and occasionally contains rounded quartz inclusions. Quartz shows undulose extinction, subgrain formation and lobate grain boundaries, and is often intergrown with K-feldspar at the margins of porphyroblasts to form myrmekite. These features are indicative of deformation at moderate to high strain rates on the retrograde path, after the fabric was formed at higher temperatures by recrystallisation of mica.

Brittle faults in the LSZ are often associated with narrow bands of intense alteration to fine-grained chlorite and white mica, suggesting infiltration by fluids. These brittle faults are more common towards the western margin, as the outcrop of the Liachar Thrust is approached. Thus rocks in the Liachar Shear Zone have experienced deformation at a range of temperatures as they have approached the surface, with deformation at lower temperatures being increasingly partitioned and brittle.

Elsewhere in the Tato Valley, orthogneisses display similar compositions with or without garnet, and varying degrees of deformation. Z134 is a garnet-bearing orthogneiss collected from the Grande Moraine at about 4000m. It is of meta-igneous origin, containing biotite (15%), garnet (10%), K-feldspar (30%, quartz (30%) and plagioclase (20%). It shows a fine-grained equigranular texture, biotite showing a slight preferred orientation but no strong schistosity. Relict garnet porphyroblasts of up to 3 mm contain quartz inclusions. Biotite near these porphyroblasts is altered to chlorite. Coarser biotite rims a leucosome which appears to cross-cut the weak fabric in the rock. The leucosome is coarse-grained,

with subhedral to euhedral crystal shapes. Plagioclase shows zoning, large strained quartz crystals have serrated grain boundaries with feldspars, and occasional biotite crystals are randomly oriented and strongly altered to chlorite.

In the Rupal Valley, muscovite is present with biotite in schists which occur along the length of the valley. A typical sample is E101, which contains about 10% each of muscovite and biotite, 25% K-feldspar, 50% quartz, about 5% plagioclase, and occasional small tourmaline crystals. Biotite and muscovite are oriented parallel to the foliation, wrapping anhedral K-feldspar porphyroblasts which contain quartz inclusions and show undulose extinction with minor alteration to sericite. Strained quartz showing subgrain formation fills leucocratic segregations (Fig. 2.12). Plagioclase is unzoned, and the assemblage appears to be in textural equilibrium, although deformation has led to some grain size reduction. The presence of primary muscovite suggests that this sample has not crossed vapour-absent muscovite breakdown reactions, in contrast to lithologies from the Tato valley.

2.3.3.2 Pelitic gneisses

Pelitic gneisses are the most useful for thermobarometric techniques, and will be described in more detail in Chapter 3. Typical metapelitic assemblages contain quartz, sillimanite, biotite, potassium feldspar and plagioclase feldspar, with variable occurrences of garnet, cordierite, spinel and muscovite. Ilmenite, pyrite and apatite are common accessory phases, with rutile, magnetite, chalcopyrite, zircon and monazite occurring more rarely. Kyanite was not observed from the field area, but has been previously observed in the MMT zone on the western margin (Misch, 1949). Muscovite is found in the Rupal Valley, and in the Tato valley on the margin of the massif (figure 2.1), but does not occur as a primary phase in the core of the massif where cordierite seams are observed.

The most recent fabrics are defined by sheaves of biotite and sillimanite, wrapping around garnets. Where inclusion trails are visible in garnet, they usually consist predominantly of quartz and opaque minerals, mostly ilmenite, at a high angle to the most recent fabrics. This observation is taken to indicate that garnet growth predated the latest deformation and metamorphism. Garnet often assumes a relict appearance (Fig. 2.13), and in more aluminous lithologies is often mantled by cordierite, though not apparently associated with leucosome formation. This texture has been observed in metapelites from the central Himalaya, and interpreted to indicate decompression at high temperatures (Inger and Harris, 1992). Further evidence for decompression is provided by plagioclase coronas between garnet and quartz, formed by the GASP reaction (Fig. 2.14).

Biotite from pelitic horizons has a relict appearance where cordierite is present, in contrast to its occurrence as the major fabric-forming phase in less aluminous lithologies. Where found to be breaking down, it is often partially replaced by ilmenite (Fig. 2.15). In higher grade rocks thin zones of cordierite ± spinel are seen intimately associated with decomposing biotite (Fig. 2.16). These textures and the significance of spinel will be investigated in Chapter 3.

Fig. 2.15. Photomicrograph of pelitic gneiss N1 from Fairy Meadows, showing biotite, garnet and sillimanite breaking down, to produce cordierite and ilmenite. Plane polarised light, long dimension of the photo is ~ 1 mm.

Fig. 2.16. Photomicrograph of pelitic gneiss Z147 collected as float from the upper Raikhot Glacier. Biotite and sillimanite are breaking down to produce cordierite and spinel. Plane polarised light, long dimension of the photograph is ~ 3 mm.

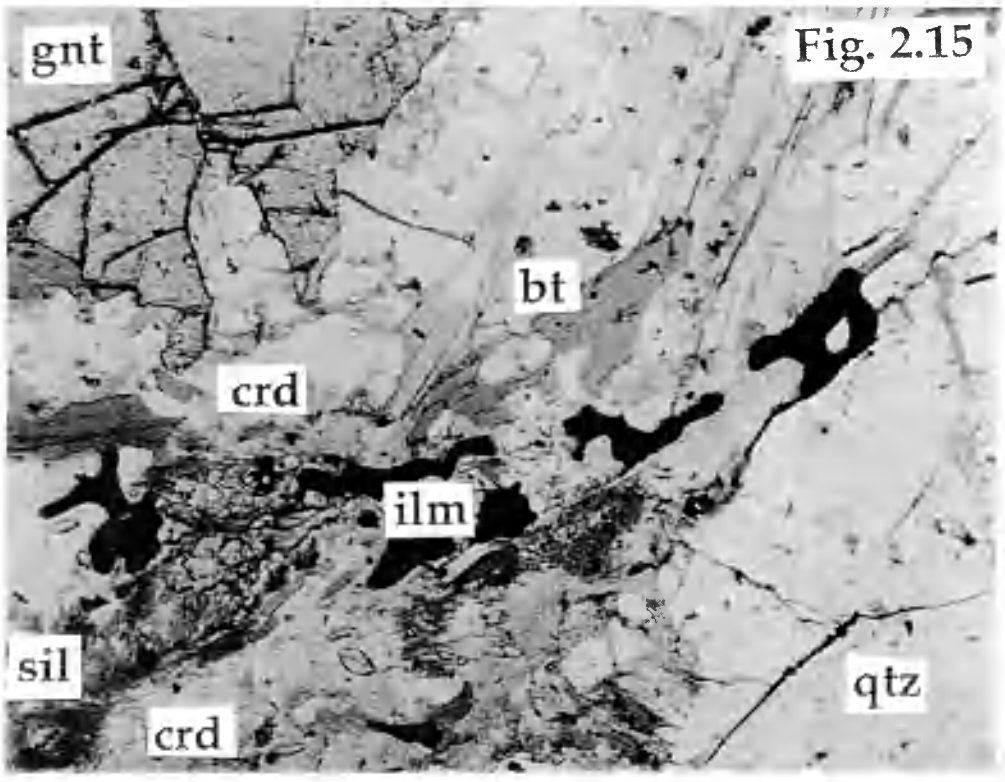
gnt
Fig. 2.15
bt
crd
ilm
sil
qtz
crd

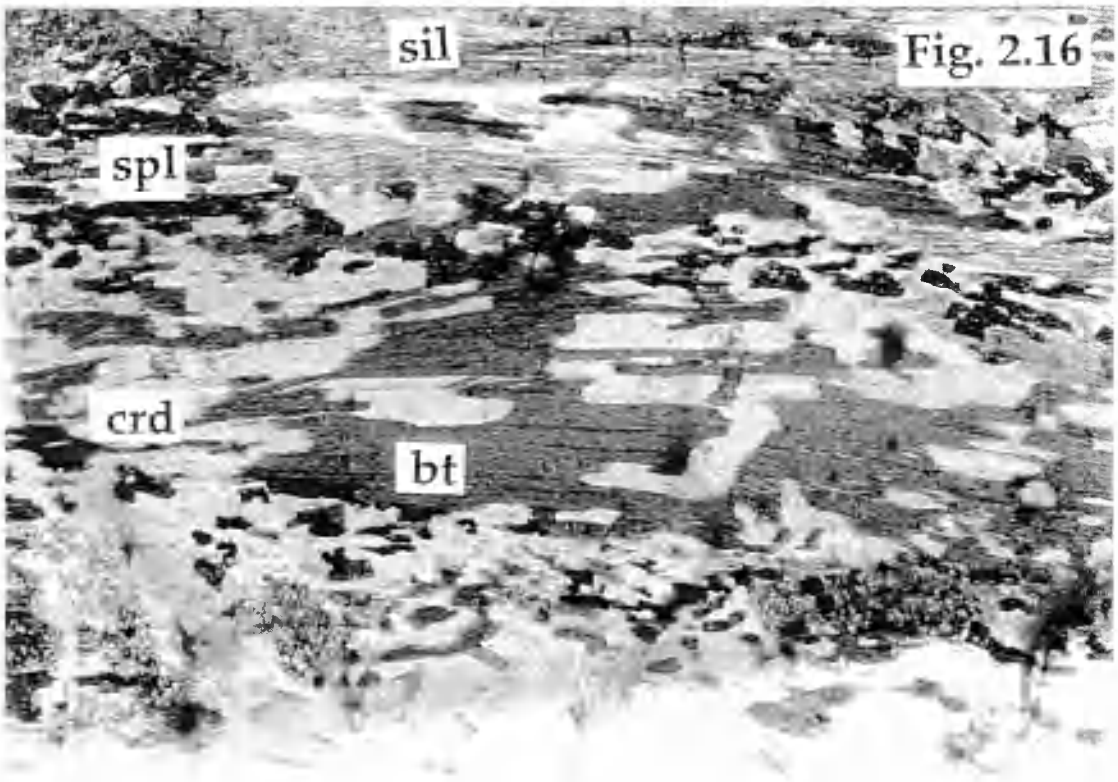
sil
Fig. 2.16
spl
crd
bt

2.3.3.3 Basement calc-silicates

True marbles are rare in the Nanga Parbat basement gneisses. Calc-silicate lithologies are more common, although they were not found in the Rupal Valley. Typical assemblages include calcite and/or dolomite, with diopside and/ or calcic amphibole. Plagioclase, quartz, wollastonite, grossular garnet, magnesium-rich spinel, epidote and phlogopite are also observed in calcium-rich lithologies. The rocks are usually banded, with pale green layers composed primarily of pyroxene alternating with white layers composed primarily of carbonate and plagioclase, and sometimes pink layers containing grossular garnet. These rocks often deform in a brittle fashion, while adjacent pelitic lithologies undergo ductile deformation, and rotation of rigid blocks of calc-silicate is a useful shear-sense indicator in the Liachar Shear Zone (Fig. 2.5). Where deformation is coaxial, green layers appear to behave as rigid bodies, while pale segregations of calcite and quartz fill boudin necks.

Z150 is a magnesian marble collected from the glacier adjacent to the Grande Moraine at an altitude of 4000m. It is white and crystalline in hand specimen, with randomly oriented elongate green crystals up to 3 mm long. In thin section, it can be seen to be comprised predominantly of polygonal matrix calcite and dolomite (60-65% combined), with cracked anhedral diopside phenocrysts (15%). Anhedral wollastonite (15%) also occurs as a coarser phase, with subhedral to euhedral green magnesian spinel (<5%) and occasional pleochroic phlogopite (<5%). The assemblage appears to be in equilibrium, and while carbonate grains occasionally have bent twin planes, the rock shows little evidence for deformation (Fig. 2.17).

Z124 is a more typical layered calc-silicate collected from below Jalipur Pass at an altitude of about 3800m. It contains tight folds which show up spectacularly due

to the colour variation across different lithological layers, which occur on a cm scale. In thin section, it is seen to be comprised of plagioclase (60%), clinopyroxene (30%), showing some replacement by amphibole and epidote (<5% combined), grossular garnet (<5%), and small euhedral sphene (<5%).

Clinopyroxene and plagioclase are very coarse, with crystals several mm in diameter, and form a granoblastic polygonal texture. There is evidence of late deformation and alteration, plagioclase feldspar shows cracked and rotated twin planes, while clinopyroxene shows fine-grained alteration along cracks, undulose extinction and subgrain formation, especially near fold hinges. Elongate clinopyroxene porphyroblasts have been pulled apart, with hornblende and epidote growing orthogonally to the direction of extension, while small anhedral orange-brown grossular is common.

The replacement of clinopyroxene by amphibole is a common feature of Nanga Parbat rocks (Fig. 2.18). This and other features of this rock provide further evidence for retrograde metamorphism accompanied by weak deformation and late alteration during exhumation of the NPHM.

Fig. 2.17. Photomicrograph of marble Z150, showing stable spinel-diopside-calcite assemblage. A small crystal of phlogopite is just visible at the right hand side, and appears to be breaking down. Plane polarised light, long dimension of photograph is ~ 3 mm.

Fig. 2.18. Photomicrograph of calc-silicate Z124, showing green hornblende replacing pale clinopyroxene in the presence of plagioclase and quartz. Plane polarised light, long dimension of the photograph is ~ 3 mm.

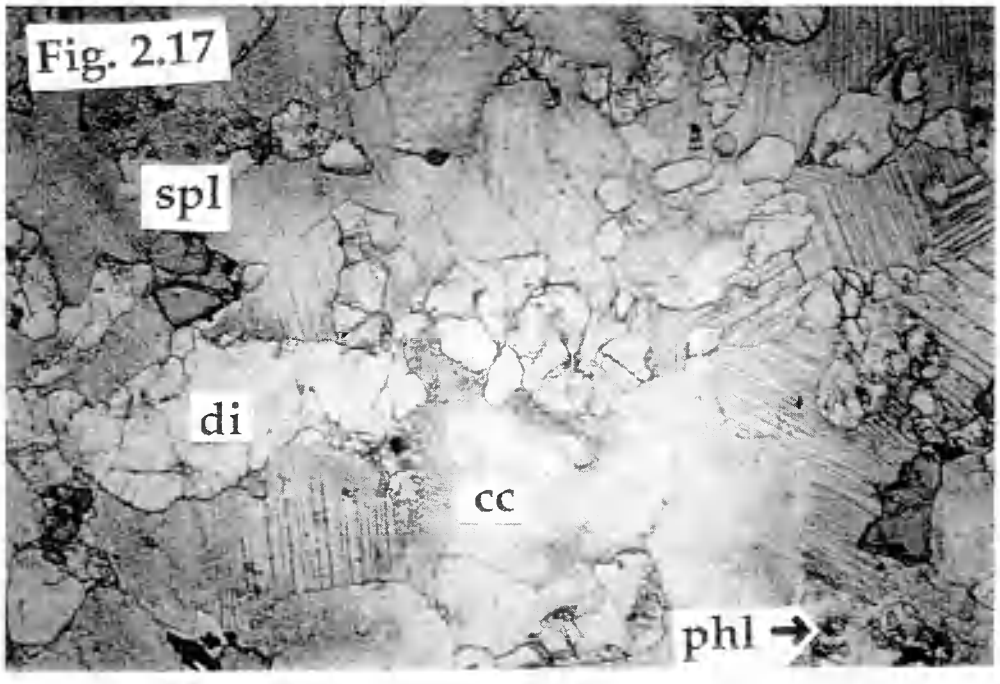
Fig. 2.17
spl
di
cc
phl

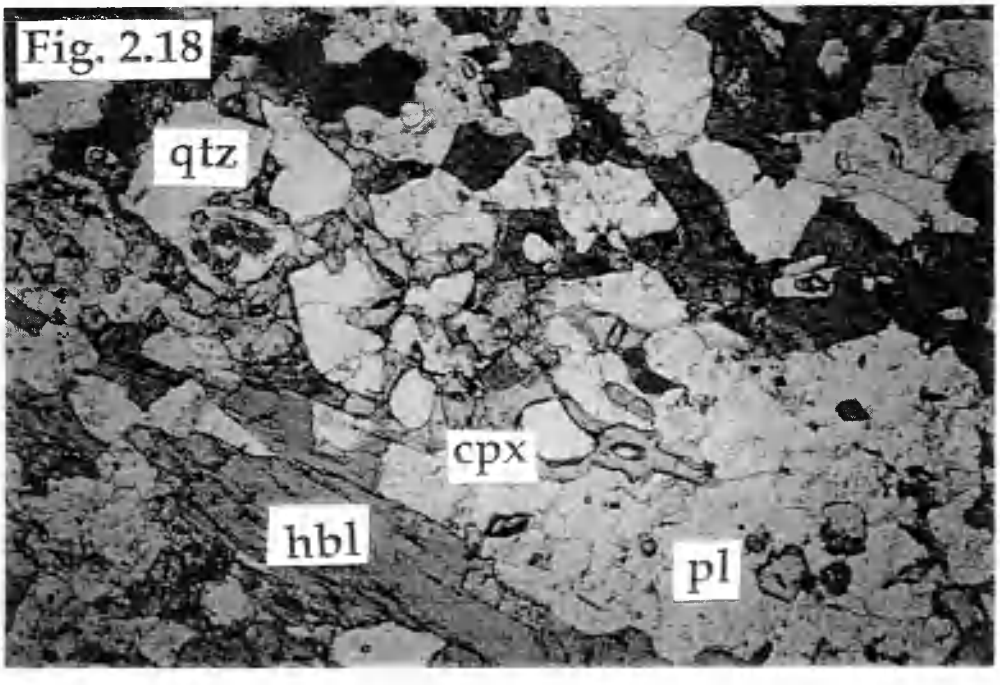
Fig. 2.18
qtz
cpx
hbl
pl

2.3.4 Amphibolite dykes

Amphibolite dykes occur frequently within the field area, and are usually strongly retrogressed to biotite and chlorite, giving them a green crumbly appearance, unsuitable for thin sectioning. Their field relations are important, because they cross-cut lit-par-lit migmatitic fabrics in basement gneisses, particularly well illustrated in the Main Mantle Thrust zone at Raikhot Bridge, where they are in turn sheared by top-to-the west ductile shear zones associated with the Liachar Shear Zone (Fig. 2.19). Within the LSZ, intense ductile deformation has resulted in near-concordance between the amphibolite sheets and basement fabrics (Winslow et al., 1995). However, several studies have documented similar sheets cross-cutting migmatitic fabrics in all parts of the NPHM (Butler et al., 1992; Butler et al., 1997; George, 1993; Pognante et al., 1993; Wheeler et al., 1995), and therefore these bodies are an important chronological marker between pre-Himalayan metamorphism and more recent fabrics.

Although the majority of dykes observed in the field were altered to lower-greenschist facies assemblages, two were found in relatively pristine condition. E104 (5 samples) was collected from an altitude of over 4000m on the south side of the Rupal Valley, near Shaigiri (Fig. 2.10), and was deformed by a north-verging shear zone. In hand specimen it is dark green, well foliated and is medium- to fine- grained.

In thin section, the rock is comprised mainly (>85%) of large acicular hornblende laths, up to 5 mm across, showing light brown to olive green pleochroism, well developed cleavages (at c. 56°), and extinction inclined at 15 to 20° from the long axes of the crystals. Plagioclase and K-feldspar (12% combined) show zoning, and contain rare small hornblende inclusions (Fig. 2.20). Small biotite crystals (2%) are aligned parallel to foliation, and show alteration to chlorite with other very fine-grained alteration products along small cracks. Subgrain formation, deformation

bands and undulose extinction within amphiboles suggest some deformation (Fig. 2.21). Amphiboles deviate in long axis orientation by up to about 15° from the main plane of foliation, and relict porphyroblasts contain rounded K-feldspar and plagioclase inclusions. Some alteration around rims may indicate late fluid infiltration.

E119 (5 samples) was collected from about 3800m on the western side of Bayal Camp, from a poorly exposed outcrop such that field relations were not clear. The amphibolite body is planar and cross-cut by a leucogranite sheet, but whether E119 is from an amphibolite dyke, a conformable paragneiss, or a syn-sedimentary volcaniclastic flow, is uncertain. This sample is fine-grained and equigranular with a strong foliation defined by acicular biotite (5-15%), subhedral pleochroic hornblende (60%) with a strong preferred orientation, subhedral to anhedral plagioclase (10-15%) and undeformed quartz (20%). There is no evidence for overprinting of a previous fabric.

A third body was sampled from 4950m on the Jalipur Pass (E155), but unfortunately field relations were obscured by snow cover. The prominence of this body on the ridge may be due to its mineralogy, containing clinopyroxene, plagioclase and brown chrome spinel.

Fluid flow appears to be preferentially channelled through amphibolites, as shown by their frequent pervasive alteration. Are the currently observed assemblages igneous, metamorphic or metasomatic? While feldspars show (igneous?) zoning, the textures appear to be metamorphic, although the near-monomineralic nature of this rock may suggest some metasomatism has occurred. The mineral chemistry of the various amphibolite bodies is described further in Chapter 3, and their geochemistry and petrogenesis are investigated in Chapter 5.

Fig. 2.19. Photograph of amphibolite dykes at Raikhot Bridge. These cross-cut the main gneissic foliation, but are themselves deformed by subsequent shears related to uplift of the Liachar Thrust. Looking south, the field of view is ~ 8 m wide.

Fig. 2.20. Photomicrograph of basic dyke E104, showing small hornblende inclusions in plagioclase feldspar. Crossed polars, long dimension of the photograph is ~ 1 mm.

Fig. 2.21. Photomicrograph of basic dyke E104, showing brittley deformed inclusion-rich hornblende . The field of view is filled with one large crystal. Crossed polars, long dimension of the photograph is ~ 3 mm.

Fig. 2.19

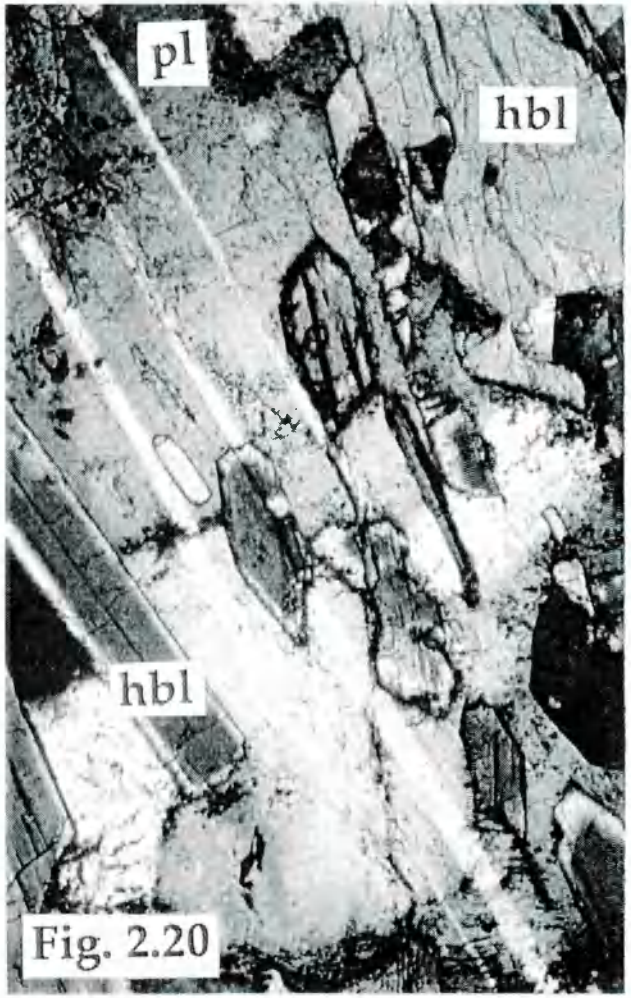

Fig. 2.20

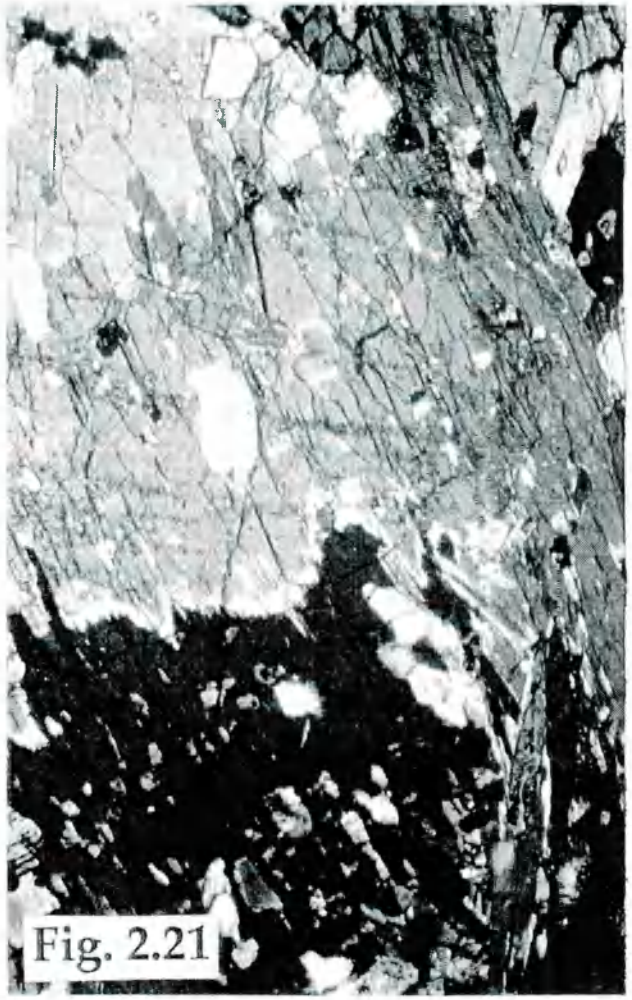

Fig. 2.21

2.3.5 Leucogranites

Leucogranite plutons from the NPHM were first reported from a poorly exposed locality at Jutial in the north-west of the syntaxis (Butler et al., 1989). In the southern part of the massif, a well-exposed pluton and numerous leucogranite sheets have been observed (Figs. 2.22 and 2.23). Post-collisional leucogranites are one of the most distinctive features of the Himalayan orogen, and the Nanga Parbat leucogranites share many features with those from the main orogen, particularly mineralogy, major- and trace-element geochemistry (Chapter 4).

2.3.5.1 Tato Pluton

The Tato pluton shows sharp contacts discordant to gneissic foliation, but no chilled margin. The pluton appears to be both compositionally homogeneous and undeformed throughout its outcrop, both horizontally over at least 2 km, and vertically throughout 500m. The pluton is a medium to coarse grained leucogranite containing quartz (30 to 35%), perthitic alkali feldspar (30 to 35%), zoned plagioclase feldspar (25 to 30%), biotite (<5%), tourmaline (< 5%), and muscovite (< 2%). Despite indicators of minor brittle deformation in the pluton, no magmatic flow fabric or pervasive deformation fabric can be observed, either in the field or in thin section (Figs. 2.24 and 2.25).

2.3.5.2 Leucogranite sheets

There are also numerous leucogranitic sheets and dykes associated with the pluton, rarely more than 1 metre in width. In the core of the massif, both on the Fairy Meadows and Rupal sides of Nanga Parbat itself, undeformed sheets are usually subhorizontal in orientation, consistent with vertical extension during

unroofing of the massif. Several sheets show textures indicative of multiple episodes of magma injection, and tourmaline crystals are often aligned at the margins of successive magma batches, or within single injection horizons.

Z105 from the Rupal Valley shows narrow zones of intense deformation and grain-size reduction in thin section. K-feldspar phenocrysts appear as augen surrounded by conjugate anastomosing shear zones, with subgrain formation and sericitisation around rims, indicating some fluid infiltration and alteration (Fig. 2.26). Subhedral plagioclase crystals preserve zoning, but also show subgrain formation and deformed twin planes. Muscovite is generally aligned parallel with shear zones, while tourmaline is undeformed. Biotite is not present in this sample. These features indicate post-crystallisation deformation at high strain.

On the western margin of the massif, leucogranitic dykes are often coarser-grained and pegmatitic, and have been deformed in the Liachar Shear Zone (Fig. 2.27). Boudinaged dykes show pre-full crystallisation deformation fabrics, indicating syn-tectonic emplacement (Butler et al., 1997). Some sheets are almost entirely quartzofeldspathic, while others contain small euhedral clean garnets, and in some cases pegmatites show tourmaline and biotite growth up to several centimetres long. Occasional late cross-cutting aplites can be found, apparently undeformed by the Liachar Shear Zone, suggesting their emplacement was very recent.

Fig. 2.22. Photograph of the Tato pluton, distinctly lighter than the surrounding gneisses of the Jalipur ridge, looking west from Fairy Meadows. The field of view is approximately 4 km wide.

Fig. 2.23. Photograph of the summit region of Nanga Parbat (8126 m), looking north from Shaigiri. Note large volumes of leucogranite (including the summit itself) and associated feeder dykes, which cross-cut fabrics in surrounding gneisses. Vertical extent of cliffs is ~ 1500 m.

Fig. 2.24. Close-up view of the Tato pluton, showing homogenous undeformed igneous texture, with biotite and tourmaline clearly visible in hand specimen. The coin is ~ 15 mm in diameter.

Fig. 2.22

Fig. 2.23

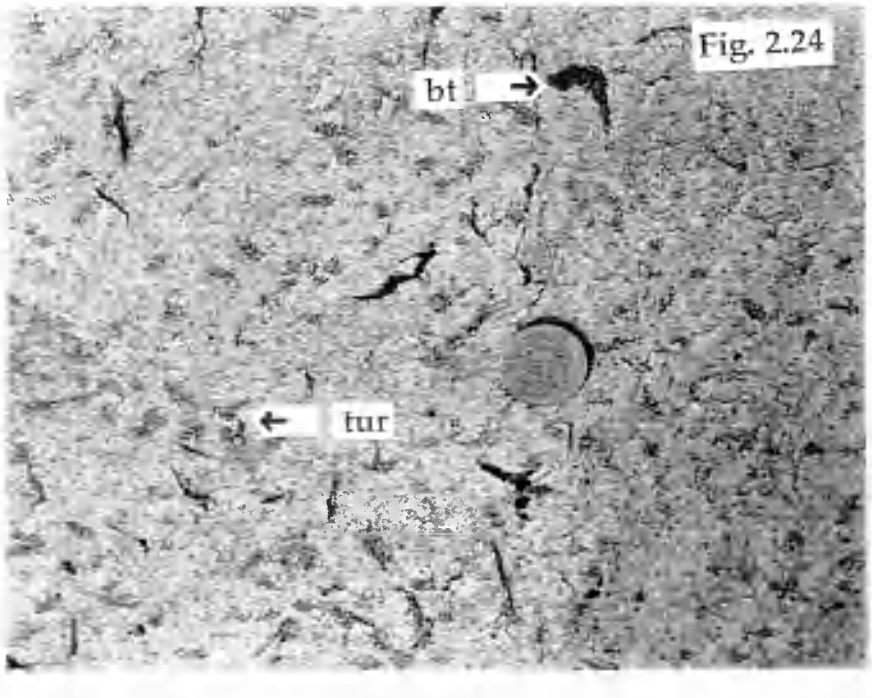

Fig. 2.24

Fig. 2.25. Photomicrograph of Z141 from the Tato Pluton at Bezar Gali. Note green compositionally zoned tourmaline crystals clumping together. Plane polarised light, long dimension of the photograph is ~ 3 mm.

Fig. 2.26. Photomicrograph of Z105, a brittley deformed leucogranite sheet collected from below the Rupal Face. Note large K-feldspar porphyroclast showing subgrain formation and undulose extinction, with grain-size reduction near the margin of the crystal. Matrix quartz shows highly irregular grain boundaries and small grain size. Micas in the matrix show minor alteration around crystal margins. Crossed polars, long dimension of the photograph is ~ 3 mm.

Fig. 2.27. Pegmatitic leucogranite dyke deformed synkinematically in the Liachar Shear Zone, viewed looking south-west. Note offset of leucocratic bands in host gneiss, which are genetically unrelated to the granite sheet. Field of view is ~ 1.5 m wide.

Fig. 2.25

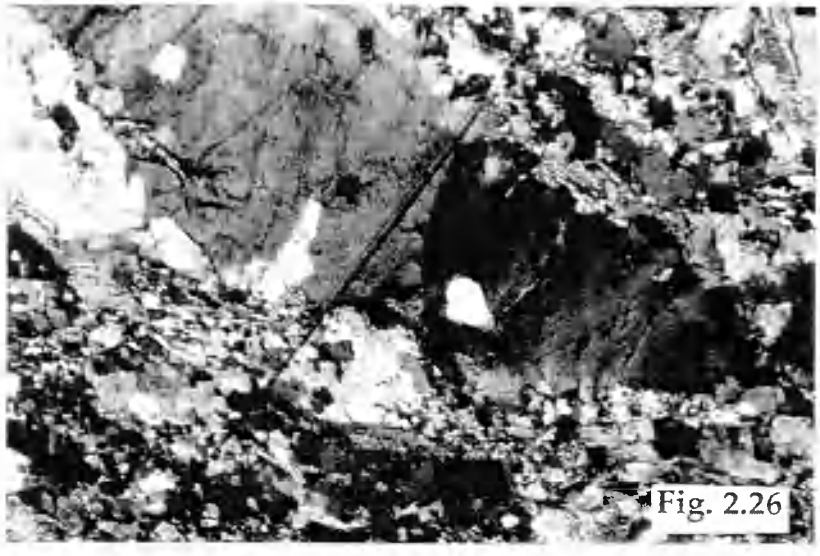

Fig. 2.26

Fig. 2.27

2.3.6 Cordierite-bearing leucosomes

Cordierite-bearing leucosomes form nebulous, bleached areas containing dark nodules which comprise about 10 to 20 percent of the exposed bleached area, and are rarely more than 50 cm across. These nodules sometimes occur as thin bands ghosting biotite foliation, indicating that biotite is an essential reactant. This latest metamorphic event is generally localised in shear zones but not offset by them. Seams appear to cross leucogranite sheets, and sheets are deformed by shear zones containing seams. Cordierite nodules are however rarely found where seams cross sheets or leucocratic bands (Fig. 2.28), perhaps due to the paucity of biotite in many sheets preventing cordierite growth. This can give the impression of sheets cross-cutting seams, and it may be that formation of the two was coeval during exhumation. The relation between cordierite seams and cordierite pegmatites is also unclear (Fig. 2.29).

Cordierite seams are found in the Tato valley south of the village itself, in a variety of biotite-bearing lithologies. They are not found *in situ* in the Rupal valley to the south of Nanga Parbat (Fig. 2.10), but occasional boulders containing seams can be found in scree and in moraine deposits, suggesting that seams do exist higher up on the Rupal Face.

Some cut faces of these seams were stained with sodium cobaltinitrite solution to identify the distribution of alkali feldspar within hand specimens. Bleached areas of seams were found to contain very large quantities of potassium feldspar, with some grains occurring as inclusions within the dark nodules (Fig. 2.30).

Fig. 2.28. Leucogranite sheet overprinted by cordierite seams (arrowed), from Fairy Meadows. Deducing relations between the cordierite (green nodules, now mostly pinite) and leucogranite is made more difficult by lack of biotite inhibiting cordierite formation in the lower seam. Note sharp cross-cutting margins to the granite sheet. Compass is ~ 7 cm across.

Fig. 2.29. Tourmaline- and cordierite-bearing leucosomes in migmatitic gneiss. Deducing relations between the two compositions is near impossible in this case, although the presence of euhedral prismatic cordierite (arrowed) which is different in appearance to that seen in most cordierite seams, suggests a pegmatitic origin.

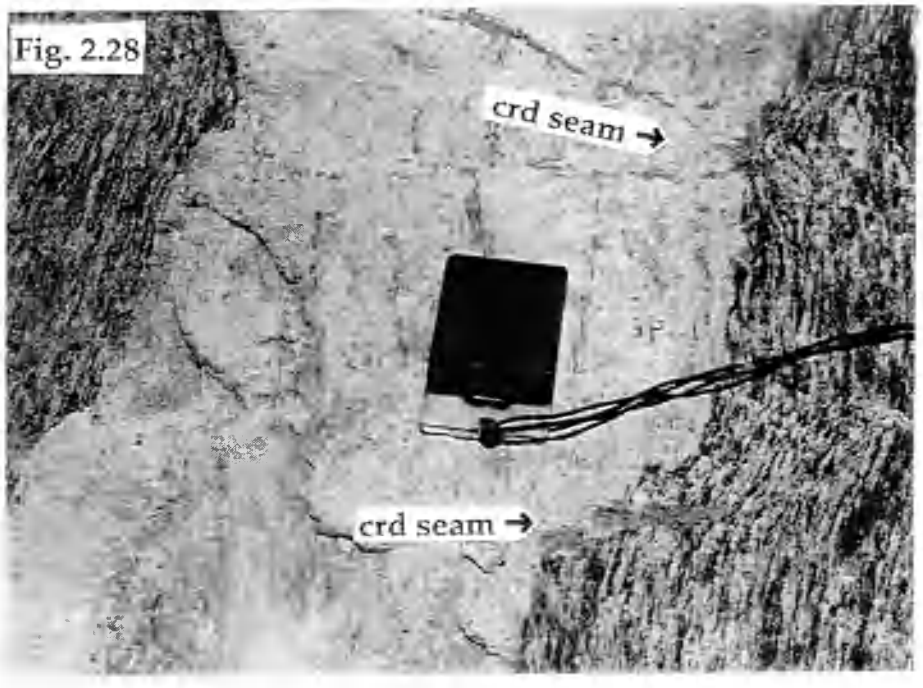

Fig. 2.28

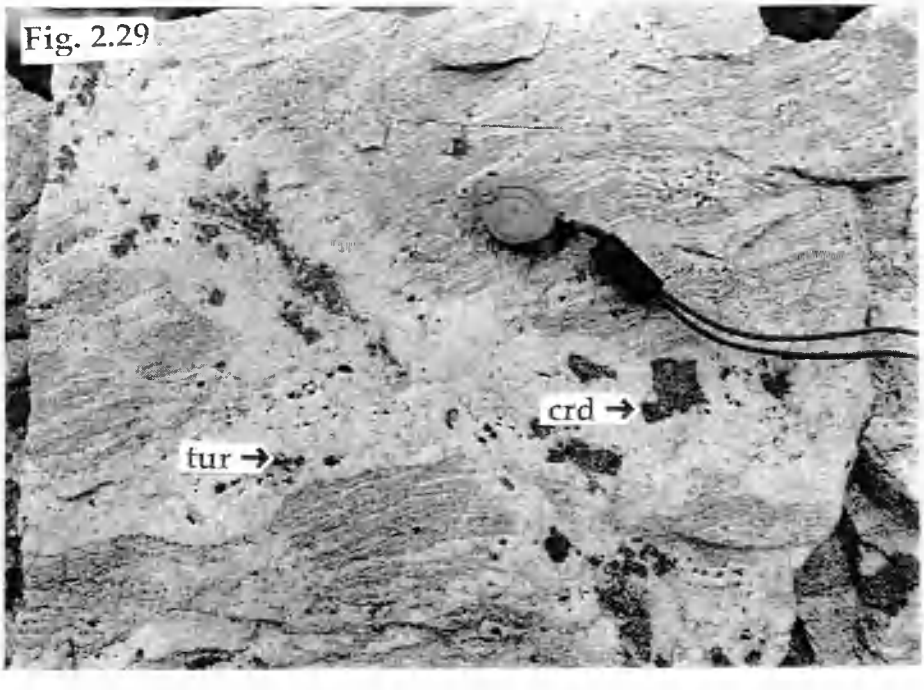

Fig. 2.29

Fig. 2.30. Cut slab of cordierite seam / pelitic gneiss sample Z130. Upper sample has been etched with HF and stained with sodium cobaltinitrite to stain K-feldspar yellow. Note substantial intergrowth of K-feldspar and cordierite (altered to green pinite), and K-feldspar rich layers in pelitic gneiss. Length of slabs is ~ 9 cm.

Fig. 2.31. Photomicrograph of cordierite seam X4, showing interlocking cordierite and K-feldspar. Cordierite has higher relief and is altered to pinite around crystal margins. Plane polarised light, long dimension of the photograph is ~ 3 mm.

Fig. 2.32. Photomicrograph of cordierite seam X4, as for Fig. 2.31 but with crossed polars. Note classic cordierite cleavage (upper left of photograph), alteration to pinite, and deformed twin planes in K-feldspar.

Fig. 2.30

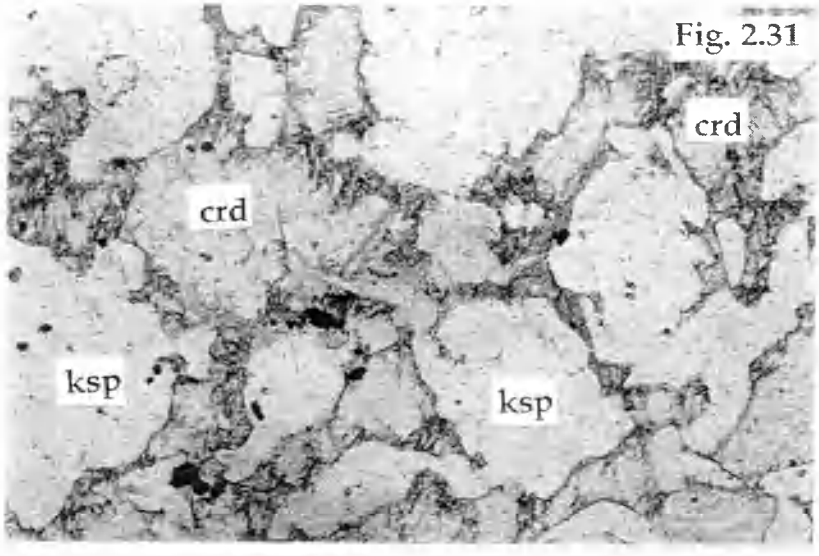

Fig. 2.31

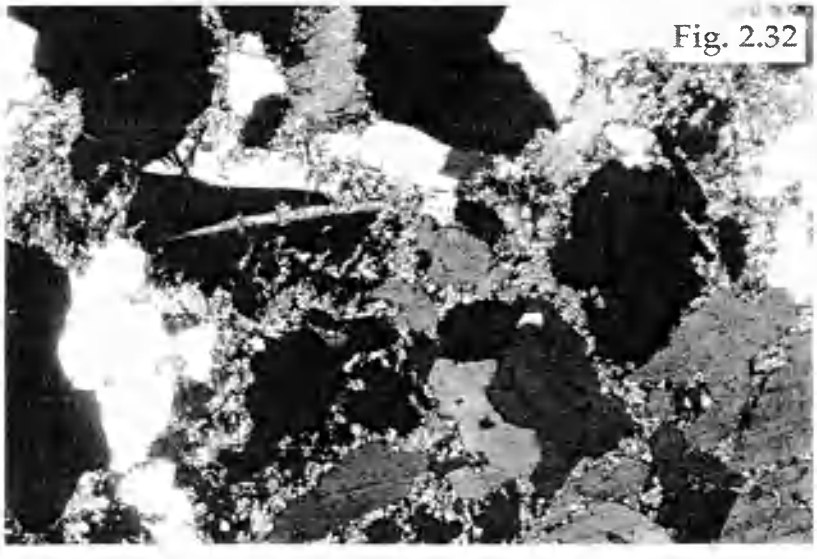

Fig. 2.32

In thin section seams are dominated by very coarse subhedral potassium feldspar crystals and interstitial cordierite, both phases enclosing generally rounded quartz grains (Figs. 2.31 and 2.32). These textures range in appearance from a cumulate texture to an interstitial grain-boundary texture, depending on the percentage area filled by cordierite. In general cordierite is usually altered around rims, and in some cases has been completely replaced by a fine-grained white mica aggregate (pinite). Further discussion of cordierite seams is contained in Chapter 4.

2.4 Summary and metamorphism-deformation history

A summary of the metamorphic and deformational history of the NPHM is shown in Table 2.1, several parts of which will be the subject of further discussion in subsequent chapters. The zircon core ages are interpreted here to date the precursors to the Iskere and Shengus gneisses, although there remains the possibility of the U-Pb system in zircon being reset during the granulite facies metamorphism which preceded the intrusion of the basic dykes. The early (pre-Himalayan) history of Nanga Parbat is discussed further in Chapter 5.

The lack of any reliable geochronology recording "Himalayan" ages from the NPHM is an interesting feature. While a few Ar-Ar ages from amphiboles have yielded apparent ages between 20 and 50 Ma, these are mostly thought to be erroneous due to incorporation of excess argon (Chapter 6). Until the unusual development of the NPHM during the late Miocene to present, the NPHM probably followed a similar P-T-t path to those parts of the Indian Plate basement which remain under the Kohistan-Ladakh arc. To the west in the nappe zones of Hazara and the Kaghan valley, currently exposed rocks experienced peak metamorphism prior to about 50 Ma. Nanga Parbat rocks will have been buried

deeper, and hence subjected to greater pressure, from the end of reverse movement on the MMT until rapid exhumation associated with syntaxial formation occurred at about 10 Ma. Even metamorphic monazite growth and zircon rim development record ages of <10 Ma, suggesting that the intervening time, about 40 Ma, was spent at temperatures greater than the U-Pb closure temperature in these minerals.

Associated with rotation of the Indian Plate and pinning of a major Himalayan thrust in the western Himalaya, syntaxial development has been rapid and has exposed rocks from different depths which have experienced different P-T-t paths across the massif. Exhumation in the eastern NPHM has been relatively passive on the limb of a crustal-scale antiform, but active tectonics on the western margin has exhumed rocks from depths of >30 km very rapidly. The gradual overprinting of reverse movement by strike-slip movement from north to south along the western margin suggests that the locus of the most rapid exhumation is migrating southwards, perhaps to the Besham area above the Indus Kohistan Seismic Zone.

Further evidence for the southwards migration of the most rapid exhumation through time comes from geochronology of leucogranites generated by decompression melting (Zeitler and Chamberlain, 1991; Butler et al., 1992; George, 1993; Butler et al., 1997; Chapter 4). Recently reported ages for the Jutial pluton in the northern NPHM are 10 ± 1 Ma and 5.2 ± 0.3 Ma for U-Pb in zircon and Th-Pb in monazite respectively (Schneider et al., 1997). These contrast with younger ages from leucogranites in the southern NPHM. The Tato pluton has been dated at 1.0 Ma by U-Pb on zircon (Zeitler and Chamberlain, 1991). The Mazeno Pass pluton is further south still, approximately 8 km west of Nanga Parbat, and has yielded U-Pb zircon and Th-Pb monazite ages of 1.4 Ma, while leucogranite dykes from the Rupal valley have yielded zircon and monazite ages of 2.2 Ma (Schneider et al., 1997). In contrast to the leucogranites, the generation of cordierite seams is controlled more by fluid flow than thermal structure, although any melting

requires temperatures in excess of 640 °C. These are discussed further in chapter 4.

Table 2.1. Summary of the metamorphism-deformation history inferred from field relations with absolute chronology from previous studies where available (references in the text).

Time	Event	Evidence
~2500 Ma	Precursor to (Shengus) gneiss	Inherited Pb component in basement zircons
~1850 Ma	Precursor to (Iskere) gneiss	Inherited Pb component in basement zircons
Precambrian?	Metamorphic event	Lit-par-lit migmatisation, granulite facies metamorphism
Precambrian?	Extensional event?	Basaltic sheets intruded
~500 Ma	Metamorphism of (Shengus) gneiss	Inherited Pb component in basement zircons
55 - 60 Ma	Himalayan collision	MMT fabric formed, subduction of NPHM beneath Kohistan. Garnets record P ≥ 10 kbar at T > 700 °C
12 Ma to present	Metamorphism,	Metamorphic monazite rims record ages between 3.3 and 11 Ma. Low pressure assemblages record P ≤ 4 kbar at T > 650 °C
	exhumation on Liachar Shear Zone,	Recrystallisation ages of 8 to 12 Ma on micas from ductile LSZ fabrics
	and crustal anatexis	Zircon leucogranite crystallisation ages of 1 to 10 Ma
		Cordierite-bearing leucosomes in shear zones
Present day	Rapid denudation and continued exhumation on LSZ	Brittle LSZ fabrics, hot springs, historic earthquakes, cooling ages <2 Ma (Ar-Ar), < 1 Ma (fission track)

From the evidence presented here, we would expect a clockwise P-T-t loop, with rapidly increasing pressure accompanying the obduction of Kohistan shortly after collision. Depending on the nature of subsequent imbrication of the combined Kohistan arc and Indian Plate rocks, different parts of the NPHM may have experienced different P-T-t paths, although no clear evidence has been found for such imbrication so far north, in contrast to the Hazara and Besham regions to the southwest. Left at depth for tens of millions of years, thermal relaxation would be expected to promote near-isobaric heating, depending on exhumation rates over this period. With rapid syntaxial development initiating at about 10 or 12 Ma, rapid exhumation would produce near-isothermal decompression along an adiabatic path, followed by rapid cooling as the surface is approached. Since thermal relaxation operates over a timescale of several tens of millions of years, this simplified P-T-t history would explain why geochronometers fail to record ages in the range 20 to 50 Ma in the NPHM, because peak temperatures were only attained at the initiation of rapid exhumation. Chapters 3 and 7 contain further discussion of the metamorphic history and P-T path followed by rocks of the southern NPHM.

Exhumation has been accommodated by a combination of erosion acting on an actively growing crustal-scale antiform, and by movement on discrete shear zones. Within the upper 8 km of crust, magmatic and meteoric fluid fluxes are channelised by active structures, providing a feedback mechanism for focussing deformation. At subsolidus temperatures meteoric fluids promote strain localisation and may trigger cataclastic deformation. These processes are still active, as demonstrated by historic seismic activity and massive hill slope failures.

CHAPTER 3 - METAMORPHISM OF THE SOUTHERN NANGA PARBAT HARAMOSH MASSIF

3.1 Introduction

The purpose of this chapter is to investigate conditions of metamorphism in the NPHM, and the direction of change of those conditions, i.e. the P-T path. Section 3.1 reviews previous work in the NPHM, and the thermobarometric techniques used in this contribution. Section 3.2 presents P-T estimates from pelitic, calc-silicate and amphibolitic lithologies using Thermocalc, and augments the existing database of P-T data from the massif. Section 3.3 reports garnet zoning profiles from metapelitic lithologies, and discusses their significance for P-T-t paths. Section 3.4 investigates the petrogenesis of spinel-bearing metapelitic assemblages which are found only in the interior of the massif, and are the first reported occurrence of spinel in metapelites from the Himalayas. The findings of this rather lengthy chapter are summarised in section 3.5.

3.1.1 Previous work

This chapter deals with the metamorphic history of the southern Nanga Parbat Massif as deduced from textural relations and thermobarometric techniques. Previous workers in the NPHM have applied standard geothermometers such as Fe-Mg exchange in biotite, and standard geobarometers such as garnet-aluminosilicate-sillimanite-plagioclase (GASP), using analyses from rims of phases in textural equilibrium. Two previous studies have undertaken modelling of P-T

paths from garnet growth zoning profiles using the Gibbs method (Spear and Selverstone, 1983). A summary of previous P-T estimates is shown in Fig. 3.1a.

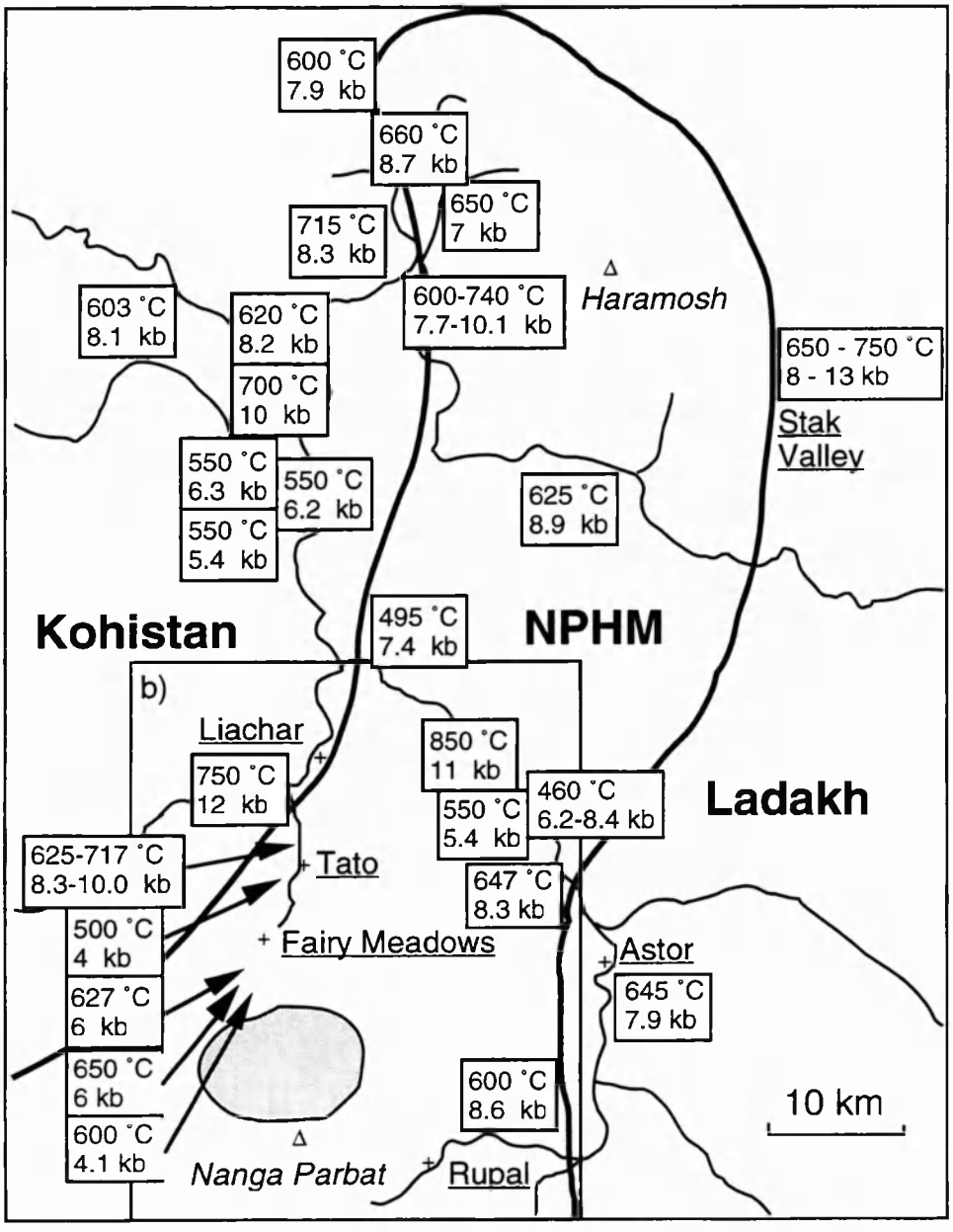

Figure 3.1a). Summary of previous thermobarometric data from the NPHM. The shaded region indicates the location of spinel-bearing samples discussed in section 3.4. Data compiled from Chamberlain et al. (1989), George (1993), Pognante et al. (1993), Zeitler et al. (1993), and Winslow et al. (1995).

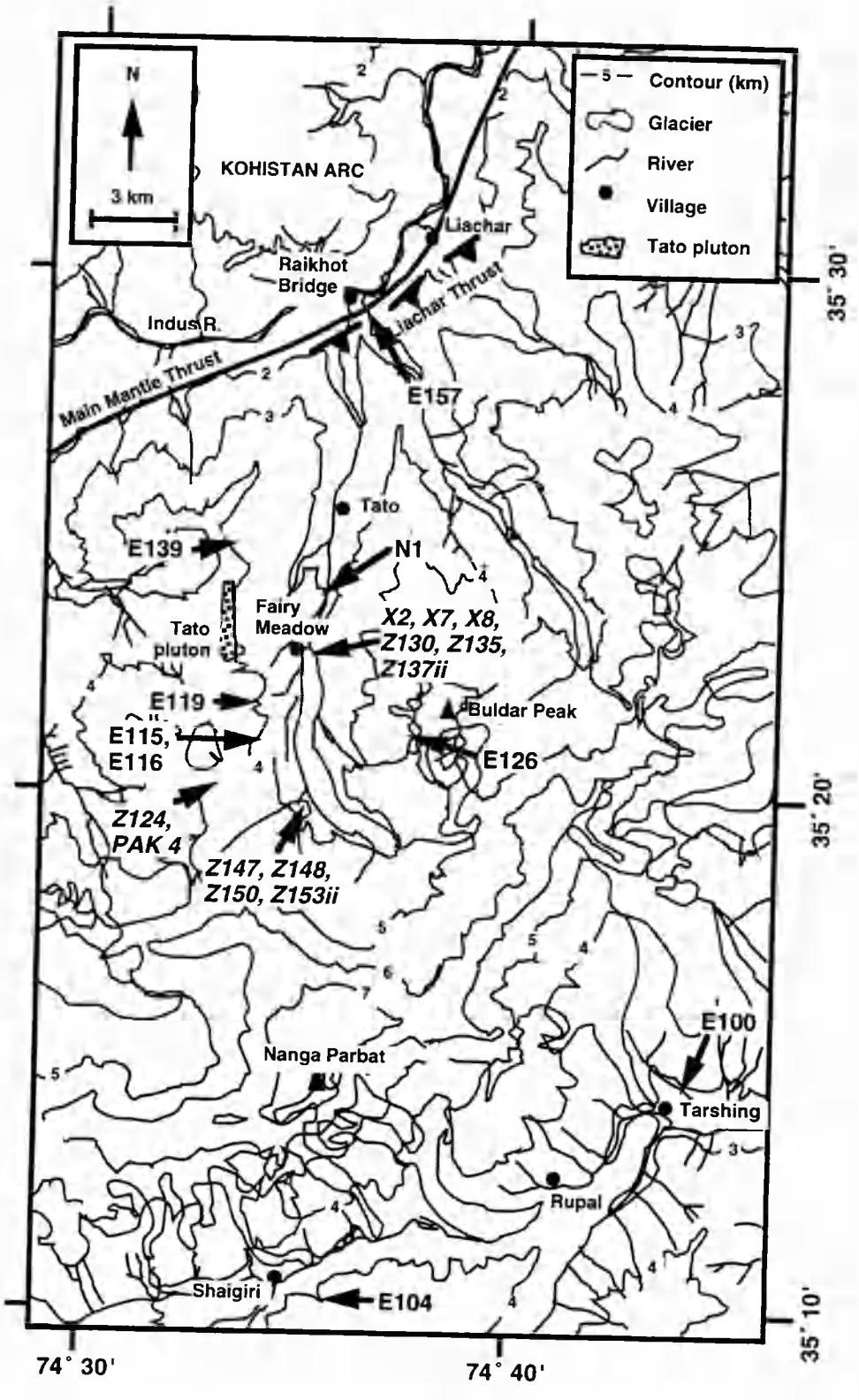

b) Location map for samples collected during this study. Italic font indicates float sample collected from glacier, normal type indicates sample was collected from outcrop.

The first metamorphic study of the massif was undertaken by Peter Misch, accompanying the German mountaineering expeditions of the 1930s. Misch (1949) described concentric isograds around Nanga Parbat, with both metamorphic grade and amount of granitic material increasing as the summit region was approached. Metamorphic grade was considered to be controlled by variation in peak temperature, while peak pressures were considered to be approximately constant throughout the massif, so that isograds were interpreted to be near-vertical. While distinguishing between late, post-tectonic tourmaline leucogranites (the Tato pluton and associated sheets), and older granitic basement, Misch (1949) attributed the increase in granitic material exposed in the interior of the massif to be due to the action of hot granitising fluids. These were considered by Misch (1949) to be both the agent of heat transfer, enabling the transformation of kyanite to sillimanite within the massif interior, and the agent of alkali transport, enabling the transformation of metapelitic gneiss to granite.

The same features which Misch (1949) attributed to granitisation are now interpreted as *in situ* migmatisation (Chapter 2), leading to lit-par-lit migmatites which show no evidence for melt injection. Had Misch (1949) noted the presence of cordierite in the interior of the massif, his interpretation of an isobaric event may have also been revised.

Misch (1964) developed his interpretation of the thermal and fluid history of Nanga Parbat by investigating calc-silicate assemblages. He divided these into three zones, which corresponded with zones previously described for pelitic assemblages (Misch, 1949). The highest grade rocks of zone 1 contained wollastonite and anorthite, with grossular absent. Zone 2 contained wollastonite, grossular, and either calcite or quartz, while the lowest grade rocks of zone 3 contained calcite and quartz, with grossular and diopside, and no wollastonite. In impure calc-silicates, the assemblage forsterite-spinel-phlogopite was noted in the highest grade rocks. Retrograde reactions producing scapolite after plagioclase,

and skeletal grossular after wollastonite and plagioclase, were also noted. Most of these petrographic observations have been reproduced in this study, but with subsequent advances in thermobarometry this chapter will attach P-T estimates to these assemblages.

Chamberlain et al. (1989) used Gibbs modelling to generate P-T paths from garnet zoning. Six samples in a traverse from Kohistan through the NPHM to Ladakh gave final temperatures and pressures between 450 and 650°C at 5.3 to 14.5 kbar for the NPHM, and 550 to 715 °C at 5.3 to 8.3 kbar in Kohistan. There was considerable overlap between conditions recorded in Kohistan and NPHM samples, and the low temperatures obtained from rim analyses in both terranes are probably due to retrograde re-equilibration. Five samples were modelled with the Gibbs method, and gave every combination of P-T path possible (Chamberlain et al., 1989, Fig. 4). NPHM samples recorded increasing pressure with increasing or decreasing temperature, while Kohistan samples recorded decreasing pressure with increasing or decreasing temperature.

Chamberlain et al. (1989) interpreted these results as recording movement on the MMT, where the NPHM was underthrust beneath Kohistan, resulting in increasing pressure during garnet growth in the NPHM. This model would imply that garnet growth was of Himalayan age, rather than Neogene, since the MMT transported Kohistan southwards over the NPHM (Butler et al., 1988b) and was not involved in syntaxial development.

George (1993) conducted a metamorphic study across the NPHM and eastern Kohistan, using Thermocalc to generate combined (PT) estimates, and showed that low pressures were recorded by rocks from Tato (4 kbar at ~500°C) and Fairy Meadows (6 kbar at 627°C), with higher pressures of 6 to 12 kbar recorded by rocks of the northern NPHM and Kohistan. George (1993) undertook Gibbs modelling on 7 samples, and obtained a path of increasing P and T for a sample

from the Kohistan arc, in contrast to the path obtained by Chamberlain et al. (1989). Decreasing P and T paths were obtained for two samples from the Astor gorge, while one sample from Astor recorded increasing P and T. No sample showed increasing P with decreasing T, in contrast to two samples analysed by Chamberlain et al. (1989). From the western margin, one sample from Sassi recorded increasing T and increasing P, while another sample from Sassi and one from Liachar showed increasing T and decreasing P.

These disagreements between studies, and between adjacent samples from the same study, may reflect the many assumptions inherent in using the Gibbs method (Florence and Spear, 1993), some of which may not be justified. The assumption of a known mineral assemblage during garnet growth depends on a complete assemblage being retained in inclusions. The assumption of continuous growth zoning unmodified by later diffusion or retrograde re-equilibration is also dubious, especially given that recorded rim temperatures of 500°C or less are anomalously low within this area, and suggests significant diffusive modification of growth profiles (Florence and Spear, 1993; Jiang and Lasaga, 1990).

Zeitler et al. (1993) obtained two P-T estimates from the Tato region of 650 ± 50°C at 6 ± 1 kbar for a pelite, and ~600 °C at 4.1 ± 1 kbar for a garnet-cordierite-sillimanite "melt sample". These estimates were taken to imply near-isothermal decompression in the core of the massif.

Pognante et al. (1993) undertook a study of the north-eastern margin of the NPHM, in the Stak and upper Turmik valleys (Fig. 6.1). Kyanite was the stable aluminosilicate phase, with no evidence for the presence of sillimanite, and some incipient migmatisation was observed. Peak P-T estimates of 650 to 700 °C at 8 to 13 kbar were determined using several geothermometers and geobarometers, and Gibbs modelling of garnet zoning suggested a path of decreasing P and T. Pognante et al. (1993) proposed a model where high convergence rates lead to

rapid subduction and exhumation, and hence lower thermal gradients than areas further east, with only incipient migmatisation. This model may explain why the preservation of eclogites around the suture zone is restricted to the western Himalaya (Tonarini et al., 1993; Spencer et al., 1995), although this would suggest that the margins of the NPHM did not share the recent high-temperature history of the interior of the massif.

Winslow et al. (1995) used standard geobarometers and geothermometers on 12 rocks, and found that cordierite-free assemblages give P-T estimates of 540 to 740°C at 7.1 to 13.1 kbar, while cordierite-bearing assemblages gave P-T estimates of 608 to 675 °C at 3.9 to 6.8 kbar. The two groups were termed "non-migmatised" (cordierite-absent) and "migmatised" (cordierite-present) by Winslow et al. (1995), with sample locations corresponding to the margins and interior of the massif respectively. Garnet zoning profiles were different between the two areas, with homogenised profiles in the massif core and growth zoning preserved on the massif margins. Gibbs modelling of P-T paths from garnet zoning indicated growth during near-isothermal decompression in a sample from Tato, and growth during increasing P and T conditions in garnets from Raikhot and Astor.

While the results obtained in previous work are interpreted to be estimates of peak conditions following Tertiary (Himalayan) collisional orogeny, Wheeler et al. (1995) have conducted a detailed study of polymetamorphism in the Indus Valley. They suggest that granulite facies metamorphism and biotite dehydration melting produced the early migmatitic fabrics, and used detailed petrography to reconstruct an anti-clockwise P-T path for this event, which reached over 800 °C (Wheeler et al., 1995). This was followed by intrusion of basaltic sheets, not necessarily in the same tectonic event. Since Tertiary basaltic magmatism within the Himalayan orogen is unknown, and would be difficult to achieve in a region of greatly thickened crust, the basaltic sheets and hence granulite facies

metamorphism are attributed to a pre-Himalayan orogeny. Basaltic sheets from the southern NPHM are discussed further in Chapter 5.

Dating metamorphism within the NPHM has proved somewhat problematic. K-Ar and Ar-Ar ages from hornblendes has provided a range of ages (Treloar et al., 1989a, 1991; Zeitler et al., 1989; Winslow et al., 1996), none of which are reliable due to incorporation of excess argon and frequent failure to provide meaningful plateau ages. In addition, peak temperatures from the NPHM exceed the closure temperature of the Ar-Ar system in hornblendes, so that the early cooling path would be constrained, and not the timing of peak metamorphism. Zircons from the Indus valley show thin rims with high uranium contents, and were dated at between 2 and 14 Ma (Zeitler, 1989; Zeitler et al., 1989). The data from these studies have since been reinterpreted to define a discordia line with a lower intercept of 21 ± 18 Ma (Smith et al., 1992). Whether the rims grew during metamorphism (Zeitler et al., 1993) or as a result of influx of a uranium-rich fluid on the retrograde path (Zeitler, 1989; Zeitler et al., 1989) is uncertain.

In the southern NPHM, no geochronometer has yielded reliable ages older than 11 Ma. Smith et al. (1992) obtained ages of between 4 and 11 Ma on monazite fractions of between 12 and 200 crystals from the Tato and Astor regions by the U-Pb method. An attempt to date garnet from the Astor valley using the Sm-Nd system constrained last equilibration to have been more recent than 25 Ma (George, 1993). Zircons from syn- to post-kinematic leucogranites in the southern NPHM have been dated at between 1 and 8 Ma (Zeitler and Chamberlain, 1991; Zeitler et al., 1993), and two monazite fractions from a migmatite yielded U-Pb ages of 3.3 Ma (Zeitler et al., 1993).

While field relations argue for a polymetamorphic history in this part of the NPHM, Zeitler et al. (1993), Winslow et al. (1995) and Chamberlain et al. (1989) have all concluded that all metamorphism and magmatism within the massif

occurred during the last 10 Ma, accompanied by rapid exhumation. A near-isothermal decompression path may be anticipated in a region of such rapid exhumation (Hodges et al., 1993), and vapour-absent (decompression) melting was suggested by Zeitler and Chamberlain (1991) as a mechanism for generating the leucogranites. This was subsequently confirmed by trace element modelling of the granites (Butler et al., 1992; George, 1993; Butler et al., 1997; Chapter 4, this thesis). Thermal modelling also suggests near-isothermal decompression at depth, followed by extremely rapid cooling as the surface is approached (Craw et al., 1994; Chapter 7).

The aims of this chapter are to provide further estimates of P-T conditions from the southern NPHM (section 3.2), and to interpret these estimates as recording either peak or retrograde conditions. In addition to Thermocalc, quantitative evaluation of garnet zoning patterns (Section 3.3) and petrogenetic grid calculations (Section 3.4) are employed to this end. The P-T evolution of the southern NPHM is summarised in section 3.5.

3.1.2 Thermobarometric techniques

In this chapter, thermobarometric calculations based on analyses of phase rims will be presented from pelitic, calc-silicate and amphibolitic lithologies. Rather than using published barometers and thermometers separately, which are each based on individual calibrations and in some cases have been recalibrated several times, I have used the Thermocalc program of Powell and Holland (1988), using the updated thermodynamic dataset of Holland and Powell (1990). In all cases, calculations have been performed using version 2.4 of the program, running on a Macintosh™ PowerPC™ 6200. Sample Thermocalc output is provided in Appendix 4.4.

Endmember activities were calculated using the "ax96" activity program written by Tim Holland. Endmember abbreviations and activity models used in the program are contained in Appendix 4.2.

The advantage of Thermocalc is that it calculates an independent set of reactions for the given phases, weighting the importance of each reaction according to both uncertainty in the thermodynamic dataset, and analytical uncertainty in endmember activities. The best P-T is required to pass a statistical test, so that the errors (quoted at 1 sigma unless otherwise specified) are realistic, although they may be larger than those quoted for other techniques. In contrast, the quoted errors on individual reaction calibrations are often smaller than the differences between calibrations for the same reaction, depending on the activity model used (e.g. the garnet-biotite Fe-Mg exchange thermometer reviewed in Kleemann and Reinhardt, 1994). Another advantage of Thermocalc is that since data for all phases is internally consistent, comparing different reactions is not subject to differences in activity models for the same phase.

Another potential pitfall where single reactions are used for P and T, for example Fe-Mg exchange between garnet and biotite for temperature and the GASP reaction for pressure, is the effective blocking temperature for these reactions. While Fe-Mg exchange typically has a blocking temperature of about 550 °C, the GASP reaction involves net transfer of elements from one site to another, rather than simple exchange. The activation energy for net transfer reactions is typically higher than that for exchange reactions, so that the blocking temperature is also typically higher. Hence the pressure recorded by the GASP reaction may refer to a blocking temperature higher than the temperature recorded by Fe-Mg exchange in biotite. Since the two reactions both have positive slopes in P-T space, there is a degree of correlation between them, and the resulting error box is an ellipse rather than a square. This correlation between different reactions is expressed in Thermocalc as the "corr" function, with a value of 0 indicating no correlation

(orthogonal reactions in P-T space) and a value of 1 indicating reactions with identical slopes in P-T space.

Although individual reactions calculated with Thermocalc have significant (realistic) errors attached, differences between the same reaction calculated for different analyses should be quite precise. This facilitates comparison of recorded P-T conditions from different rocks in this study with more certainty than the absolute conditions recorded.

To summarise, the approach used in this chapter is internally consistent, allowing comparison between different assemblages across the southern NPHM. Errors are larger than those quoted for many single-reaction thermometers and barometers, but are statistically valid given the uncertainties in both analytical and thermodynamic data required for thermobarometric calculation.

3.2 Thermobarometry

This section presents P-T calculations using Thermocalc on a variety of lithologies from across the southern NPHM. Calculations on a metapelite containing a cordierite seam (Z130) are presented in Chapter 4. Calculations on spinel-bearing metapelites are presented in Section 3.4, and calculations from an unmelted pelite (N1) are presented in Chapter 7. The results from all these assemblages are considered in the summary (Section 3.5, Fig. 3.13, Table 3.15), but the details of calculations from other chapters are not repeated in this section.

3.2.1 Pelitic lithologies

3.2.1.1 E157 is a mylonitic metapelite from the MMT zone on the western margin of the NPHM at Raikhot Bridge. Deformation in this rock relates to underthrusting of the NPHM beneath Kohistan during convergence, followed by extensional reactivation of the fabric during formation of the syntaxis (Chapter 2). Ar-Ar dating suggests that muscovite last recrystallised at about 12 Ma (Chapter 6). E157 contains quartz ribbons, cracked and sheared garnet porphyroblasts, fabric-forming muscovite and biotite, and plagioclase feldspar. Aluminosilicate is absent, and cracks in garnet are often filled with chlorite.

Garnet is homogeneous, with typical composition alm_{66} prp_{22} sps_1 gr_{11} and an Fe# of 75, where Fe# = $100*Fe^{2+}/(Fe^{2+} + Mg)$, although these vary slightly between different porphyroblasts (section 3.3). Biotite has an Fe# of about 63 which varies with degree of chloritisation, and with composition of nearby garnet. Muscovite has a small celadonite component (Fe, Mg and Si substitution for Al). Plagioclase is albitic, with An content of about 15 mol. %, while K-feldspar has an Or content of about 70 mol. %. Three different domains within a single thin section were analysed, each containing a garnet porphyroblast, and average (PT) calculations have been conducted on each ring.

The results indicate disequilibrium between the analysed phases, since at least two endmembers had to be eliminated before Thermocalc could find a statistically valid (PT) estimate. Usually P and T had to be calculated separately, since there was a high degree of correlation between the two (0.8 for ring 2). Average (PT) conditions were at about 1000°C and 13 kbar for domains 1 and 2, with large errors of about 200 °C and 2.5 kbar (1 sigma errors). Calculations omitting all muscovite endmembers gave average (P) and average (T) curves that were identical, due to the low number of phases available for constructing reactions, so that without an additional constraint no unique answer could be achieved.

The presence of stable muscovite suggests that during re-equilibration temperatures were below about 700 °C, or pressures were very high, but there remains the strong possibility that muscovite formed on the retrograde path during extensional deformation and is not in equilibrium with garnets which clearly predate the extensional episode. Hence no (PT) estimate can be achieved for this rock.

3.2.1.2 E126 is a garnet-bearing metapelite from the eastern side of the Raikhot valley, 5 km south-west of Buldar Peak. Garnet forms very large unzoned porphyroblasts up to 5 mm across, with quartz pressure shadows and wrapped by biotite foliation. Garnet is cracked and anhedral, and in some cases it appears that part of a crystal is either missing or has been replaced by quartz and feldspar. Biotite shows incipient chloritisation and exsolution of iron oxides, often combined with a feathery appearance and lack of good crystal shape. There is no sign of cordierite, and fibrolitic sillimanite occurs sporadically with biotite.

Domain 1 contains almandine-rich garnet ($alm_{0.78}$ $prp_{0.07}$ $gr_{0.03}$ $sps_{0.12}$) with an Fe# of 91, homogeneous biotite with Fe# of 70 irrespective of whether it is inside or outside the garnet, unzoned plagioclase of bytownite composition, with quartz and minor sillimanite and orthoclase. Average (PT) calculations required the omission of pyrope to find a statistically acceptable result, and are summarised in Table 3.1. Domain 2 contains a similar assemblage with similar compositions, suggesting equilibration between phases on the scale of a thin section. Average (PT) calculations were statistically acceptable with all phases present, and are summarised in Table 3.1.

Table 3.1. Average (PT) calculations for E126 domains 1 and 2

water activity	T (°C)	±	P (kbar)	±	f (fit parameter)
E126 domain 1, calculations exclude pyrope					
$X_{H2O} = 1.0$	636	48	5.5	1.7	1.07
$X_{H2O} = 0.5$	585	40	4.9	1.6	1.03
$X_{H2O} = 0.1$	470	31	3.6	1.3	0.94
$a_{H2O} = 0.9$	624	47	5.4	1.7	1.06
$a_{H2O} = 0.5$	560	39	4.6	1.5	1.01
$a_{H2O} = 0.1$	424	28	3.1	1.2	0.89
E126 domain 2, calculations include all garnet endmembers					
$X_{H2O} = 1.0$	685	43	5.5	1.9	0.77
$X_{H2O} = 0.5$	633	37	4.8	1.8	0.75
$X_{H2O} = 0.1$	519	29	3.5	1.6	0.93
$a_{H2O} = 0.9$	673	42	5.3	1.9	0.76
$a_{H2O} = 0.5$	611	37	4.5	1.7	0.76
$a_{H2O} = 0.1$	480	30	2.9	1.6	1.08

Calculations on domain 2 are more reliable because they incorporate all garnet endmembers. The best statistical fits are obtained for water activities between 0.5 and 1.0, and the average PT conditions are about 670 ± 50°C and 5.3 ± 2.0 kbar for fluid-absent conditions with a water activity of 0.9. Fluid-absent conditions are thought to prevail because otherwise melting would progress rapidly to large melt fractions at these temperatures. At low water activities, subsolidus biotite breakdown would occur, although the calculated PT conditions for low water activities are in any case much lower than those obtained from other nearby rocks. Calculated pressures at high water activities are not significantly higher than those from some rocks where cordierite is present (e.g. N1, chapter 7). This may suggest a combination of rapid cooling preventing the growth of cordierite from garnet, and the bulk composition of this rock. A more aluminous composition would favour cordierite growth, since sillimanite is a reactant. In rocks where cordierite

has grown at the expense of garnet, sillimanite is much more abundant, even after cordierite growth, than in E126.

3.2.1.3 Z137ii is a leucocratic gneiss collected from near the snout of the Raikhot Glacier, and hence is must therefore have been transported from the upper Raikhot Glacier. It contains small (< 1 mm) subhedral garnets, ragged biotite which appears to be breaking down, with partially altered cordierite rimming biotite and garnet. The rock is predominantly leucocratic, containing about 80 modal % quartz and feldspars. Potassium feldspar is often poikiloblastic, containing rounded quartz inclusions, and sparse fibrolitic sillimanite occurs parallel to the weak fabric defined by biotite. Ilmenite inclusions occur in cordierite, probably where biotite has been replaced.

Garnet is almandine-rich and homogeneous, with composition prp_{84} alm_8 sps_6 gr_2, and an Fe# of 92. Biotite is also homogeneous, with an Fe# of about 72. Cordierite was not analysed due to complete alteration to pinite. Potassium feldspar typically has an Or content of 68 mol. %, while plagioclase feldspars are albitic, with Ab contents of 86 mol. %. Sillimanite and quartz were also used in average (PT) calculations (Table 3.2).

Table 3.2. Average (PT) calculations for Z137ii

water activity	T (°C)	±	P (kbar)	±	f (fit parameter)
$X_{H_2O} = 1.0$	623	42	7.0	2.2	1.06
$X_{H_2O} = 0.5$	581	40	6.4	2.4	1.15
$X_{H_2O} = 0.1$	483	41	4.9	2.8	1.49
$a_{H_2O} = 0.9$	612	42	6.8	2.2	1.08
$a_{H_2O} = 0.5$	559	42	5.9	2.4	1.21
$a_{H_2O} = 0.1$*	432	44	4.2	2.8	1.67

* eastonite (east) was omitted from this calculation

The results of (PT) calculations produce lower temperatures than would be expected, and higher pressures than are compatible with the observation of cordierite growth, although cordierite was not included in the input file. Pressures have significant errors attached, due to the low anorthite content of plagioclase and the low grossular content of garnet, since the GASP reaction controls the calculated pressure. Temperatures are controlled by the Fe/Mg distribution between biotite and garnet, but these will also be affected by the presence of cordierite. Hence these calculations should be treated with some caution, although the results are within error of those on similar rocks.

3.2.1.4 E139 is a metapelite from less than 100m below the Tato pluton at Bezar Gali, about 5 km west of Tato village, and contains garnet, cordierite, biotite, sillimanite, plagioclase and orthoclase feldspar, quartz and opaque oxides. Cordierite was not analysed due to extensive alteration, but it can be seen surrounding biotite, sillimanite and garnet. Garnet is small and subhedral, while biotite appears quite ragged and is replaced by cordierite, leaving opaque oxide minerals, probably ilmenite. Garnet is essentially almandine (70 mol. %) with significant spessartine (12 mol. %) and pyrope (14 mol. %) solid solution, while grossular is a minor component (<4 mol. %). The remaining garnet crystals are small (< 0.5 mm across) and homogeneous, while biotite composition is variable. Biotite enclosed in cordierite has an Fe# of 0.66, while biotite only 1 mm away and partially enclosed in cordierite has an Fe# of 0.56. Biotite will become more Fe-rich while breaking down to produce cordierite, or when re-equilibrating with cordierite rather than garnet, since cordierite is more magnesian than garnet. Average (PT) calculations have been conducted using these two different biotite compositions to indicate the size of the uncertainty introduced from an unknown original biotite composition in equilibrium with garnet (Table 3.3). Plagioclase is uniformly oligoclase, with An content typically 25 mol. %.

Table 3.3. Average (PT) calculations for metapelite E139, with both Fe-rich and Fe-poor biotite compositions (analyses in Appendix 4).

water activity	T (°C)	±	P (kbar)	±	f (fit parameter)
E139 domain 1, using high-Fe biotite composition					
X_{H2O} = 1.0	712	60	5.9	2.0	1.32
X_{H2O} = 0.5	658	62	5.3	2.2	1.58
X_{H2O} = 0.1*	484	33	3.5	1.2	0.04
a_{H2O} = 0.9	700	61	5.8	2.0	1.38
a_{H2O} = 0.5	638	66	5.0	2.3	1.70
a_{H2O} = 0.1*	438	33	3.0	1.1	0.03
E139 domain 1, using low-Fe biotite composition					
X_{H2O} = 1.0	703	59	6.1	1.5	0.16
X_{H2O} = 0.5	641	50	5.3	1.4	0.14
X_{H2O} = 0.1	510	38	3.8	1.2	0.10
a_{H2O} = 0.9	688	58	5.9	1.5	0.15
a_{H2O} = 0.5	615	50	5.0	1.4	0.14
a_{H2O} = 0.1	463	36	3.3	1.1	0.07

Average (PT) calculations involved endmembers alm, prp, sps, gr, phl, ann, east, naph, an, ab, ksp, sill and q, except that for the Fe-rich biotite composition eastonite (east) was excluded in each case. For X_{H2O} = 0.1 and a_{H2O} = 0.1, pyrope (prp) was also excluded for the Fe-rich biotite composition, in order to produce a statistically valid calculation. This is part of the reason for the unusually low temperature estimates for the Fe-rich composition.

The Fe-poor composition is thought to be nearer to the original biotite composition, and generates lower temperatures, higher pressures, and better statistical fits, than the Fe-rich composition. However, the differences are always within one standard deviation, so that even if the original composition is not preserved, the difference between the calculated and "true" (PT) estimates are likely to be small. At these conditions, melting would have occurred if an aqueous

fluid was present, so that a free fluid phase was probably absent. However, biotite breakdown will release more water than will be incorporated into the growing cordierite structure, so that water activity was probably high. In conclusion, pressure-temperature conditions of about 690 ± 60 °C and 5.9 ± 1.5 kbar are thought to have prevailed during the most recent equilibration of this rock.

3.2.1.5 Z153ii is a garnet-cordierite metapelite collected from the Raikhot glacier near Advance Base Camp, and its origin is therefore constrained to be from the Raikhot Face. Part of a large garnet (~ 1 cm across) has been analysed, and is homogeneous with the exception of diffusion rims of about 100μm extent (section 3.3). The garnet is largely surrounded by subhedral cordierite porphyroblasts of up to several mm diameter, which show minor alteration to chlorite and fine-grained mica around rims. The garnet-cordierite assemblage is hosted by a small leucosome composed of a quartz matrix, with minor plagioclase and potassium feldspar, small relict biotite crystals, and occasional small euhedral apatite crystals.

The garnet is almandine-rich, with typical composition alm_{78} prp_{13} sps_8 gr_2, with an Fe# of about 86. Cordierite is very uniform across individual porphyroblasts and between crystals, with an Fe# of about 51, while biotite has an Fe# of about 72. Plagioclase feldspar is oligoclase, with An content typically 15 mol. %, while potassium feldspar is sanidine, with Or content typically 70 mol. %.

Average (PT) calculations involved the endmembers alm, prp, sps, gr, phl, ann, naph, crd, fcrd, mncrd, an, ab, ksp, sill, and q, but the eastonite endmember (east) was omitted to enable statistically acceptable calculations. The results are summarised in Table 3.4.

Table 3.4. Average (PT) calculations on metapelite Z153ii.

water activity	T (°C)	±	P (kbar)	±	f (fit parameter)
$X_{H_2O} = 1.0$	646	38	4.3	0.4	0.86
$X_{H_2O} = 0.5$	599	33	3.7	0.4	0.94
$X_{H_2O} = 0.1$	496	34	2.6	0.4	1.26
$a_{H_2O} = 0.9$	635	37	4.2	0.4	0.88
$a_{H_2O} = 0.5$	579	33	3.6	0.4	0.99
$a_{H_2O} = 0.1$	461	38	2.3	0.4	1.43

The highest temperatures and pressures, and best statistical fits, were obtained for the highest water activities, and are close to the vapour-present solidus for metapelites (Le Breton and Thompson, 1988). The textures in this rock are metamorphic rather than igneous, and it is thought that the leucosome was formed by subsolidus processes, although the petrography is similar to the cordierite seams discussed in Chapter 4, except that large garnet porphyroblasts are not present in cordierite seams. Temperatures of at least 600 °C combined with pressures of about 4 kbar suggest an average geotherm of about 50 °C / km in the top 12 km of the crust at the time this assemblage last equilibrated.

3.2.2 Calc-silicate lithologies

3.2.2.1 E115 is a calc-silicate rock from Bayal Camp (Fig. 3.1). It contains clinopyroxene, garnet, plagioclase, quartz, calcite and wollastonite. Three domains from a single thin section were analysed. Domain 1 contains plagioclase feldspar, with An content of about 94 mol. %, pale green clinopyroxene of the diopside-hedenbergite series with a variable Fe# of about 40, and quartz. Domain 2 contains the same assemblage with the addition of small anhedral Ca-rich garnet crystals, composed of approximately equal molecular proportions of andradite

and grossular. Domain 3 contains clinopyroxene, plagioclase, calcite, and minor sphene and wollastonite, in the apparent absence of quartz. Calcite has been partially replaced by wollastonite along deformed cleavage planes, and the characteristic pairs of calcite cleavages are only seen in a few small crystals.

While garnet and quartz do not coexist with wollastonite and calcite in this slide, Thermocalc failed to find an acceptable average (PT) unless garnet, quartz, wollastonite, clinopyroxene and plagioclase were input. In this case, which assumes equilibrium on the scale of a thin section, an average (PT) of 745 ± 106 °C at 1.8 ± 1.9 kbar was calculated. This estimate has a strong correlation between P and T (cor = 0.962) indicating the influence of the reaction:

grossular + quartz = anorthite + 2 wollastonite

on both average (P) and average (T) calculations. This reaction has a positive slope in P-T space. The other two reactions with usefully low uncertainties are:

Ca-tschermakite + wollastonite = grossular

which also has a positive slope in P-T space, and:

Ca-tschermakite + quartz = anorthite

which has a negative slope in P-T space, and provides the upper limit on average (PT) calculations. None of these reactions is sensitive to fluid activity or composition, and the introduction of calcite into the data file prevents Thermocalc from achieving statistically acceptable P-T calculations, confirming the petrographic observation that calcite is no longer in equilibrium with the main assemblage. The replacement of calcite by wollastonite will release CO_2, and will be favoured by low CO_2 activity. This does not necessarily imply fluid-absent conditions, but if a fluid is present it is likely to be mostly aqueous. This constraint is useful for calculations on other lithologies (section 3.2.1).

3.2.2.2 E116 is a banded metapelite / calc-silicate from Bayal Camp, collected only 300m south of E115. Two thin sections were cut from the hand specimen, which show variations in mineralogy from garnet-biotite-plagioclase-quartz to clinopyroxene-amphibole-plagioclase on a sub-centimetre scale.

Domain 1 of section 1 contains a skeletal garnet porphyroblast, about 3 mm long, with ragged biotite partially altered to chlorite and ilmenite, polygonal quartz and plagioclase feldspar. Garnet is predominantly almandine, typically of composition alm_{61} prp_{11} sps_6 gr_{23} with an Fe# of 78, and biotite has Fe# of 59. Plagioclase is anorthitic (An about 86 mol. %). There is no sillimanite present, and this may be the reason for the survival of the remaining garnet, since without sillimanite it cannot break down to form plagioclase or cordierite.

Thermobarometric calculations without sillimanite produced an average (PT) of 710 ± 160 °C at 4.3 ± 2.3 kbars. This estimate was the same under fluid-present or fluid-absent conditions, decreasing by only 10 °C and 0.1 kbar for a water activity of 0.1 under fluid-absent conditions.

Domain 2 of section 1 contains quartz, anhedral pale green clinopyroxene, rounded anhedral dark green amphibole apparently replacing pyroxene, dusty plagioclase and minor sphene. Plagioclase has an anorthite content of about 93 mol. %, and clinopyroxene belongs to the diopside-hedenbergite series, with an Fe# of 46. Amphibole is near to the composition of hornblende *sensu stricto*, but with significant Fe^{3+} and (K, Na) substitution and has an Fe# of about 60.

Thermobarometric calculations yielded an average (PT) of 1083 ± 266 °C at 2.9 ± 3.4 kbar, independent of fluid composition or the activity of vapour components. Domain 3 of section 1 contains a similar assemblage to domain 2, with similar mineral chemistry, confirming that the endmember activities calculated for

domain 2 represent a chemical equilibrium. Average (PT) conditions were only statistically acceptable with the exclusion of the tremolite endmember, at 838 ± 208 °C and 4.0 ± 2.9 kbar, again independent of fluid composition or activity.

The same assemblages also occur in the other thin section cut from the hand specimen, and mineral composition is also the same, confirming chemical equilibrium on a hand specimen scale (several cm). In domain 1 of section 2, calculations on coexisting biotite, garnet, plagioclase and quartz yield average (PT) conditions of 730 ± 166 °C at 4.1 ± 2.5 kbar, again independent of fluid composition or activity.

In domain 2, garnet coexists with clinopyroxene and amphibole, in addition to ilmenite, and magnetite with significant Ti substitution (possibly an intergrowth of ilmenite and magnetite unresolvable by the 20μm spot size used). Thermobarometric calculations on this assemblage were only acceptable with the exclusion of the pyrope endmember, and varied from 845 ± 158 °C at 9.7 ± 2.5 kbar in the presence of an aqueous fluid, to 806 ± 150 °C at 9.3 ± 2.4 kbar for vapour-absent conditions with a_{H_2O} = 0.3. For lower water contents or activities, more endmembers must be excluded to produce statistically valid results.

Analyses from pelitic and calc-silicate assemblages within the same thin section, and on two thin sections from the same hand specimen, have established that chemical equilibrium was achieved on a scale of several cm. Calc-silicate assemblages yielded higher temperatures than pelitic assemblages, and at similar pressures. The exception to this is that pressure estimates from one domain were considerably higher when pyrope had been excluded. This suggests that for this assemblage, where garnet occurs in contact with pyroxene and amphibole, retrograde exchange between phases may have occurred. Sufficient fluid-independent calculations have been performed to place this rock at low pressures,

about 4 ± 3 kbar, and high temperatures, about 730 ± 170°C or possibly higher. Although the errors on these estimates are large, they are probably realistic.

3.2.2.3 Z124 is a calc-silicate collected from below the Jalipur Pass, showing compositional banding on a cm scale and open folding on a scale of 10 cm. Two different areas of 5 mm by 5 mm were studied on the same thin section.

Domain 2 contains large (~2 mm) subhedral amphibole porphyroblasts, found replacing inclusion-rich and corroded clinopyroxene porphyroblasts. Clinopyroxenes belong to the diopside-hedenbergite solution series, and are zoned between $di_{23}hed_{77}$ in contact with amphibole, and more Fe-rich compositions of $di_{34}hed_{66}$ in contact with plagioclase. Feldspar shows minor alteration to meionite-rich scapolite along rims with clinopyroxene. Anorthite and orthoclase are both present, and anorthite shows deformation bands disrupting twin planes. Clinozoisite occurs as a large anhedral porphyroblast, with an embayment filled with scapolite apparently replacing plagioclase. Pressure-temperature conditions calculated using these phases are tabulated below (Table 3.5), using endmembers tr, ftr, ts, parg, di, hed, cats, acm, cz, ps, ksp, ab, an, H_2O (abbreviations listed in Appendix 4).

Domain 4 contains anhedral clinopyroxene porphyroblasts, intermediate between diopside and hedenbergite, with embayed edges. These porphyroblasts are zoned, between $di_{33}hed_{67}$ in the core to $di_{43}hed_{57}$ at the rim. The analysis used in PT calculations is from the rim, and hence Fe-rich. The matrix is composed mostly of anorthite, with some quartz and occasional small euhedral sphene crystals. Andradite garnet and clinozoisite are found growing together along matrix grain boundaries, and around the embayed rims of some clinopyroxene porphyroblasts. Microprobe analyses of clinopyroxene, plagioclase, garnet and clinozoisite can be found in Appendix 4.

In addition to these phases, quartz and H_2O were added to the data file for domain 4. Diopside was excluded due to the absence of other Fe-bearing phases, and the grossular and almandine garnet endmembers had to be discarded for Thermocalc to achieve statistically valid average (PT) calculations. The results are tabulated below, using the endmembers hed, cats, acm, an, ab, andr, cz, ps, q, and H_2O (abbreviations tabulated in Appendix 4).

Table 3.5. Calculated average (PT) conditions for Z124 rim compositions.

	Domain 2		Domain 4	
Water activity	T (°C)	P (kbar)	T (°C)	P (kbar)
Fluid present				
$X_{H2O} = 1$	643 ± 72	6.2 ± 2.3	729 ± 72	6.8 ± 1.9
$X_{H2O} = 0.9$	640 ± 71	6.3 ± 2.3	724 ± 71	6.8 ± 1.8
$X_{H2O} = 0.5$	628 ± 71	6.5 ± 2.4	704 ± 68	7.0 ± 1.8
$X_{H2O} = 0.1$	589 ± 70	7.5 ± 2.5	640 ± 59	7.3 ± 1.7
Fluid absent				
$a_{H2O} = 0.9$	639 ± 71	6.3 ± 2.3	723 ± 71	6.8 ± 1.8
$a_{H2O} = 0.5$	621 ± 71	6.7 ± 2.4	693 ± 67	7.0 ± 1.8
$a_{H2O} = 0.1$	573 ± 70	7.9 ± 2.6	617 ± 58	7.4 ± 1.7

Pressure-temperature calculations are affected little by fluid composition and water activity, except where fluid composition is very CO_2-rich or water activity is very low. For a water activity of 0.1, or where a CO_2-rich fluid is present (a_{H2O} = 0.1 and X_{H2O} = 0.1 respectively), calculated (PT) conditions shift to lower temperatures and higher pressures. However, the shift is within one standard deviation of the (PT) calculations for a water activity of 1 in each case.

Scapolite often occurs as a metasomatic mineral, and the presence of meionite rather than zoisite is indicative of high CO_2/H_2O pressure (Deer et al., 1992). In Z124 however, clinozoisite does appear to be stable, with only minor alteration to

scapolite. This may indicate the presence of CO_2-rich fluids (or Cl- or SO_4-rich fluids) during retrogression, but also suggests that peak metamorphism occurred in a more aqueous environment, although not necessarily in the presence of a fluid. Calculated average (PT) conditions are 630 ± 80 °C at 6.4 ± 2.4 kbar for domain 1, and 720 ± 70 °C at 6.9 ± 1.9 kbar for domain 2. While the pressures converge at low a_{H_2O}, the preferred interpretation for the differences in calculated (PT) conditions is that retrograde exchange may have been more significant in domain 2, where clinopyroxene and amphibole are in contact. In contrast, garnet in domain 4 is not in contact with clinopyroxene, and could not exchange easily without the presence of a fluid. The calculated average (PT) conditions for domains 2 and 4 are only one standard deviation apart in any case, and the difference may reflect the realistic uncertainties involved in such calculations.

3.2.2.4 Z148 is a calc-silicate collected from the Raikhot glacier near Advance Base Camp, and its origin is therefore constrained to be from the Raikhot Face. Z148 contains plagioclase and garnet in some bands, and plagioclase, clinopyroxene and amphibole in others. Sphene is distributed throughout the rock.

Domain 1 contains anorthite, anhedral andradite garnet and minor sphene. There is no sillimanite or quartz, and so no reactions can be calculated. Domain 2 contains anhedral amphibole and clinopyroxene, plagioclase (An content 90 to 95 %), and minor potassic feldspar and magnetite. Pyroxenes are of the diopside-hedenbergite solid solution, with an Fe# of 30 to 33 and are not found in contact with amphibole, which is typically of composition $Si_{6.2}(Al,Fe)_{2.5}(Fe,Mg)_4Ca_2(Na,K)_{0.7}$, with an Fe# of about 50. Where the amphibole appears brown, rather than green, in plane polarised light, the composition is $Si_7(Al,Fe)_{1.3}(Fe,Mg)_{4.5}Ca_2(Na,K)_{0.3}$, with an Fe# of about 40. In both cases the amphibole is calcic, intermediate in composition between hornblende, tschermakite, edenite and pargasite, with significant Fe substitution for Al. The differences in composition

do not appear related to alteration, which has affected pyroxene much more than amphibole.

Table 3.6. Average (PT) conditions calculated from Z148, combining domains 1 and 2.

water activity *	T (°C)	±	P (kbar)	±	f (fit parameter)
1. Low silica amphibole composition					
$X_{H2O} = 1.0$	632	70	8.5	1.8	0.93
$X_{H2O} = 0.5$	608	66	8.9	1.7	0.99
$X_{H2O} = 0.1$	544	65	10.1	1.9	1.15
$a_{H2O} = 0.9$	626	70	8.6	1.8	0.95
$a_{H2O} = 0.5$	594	68	9.2	1.8	1.02
$a_{H2O} = 0.1$	513	70	10.7	2.0	1.23
2. High silica amphibole composition					
$X_{H2O} = 1.0$	680	80	3.3	2.6	1.46
$X_{H2O} = 0.5$	659	76	3.8	2.6	1.47
$X_{H2O} = 0.1$	606	68	4.8	2.7	1.51
$a_{H2O} = 0.9$	675	78	3.4	2.6	1.46
$a_{H2O} = 0.5$	651	75	3.9	2.7	1.47
$a_{H2O} = 0.1$	587	67	5.2	2.7	1.53

* a_{H2O} indicates water activity under vapour-absent consitions, X_{H2O} indicates water content of fluid under vapour-present conditions

A combined dataset has been used in thermobarometric calculations, with plagioclase, amphibole and pyroxene compositions from domain 2 with garnet compositions from domain 1. Without the addition of garnet, insufficient reactions were found for average (PT) calculations, although the separation of these phases of about 1 cm may render the assumption of equilibrium between phases invalid. Calculations were performed using both low-silica and high-silica amphibole compositions, and a statistically acceptable calculation could only be performed with the omission of the almandine garnet endmember. Results are

summarised in Table 3.6, using the endmembers gr, andr, di, hed, cats, acm, tr, ftr, ts, parg, an, ab, with the additional omission of tremolite for calculations involving the low-silica amphibole composition.

Temperatures exceed 600 °C in most cases for values of a_{H_2O} or X_{H_2O} in excess of 0.5, and the best statistical fits are obtained for high water activities, or the presence of an aqueous fluid. The significant difference between the two amphibole compositions used is the calculated pressure, which is high for the low-silica composition predominant in Z148, and low for the high-silica composition. There is no apparent zoning in clinopyroxene composition, although only a small number of analyses were performed. The different pressures may indicate re-equilibration of some amphiboles during decompression, which would also require the presence of a fluid since amphibole and pyroxene are not in contact. Whether the differences in calculated P-T conditions are ascribed to alteration or re-equilibration, temperatures recorded from Z148 are apparently in excess of 600 °C, as would be expected from other calculations performed on rocks from the interior of the NPHM.

3.2.2.5 Z150 is a marble, also collected from the Raikhot glacier. Z150 contains calcite, dolomite, spinel, olivine, clinopyroxene, and biotite, with no free quartz. Three different domains of about 5 mm by 5 mm were investigated using the microprobe.

Domain 1 contains calcite, Mg-rich spinel, diopside and phlogopite. Large diopside porphyroblasts are ragged, anhedral and embayed, while spinel is subhedral or euhedral. Spinel and clinopyroxene are not found in contact, and matrix calcite around spinel is coarser than near clinopyroxene, possibly indicating recrystallisation or new growth of calcite. Domain 2 contains calcite, Mg-spinel, forsterite and phlogopite, and exhibits a much narrower range of grain

sizes than domains 1. Olivine and spinel are both subhedral and rounded, and appear to coexist stably, while phlogopite is anhedral and appears corroded. Calcite is often rounded and embayed, but shows one or two good cleavages. Domain 3 contains calcite, dolomite, spinel and forsterite. Spinel and forsterite are both anhedral, and coexist stably. Calcite shows no cleavages and appears anhedral and altered, while dolomite shows good cleavages and no alteration.

Thermocalc was unable to conduct average (PT) calculations on any of these assemblages. Individual reactions such as Fe-Mg exchange between clinopyroxene and spinel, or olivine and spinel, have large errors attached and are not very useful. The assemblage forsterite-spinel-phlogopite was found only in the core of the massif by Misch (1964) and attributed to the highest temperatures recorded from the NPHM. The high temperatures obtained from pelitic rocks in the vicinity support this conclusion (Section 3.4).

3.2.3 Amphibolite sheets

The bulk geochemistry of the amphibolite sheets is discussed in Chapter 5. These bodies are highly deformed, so that they appear sub-concordant with pervasive gneissic foliation in the NPHM basement (Winslow et al., 1995), however sufficient examples of discordance have been noted to restrict these sheets to an age older than the pre-Himalayan granulite facies metamorphism (Wheeler et al., 1995; Butler et al., 1997; this thesis), and so they have undergone polymetamorphism.

Two sheets were sampled, E104 and E119, which are both now amphibolites composed predominantly of hornblende and plagioclase, with some biotite and minor alteration to chlorite. While amphibolite sheets from the Indus valley contain relict clinopyroxene inclusions within hornblende (Wheeler et al., 1995),

replacement of pyroxene by amphibole has been complete within the two sheets sampled from the southern NPHM.

E104 has been analysed extensively as part of a study to test the reliability of activity models for amphiboles in assigning Fe^{2+} and Fe^{3+} cations from microprobe analyses. This preliminary study on iron oxidation state was carried out with Dr. Phil Bland, who performed Mössbauer analyses on a powdered whole-rock sample of E104A and obtained a bulk Fe^{3+} content of 20% of Fe cations. Over three hundred analyses were conducted on a thin section of sample E104A, which showed that hornblende grains were not systematically zoned. The average Fe^{3+} content of 328 hornblende analyses was 8.11 ± 2.84 % (percentage of total iron cations). This was calculated using the ideal mixing-on-sites activity model (Holland and Powell, 1990) combined with ferric iron calculations from Holland and Blundy (1994), incorporated into the ax96 program written by Tim Holland. The results are illustrated in a histogram in Fig. 3.2.

Although the whole-rock analysis does include a small amount of Fe from biotite, the modal proportion of biotite in E104A is less than 5%, compared to about 85% for hornblende. In addition, the Fe^{3+} content of biotite has been calculated to be between 0 and 18 % of Fe cations (the average calculated content of 26 analyses is 8.3 ± 5.4 %), using the site-mixing activity model of Holland and Powell (1990). Ferric iron was calculated using the constraint that the sum of cations in tetrahedral and octahedral sites should be 6.9 for 11 oxygens. The discrepancy between the measured whole-rock Fe^{3+} content and the calculated hornblende Fe^{3+} content cannot therefore be explained by Fe^{3+} in biotite incorporated into the whole-rock Mössbauer analysis.

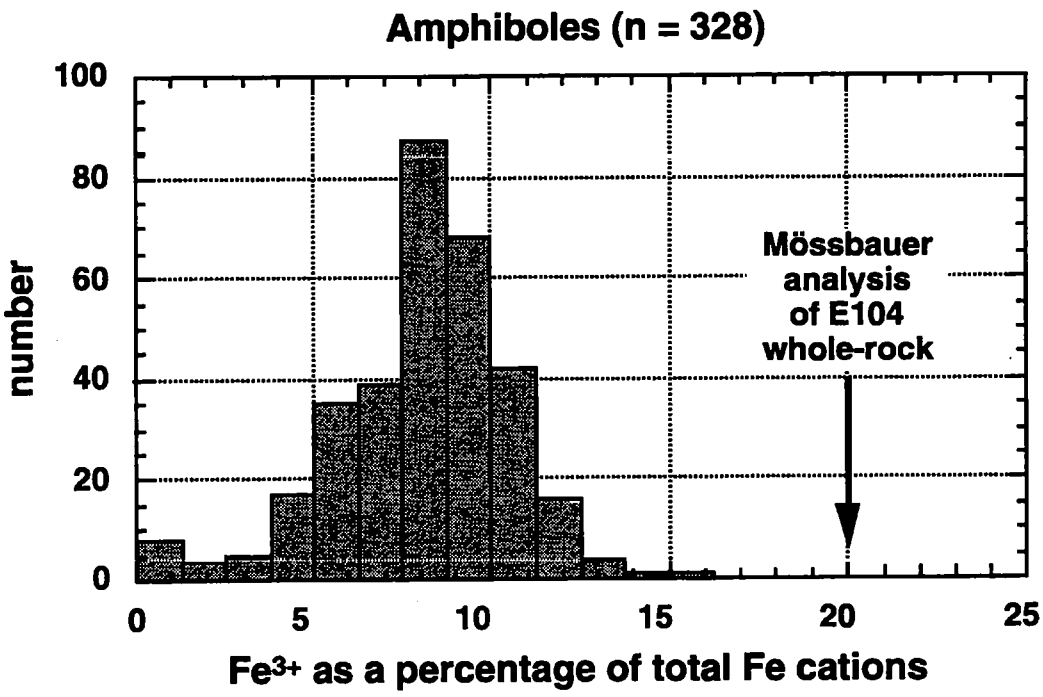

Figure 3.2. Histogram of calculated Fe^{3+} contents of 328 amphibole analyses from E104A, calculated using the activity-composition model of Holland and Blundy (1994), incorporated into the ax96 program (Tim Holland, pers. comm.). Also shown is the Fe^{3+} percentage of total Fe in the bulk rock determined by Mössbauer analysis (Phil Bland, pers. comm.). This will be dominated by hornblende, which makes up 85 % of E104, and indicates that the model used to assign Fe^{2+} and Fe^{3+} is not appropriate in this case.

The implication is that the activity-composition model used here is inappropriate for the amphibole composition found in E104. The most relevant repercussion of this conclusion for the present study is in the calculation of metamorphic pressure-temperature conditions, since the activities of Fe^{2+} endmembers will be overestimated. While the average Fe# was calculated to be 39.65 ± 2.28, the true Fe# may be at least 10 % lower, i.e. outside the uncertainties of compositional variability. In particular, calculations on Fe-Mg exchange reactions between biotite and hornblende will be affected. As is discussed below however, the

magnitude of this error is likely to be minor compared with the uncertainties on plagioclase compositions from this sample.

Three different hornblende analyses were used in thermobarometric calculation (Table 3.7), a near-average analysis (#10), a silica-poor analysis (#126), and a silica-rich analysis (#4.3). These represent the extremes of analysed compositions, to fully evaluate the potential uncertainties.

Feldspars in E104 can be assigned to three compositional groups, orthoclase (n = 6), albite (n = 8), and plagioclase with variable composition averaging $Ab_{55}An_{43}$ (n = 26). There is no evidence for zoning within individual grains where traverses have been conducted, although cores may be one or two mol.% more albitic than rims. Individual crystals appear fairly homogeneous in most cases, but the presence of three distinct feldspar compositions suggests some chemical disequilibrium, and the range of compositions makes thermobarometry problematic. Three different plagioclase compositions were used (Table 3.7), a near average analysis (#157), an albitic composition (#36) and an anorthitic composition (#237). Quartz was not found in the thin section.

Average (PT) calculations and average temperatures could not be calculated by Thermocalc for the analyses and endmember activities listed in Table 3.7. Calculations on average pressure and average temperature were successful when conducted separately, although the errors were typically ± 3 kbar and ± 300 °C. With the addition of quartz, errors were significantly reduced but calculated pressures increased by several kbars. Since quartz is not present in the thin section, these calculations are invalid and the results are not reported here.

Table 3.7 Mineral compositions from amphibolite E104A

Mineral	amphibole						biotite		
Analysis	average	stdev	#10	#126	#4.3		average	stdev	#117
SiO_2	45.33	1.45	45.03	43.17	50.88		35.73	1.25	36.87
TiO_2	0.63	0.09	0.67	0.60	0.29		2.52	0.56	2.54
Al_2O_3	11.41	1.54	11.37	14.40	5.07		16.01	0.61	15.59
Cr_2O_3	0.11	0.16	0.02	0.01	0.19		0.05	0.01	0.05
Fe_2O_3	1.30	0.47	1.68	1.53	0.9		1.66	1.12	0.53
FeO	13.26	0.52	13.19	13.37	14.68		16.27	0.69	16.87
MnO	0.24	0.01	0.23	0.25	0.26		0.15	0.01	0.14
MgO	11.35	0.76	11.32	10.03	12.69		13.10	0.66	12.89
CaO	11.95	0.21	11.98	11.73	12.13		0.31	0.88	0.02
Na_2O	1.10	0.13	1.08	1.24	0.49		0.14	0.03	0.15
K_2O	0.85	0.20	0.90	1.11	0.19		8.08	1.34	8.99
Total	97.54	0.47	97.49	97.43	97.77		94.03	0.82	94.65
Oxygens			23	23	23				11
	n = 328						n = 13		
Cations pfu*									
Si	6.681	0.179	6.653	6.395	7.434		2.722	0.081	2.794
Ti	0.070	0.010	0.074	0.067	0.032		0.145	0.033	0.145
Al	1.985	0.275	1.981	2.515	0.873		1.439	0.060	1.393
Cr	0.013	0.019	0.002	0.002	0.021		0.003	0.001	0.003
Fe^{3+}	0.145	0.052	0.187	0.170	0.099		0.095	0.065	0.030
Fe^{2+}	1.635	0.071	1.629	1.657	1.794		1.037	0.044	1.069
Mn	0.030	0.001	0.029	0.031	0.032		0.010	0.001	0.009
Mg	2.493	0.153	2.494	2.214	2.763		1.487	0.079	1.456
Ca	1.887	0.030	1.897	1.862	1.899		0.026	0.072	0.002
Na	0.316	0.039	0.310	0.357	0.140		0.020	0.004	0.022
K	0.160	0.038	0.170	0.209	0.036		0.785	0.127	0.870
Sum			15.427	15.478	15.124				7.794
Fe3 %	8.11	2.84	10.30	9.30	5.23		8.28	5.44	2.73
Fe#	39.65	2.28	39.51	42.81	39.4		41.09	1.69	42.34
Endmember activities*									
tr			0.00247	0.000649	0.0218	phl			0.0949
ftr			0.000294	0.000152	0.00251	ann			0.0376
ts			0.00918	0.0162	0.001	east			0.0288
parg			0.0171	0.0178	0.00098	naph			0.00242

* Calculated using the "ax" program, written by Tim Holland

Table 3.7 continued.

Mineral	plagioclase					ksp	ab
Analysis	average	stdev	#157	#237	#36	#88	#169
SiO_2	56.76	3.08	56.93	50.92	63.01	64.56	67.25
TiO_2	0.00	0.01	0.00	0.00	0.00	0.01	0.00
Al_2O_3	26.95	1.87	26.84	30.79	23.40	18.05	20.30
Cr_2O_3	0.00	0.00	0.00	0.00	0.01	0.00	0.00
Fe_2O_3	0.13	0.11	0.19	0.16	0.29	0.27	0.16
FeO	0.00	0.00	0.00	0.00	0.00	0.00	0.00
MnO	0.00	0.00	0.00	0.00	0.01	0.00	0.01
MgO	0.01	0.03	0.01	0.01	0.00	0.00	0.00
CaO	9.07	2.22	9.05	13.50	4.58	0.02	1.02
Na_2O	6.34	1.42	6.54	3.90	9.14	0.38	11.16
K_2O	0.36	0.89	0.12	0.08	0.24	15.98	0.18
Total	99.62	0.53	99.68	99.36	100.68	99.28	100.08
Oxygens			8	8	8	8	8
	n = 26					n = 6	n = 8
Cations pfu*							
Si	2.558	0.112	2.563	2.331	2.775	3.004	2.946
Ti	0.000	0.000	0.000	0.000	0.000	0.000	0.000
Al	1.434	0.113	1.425	1.662	1.215	0.990	1.048
Cr	0.000	0.000	0.000	0.000	0.000	0.000	0.000
Fe^{3+}	0.004	0.004	0.006	0.005	0.010	0.009	0.005
Fe^{2+}	0.000	0.000	0.000	0.000	0.000	0.000	0.000
Mn	0.000	0.000	0.000	0.000	0.000	0.000	0.000
Mg	0.001	0.002	0.001	0.000	0.000	0.000	0.000
Ca	0.439	0.111	0.436	0.662	0.216	0.001	0.048
Na	0.553	0.119	0.571	0.346	0.781	0.034	0.948
K	0.021	0.052	0.007	0.005	0.013	0.950	0.010
Sum			5.010	5.011	5.010	4.988	5.006
X(An)	0.43	0.11	0.43	0.65	0.21	0.00	0.05
X(Ab)	0.55	0.12	0.56	0.34	0.77	0.03	0.94
X(Or)	0.02	0.05	0.01	0.00	0.01	0.96	0.01
Endmember activities*							
an			0.43	0.654	0.214		0.0477
ab			0.563	0.342	0.773	0.0344	0.942
ksp						0.965	

* Calculated using the "ax" program, written by Tim Holland

There are two hornblende-plagioclase thermometers, based on the following reactions:

Edenite + 4 quartz = tremolite + albite

Edenite + albite = riebeckite + anorthite

These have been incorporated into the "hb-plag program" (Tim Holland, pers. comm.), using the calibrations of Holland and Blundy (1994). This program was used to calculate temperatures of equilibration for various plagioclase compositions (Table 3.7). Note that the edenite-tremolite reaction is only valid for quartz-bearing rocks, so that this thermometer cannot be used in this case. For the average amphibole composition (#10, Table 3.7), the edenite-riebeckite reaction was not solved.

Table 3.8 Variability of calculated P-T conditions from E104A (analyses listed in Table 3.7)

		P (kbar)*	Plag # 157	Plag # 237	Plag incl.
hbl #10	(5 kbar)	6.43	769	803	710
	(10 kbar)		692	717	637
hbl #4.3	(5 kbar)	0.86	585	597	545
	(10 kbar)		522	528	484
hbl #126	(5 kbar)	9.12	827	869	761
	(10 kbar)		745	778	684

*Pressures using the barometer of Hammarstrom andZen (1986)
Temperatures use the thermometer of Blundy and Holland (1990)

The hornblende-plagioclase thermometer of Blundy and Holland (1990) is calibrated for temperatures between 500 and 1100 °C, with quoted errors of ±75 °C, for plagioclase with X(An) <0.92 and amphibole with Si < 7.8 cations per formula unit. The barometer of Hammarstrom and Zen (1986) depends only on the total Al content of amphibole, and assumes a temperature of 700 °C. This is about the peak temperature expected from thermobarometry on other assemblages, but has quoted errors of ± 3 kbar. P-T conditions calculated from these reactions (Table

3.8), for the three hornblende and plagioclase analyses listed in Table 3.7, illustrate the uncertainty introduced through variability in composition, which is far greater than that introduced by imperfect activity-composition models.

While the errors on each of the methods described above are considerable, a compilation of all the results suggests a P-T field of 650 to 750 °C at 6 to 7 kbar (Fig. 3.3), in broad agreement with those obtained from other lithologies.

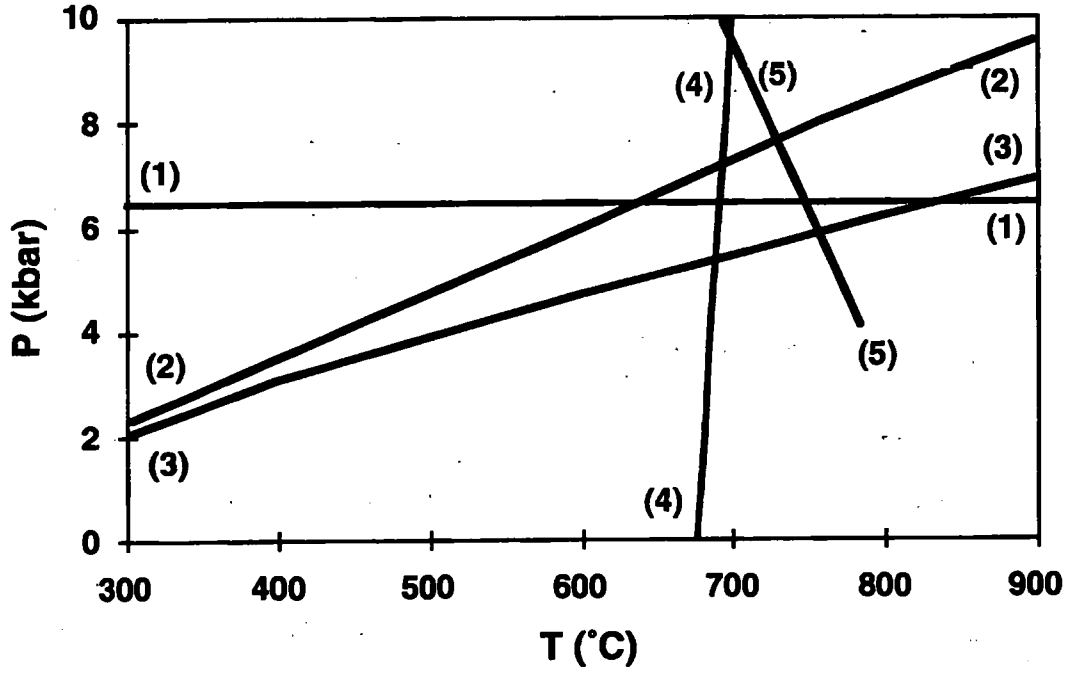

Figure 3.3. Summary P-T diagram for amphibolite E104, using hornblende analysis #10 and plagioclase analysis #157 (Table 3.7). Labelled curves are as follows: (1) Barometer of Hammarstrom and Zen (1986), (2) Thermocalc average temperature, (3) Thermocalc average pressure, (4) Edenite-tremolite thermometer of Holland and Blundy (1994), (5) thermometer of Blundy and Holland (1990) . Note that since quartz is not present in E104, curve (4) is invalid for this rock, and is included for comparison only.

3.3 Garnet zoning patterns in metapelites

3.3.1 Fabric relations

The most recent fabrics in metapelitic lithologies are defined by sheaves of biotite and sillimanite, wrapping around garnets. Garnets throughout the southern NPHM appear corroded and are usually subhedral to anhedral in appearance, with mats of sillimanite often found in embayments. Where inclusion trails are visible in garnet, they usually consist predominantly of quartz and opaque minerals, mostly ilmenite, at a high angle to the most recent fabrics (Chapter 2). This observation is usually taken to indicate that garnet growth predated the latest deformation, although this simple interpretation has recently been put in doubt by the work of Bell and Rubenach (1980), and Bell (1985), which suggests that porphyroblasts do not rotate during deformation.

In the interior of the massif, spinel is often associated with bands of sillimanite and cordierite wrapping corroded garnet, and these assemblages are discussed in more detail in section 3.4. In the MMT zone on the eastern margin of the massif at Raikhot Bridge, garnet has been broken and rotated during mylonitic deformation (Chapter 2). Thus garnets from different parts of the massif have undergone deformation under different conditions and in different assemblages.

3.3.2 Garnet zoning at Nanga Parbat

Microprobe traverses were conducted on a total of 23 garnets from 10 rocks across the southern NPHM, from the MMT zone to the high-grade interior of the massif. Zoning of major elements was rarely observed, and in some cases homogenisation appears to have occurred between different garnets in the same thin section, as

well as within individual crystals. A summary of the traverses is shown in Table 3.9.

Table 3.9. Summary of garnet zoning profiles from the southern NPHM, arranged by lithology.

Name	Rock type	Length (mm)	Fe (pfu)	Mg (pfu)	Ca (pfu)	Mn (pfu)	Notes
E157 g1	MMT	1.8	2.0	0.7	0.3	<0.1	homogenised
E157 g2	zone	1.4	2.1	0.7	<0.1	<0.1	homogenised
E157 g2	pelitic	1.2	2.1	0.7	<0.1	<0.1	diffn rim*
E157 g3	mylonite	2.2	2.2	0.7	<0.1	<0.1	diffn rim*
E157 g3		1.5	2.2	0.7	<0.1	<0.1	diffn rim*
Z130	crd seam	0.7	2.5	0.2	<0.1	0.2	minor zoning
E116(1)a		1.6	1.8	0.3	0.6	0.2	variable
E116(1)b	Ca-rich	1.1	1.7	0.3	0.8	0.2	strong zoning
E116(2)a	banded	0.6	1.8	0.3	0.7	0.2	variable
E116(2)b	pelite	0.8	1.8	0.3	0.8	0.2	diffn rim*
E116(2)c		0.6	1.8	0.3	0.7	0.2	variable
N1	pelite	4.6	2.2	0.4	0.2	0.1	crd rim*
E126 g1	pelite	4.0	2.3	0.2	0.1	0.4	homogenised
E126 g2	pelite	2.8	2.3	0.2	0.1	0.4	homogenised
Z137ii 1.1	pelite	0.7	2.5	0.2	<0.1	0.2	homogenised
Z137ii 1.2	pelite	0.7	2.5	0.3	<0.1	0.2	homogenised
Z137ii 2.1	pelite	0.9	2.5	0.2	<0.1	0.2	homogenised
Z153ii	pelite	8.0	2.3	0.4	<0.1	0.3	diffn rim*
Z147.1g1	spl pelite	0.8	2.2	0.5	0.2	0.2	homogenised
Z147.3g1	spl pelite	3.0	2.2	0.5	0.2	<0.2	variable Mn
P4a 1.1	spl pelite	0.9	2.5	0.3	<0.1	0.2	homogenised
P4b 1.1	spl pelite	1.1	2.5	0.3	<0.1	0.3	homogenised
P4b 1.2	spl pelite	2.4	2.5	0.3	<0.1	0.3	2 garnets**
P4b 1.3	spl pelite	1.0	2.5	0.3	<0.1	0.3	2 garnets**
P4b 2.1	spl pelite	1.2	2.4	0.3	<0.1	0.3	homogenised
P4b 2.2	spl pelite	1.0	2.4	0.3	<0.1	0.3	homogenised
P4c 1.1	spl pelite	1.2	2.5	0.3	<0.1	0.2	homogenised
P4c 2.1	spl pelite	0.9	2.5	0.3	<0.1	0.2	homogenised

* indicates the presence of a retrograde diffusion rim
** indicates traverse crosses contiguous crystals.

Diffusion rims were more frequently observed, although these were usually less than 100μm in width. While not all traverses are likely to have intersected the true garnet core, the lack of Mn zoning in all but one profile suggests internal diffusive homogenisation is responsible. Mn behaves as a trace element in garnet, and can record strong zoning profiles in the absence of post-crystallisation diffusion (e.g. Ayres and Vance, 1997). In some cases several traverses were conducted on the same crystal in different orientations, but in no such traverses was zoning observed.

Garnet compositions vary between different lithologies, but are always predominantly almandine. Fe/Mg ratios are lower in the MMT zone than in pelitic lithologies from the interior of the massif, and garnets from a calcium-rich banded pelite (E116) contain more grossular.

Almandine-rich garnets from a pelitic mylonite in the MMT zone (E157, Fig. 3.4), are strongly cracked, with chlorite filling the cracks. These garnets are internally homogeneous, but show increasing grossular content, and decreasing almandine and pyrope contents, in narrow diffusion rims.

Grossular-rich garnets from a calcic banded pelite near Fairy Meadows (E116, Fig. 3.5), show the strongest internal zoning, with cores more Ca-rich and Fe-poor than rims. While Mg and Mn contents are homogeneous throughout the traverses, Ca and Fe profiles mirror each other, and often show great variability, perhaps due to the proximity of inclusions or cracks.

Almandine-rich garnets from high-grade pelitic rocks near Fairy Meadows contain higher Mn abundances than those from the massif margins, and show less pronounced diffusion rims (Fig. 3.6). The longest traverse is 8 mm long (Z153ii), which shows Fe-rich and Mg-poor diffusion rims. Z137ii is spinel-absent, and largely homogeneous with small diffusion rims in at least one garnet (Fig. 3.6).

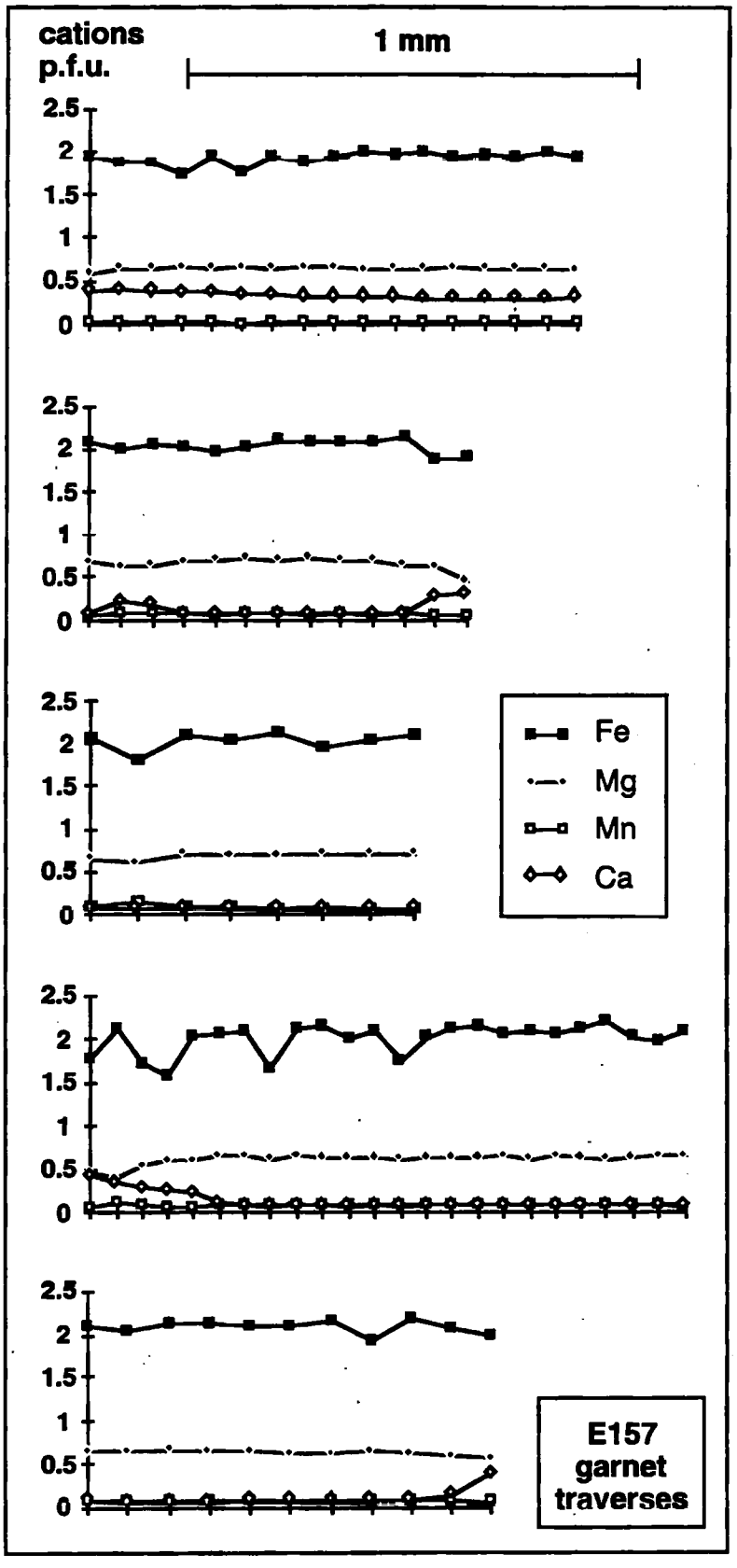

Figure 3.4. Garnet traverses for E157 from the MMT zone. Cation contents are expressed as cations per formula unit, assuming 12 oxygens. 1 mm scale applies to all traverses.

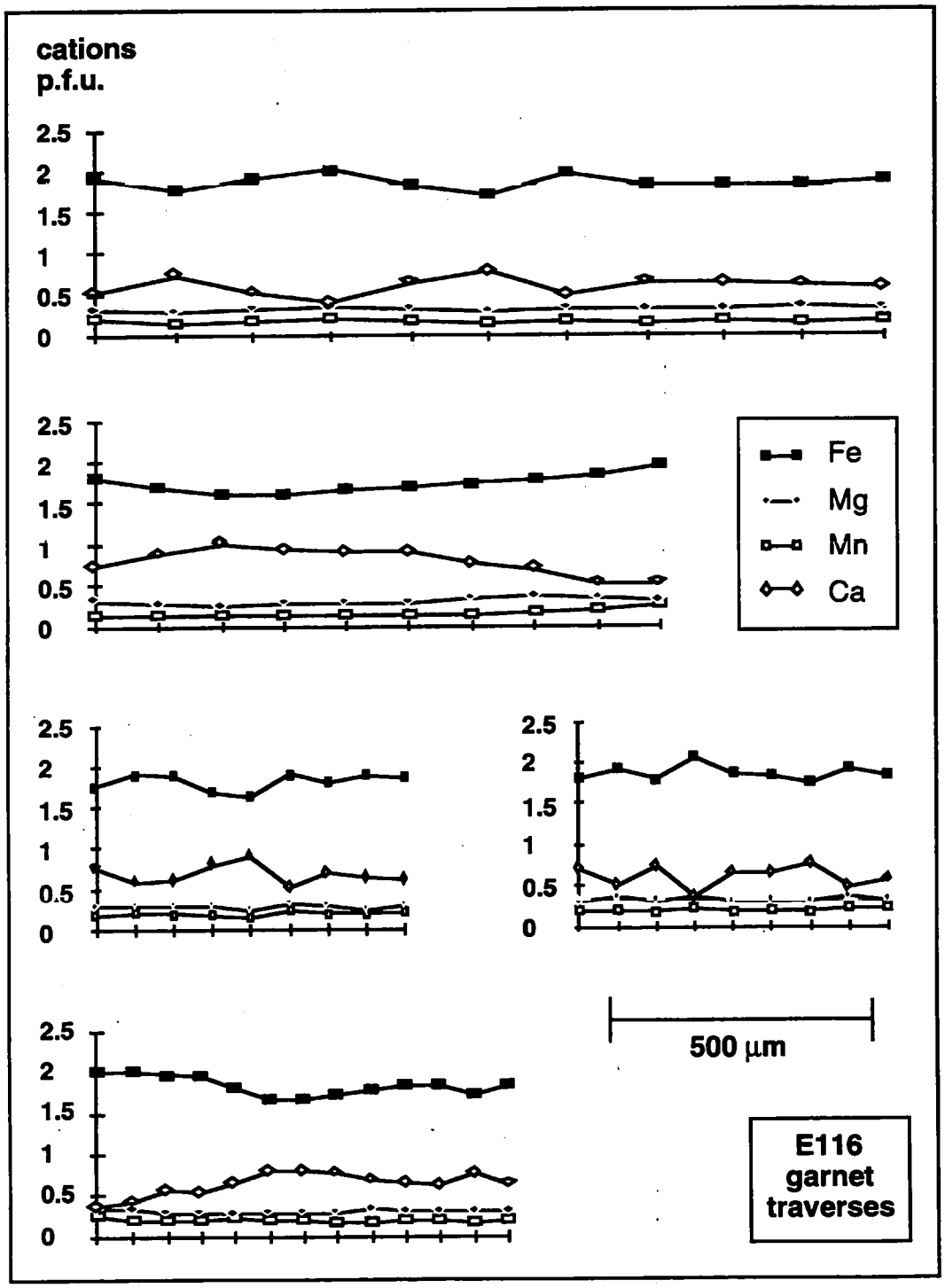

Figure 3.5 Garnet traverses for E116, a banded calcic pelite from the massif interior. 500μm scale applies to all traverses.

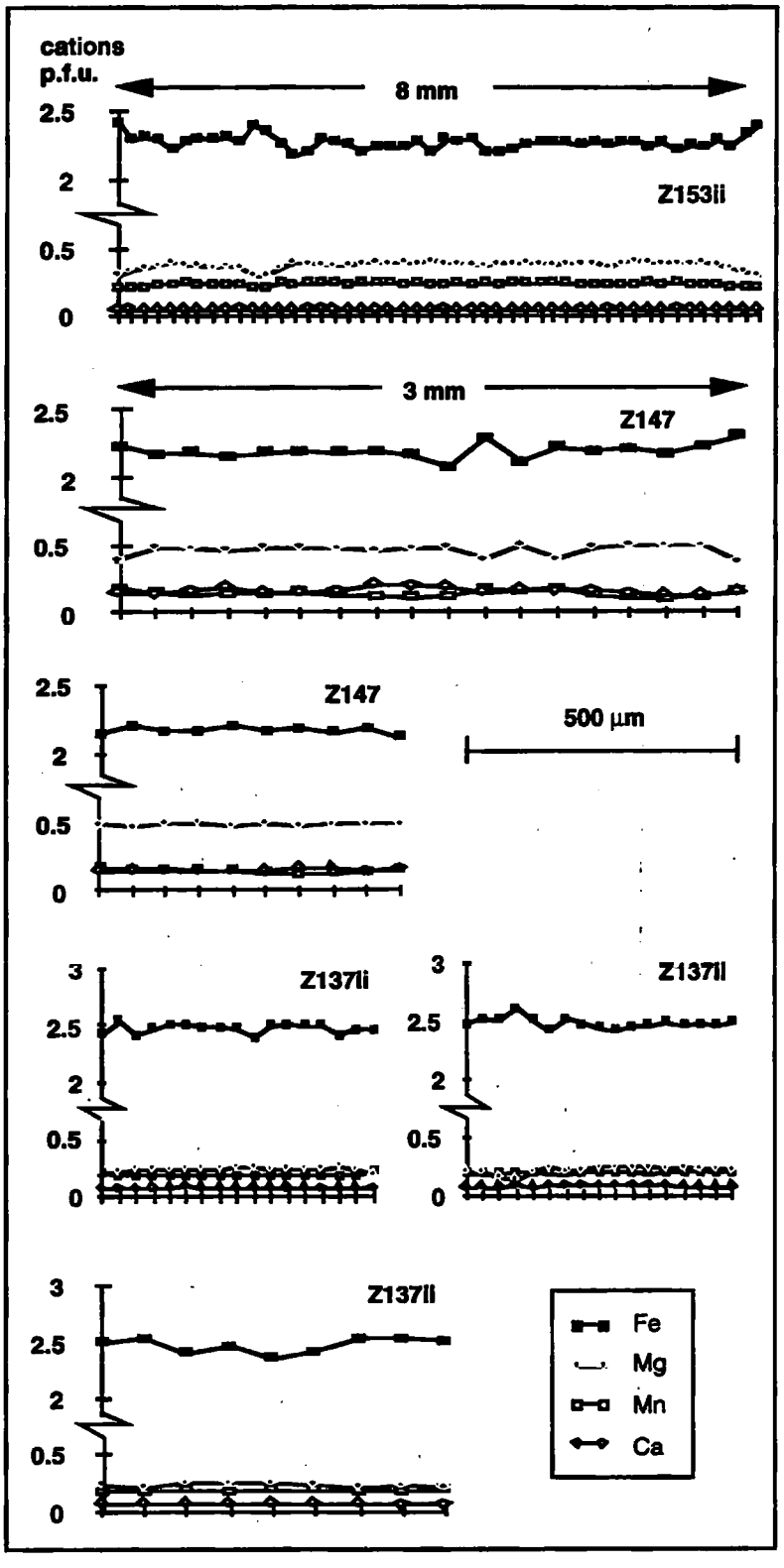

Figure 3.6 Garnet traverses for high grade pelites from the massif interior. Z137ii and Z153ii are spinel-absent, while Z147 contains spinel. 500 µm scale applies to lower four traverses, individual scales shown for top two traverses.

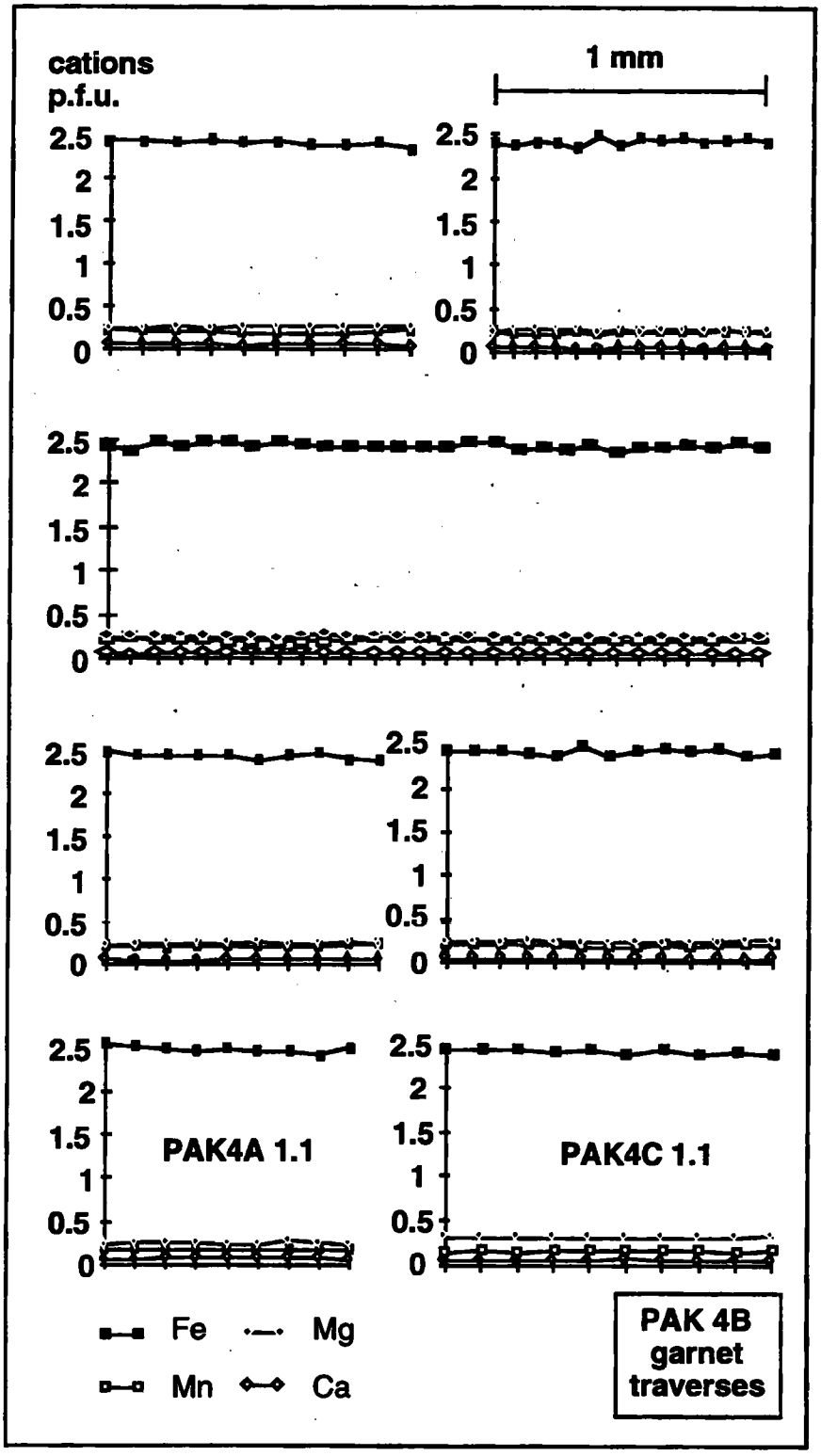

Figure 3.7 Garnet traverses for PAK4, a spinel-bearing metapelite from the massif interior. The exceptional degree of homogenisation within individual crystals, within different crystals from the same thin section (the top 5 traverses are all from section PAK4B), and within a hand specimen (all 7 traverses) indicates equilibrium was attained on at least a decimetre scale.

Spinel-bearing pelitic rocks from the massif interior contain garnets with similar zoning profiles to those in spinel-absent rocks, although the only example of Mn zoning occurs in a garnet from Z147 (Fig. 3.6) in the same thin section as spinel-cordierite intergrowths (Section 3.4). This zoning is weak, and undulates, so that either the garnet has formed from two smaller crystals which subsequently grew together, or the observed trends may be influenced by submicroscopic inclusions. Despite small antipathetic fluctuations in Fe and Mg content, there is no evidence of a partially homogenised Rayleigh growth profile, so that homogenisation again appears to be complete.

The scale of homogenisation in the examples discussed above is both within single crystals, and also between crystals in the same thin section. The extent of homogenisation in the interior of the massif (spinel zone) can be appreciated through seven traverses from different thin sections of the same hand specimen (PAK4, Fig. 3.7). Five traverses from the same thin section show complete homogenisation, no diffusion rims, and equilibration between different crystals. Garnets from two other thin sections from the same hand specimen (PAK4A and PAK4C) also show internal homogenisation and identical composition.

Thus in the southern NPHM, mm-scale garnets have been internally homogenised in both the margins and interior of the massif. The largest diffusion rims are from garnets which grew in the massif margins, with little or no evidence of retrograde diffusion in garnets from the massif interior. Homogenisation occurred not only on the scale of a single crystal (mm scale) or thin section (cm scale), but also on the scale of a hand specimen (dm scale).

3.3.3 Obtaining P-T information from garnet zoning profiles

Compositional zoning is widespread in many metamorphic garnets (although apparently not at Nanga Parbat). Growth zoning occurs during prograde garnet growth, where the composition of new garnet depends on bulk rock composition, mineralogy, and pressure-temperature conditions (Florence and Spear, 1993). In general, prograde metamorphic garnets in pelitic lithologies have more magnesium- and manganese-rich cores, and more iron- and calcium-rich rims. The distribution of iron and magnesium depends on the coexisting mineralogy at the time of garnet growth. For example, coexisting biotite will always have a lower X_{Fe} than garnet, where X_{Fe} = Fe /(Fe+Mg), but the relative distribution of Fe and Mg between garnet and biotite depends almost entirely on the temperature of garnet growth. This distribution is described by

$$K_d(Fe\text{-}Mg)_{gnt\text{-}bt} = [X_{Fe}/X_{Mg}]_{bt} / [X_{Fe}/X_{Mg}]_{gnt}$$

Since lines of constant K_d for this simple exchange reaction have very steep slopes in P-T space, temperature has by far the dominant effect on the relative distribution of Fe and Mg between garnet and biotite.

Manganese is partitioned very strongly into garnet, relative to all other common phases in metapelitic rocks. During garnet growth, the manganese concentration in garnet will be determined largely by Rayleigh fractionation (Hollister, 1966) as other Mn-bearing phases break down. Once this profile has been incorporated during garnet growth, it will homogenise through volume diffusion. At the same time, the garnet rim will attempt to re-equilibrate with coexisting minerals in the matrix. In pelitic rocks this effect is usually strongest with regard to iron and magnesium, in particular where biotite rims the garnet. This exchange will continue down to a blocking temperature, below which rates of diffusion are insignificant.

The original Rayleigh distribution of manganese can be reconstructed, assuming that the bulk Mn content of the garnet has not changed, and with a known or assumed distribution coefficient between garnet and the bulk rock. A Kd for Mn between garnet and whole-rock of about 80 was obtained by Ayres and Vance (1997), in broad agreement with previous estimates (Atherton, 1968; Dempster, 1985). If the profile is only partly homogenised, and the diffusion coefficient for manganese within garnet is known, then constraints can be placed on the temperature-time history of the garnet.

Ayres and Vance (1997) used garnet zoning profiles from Zanskar to calculate diffusion rates empirically, and hence the diffusion coefficient, for Mn in garnet. Note that strictly this is an effective bulk diffusion coefficient (EBDC) since Mn must exchange with other cations (Fe^{2+}, Mg, Ca) in order to diffuse. Although their calculated diffusion coefficient of $6 \pm 3.2 \times 10^{-23}$ m^2s^{-1} has significant errors attached, it can be used to place constraints on the minimum duration spent above a given temperature for garnets which show complete homogenisation of growth zoning.

The equation relating the extent of homogenisation to diffusion rate, diffusion radius, temperature and time is

$$t' = \frac{D_{(T_{CH})} \times t}{a^2}$$

where D is the diffusion rate of Mn in garnet at the temperature at which all diffusion is assumed to occur (T_{CH}), t is the time spent at T_{CH}, and a is the diffusion length scale. If no diffusive homogenisation has occurred t' is 0, and for $t' \geq 0.25$ homogenisation is complete. $T_{CH} \approx 0.97 \times T_{PEAK}$ for typical regionally metamorphosed terranes (Chakraborty and Ganguly, 1990), and is an approximation to eliminate the temperature dependence of diffusion rates.

For Nanga Parbat garnets, metamorphic conditions are constrained by complete homogenisation of Mn in garnet over length scales of at least 4 mm (the radius of garnet Z153ii, Table 3.9), corresponding to a t' value of 0.25 or greater. Calculations using the Mn diffusion coefficient of Ayres and Vance (1997) suggest that this garnet must have spent a time of at least 1378 to 4527 Ma at a peak temperature of 720°C (T_{CH} = 690 °C). These timescales are two orders of magnitude greater than the timescale of the Himalayan orogeny, but since maximum temperatures are thought to be higher than this in the massif interior where spinel occurs (Section 3.4), the duration of peak temperatures may be lower. For a peak temperature of 830°C (T_{CH} = 800 °C), which would exceed the vapour-absent biotite dehydration solidus and hence is unrealistically high, the minimum duration of the thermal event is calculated to be between 160 and 13 Ma. This constraint is not particularly enlightening, especially when the full uncertainties on the diffusion coefficient of four orders of magnitude are considered (Ayres and Vance, 1997, Fig. 10).

Although many garnets from the southern NPHM are internally homogeneous, and homogenisation also appears to have occurred between different garnets within the same thin section, retrograde diffusion rims are apparent in many samples. These rims typically occur over distances of only 100μm in homogenised garnets, suggesting that cooling to below effective diffusion temperatures was rapid.

Very high cooling rates within the NPHM have been documented by unusually young metamorphic monazite and zircon growth (Zeitler et al., 1989; Zeitler and Chamberlain, 1991; Smith et al., 1992; Zeitler et al., 1993). Such high cooling rates will result in high blocking temperatures for both net transfer reactions and cation exchange reactions, explaining why the garnet-biotite exchange reaction records higher temperatures in the NPHM than those commonly obtained in other regions, where cooling rates were lower.

Perhaps of more interest is the qualitative significance of complete Mn homogenisation within garnets from both the interior and the margin of the NPHM. This suggests that all rocks now exposed within the NPHM have experienced high temperatures over a prolonged period. A comparison may also be made with garnet-bearing lithologies from the main Himalayan range in Zanskar.

3.3.4 Comparison of garnet zoning between Nanga Parbat and Zanskar

Garnet zoning patterns can be used to compare the P-T-t histories of different rocks. Where inclusion assemblages are available for thermobarometric calculation, and geochronological techniques can be used to date garnet growth and / or peak metamorphism, more precise limits can be placed on P-T-t paths (e.g. Vance and O'Nions, 1990). P-T-t paths of individual rocks are controlled by many factors, and will be expected to vary within a single orogen across strike, with structural level, position in relation to major faults, and different erosion rates and processes (Batt and Braun, 1997). The effect of these differences on patterns of garnet zoning are evident within the southern NPHM by comparing E157 from the MMT zone, and PAK4 from the interior of the massif (Figs. 3.4 and 3.7).

Garnets from Zanskar show variable degrees of homogenisation, depending on grain size, although the observation that smaller garnets are depleted in Mn with respect to larger garnets suggests that garnet nucleation was diachronous (Ayres and Vance, 1997). The most significant difference between the two areas is that large garnets from Zanskar (>3 mm radius) show little or no diffusive modification of Rayleigh Mn zoning profiles (Ayres and Vance, 1997, Fig. 4), in stark contrast to large garnets from Nanga Parbat (e.g. Z153ii, Fig. 3.6). Bulk MnO contents are similar between Z153ii (average MnO content is 3.5 wt.%) and large

garnets from Zanskar (zoned from >5 wt.% in the core to <1 wt.% at the rim), so that the lack of zoning in Z153ii is not due to lack of Mn in the bulk rock.

Diffusion rims are often small or lacking in garnets from Zanskar (Ayres and Vance, 1997), suggesting that rapid cooling from high temperatures is a feature common to both areas. Peak temperatures are similar in both areas, with Thermocalc P-T estimates of 690 to 750 °C at 8 to 12 kbar for garnet-bearing assemblages from Zanskar (Searle et al., 1992b; Ayres and Vance, 1997). These compare with a range of estimates between 630 and 720 °C at 3 to 9 kbar for garnet-bearing assemblages from Nanga Parbat (section 3.2). Although Thermocalc P-T estimates are similar for the two areas, temperatures of 700 to 750 °C may record partial re-equilibration on the retrograde path rather than true peak conditions (Spear and Peacock, 1989; Jiang and Lasaga, 1990). Garnets from Zanskar have not been homogenised, so that temperatures calculated from these assemblages are likely to represent peak conditions. In addition, garnets from neither area show strong diffusion rims, suggesting rapid cooling with little time for re-equilibration.

The timing of peak metamorphism at Zanskar is constrained by Ar-Ar geochronology on hornblende, which gives ages of about 30 Ma at the top of the slab near the Zanskar Shear Zone (ZSZ), and 22 Ma or younger in the middle of the slab (Searle et al., 1992b). Exhumation at Zanskar at about 22 Ma was due to movement on the extensional ZSZ (Searle, 1986; Herren, 1987), resulting in genesis of High Himalayan leucogranites by vapour-absent muscovite breakdown (Inger and Harris, 1993). Cooling ages at Nanga Parbat are almost exclusively less than 10 Ma for all geochronological systems, including U-Pb on monazite and zircon (Zeitler et al., 1989; Smith et al., 1992; Zeitler et al., 1993), Ar-Ar on micas (George, 1993; Winslow et al., 1996; Chapter 6) and fission track dating (Zeitler et al., 1982a, b; Zeitler, 1985).

The contrast in garnet profiles between Nanga Parbat and Zanskar thus reflects the longer time spent at high temperatures by the Nanga Parbat lithologies. For collision at circa 50 Ma (discussion in Chapter 1), Zanskar rocks were metamorphosed and exhumed to low temperatures within 30 Ma of collision, while those at Nanga Parbat have only been exhumed within the past 5 or 10 Ma. Peak temperatures may have been higher at Nanga Parbat, but this cannot be firmly established due to the likelihood of re-equilibration during cooling and decompression. An additional possibility is that garnets at Nanga Parbat did not grow during the Himalayan orogeny, but have been exhumed from great depths in the Indian Plate, in which case they may have grown prior to Himalayan metamorphism. This hypothesis would explain why Mn growth profiles are now homogeneous over distances of several mm, and may be tested by garnet chronometry.

3.4 Spinel-bearing assemblages in metapelites

Author's note: This manuscript has been accepted for publication in a Geological Society of London Special Publication, the proceedings volume of the Metamorphic Studies Group meeting in Kingston, September 1996.

"Low pressure crustal anatexis: the significance of spinel and cordierite from metapelitic assemblages at Nanga Parbat, northern Pakistan"

by Alan Whittington, Nigel Harris and Judy Baker

3.4.1 Abstract

Spinel-bearing domains in high grade metapelitic rocks from Nanga Parbat represent zones of partial melting during biotite breakdown under vapour-undersaturated conditions. Spinel is essentially of the $MgAl_2O_4$-$FeAl_2O_4$ solid solution, and is therefore not stabilised by the presence of trace elements such as zinc, but is restricted to a quartz-absent petrogenesis. A new petrogenetic grid for metapelites has been constructed to allow for both vapour-undersaturated and quartz-undersaturated conditions. This grid contains a quartz-absent invariant point in KFASH that predicts quartz-absent melting will occur in biotite-sillimanite assemblages at low pressures.

A P-T pseudosection drawn for bulk compositions with intermediate Fe/Mg ratios shows that at low pressures biotite will break down initially in the presence of quartz, to produce cordierite and K-feldspar and melt. At higher temperatures the quartz-absent reaction will be crossed, and biotite will break down to produce spinel in addition to cordierite, K-feldspar and melt. The sequence of assemblages is biotite-cordierite, biotite-cordierite-spinel, and finally cordierite-spinel. This biotite-absent assemblage is not observed, indicating that the quartz-absent reaction did not go to completion. Limits can be placed on the pressures and temperatures at which the biotite breakdown reaction is crossed, from the coexistence of solid phases and granite melt over a range of water activities. For the Nanga Parbat assemblages, pressures and temperatures lay at about 720 °C and 5 kbars at $a_{H_2O} \geq 0.6$. These conditions are consistent with a rapidly exhuming terrane, as suggested by isotopic constraints and thermal modelling of the region.

3.4.2 Introduction

Crustal anatexis of metapelitic assemblages in the absence of a free fluid phase usually involves the breakdown of biotite and/or muscovite leading to the coexistence of a melt and anhydrous peritectic phases (Gardien et al., 1995; Le Breton and Thompson, 1988; Patiño Douce and Johnston, 1991; Vielzeuf and Holloway, 1988). In Himalayan lithologies, Miocene leucogranites have been associated with sillimanite formation during the dehydration melting of muscovite (Harris et al., 1995), but temperatures were insufficient for biotite breakdown to occur. Cordierite-spinel metapelitic assemblages are reported here for the first time from the Himalayas. The significance of spinel formation and its possible relationship with melt formation are investigated, using standard thermobarometric techniques combined with theoretical calculations in the K_2O-FeO-MgO-Al_2O_3-SiO_2-H_2O (KFMASH) system.

The rocks we have used in this study are from the Nanga Parbat-Haramosh Massif in northern Pakistan. The massif, which marks the western extremity of the High Himalayas, is a polymetamorphic terrain comprising granitic orthogneisses and psammitic, pelitic and calcareous paragneisses which have experienced metamorphism both as part of the Indian craton, and more recently during the Himalayan orogeny. The most recent metamorphic episode is associated with rapid exhumation of the massif over the last 10 Ma (Zeitler et al., 1982a; Zeitler, 1985), which has led to leucogranite generation through fluid-absent muscovite breakdown (Zeitler and Chamberlain, 1991; Butler et al., 1997; Whittington et al., 1997a) and high-T low-P metamorphic assemblages containing cordierite, sillimanite and K-feldspar. These assemblages fall into two categories: cordierite-K-feldspar leucosomes localised in shear zones, and biotite-sillimanite-K-feldspar ± spinel domains within migmatitic pelitic gneisses. The leucosomes have been attributed to fluid infiltration and localised fluid-present melting in shear zones

(Whittington et al., 1997a). This paper investigates the origins of spinel-bearing domains in the pelitic gneisses.

3.4.3 Petrography

Metapelitic gneisses from the core of the Nanga Parbat Massif typically contain biotite, garnet, sillimanite, quartz, K-feldspar and plagioclase, with cordierite commonly occurring, and more rarely green hercynitic spinel. Ilmenite, pyrite and apatite are common accessory phases, with rutile, magnetite, chalcopyrite, zircon and monazite occurring more rarely. Small (cm scale) granitic leucosomes are common in these gneisses and some melting is inferred to have occurred.

The most recent fabrics are defined by sheaves of biotite and sillimanite, wrapping around garnets which show inclusion trails at steep angles to foliation (Fig. 3.8a). This suggests that garnet was present before the most recent metamorphism. Garnet is often mantled by cordierite (Fig. 3.8b), which is not apparently associated with leucosome formation, and which is readily explained by the solid-state decompression reaction:

garnet + sillimanite + quartz = cordierite (3.1)

In many thin sections, biotite is observed to be breaking down in the presence of sillimanite. Microprobe investigation shows that cordierite-K-feldspar intergrowths are common. These textures may be explained by the reaction:

biotite + sillimanite + quartz = cordierite + K-feldspar + melt (3.2)

Figure 3.8. Photomicrographs of thin sections, mineral abbreviations follow Kretz (1983).

a) Garnet showing inclusion trail (S_i) oriented at a steep angle to external foliation (S_e) defined by biotite and sillimanite in the presence of quartz and cordierite.

b) Cordierite rimming garnet and biotite, which are breaking down. Plain polarised light, long dimensions of photographs are 3mm..

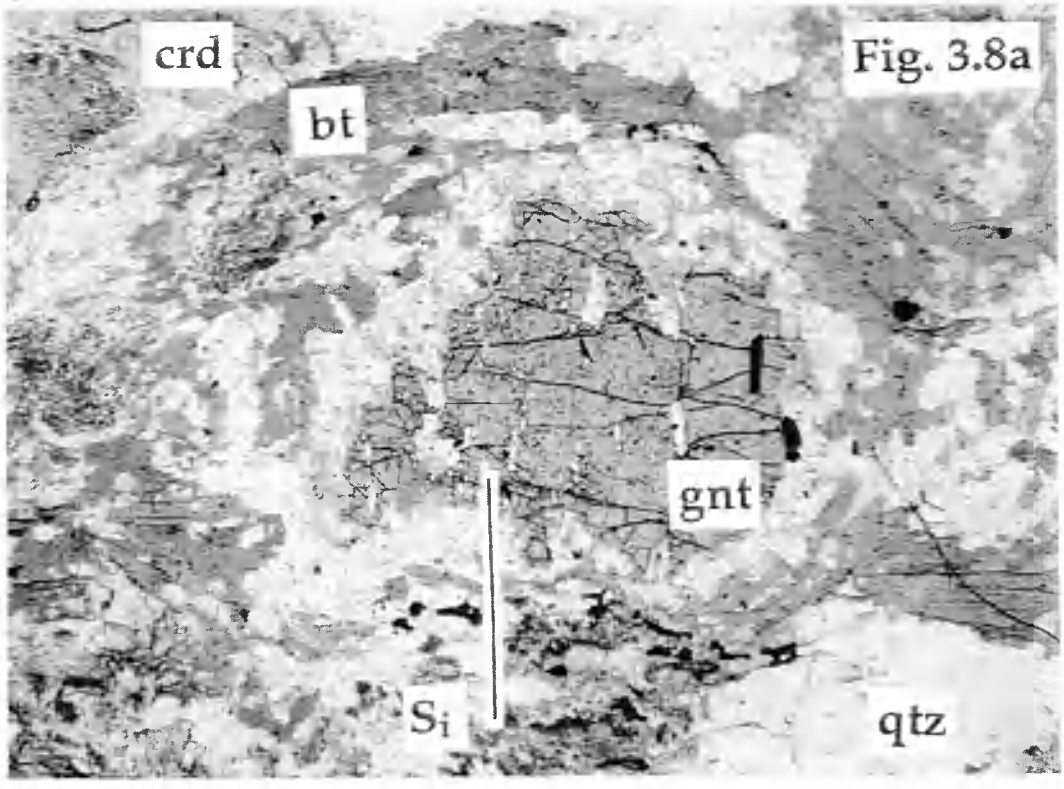
crd
bt
Fig. 3.8a
gnt
S_i
qtz

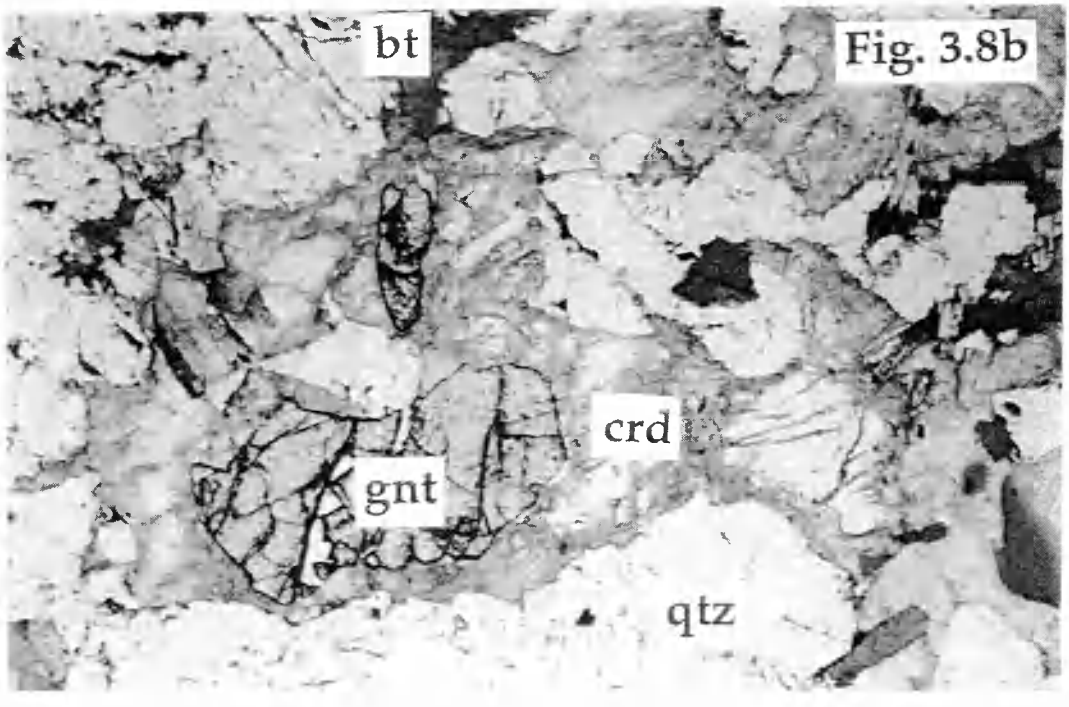
bt
Fig. 3.8b
crd
gnt
qtz

Figure 3.8 (continued)

c) Back-scattered electron image of spinel-bearing zone, showing biotite and sillimanite breaking down, with intimately associated cordierite and spinel. Scale bar is 500 μm.

d) Spinel - cordierite intergrowth, and spinel rimming decomposing biotite and sillimanite. Scale bar is 100 μm.

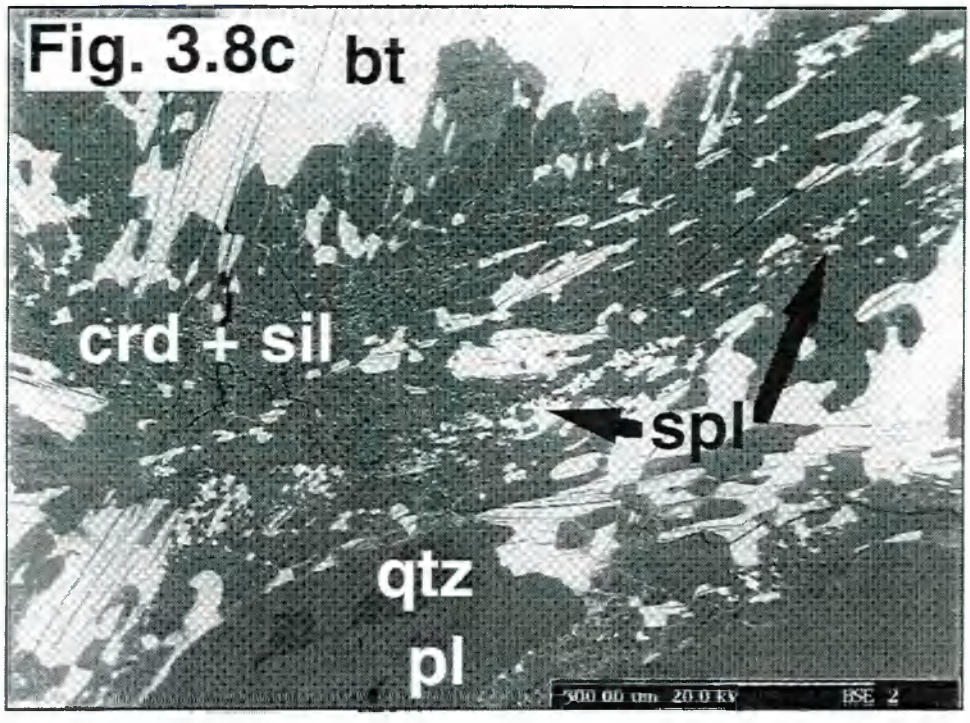
Fig. 3.8c
bt
crd + sil
spl
qtz
pl
500.00 um 20.0 kV
BSE 2

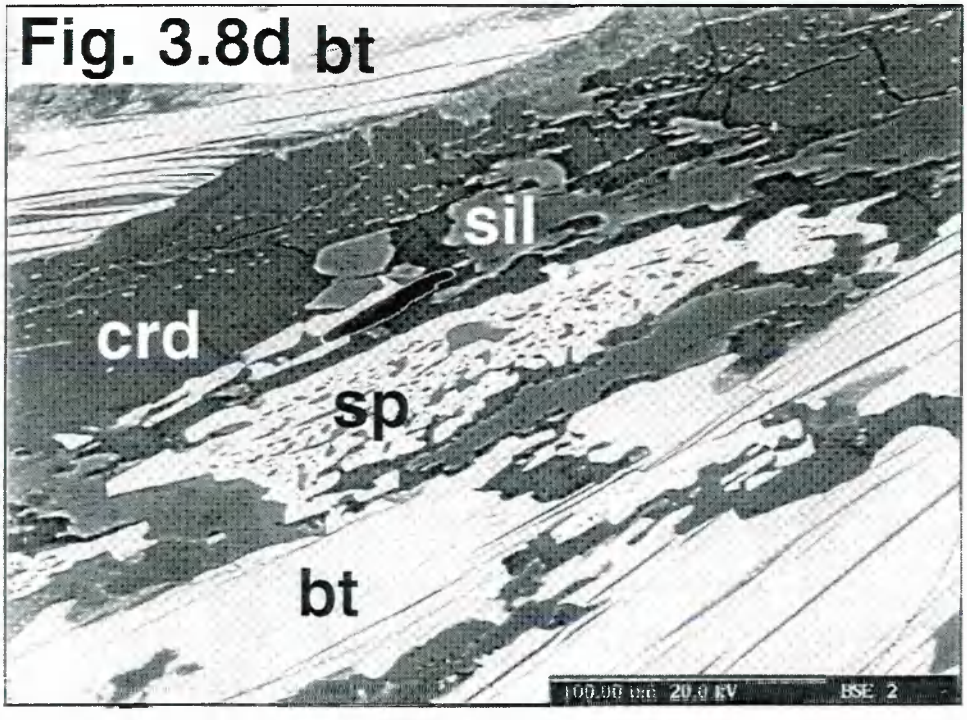
Fig. 3.8d
bt
sil
crd
sp
bt
100.00 um 20.0 kV
BSE 2

Carrington and Watt (1995) found that for the KFMASH system, reaction (3.2) was close to K-feldspar-absent degeneracy, and that K-feldspar was a reactant in experiments where the H_2O/K_2O ratio in the melt was less than the H_2O/K_2O ratio in reacting biotite. In previous experiments on reaction (3.2), where cordierite is a product, LeBreton and Thompson (1988) found K-feldspar was a product phase, but Vielzeuf and Holloway (1988) and Patiño-Douce and Johnston (1991) found no K-feldspar generated by the reaction. While K-feldspar is common throughout Nanga Parbat metapelites, its occurrence as an intergrowth with cordierite suggests that in this case it is a reaction product.

In some sections, thin zones of cordierite-spinel intergrowths are seen intimately associated with decomposing biotite (Fig. 3.8c). Where spinel is found in these zones, quartz is absent or present only as inclusions within other phases, for example plagioclase, and hence is texturally isolated from reaction (3.2). All available quartz has been consumed within these domains, although quartz coexists with biotite elsewhere in the same thin section, indicating chemical disequilibrium on a very small (sub-centimetre) scale. Spinel can be clearly seen overgrowing biotite, and spinel-cordierite intergrowths also occur (Fig. 3.8d), hence both these phases are reaction products.

3.4.4 Mineral chemistry

In this paper we have studied several spinel-bearing assemblages through microprobe analyses of coexisting biotite, cordierite and spinel. Spinel data are given in Table 3.10, and representative analyses of all phases used in thermobarometry are given in Table 3.11, including a silica-saturated biotite-cordierite-garnet metapelite (N1) for comparison. Of particular interest is the

variation in mineral chemistry within a single thin section, depending on textural relations.

As an example, X8 is a spinel-bearing metapelite which also contains a garnet porphyroblast, rimmed by stable fabric-forming biotite and plagioclase. Biotite and plagioclase are also found as inclusions within the garnet, and biotite is observed breaking down in the presence of spinel elsewhere in the thin section. Garnet cores are of composition $alm_{76}prp_{15}grs_5sps_4$. Rims are less Mg-rich, but more Fe- and Mn-rich, with composition $alm_{79}prp_{11}grs_4sps_6$ where in contact with biotite. Fe# varies from 84 in the core to 89 in the rim, where Fe# = (mol.% Fe^{2+}) / (mol.% Fe^{2+} + mol.% Mg) * 100. Biotite from X8 shows systematic variations in Fe number with its petrographic location (Table 3.11). Biotite inclusions in garnet have an average Fe# of 60, while biotite rimming garnet has an average Fe# of 65. Biotite analyses from the spinel zone show even higher Fe# of 67. Matrix plagioclase shows zoning, from about An_{28} in cores to An_{35} in rims. Plagioclase inclusions in garnet contain An_{30}, approximately the core composition of matrix plagioclase.

In spinel zones, cordierite has a fairly uniform composition within a single thin section, and even between different thin sections. Spinel has a limited range of Fe/Mg ratio, with Fe# varying only between 86 and 89, with only zinc abundances varying significantly. In contrast, biotite varies in composition across a single decomposing grain; for example X2 analyses 28 and 30 shows variation of Fe# between 59 and 64 in a single grain. Holtz and Johannes (1991), and Patiño Douce and Johnston (1991) reported that biotite compositions in equilibrium with a melt become more Mg-rich as biotite melting progresses. Since unmelted matrix biotite from this same thin section has an Fe# of 64, this was probably the original biotite composition, and the more Mg-rich composition from the spinel zone reflects the coexistence of a melt. Furthermore, Patiño Douce and Johnston (1991) noted an increase in TiO_2 content of biotite with increasing temperature, and biotites from

spinel-bearing zones at Nanga Parbat are also more Ti-rich than biotites from garnet-bearing zones (e.g. Z147 and X7, Table 3.11).

3.4.5 Spinel stability

The presence of spinel in metapelitic assemblages has been accredited to a number of factors. At temperatures greater than 900 °C and pressures less than 8 kbars, spinel is stable in the presence of quartz and cordierite following garnet breakdown (Hensen and Green, 1973). The stability field of spinel may be extended to lower temperatures by the presence of additional components such as ferric iron (Dasgupta et al., 1995) and chromium, which substitute for aluminium, or zinc (Dasgupta et al., 1995; Nichols et al., 1992; Waters, 1991), which substitutes for iron and magnesium. In such cases, spinel cannot be used as a guide to metamorphic grade in petrogenetic grids constructed in the KFMASH system, which can strictly only account for the hercynite ($FeAl_2O_4$) and spinel *sensu stricto* ($MgAl_2O_4$) endmembers.

Microprobe analyses in Table 3.10 have been recalculated by site allocation to estimate the ferrous/ferric iron ratios in spinel. Ferric iron averages between 3 and 5 weight percent of spinel, comprising less than 10 percent of trivalent cations. Zinc, chromium and titanium occur in concentrations of up to 10.3, 1.2 and 0.3 weight percent respectively. Zinc is clearly the most significant component outside the KFMASH system.

Table 3.10. Microprobe analyses of spinel from metapelitic assemblages at Nanga Parbat.

oxides	Z135r4 avge.	Z135r4 stdev.	Z147r1 avge.	Z147r1 stdev.	X8 avge.	X8 stdev.	X7 avge.	X7 stdev.	X2 avge.	X2 stdev.	004A avge.	004Cr1 avge.	004Cr2 avge.
SiO_2	0.42	0.35	0.26	0.27	0.35	0.40	0.29	0.30	0.25	0.26	0.11	0.21	0.50
TiO_2	0.09	0.02	0.12	0.03	0.11	0.04	0.11	0.03	0.12	0.03	0.04	0.07	0.03
Al_2O_3	56.80	0.68	56.52	0.49	56.14	0.96	57.02	0.83	55.72	0.63	56.49	57.16	57.16
Cr_2O_3	0.19	0.07	0.18	0.14	0.13	0.06	0.32	0.32	0.21	0.23	0.01	0.00	0.02
Fe_2O_3	2.71	0.96	2.36	0.78	4.27	1.08	3.01	0.97	3.23	0.72	5.75	3.01	5.57
FeO	34.47	0.77	35.91	0.46	34.93	0.89	34.50	0.78	33.76	0.89	29.80	33.11	24.68
MnO	0.31	0.01	0.18	0.01	0.35	0.02	0.32	0.02	0.37	0.02	0.21	0.22	0.22
MgO	2.88	0.06	2.50	0.10	2.72	0.11	3.37	0.11	3.04	0.13	1.55	2.18	2.17
CaO	0.00	0.00	0.00	0.01	0.01	0.01	0.01	0.01	0.01	0.01	0.00	0.00	0.04
Na_2O	0.07	0.02	0.02	0.01	0.05	0.02	0.03	0.02	0.05	0.02	0.48	0.28	0.89
K_2O	0.00	0.00	0.05	0.05	0.09	0.09	0.04	0.02	0.05	0.05	0.04	0.02	0.00
ZnO	2.25	0.05	0.87	0.11	1.48	0.29	1.28		1.40	0.47	6.75	3.43	10.20
Total	100.11 (n = 17)		98.96 (n=47)		100.61 (n = 34)		100.28 (n = 22)		98.20 (n = 63)		101.13 (n = 3)	99.65 (n = 3)	100.91 (n = 2)
Cations													
Si	0.012	0.010	0.008	0.008	0.010	0.011	0.008	0.008	0.007	0.007	0.003	0.006	0.014
Ti	0.002	0.000	0.002	0.001	0.002	0.001	0.002	0.001	0.002	0.001	0.000	0.001	0.001
Al	1.916	0.008	1.930	0.010	1.893	0.017	1.914	0.013	1.914	0.011	1.907	1.940	1.913
Cr	0.004	0.002	0.004	0.003	0.003	0.001	0.007	0.007	0.005	0.005	0.000	0.000	0.001
Fe^{3+} [1]	0.059	0.021	0.051	0.017	0.092	0.024	0.065	0.021	0.071	0.016	0.132	0.065	0.119
Fe^{2+}	0.825	0.014	0.870	0.010	0.835	0.018	0.821	0.017	0.823	0.019	0.711	0.798	0.586
Mn	0.008	0.000	0.004	0.001	0.009	0.001	0.008	0.000	0.009	0.001	0.004	0.005	0.005
Mg	0.123	0.002	0.108	0.004	0.116	0.004	0.143	0.004	0.132	0.005	0.065	0.094	0.092
Ca	0.000	0.000	0.000	0.000	0.000	0.000	0.000	0.000	0.000	0.000	0.000	0.000	0.002
Na	0.004	0.001	0.001	0.001	0.003	0.001	0.002	0.001	0.003	0.001	0.031	0.015	0.049
K	0.000	0.000	0.002	0.002	0.003	0.003	0.001	0.001	0.002	0.002	0.000	0.001	0.000
Zn	0.048	0.001	0.019	0.002	0.031	0.006	0.027	0.008	0.030	0.010	0.141	0.073	0.214
total	2.999	0.001	2.999	0.001	2.997	0.001	2.998	0.001	2.998	0.001	2.993	2.999	2.995
Endmember activities [2]													
Spinel	0.115	0.002	0.102	0.004	0.106	0.004	0.133	0.005	0.123	0.006	0.062	0.079	0.090
Hercynite	0.771	0.018	0.821	0.016	0.764	0.024	0.764	0.020	0.766	0.019	0.675	0.732	0.579
Gahnite	0.044	0.001	0.018	0.002	0.029	0.006	0.025	0.008	0.028	0.010	0.134	0.098	0.211
Galaxite	0.007	0.000	0.004	0.000	0.008	0.000	0.007	0.000	0.008	0.000	0.000	0.000	0.000
Fe# [3]	87.0	0.3	89.0	0.4	87.8	0.5	85.2	0.6	86.2	0.6	91.6	89.1	87.5

[1] Fe3+ calculated by site allocation. [2] Endmember activities assume ideal mixing. [3] Fe# = $(Fe^{2+})/(Fe^{2+} + Mg)$ cations. Analyses were carried out on a Cameca SX-100 at the Open University, and a Cameca SX-50 at Cambridge University (004A, 004C) using 1μm beam size and 20 nA beam current.

Table 3.11. Representative mineral analyses used in thermobarometric calculations.

	Z135 spinel zone [1]				Z147 garnet rim [2]				Z147 spinel zone [1]	
	crd	spl	bt	ksp	gnt	plag	bt	ksp	bt	spl
	#42	#31	#135	#119	#136	#141	#144	#166	#108	#47
SiO_2	48.03	0.25	33.99	64.13	37.24	60.51	34.28	63.82	34.26	0.08
TiO_2	0.00	0.06	3.40	0.18	0.00	0.06	1.81	0.00	5.63	0.09
Al_2O_3	32.44	57.19	17.37	18.48	20.79	24.46	18.67	18.16	18.80	57.77
Cr_2O_3	0.00	0.18	0.07	0.00	0.05	0.03	0.07	0.04	0.05	0.18
Fe_2O_3	1.62	2.73	0.00	0.26	1.73	0.03	0.00	0.13	0.00	1.60
FeO	9.57	34.30	23.54	0.00	32.65	0.00	20.21	0.00	22.29	36.29
MnO	0.29	0.31	0.26	0.00	2.06	0.00	0.21	0.00	0.06	0.18
MgO	6.58	2.83	6.92	0.00	4.21	0.00	9.07	0.00	6.38	2.42
CaO	0.01	0.00	0.00	0.08	1.73	6.29	0.00	0.10	0.00	0.00
Na_2O	0.26	0.07	0.13	2.76	0.00	7.74	0.42	1.95	0.17	0.02
K_2O	0.00	0.00	9.33	12.93	0.02	0.47	9.37	14.02	9.23	0.03
ZnO	n/a	2.28	n/a	n/a	n/a	n/a	n/a	n/a	n/a	0.90
Totals	98.80	100.20	95.01	98.83	100.48	99.58	94.11	98.24	96.87	99.55
Si	4.980	0.007	2.667	2.974	2.970	2.705	2.667	2.987	2.607	0.002
Ti	0.000	0.001	0.201	0.006	0.000	0.002	0.106	0.000	0.322	0.002
Al	3.966	1.927	1.607	1.010	1.955	1.289	1.712	1.002	1.687	1.956
Cr	0.000	0.004	0.004	0.000	0.003	0.001	0.004	0.001	0.003	0.004
Fe^{3+}	0.126	0.059	0.000	0.009	0.104	0.001	0.000	0.004	0.000	0.034
Fe^{2+}	0.830	0.820	1.545	0.000	2.178	0.000	1.315	0.000	1.419	0.872
Mn	0.026	0.008	0.017	0.000	0.139	0.000	0.014	0.000	0.004	0.004
Mg	1.017	0.121	0.809	0.000	0.500	0.000	1.052	0.000	0.724	0.104
Ca	0.002	0.000	0.000	0.004	0.148	0.301	0.000	0.005	0.000	0.000
Na	0.053	0.004	0.020	0.248	0.000	0.670	0.064	0.177	0.024	0.001
K	0.000	0.000	0.935	0.766	0.002	0.027	0.931	0.838	0.897	0.001
Zn	n/a	0.048	n/a	n/a	n/a	n/a	n/a	n/a	n/a	0.019
Sum	11.000	2.999	7.804	5.017	8.000	4.996	7.866	5.016	7.687	3.000
Fe #	44.9	87.2	65.2	-	81.3	-	55.6	-	66.2	89.3

Analyses were carried out on (1) a Cameca SX-100 at the Open University using a 1μm beam size and 20 nA beam current; (2) on a Cameca SX-50 at Cambridge University using a 20μm beam size and 20 nA beam current; (3) on a Cameca SX-50 at Leeds University using a 20 μm beam size and 20 nA beam current. n/a indicates not analysed. Fe^{3+} by site allocation.

Table 3.11 continued.

	X2 spinel zone [1]					X2 garnet rim [3]			X7 garnet rim [3]				X7 spinel zone [1]		
	crd #53	bt #28	bt #30	spl #36	ksp #6	gnt #9	bt #7	plag #23	ksp 4r1	plag 1r1	gnt 2.2	bt 2.1	spl #198	fsp #222	bt #175
SiO_2	47.24	34.17	38.29	0.88	65.37	37.11	34.14	60.15	65.10	61.08	37.01	33.97	0.07	52.31	34.09
TiO_2	0.00	3.16	3.06	0.12	0.00	0.07	2.98	0.00	0.00	0.00	0.00	2.06	0.09	0.07	5.38
Al_2O_3	32.25	20.12	21.82	56.57	18.34	20.98	17.75	24.48	18.75	24.25	20.74	17.50	56.95	35.16	18.77
Cr_2O_3	0.00	0.12	0.12	0.10	0.00	0.02	0.00	0.00	0.00	0.00	0.11	0.00	0.13	0.00	0.27
Fe_2O_3	2.10	3.17	0.00	2.00	0.00	0.49	0.00	0.19	0.07	0.00	0.41	2.85	3.72	1.81	0.00
FeO	8.59	19.77	20.08	35.75	0.00	33.97	23.71	0.00	0.00	0.00	33.60	22.17	34.54	0.00	22.37
MnO	0.32	0.22	0.12	0.36	0.00	3.64	0.18	0.04	0.03	0.02	4.21	0.31	0.30	0.01	0.09
MgO	6.98	7.75	6.21	3.17	0.00	3.16	7.52	0.00	0.00	0.00	2.63	7.75	3.49	0.72	6.78
CaO	0.04	0.06	0.10	0.01	0.10	1.17	0.00	6.98	0.11	6.02	1.46	0.03	0.00	0.03	0.00
K_2O	0.17	0.19	0.22	0.03	1.81	0.00	0.20	7.66	1.77	7.71	0.00	0.23	0.01	0.31	0.18
K2O	0.01	6.56	8.24	0.01	14.53	0.00	9.47	0.51	13.77	0.63	0.00	8.64	0.01	8.79	9.23
ZnO	n/a	n/a	n/a	1.17	n/a	n/a	n/a	n/a	n/a	n/a	n/a	n/a	0.69	n/a	n/a
Totals	97.70	95.30	98.26	100.16	100.16	100.61	95.96	100.01	99.61	99.71	100.17	95.51	100.02	99.22	97.17
Si	4.945	2.591	2.778	0.025	3.000	2.980	2.652	2.687	2.992	2.724	2.992	2.644	0.002	2.378	2.591
Ti	0.000	0.180	0.167	0.003	0.000	0.004	0.174	0.000	0.000	0.000	0.000	0.121	0.002	0.002	0.307
Al	3.980	1.798	1.866	1.903	0.992	1.986	1.626	1.289	1.016	1.275	1.977	1.606	1.915	1.884	1.682
Cr	0.000	0.007	0.007	0.002	0.000	0.001	0.000	0.000	0.000	0.000	0.007	0.000	0.003	0.000	0.016
Fe^{3+}	0.165	0.181	0.000	0.043	0.000	0.030	0.000	0.006	0.002	0.000	0.025	0.167	0.080	0.062	0.000
Fe^{2+}	0.752	1.254	1.218	0.853	0.000	2.281	1.541	0.000	0.000	0.000	2.272	1.443	0.824	0.000	1.422
Mn	0.028	0.014	0.007	0.009	0.000	0.248	0.012	0.002	0.001	0.001	0.288	0.020	0.007	0.000	0.006
Mg	1.090	0.876	0.671	0.135	0.000	0.378	0.871	0.000	0.000	0.000	0.317	0.899	0.148	0.049	0.768
Ca	0.005	0.005	0.008	0.000	0.005	0.101	0.000	0.334	0.005	0.288	0.127	0.003	0.000	0.001	0.000
Na	0.035	0.027	0.031	0.002	0.161	0.000	0.030	0.664	0.158	0.667	0.000	0.035	0.001	0.027	0.027
K	0.001	0.635	0.763	0.000	0.852	0.000	0.940	0.029	0.808	0.036	0.000	0.859	0.000	0.510	0.896
Zn	n/a	n/a	n/a	0.025	n/a	n/a	n/a	n/a	n/a	n/a	n/a	n/a	0.015	n/a	n/a
Sum	11.000	7.568	7.516	2.999	5.010	8.008	7.846	5.011	4.982	4.990	8.004	7.796	2.998	4.915	7.715
Fe #	40.8	58.9	64.5	86.4	-	85.8	63.9	-	-	-	87.8	61.6	84.8	-	64.9

Table 3.11 continued.

	X8 spinel zone [1]		X8 garnet core [3]			X8 garnet rim [3]			N1 garnet rim [3]			
	spl	bt	bt	gnt	plag	bt	gnt	plag	crd	gnt	ksp	bt
	#53	#4/1	#6/3	5c3	#2/2	#8/3	#3r4	#1/2	crd.2/3	gnt.2r2	ksp.1r2	bt.1/1
SiO_2	0.40	33.59	34.80	37.81	60.99	34.77	37.38	60.39	47.56	36.20	64.86	33.97
TiO_2	0.10	4.45	4.27	0.00	0.00	0.96	0.06	0.00	0.00	0.03	0.00	4.13
Al_2O_3	55.43	18.54	18.73	21.42	23.99	18.69	20.99	25.18	31.88	20.80	18.61	18.58
Cr_2O_3	0.26	0.00	0.00	0.00	0.00	0.00	0.09	0.00	0.00	0.02	0.00	0.00
Fe_2O_3	4.24	0.00	0.00	0.00	0.29	0.00	0.54	0.17	0.00	0.61	0.40	0.00
FeO	35.00	23.43	21.21	34.02	0.00	25.31	35.22	0.00	11.07	36.93	0.00	22.54
MnO	0.37	0.13	0.05	2.44	0.06	0.12	1.91	0.00	0.06	1.85	0.06	0.10
MgO	2.58	6.49	7.92	3.69	0.00	7.11	3.20	0.00	6.43	2.02	0.00	6.64
CaO	0.01	0.00	0.05	1.69	6.28	0.00	1.69	7.36	0.00	1.39	0.08	0.00
Na_2O	0.04	0.20	0.26	n/a	7.93	0.26	0.00	7.35	0.22	0.00	2.95	0.28
K_2O	0.05	9.37	8.87	n/a	0.66	8.92	0.00	0.54	0.00	0.00	12.38	9.28
ZnO	1.50	n/a	n/a	n/a	n/a	n/a	n/a	n/a	n/a	n/a	n/a	n/a
Totals	99.96	96.20	96.16	101.09	100.21	96.14	101.08	101.01	97.22	99.83	99.34	95.52
Si	0.012	2.599	2.646	2.999	2.717	2.696	2.984	2.671	5.018	2.958	2.983	5.262
Ti	0.002	0.259	0.244	0.000	0.000	0.057	0.003	n/a	0.000	0.002	0.000	0.481
Al	1.885	1.690	1.679	2.002	1.259	1.708	1.975	1.313	0.977	2.003	1.009	3.393
Cr	0.006	0.000	0.000	0.000	0.000	0.000	0.006	n/a	0.000	0.001	0.000	0.000
Fe^{3+}	0.092	0.000	0.000	0.000	0.010	0.000	0.033	0.006	0.000	0.038	0.014	0.000
Fe^{2+}	0.844	1.516	1.349	2.256	0.000	1.642	2.351	0.000	0.977	2.524	0.000	2.921
Mn	0.009	0.009	0.004	0.164	0.002	0.008	0.129	0.000	0.006	0.128	0.002	0.013
Mg	0.111	0.749	0.898	0.436	0.000	0.822	0.381	0.000	1.012	0.246	0.000	1.533
Ca	0.000	0.000	0.004	0.144	0.300	0.000	0.144	0.349	0.000	0.122	0.004	0.000
Na	0.002	0.030	0.038	n/a	0.685	0.040	n/a	0.630	0.045	0.000	0.263	0.083
K	0.002	0.926	0.861	n/a	0.038	0.883	n/a	0.030	0.000	0.000	0.727	1.835
Zn	0.032	n/a	n/a	n/a	n/a	n/a	n/a	n/a	n/a	n/a	n/a	n/a
Sum	2.997	7.775	7.721	8.001	5.010	7.855	8.006	5.000	11.022	8.020	5.001	19.520
Fe #	88.4	67.1	60.1	84.7	-	66.8	86.8	-	49.1	91.1	-	65.6

The gahnite endmember ($ZnAl_2O_4$) may have an activity of up to 0.214 in spinel from these rocks, while coexisting phases contain no detectable zinc. Within a single domain, on the scale of a few millimetres, zinc concentrations are relatively constant, although zinc concentrations vary considerably between different samples and even between different domains in the same thin section (e.g. sample 004 rings 1 and 2, Table 3.10), suggesting a local bulk compositional control. However, since in some sections spinel contains an average of less than one weight percent of zinc (e.g. sample Z147, Table 3.10), it appears unlikely that spinel is stabilised primarily by the zinc content of the rock. Rather, it has scavenged available zinc during its formation (Stoddard, 1979). This view is supported by the lack of correlation between zinc content and modal abundance of spinel.

Thus spinel does not appear to be stabilised primarily by significant components outside the hercynite-spinel solid solution series, and its stability can be investigated within the KFMASH system.

3.4.6 Phase equilibria

For the AFM diagram (Fig. 3.9a), the coexistence of cordierite-sillimanite-biotite is illustrated in the presence of K-feldspar, quartz and granitic liquid (Figure 3.9b). However, the coexistence of spinel and cordierite in the absence of quartz suggests a new spinel-cordierite tie-line. The relative Fe/Mg ratios of the ferromagnesian phases can be seen to be $Fe\#_{spl} > Fe\#_{bt} > Fe\#_{crd}$ (Table 3.11). This implies that biotite and sillimanite coexist with cordierite and spinel in the absence of quartz through the reaction:

biotite + sillimanite = cordierite + spinel + K-feldspar + melt (3.3)

Alternatively it could be argued that spinel is not a product of a quartz-absent melting reaction, but is a reactant in the production of cordierite from the solid-state reaction:

spinel + quartz = cordierite (3.4)

Whilst this accounts for the incompatibility between spinel and quartz, it does not explain the complex intergrowths between spinel and cordierite as apparent reaction products of biotite breakdown (Fig. 3.8d). Reaction (3.4) should lead to cordierite rims separating spinel from quartz-rich domains which are not observed.

We can further explore quartz-absent stability through the HS(FM) diagram (Fig. 3.9c) that can illustrate the effect of changing bulk silica and water content on phase compatibilities. On this diagram it is clear that as H_2O and/or SiO_2 contents decrease the stable assemblage for the given bulk composition will change from biotite-cordierite-quartz to biotite-cordierite-spinel. The local stability of spinel may then be explained if melting occurs and melt is removed, which will reduce the H_2O content of the rock since melts are significantly more hydrous than the bulk rock, and leading to the assemblage biotite-cordierite-spinel. Some compositional variation within Nanga Parbat metapelites has been observed on a sub-centimetre scale as banding visible in hand specimen, and removal of melt from a silica-poor band will result in movement away from both H and S apices (Fig. 3.9c).

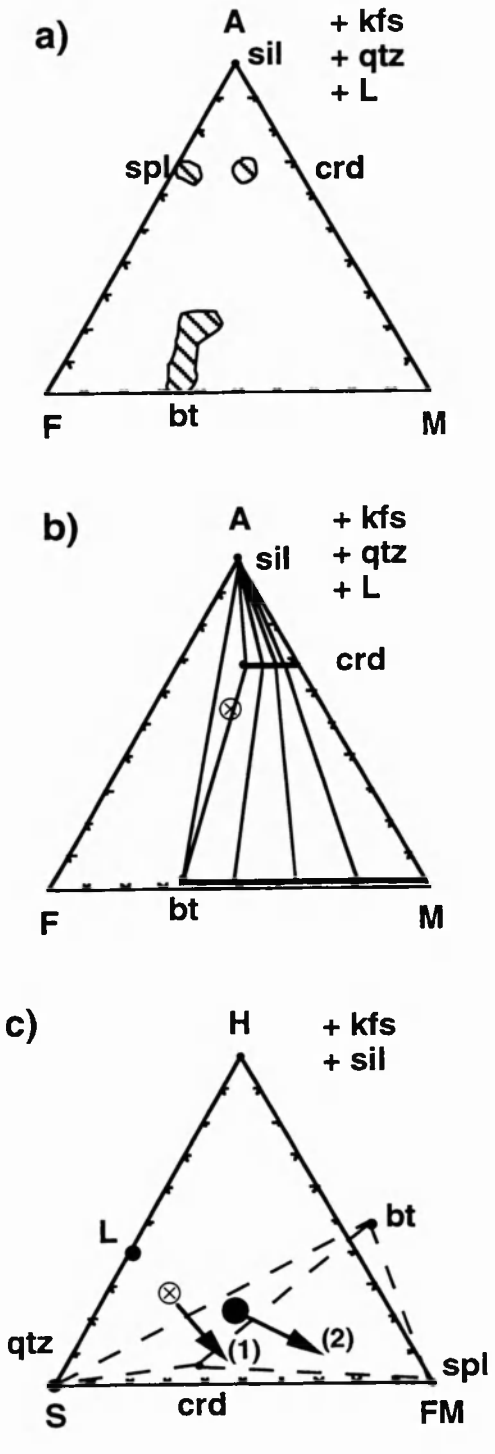

Figure 3.9. $AlO_{1.5}$-FeO-MgO and $HO_{1.5}$-SiO_2-(FeO + MgO) diagrams for Z135. Phase compositions in table 2. The crossed circle indicates the bulk composition of Z147, a typical spinel-bearing metapelite, measured by XRF analysis. a) AFM diagram projected from quartz, liquid, and K-feldspar, showing composition fields (striped) of all phases analysed in spinel-bearing zones . The average leucogranite of Whittington et al. (1997a) was used for the liquid composition in all diagrams, assuming a water content of 7 wt.%. b) AFM diagram showing phases analysed in a spinel-bearing zone of Z135. Tie-lines drawn for coexistence of biotite-cordierite-sillimanite, as observed outside spinel-bearing zones. c) HS(FM) composition diagram showing phase analyses from Z135. In order to achieve the assemblage biotite-cordierite-spinel, the bulk composition of Z147 requires reduction of the water content, which may be achieved by removal of melt. This process is illustrated by arrow (1). More mafic compositions (solid circle) will have both silica and water contents reduced by melt removal, shown by arrow (2). Note that the because FeO and MgO should be considered as separate components, the three-phase triangles shown (dashed lines) are actually four-phase tetrahedra with L as the fourth phase.

Unfortunately it is not possible to show separate FeO and MgO components (in addition to SiO_2 and water) rigorously on a two-dimensional ternary plot. The extra degree of freedom generated by separate consideration of FeO and MgO components is accounted for by the coexistence of a liquid phase (L) with each of the three-phase assemblages shown in Fig. 3.9c.

We conclude that anatexis and melt removal will favour the formation of spinel in the restite, as has been invoked by Srogi et al. (1993) for similar anatectic assemblages from the Wilmington complex, although Fig. 3.9 suggests the role of melt in removing silica may be less significant than its effect in depleting H_2O content. In the Wilmington example silica depletion was more marked, and corundum was stabilised locally within restitic melanosomes.

3.4.7 KFMASH petrogenetic grid

The K_2O-FeO-MgO-Al_2O_3-SiO_2-H_2O (KFMASH) system incorporates the major chemical components in pelitic rocks. It is, however, a simplification of the natural system: omission of TiO_2 and Fe_2O_3 from KFMASH precludes consideration of the Fe-Ti oxides, and omission of CaO and Na_2O precludes consideration of plagioclase and natural granitoid melts. The KFMASH grid for dehydration melting of biotite at moderate pressures (>5 kbar) has been established by Powell and Downes (1990) and Hensen and Harley (1990), and developed at higher temperatures by Carrington and Harley (1995). In this study we have extended this grid to lower pressures, where cordierite rather than garnet is the stable peritectic phase under vapour-absent conditions in normal pelitic bulk compositions. We have also investigated equilibria under quartz-absent conditions.

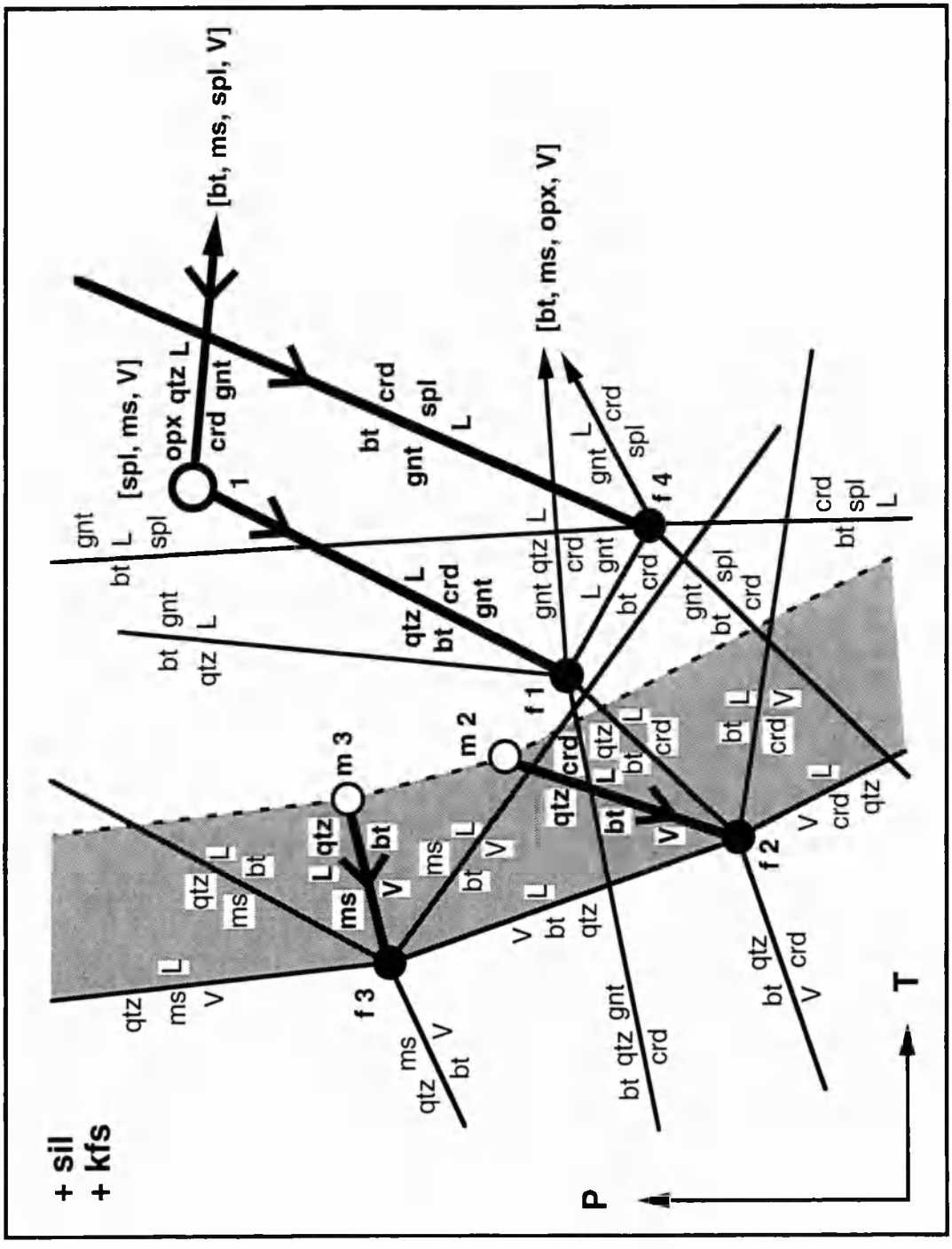
+ sil
+ kfs
P
T
[bt, ms, spl, V]
[bt, ms, opx, V]
[spl, ms, V]
opx qtz L
crd gnt
1
m 2
m 3
f 1
f 2
f 3
f 4
qtz L
bt
crd
gnt
spl
ms
V
bt qtz gnt
crd

Figure 3.10. Low-pressure petrogenetic grid for metapelites in the KFMASH system, assuming excess orthoclase and sillimanite, adapted from Powell and Downes (1990) to allow for silica-undersaturation. Other mineral abbreviations follow Kretz (1983), with melt phase (L) and vapour phase (V). Solid lines are univariant reactions in KFASH, and thick solid lines are univariant reactions in KFMASH. Large arrows indicate direction of increasing Fe. Filled circles are invariant points in KFASH (f1, etc.), open circles are invariant points in KMASH (m1, etc.), and the bold open circle is invariant point 1 in KFMASH. The shaded field is the zone of water-saturated melting for compositions between pure Fe- and Mg- endmembers. Invariant points are: f1, m1 [ms, opx, spl, V]; f2, m2 [gnt, ms, opx, spl]; f3, m3 [crd, gnt, opx, spl] and f4 [qtz, ms, opx, V].

A low pressure KFMASH grid is shown in Fig. 3.10, assuming excess orthoclase and sillimanite. The grid was constructed for Fe# (Spl) > Fe# (Gnt) > Fe# (L) > Fe# (Bt) > Fe# (Crd), in accordance with analysed minerals from Nanga Parbat (Table 3.11). The average leucogranite of Whittington et al. (1997a) was used for the liquid composition. Invariant points in the KFASH system and in the KMASH system are linked by a univariant line in the KFMASH system, so that for example f2 and m2, which are both garnet, muscovite, orthopyroxene and spinel absent, are linked by the KFMASH univariant reaction (3.2). The single KFMASH invariant point (marked 1), is vapour, muscovite, and spinel absent, and has been fixed in P-T space at about 890-910 °C and 9 kbar (Carrington and Harley, 1995).

The shaded field low-temperature field between the KFASH and KMASH endmember reactions represents the water-saturated solidus for bulk compositions of intermediate Fe/Mg ratio. The reaction linking f2 and f3 is annite + sillimanite + quartz + V = melt, and occurs at higher temperatures for phlogopite + sillimanite + quartz + V = melt, which links m2 and m3. At higher pressures than f3-m3, muscovite is a reactant during vapour-present melting, and at lower pressures than f2-m2, cordierite is a reactant during vapour-present melting. None of these reactions leads to cordierite or spinel as product phases, suggesting that if spinel is a peritectic phase, melting must have been vapour-

undersaturated (i.e. at higher temperatures, and to the right of, the shaded field). The KFASH invariant point f2 has been fixed in P-T space at around 725 °C and 2.5 kbar (Fig. 5 of Vielzeuf and Holloway, 1988). This is a considerably higher temperature than the water-saturated haplogranite solidus, because f2 was determined for the Na-absent KFASH system. A quartz-absent invariant point (f4) occurs at the intersection between the quartz-absent reactions from f1, and from a higher temperature KFASH invariance [bt, ms, opx] which stabilises the coexistence of spinel and quartz.

In the full KFMASH system, there are two vapour-absent univariant reactions relevant to the Nanga Parbat assemblages:

biotite + sillimanite + quartz = cordierite + garnet + K-feldspar + melt (3.5)

linking f1 and 1, and

biotite + sillimanite + garnet = cordierite + spinel + K-feldspar + melt (3.6)

This reaction is terminated at low pressures by the KFASH invariant point f4, which is both vapour-absent and quartz-absent. With increasing temperature, crossing reaction (3.5) consumes quartz and produces peritectic cordierite, consistent with assemblages at Nanga Parbat. Reaction (3.6) consumes both biotite and garnet, and results in cordierite and spinel forming as peritectic phases with a melt.

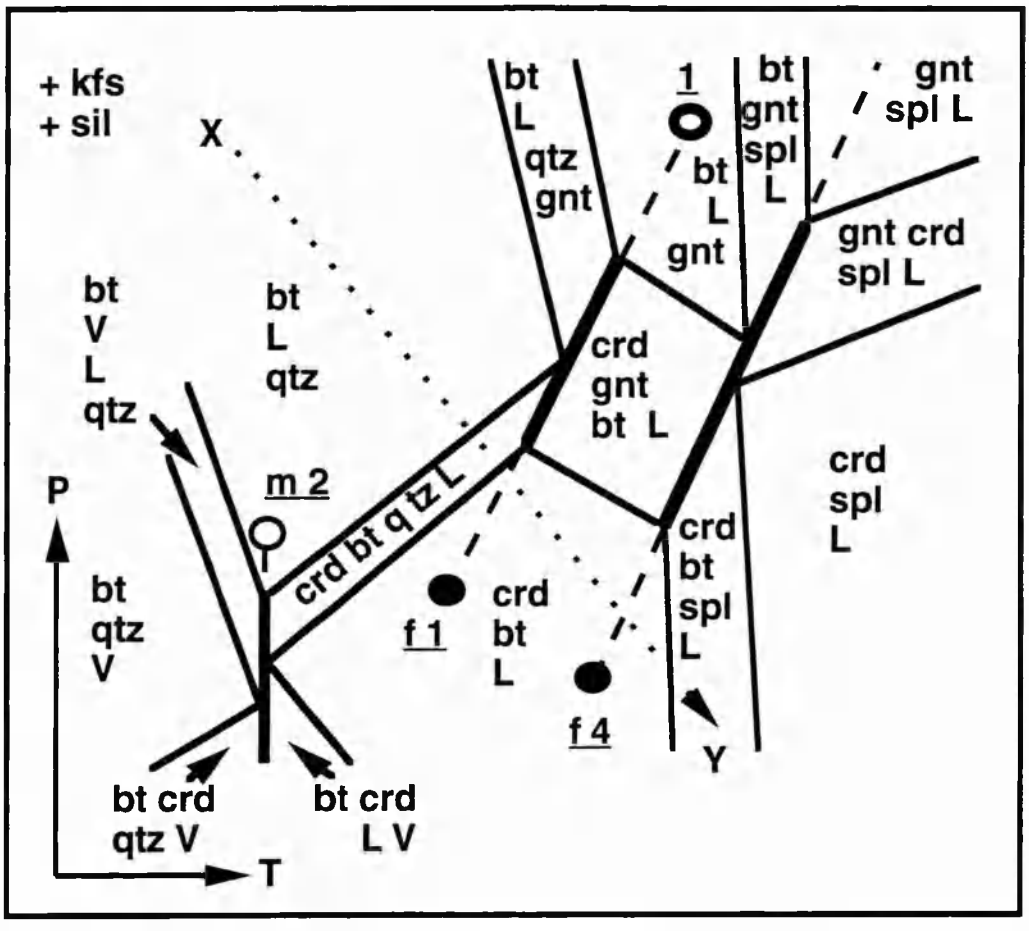

Figure 3.11. P-T pseudosection constructed for a fixed intermediate bulk composition, adapted from Powell and Downes (1990) to allow for silica-undersaturation. Mineral abbreviations and invariant point symbols as for figure 4. Dotted line X-Y is a qualitative P-T path for Nanga Parbat rocks consistent with petrographic observation.

The absence of garnet in the Nanga Parbat assemblages results from low pressures during prograde metamorphism, as can be illustrated by a P-T pseudosection constructed for a fixed bulk composition of intermediate Fe# (Hensen, 1971), between pure KFASH and pure KMASH endmember reactions (Fig. 3.11), after Powell and Downes (1990). A qualitative P-T path for Nanga Parbat rocks in the pseudosection has been drawn (X-Y on Fig. 3.11), illustrating the change in mineralogy consistent with petrographic observation. This path does not extend into the orthopyroxene field, because we have found no evidence for orthopyroxene in these assemblages.

For assemblages at `X', a melt will be present only if fluid-present conditions prevail. Under fluid-absent conditions, with either an increase in temperature or decompression, fluid-absent melting results in the formation of cordierite as the cordierite-biotite-quartz-melt field is entered, from reaction (3.2). Note that for higher Fe/Mg ratios or pressures, both garnet and cordierite would be formed. For compositions of low to moderate bulk SiO_2 content, melting will exhaust quartz, and spinel is formed as the cordierite-biotite-spinel-melt field is entered from reaction (3.3). Further increase in temperature and/or decompression results in biotite-absent cordierite-spinel assemblages, which are not observed. The presence of minor non-KFMASH components in biotite, such as Ti and F, will contribute to the broadening of this reaction interval in natural systems.

3.4.8 Thermobarometry

Petrogenetic grid topologies of potential reactions provide essential constraints on qualitative P-T paths. However, with only two points on the KFMASH grid of Fig. 3.10 fixed experimentally, quantitative P-T information on the Nanga Parbat assemblages requires thermobarometry based on analysed activities from coexisting phases. To calculate pressure and temperature conditions, we have used version 2.4 of the Thermocalc program (Powell and Holland, 1988) and the extended internally consistent thermodynamic dataset of Holland and Powell (1990).

The early metamorphic history of the Nanga Parbat assemblages may be constrained by garnet-bearing assemblages. X8 is a spinel-bearing metapelite which also contains garnet with inclusions of biotite, plagioclase and quartz. The garnet is rimmed by stable fabric-forming biotite apparently in textural equilibrium with garnet, in contrast to biotite found in spinel-bearing zones in the same thin section, which is breaking down. Biotite rimming garnet has a low Ti

content of less than 1 wt. %, in contrast to biotite in the spinel zone which has a Ti content of over 4 wt. %, and hence may have grown via retrograde garnet breakdown.

Average (PT) conditions for the core and rim were computed by Thermocalc using the endmembers almandine, pyrope, grossular, anorthite, orthoclase, annite, phlogopite, sillimanite and quartz, and a range of water activities under fluid-absent conditions. Analyses of phase compositions used in calculations are provided in Table 3.11. These calculations suggest conditions of 720 ± 50 °C at 7.6 ± 1.5 kbar for the core, and 670 ± 40 °C at 6.3 ± 1.4 kbar for the rim, assuming a water activity of 0.9. For a water activity of 0.5, the results are 655 ± 50 °C at 6.7± 1.7 kbar for the core, and 610 ± 40 °C at 5.5 ± 1.3 kbar for the rim. The differences in P-T conditions between core and rim are within error, but probably represent some decompression and cooling.

For determining conditions during melt formation, thermobarometry on the cordierite-spinel assemblages is required. From petrographic observation, we infer that some degree of partial melting during fluid-absent biotite breakdown has occurred. The presence of a melt phase makes thermobarometric calculations on these assemblages more problematic, as it is not currently possible to introduce a melt phase to Thermocalc without further experimental constraints (Holland et al., 1996). However, both solid-phase equilibria and melt must coexist under conditions of identical water activities. Hence if P-T fields from solid phases are calculated for a range of a_{H_2O} and overlain on the granite solidii determined at varying a_{H_2O}, both solids and melt will coexist where water activities for the melt and for the mineral assemblage are equal (Fig. 3.12; c.f. Fig. 4 of Waters, 1991).

Table 3.12 Endmember activities and Thermocalc P-T results

Endmember activities

Mineral	Endmember	Formula	activity [1]
Biotite	phlogopite	$KMg_3Si_3AlO_{10}(OH)_2$	0.0162
	annite	$KFe_3Si_3AlO_{10}(OH)_2$	0.113
Cordierite	Fe-cordierite	$Fe_2Si_5Al_4O_{18}$	0.196
	Mg-cordierite	$Mg_2Si_5Al_4O_{18}$	0.295
Spinel [2]	hercynite	$FeAl_2O_4$	0.772
	spinel	$MgAl_2O_4$	0.113
K-feldspar	orthoclase	$KAlSi_3O_8$	0.752
Sillimanite		Al_2SiO_5	1
Quartz		SiO_2	variable
Fluid	water	H_2O	variable

THERMOCALC P-T calculations [3]

$a(H_2O)$	T (°C)	sd	P (kbar)	sd	cor [4]	f [5]
1.0	785	66	6.3	1.2	0.87	1.18
0.9	768	64	6.0	1.2	0.86	1.18
0.8	750	63	5.7	1.1	0.86	1.19
0.7	731	61	5.3	1.1	0.85	1.20
0.6	710	59	5.0	1.1	0.84	1.22
0.5	687	58	4.6	1.0	0.84	1.24
0.4	661	56	4.3	1.0	0.83	1.26
0.3	631	54	3.8	1.0	0.82	1.29
0.2	593	52	3.4	0.9	0.81	1.34
0.1	539	49	2.9	0.9	0.79	1.44

[1] Acitivities were calculated using the "ax" program written by Tim Holland, using mixing models from Holland and Powell (1990) and references therein.

[2] Spinel activities assume ideal mixing, ferric iron calculated by site allocation.

[3] Calculations assume fluid-absent conditions, and include all endmembers listed above, with fixed $a(SiO_2) = 0.95$ and variable $a(H_2O)$.

[4] Correlation between P and T. These values indicate significant correlation, and hence an elongate error ellipse.

[5] Statistical fit parameter. All results are statistically acceptable.

Calculations were conducted on a spinel-cordierite metapelite (Z135), using the analyses listed in Table 3.11. Calculated endmember activities and P-T results are listed in Table 3.12, using a silica activity of 0.95 to represent the quartz-absent nature of the assemblage. For this rock, the minimum water activity required for the biotite-cordierite-spinel assemblage to coexist with a melt is 0.5 at conditions of 687 ± 58 °C at 4.6 ± 1.0 kbar, although if the 2 sigma uncertainties on the PT results are considered, a_{H_2O} could be as low as 0.4 (Fig. 3.12). The actual intersection is at a water activity of 0.6, suggesting conditions of 710 ± 60 °C at 5.0 ± 1.1 kbar.

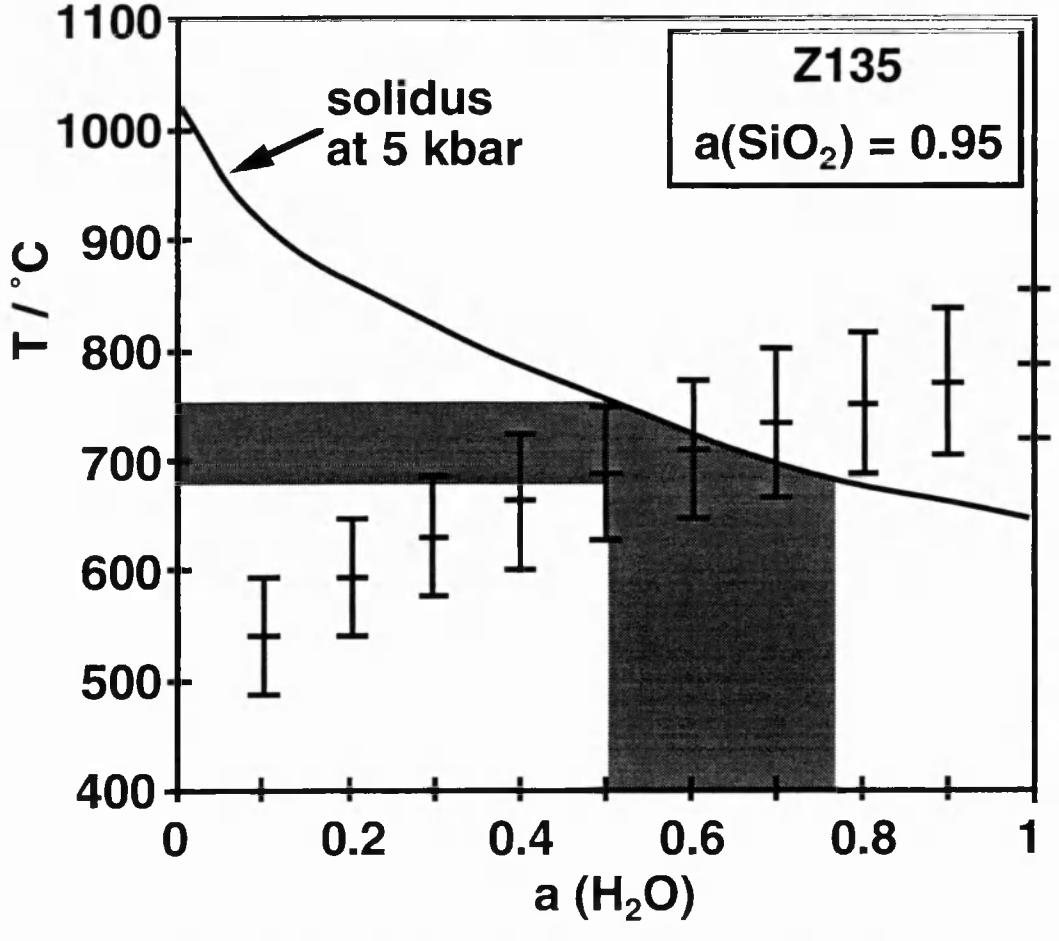

Figure 3.12. Average (PT) calculations for a spinel-bearing assemblage (Z135) for $a(SiO_2)$ = 0.95 and variable $a(H_2O)$, compared with the 5 kbar haplogranite solidus of Holtz and Johannes (1990). Endmember activities and results of calculations are listed in Table 3, and error bars shown are ± 1 sigma. This indicates that $a(H_2O)$ must have been greater than 0.4 for melting to have occurred (allowing 2 sigma errors), and probably lay within the range 0.5 to 0.7, at temperatures between 700 and 760 °C (shaded bands).

Although such a water activity could be achieved from the hydroxyl component of biotite that is released as water on biotite breakdown, these temperatures are significantly below those obtained from experimental studies of biotite breakdown under fluid-absent conditions (Gardien et al., 1995; Patiño Douce and Johnston, 1991; Vielzeuf and Holloway, 1988). Low pressures and Fe-rich bulk compositions will enable melting to occur at lower temperatures, but there is no evidence to suggest that dehydration melting of biotite at 5 kbars can occur below 800 °C. We infer that some fluid ingress is required to allow limited melting. In other words, while final equilibration of the analysed assemblage probably took place at a water activity of about 0.6 (Fig. 3.12), a higher water activity was probably required to initiate melting at the P-T conditions encountered by rocks from Nanga Parbat, followed buffering of the water activity by the melt phase at about 0.6. Similar calculations for a cordierite-bearing leucosome indicate that a_{H_2O} must have been at least 0.7 and probably greater than 0.9 for melting to occur, consistent with fluid-present melting localised in shear zones (sample Z130, Whittington et al., 1997a).

Quantitative P-T constraints for the petrogenetic grid (Fig. 3.10) can now be obtained by considering biotite breakdown reaction (3.2). If it is assumed that water activity is buffered by the melt, rather than being externally controlled, the reaction can be constrained in P-T space (Fig. 3.13), following the approach of Waters (1991). This will be valid even with limited influx of external fluid, provided the water activity remains buffered by the melt. Such an approach can only be applied to reaction (3.2), since the granitic solidii are for a silica-saturated melt. Some uncertainty is introduced in this case since the granitic solidii are for the sodium-bearing NaKASH system, whereas the reaction is calculated in KFMASH. K-feldspar will be the only phase sensitive to Na content, and an orthoclase activity of 0.752 was used in the calculation, from analysis #119 (Table 3.11). The addition of components FeO and MgO to NaKASH would reduce the

temperatures of the granitic solidii by only a few degrees, within the error of thermobarometric calculations. The melt-free equivalent of reaction (3.2) is:

biotite + sillimanite + quartz = cordierite + K-feldspar + [H_2O] (3.7)

When calculated for coexisting phases from Z135, this reaction occurs at 720 °C at 5 kbar for a melt-buffered water activity of 0.6, in excellent agreement with average (PT) calculations (Fig. 3.13).

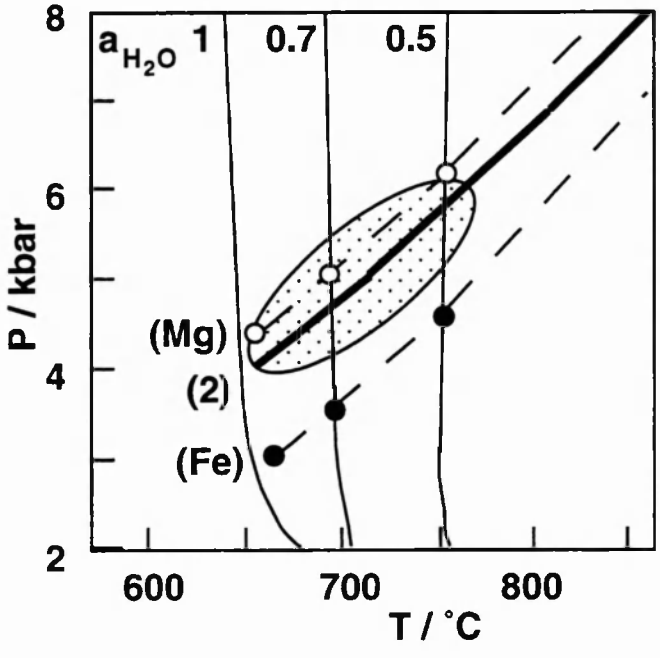

Figure 3.13. Biotite breakdown reaction (2) (thick solid line) calculated using mineral compositions from the spinel-bearing zone of Z135, and assuming that water activity is buffered by the melt, using water activities in granitic melts for a_{H_2O} = 1.0, 0.7, and 0.5, from Holtz and Johannes (1990). Dashed lines indicate Fe and Mg endmember curves for reaction (2), intersections of reaction curves with solidii at a_{H_2O} = 0.9, 0.7, and 0.5 shown as filled circles (Fe) and open circles (Mg). Note the significant effect of bulk composition on P-T conditions of the reaction. Shaded field is the average (PT) estimate for a_{H_2O} = 0.6, with 1 sigma errors, from Table 3.

Hence P-T conditions during partial melting are constrained between about 650 and 770 °C, at between 3.9 and 6.1 kbars. It is not possible to calculate reaction (3.3) until a silica-undersaturated liquid phase can be introduced to Thermocalc, but it is expected to occur at higher temperatures and/or lower pressures than reaction (3.2), from the petrogenetic grid (Fig. 3.10). The melt-absent equivalent reaction is:

biotite + sillimanite = cordierite + spinel + K-feldspar + [H_2O] (3.8)

This reaction was calculated for Z135, and occurs at temperatures a few tens of degrees higher than reaction (3.7) for pressures less than 6 kbars, as predicted.

3.4.9 Discussion

The P-T-a_{H_2O} constraints obtained from thermodynamic considerations can be related to the tectonothermal history of the NPHM. Thermal modelling of Nanga Parbat suggests a very steep decompression path, attributed to rapid erosion in the absence of extensional structures (Whittington, 1996). P-T estimates from Thermocalc do not appear to record higher pressure stages of this path in many pelitic rocks, probably due to peak temperatures being maintained throughout most of the decompression history.

Thermobarometry on biotite and plagioclase inclusions records early garnet growth at about 720 °C and 7.6 kbar (A, Fig. 3.14) with final garnet rim equilibration at 670 °C and 6.3 kbar (B, Fig. 3.14). Water activities are likely to have been close to unity prior to melting, due to subsolidus dehydration reactions,

hence calculations assuming a_{H_2O} of 0.9 are shown. If a_{H_2O} is assumed to be 0.5 then calculated pressures and temperatures are reduced by 0.8 kbar and 60 °C respectively for both sets of calculations. Independent of assumed a_{H_2O}, the difference between core and rim conditions is about 1.3 kbar and 50 °C, the equivalent of decompression though 4 or 5 km.

Although in many studies it is assumed the garnet core preserves the "peak" P-T conditions, for these assemblages the spinel-bearing assemblages clearly post-date garnet growth. Vapour-absent melting reactions have positive slopes in P-T space, and hence "prograde" reactions can occur during decompression even if accompanied by slight cooling.

Initial melting in the massif is likely to be controlled by local fluid distribution; where a local grain-boundary fluid is present, small melt fractions may be generated at higher pressures (greater than about 6 kbars), but no peritectic phases will result. The first melt reaction to occur during decompression is the vapour-absent muscovite breakdown reaction:

muscovite + quartz + plagioclase + vapour ± biotite

= sillimanite + K-feldspar + melt (3.9)

which is associated with leucogranite formation (Whittington et al., 1997a). This reaction will terminate once muscovite is exhausted (C, Fig. 3.14). With further decompression, reaction (3.5) allows a liquid to form from fluid-absent biotite melting with peritectic cordierite and/or garnet. At low pressures, a bulk composition with intermediate Fe/Mg ratio will not necessarily produce garnet. These assemblages have equilibrated between 650 and 770 °C, and between 3.9

and 6.1 kbar (D, Fig. 3.14). Reaction (3.5) will continue until quartz or biotite are entirely consumed. In the absence of quartz, the ensuing melt reaction (3.6), or the divariant reaction (3.3), generates both cordierite and spinel with melt at higher temperatures and/or lower pressures. At Nanga Parbat neither reaction (3.6) nor (3.3) has gone to completion, since biotite and sillimanite have not been exhausted in spinel-bearing zones. A similar interpretation has also been made for silica-poor metapelitic migmatites from Antarctica (Fitzsimons, 1996).

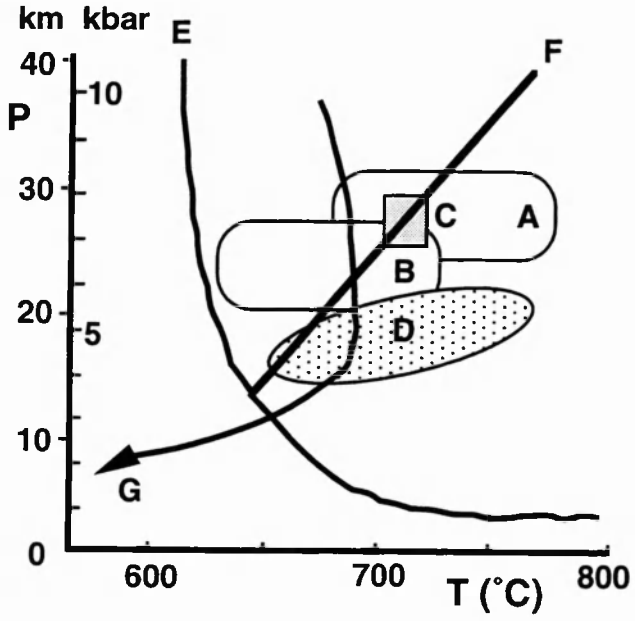

Figure 3.14. Summary diagram of P-T information from the Tato Valley of the NPHM. A: garnet inclusion thermobarometry from this study. B: garnet rim thermobarometry from this study. C (shaded): P-T conditions of leucogranite formation by vapour-absent muscovite breakdown (Butler et al., 1997). D (shaded): Thermobarometry from a spinel-bearing zone in metapelite Z135, from this study. E: Water-saturated granitic solidus from Holtz and Johannes (1990). F: Vapour-absent muscovite melting reaction, from Petö (1976). G: Modelled exhumation path for rocks currently exposed in the Tato Valley from Whittington (1996).

For the Nanga Parbat assemblages it seems probable that some fluid ingress occurred initially to allow biotite melting reactions to progress at temperatures less than 800 °C. However, any such fluid infiltration was insufficient to saturate the melt, and a_{H_2O} was buffered at about 0.6.

While this approach constrains conditions of melting, it does not constrain the slope of the P-T path, which requires only that the melting reaction is crossed in the prograde direction (Vernon, 1996). Such a path is possible by either heating or cooling during decompression, or even by isobaric heating. For the assemblages at Nanga Parbat however, rapid exhumation has been documented by several geochronological techniques (Zeitler et al., 1982a; Zeitler, 1985; Smith et al., 1992; Zeitler et al., 1993; Winslow et al., 1994; Whittington, 1996). The modelled P-T path for this scenario (Whittington, 1996) suggests a near-isothermal decompression path for this latest metamorphic episode (G, Fig. 3.14), followed by rapid cooling as rocks approached the surface and isotherms are telescoped.

3.5 Summary

The main points of this chapter may be summarised as follows:

1. Within the southern NPHM, metamorphic rocks from both pelitic and calc-silicate rocks record pressures and temperatures in the range 610 to 720 °C and 3.0 to 8.6 kbar (Table 3.15). Thermobarometry in this work was mostly conducted using the Thermocalc program in average (PT) mode, and the results are comparable with previous estimates using standard geothermometers and geobarometers. The possibility of re-equilibration and homogenisation during decompression leading to underestimation of peak P-T conditions cannot be ruled out, hence these estimates are referred to in the text as conditions of final equilibration.

Table 3.13. Summary of Thermocalc average (PT) calculations from the NPHM

Rock	Lithology	a(H_2O)	T (°C)	±	P (kbar)	±	fit
N1	pelite	0.9	720	60	4.4	0.6	
E126	pelite	0.9	673	42	5.3	1.9	0.76
Z137ii	pelite	0.9	612	42	6.8	2.2	1.08
E139	pelite	0.9	688	58	5.9	1.5	0.15
Z153ii	pelite	0.9	635	37	4.2	0.4	0.88
Z130	crd seam	1.0	630	30	3.0	0.4	
Z135	gnt core	0.9	720	50	7.6	1.5	
Z135	gnt rim	0.9	670	40	6.3	1.4	
Z135	crd-spl	0.6	710	59	5.0	1.1	1.22
Z124	calc-silicate	0.9	723	71	6.8	1.8	
Z148	calc-silicate	0.9	626	70	8.6	1.8	0.95
Z148	calc-silicate	0.9	675	78	3.4	2.6	1.46

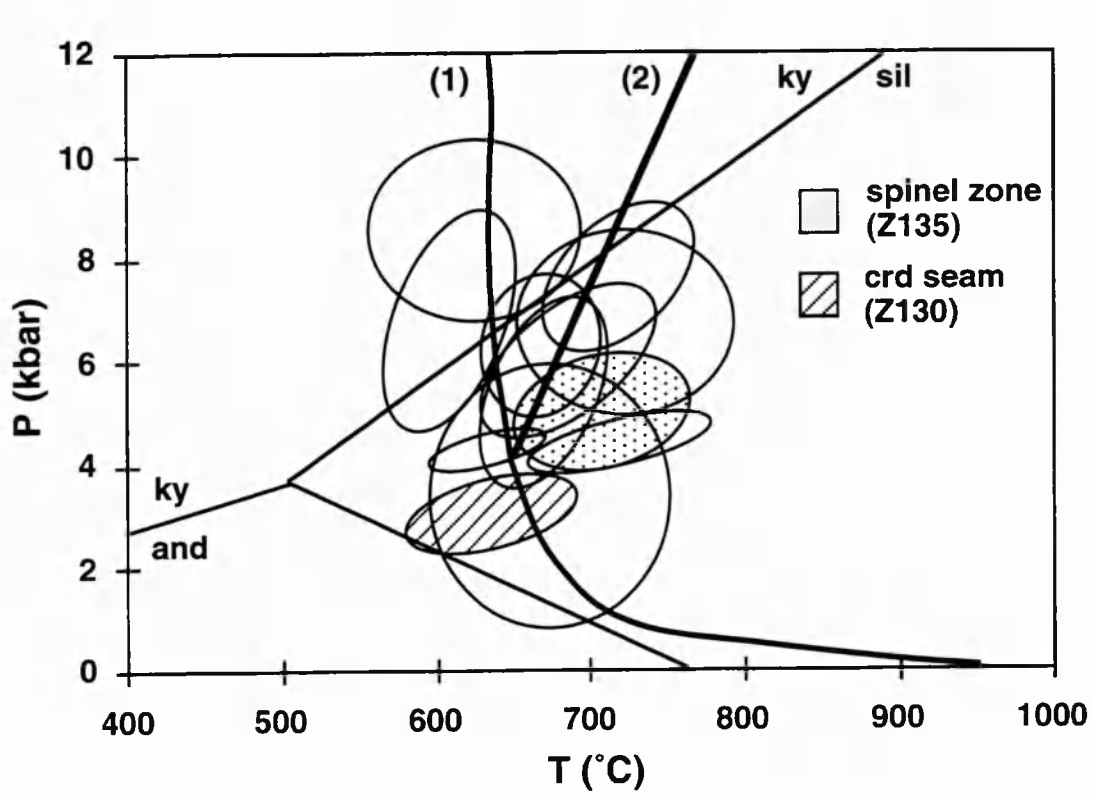

Figure 3.15 Summary P-T diagram for the southern NPHM, showing the "best estimate" P-T fields obtained for each sample in this chapter (Table 3.13). Curve (1) is the water-saturated haplogranite solidus of Johannes and Holtz (1990), and curve (2) is the vapour-absent muscovite melting reaction of Le Breton and Thompson (1988). The aluminosilicate triple point of Holdaway (1971) is shown for reference. The shaded field is the P-T field determined for formation of spinel in Z135, and the striped field is the P-T field determined for formation of cordierite seams in Z130.

2. When plotted on a P-T diagram, these calculations suggest a path of near-isothermal decompression, indicated by cooling of less than 100 °C during exhumation of more than 15 km (Figs. 3.14 and 3.15). The eastern margin of the NPHM has experienced similarly rapid exhumation from over 10 kbar with little or no medium-pressure equilibration, but never entered the sillimanite field (Pognante et al., 1993). Lower peak pressures are recorded by rocks from the southern NPHM than from the eastern margin, possibly suggesting that peak

temperatures were reached in the south only during decompression, rather than at its initiation. This is supported by the total absence of kyanite from the field area studied, although kyanite has been reported from adjacent areas on the eastern margin south of Astor, and on the western margin along the MMT (Misch, 1949). Sillimanite found in the southern NPHM does not appear to be a pseudomorph of kyanite, but is fibrolitic and is probably a peritectic product of muscovite breakdown. Temperatures on the eastern margin were too low for granite production, and this may reflect the different thermal structures resulting from active exhumation via the Liachar thrust on the western margin, and passive exhumation on the eastern margin.

3. A detailed investigation of microscopic spinel-bearing quartz-absent zones in pelitic assemblages, restricted to the interior of the NPHM, suggests that spinel in these zones is not stabilised by the presence of zinc, and may therefore be treated in the KFMASH system.

4. A petrogenetic grid has been constructed for the KFMASH system, which allows for both silica- and water-undersaturation. This grid contains an invariant point in KFASH (f4) which is both vapour-absent and quartz-absent. The reaction linking this point to the KMASH equivalent (m4) will produce liquid, peritectic spinel, cordierite and K-feldspar, while consuming biotite and sillimanite. Petrographic observation suggests that this is the reaction responsible for generation of spinel in these zones. A pseudosection constructed from this grid suggests a path of decompression and heating is required to account for the presence of spinel.

5. Conditions required to form spinel were only achieved in very small zones in a limited area, and would require lowering of bulk silica from normal pelitic compositions. This process could be achieved by removal of melt formed from the first biotite breakdown reaction, which produces peritectic cordierite and K-

feldspar. Melt volumes would have been very small, although melt fraction was probably high (~0.4), so that removal of melt from these zones would have been easily achieved. The small (cm-sized) leucosomes commonly found in high grade pelitic gneisses from the interior of the NPHM may be the crystallised equivalents of these melts.

6. Garnet zoning profiles from the southern NPHM are mostly homogeneous, even in garnets over 1 cm across, indicating that temperatures were high and sustained for some time after garnet growth. Retrograde diffusion rims are limited to less than 100 μm in most cases, suggesting that cooling below the blocking temperature for Fe-Mg exchange between garnet and biotite was rapid. Simple calculations of the time required to achieve this homogenisation suggest that garnet-bearing rocks must have been in excess of 700 °C for at least 1400 Ma, although these calculations have order-of-magnitude errors attached.

7. Comparison with garnets found in the High Himalayan Crystalline sequence in Zanskar suggests that rocks from the NPHM enjoyed high temperatures for longer than those exposed further to the west. Whilst some variation in P-T-t paths from different structural levels across strike may be expected, the main reason for this difference in T-t conditions experienced by garnet-bearing rocks in the two areas may equally be related to the timing of exhumation: extensional tectonics in Zanskar led to significant exhumation by 20 Ma, while rocks currently exposed at Nanga Parbat have only been exhumed within the last 10 Ma (Chapters 6 and 7). Since the timing of collision was probably similar for both the NPHM and Zanskar, rocks currently exposed at Nanga Parbat have been at high pressures and temperatures for between 10 and 20 Ma longer than rocks exposed at Zanskar. This argument is only relevant if garnet grew on the prograde path, subsequent to collision, in each case. Although garnet from other parts of the Himalaya appears to be Oligocene in age (Prince et al., 1997; Vance et al., 1997), further work is required to date garnet growth at Nanga Parbat.

CHAPTER 4 - GEOCHEMISTRY AND PETROGENESIS OF GRANITIC ROCKS OF THE SOUTHERN NPHM

Author's note: This manuscript has been accepted for publication in a Geological Society of America Special Paper, the proceedings of the 11th Himalaya-Karakorum-Tibet workshop in Flagstaff, Arizona, 1996.

"Contrasting anatectic styles at Nanga Parbat, northern Pakistan"

by Alan Whittington, Nigel Harris and Rob Butler

4.1 Abstract

Tourmaline-bearing two-mica granite plutons and sheets intruding the basement lithologies of the Nanga Parbat-Haramosh Massif (NPHM) represent the youngest known occurrence of High Himalayan leucogranite magmatism. Trace element modelling using Rb, Sr and Ba indicates an origin by vapour-absent muscovite melting. Accessory phase modelling suggests that anatexis occurred at temperatures of ~720°C, and therefore depths of 20-25 km. The source of one such intrusion (the Tato pluton) is considered to be metapelitic gneiss similar to that outcropping in the massif, and isotopically distinct from the source of the Miocene Himalayan leucogranites. Initial $^{87}Sr/^{86}Sr$ ratios of ~0.88 for the Tato pluton compare with 0.74-0.78 for Miocene granites intruded into the central Himalayan orogen.

Subsequent to, or coeval with, leucogranite emplacement, small cordierite-bearing leucosomes have been generated in ductile shear zones within the interior of the massif. These are geochemically variable, but are consistently characterised by strong depletion in HFSEs and other incompatible trace elements. Petrographic and geochemical constraints indicate that at least some seams may be restitic, following localised incongruent melting of biotite in the presence of a fluid yielding a high melt fraction (F ~ 0.5). Other seams may be wholly or partially subsolidus in nature. Thermobarometric data from these seams indicate channelled fluid migration within the massif occurred at pressures <400 MPa and temperatures of about 630°C.

Geochemical constraints on contrasting granitic rocks from the interior of the NPHM therefore chart a changing regime from fluid-absent anatexis in the mid-crust (~20 km depth) to fluid-infiltration during ductile deformation in the upper

crust (~10 km depth). These findings are consistent with the rapid exhumation of the NPHM with more modest exhumation rates around the margins.

4.2 Introduction

The Nanga Parbat-Haramosh Massif (NPHM) in northern Pakistan is the most northerly outcrop of Indian continental crust within the Himalayan orogen (Fig. 4.1). The NPHM exhibits unusually young metamorphism, high exhumation rates, and the most recent melting event in the Himalaya, making it ideal to study the interaction between deformation, magmatism, and the thermal state of the crust during active thickening (Zeitler et al., 1993; Zeitler and Chamberlain, 1991; Winslow et al., 1994; Whittington, 1996; Butler et al., 1997).

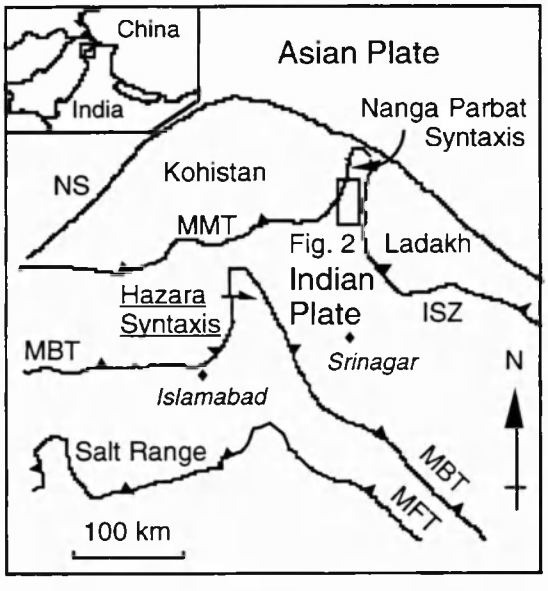

Figure 4.1. Tectonic sketch map of the western Himalaya. NS = Northern Suture, ISZ = Indus Suture Zone, MMT = Main Mantle Thrust, MBT = Main Boundary Thrust, MFT = Main Frontal Thrust.

Intruding the basement gneisses are a swarm of peraluminous leucogranite sheets and discrete plutons, the most accessible being the Tato pluton exposed about 6 km south-west of the village of Tato (Fig. 4.2). Rapid exhumation of up to several mm/yr has been reported from the NPHM (Zeitler et al., 1982a; Zeitler, 1985; Whittington, 1996) and vapour-absent melting has been suggested as a mechanism for leucogranite formation at Nanga Parbat on the basis of the temporal coincidence of melting and exhumation (Zeitler and Chamberlain, 1991). Vapour-absent melting, also called dehydration melting, occurs when the breakdown of a hydrous phase produces a water-undersaturated melt and anhydrous solid products without the direct participation of a vapour phase.

Leucogranites intruding the NPHM are of broadly similar geochemical composition to Miocene (~20 Ma) plutons described from the High Himalaya (George et al., 1993; Butler et al., 1997) but isotopic studies indicate zircon ages between 7.0 and 1.0 Ma for the NPHM leucogranites (Zeitler and Chamberlain, 1991; Zeitler et al., 1993). While rapid decompression in the main Himalayan orogen was achieved by extension on the South Tibet Detachment System, at Nanga Parbat exhumation is achieved solely by erosion in the absence of extensional structures (Whittington, 1996; Butler et al., 1997)

Various models suggested for Himalayan leucogranite formation include shear heating on the Main Central Thrust (Le Fort, 1975; England et al., 1992), contrasting thermal conductivity and internal heat production (Pinet and Jaupart, 1987), pervasive fluid infiltration of the mid-lower crust from dehydrating sediments (Le Fort et al., 1987) and vapour-absent melting due to rapid decompression (Swapp and Hollister, 1991; Harris et al., 1993; Harris and Massey, 1994). Each of these models requires a specific thermal regime, which will control the melt reaction involved in leucogranite formation. By correct interpretation of

geochemical signatures, important constraints can be placed on the thermal and tectonic evolution of mountain belts.

In addition to leucogranite formation, there is evidence of recent metamorphism involving biotite breakdown, cordierite growth, and of a leucosome-forming event resulting in leucocratic seams containing cordierite. Cordierite has previously been described from metapelites in the Himalaya (Brunel and Kienast, 1986; Inger and Harris, 1992), but has only been reported once from granitic rocks (Hodges et al., 1993). This paper presents a geochemical study of both the leucogranites and cordierite seams found at Nanga Parbat, and specifically addresses the conditions of leucogranite and cordierite seam formation, and the relationship between their petrogenesis and the thermal evolution of the NPHM.

4.3 Geotectonic setting

Nanga Parbat basement formed the footwall to the collision suture, locally named the Main Mantle Thrust (MMT), but has been exhumed through the Kohistan-Ladakh arc that originally lay in the hanging-wall. The NPHM may be broadly described as a north-plunging crustal-scale antiformal structure (Coward et al., 1986; Treloar et al., 1991), although the youngest structures for shear zones which lie along the western margin of the Nanga Parbat Massif. The reverse dip-slip Liachar Shear Zone (LSZ) carries the massif back across the suture onto the Kohistan arc, and locally over Holocene sediments (Butler and Prior, 1988a). Further north the western margin shows a transition from reverse dip-slip to oblique dextral reverse faulting over time (Butler et al., 1989; Treloar et al., 1991), with over 15 km of dextral Quaternary displacement (Madin et al., 1989).

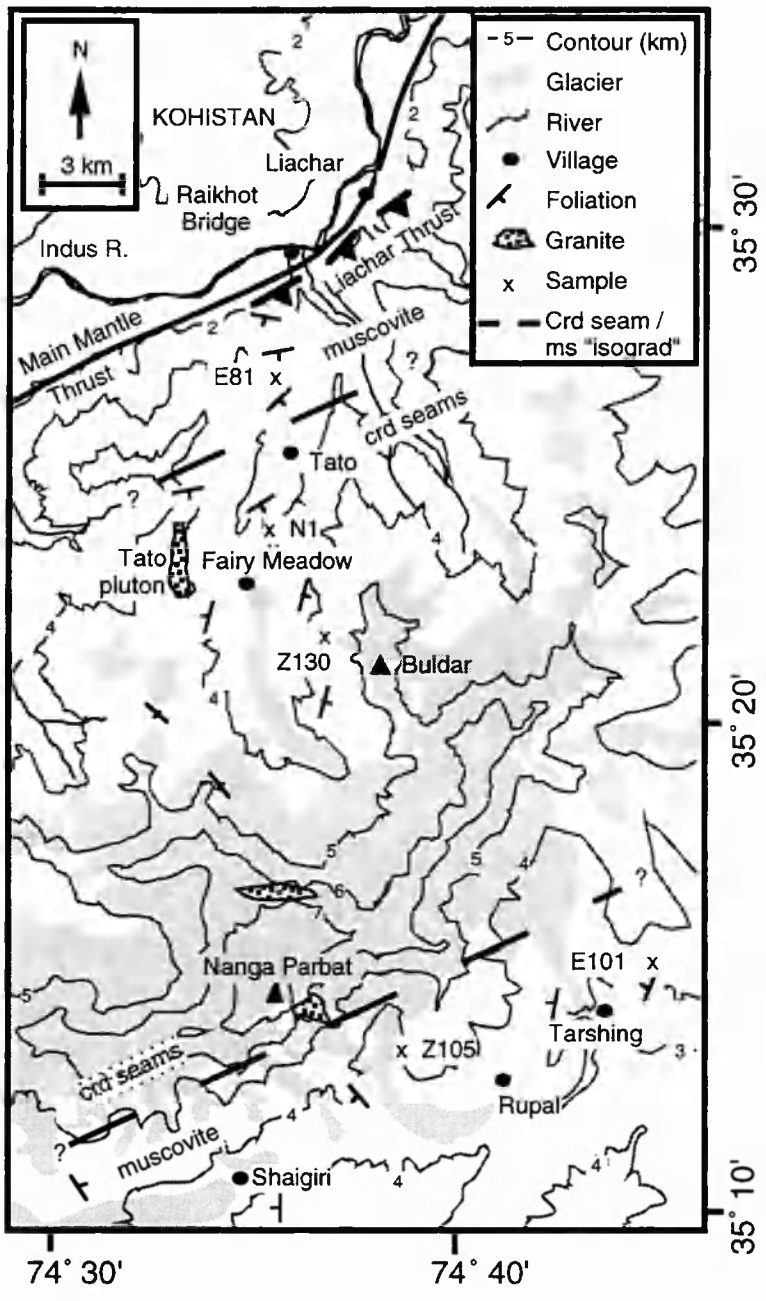

Figure 4.2. Map showing field area and sample locations, samples listed in Table 4.1. "Isograds" for occurrence of primary muscovite and cordierite seams are shown as dashed lines. Geography based on the map of R. Finsterwalder (1936), Alpensvereinkarte no. 0/7.

The structurally deepest outcrops are exposed in the central and western parts of the massif, and consist of upper amphibolite grade ortho- and paragneisses

showing evidence for polymetamorphism (Wheeler et al., 1995). The margins of the NPHM show lower grade muscovite-bearing assemblages, and the term "interior" is used to denote muscovite-absent rocks from south of the LSZ and north of the Rupal valley (Fig. 4.2). The true core of the massif lies at over 6000m on Nanga Parbat itself, and currently eludes geological investigation except by the use of binoculars.

4.4 Petrography and field description

4.4.1 Leucogranites

Leucogranite plutons from the NPHM were first reported from a poorly exposed locality at Jutial in the north-west (Butler et al., 1992). We present here a detailed geochemical study of the Tato pluton (Fig. 4.2) which shows sharp contacts discordant to gneissic foliation (Fig. 4.3a), but no chilled margin. The pluton appears to be compositionally homogeneous and non-deformed throughout its outcrop, both horizontally over at least 3 km and vertically throughout 500 m.

The pluton is a medium- to coarse-grained leucogranite containing quartz (30 to 35%), perthitic alkali feldspar (30 to 35% by volume), plagioclase feldspar (25 to 30%), biotite (<5%), tourmaline (< 5%), and muscovite (< 2%) (Table 4.1). Plagioclase feldspar is commonly zoned, typically from $An_{0.31}$ to $An_{0.06}$, core to rim. While biotite and muscovite are evenly distributed, strongly pleochroic and zoned tourmaline grains often occur in small clusters of subhedral crystals. The granite shows an interlocking seriate igneous texture in thin section, with late-crystallizing alkali feldspar sometimes containing inclusions of plagioclase and quartz (Fig. 4.3b).

Figure 4.3.

a) Contact of Tato pluton with orthogneiss wall-rock. Photo looking west, hammer head is 20 cm across.

b) Photomicrograph of Tato pluton sample under crossed polars showing tourmaline, muscovite, biotite, and potassium feldspar with inclusions of plagioclase feldspar and quartz. Long dimension is 3 mm.

c) Deformed leucogranite sheets in Liachar shear zone showing boudinage with a top-to-N shear sense, looking west. Hammer is 30 cm long.

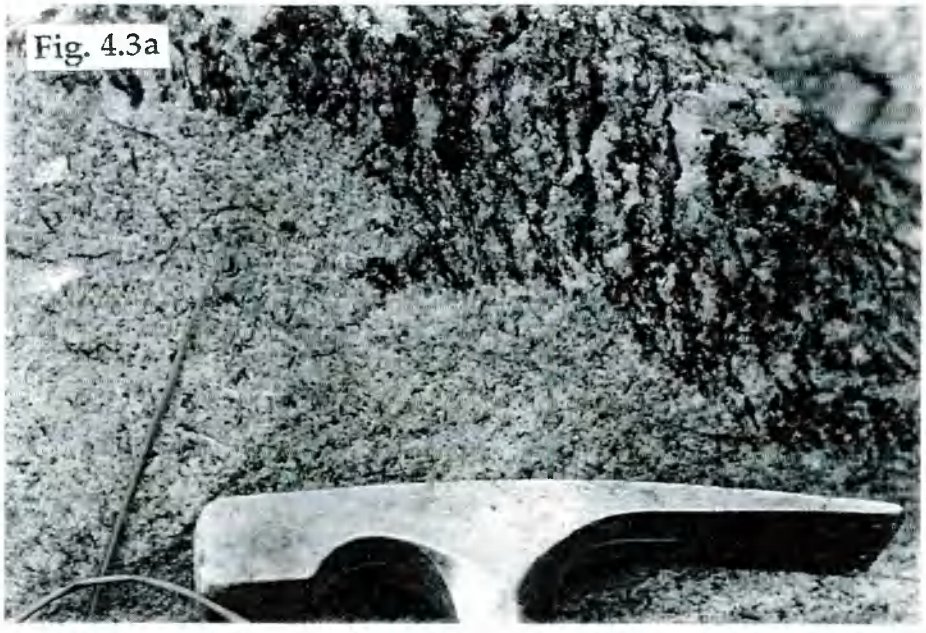
Fig. 4.3a

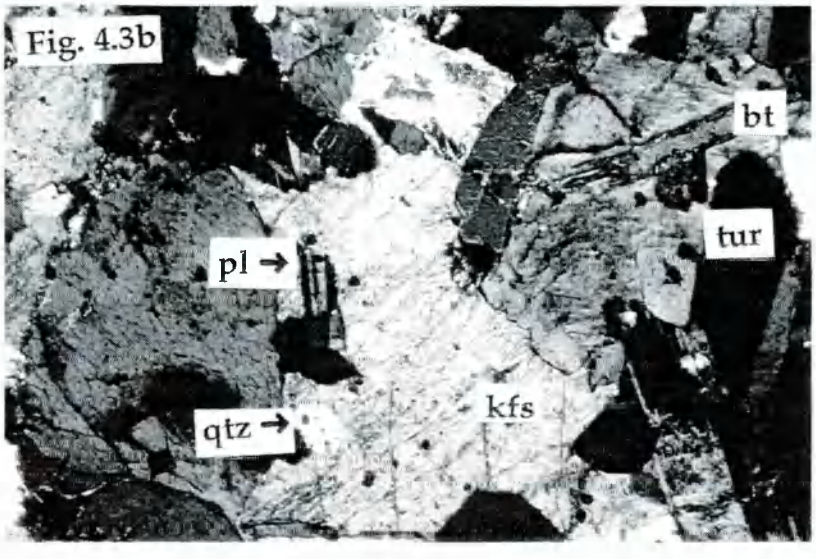
Fig. 4.3b
bt
tur
pl →
kfs
qtz →

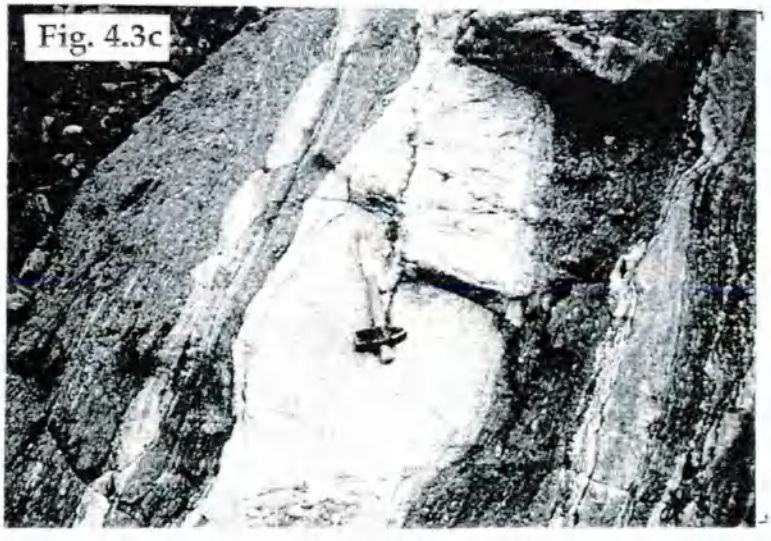
Fig. 4.3c

In thin section, alkali feldspar often shows irregular or deformed twin planes, sometimes with minor alteration to sericite. Quartz shows undulose extinction indicative of strain, and serrated grain boundaries suggesting grain boundary migration. Despite these indicators of deformation in the pluton, no pervasive fabric which might result from deformation or magmatic flow can be observed in the pluton, either in the field or in thin section.

There are also numerous leucogranitic sheets and dikes associated with the pluton, rarely more than 1 metre in width. Some of these disappear into the base of the pluton, and are probably feeder dikes, indicating emplacement through brittle fractures, driven either by buoyancy or injection pressure (Clemens and Mawer, 1992). In the interior of the massif, both on the Fairy Meadows and Rupal sides of Nanga Parbat itself, they are usually subhorizontal in orientation, consistent with vertical extension during unroofing of the massif. Several sheets show textures indicative of multiple episodes of magma injection, and tourmaline crystals are often aligned at the margins of successive magma batches, or within single injection horizons. At least one sheet from the Rupal valley shows narrow mylonitic zones in thin section, indicating post-crystallization deformation at high strain.

On the western margin of the massif these leucogranitic dikes are often very coarse-grained and pegmatitic, and have been deformed in the Liachar Shear Zone (Fig. 4.3c). Boudinaged dikes show syn-crystallization deformation fabrics, indicating syn-tectonic emplacement (Butler et al., 1997). Some sheets are almost entirely quartzofeldspathic, others contain small euhedral inclusion-free garnets, and in some cases pegmatites show tourmaline growth up to several cm long. Occasional late cross-cutting aplites are not deformed by the Liachar Shear Zone, suggesting that their emplacement was very recent.

4.4.2 Basement gneisses

The basement of the Nanga Parbat Massif is composed of Indian plate gneisses metamorphosed under upper-amphibolite facies conditions. Compositions range from metapelites and metagreywackes with occasional calc-silicate layers to granitic orthogneisses. Since metapelites are the most likely source material for crustally derived granitic melts (Wyllie, 1977), these lithologies will be described in more detail. Lit-par-lit migmatites found in some locations are unlikely to represent the source of the leucogranites, since migmatitic fabrics are cross-cut by metabasaltic sheets of probable pre-Himalayan age (Wheeler et al., 1995).

Typical metapelitic assemblages contain quartz, sillimanite, biotite, potassium feldspar and plagioclase feldspar, with variable occurrences of garnet, cordierite, spinel and muscovite. Kyanite was not observed from the interior of the massif. Muscovite is found in the Rupal valley and in the Tato valley on the margin of the massif (Fig. 4.2) but does not occur as a primary phase in the central region of the massif.

Garnets enclose quartz inclusion trails oriented at a high angle to external fabrics, indicating that garnet growth predated the latest metamorphism and deformation. In more aluminous lithologies, garnet is often mantled by cordierite. This texture has been observed in metapelites from the central Himalaya (Inger and Harris, 1992), and is indicative of heating and/or decompression. Biotite from pelitic horizons has a ragged appearance, in contrast to its occurrence as the major fabric-forming phase in less aluminous lithologies, and shows partial breakdown to an ilmenite-bearing assemblage. Cordierite reaction rims separate biotite from fibrolitic sillimanite and from small equant spinel crystals. Similar textures have been recognized in the Wilmington Complex (Srogi et al., 1993) and ascribed to dehydration partial melting of biotite. The significance of these textures is discussed in a separate paper (Whittington et al., 1997b).

4.4.3 Cordierite seams

Cordierite-bearing seams consist of dark nodular masses in a pale biotite-free host material which has somewhat indistinct boundaries against the surrounding biotite gneiss. The dark cordierite nodules comprise about 20 to 30 percent of the seams, which are rarely more than 50 cm across. These nodules sometimes occur as thin bands replicating biotite foliation, indicating that biotite is an essential reactant (Fig. 4.3d). In addition to quartz, potassium feldspar and cordierite, which comprise over 90 % of the modal mineralogy of seams, small plagioclase crystals and myrmekitic quartz-plagioclase intergrowths can be found near the margins of bleached zones. Relict biotite and more rarely garnet crystals and ilmenite occasionally occur as inclusions within interstitial cordierite (Table 4.1).

This latest metamorphic event is generally localized in steeply dipping reverse shear zones but not offset by them (Fig. 4.3e). Where not in shear zones the seams are generally sub-horizontal, both orientations consistent with vertical stretching during rapid unroofing (Butler et al., 1997). The seams appear to cross leucogranite sheets, and the sheets are deformed by shear zones containing seams. Cordierite nodules are however rarely found where seams cross sheets or leucocratic bands (Fig. 4.3d), perhaps due to the paucity of biotite in many sheets which prevents cordierite growth. This can give the impression that sheets cross-cut seams, and it may be that formation of the two was coeval during exhumation.

Cordierite seams are found in the Tato valley south of the village itself, in a variety of biotite-bearing lithologies. They are not found *in situ* in the Rupal valley to the south of Nanga Parbat (Fig. 4.2), but occasional boulders containing seams can be found in scree and in moraine deposits, suggesting that seams do exist higher up on the Rupal face.

Figure 4.3 (continued)

d) Cordierite exhibiting "ghost foliation" after biotite, with a biotite-free rim in pelitic gneiss, apparently truncated by a granitic leucosome (see text for discussion). Lens cap is 6 cm across. Very dark patches are lichen.

e) Cordierite seam in shear zone displaying vertical displacement. Photo looking north-west, compass is 8 cm long.

f) Photomicrograph of cordierite seam under crossed polars showing rounded restitic quartz set within interstitial cordierite, largely altered to pinite (pin). Long dimension is 3 mm.

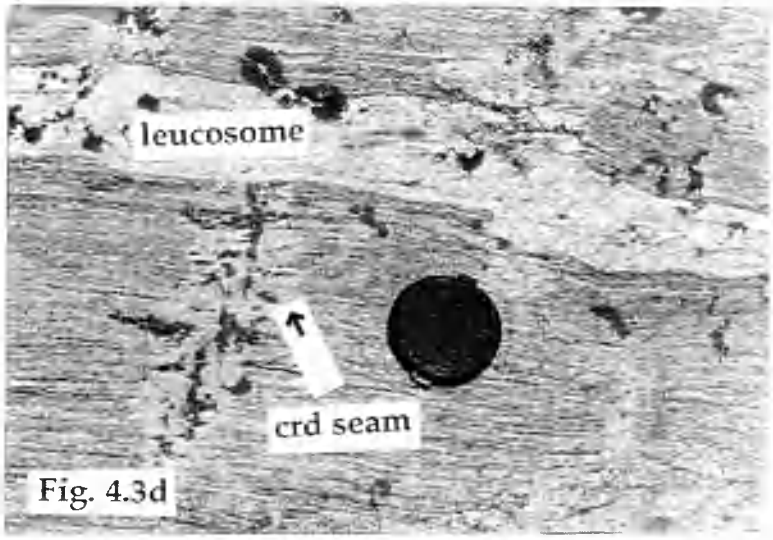

Fig. 4.3d

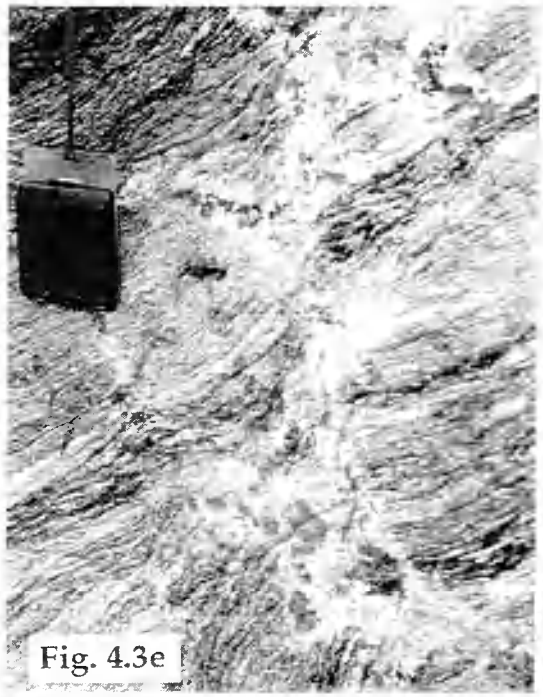
Fig. 4.3e

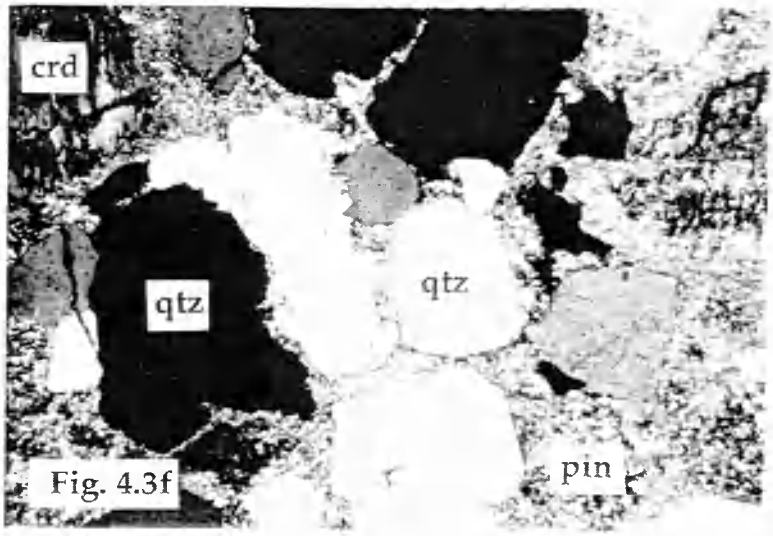

Fig. 4.3f

Some cut slabs of these seams were stained with sodium cobaltinitrite solution to identify the distribution of alkali feldspar within hand specimens. Seams were found to contain large quantities of potassium feldspar (locally > 80 %), with some grains occurring as inclusions within the dark nodules.

In thin section seams are dominated by coarse subhedral potassium feldspar crystals and interstitial cordierite, both phases enclosing generally rounded quartz grains. These textures range in appearance from a cumulate texture (Fig. 4.3f) to an interstitial grain-boundary texture, depending on the percentage area filled by cordierite. The proportion of cordierite present decreases towards the margins of seams. In general cordierite is usually altered around rims, and in some cases has been completely replaced by a fine-grained white mica aggregate (pinite). Cordierite shows different textures in aluminous layers in metapelites and in cordierite seams, and it is therefore argued that these were two quite separate cordierite-forming events.

Two sample pairs of unaltered gneiss and adjacent cordierite seam were analysed (Z130a and Z130b) and are discussed in detail.

Table 4.1. Sample mineralogy and location

Sample	Location	Type	Qtz	Kfs	Pl	Crd	Bt	Grt	Sil	Tur	Ms	Ilm
E5a/i	Tato pluton	Pluton	√	√	√	-	tr	-	tr	√	tr	-
E5a/ii	Tato pluton	Pluton	√	√	√	-	tr	-	-	√	tr	-
Z66a	Tato pluton	Pluton	√	√	√	-	tr	-	-	√	tr	-
E70a	Tato pluton	Pluton	√	√	√	-	tr	-	-	√	tr	-
E111	Tato pluton	Pluton	√	√	√	-	tr	-	-	√	tr	-
Z140	Tato pluton	Pluton	√	√	√	-	tr	-	tr	√	tr	-
Z141	Tato pluton	Pluton	√	√	√	-	tr	-	-	√	tr	-
E64	Tato pluton	Dike	√	√	√	-	tr	-	tr	tr	tr	-
E81*	LSZ	Dike	√	√	√	-	tr	-	-	-	tr	-
Z105*	Rupal	Dike	√	√	√	-	tr	-	-	tr	tr	-
X1	Fairy Meadow	Crd seam	√	√	√	√	tr	tr	tr	-	-	-
X10	Fairy Meadow	Crd seam	√	√	tr	√	tr	-	-	-	-	tr
Z42i	Fairy Meadow	Crd seam	√	√	tr	√	tr	-	-	-	-	tr
Z42iv	Fairy Meadow	Crd seam	√	√	tr	√	tr	-	tr	-	-	-
Z46Ci	Fairy Meadow	Crd seam	√	√	tr	√	tr	-	-	-	-	-
Z46Civ	Fairy Meadow	Crd seam	√	√	tr	√	tr	-	-	-	-	-
Z130a/i*	Buldar	Crd seam	√	√	tr	√	tr	-	tr	-	-	-
Z130b/i*	Buldar	Crd seam	√	√	tr	√	tr	tr	tr	-	-	tr
Z130a/ii*	Buldar	Pelitic gneiss	√	√	√	√	√	√	√	-	-	tr
Z130b/ii*	Buldar	Pelitic gneiss	√	√	√	√	√	√	√	-	-	tr
N1*	Fairy Meadow	Pelitic gneiss	√	√	tr	√	√	√	√	-	-	tr
Z9/i*	Fairy Meadow	Pelitic gneiss	√	√	√	√	√	√	√	-	-	tr
E101*	Tarshing	Pelitic gneiss	√	√	√	-	√	tr	√	-	√	-

Note: √ indicates major phase, tr indicates minor phase, - indicates absent. Sample locations refer to place names on Fig. 2, samples marked * are labelled individually. Mineral abbreviations follow Kretz (1983).

Table 4.2. Geochemical composition of representative samples

Type	Tato Lcg	Tato Lcg	Tato Lcg	Tato Lcg	Tato Lcg	Lcg Dike
Sample	E5a/i	E5a/ii	Z66a	E70a	E111	E64
SiO_2	73.7	73.36	74.74	73.95	73.83	74.84
TiO_2	0.07	0.09	0.08	0.09	0.08	0.06
Al_2O3	14.33	14.30	14.02	14.11	14.23	14.09
Fe_2O_3	1.08	1.15	1.04	1.18	1.14	0.90
MnO	0.03	0.04	0.03	0.03	0.04	0.05
MgO	0.09	0.11	0.06	0.11	0.13	0.07
CaO	1.21	1.24	1.18	1.41	1.37	0.87
Na_2O	3.43	3.61	3.44	3.48	3.47	3.87
K_2O	4.80	4.80	4.92	4.91	4.77	4.55
P_2O_5	0.09	0.09	0.05	0.06	0.06	0.07
LOI	0.52	0.60	0.14	0.42	0.52	0.49
TOTAL	99.35	99.38	99.70	99.75	99.64	99.86
Rb	453	458	444	395	474	497
Sr	58.5	60.0	57.6	71.7	67.5	35.7
Y	38.8	41.2	46.7	44.6	41.5	40.5
Zr	60	62	70	74	76	44
Nb	11.2	12.1	11.2	11.1	11.7	13.4
Ba	164	166	147	195	182	94
Pb	77	77	90	89	91	65
La	18.5	17.9	19.3	22.2	18.9	15.7
Ce	38.0	36.0	44.0	44.0	38.1	31.8
Nd	21.7	20.7	21.5	24.4	20.6	17.4
Sm	3.47	3.47	3.93	3.72	3.30	3.12
Eu	0.36	0.38	0.36	0.45	0.38	0.24
Tb	0.83	0.83	0.95	0.90	0.87	0.82
Yb	5.01	5.11	5.48	5.29	4.76	5.65
Lu	0.76	0.74	0.85	0.77	0.70	0.82
Th	16.4	16.1	20.7	20.9	17.2	16.0
U	43.7	40.5	33.0	39.4	33.8	27.0
Ta	3.8	4.02	3.4	2.47	2.86	5.5
Hf	2.6	2.58	3.1	3.29	3.16	2.1
Cs	67.7	68.6	64.5	36.0	70.5	47.3
Zn	32	33	30	32.2	29	28
$^{87}Sr/^{86}Sr$	0.877338	0.873819	0.880229	0.885434	0.873006	0.898259
$^{143}Nd/^{144}Nd$	0.511399	0.511439	0.511424	0.511415	N.D.	N.D.

Note: Major and trace elements determined by XRF analysis at the Open University. Rare earth elements, Th, U, Ta, Hf, Cs and Zn determined by INAA at the Open University.

Table 4.2 (continued)

Type Sample	crd seam X1	crd seam X10	crd seam Z42/i	crd seam Z42/iv	crd seam Z130a/i	crd seam Z130b/i
SiO_2	73.29	74.05	74.48	74.34	73.97	73.45
TiO2	0.25	0.10	0.04	0.04	0.04	0.05
Al_2O_3	13.79	13.92	14.13	14.24	14.27	14.71
Fe_2O_3	2.19	2.52	0.56	0.33	0.78	0.66
MnO	0.02	0.06	0.01	0.01	0.02	0.02
MgO	0.43	0.67	0.10	0.06	0.13	0.09
CaO	0.72	0.52	0.57	0.6	1.03	0.98
Na_2O	3.24	2.30	2.64	2.63	2.48	2.39
K_2O	5.58	4.08	6.82	6.45	6.68	6.86
P_2O_5	0.24	0.18	0.31	0.28	0.14	0.12
LOI	0.35	1.34	0.54	0.39	0.58	0.65
TOTAL	100.10	99.74	100.20	99.36	100.11	99.98
Rb	391	200	341	316	326	315
Sr	65.7	66.2	81.5	78.0	168.9	176.7
Y	14.8	10.1	1.8	2.5	24.5	21.4
Zr	133	41	7	8	18	26
Nb	15.1	4.4	1.1	1.8	0.1	1
Ba	196	210	385	359	884	881
Pb	30	23	36	34	48	48
La	26.9	7.9	3.7	4.3	9.5	8.8
Ce	62.4	17.5	7.2	8.8	17.1	15.7
Nd	30.1	7.7	3.0	3.6	8.5	7.5
Sm	6.66	1.44	0.60	0.69	1.92	1.65
Eu	0.35	0.26	0.42	0.51	1.13	1.14
Tb	0.78	0.29	0.10	0.14	0.54	0.45
Yb	1.27	1.35	0.45	0.51	2.86	2.29
Lu	0.15	0.20	0.06	0.07	0.42	0.32
Th	25.4	4.6	0.2	0.2	4.4	3.9
U	13.8	6.6	3.2	3.3	9.5	5.1
Ta	1.05	0.57	0.26	0.23	0.53	0.60
Hf	4.43	1.22	0.29	0.35	1.22	1.27
Cs	4.3	6.6	3.9	4.4	11.5	8.4
Zn	50	26	16	50	12	10
$^{87}Sr/^{86}Sr$	1.195309	1.034157	1.003043	1.004531	0.846666	0.84736
$^{143}Nd/^{144}Nd$	0.511619	N.D.	0.511318	N.D.	0.511503	0.511474

Table 4.2 (continued)

Type	pelite	pelite	pelite	pelite	pelite
Sample	Z130a/ii	Z130b/ii	E101	N1	Z9/i
SiO_2	73.41	68.94	69.24	51.06	74.00
TiO_2	0.05	0.52	0.66	0.75	0.21
Al_2O3	14.72	14.91	14.28	25.78	13.88
Fe_2O_3	0.67	4.53	4.58	10.99	2.01
MnO	0.02	0.05	0.06	0.06	0.02
MgO	0.12	1.04	1.24	4.43	0.36
CaO	0.99	1.97	1.49	0.24	0.68
Na_2O	2.53	2.98	3.26	0.52	3.16
K_2O	6.94	4.25	4.64	3.96	4.95
P_2O_5	0.12	0.19	0.11	0.05	0.21
LOI	0.68	0.75	0.74	2.25	0.67
TOTAL	100.25	100.13	100.29	100.08	100.16
Rb	258	273	240	233	355
Sr	142.8	155.2	155.0	46.1	58.9
Y	24.2	24.0	35.1	17.5	10.8
Zr	207	199	211	108	102
Nb	21.7	23.5	13.0	13.5	15.1
Ba	434	463	608	568	184
Pb	28	31	37	14	30
La	53.8	46.3	66.0	54.4	21.0
Ce	112	107	143	104	48
Nd	47.9	46.0	62.9	41.2	22.8
Sm	10.2	9.45	11.50	7.03	4.44
Eu	0.95	1.05	1.02	1.59	0.31
Tb	1.21	1.16	1.23	0.80	0.59
Yb	1.85	1.75	4.67	1.98	1.06
Lu	0.25	0.23	0.69	0.30	0.11
Th	28.8	26.7	37.2	18.1	16.6
U	8.9	6.3	7.1	1.9	11.9
Ta	4.18	3.89	1.52	0.91	1.62
Hf	6.00	6.42	6.65	3.10	3.33
Cs	9.9	11.0	6.4	11.1	11.5
Zn	80	74	78	140	57
$^{87}Sr/^{86}Sr$	0.849488	0.853131	0.834937	0.887008	1.261783
$^{143}Nd/^{144}Nd$	0.511438	0.511409	0.511147	0.511064	0.511524

4.5 Geochemistry

4.5.1 Major element geochemistry

Quartz and feldspars comprise more than 90% of the modal mineralogy of both the leucogranites and cordierite seams at Nanga Parbat. Hence their petrogenesis will be interpreted in part from major element compositions plotted on a quartz (Qtz) - albite (Ab) - orthoclase (Or) diagram (Fig. 4.4).

(i) Tato leucogranites

Tato leucogranites are peraluminous, with normative compositions of $Qtz_{33.5\text{-}36.1}Ab_{32.0\text{-}35.5}Or_{29.1\text{-}33.3}$. These compositions are compared with a range of experimental melt compositions from the literature (Fig. 4.4). Seventeen samples from the Tato pluton plot close to experimental minimum melts in the haplogranitic system at 200 MPa and a water activity of 0.3 (Johannes and Holtz, 1990). With increasing pressure, experimental minimum melt compositions become less quartz-rich, and with increasing water activity the modal percentage of albite increases at the expense of orthoclase. It is unlikely that leucogranite formation occurred at such a low pressure, but some deviation from the haplogranite system may be expected due to the complex chemistry of natural source rocks, particularly the abundance of volatile elements at the magmatic stage (France-Lanord and Le Fort, 1988). To examine the effects of a more complex system, Tato is compared to experimental melts of metapelitic protoliths.

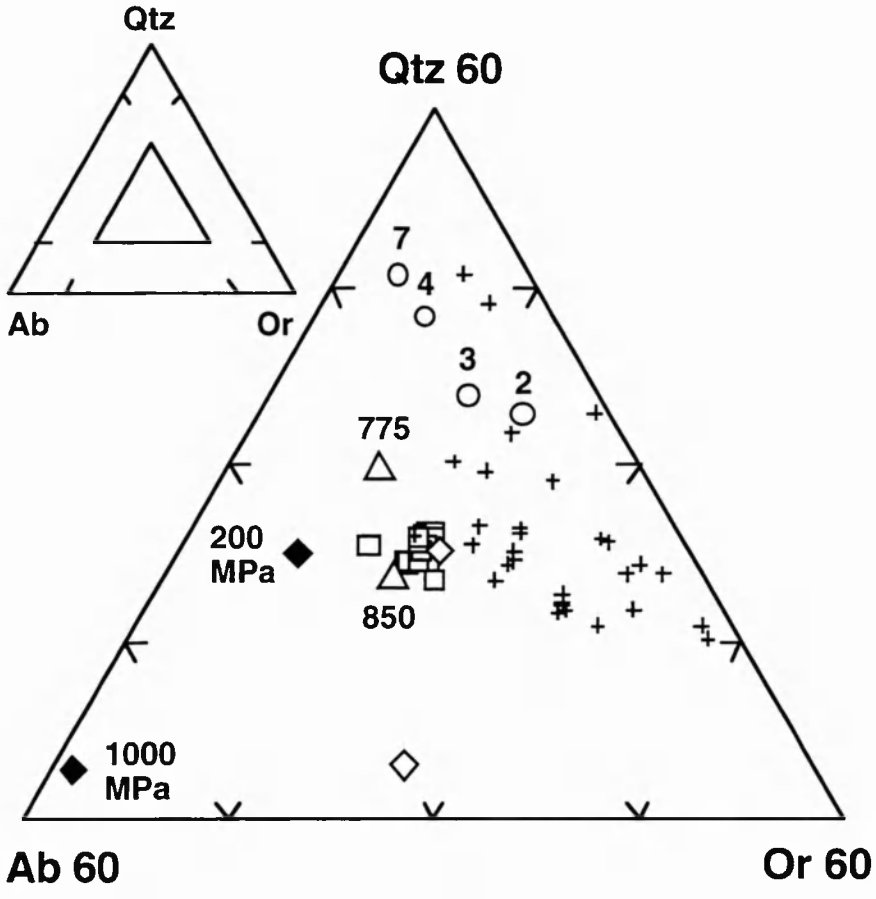

Figure 4.4. CIPW normative compositions of Tato leucogranites (open squares) and cordierite seams (crosses). Insert shows location of main plot in Q-Pl-KF ternary system. Also shown are experimental melts in the haplogranitic system for 200 MPa and 1000 MPa, a_{H_2O} = 1 (filled diamonds) and a_{H_2O} = 0.3 (open diamonds) from Johannes and Holtz (1990); experimental melts of a muscovite-rich pelite under vapour absent conditions (Patiño Douce, pers. comm.) at 850 °C and 775 °C at 600 MPa(open triangles); and experimental melts from a biotite gneiss under vapour present conditions at 750 °C and 500 MPa (open circles) from Holtz and Johannes (1991), numbers refer to added wt.% H_2O.

An experimental vapour-present biotite gneiss melt at 750 °C and 0.5 GPa (Holtz and Johannes, 1991) is considerably more quartz-rich than Tato compositions, with a modal composition of $Qtz_{50.8}Ab_{26.3}Or_{22.9}$ (7 wt.% added H_2O). For lower

percentages of added water, the experimental compositions become slightly less quartz-rich.

Experimental melts of a Himalayan muscovite- schist formed at 600 MPa under vapour-absent conditions (Patiño Douce and Harris, unpublished data) have similar modal compositions to those of the Tato pluton; $Qtz_{33.3}Ab_{35}Or_{31.7}$ at 850 °C, and $Qtz_{39.6}Ab_{32.8}Or_{27.5}$ at 775 °C. While the melt at 850 °C is the closest match to Tato, we suggest that the elevated temperatures required for melting under experimental conditions and timescales may not necessarily imply that such high temperatures are required under geologically realistic conditions. While normative Tato compositions are more compatible with an origin through vapour-absent muscovite melting, firm conclusions about pressure, water activity, and melting reaction cannot be drawn from these data.

Leucogranite sheets exhibit more varied normative compositions, from $Qtz_{44.1}Ab_{40.5}Or_{5.4}$ to $Qtz_{32.8}$ $Ab_{25.2}Or_{42.0}$, consistent with fluid/melt interaction during crystallization. Eleven analyses define a roughly linear trend away from the normative orthoclase apex, passing through the well defined Tato pluton field, while quartz/albite ratios remain roughly constant.

(ii) Cordierite seams

Cordierite seams plot as a widely scattered field at low albite (Ab <30) and high silica (Qtz 30-50) and orthoclase (Or 30-50). Cordierite seams are less albite-rich than the Tato pluton, and much more heterogeneous. They are also considerably less albite-rich than haplogranite minimum melts of Johannes and Holtz (1990), and experimental vapour-absent muscovite breakdown melts (Patiño Douce and Harris, unpublished data). The field of cordierite seams does overlap with the experimental vapour-present biotite melts of Holtz and Johannes (1991),

particularly for melts produced with little added H_2O. The cordierite seams also extend to compositions far more orthoclase-rich than experimental melts however, suggesting that some seams cannot be pure melts.

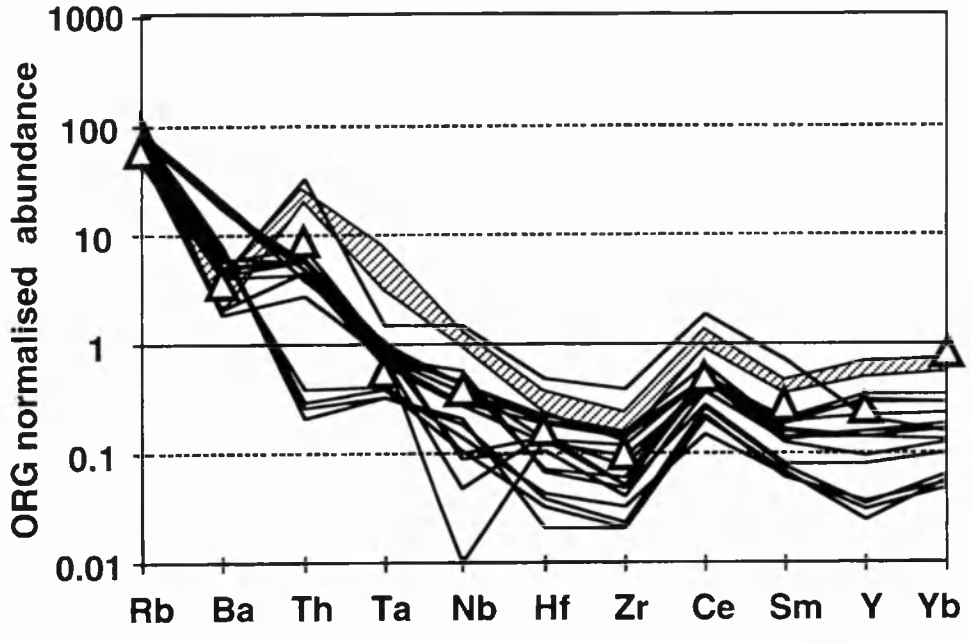

Figure 4.5. Spidergram of trace elements normalized to theoretical Ocean Ridge Granite abundance of Pearce and others (1984). Average Langtang leucogranite of Inger and Harris (1993) shown as open triangles, 17 Tato leucogranites shown as striped field, and 16 cordierite seams shown as solid lines.

4.5.2 Trace element geochemistry

(i) Tato leucogranites

Trace element concentrations have been illustrated on a spidergram (Fig. 4.5), normalised to the theoretical Ocean Ridge Granite (ORG) composition of Pearce et al., (1984). Tato leucogranites show enrichments in the High Field Strength Elements (HFSE) Nb, Ta, Hf and Zr and Rare Earth Elements (REE), except Yb,

with respect to an average of 8 Langtang leucogranites (Inger and Harris, 1993), selected as a typical Miocene High Himalayan leucogranite. The overall pattern is similar however, with positive Th and Ce anomalies, and strong depletion of Ba with respect to Rb. The distinctive chemistry of the Tato leucogranite is shared by the Jutial intrusion emplaced into the NPHM 70 km to the north (George, 1993; George et al., 1993).

Tato granites all show very similar REE patterns, at the lower abundance limit of the representative Nanga Parbat metapelite field for LREE and Eu (Fig. 4.6a). Tato LREE show a negative slope, with a pronounced negative Eu anomaly and slight enrichment in HREE, while the metapelite field shows a negative slope in both LREE and HREE. The negative Eu anomaly of the leucogranites may indicate either residual feldspar in the source, production of peritectic feldspar left in the source, fractional crystallization of feldspar, or simply a negative Eu anomaly in the source. It is likely that the distribution of other rare earth elements will be controlled largely by the accessory phases monazite, apatite and zircon (Watt and Harley, 1993).

Seventeen analyses of the Tato leucogranites define a narrow range of trace element compositions, confirming chemical homogeneity within the pluton. In contrast, trace element patterns are heterogeneous in leucogranite sheets, which also have a more variable mineralogy.

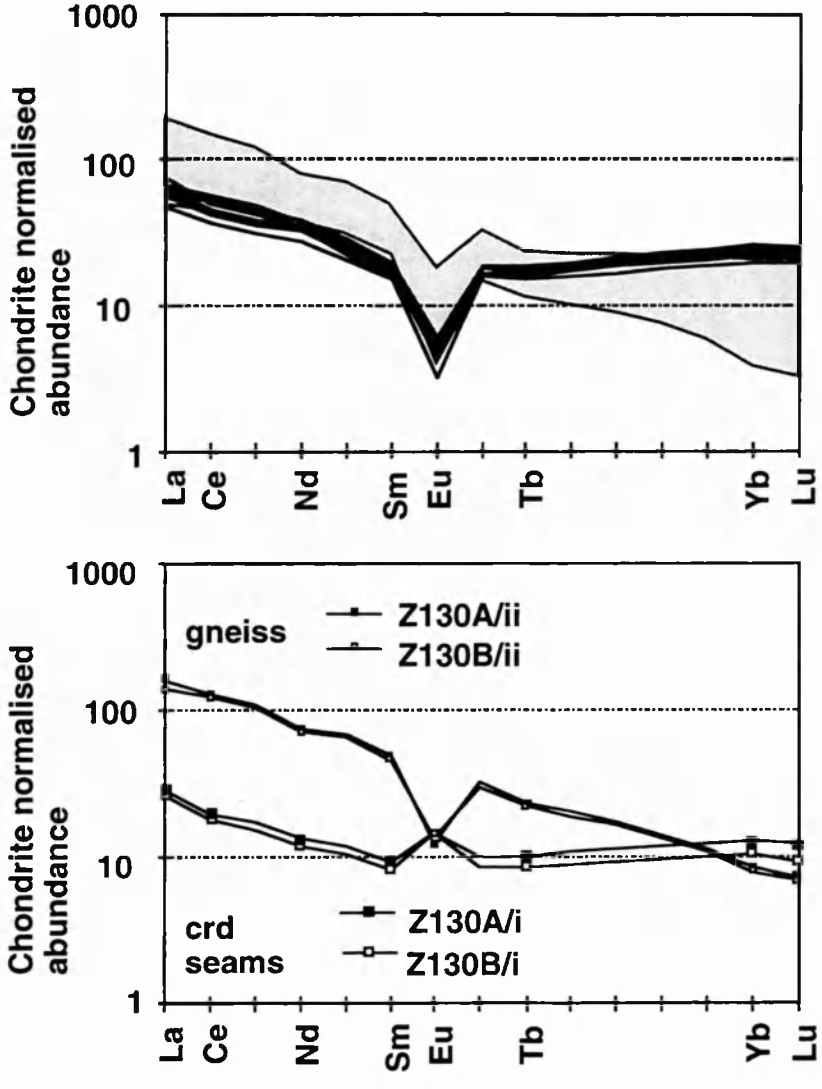

Figure 4.6. a) Chondrite-normalised plot of rare earth element concentrations in 12 Tato leucogranites and 10 metapelites (shaded field). b) Chondrite-normalised plot of rare earth elements in cordierite seams Z130a/i (large filled squares) and Z130b/i (large open squares), and paired gneiss samples Z130a/ii (small filled squares) and Z130b/ii (small open squares). Average chondrite composition taken from Sun and McDonough (1989).

(ii) Cordierite seams

In general, the geochemistry of 16 cordierite seams is highly variable, both in element concentration and relative enrichments and depletions (Table 4.2). This may be in part due to source heterogeneity, since they are localised phenomena. With one exception they are generally more depleted than the Tato leucogranites in most trace elements, but particularly Th, Ta, Nb and the REE. Since Rb and Ba show similar concentrations or even enrichment in the seams relative to the leucogranites, depletion in other trace elements may reflect removal or dissolution of trace element-rich accessory phases from seams. Of particular note are pronounced negative Nb and Ba anomalies in some seams.

Metapelites often show negative Eu anomalies and a general decrease in chondrite-normalised abundance from LREE through HREE (Fig. 4.6a). The two paired seams from Z130 both show depletion relative to their host metapelites in LREE and MREE, and the heaviest elements (Yb and Lu) have similar concentrations in both metapelites and seams (Fig. 4.6b). While the metapelites have a negative Eu anomaly, the cordierite seams have a positive anomaly so that Eu concentrations in both groups are similar.

4.5.3 Isotope Geochemistry

(i) Tato leucogranites

The Tato pluton shows a restricted isotopic range of values, with an average $(^{87}Sr/^{86}Sr)_5$ ratio of 0.877 ± 0.011 and $(^{143}Nd/^{144}Nd)_5$ ratio of 0.511424 ± 0.000017 (Fig. 4.7, Table 4.2). Such low variance suggests either a homogeneous source or thorough mixing prior to crystallization. These initial Sr values are higher than

those from other Himalayan leucogranites which typically range from 0.74 to 0.78 corrected to 20 Ma (Le Fort et al., 1987 and references therein). Epsilon Nd values for the Tato pluton (at 5 Ma) are about -23, compared with -13 to -17 for the Miocene Manaslu leucogranite (Le Fort et al., 1987).

Leucogranite sheets show more variable initial Sr ratios, particularly for sheets emplaced syn-tectonically in the Liachar Shear Zone, possibly due in part to interaction with fluids. Initial Nd ratios are also more variable in the sheets, perhaps due to fluid involvement, the effect of syn-tectonic emplacement leading to accessory phase concentrations in boudin necks, or to crystal fractionation.

(ii) Cordierite seams

The large range of initial Sr isotopic compositions for basement gneisses (from 0.72 to 1.26) suggests that pervasive fluid influx has not occurred. Cordierite seams show a similarly wide range of compositions, the clusters being due to several seams taken from the same host gneiss outcrop. This indicates that the host gneiss exerts the major control over the Sr isotopic composition of the seams, although there is a small but significant shift between isotopic compositions in host gneiss and cordierite seam. The shift in $(^{87}Sr/^{86}Sr)_5$ is -0.003 for Z130A and -0.006 for Z130B, the seams having the lower ratio. This suggests either a very limited effect of a fluid of unknown composition, or it is possible that the systematic shifts result from disequilibrium melting where the melt, with a slightly higher $^{87}Sr/^{86}Sr$ ratio than the pelite due to reactant biotite, is extracted before equilibrating with restitic feldspar. However, the range of ratios in both gneisses and seams suggests seam ratios depend much more on host gneiss than on fluid composition.

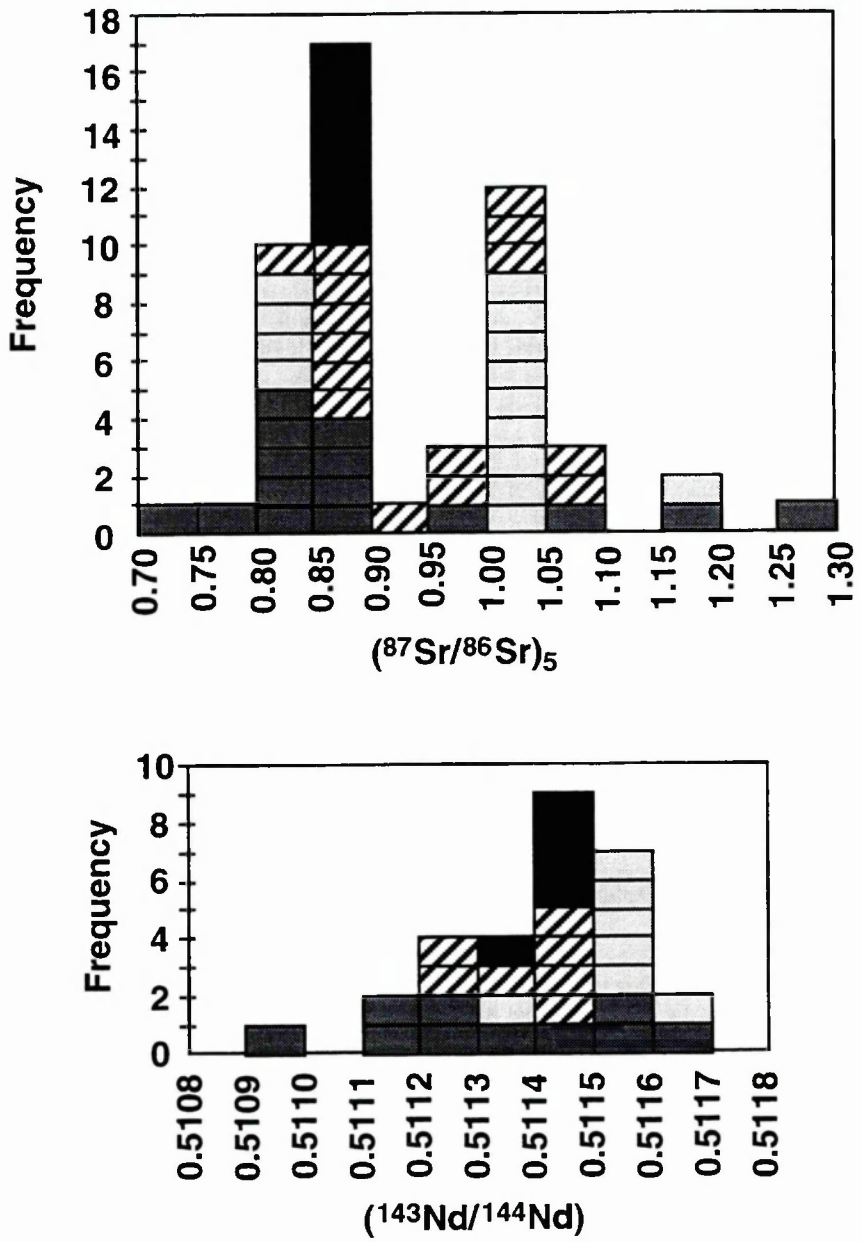

Figure 4.7. a) Histogram of calculated $(^{87}Sr/^{86}Sr)_5$ ratios. b) Histogram of calculated $(^{143}Nd/^{144}Nd)_5$ ratios. Filled boxes are Tato pluton, striped boxes are leucogranite sheets, shaded boxes are basement gneisses and plain boxes are cordierite seams. Strontium analyses for 8 leucogranite sheets and 8 basement gneisses, and Nd analyses for 1 leucogranite sheet and 3 basement gneisses are from George (1993).

Fewer Nd analyses have been undertaken, but available data are consistent with the larger Sr-isotope database, with a wide range in composition of both basement rocks and cordierite seams (Fig. 4.7). The shift in $(^{143}Nd/^{144}Nd)_5$ between gneiss and seam is +0.000065 for both samples Z130A and Z130B, the seams having the higher ratio. Since Nd is relatively immobile in hydrous fluids (Bau, 1991; Rollinson, 1993 and references therein), this may suggest that the shift in both Sr and Nd ratios may not be due to influx of aqueous fluids.

4.6 Thermobarometry

Sample Z130, taken across the seam/gneiss contact zone, was investigated to determine thermobarometric conditions of seam formation. The seam assemblage consists of cordierite, alkali feldspar and quartz, while the adjacent gneiss includes garnet rimmed by cordierite coexisting with biotite, sillimanite, alkali feldspar and quartz.

Thermobarometric calculations, used version 2.3 of the THERMOCALC program of Powell and Holland (1988) and the internally consistent thermodynamic dataset of Holland and Powell (1990). All phases analysed (see Table 4.3 for sample rim analyses and Table 4.4 for endmember activities used in calculations) were used to calculate an average pressure and temperature of 310 ± 40 MPa at 643 ± 43 °C for an assumed water activity of unity. When P and T were tested independently, the best fit was 300 ± 40 MPa at 630 ± 30 °C. For a lower water activity of 0.5 in the presence of CO_2, a lower average (PT) of 240 ± 40 MPa at 586 ± 37 °C was obtained. The dominant control on the pressure result was the reaction:

$$Gnt + Sil + Qtz = Crd \qquad (4.1)$$

which is observed in thin section. The dominant control on the temperature result was the dehydration reaction:

$$Bt + Sil + Qtz = Crd + Kfs + H_2O \quad (4.2)$$

If the cordierite seams are subsolidus in origin this represents the most likely reaction for seam formation, although the calculated P-T conditions overlap the vapour-present pelitic solidus of Le Breton and Thompson (1988), indicating that fluid influx into the rock would induce anatexis. These conditions also overlap the field of the divariant dehydration-melting reaction:

$$Bt + Sil + Pl + Qtz = Crd + Kfs + L \quad (4.3)$$

for the mineral compositions observed. Alkali feldspar may be a reactant, provided it is present in the protolith. This is the first (and only) biotite dehydration-melting reaction accessible to these rocks, and will produce a melt only slightly undersaturated in H_2O. The amount of melt produced will not be very much greater than the amount of biotite consumed. To discern between the possible melt reactions, trace element modelling is employed below.

Table 4.3. Sample rim analyses of phases used in thermobarometric calculations

Mineral	biotite	garnet	k-feldspar	cordierite
number	106	64	41	134
SiO_2	35.41	36.38	64.82	47.03
TiO_2	4.31	0.01	N.D.	0.01
Al_2O_3	17.54	20.97	18.77	32.50
Cr_2O_3	N.D.	0.04	N.D.	N.D.
FeO	26.47	37.93	0.02	14.98
MnO	0.11	2.37	N.D.	0.31
ZnO	N.D.	0.04	N.D.	N.D.
MgO	3.72	1.51	N.D.	3.47
CaO	0.00	0.65	0.15	0.02
BaO	0.04	N.D.	0.05	N.D.
Na_2O	0.23	N.D.	3.29	0.28
K_2O	8.53	N.D.	11.14	0.02
F	1.03	N.D.	N.D.	0.00
Cl	0.18	N.D.	N.D.	0.01
Total (wt.%)	97.56	99.90	98.23	98.62
Si	5.427	2.978	2.992	4.985
Ti	0.497	0.000	N.D.	0.001
Al	3.168	2.023	1.021	4.061
Cr	N.D.	0.003	N.D.	N.D.
Fe	3.393	2.596	0.001	1.328
Mn	0.014	0.165	N.D.	0.028
Zn	N.D.	0.002	N.D.	N.D.
Mg	0.850	0.184	N.D.	0.548
Ca	0.000	0.057	0.007	0.002
Ba	0.003	N.D.	0.001	N.D.
Na	0.069	N.D.	0.294	0.058
K	1.668	N.D.	0.656	0.003
O = F	-0.432	N.D.	N.D.	0.000
O = Cl	-0.041	N.D.	N.D.	-0.002
Total (cations)	14.616	8.005	4.972	11.012

N.D. denotes no data.

Table 4.4. Endmember activities used in thermobarometric calculations

Endmember	Activity
Biotite no. 106	
phlogopite	2.33×10^{-3}
annite	1.48×10^{-1}
eastonite	4.93×10^{-3}
Na-phlogopite*	9.65×10^{-5}
Cordierite no. 134	
Mg-cordierite	9.92×10^{-2}
Fe-cordierite	4.49×10^{-1}
Mn-cordierite*	2.18×10^{-4}
Alkali feldpsar no. 41	
orthoclase	6.85×10^{-1}
albite	3.07×10^{-1}
Garnet no. 64	
pyrope	2.30×10^{-4}
grossular	6.80×10^{-6}
almandine	6.29×10^{-1}
spessartine*	1.65×10^{-4}
sillimanite	1
quartz	1
H_2O	variable
CO_2	variable

Note: Phases marked with an asterisk were not used for thermobarometric calculations

4.7 Petrogenesis of granitic rocks

4.7.1 Tato leucogranites

The homogeneous nature of the Tato pluton, in both major element composition, which is similar to experimental minimum melts, and in trace element geochemistry, combined with interlocking equigranular igneous textures support the conclusion that Tato leucogranites are crystallised granitic melts. In general tourmaline and two micas coexist in the same assemblages, whereas in Miocene granites from the central Himalaya two distinct facies of tourmaline-muscovite granites and biotite-muscovite granites have been identified (Reddy et al., 1993; Guillot and Le Fort, 1995). It has been suggested that tourmaline is favoured over biotite during water-undersaturated melting, independent of source composition (Guillot and Le Fort, 1995), although the presence of boron is also required.

The source of the Tato leucogranite must in any case be different to that of Miocene leucogranites because it displays extremely high initial Sr ratios and low initial Nd ratios compared to other Himalayan plutons. The source rocks are isotopically similar to metapelitic gneisses outcropping within the NPHM. Hence trace element concentrations in the Tato granite have been normalised against an average metapelitic composition from the NPHM to investigate possible trace element enrichment trends during anatexis (Fig. 4.8).

In general, the Tato pluton shows slight enrichment in Rb, Ta, Y and heavy rare earth elements, and slight depletion in Ba, Th, Nb, Hf, Zr and light rare earths, relative to a range of metapelitic compositions. An experimental vapour-absent

melt from a metapelitic gneiss at 870 °C and 700 MPa (Cavallini et al., 1995) shows a similar pattern of trace element partitioning between protolith and melt, except for the HREE which mostly reside in accessory phases such as zircon. The release of HREE into the melt will therefore be controlled by dissolution of accessory phases, and equilibrium is unlikely to be reached on experimental timescales.

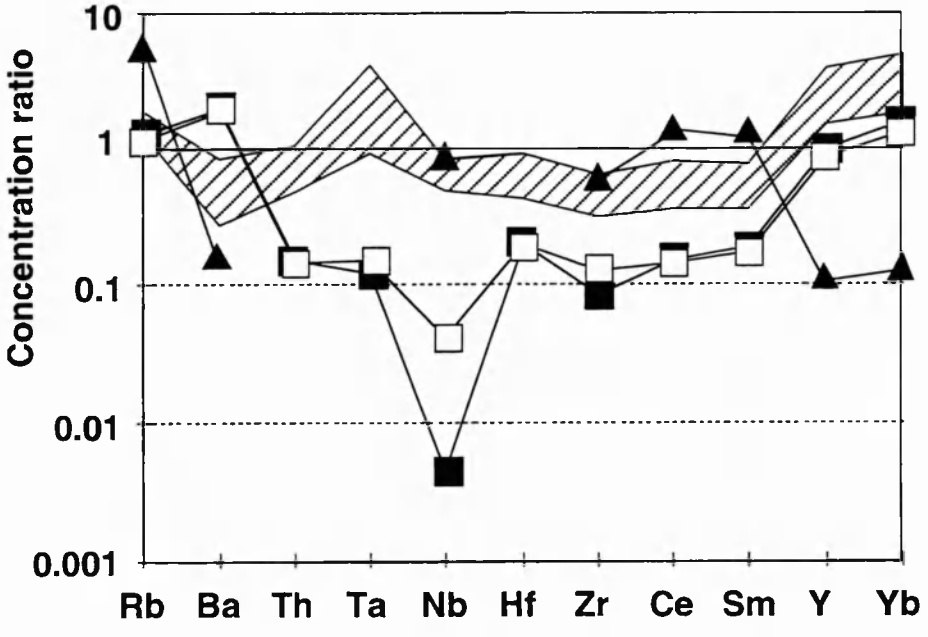

Figure 4.8. Trace element concentrations in melts. The Tato granite is normalised to a range of 5 metapelites from the field area (striped field). Two cordierite seams ratioed to their adjacent gneiss pairs are shown, Z130a (filled squares) and Z130b (open squares), and data from an experimental pelitic melt at 700 MPa and 870 °C (filled triangles) from Cavallini and others (1995).

On geological timescales however, zirconium and rare earth elements should equilibrate with a coexisting magma, and a temperature of magma formation can be calculated using the techniques of Watson and Harrison (1983) for zircon, and Montel (1993) for monazite. The Tato pluton yields generally consistent results of 710 to 730 °C for both thermometers (Table 4.5, Fig. 4.9). Some inheritance of

accessory phases not in equilibrium with the melt is anticipated, but this is likely to be a random process, and wide variations in modelled temperatures would be expected within the pluton if a significant proportion of accessory phases was inherited. Discordance between the two thermometers would also be expected if there was disequilibrium between melt and restite due to rapid melt extraction (Ayres et al., 1997). These temperatures of melting are too low for biotite melting under vapour-absent conditions, so either vapour-present melting or vapour-absent muscovite melting is implied. These alternatives can be distinguished by the use of a Rb/Sr vs Ba diagram.

Table 4.5. Accessory phase thermometry data

Type	Sample	Zr (ppm)	Zircon thermometer (°C)*	Σ LREE (ppm)	Monazite thermometer (°C)†
Tato pluton	E5a/i	60	713	0.611	725
	E5a/ii	62	712	0.584	715
	Z66A	70	722	0.664	726
	E70A	74	723	0.706	724
	E111	76	728	0.605	718
	Z140	81	731	0.694	725
	Z141	66	717	0.614	719
Lcg sheets					
	E64	44	690	0.509	711
	E81	25	645	0.182	628
	Z105	31	671	0.425	712
Cordierite seams					
	Z42/i	7	575	0.108	612
	Z42(IV)	8	585	0.130	630
	Z45B	29	664	0.287	679
	Z46C/i	32	689	0.198	691
	Z46C/iv	52	704	0.247	665
	Z130a/i	18	629	0.276	667
	Z130b/i	26	654	0.251	666
	Z130C	14	615	0.207	654
	Z130d	18	625	0.271	659

Note: All calculations assume a magmatic H_2O content of 7 weight %.
*Using the zircon thermometer of Watson & Harrison (1983)
†Using the monazite thermometer of Montel (1993).

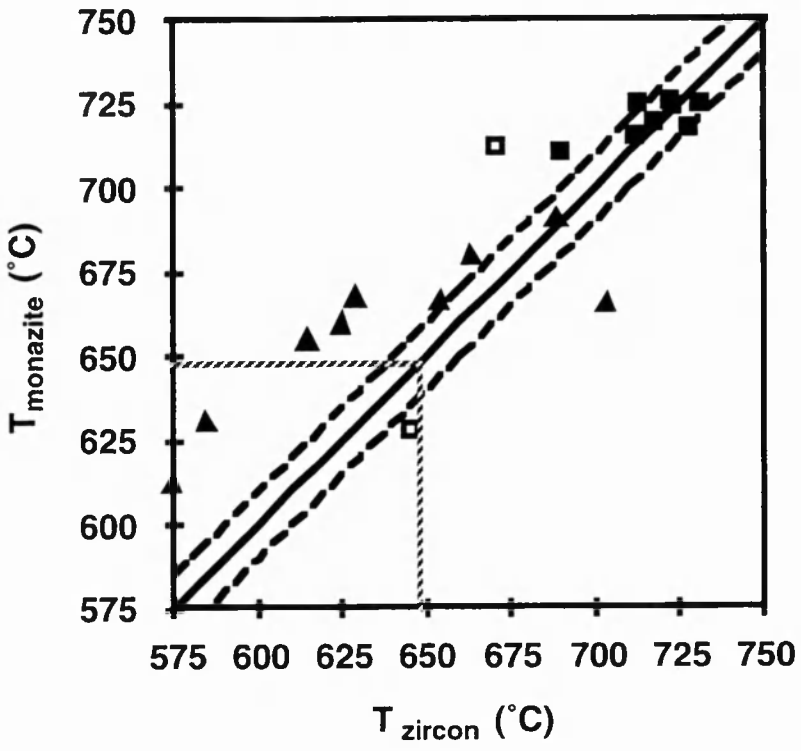

Figure 4.9. Accessory phase thermometry. Calculated temperatures shown use the zirconium thermometer of Watson and Harrison (1983) and the LREE thermometer of Montel (1993), assuming a magma water content of 7 wt.%. Solid line is for T (Zr) = T (LREE), and dashed lines enclose data within 10 °C of concordance. Thick dotted line shows vapour present solidus at 500 MPa. Filled squares are Tato pluton samples (n=8), open squares are leucogranite dykes (n=2), and filled triangles are cordierite seams (n=9).

Rubidium, Sr and Ba are the trace elements that reside in the major reactants and products of melting reactions (feldspars and micas). Quantitative modelling is undertaken in three stages; (i) Balanced reactions are obtained from given mineral and melt compositions and variable melt fraction; (ii) Restite modes are obtained by mass balance using stoichiometric coefficients and modes for the gneiss protolith (Harris and Inger, 1992); (iii) Concentration ratios in the liquid relative to the source (Cl/Co) are calculated from appropriate partition coefficients (Kd) for granitic melts, using a range of values from Blundy and Wood (1991), Harris et al.,

(1993) and Nash and Crecraft (1985). Simple melts have well-defined Cl/Co ratios for Rb, Sr and Ba whether controlled by mineral fractionation or by the partial melting reaction. For example fluid-absent melting results in high Rb/Sr ratios and depleted Ba relative to their source as seen in the Tato granite (Fig. 4.10).

Compositions from basement pelites define quite a large field, but Tato pluton analyses extend well beyond its limits. Harris et al. (1993) report that Rb/Sr ratios greater than 3.5 cannot be achieved by vapour-present melting. The Tato granite ranges in Rb/Sr ranges between 5 and 14, defining an array similar to that modelled by Inger and Harris (1993) for vapour-absent muscovite melting. An alternative cause of such a trend is crystal fractionation of alkali feldspar, but petrographic evidence shows alkali feldspar to be a late-crystallizing phase containing both quartz and plagioclase inclusions, and hence this explanation can be discounted.

We conclude that the Tato pluton was formed by vapour-absent muscovite melting of a metapelitic protolith at temperatures of around 720 °C. From the fluid-absent muscovite solidus of Petö (1976), this implies a pressure of 700 to 800 MPa, and hence a depth for the onset of melting between 20 and 25 km.

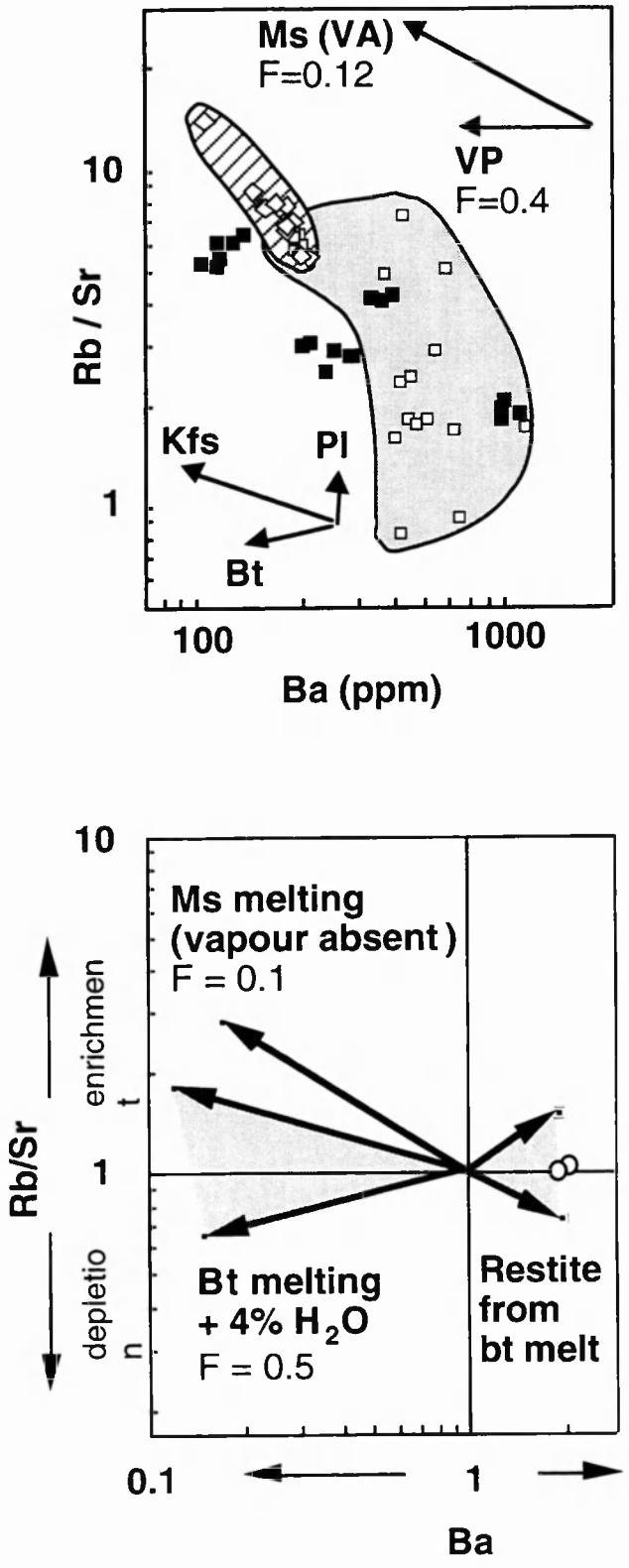

Figure 4.10. LILE covariation in Nanga Parbat gneisses, leucogranites and cordierite seams. (a) Basement pelites (open squares, shaded field), Tato leucogranite (open diamonds, striped field) and cordierite seams (filled squares). Melting vectors indicate the significance of compositional displacement of a melt from its source (Ms (VA) = vapour-absent muscovite melting, VP = vapour-present melting), and fractional crystallisation vectors indicate compositional displacement of a melt which undergoes 10% fractional crystallisation of Kfs, Pl and Bt. . Vectors from Inger and Harris (1993). (b) Modelled evolution vectors for vapour-present biotite melting of Z130 gneisses, with F = 0.5. Open circles are seam/gneiss pairs from Z130. Also shown is the evolution vector for a restite associated with melting. Shaded field indicates propagated uncertainties in Kd values for Rb and Sr in biotite. Distribution coefficients from Henderson (1982) and Nash and Crecraft (1985).

4.7.2 Cordierite seams

The following section investigates whether formation of cordierite seams was a metasomatic process, or if a melt phase was involved. There are four possible origins for the seams:

(i) Seams are metasomatic

The argument for a purely metasomatic origin for the seams rests on the *in situ* nature of the outcrops (e.g. biotite foliation is undisturbed locally) and their non-magmatic modal composition (rich in cordierite and alkali feldspar) and textures. A study of apparently similar seams from the Massif Central (Didier and Dupraz, 1985) describes nodules of poikilitic cordierite containing inclusions of quartz surrounded by biotite-free patches; these 'nodules' occur along structural discontinuities within a granite. They are ascribed to a metasomatic origin in the absence of geochemical evidence. An infiltrating metasomatic fluid will be either aqueous, i.e. the dominant anion is hydroxyl, or non-aqueous (probably carbonic in the absence of sulphides, phosphates or halides).

In general, the trace element variations between seams and gneiss are difficult to reconcile with an aqueous fluid causing metasomatism. Aqueous fluids transport the alkalis Rb and Cs, together with Ba and U, much more readily than HFS elements such as Zr, Nb and Th. Typically infiltration by a hydrous fluid causes a high U/Th ratio, while in fact U appears to be immobile during seam formation, as do alkalis, whereas the strongest depletion is for Nb; Th and other HFS elements are also depleted.

If formation of seams is a subsolidus event occurring at peak metamorphic conditions then fluid must be poor in H_2O and F in order to destabilise biotite without forming a melt. A non-aqueous fluid will probably be carbonic as inferred by Didier and Dupraz (1985). The general reaction inferred from that study requires the generation of an alkali-rich fluid. In the case of the Nanga Parbat seams however, there is little change in alkali concentrations between gneiss and seam (Fig. 4.8b).

(ii) Seams are melts resulting from equilibrium anatexis

Both field evidence and geochemical parameters preclude simple melt injection; K_2O and MgO concentrations are too high in some seams for a magmatic origin, the positive Eu anomaly in many seams is inconsistent with residual feldspar, and Nb/Ta ratios are anomalously high for a magmatic rock. Textures of subrounded quartz, subhedral alkali feldspar and interstitial cordierite are non-magmatic, in that igneous cordierite is likely to form stubby subhedral crystals (Clarke, 1995).

Alternatively the cordierite may be an entrained peritectic phase generated through a biotite-breakdown melting reaction, which would account for the elevated MgO concentration. Abundant alkali feldspar in the source implies it would be a reactant, together with plagioclase and quartz. At the pressures and temperatures obtained by thermobarometry of the seam Z130, a melt could only form in response to fluid infiltration, since the assemblage is muscovite-absent. Both the starting assemblage and PT conditions are similar to those used by Holtz and Johannes (1991) for experimental melting; at 750 °C and 500 MPa, granitic melts were formed from a pelitic gneiss with added H_2O (for 4 wt.% H_2O, F~0.5). Note that the melt is undersaturated in H_2O despite the fact that water is required for the reaction. In general Rb-Sr-Ba modelling for melting the metapelitic protolith in this experiment results in modest enrichment (in the melt) of Rb,

modest to strong depletion of Sr, and strong depletion of Ba (Fig. 4.10b). Strontium is sensitive to modal plagioclase and alkali feldspar in the restite, while Rb and Ba are sensitive to modal alkali feldspar (and/or biotite) in the restite. Under equilibrium conditions it is not possible to model enriched Ba without enriching Rb in the melt, thus confirming that the cordierite seams are not simple intrusive melts.

(iii) Seams are melts resulting from disequilibrium anatexis

Some evidence for disequilibrium melting comes from calculated accessory phase temperatures from cordierite seams. These form a scattered field, generally displaced towards higher monazite temperatures (Fig. 4.9), implying either an excess of LREE, undersaturation of zirconium, or a non-anatectic origin. This could be due to incomplete dissolution of zircon, either due to shielding in restitic phases or lack of time for dissolution of trace elements into the melt (disequilibrium melting). Some seams give temperatures below the wet solidus, and it is concluded that calculated temperatures for the seams are meaningless.

Disequilibrium melting can be modelled if the distribution of trace elements between coexisting phases in the protolith is known from ion-probe data. If it is assumed that Ba does not have time to partition between melt and restite phases (i.e. disequilibrium), then enrichment of Ba can be modelled at high melt fractions (F = 0.6-0.7) provided that rapid melting leads to consumption of virtually all alkali feldspar in the source.

There are some problems with this model: (i) Abundant alkali feldspar is observed in seams before and after melting. (ii) Both Rb and Sr are also enriched in melt by disequilibrium melting although Rb/Sr may remain fairly constant. The modelled enrichment in Rb and Sr can only be prevented if diffusion rates for

Ba are substantially slower than for the other phases; this is not supported by diffusion data for Sr and Ba in plagioclase (Giletti, 1991), although not all seams show Ba enrichment relative to basement gneisses (Fig. 4.10). (iii) Textures are not indicative of a magmatic origin of any kind. One might expect to observe an aplitic texture for a melt formed and crystallised very rapidly.

(iv) Seams are restites following anatexis and melt extraction

Influx of an aqueous fluid along shear zones may have generated a melt along grain boundaries that was extracted leaving a restite with minor melt entrapment. The biotite-alkali feldspar gneiss is similar in composition to a granite (approximate modal composition Qtz 30 %, Kfs 35 %, Pl 20 %, Bt 10 %, Sil 5 %) so the major-element composition is not greatly changed by melt extraction. However large changes in trace elements are observed. In order to double Ba abundances between protolith and restite, the melt fraction cannot be less than 0.5 (although lower F values are possible if the fluid enriches the seam in Ba). The extraction of higher melt fractions is precluded by the relatively small enrichment of Sr in the seam. We have assumed F=0.5 for modelling.

From mass balance of major phases, the composition of the melt extracted from Z130 is that of a cordierite granite (Kfs=0.47, Pl=0.16, Qtz=0.29, Crd=0.05, Sil=0.02). A balanced melt reaction for such a melt (F = 0.5; 4 wt.% H_2O added) is given by:

$$0.11\ Bt + 0.19\ Pl + 0.08\ Sil + 0.22\ Qtz + 0.44\ Kfs + 0.07\ H_2O = L + 0.11\ Crd \quad (4.4)$$

Both plagioclase and biotite must be virtually exhausted by the melt phase in order to generate the observed values of Cr/Co (Rb=1.2; Sr=1.1 ; Ba=1.9 ; see Fig. 4.10b). High Ba and the appropriate modest enrichments in Rb and Sr can be generated for an alkali feldspar-rich restite for F = 0.5. A restite model also accounts for residual quartz textures (Fig. 4.3f). The textures are suggestive of restitic quartz and alkali feldspar with peritectic cordierite occupying intergranular areas.

The positive Eu anomaly in the high Ba seams is consistent with a restite origin, generating a liquid with a negative Eu anomaly due to restitic alkali feldspar. Rare earth elements and other trace elements in seams appear to mirror the trends seen in the experimental study of trace element distribution during anatexis of a pelite (Cavallini et al., 1995 and Fig. 4.8, this study). This suggests that in the case of the cordierite seams the melt was enriched in HFS elements, by entrainment of accessory phases rather than dissolution, leaving behind a depleted restite in the seams (Table 4.2). Zircon (Zr, Hf), monazite (LREE, Th) and ilmenite (Nb, Ta) would all have been extracted with the melt, released from inclusions in biotite, along grain boundaries or (for ilmenite) as peritectic phases of the melt reaction.

The interstitial texture of cordierite from the seams contrasts with the reactant texture of cordierite seen between biotite and sillimanite in aluminous layers from some anatectic metapelitic gneisses (e.g. N1). This may be because the seams represent restites from melting after a high melt fraction has been extracted (F = 0.5), and the aluminous layers represent *in situ* melting of much smaller melt fractions in the absence of fluid channelled along shear zones.

In summary, while the restite model fits our detailed analysis of seam Z130, and from petrographic evidence the model should fit many other seams, it is not necessarily a unique explanation. In many cases there may be traces of melt retained in the seams. The melt reaction would yield a melt fraction of about 0.5

for 4 wt.% added H_2O. Since most seams occur in shear zones, and melting was probably triggered by fluid influx along these zones, it seems reasonable to suggest that the melt also escaped along these channels. Although small in volume, such a large melt fraction could segregate rapidly from the source, especially under conditions of active deformation (Clemens and Mawer, 1992; Rutter and Neumann, 1995).

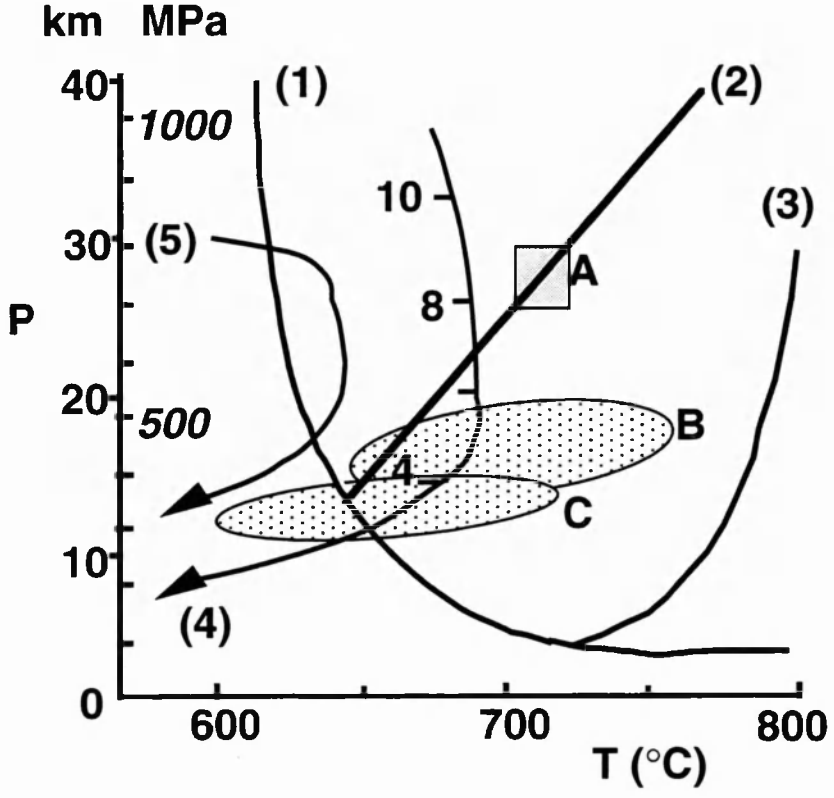

Figure 4.11. Pressure-temperature graph of vapour-present solidus for metapelites (1), vapour-absent melting of muscovite (2) and vapour-absent melting of biotite (3). Data from Le Breton and Thompson (1988) and Petö (1976). Modelled exhumation path for lithologies currently exposed in the core of the massif (4) from Whittington (1996), and inferred qualitative path of rocks at the massif margin (5). Numbered ticks indicate time in Ma. Field of leucogranite formation (A) determined from accessory phase thermometry. Fields of basement metamorphism (B) and cordierite seam formation (C) from solid-phase thermobarometry.

4.8 Discussion

Nanga Parbat leucogranites formed by vapour-undersaturated muscovite breakdown synchronous with rapid exhumation (Fig. 4.11). A zircon age of 1.0 Ma has been obtained from the Tato pluton (Zeitler et al., 1993), and so cooling and exhumation to the surface occurred on timescales shorter than this.

The rate-determining step for melt extraction is critically dependant on both the deviatoric stress and on the viscosity of the magma, which in turn depends on its water content and temperature. Applying equation 23 of Rutter and Neumann (1995) to Himalayan leucogranite melts formed under fluid-absent conditions at temperatures of 700 to 750 °C, a viscosity in the range 10^7 to 10^9 Pa s is obtained. Under these conditions the rate-determining step is more likely to be flow though the vein network (Fig. 16 of Rutter and Neumann, 1995); extraction of a 10% melt fraction by this process will occur over a period of 1 to 50 ka.

Rapid transport of melt can be effected by fracture propagation, over a timescale <1000 years (Clemens and Mawer, 1992; Petford et al., 1993). Magma transport through dikes is suggested by the abundance of both sheets and dikes displaying several episodes of magma injection, and feeder dikes connecting with the Tato pluton. Some leucogranitic sheets were emplaced syn-tectonically in the Liachar Shear Zone, which itself partially accommodates exhumation, while in the interior of the massif sheets are generally found as undeformed sub-horizontal sills, suggesting emplacement in a vertical extensional regime, probably due to rapid unroofing.

A subsequent event led to formation of cordierite-bearing seams, which show a range of textures and geochemistry. Although several models may account for their origin, all involve biotite breakdown, cordierite growth, and require a fluid influx. Trace element modelling of the biotite breakdown reaction allows Ba depletion in magma with a modest depletion in Rb and Sr provided virtually all plagioclase and biotite are exhausted. Thus the seams could be restites that include some peritectic cordierite and variable proportions of melt. If so, about 4 wt.% water is required to generate a melt fraction of about 0.5. Such a melt will be undersaturated in H_2O and be able to rise through the crust prior to crystallization. Although small in volume, the melt could segregate rapidly from the source, especially under conditions of active deformation along the shear zones in which they are found.

New thermobarometric data show the conditions of seam formation to be 300 ± 40 MPa and 630 ± 50 °C, which allows the possibility that some seams formed at subsolidus temperatures (Fig. 4.11). However, whether seams are restites or a purely metasomatic feature, fluid influx is required, and hence the seams are indicative of channelled fluid migration within the massif at pressures of at least 300 MPa.

These P-T calculations on a seam compare with similar calculations on an unmelted pelitic gneiss (Whittington, 1996) of 440 ± 60 MPa at 700 ± 60 °C. If the two rocks were exhumed on the same path, that is their relative positions have not been tectonically altered since closure to elemental diffusion, then the metamorphic geotherm shows decompression of about 150 MPa and cooling of about 80 °C. This would indicate some combination of a gentle geothermal gradient at depth, contrasting with the steep near-surface geotherm (Winslow et al., 1994; Whittington, 1996), and rapid exhumation leading to advection of heat faster than heat loss by conduction.

Intriguingly, seams are restricted to the interior of the massif, whereas outcrops of gneisses from the Rupal valley and western margin are characterised by muscovite-bearing subsolidus assemblages. Considerations of the likely P-T-t path during exhumation of the massif suggests that this mutual exclusivity is no coincidence. Assemblages that have been exhumed very rapidly in the interior of the massif (path 4, Fig. 4.11) crossed the vapour-absent muscovite solidus before cooling below the wet pelite solidus. Along this path, micaceous assemblages could melt twice; firstly from muscovite breakdown during decompression to produce leucogranites, and subsequently during fluid infiltration resulting in cordierite seams. In contrast, assemblages from the margins of the massif have been exhumed less rapidly, and so cooled earlier during exhumation. Juxtaposition of marginal rocks against the cooler hangingwall during thrusting will also lead to earlier cooling, although not necessarily due to slower exhumation, and the P-T-t path of marginal zones need not cross the vapour-absent muscovite solidus. In this case cordierite seams will not be formed since by the time these rocks had reached the depths at which focused fluid flow occurred, temperatures were subsolidus relative to the fluid-present reaction.

Thus the Neogene magmatic history of the Nanga Parbat - Haramosh Massif results from the complex interaction between its thermal structure, tectonic evolution and fluid advection, reflecting both the broad Himalayan affiliation of the massif, and its singular neotectonic activity which is anomalous within the orogen.

CHAPTER 5 - MAFIC AND ULTRAMAFIC ROCKS OF THE SOUTHERN NPHM

5.1 Introduction

The amphibolite sheets of the Nanga Parbat-Haramosh massif are important for two reasons. Firstly, they are clearly seen to be cross-cutting early migmatitic fabrics in the NPHM basement, both at Raikhot Bridge (Chapter 2) and in the Indus Valley (Wheeler et al., 1995). Thus if the intrusion age of the sheets can be obtained, a lower limit can be imposed on the timing of early migmatisation. Secondly, their geochemistry will have implications for the geochemistry of the mantle beneath the northern edge of the Indian Plate. These are the northernmost examples of basic rocks within the Indian Plate, and if a correlation can be found it may reveal more about previously documented magmatic episodes.

The samples are described in section 5.2, and their geochemistry is described in section 5.3. The petrogenesis of these bodies is discussed in section 5.4, including a comparison with similar basic rocks from the northern edge of the Indian Plate. Their isotope systematics and timing relations to metamorphic events in the NPHM are discussed in section 5.5.

5.2 Sample description

All amphibolite sheets within the NPHM have undergone some combination of deformation, metamorphism and fluid flux. Evidence for these processes includes the metamorphic mineralogy and textures (Chapter 3), combined with frequent examples of boudinaged amphibolite sheets intruded by granitic

pegmatites in the Liachar Shear zone, and the field observation that the majority of amphibolite sheets are retrogressed to predominantly chlorite. Samples were collected from three different amphibolite bodies (Fig. 5.1), chosen for their apparent lack of low-grade alteration. Their petrography has been described in Chapter 2, where it is noted that chlorite occurs rarely.

The three amphibolite bodies sampled are:

(i) An olivine-clinopyroxene-spinel body from about 5000m on the Jalipur Pass (E155, one sample). No field relations were visible, due to snow cover.

(ii) A hornblende-biotite-plagioclase metabasic dyke from about 4000m on the south side of the Rupal valley, folded in a 10m-scale hanging-wall antiform to a north-verging reverse shear zone (E104, five samples). The dyke was discordant to gneissic foliation, though later deformation has resulted in the discordance being at only a slight angle.

(iii) A hornblende-biotite-plagioclase-quartz sheet from the west side of Bayal Camp (E119, five samples), intruded by a pegmatitic feeder dyke to the Tato Pluton. This body is either conformable or near-conformable with gneissic foliation in core of massif, so that it may be an "amphibolite dyke" or a more calcic layer in the NPHM basement gneisses with unclear relations to host gneiss.

There are also two samples of Kohistan origin. E156 is part of a large dioritic pluton exposed on the roadside north-east of Raikhot Bridge, containing amphibole-clinopyroxene phenocrysts. E160 is a strongly deformed meta-diorite from the MMT zone. Although not part of the geological evolution of the NPHM, these samples represent magma of intermediate composition generated within an island arc, and will be contrasted with basic sheets intruding the NPHM.

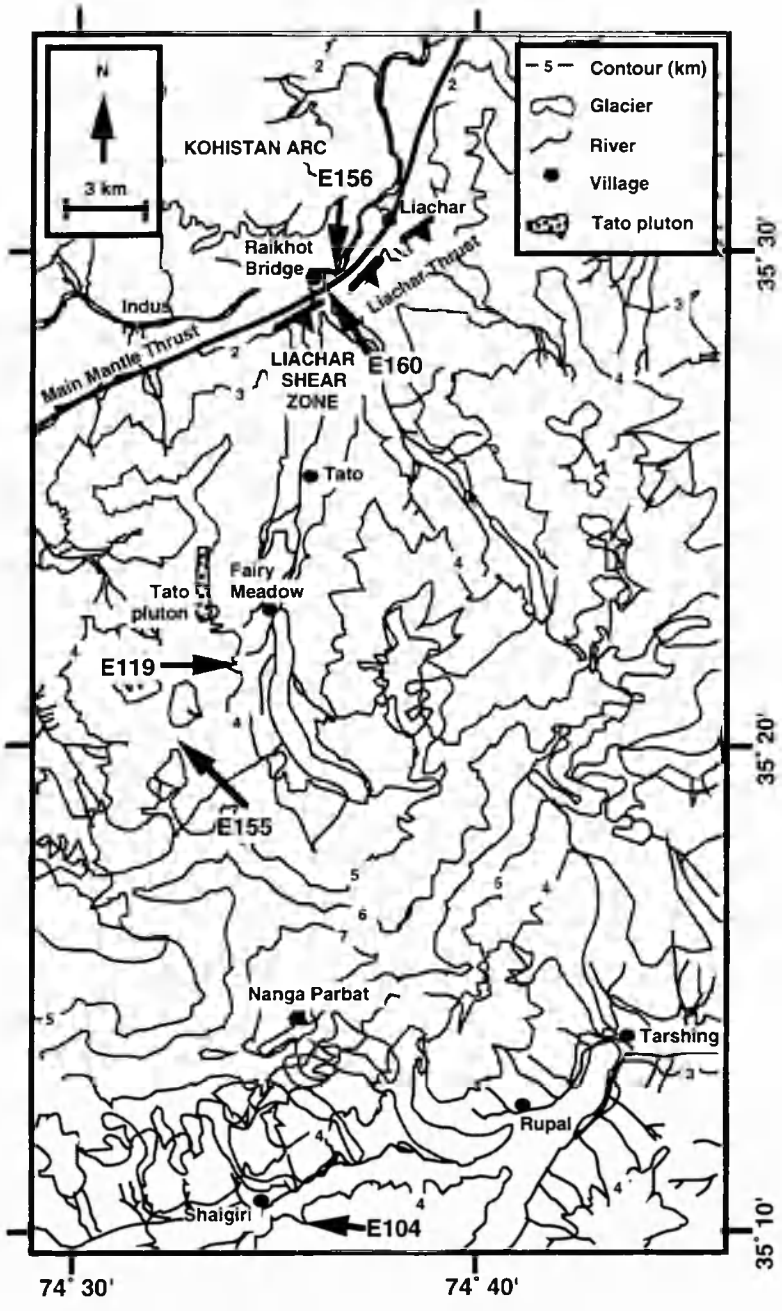

Figure 5.1. Location map showing sample localities for metabasic rocks.

5.3 Geochemistry

5.3.1 Alteration

Before the petrogenesis of these lithologies can be interpreted from their geochemistry, it is essential to discern how altered the rocks are from their primary composition. The Kohistan diorite (E156) is likely to best preserve original mineralogy, textures and chemistry from the time of emplacement, since all the others have undergone deformation and metamorphism. The MMT zone sample (E160) is the most strongly affected by low grade alteration, showing epidotisation and calcitisation along microscopic veinlets (Chapter 2), but even this alteration affects only a fraction of the volume of the sample. The chemistry of the amphibolites is likely to have been affected by Himalayan high-grade metamorphism (Chapter 3) but they are thought to be relatively unaffected by fluid infiltration.

Possible indicators of alteration by fluids include an increased loss on ignition (LOI), indicating an abundance of hydrous phases or carbonates, and depletion of mobile elements such as K and Sr. A negative correlation between K_2O and H_2O contents, or Sr and H_2O contents, may indicate removal of these mobile elements during fluid fluxing. Similarly, a positive correlation between Sr and K_2O contents may indicate a similar process where evidence in the form of a hydrated assemblage is no longer present.

No correlation is found between Sr and LOI, or Sr and K_2O, for the five samples of E104. The five samples of E119 show no obvious trend, and E155 has low LOI, K_2O and Sr. Hence there is no compelling evidence for removal of Sr or K_2O during metamorphism, although the possibility cannot be discounted. Since these

elements are particularly susceptible to removal during metasomatism, it is certainly worth investigating these samples further.

5.3.2 Major element geochemistry

The bulk geochemistry of the metabasic lithologies will first be examined through the total alkalis vs. silica plot for volcanic rocks, after Le Maitre et al. (1989). Volcanic, rather than plutonic, names have been used for the sheets since E104 and E155 are likely to be feeder dykes associated with volcanism, while E119 may be metavolcanic even if it is conformable with nearby metapelites.

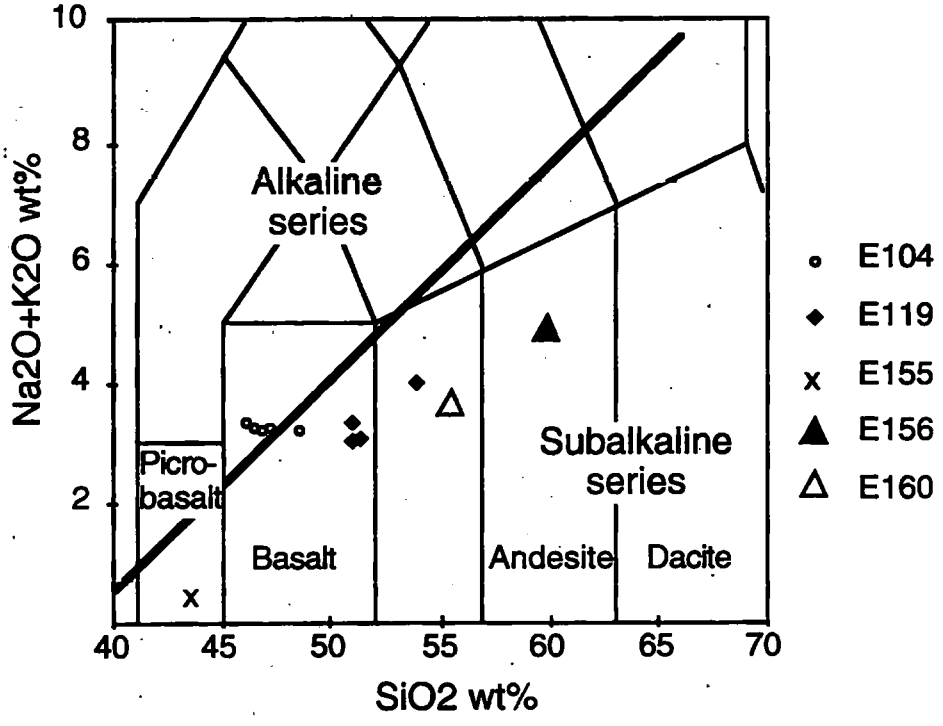

Figure 5.2. Total alkalis vs. silica (TAS) diagram for basic lithologies from the southern NPHM and Kohistan (Chilas complex). Fields from Le Maitre et al. (1989). Data from Table 1. Black triangles = E156 (Kohistan diorite), open triangle = E160 (MMT zone diorite), open circles = E104 (Rupal dyke), filled diamonds = E119 (Bayal Camp), cross = E155 (Jalipur Pass).

Table 5.1. Whole-rock geochemical data for basic lithologies from the southern NPHM and Kohistan. Samples described in text. Major oxides (wt. %) and trace elements determined by XRF analysis at the Open University.

SAMPLE	E156	E160	E104A	E104B	E104C	E104D	E104E
SiO_2	60.06	55.58	46.81	48.45	46.14	46.49	47.08
TiO_2	0.76	0.80	0.69	0.63	0.63	0.67	0.64
Al_2O_3	16.33	16.79	15.23	14.43	14.87	15.15	14.99
Fe_2O_3	7.48	8.11	12.64	11.76	12.03	12.48	12.09
MnO	0.14	0.13	0.18	0.18	0.19	0.18	0.19
MgO	3.15	5.02	8.56	8.61	8.40	8.46	8.60
CaO	6.43	8.18	11.05	10.98	11.62	11.26	10.92
Na_2O	3.13	3.19	2.08	2.31	2.09	2.08	2.25
K_2O	1.73	0.42	1.10	0.85	1.22	1.15	1.02
P_2O_5	0.16	0.17	0.07	0.07	0.07	0.07	0.07
LOI	0.36	1.97	1.22	1.65	2.49	1.68	1.89
TOTAL	99.73	100.36	99.63	99.92	99.75	99.67	99.73
Rb	49.5	7	68.3	56.7	91.7	72.7	72.1
Sr	392.5	372.8	160.0	154.2	157.6	160.7	158
Y	23.2	18.3	20.5	19.3	18.2	19.4	18.6
Zr	128	59	66	64	64	65	62
Nb	2.9	2.4	2.4	3.7	2.4	3.1	3.4
Ba	463	121	161	132	127	122	162
Pb	19	8	15	9	12	15	13
Sc	20	23	36	36	32	38	37
V	176	210	276	255	261	262	266
Cr	23	103	462	406	460	477	467
Co	20	32	62	56	58	59	59
Ni	12	42	157	150	157	155	161
Cu	46	51	104	9	130	123	69
Zn	76	80	94	102	104	94	104
Ga	18	16	18	17	18	16	17
S	111	132	99	87	98	127	99
La	18.2	n/a	9.9	9.3	10.2	10.3	9.4
Ce	37.0	n/a	19.3	18.5	18.3	19.7	18.3
Nd	18.2	n/a	10.3	10.3	10.2	10.9	9.7
Sm	3.98	n/a	2.50	2.47	2.48	2.57	2.44
Eu	1.00	n/a	0.76	0.78	0.76	0.80	0.77
Tb	0.64	n/a	0.58	0.56	0.52	0.58	0.54
Yb	2.21	n/a	1.66	1.59	1.60	1.63	1.60
Lu	0.36	n/a	0.24	0.24	0.23	0.25	0.24
Hf	3.9	n/a	1.8	1.7	1.8	1.8	1.8
Ta	0.2	n/a	0.2	0.2	0.2	0.2	0.2
Th	2.8	n/a	3.3	3.1	3.2	3.4	3.1
U	0.8	n/a	0.6	0.7	1.0	0.6	0.5
Cs	2.2	n/a	3.6	7.2	5.9	3.1	8.2
Mg#	35.5	44.7	47.0	48.9	47.7	47.0	48.2
(La/Yb)n	5.5		4.0	3.9	4.3	4.2	3.9

Rare earth elements and Th, U, Hf, Ta, and Cs determined by INAA at the Open University. Analytical techniques described in Appendix 1. bd = below detection limit, na = not analysed.

SAMPLE	E119A	E119B	E119C	E119D	E119E	E155
SiO_2	51.60	51.46	50.96	51.04	53.95	43.87
TiO_2	1.60	1.58	1.63	1.52	1.42	0.32
Al_2O_3	14.31	14.47	14.18	13.78	14.90	6.13
Fe_2O_3	12.78	12.72	12.99	13.68	11.88	14.01
MnO	0.22	0.22	0.23	0.23	0.18	0.19
MgO	6.35	6.30	6.41	7.17	6.08	28.31
CaO	8.85	8.93	8.93	7.98	6.41	5.29
Na_2O	2.07	2.12	1.92	1.63	1.93	0.22
K_2O	1.01	0.94	1.04	1.69	2.05	0.11
P_2O_5	0.14	0.14	0.14	0.14	0.14	0.04
LOI	1.01	1.08	1.03	1.11	0.59	0.34
TOTAL	99.93	99.95	99.46	99.96	99.53	98.84
Rb	47.6	40.4	54.6	143.0	139.9	6.8
Sr	381.4	391.7	344.0	225.6	211.8	13.3
Y	24.2	24.1	25.4	22.1	24.2	9.1
Zr	120	114	125	115	144	31
Nb	7.1	7.4	7.9	6.8	11.9	1.2
Ba	229	202	230	411	362	13
Pb	23	24	24	17	36	2
Sc	37	33	32	31	30	24
V	300	307	306	296	254	151
Cr	213	209	211	197	162	3969
Co	49	49	50	54	44	136
Ni	56	57	55	55	44	1589
Cu	80	94	78	63	52	183
Zn	114	113	115	131	265	86
Ga	22	21	23	20	21	9
S	121	123	140	142	72	957
La	15.5	n/a	n/a	n/a	n/a	4.1
Ce	31.2	n/a	n/a	n/a	n/a	8.4
Nd	17.5	n/a	n/a	n/a	n/a	4.4
Sm	4.24	n/a	n/a	n/a	n/a	1.07
Eu	1.41	n/a	n/a	n/a	n/a	0.31
Tb	0.78	n/a	n/a	n/a	n/a	0.25
Yb	2.01	n/a	n/a	n/a	n/a	0.82
Lu	0.29	n/a	n/a	n/a	n/a	0.13
Hf	3.2	n/a	n/a	n/a	n/a	0.8
Ta	0.5	n/a	n/a	n/a	n/a	0.1
Th	3.2	n/a	n/a	n/a	n/a	1.2
U	1.2	n/a	n/a	n/a	n/a	0.5
Cs	2.1	n/a	n/a	n/a	n/a	0.8
Mg#	39.4	39.3	39.2	40.7	40.1	72.5
(La/Yb)n	5.2					3.3

The three groups form a curved trend from basalt (E104) through basaltic andesite (E119 and E156) to andesite (E160), with increasing alkali content (Fig. 5.2), although no genetic link should be inferred from this trend. The plutonic equivalent names for the Kohistan rocks are gabbro or diorite for E160, and diorite for E156, and will be used for the two Kohistan samples. E119, E156 and E160 are all tholeiitic, while E104 crosses the tholeiitic/calc-alkaline boundary of MacDonald (1968). E104 shows no correlation between alkali and silica content, while E119 shows some positive correlation. E155 plots in the tholeiitic picro-basalt field at very low alkali content (0.33 wt. %), and shows many characteristics typical of a very primitive magma, including a high Mg number of 72, and high Ni and Cr contents (Table 1).

Further subdivision of the subalkaline series is possible by considering potassium content (Fig. 5.3). On a plot of K_2O vs. SiO_2, only the primitive sheet (E155) and the MMT diorite (E160) fall in the low-K (tholeiitic) series, following the subdivisions of Le Maitre et al. (1989), while the Kohistan diorite (E156) and the basaltic sheets (E104 and E119) plot in the calc-alkaline series (Fig. 5.3a). E119 shows some scatter, which may be due to post-magmatic processes, while E104 shows a remarkably linear trend towards lower K_2O values with increasing silica content, possibly due to fractionation of a potassic phase such as phlogopite. On a plot of K_2O vs. Na_2O content, the basaltic sheets E104 and E119 both show a spread crossing the boundary of the calc-alkaline and shoshonitic fields (Fig. 5.3b). The Kohistan diorite (E156) plots in the Shoshonitic field, while the MMT diorite (E160) plots in the calc-alkaline field. The scatter in the basaltic sheets E104 and E119 indicate much greater variability in K_2O content than in Na_2O content.

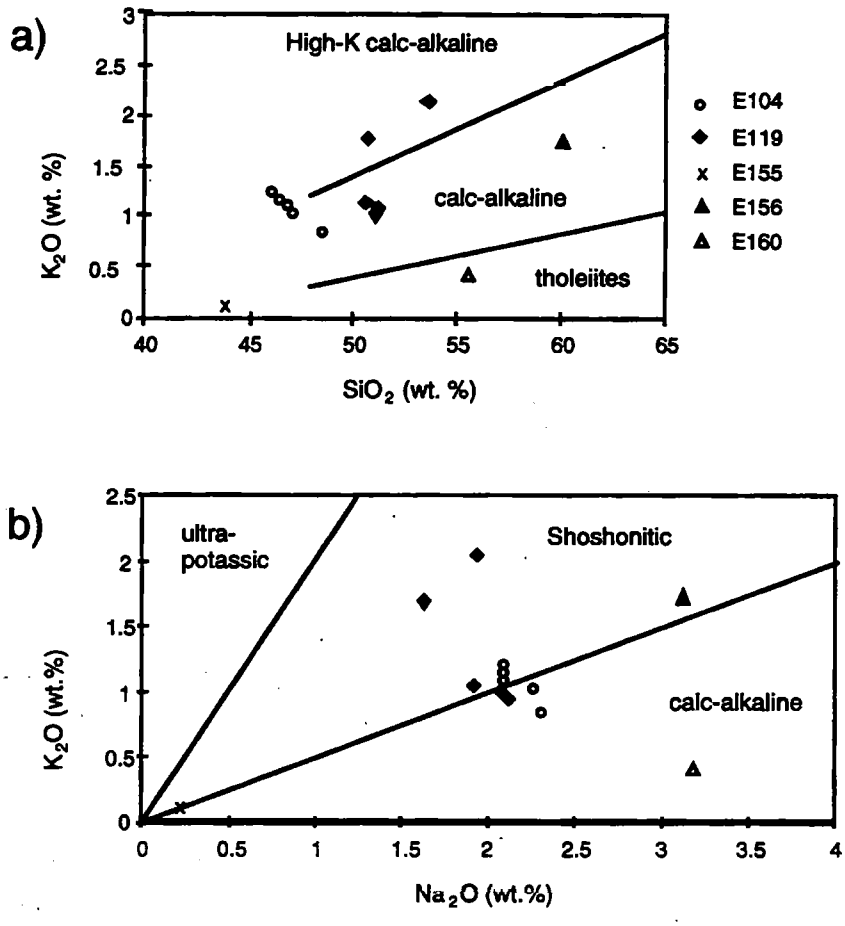

Figure 5.3. a) K_2O vs. SiO_2 diagram and b) K_2O vs. Na_2O diagram for basic lithologies from the southern NPHM. Data in Table 1. Symbols as for Fig. 5.2.

Since Si, Ca, Na and K are mobile during amphibolite-grade metamorphism of basalts (Rollinson, 1983), and the surrounding basement to the amphibolites is predominantly metagranitic, silica and alkali contents would probably be increased in the amphibolites during metamorphism. This may explain the Shoshonitic classification of sheets E104 and E119. Fe, Mg, Na and K are also mobile during greenschist-facies metamorphism of basalts (Pearce, 1976; Gelinas

et al., 1982), so that further investigation will be conducted through the use of trace elements.

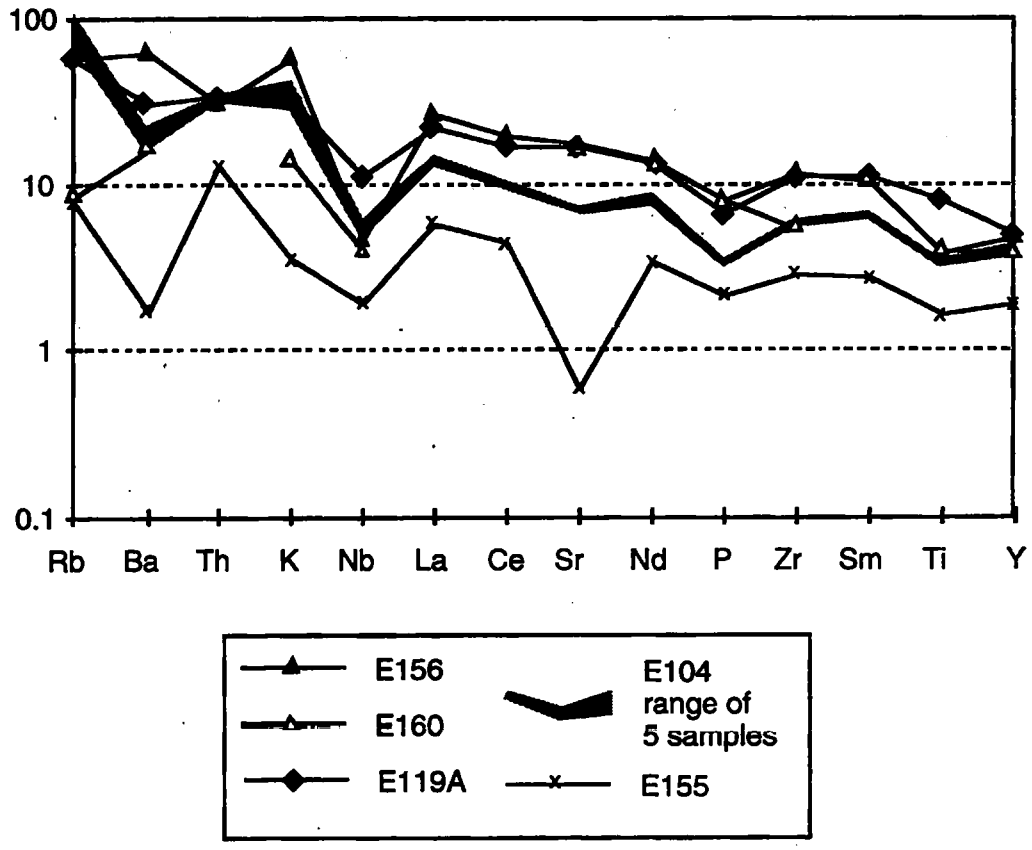

Figure 5.4. Spider diagram of trace element concentrations normalised to the primitive mantle composition of Wood et al. (1979), arranged in order of increasing mantle incompatibility after Rollinson (1993, Fig. 4.23). Data in Table 1. Symbols as for Fig. 5.2.

5.3.3 Trace element geochemistry

The trace element geochemistry of the samples is investigated via a spidergram (Fig. 5.4), normalised to the primitive mantle values of Wood et al. (1979), and arranged in order of increasing compatibility with respect to a small percentage mantle melt after Rollinson (1993). The pattern of the Kohistan diorite (E156) will

be described first, and used as a reference pattern for other samples, since its origin is the best-constrained of any of the samples.

The Kohistan diorite (E156) shows an overall trend of decreasing concentration of more incompatible elements (from left to right on Fig. 5.4), with strong Nb depletion and also negative Th, P and Ti anomalies. The deformed diorite from the MMT zone (E160) shows strong depletion relative to E156 in the large ion lithophile (LIL) elements (Rb Ba and K but not Sr) and Zr, but not in the incompatible elements Nb, Sr, P, Ti and Y.

E119A appears very similar to E156, with minor depletions in Ba and K, and minor enrichments in Nb and Ti, relative to E156. The five samples of E104 show a very narrow range of trace element concentrations, with a similar pattern to the Kohistan diorite but at lower concentrations for many elements. The strongest depletion is again in Nb, with minor depletions in Ba, Sr, P and Ti.

The picro-basalt E155 is only slightly enriched in many elements compared to primitive mantle values, having much lower concentrations of all elements than all the other samples, and is extremely depleted in Ba and Sr, with minor depletions in K, Nb and Ti.

While minor anomalies in figure 5.4 may be simply due to plotting order, there are a few obvious features which cannot be explained by this alone. Every sample exhibits a pronounced negative Nb anomaly, a characteristic of the continental crust, or of melts derived from enriched sub-continental lithospheric mantle (Turner et al., 1996). In addition, the high Ti/Y ratios exhibited by the amphibolites (Ti/Y ≈ 200 for E104, E156, E160; Ti/Y ≈ 300 for E119) cannot be attributed to contamination by crustal material since Ti/Y ratios in NPHM basement rocks rarely exceed 100.

The MMT zone diorite (E160) is depleted in the LIL elements Rb, Ba and K, although not in Sr. This may indicate removal of these elements by a fluid in the shear zone, a hypothesis supported by the highly altered nature of some of the MMT zone rocks.

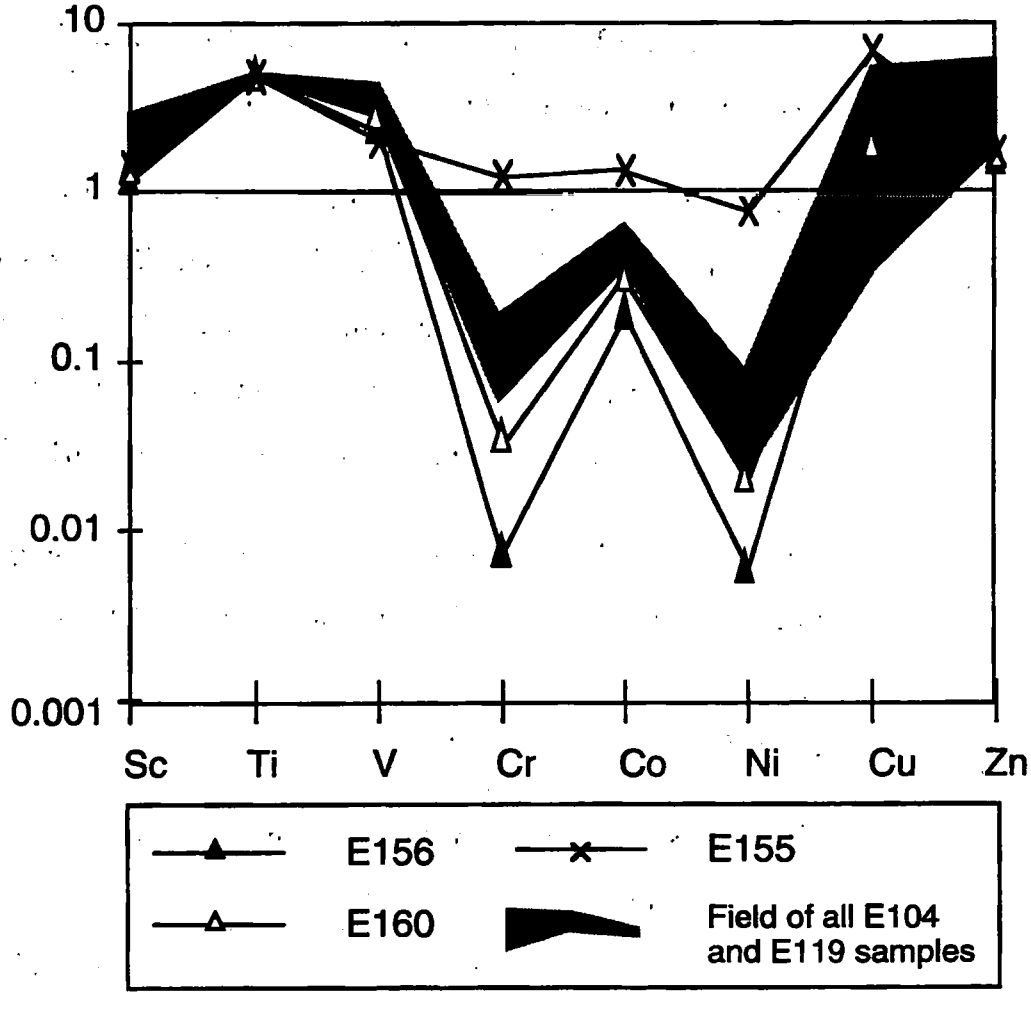

Figure 5.5. Spider diagram of transition metal concentrations in E155 (crosses), E156 (filled triangles), E160 (open triangles), and E104 and E119 (shaded field) normalised to an average of six ultramafic nodules from Jagoutz et al. (1979).

The picrobasalt (E155) is distinctly depleted with respect to all the other samples, which may be a primary feature relating to its petrogenesis, although the strong

negative Ba and Sr anomalies again suggest the involvement of a fluid. When transition element concentrations are normalised to an average of six ultramafic xenoliths (Jagoutz et al., 1979), E155 deviates little from their composition, with slight enrichment in Sc to Co and slight depletion in Ni (Fig. 5.5). In contrast, MORB is depleted in Cr and Ni by a factor of 10 (Langmuir et al., 1977) due to fractionation of spinel (Cr), olivine (Ni) and pyroxene (Cr and Ni). The basaltic sheets E104 and E119 show MORB-like patterns, while the Kohistan and MMT diorites show even greater depletion in Cr, Co and Ni (Fig. 5.5). Cu and Zn are known to be quite mobile during metamorphsm, confirmed by the wider spread in analyses from E104 and E119.

The Cr and Ni pattern of E155 suggests an origin either as a mantle xenolith, or a cumulate. The very high Mg number (MgO / FeO+MgO = 0.72) is strongly primitive, but does not resolve this question, since a fractionating assemblage of olivine + spinel would be from a primitive melt, but enrichment of Mn and Fe by several orders of magnitude compared to the average xenolith value of Jagoutz et al. (1979) favours a cumulate origin. Since the rock was emplaced into crustal basement rocks, it is likely to be strictly a xenolith, whether cumulate or primitive mantle. Alternatively, it could originate from *in situ* crystal settling of a sill-like body, but field relations were not visible and the sample has been recrystallised during subsequent metamorphism so that original textures are destroyed.

The rare earth element (REE) patterns of each sample follow similar patterns, with mantle-normalised $(La/Yb)_N$ values between 3.3 and 5.5 (Fig. 5.6; Table 1). Small negative Eu anomalies are exhibited by all except E119A, suggesting some fractionation of plagioclase or residual plagioclase in the source. This similarity in patterns may reflect origin from a similar source, or simply a similar fractionation history with REE concentrations controlled by their (in)compatibility in the same fractionating phases.

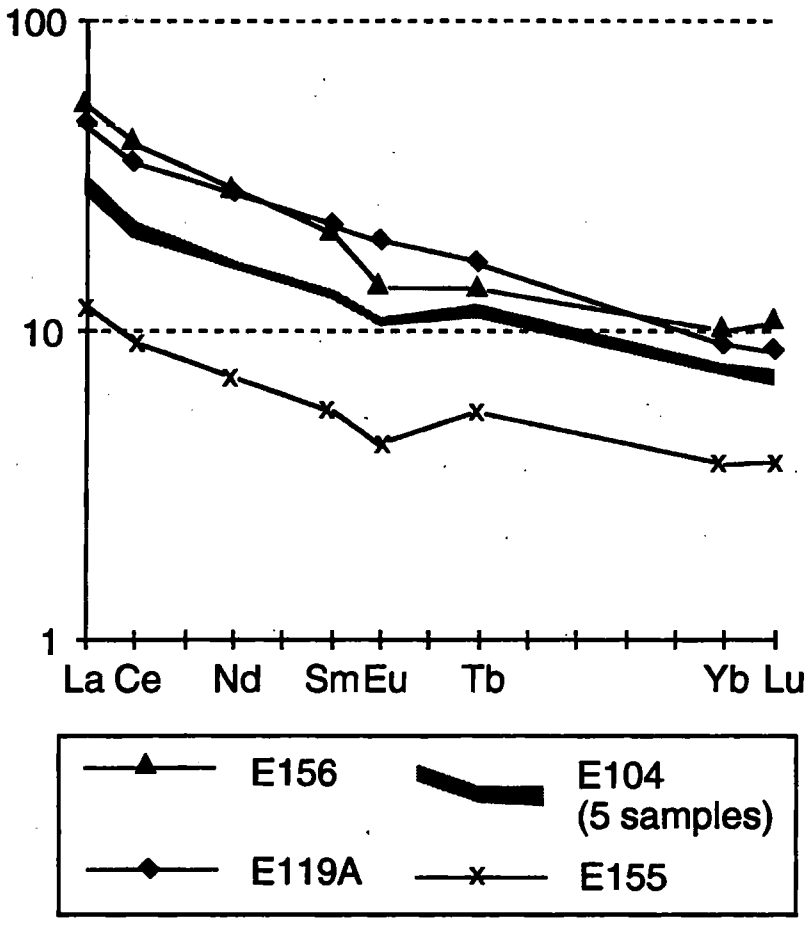

Figure 5.6. Rare earth element plot for basic lithologies from the southern NPHM and Kohistan, normalised to the average chondrite values of Nakamura (1974). Data in Table 1. Filled triangles = E156, filled diamonds = E119A, shaded field is E104 (5 samples), crosses = E155.

Fractionation of clinopyroxene would result in preferential enrichment of LREE, while fractionation of olivine will have a similar but much smaller effect due to its very low REE partition coefficients. Residual garnet in the source would have a much greater effect than either, due to its strong partitioning of the HREE, with measurements of Kd $(La/Yb)_{gt}$ between $1.4x10^{-4}$ and $6.3x10^{-4}$ in basaltic liquids (Irving and Frey, 1978).

E155 shows much lower REE concentrations than the other samples, as with other trace elements (Fig. 5.6), but no difference in pattern. These low concentrations reflect the incompatibility of REE in the phases which comprise E155, particularly olivine. The $(La/Yb)_N$ ratio of 3.34, despite the greater compatibility of the HREE relative to the LREE in these phases, suggests that the magma from which these phases crystallised was significantly enriched in LREE, possibly due to residual garnet in the source.

5.3.4 Summary

Major and trace element data have been presented for a range of basic lithologies from the southern Nanga Parbat-Haramosh Massif. The Kohistan pluton sample (E156) is an unaltered calc-alkaline diorite belonging to the Kamila amphibolite suite (Bard, 1980; Jan and Howie, 1981). The MMT zone diorite (E160) has a low K_2O content and is apparently tholeiitic, although it is also depleted in the mobile alkali elements Rb and Ba, suggesting that K may also have been lost during deformation and fluid infiltration.

E155 is classified as a picro-basalt, although generally low trace element concentrations combined with high MgO content and high Mg number lead to its interpretation as a xenolith. High concentrations of Fe and Mn relative to other xenoliths suggest a cumulate origin, and high Ni and Cr concentrations confirm the fractionating assemblage was olivine + chrome-spinel + clinopyroxene, as observed in thin section. The cumulate was probably deposited in a magma chamber and transported in a dyke as a xenolith.

The other metabasaltic sheets, E104 and E119, are both classified as calc-alkaline basalts. They display considerable variation in K_2O contents, although whether their original value was high or low is uncertain. Five samples of E104 show little

variation on a spidergram, although negative Ba anomalies may be attributable to the action of fluids. REE patterns appear to be primary, with LREE enrichment due to a combination of clinopyroxene fractionation and residual garnet in the source.

The change in amphibolite composition in the presence of a fluid will be controlled by the fluid composition, likely to be enriched in mobile elements, and the fluid-rock ratio. The REE and HFSE are generally immobile during metasomatism of basic rocks due to their high ionic potential, although the behaviour of the REE may be unpredictable in the presence of highly evolved magmas or aqueous fluids enriched in components such as H_2O, Li, B, F and P (Bau, 1991). Such components are likely to be associated with granitic magmas, especially magmas known to contain B and probably F as in the case of the tourmaline-bearing Tato granite and its associated pegmatites.

Bulk compositional change may also have been assisted by deformation, particularly in the Liachar Shear Zone. In a study of granitic mylonitisation, Condie and Sinha (1996) found that almost all major and many trace elements were mobilised during mylonitisation, but that the direction of change in composition was different in two different shear zones. Rare earth elements and incompatible trace elements were relatively immobile, with Sm/Nd ratios stable during mylonitisation.

Since both the MMT zone diorite E160 and the basaltic sheets E104 and E119 are strongly deformed, and amphibolite sheets are observed to be fluid conduits in the LSZ (Butler et al., 1997), both of the above mechanisms may have affected bulk rock chemistry. The effect of fluids will be investigated further, in the light of isotopic evidence, in section 5.5.

5.4 Petrogenesis

In this section, the petrogenesis of the meta-basalt sheets E104 and E119 will be investigated, in part using tectonic discrimination diagrams. E155 is not plotted as it is considered to be a cumulate rock, and hence unsuitable for such analysis. Comparisons with other occurrences of basaltic rocks from the Indian Plate will then be made, using the same diagrams to identify possible correspondences.

5.4.1 Tectonic discrimination diagrams

Interpretation of tectonic discrimination diagrams relies on crustal contamination being insignificant for the trace elements concerned. Both meta-basaltic sheets and both Kohistan samples show low Mg numbers and negative Nb, P and Ti anomalies on the spidergram (Fig. 5.3). These are characteristics of the continental crust, or of melts derived from enriched sub-continental lithospheric mantle (Turner et al., 1996). In the case of the Kohistan samples, the involvement of subducted sediment from the Indian Plate in melt generation may be responsible for these signatures. In the case of sheets E104 and E119, some crustal assimilation may have occurred. However, concentrations of immobile incompatible elements in E104 and E119 are much lower than in NPHM basement, arguing against significant contamination. High Ti/Y ratios exhibited by the amphibolite sheets (Ti/Y ≈ 200 for E104, E156, E160; Ti/Y ≈ 300 for E119) cannot be attributed to assimilation of crustal material since Ti/Y ratios in NPHM basement rocks rarely exceed 100. There is no correlation between Ti/Y and Rb/Ba, so that while mobile elements show considerable variation, this is attributed to the action of crustal fluids rather than to crustal assimilation, and tectonic discrimination diagrams using only immobile elements should be valid.

Nb/Y ratios are used to screen alkali basalts, which are unsuitable for other discriminant plots (Winchester and Floyd, 1977). No sample has Nb/Y greater than 0.5, confirming that none of the rocks are alkaline basalts. On the Ti/100 - Zr - Y*3 triangular plot of Pearce and Cann (1973), the Kohistan diorite (E156) plots in the calc-alkaline basalt (CAB) field, while the MMT diorite (E160) is in the field which includes CAB, mid-ocean ridge basalts (MORB) and island arc tholeiites (IAT) (Fig. 5.7). E119 plots in the within-plate basalt (WPB) field, and E104 is transitional between the CAB and CAB-MORB-IAT fields. It has been noted that continental flood basalts do not necesarily plot in the WPB field (Holm, 1982; Duncan, 1987), but it is clear that E104 and E119 have quite different geochemical signatures.

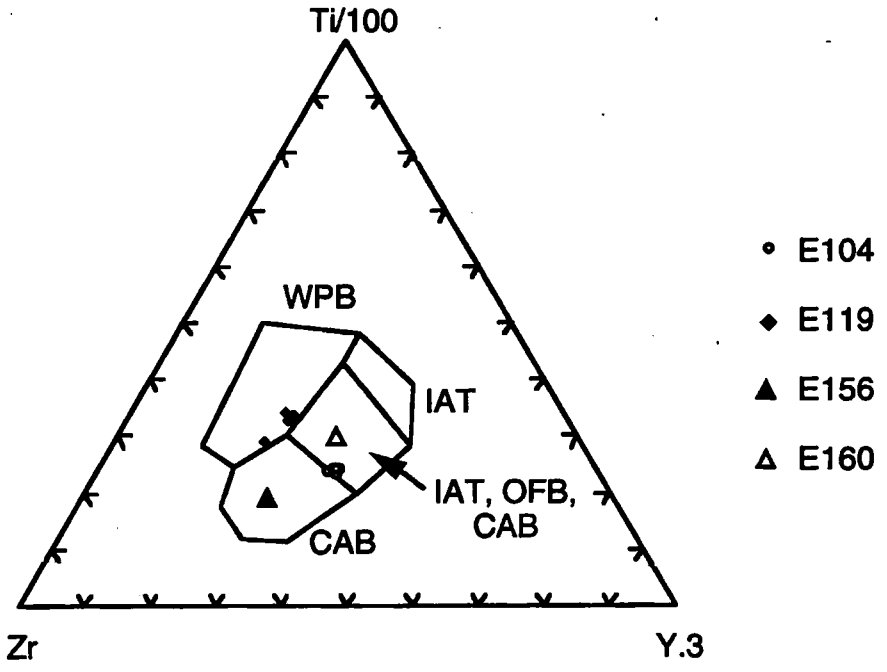

Figure 5.7. Ti/100 - Zr - Y*3 triangular plot with field classifications from Pearce and Cann (1973). Symbols as for Fig. 5.2.

The Ti vs. Zr diagram of Pearce and Cann (1973) is used to discriminate between samples plotting in the CAB-MORB-IAT field of Fig. 5.7. The Kohistan diorite (E156) again plots in the calc-alkali basalt field, while the MMT diorite (E160) is transitional between the IAT and MORB-CAB-IAT fields (Fig. 5.8). E119 plots in the MORB field, and E104 is transitional between the island-arc tholeiite and calc-alkali basalt fields. On the logarithmic scale version of the Ti vs. Zr diagram (Pearce, 1982), the Kohistan diorite (E156) plots in the volcanic arc field (not shown). E104 and the MMT diorite (E160) are transitional between volcanic arc and MORB fields, and E119 is transitional between MORB and WPB fields. E119 and E104 again have different geochemical signatures.

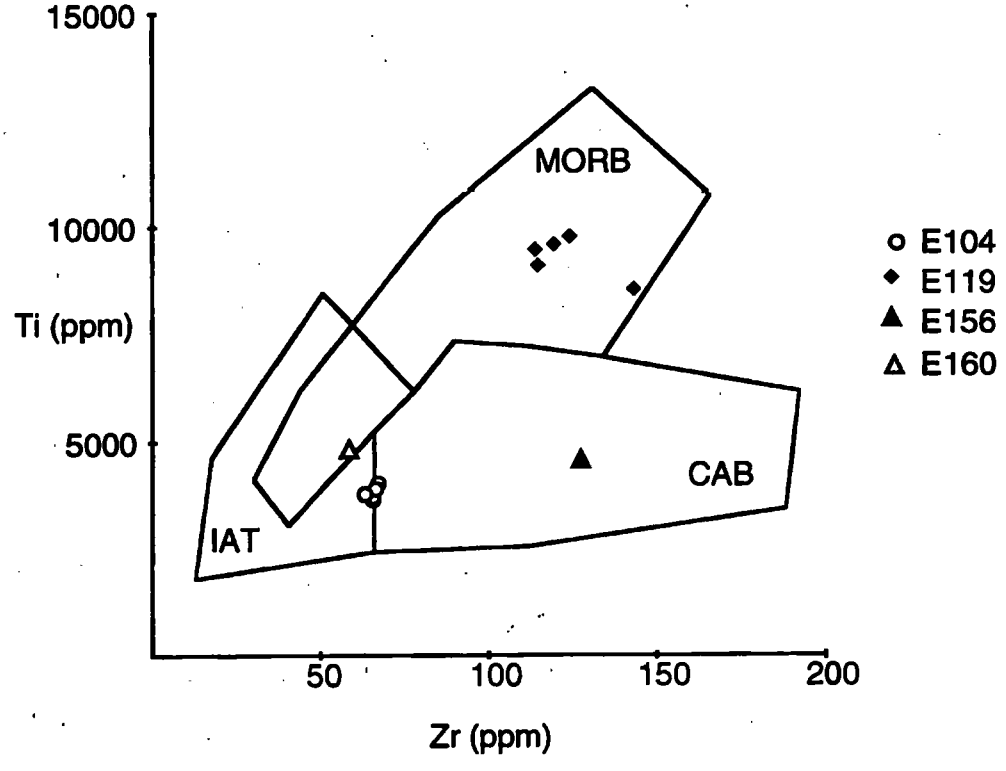

Figure 5.8. Ti vs. Zr diagram with field classifications from Pearce and Cann (1973). Symbols as for Fig. 5.2.

On a Zr/Y vs. Ti/Y diagram (Pearce and Gale, 1977), all samples plot in the plate-margin basalt field except for E119, which is transitional with the within-plate basalt field (not shown). On a Zr/Y vs. Zr diagram (Pearce and Norry, 1979), E160 and E104 plot in the overlap between the MORB and volcanic arc basalt (VAB) fields (not shown). E119 and the Kohistan diorite (E156) plot in the overlap of the MORB and WPB fields. On a Ti/Y vs. Nb/Y diagram (Pearce, 1982), all samples plot in the VAB / MORB field except for E119, which plots on the boundary with the WPB field (not shown).

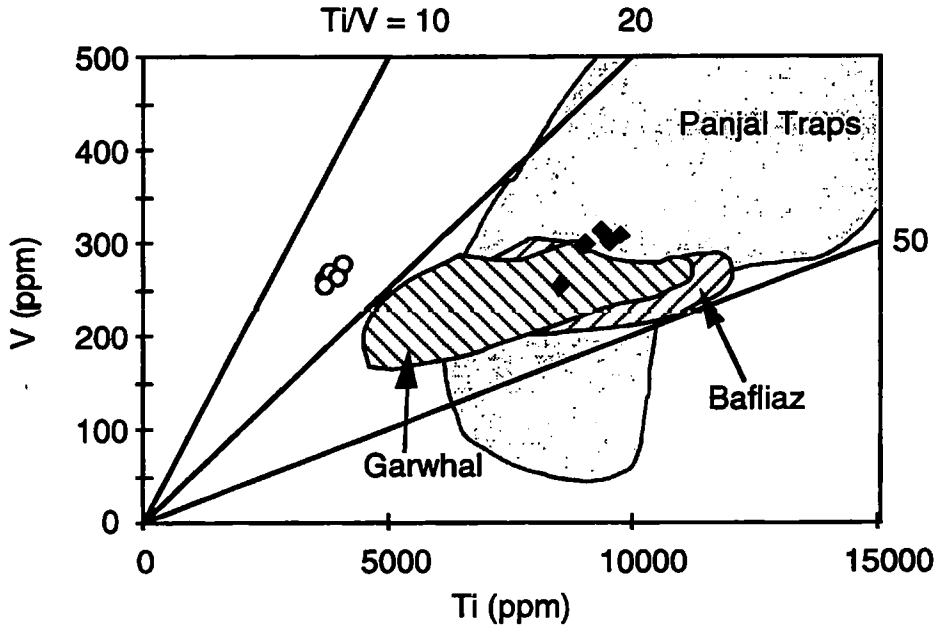

Figure 5.9. V vs. Ti diagram. Symbols as for Fig. 5.2. Fields of the Panjal Traps (dotted line), Bafliaz volcanics (left-slanted hatching) and Garwhal volcanics (right-slanted hatching) are included. Lines of Ti/V = 20 and 50 approximately divide basalts from different tectonic settings (see text for discussion). Data from Table 1. Garwhal and Bafliaz sources listed in caption to Table 2.

On a plot of V against Ti (Fig. 5.9), the amphibolite sheets E104 and E119 are separated by their very different Ti contents. Shervais (1982) used the diagram for tectonic discrimination on the basis of Ti/V ratio. Although there is some overlap between fields, E104 plots in the IAT/CAB field with Ti/V ratios of about 15. E119 is quite distinct, plotting in the MORB/CFB fields with Ti/V ratios of about 32.

On a range of tectonic discrimination diagrams, the Kohistan diorite (E156) is classified as a volcanic arc calc-alkaline rock. The altered sample from the MMT zone (E160), is depleted in Zr but not in Nb, Y, TiO_2 or P_2O_5 with respect to E156. This may reflect its original chemistry or subsequent alteration, but affects its classification relative to E156 only on those diagrams using Zr as a discriminant. E160 consistently plots in IAT/MORB fields.

E119 consistently plots in MORB or WPB fields, compatible with a rift tectonic setting. In contrast, E104 plots in CAB or IAT fields and may be related either to Kohistan or to an earlier event that resulted in an enriched mantle at a destructive plate margin.

5.4.2 Comparison with other basic rocks of the Himalaya

Amphibolitic dykes have been noted in the NPHM previously (Butler and Prior, 1988b; Butler et al., 1992; George, 1993; Treloar et al., 1991; Wheeler et al., 1995; Butler et al., 1997), and their field relations interpreted to indicate a pre-Himalayan intrusion age, although geochronological data are still lacking. In the absence of a reliable isotopic age (section 5.5), in this section I will attempt to correlate the amphibolite dykes of the NPHM with other occurrences of basic igneous activity from elsewhere along the northern edge of the Indian Plate, using

their geochemical signatures. These occurrences are briefly described below, divided for convenience into seven Precambrian and Phanerozoic groups:

(i) Several major occurrences of basic magmatism of Precambrian age have been recognised in the lesser Himalaya (Bhat, 1987). Absolute ages determined through radiometric dating are still lacking for some these, so that whether there were two or more major phases is currently unclear. The Rampur metavolcanics (RV) in the north-west Indian Himalaya have yielded a 2510 Ma Sm-Nd whole-rock isochron (Bhat and Le Fort, 1992), and are the oldest known occurrence in the Himalayan belt. The RV form a series of flows and have been classified as continental tholeiites with a mantle isotopic signature. They display geochemical characteristics typical of assimilation and fractional crystallisation (AFC) processes, but these signatures are attributed instead to source enrichment through a hydrous silicate melt phase contemporaneous with melting (Bhat and Le Fort, 1992).

(ii) The Mandi-Darla Volcanics (MDV), which occur as flows within low-grade metasediments of the lesser Himalayas, are continental tholeiites generated by different extents of isobaric melting of a heterogeneous enriched mantle source (Ahmad and Bhat, 1987). The MDV and RV units, which outcrop in the same vicinity, are thought to be coeval (Bhat and Le Fort, 1992).

(iii) The Garwhal volcanics (GV), widely thought to be mid-Proterozoic, are also tholeiitic, occurring as flows intercalated with psammites and pelites, with associated dyke sheets showing more Fe-enrichment than the flows (Ahmad and Tarney, 1991). Again the rocks are enriched in incompatible elements and LREE relative to primordial mantle, but show a distinct continental signature (Ahmad and Tarney, 1991).

(4) Major occurrences of Palaeozoic mafic volcanics are restricted to the two syntaxial bends in the Himalaya (Bhat et al., 1994). The lower Palaeozoic Bafliaz

volcanics (BV) occur in the Pir Panjal range of the Kashmir Himalaya as a succession of flows showing an overall trend of tholeiitic basal flows to predominantly alkaline uppermost flows, the oldest known alkaline volcanics in the Himalaya (Bhat et al., 1994).

(5) The Baralacha La dyke swarm (BL) in Upper Lahul, have a fairly constant NW-SE orientation, are 1-20m thick, and are frequently injected along synsedimentary transtensional faults of Lower Carboniferous age (Vannay and Spring, 1993). These dykes have been shown to be magmatically unrelated to the nearby Panjal Traps (Vannay and Spring, 1993).

(6) The Kashmir Panjal Traps (PT) cover an area of approximately 12,000 km^2 (Lydekker, 1878, 1883; Wadia, 1961). Volcanic activity began in the Upper Carboniferous but was most prolific during the Mid-Lower Permian, producing voluminous basaltic flows of both tholeiitic and alkaline affinity (Honegger et al., 1982). The geochemistry is indicative of a rift tectonic setting, and the timing coincides with initial phase of break-up of the Indian and Siberian plates (Bhat et al., 1981). Data have been compiled from several studies (Bhat et al., 1981; Honegger et al., 1982; Vannay and Spring, 1993).

The Abor volcanics (AB) in the eastern syntaxial bend of the Himalayan chain have been correlated with the Late Carboniferous-Triassic Panjal Traps (Gansser, 1964), and their geochemistry indicates a within-plate tectonic setting (Bhat and Ahmad, 1990) with transitional tholeiitic to alkalic compositions (Bhat, 1984). They are not considered separately from the Panjal Traps since their geochemistry is very similar, although recent work suggests an Upper Palaeocene to Middle Eocene age for the Abor volcanics on the basis of intercalated fossiliferous sediments (Sengupta et al., 1996). If this interpretation is correct, the Abor volcanics may have been erupted in a foreland basin setting (Sengupta et al.,

1996), and are the only known occurrence of Tertiary basaltic magmatism within the Himalayan region.

(7) Lower Triassic alkaline volcanics have been described from exotic blocks along ophiolitic melange zones of the Peri-Indian suture zone, and intercalated in the Lamayuru unit of Ladakh (Honegger et al., 1982).

All these examples of basic magmatism are considered to be Pre-Himalayan and generated in a rift tectonic setting (Bhat, 1987), with the possible exception of the Abor volcanics, and all share many similarities in their geochemistry. It is to be expected that metabasaltic lithologies from Nanga Parbat will also share many of these characteristics, but it is hoped that sufficient differences will be preserved to narrow the options for correlation with previously documented examples.

Data from each of these occurrences have been plotted on spidergrams and chondrite-normalised REE plots, but little can be deduced from such diagrams. A comparison of trace element concentrations normalised to primitive mantle (Fig. 5.10) reveals that the two most consistent features are low Sr and Nb concentrations, and a gradual decrease in normalised concentration from compatible to incompatible elements. The only significant departures from this trend are in the alkaline Bafliaz volcanics, the Kashmir alkaline volcanics, and the Baralacha La dykes, which do not show depletion in Nb. The Kashmir alkaline volcanics (Honegger et al., 1982) actually have a strong enrichment in Nb, which cannot be explained by alteration since Nb is highly immobile in aqueous fluids. It is concluded that the Nanga Parbat dykes are not related to any of these three suites.

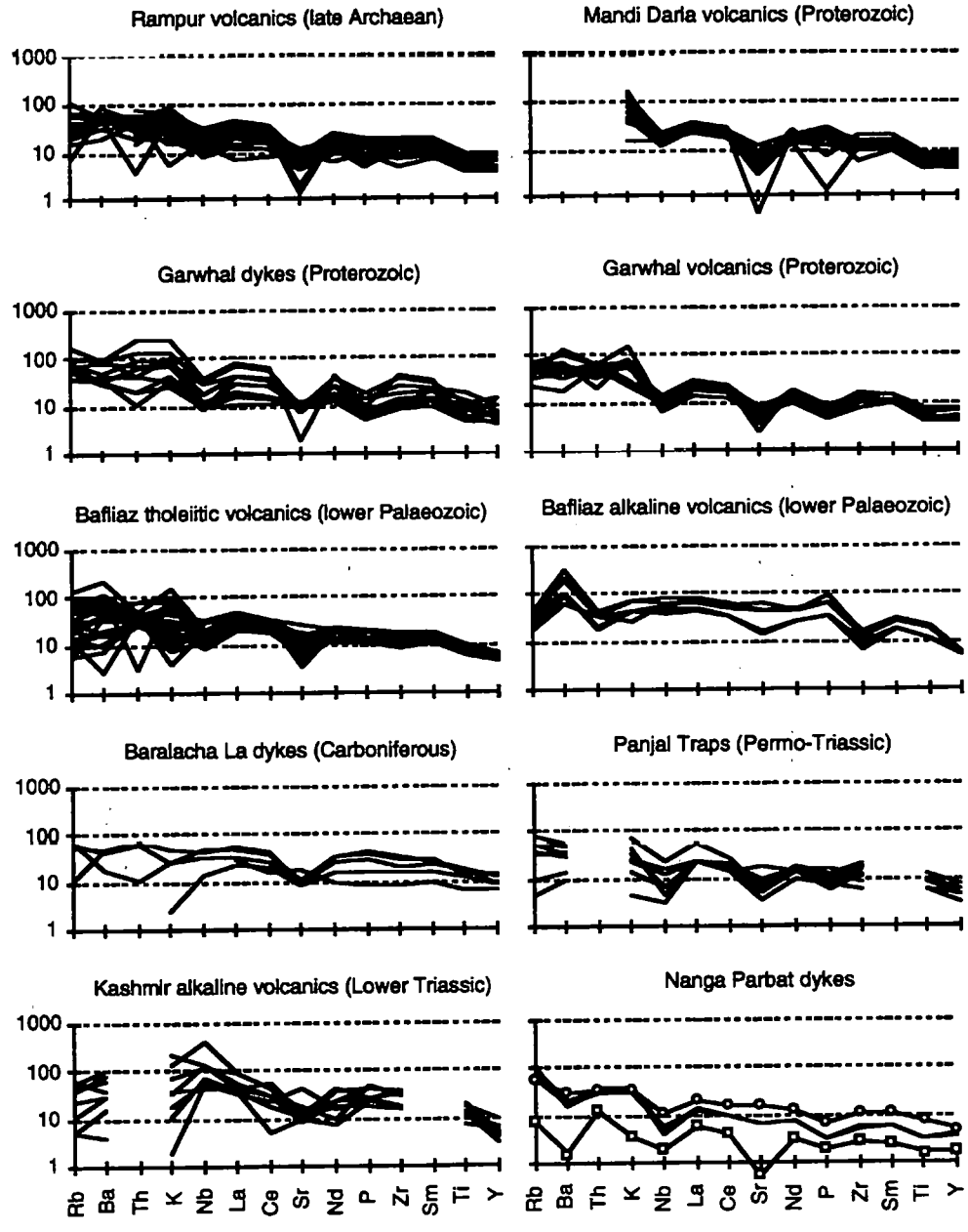

Figure 5.10. Spider diagram of trace element concentrations in a range of pre-Himalayan occurrences of basic magmatism, normalised to the primitive mantle values of Wood et al. (1979). Data sources in Table 2. Nanga Parbat dykes shown for comparison are E104 (no ornament), E119 (open circles) and E155 (open squares).

Table 5.2. Correspondences between Nanga Parbat amphibolite bodies E104 and E119, and other pre-Himalayan occurrences of basic magmatism. Data compiled from: Bhat et al., 1981 (Panjal Traps); Honegger et al., 1982 (Panjal Traps, Kashmir Triassic volcanics); Bhat and Le Fort, 1992 (Rampur); Vannay and Spring, 1993 (Baralacha La, Panjal Traps), Ahmad and Bhat, 1987 (Mandi-Darla); Ahmad and Tarney, 1991 (Garwhal); Bhat, 1984 (Abor).

	V-Ti		Zr/TiO_2-Nb/Y		TiO_2-Zr		TiO_2-Zr-Y	
Rock suite	E104	E119	E104	E119	E104	E119	E104	E119
Panjal Traps (Permo-Triassic)	x	√	√	√	x	√	√	x
Bafliaz (lower Palaeozoic)	x	√	√	√	x	√	√	?
Mandi Darla (Proterozoic)	n/a	n/a	x	√	x	√	?	√
Garwhal (mid-Pz)	x	√	√	√	?	x	√	?
Rampur (Late Archaean)	n/a	n/a	√	√	?	?	√	?

REE patterns are similar for each dataset, with similar normalised $(La/Yb)_N$ ratios of between about 5 and 10. There is some variation in absolute concentrations, but the spread within each dataset is generally greater than the differences between datasets. Further comparisons will therefore be attempted through the use of trace element tectonic discrimination diagrams. Lack of correlation will be used to eliminate potential equivalents, assuming that the discriminant variables used have not been significantly affected by metamorphism. Since all occurrences have been involved to some extent in the Himalayan orogeny, the more mobile elements are unreliable, and only diagrams using the immobile trace elements Ti, V, Nb, Zr and Y will be employed.

On the V-Ti plot, E119 is compatible with the Bafliaz tholeiites, the Garwhal volcanics and the Panjal Traps, while E104 is compatible with none of these. On the Zr/TiO_2 vs. Nb/Y plot, E119 is compatible with all five groups, but E104 is not compatible with Mandi Darla. This leaves Rampur as the only possible correlation with E104. The TiO_2-Zr diagram eliminates Garwhal as an equivalent to E119, while the match with Rampur is poor. The TiO_2-Zr-Y plot further eliminates the Panjal Traps as an equivalent to E119, while matches between E119 and Bafliaz, Garwhal and Rampur are poor. These correlations are summarised in Table 5.2.

5.4.3 Summary

Using various tectonic discrimination diagrams to identify correlations between the Nanga Parbat dykes E104 and E119, and other known occurrences of basaltic rocks in the Himalayan orogen (Table 2), some conclusions can be drawn.

E104 appears to correlate only with the late Archean Rampur metavolcanics using a range of tectonic discriminants. The two suites share similar features such as negative Nb, Ti and P anomalies and low Mg number, but the Rampur metavolcanics are classified as continental tholeiites by Bhat and Le Fort (1992) while E104 is calc-alkaline and appears to be arc-related from tectonic discrimination diagrams. The calc-alkaline classification depends largely on the K_2O content being unaffected by fluids, but combined tholeiitic and calc-alkaline suites are known in the Himalayan region, for example the Bafliaz volcanics and the Panjal Traps.

Both E104 and the Rampur volcanics exhibit negative Eu anomalies and low Sr, suggesting either the presence of plagioclase in the source or plagioclase fractionation. Bhat and Le Fort (1992) attribute the trace element patterns of the

Rampur metavolcanics to source enrichment by a hydrous silicate melt phase penecontemporaneous with melt generation. If E104 was generated at a destructive plate margin, these features may be attributed to the involvement of subducted continental sediments in the melt generation process.

E119 correlates best with the Proterozoic Mandi Darla suite, and does not correspond with either the Panjal Traps or mid-Proterozoic Garwhal volcanic suite. E119 appears to be the product of a continental rifting event. Its high Sr concentrations and lack of Eu anomaly indicate that the source was plagioclase-free, and hence probably located in the mantle.

These correspondences suggest that the two amphibolite sheets E104 and E119 are not related to each other, either temporally or petrogenetically. There have been continental rifting episodes within the Indian Plate from the Archean to the Triassic, and although the preferred correlation for E119 is with a Proterozoic suite, this geochemical correspondence may be coincidental. The northern margin of the Indian Plate has not been a destructive plate margin during at least the last 250 million years, when the Lhasa block rifted away from Gondwana, the separation marked by the Panjal Traps, so that E104 is likely to be considerably older than Mesozoic, and may be as old as Archean if this sheet is related to the Rampur metavolcanics.

Further constraints on the timing of amphibolite emplacement will be investigated through the use of the Rb-Sr and Sm-Nd isotopic systems, discussed in section 5.5.

5.5 Isotope geochemistry

5.5.1 Amphibolite sheets

Isotopic data for the amphibolite sheets is presented in Table 5.3. When the data are plotted on Rb-Sr and Sm-Nd isochron diagrams, the low range of Rb/Sr and Sm/Nd elemental ratios preclude any meaningful age information. Model ages have been calculated for these samples (Table 3), but if the isotope systems have been disturbed they may be misleading. Nd model ages calculated assuming extraction of melts from depleted mantle (DM) give ages of 2.3 to 2.6 Ga for E104. Sr model ages range from 2.0 Ga to 13.9 Ga, the older ages suggesting fractionation of Rb/Sr since formation.

A striking feature is the extremely radiogenic nature of both Rb-Sr and Sm-Nd isotopic systems, with ratios more commonly associated with Precambrian granitoid rocks. There are three possible explanations for this: (i) the amphibolites are Precambrian in age, as suggested by their Nd model ages (Table 3), (ii) both isotope systems have exchanged with fluids of isotopic composition similar to surrounding crustal rocks, (iii) the amphibolite sheets have assimilated a considerable quantity of crustal material. The third explanation is rejected on trace element grounds (section 5.4), and the calculation of erroneously old Sr model ages suggests that some fluid interaction has occurred. If the timing of this isotopic exchange event can be determined, a minimum age constraint can be placed on the timing of dyke emplacement, and hence on the age of migmatitic fabrics in the massif basement.

Table 5.3. Whole-rock isotopic data. Analytical techniques described in Appendix 2.
$^{87}Rb/^{86}Sr$ and $^{147}Sm/^{144}Nd$ determined from elemental ratios.

Sample	Type	Rb	Sr	$^{87}Rb/^{86}Sr$	Sm	Nd	$^{147}Sm/^{144}Nd$	$^{87}Sr/^{86}Sr$	$^{143}Nd/^{144}Nd$	t^{Sr}_{CHUR} (Ma)	t^{Nd}_{CHUR} (Ma)	ε_{Sr}	ε_{Nd}
E156	Kohistan	49.5	392.5	0.3652	3.98	18.2	0.1323	0.705394	0.512639	517	768	10	0.02
E104A	dyke	68.3	160.0	1.2362	2.50	10.3	0.1468	0.749876	0.511907	2723	2351	641	-14.3
E104B	dyke	56.7	154.2	1.0649	2.47	10.3	0.1449	0.751775	0.511887	3298	2334	668	-14.7
E104C	dyke	91.7	157.6	1.6850	2.48	10.2	0.1471	0.750259	0.511893	2003	2387	646	-14.5
E104D	dyke	72.7	160.7	1.3101	2.57	10.9	0.1423	0.752296		2696		675	
E104E	dyke	72.1	158.0	1.3215	2.44	9.7	0.1522	0.750550	0.511874	2580	2595	651	-14.9
E119A	dyke	47.6	381.4	0.3614	4.24	17.5	0.1466	0.757660	0.511979	11332	2203	752	-12.9
E119B	dyke	40.4	391.7	0.2987				0.757680		13916		752	
E119C	dyke	54.6	344.0	0.4597	4.24	17.5	0.1466	0.760182	0.512013	9165		787	-12.2
E119D	dyke	143.0	225.6	1.8357	4.24	17.5	0.1466	0.761970	0.511982	2284		813	-12.8
E119E	dyke	139.9	211.8	1.9129	4.24	17.5	0.1466	0.770687	0.511810	2509		936	-16.2
E155	cumulate	6.8	13.3	1.4807	1.07	4.4	0.1471	0.736207	0.512002	1612	2173	447	-12.4

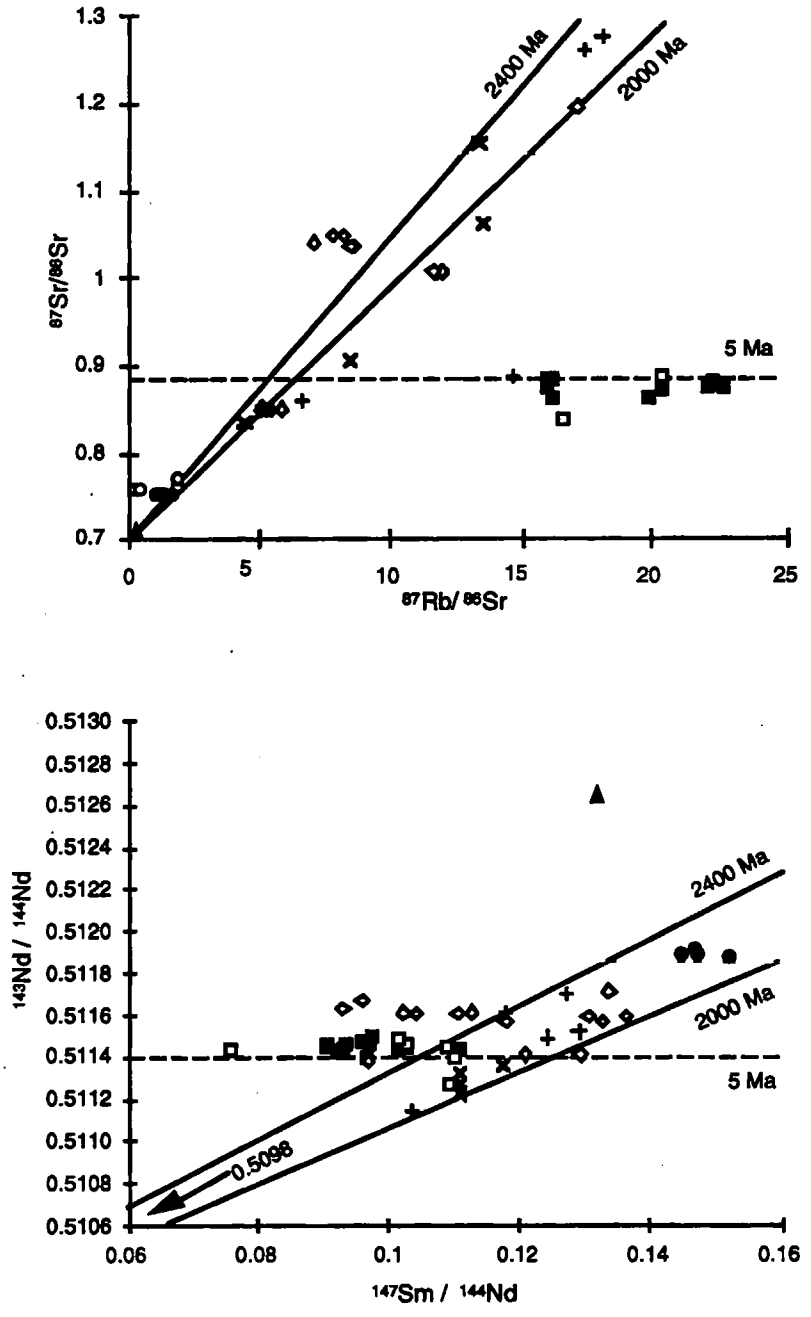

Figure 5.11. Radiogenic isotope diagrams for basement lithologies. Data from Table 5.3 and Appendix 2. Filled circles = E104, open circles = E119, filled triangle = E156. Analytical error smaller than symbol size for Rb-Sr, approximately equal to symbol size for Sm-Nd. a) $^{87}Sr/^{86}Sr$ vs. $^{87}Rb/^{86}Sr$ diagram showing 5 Ma reference line (dashed), and 2000Ma and 2400 Ma isochrons with an ($^{87}Sr/^{86}Sr$) intercept of 0.70000. b) $^{143}Nd/^{144}Nd$ vs. $^{147}Sm/^{144}Nd$ diagram (E104 and E156 only) showing 5 Ma reference line (dashed), and 2000 and 2400 Ma isochrons with a ($^{143}Nd/^{144}Nd$) intercept of 0.50975, the bulk earth ratio at 2250 Ma.

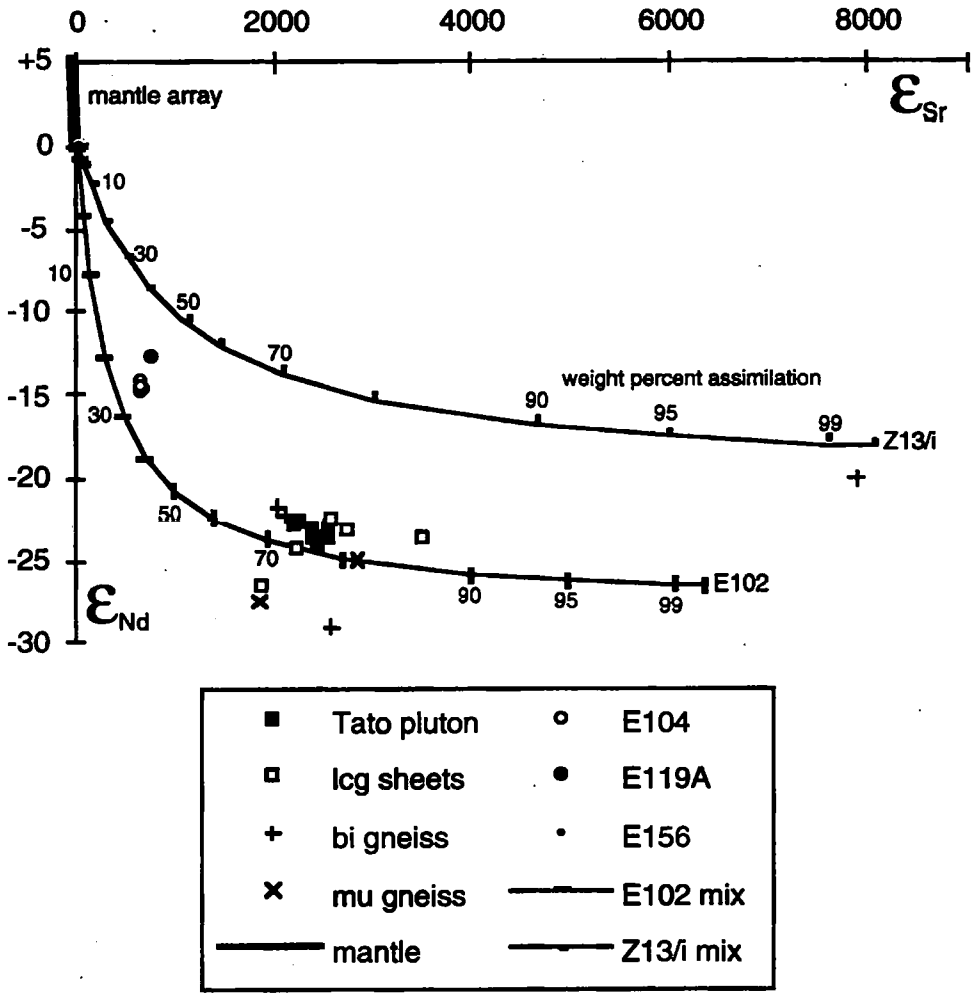

Figure 5.12. Epsilon diagram for basement lithologies. Data from Table 3 and Appendix 2. Symbols as for Fig. 5.11. Mixing line between E119, but assuming mantle $^{87}Sr/^{86}Sr$ and $^{143}Nd/^{144}Nd$ ratios, with pelitic rocks Z13/i and E102. Tick marks are at 1, 5, 10, 20, ...80, 90, 95 and 99 weight percent of mixing with pelitic compositions.

5.5.2 Evidence for basement homogenisation

The next step is to look for evidence of a homogenisation event in the basement, whether due to regional metamorphism or fluid infiltration. When all Rb-Sr and Sm-Nd data for the massif are plotted, there is a striking trend defined by the basement lithologies (Fig. 5.11). While there is considerable spread, particularly in the Sm-Nd data, the trend appears to be significant.

Errorchron calculations yield an age of about 2250 Ma for the Rb-Sr system on basement gneisses from Nanga Parbat. This calculation involved nine samples, including muscovite-bearing lithologies from the Rupal valley, two gneisses hosting cordierite seams from Buldar peak in the Tato valley, and four pelitic lithologies from the Tato Valley. Separate calculations on the four muscovite-bearing samples from the Rupal valley yield an errorchron of 2147 Ma, and calculations on the six samples from the Tato valley yield an errorchron of 2316 Ma. The relative consistency of these calculations on either side of Nanga Parbat, in lithologies which have undergone different degrees of metamorphism with variable fluid influx, suggests that isotopic systems within the basement were reset in the early Proterozoic.

A pre-Himalayan trend has been noted for basement lithologies in the Zanskar region of the main Himalayan orogen (Ayres, 1997), with an errorchron of about 500 Ma. If such whole-rock arrays reflect basement isotopic equilibration, the difference in age for the two regions may reflect differences in structural level exposed in the two areas, or different pre-Himalayan histories.

If the isotopic trend reflects basement homogenisation, were the amphibolites emplaced prior to, or after, this event? The errorchrons have been recalculated incorporating the two amphibolite sheets, E104 from the Rupal valley and E119 from the Tato valley, giving an age of 1990 Ma. Although the amphibolites have very different $^{87}Sr/^{86}Sr$ and $^{87}Rb/^{86}Sr$ ratios to the basement gneisses, they lie very close to the basement trend on the scale of Fig. 5.11. The difference in calculated age is small enough to be consistent with the amphibolites being emplaced prior to basement homogenisation.

There remains the possibility that the basement trend is caused by mixing with an exceptionally high $^{87}Sr/^{86}Sr$ ratio fluid, and the next section models the effects of pervasive fluid infiltration.

5.5.3 Evidence for fluid infiltration

An ε_{Sr} - ε_{Nd} diagram for all lithologies, using ratios calculated for 5 Ma, shows the large displacement of the amphibolite sheets from the Kohistan Arc and the mantle array (Fig. 5.12). Particularly noticeable is the variation in ε_{Sr} in basement rocks compared to the relatively narrow, though extremely low, values of ε_{Nd}. Mixing calculations have been performed using two possible endmember types. Pelitic compositions with extremely high $^{87}Sr/^{86}Sr$ could be responsible for basement homogenisation, while granitic compositions associated with pegmatitic fluids are more likely to be associated with recent fluid activity in the massif, and disturbance of isotope systematics in the amphibolites.

Calculations were performed using combined Nd and Sr data, mixing amphibolite E119, but assuming mantle ratios at 5 Ma, with two typical pelites. A muscovite gneiss from Rupal (E102) and a pelitic rock from Tato (Z13/i) have been chosen since they have extremely high $^{87}Sr/^{86}Sr$ ratios, and hence will represent the minimum amount of crustal contamination or fluid exchange required to shift isotopic ratios in the amphibolites to their current values.

This calculation shows that the isotopic values of the amphibolites could be achieved by assimilation of about 40 weight percent of crustal material with isotopic composition similar to those found in the massif, or by exchange with a fluid in equilibrium with this composition (Fig. 5.12). Similar calculations using the lower Sr and Nd concentrations in E104 show that only about 20 weight percent assimilation or exchange is required. The amount of exchange required is similar for both Nd and Sr, but since Sr is much more soluble in aqueous fluids, the relatively high Nd/Sr of the rocks used for the mixing calculations are unlikely to be achieved in fluids. Hence fluid exchange appears unable to provide the significant change in ε_{Nd} required to explain the low ε_{Nd} values of the amphibolites. Assimilation of an Nd-rich crustal rock, could achieve the required

isotopic shift, but significant crustal assimilation has already been eliminated on trace element grounds.

In order to assess the effect of a fluid associated with magmatic activity, similar calculations were performed with two typical samples from the Tato pluton (Z141 and E5A), and a cordierite seam (Z46C/iv), as mixing endmembers. The amount of Sr and Nd exchange was similar in each case, varying between about 0.2 and 0.8 for both elements. Again, since fluids will usually have much lower Nd/Sr ratios than these endmembers, they will not be able to achieve the required amphibolite compositions.

5.5.4 Discussion

Some disturbance due to fluid action may have occurred in the amphibolites, to explain their homogeneous $^{87}Sr/^{86}Sr$ ratios. The isotopic shifts required to achieve this are relatively small however, and may be explained by preferential leaching of Sr during recent fluid activity, supported by variable Sr concentrations in E119 (Table 5.1). Thermal resetting during recent metamorphism may also have occurred. ε_{Sr} - ε_{Nd} modelling shows that an unusually Nd-rich fluid composition would be required to achieve either basement homogenistion or displacement of the amphibolites to their present $^{87}Sr/^{86}Sr$ and $^{143}Nd/^{144}Nd$ ratios. It is concluded that the amphibolite sheets E104 and E119 were emplaced in the early Proterozoic, possibly during the thermal event that led to partial isotopic homogenisation of the basement.

Further evidence for this is provided by the coincidence between Nd model ages for the amphibolites and the calculated basement errorchron ages. Nd model ages range from 2140 to 2500 Ma, also in agreement with the basement errorchron and reflecting this homogenisation event. Sr model ages are more variable than

Nd, but this is due to recent fluid activity which has resulted in variable Rb/Sr ratios in the amphibolite sheets. The youngest Sr model ages are also in broad agreement with the Nd model ages at about 2.3 Ga (Table 3).

5.6 Conclusions

Metabasaltic dykes in the southern NPHM cross-cut early migmatitic fabrics, and are therefore important time markers for early metamorphism of the massif. In this chapter the geochemistry of three such dykes has been described, and compared with that of nearby Kohistan island arc diorites and other basaltic rocks of the Himalaya.

E104 and E119 are calc-alkaline basalts which show different trace element patterns and tectonic affinities on trace element discrimination diagrams. E119 appears to have been emplaced in a rift tectonic setting, while E104 is generally classified as an island arc rock. Tectonic discrimination diagrams rely on fresh samples however, so that these inferences may be misleading. The Nanga Parbat dykes were therefore compared with other occurrences of basaltic rocks in the Himalayan belt, which will have also been affected by the Himalayan orogeny, though not to the same degree as the Nanga Parbat samples.

Through comparison on a series of trace element diagrams chosen for their use of immobile trace elements, possible correlations with seven sets of Phanerozoic and Proterozoic basic rocks were investigated. E104 appears to correlate only with the 2.5 Ga Rampur metavolcanics, while E119 could be correlated with the Proterozoic Mandi Darla suite, although no actual connection should be inferred. Neither of the Nanga Parbat dykes correlate with the Permo-Triassic Panjal Traps,

which were extruded during the most recent rifting event to affect the northern edge of the Indian Plate.

Isotopic studies reveal an apparent trend in basic lithologies corresponding to a 2.0 to 2.4 Ga errorchron. Metabasalts from Nanga Parbat lie within this trend at extremely high ε_{Sr} and low ε_{Nd} values, with Nd model ages between 2.1 and 2.6 Ga. This observation may be interpreted as due to assimilation of crustal material during magma ascent or emplacement, due to mixing with fluids, possibly associated with recent magmatic activity, or to Proterozoic emplacement ages. Crustal assimilation is ruled out on trace element grounds, and mixing calculations with fluids of Sr and Nd isotopic composition in equilibrium with basement gneisses or leucogranites show that an only an exceptionally Nd-rich fluid would be able to achieve the isotopic values observed in the amphibolites. A fluid would be able to provide the observed Rb-Sr systematics of the sheets, and some evidence for this is provided by their variable Rb/Sr ratios, but a fluid could not achieve the large displacement from mantle values required in both Sr and Nd systems.

The coincidence of basement errorchron trend and Nd model ages of the amphibolites is interpreted to show that the amphibolites were emplaced prior to or during a basement homogenisation event at between 2.0 and 2.5 Ga. This age corresponds with ~2.5 Ga zircon core ages determined the Shengus gneiss (Zeitler et al., 1989), and provides a tentative constraint on the age of early basement migmatisation, which may have been the same event that resulted in isotopic homogenisation of the basement and basalt intrusion. The coincidence in geochemistry between E104 and the Rampur metavolcanics, and the 2.5 Ga age of the Rampur metavolcanics (Bhat and Le Fort, 1992) is interesting but further study of the amphibolites is required before any firmer conclusions can be drawn.

Zircon cores from the Iskere gneiss exposed in the north-western NPHM record younger ages of ~1850 Ma (Zeitler et al., 1989; Zeitler et al., 1993), and the relation between the Iskere and Shengus gneisses is still not clear. The two units appear to have experienced a different pre-Himlayan history, and future work should seek to resolve both the timing and nature of their juxtaposition.

CHAPTER 6 - COOLING HISTORY AND FLUID EVOLUTION DOCUMENTED BY AR-AR LASERPROBE

6.1 Introduction

Isotopes have several uses, depending on their chemical characteristics. Radiogenic isotopes are used primarily in geochronology, while stable isotopes are used as tracers in fluids and magmatic systems. Argon is a mobile element, with both stable and radiogenic isotopes, and so has applications as both a geochronometer and a tracer. This chapter presents an extensive database of argon isotope data from micas across the southern NPHM, with the combined purpose of timing the closure of micas to argon diffusion as they cooled during uplift and exhumation, and investigating fluid movement through the inherited isotopic ratios they exhibit at the time of closure.

6.1.1 Previous work

The NPHM has long been known to record exceptionally young cooling ages from a variety of different systems, from fission tracks in apatite and zircon (Zeitler et al., 1982a; Zeitler, 1985), to ^{40}Ar-^{39}Ar dating of feldspars, micas and amphiboles (Zeitler, 1985; Zeitler et al., 1989; Treloar et al., 1989c; Treloar et al., 1991, Winslow et al., 1994; George et al., 1995; George and Bartlett, 1996; Whittington, 1996; Winslow et al., 1996). These young ages have been interpreted as indicating rapid and relatively recent cooling of the massif due to exhumation (Zeitler et al., 1982a).

Regional cooling ages for the Indian Plate in northern Pakistan are typically in the range 30 to 50 Ma (Maluski and Matte, 1984; Treloar et al., 1989c), with hornblende cooling ages in the Kamila amphibolites of southern Kohistan indicating cooling below 500 °C at about 76 to 80 Ma (Treloar et al., 1989c; Wartho et al., 1996). In contrast, the NPHM records closure of all isotopic systems more recently than 10 Ma, with cooling ages for Kohistan samples decreasing towards the boundary with the NPHM (Zeitler et al., 1985; Treloar et al., 1989c; Zeitler et al., 1989; George et al., 1995). Detailed studies have been conducted along the Indus river gorge (Zeitler et al., 1989; Treloar et al., 1991), and recent studies have investigated cooling ages from the shear zones bordering the western margin of the massif near its northern end (George et al., 1995; George and Bartlett, 1996), at Sassi (Reddy et al., 1997) and in the Liachar Shear Zone (Winslow et al., 1996).

The cooling pattern for the region as a whole is best displayed by contouring the fission track ages of Zeitler et al. (1982b) and Zeitler (1985) (Fig. 1a). This shows that cooling ages are much younger within the NPHM than within the adjacent terranes, and that the sharpest change in cooling ages is found across the western margin of the massif (Fig. 1b; Zeitler, 1985). These findings are supported by other east-west traverses across the massif using the Ar-Ar method (Treloar et al., 1989c; Treloar et al., 1991; George et al., 1995; Winslow et al., 1996).

This study concentrates on the southern part of the NPHM. Previous published data in this area includes the fission track data of Zeitler et al. (1982a, b) and Zeitler (1985), the ^{40}Ar-^{39}Ar data of Zeitler (1985), Treloar et al. (1989c), Zeitler et al. (1989), and Winslow et al. (1996), U-Pb studies on metamorphic monazite by Smith et al. (1992) and Zeitler et al. (1993), and U-Pb studies on zircon from metamorphic and igneous lithologies by Zeitler et al. (1989), Zeitler and Chamberlain (1991), Zeitler et al. (1993) and Winslow et al. (1996).

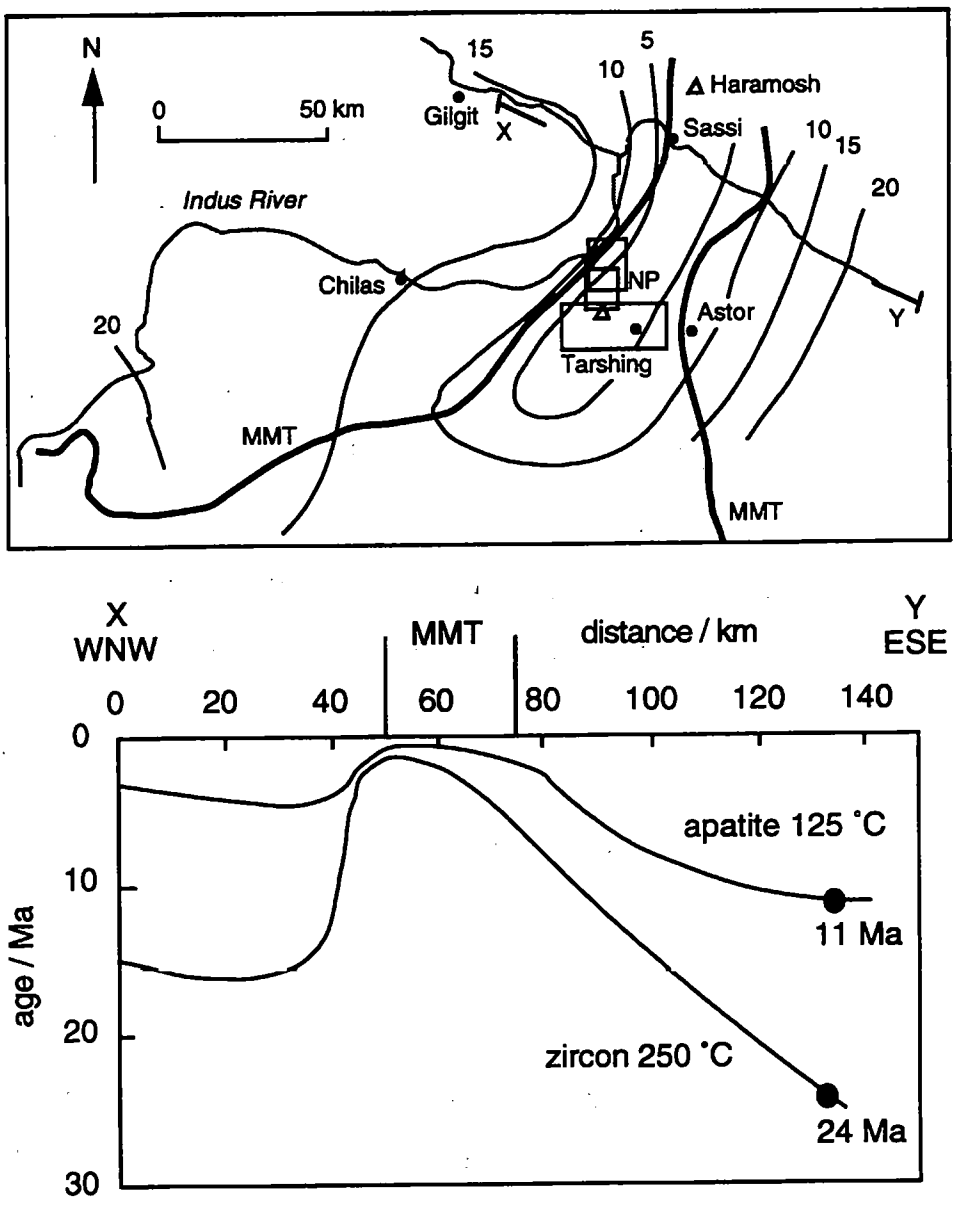

Fig. 6.1. a) Contoured plot of zircon fission track data for the NPHM region. Contours are at 5 Ma intervals. Boxes around Nanga Parbat (NP) indicate detailed maps (Figs. 6.4, 6.6 and 6.9). b) Cross-section X-Y (Fig. 6.1a) along the Indus river through the NPHM with apatite and zircon fission track age profiles. Data from Zeitler et al. (1982) and Zeitler (1985).

6.1.2 Aims of this work

The aims of this work are (i) to investigate the timing relations between leucogranite emplacement and regional-scale cooling of the basement, with particular regard to magmatic fluids as potential sources for excess argon, (ii) to investigate patterns of excess ^{40}Ar within the southern NPHM, and to relate these patterns to fluid activity during recent metamorphism, magmatism and exhumation, and (iii) to add to the existing geochronological database, particularly on the eastern side of the Tato Valley and in the Rupal Valley. Thermal models to account for the ages recorded by these different systems, each of which give time information over a different temperature range, are discussed in Chapter 7.

6.2 The ^{40}Ar-^{39}Ar technique

This section discusses the concepts of closure temperature, the phenomenon of excess argon, and how useful information may be extracted from this normally unwelcome feature. The principles of the ^{40}Ar-^{39}Ar technique are discussed in detail by McDougall and Harrison (1988), but an introduction to the closure temperature concept and excess argon is given below.

6.2.1 Closure Temperature

Many absolute systems of dating geological samples rely on the accumulation of a daughter product from radioactive decay of a parent species, at a known decay rate (usually expressed as a half-life), which is assumed to be constant over time and under different conditions. The age obtained from measurement of parent

and daughter species also assumes (i) once the clock was set, the system remained closed to incorporation or loss of parent and daughter species, and (ii) no initial daughter species were present at the time the clock was set. In many cases, neither of these assumptions is the case, particularly with ^{40}Ar-^{39}Ar dating, and a fair amount of interpretation is required to elucidate useful information from the data. This section discusses the first of these assumptions, and section 6.2.2 will address problems associated with the second.

The closure temperature of a system is defined as the temperature represented by its apparent age (Dodson, 1973), which is slightly higher than the temperature at which loss of the daughter product ceases completely. The closure temperature may be estimated empirically, or calculated using the equation governing closure temperature, obtained by Dodson (1973) assuming volume diffusion during linear cooling:

$$Tc = \frac{E/R}{\ln\left\{\left(ART^2 D_0 / a^2\right) \Big/ E\,dT/dt\right\}} \qquad \text{(equation 6.1)}$$

where E is the activation energy for diffusion, R is the gas constant, A is a geometrical constant, D_0 is the diffusion coefficient, and a is the diffusion distance. E and D_0 may be obtained through experimental work, and data exist for a range of minerals. These data are the subject of much debate, and do not always agree with empirical estimates.

Table 6.1 lists closure temperatures calculated using equation 6.1 (Dodson, 1973) and the experimental diffusion parameters of Harrison et al. (1985) for biotite, and the inferred diffusion parameters of Hamilton et al. (1989) for muscovite. Closure temperatures have been calculated for a range of grain sizes and cooling rates, and the dependence of closure temperature on these factors is quite significant. For

example, calculated muscovite closure temperatures range from about 300 to nearly 450 °C dependent on grain size and cooling rate (Table 6.1). These compare with previous estimates of 350 °C (Purdy and Jäger, 1976), 325 to 270°C depending on cooling rate (Snee et al., 1988), and about 410 °C at a cooling rate of 40°C / Ma in the Alps (Blanckenburg et al., 1989).

Table 6.1. Closure temperatures calculated for different cooling rates and grain sizes using the equation of Dodson (1973) and diffusion parameters of Harrison et al. (1985) for biotite, and Hamilton et al. (1989) for muscovite.

Biotite (Harrison et al. 1985)

Grain radius (μm)	Cooling rate (°C / Ma)	Closure temperature (°C)
250	10	324
250	60	350
250	200	370
125	10	305
125	60	330
125	200	348
62	10	287
62	60	310
62	200	327

Muscovite (Hamilton et al. 1989)

Grain radius (μm)	Cooling rate (°C / Ma)	Closure temperature (°C)
250	10	393
250	60	423
250	200	445
125	10	294
125	60	322
125	200	420

The range in calculated biotite closure temperature using Dodson's equation from slow cooling of small grains (287 °C for 62 μm radius at 10°C / Ma) to rapid cooling of large grains (370 °C for 250 μm radius at 200 °C / Ma) is nearly 100°C. In a recent study of the Larderello geothermal field, Villa and Puxeddu (1994) found argon retention in biotites at temperatures in excess of 450°C, suggesting that laboratory diffusivities may be orders of magnitude too high.

One problem with using Dodson's equation is the estimation of an appropriate diffusion distance. The maximum diffusion distance will be the grain radius, but it is likely to be considerably smaller, particularly in deformed or fractured grains, thereby reducing the actual closure temperature (Harrison and Fitzgerald, 1986; Baldwin et al., 1990). For example, Harrison et al. (1985) and Wright et al. (1991) found that the maximum diffusion distances in single biotite grains from different areas were approximately 150μm and 225 μm respectively. Another factor is cooling rate, which is in turn usually derived from the calculated closure temperature and age (Chapter 7). Since cooling rates at Nanga Parbat are known to be unusually high, calculated closure temperatures are also higher than normally quoted. A further issue is the effect of composition, within individual mineral groups, on diffusion parameters (Dahl, 1996). This potential problem is not considered in this study, since Blanckenburg et al. (1989) found identical cooling ages from biotites from the same locality with annite contents ranging from 33 to 56%, and Gnos (1992) found similar ages for phlogopites and fresh Fe-rich biotites (annite content 50 to 60%), although some Fe-rich biotites in this study were found to give erroneous ages due to alteration.

The application of the closure temperature concept to cooling history is only valid where isotope mobility is determined by volume diffusion, which is not always the case. In zones of deformation, a recrystallisation age may be obtained (e.g. Reddy et al., 1997). Such zones may also be affected by excess argon, since they act as pathways for metamorphic fluids. Fractures and defects within grains may

also allow a faster argon transport mechanism than volume diffusion (Lee, 1993, 1995).

In a study of the Remendok leucotrondjhemite, which cross-cuts the Indus-Tsangpo Suture Zone at the north-eastern margin of the NPHM, Villa et al. (1996) found a 1 Ma difference in argon ages of muscovite grains from nearby samples of the same pluton. This variation was explained in terms of microstructure, since battered grains will have lower retentivity and closure temperature, and may exchange with ambient argon down to lower temperatures.

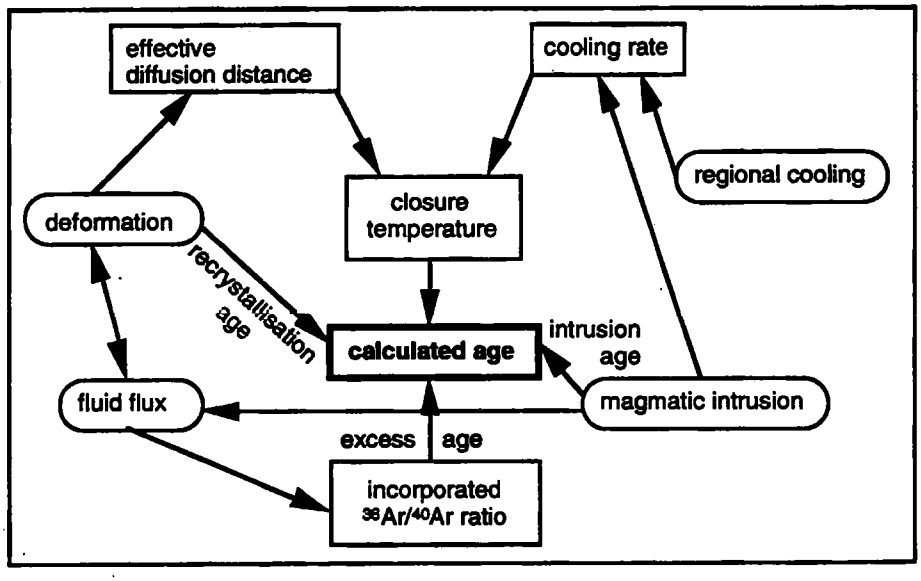

Fig. 6.2. Schematic diagram showing the processes (rounded boxes) affecting the calculated age and parameters required for closure temperature calculation (square boxes).

In igneous provinces, ages may record the age of contact metamorphism, rather than regional cooling. For any igneous body, rapid cooling following emplacement may result in a crystallisation age, but nearby country rocks may be wholly or partially reset (Hanson and Gast, 1967; Hanson et al., 1975), in which

case the age will need particularly careful interpretation since diffusion below the calculated closure temperature may be significant (Reddy et al., 1996).

The relations between calculated age, closure temperature, and a variety of other factors are summarised in Fig. 6.2. This is intended as an indication of the complexity of geochronological systems rather than a comprehensive guide. Interpretations must be made as to whether the calculated age is affected by excess argon, and whether it represents crystallisation, recrystallisation or closure to volume diffusion during cooling. Calculated closure temperatures based on experimental data are probably the best indicators of true closure temperatures, but should be assigned reasonable errors. Since cooling rates at Nanga Parbat are high, estimated closure temperatures using Dodson's equations are also high.

6.2.2 Correlation diagrams and excess argon

The incorporation of daughter species at the time of closure is overcome by measuring several samples with different parent/daughter ratios, for example in an Rb-Sr isochron plot where the parent (^{87}Rb) and daughter (^{87}Sr) are both ratioed to a non-radiogenic isotope (^{86}Sr). By choosing samples, or preferably mineral separates from the same sample, with different Rb/Sr ratios, a sufficient range in ($^{87}Rb/^{86}Sr$) should be achieved to tightly constrain the slope of the line, and hence the age.

In the case of ^{40}Ar-^{39}Ar geochronology, the decay scheme being measured is the decay of ^{40}K to ^{40}Ar, with the non-radiogenic isotope ^{36}Ar used for argon correlation diagrams (Turner, 1971; Roddick, 1978; Roddick et al., 1980; Heizler and Harrison, 1988), which are the equivalent of the isochron plot for the Rb-Sr system. The technique relies on all the measured ^{40}Ar in the sample being composed of a radiogenic component (abbreviated to $^{40}Ar^*$) which has

accumulated since the time of closure, and an initial component which is assumed to have the same composition as today's atmosphere. On a correlation diagram, of $^{36}Ar/^{40}Ar$ vs. $^{39}Ar/^{40}Ar$, the $^{36}Ar/^{40}Ar$ intercept is assumed to be 0.003384, the present-day atmospheric value.

The slope of the line through this intercept and the analysed data points gives the age, which is determined by the $^{39}Ar/^{40}Ar$ intercept ratio. Incorporation of "excess argon", i.e. any ^{40}Ar other than that which has accumulated since closure, will lead to an older calculated age because it will lower the analysed $^{36}Ar/^{40}Ar$ and $^{39}Ar/^{40}Ar$ ratios (Fig. 6.3). Hence the youngest cooling age calculated for a sample assuming an atmospheric ($^{36}Ar/^{40}Ar$) ratio will only be a maximum estimate of the true cooling age if it has been affected by excess argon. Ages from samples affected by excess argon will never give underestimates of the true age unless radiogenic argon has subsequently been lost. Since ages at Nanga Parbat are very young, even with incorporation of excess argon, the resulting uncertainty is small, although it should be noted that atmospheric intercepts have been obtained from biotites containing unambiguous excess argon (Foland, 1983).

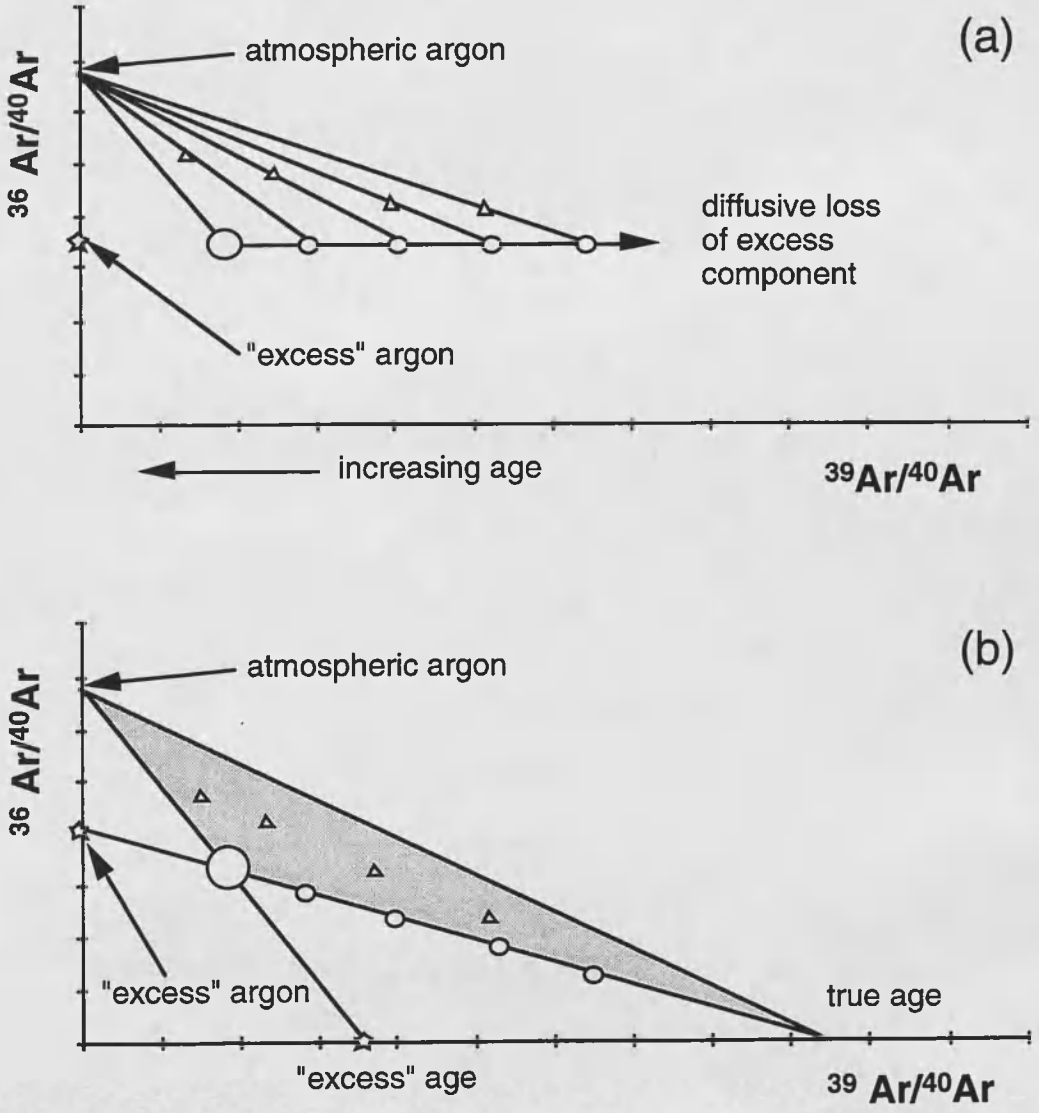

Fig. 6.3. Excess argon plots after Roddick, 1978. a) Situation at time of closure (t_c). Large open circle is the initial composition of a grain, with small circles indicating the effect of diffusive loss of the excess component (star) if argon partial pressure decreases prior to closure. Small triangles indicate the effect of mixing with an atmospheric component. b) Situation at time of analysis. The data now occupy a triangular field (shaded) bounded by lines joining the atmospheric intercept and the "true" $^{39}Ar/^{40}Ar$ ratio, the excess intercept and the "true" $^{39}Ar/^{40}Ar$ ratio, and the atmospheric intercept and the excess $^{39}Ar/^{40}Ar$ ratio. The analysed points (small triangles) may now define a spurious trend giving a false old age (Arnaud and Kelley, 1995).

Some samples display complicated patterns, because samples resulting from a variable mixture of radiogenic and excess argon will lie within an envelope defined by the true age, the atmospheric intercept and the excess intercept (shaded field on Fig. 6.3b). Arnaud and Kelley (1995) showed that spurious linear trends will be produced as this envelope becomes tighter over time, all leading to a considerable overestimate of the true age of the sample. For samples less than 10 Ma this effect will be minor because there has been little time for the envelope to tighten up, although the error may be significant as a fraction of the calculated age. Arnaud and Kelley (1995) also showed that stepped heating can lead to anomalous results if the first few steps are used.

On correlation diagrams presented here (Figs. 6.5, 6.7, 6.8 and 6.10), a line has been drawn through the analysis giving the youngest age, and joined with an atmospheric intercept, since this is the standard interpretation of such diagrams. In cases where an excess argon component is detected, a line with a lower ($^{36}Ar/^{40}Ar$) intercept is also shown for reference. Error bars are omitted for clarity, and discussion of errors is included in the results section.

6.3 Sample description and results

Data from all three irradiation batches is shown in Table 6.2. The samples are divided into three groups based on location and metamorphic grade: muscovite-bearing schists from the Rupal Valley, biotite gneisses from the interior of the massif south of Tato, and samples from the Liachar Shear Zone.

Table 6.2. Argon data. Analytical techniques are detailed in Appendix 1.

Sample	Grain size	40/39	38/39	37/39 (1)	36/39 (2)	39Ar (3)	40*/39	Age (Ma)	error (4)
Rupal valley samples (Fig. 6.5)									
E101 bi	250-425	1.11	0.0346	0	0.919	108.84	0.998	5.73	0.17
E101 bi	250-425	1.19	0.0325	0.09	1.106	99.42	1.056	6.06	0.28
E101 bi	425-500	1.18	0.0358	3.44	1.06	217.05	1.05	6.03	0.19
E101 bi	425-500	1.1	0.0352	-0.21	0.809	160.66	0.999	5.74	0.12
E101 bi	425-500	1.46	0.0366	3.02	0	35.1	1.455	8.35	0.47
E101 mu	250-425	2.27	0.0166	3.03	8.302	198.74	1.241	7.12	0.19
E101 mu	425-500	1.91	0.0129	0.49	1.579	120.31	1.714	9.83	0.23
E101 mu	425-500	1.76	0.0131	-0.11	1.778	151.86	1.534	8.8	0.19
E101 mu	425-500	1.94	0.0134	0.16	0.382	52.31	1.89	10.83	0.42
E101 mu	500-2000	1.41	0.013	1.63	0.973	1058.55	1.289	7.39	0.15
E101 mu	500-2000	1.47	0.0143	0.83	2.096	491.38	1.212	6.96	0.13
E101 mu	500-2000	1.53	0.0132	0.49	1.962	601.53	1.288	7.39	0.15
E101 mu	500-2000	1.15	0.0129	1.17	0.738	108.38	1.057	6.07	0.2
E101 mu	500-2000	1.65	0.014	1.08	2.326	657.76	1.363	7.82	0.14
E101 mu	500-2000	1.24	0.0196	0.29	0.366	245.98	1.198	6.88	0.19
E102 bi	250-425	0.99	0.0192	5.3	4.215	132.86	0.461	2.65	0.27
E102 bi	250-425	0.44	0.0196	2.09	2.817	28.4	0.086	0.5	1.26
E102 bi	425-500	0.44	0.0182	-0.9	0	9.4	0.444	2.55	1.69
E102 mu	250-425	0.74	0.0125	0	2.398	187.66	0.438	2.52	0.21
E102 mu	250-425	0.44	0.0122	1.86	0.862	139.21	0.33	1.89	0.19
E103 bi	425-500	0.53	0.0241	0.73	0.612	555.35	0.453	2.6	0.05
E103 bi	425-500	0.52	0.0255	0.22	0.739	284.21	0.432	2.48	0.07
E103 bi	425-500	0.37	0.0259	0.08	0.093	107.32	0.354	2.03	0.15
E103 mu	250-425	0.67	0.0128	-0.12	1.255	71.72	0.517	2.97	0.42
E103 mu	250-425	0.89	0.0133	1.83	4.413	224.32	0.337	1.94	0.11
E103 mu	250-425	1.52	0.0139	2.32	6.467	120.62	0.716	4.11	0.25
E103 mu	250-425	0.51	0.0129	-0.54	-3.18	31.45	0.905	5.19	0.72
E103 mu	425-500	1.08	0.0133	-0.17	2.653	150.75	0.754	4.33	0.19
E103 mu	425-500	0.8	0.0125	0.05	1.561	320.24	0.602	3.46	0.1
E103 mu	425-500	0.62	0.0128	-0.23	0.452	221.21	0.56	3.22	0.13
E103 mu	425-500	0.65	0.0129	0.07	1.2	291.69	0.503	2.89	0.12
E106 bi	425-500	0.95	0.0264	0.15	1.519	223.78	0.76	4.36	0.13
E106 bi	425-500	0.83	0.0262	-0.19	1.067	206.21	0.693	3.98	0.09
E106 bi	425-500	0.84	0.0265	-0.09	1.256	230.83	0.684	3.93	0.1
E106 bi	425-500	0.64	0.0258	1.38	0.38	184.23	0.593	3.4	0.09
E106 bi	425-500	0.52	0.0246	-0.11	-0.522	38.3	0.587	3.37	0.27
E106 mu	250-425	1.05	0.0131	0.17	3.465	334.75	0.617	3.55	0.16
E106 mu	250-425	0.58	0.0117	1.06	1.861	333.16	0.345	1.98	0.09
E106 mu	250-425	0.39	0.012	1.45	0.587	204.37	0.312	1.79	0.13
E106 mu	425-500	0.88	0.0127	0.14	1.389	237.53	0.71	4.08	0.14
E106 mu	425-500	1.82	0.0133	0.1	5.729	251.37	1.109	6.37	0.19
E106 mu	425-500	0.76	0.0127	1.26	1.45	255.12	0.581	3.34	0.09
E106 mu	425-500	0.97	0.0129	0.14	1.514	997.38	0.784	4.5	0.07
E106 mu	500-2000	1.16	0.0129	0.09	2.35	434	0.873	5.01	0.1
E106 mu	500-2000	0.63	0.0129	-0.07	0.163	306.57	0.609	3.5	0.08
E106 mu	500-2000	0.68	0.0128	-0.94	-0.498	180.82	0.74	4.25	0.2

Sample	Grain size	40/39	38/39	37/39 (1)	36/39 (2)	39Ar (3)	40*/39	Age (Ma)	error (4)
E106 mu	500-2000	0.59	0.0125	0.03	-0.041	246.36	0.594	3.41	0.1
E106 mu	500-2000	0.75	0.0128	0.62	0.991	645.87	0.631	3.63	0.07
E106 mu	500-2000	0.54	0.0122	0.43	-1.182	126.9	0.691	3.97	0.21
E106 mu	500-2000	1.05	0.013	0.13	2.744	1155.41	0.708	4.07	0.07
E106 mu	500-2000	0.64	0.0127	-0.25	0.432	439.79	0.581	3.34	0.07
E106 mu	500-2000	0.58	0.0127	6.13	0.34	117.62	0.54	3.1	0.22
E107 mu	250-425	0.91	0.0127	1.02	5.007	149.78	0.289	1.66	0.26
E107 mu	250-425	1.39	0.013	35.12	6.835	84.85	0.545	3.13	0.61
E107 mu	250-425	0.36	0.0128	1.4	1.122	285.1	0.224	1.29	0.14
E107 mu	425-500	0.92	0.0129	-0.01	3.859	404.2	0.439	2.52	0.06
E107 mu	425-500	0.75	0.0129	0.79	2.752	334.26	0.407	2.34	0.11
E107 mu	425-500	0.32	0.0122	0.06	0.793	227.04	0.217	1.25	0.05
E107 mu	425-500	0.23	0.0122	2.52	0.182	164.83	0.205	1.18	0.06
Tato pluton samples (Fig. 6.7)									
E5A mu	250-425	2.47	0.0139	0.18	14.584	171.42	0.657	0.5	0.07
E5B bi	425-500	1.41	0.0037	-0.88	0.04	141.74	1.404	1.06	0.11
E5B bi	250-425	4.34	0.0159	1.71	19.24	34.3	1.954	1.48	0.2
E5B bi	125-250	1.3	0.004	-0.77	1.786	81.57	1.078	0.82	0.17
E5B mu	125-250	0.54	0.0023	-1.19	4.67	39.76	-0.035	-0.03	0.29
E63 bi	500-2000	2.5	0.0017	-0.39	0.777	110.26	2.402	1.82	0.1
E63 bi	425-500	2.18	0.0035	-0.75	0.763	125.44	2.089	1.58	0.14
E63 bi	425-500	1.95	0.0046	-0.87	1.503	130.2	1.759	1.33	0.28
E63 bi	425-500	2.4	0.0022	-0.64	2.06	56.14	2.142	1.62	0.19
E63 bi	500-2000	2.49	0.0024	-1.97	2.134	49.51	2.228	1.69	0.21
E63 bi	425-500	6.7	0.0168	-2.79	36.733	18.24	2.14	1.62	0.29
E63 bi	425-500	2.87	0.012	-2.36	6.028	29.86	2.125	1.61	0.34
E64 bi	250-425	5.19	0.0198	-1.27	6.581	64.67	4.374	3.31	0.19
E64 mu	250-425	1.44	0.0016	0.33	2.699	68.8	1.105	0.84	0.15
E64 mu	425-500	1.15	0.0031	-0.86	-0.112	127.75	1.161	0.88	0.12
E70B bi	425-500	2.58	0.0005	-2.99	-0.727	19.7	2.673	2.02	0.54
E70B bi	250-425	5.94	0.0136	0	15.97	23.17	3.954	2.99	0.39
E70C bi	250-425	5.01	0.005	3.22	3.212	113.84	4.61	3.49	0.11
E70C bi	425-500	5.32	0.0036	-0.82	2.641	62.74	4.991	3.78	0.19
Fairy Meadow samples (Fig. 6.8)									
N1 bi	425-500	5.85	0.1008	-22.49	48.205	6.76	-0.131	-0.1	3.55
E4 bi	425-500	2.19	0.0018	-1.51	1.339	41.58	2.027	1.54	0.26
T14 bi	250-425	39.27	0.0937	45.99	227.542	22.5	25.825	2.33	0.12
T14 mu	250-425	28.98	0.0755	35.32	161.515	36.88	19.434	1.75	0.11
T15 bi	250-425	43.32	0.0543	9.94	147.549	10.72	34.597	3.12	0.1
T15 bi	125-250	34.39	0.2456	189.06	-126.74	1.76	41.885	3.77	0.7
T15 bi	125-250	37.04	0.1334	103.12	93.706	5.67	31.505	2.84	0.27
T15 mu	250-425	32.65	0.0589	22.32	188.492	35.95	21.508	1.94	0.06
T25 bi	250-425	43.02	0.1221	58.26	279.152	13.53	26.518	2.39	0.17
T25 mu	250-425	105.39	0.1898	9.11	1414.28	1.59	21.81	1.97	0.42

Sample	Grain size	40/39	38/39	37/39 (1)	36/39 (2)	39Ar (3)	40*/39	Age (Ma)	error (4)
T25 mu	250-425	25.67	0.0865	57.99	63.31	25.56	21.925	1.98	0.1
E47 bi	425-500	4.97	0.0146	-2.6	1.579	47.92	4.773	3.61	0.43
E72 bi	425-500	9.41	0.0153	-1.32	22.298	29.6	6.64	5.02	0.21
E75 bi	425-500	12.13	0.0035	-1.3	4.377	72.12	11.586	8.76	0.16
E122 bi	425-500	0.25	0.0173	0.77	0.602	132.87	0.17	0.98	0.19
E122 bi	425-500	0.2	0.0163	-0.36	0.095	211.19	0.186	1.07	0.08
E122 bi	425-500	0.2	0.0169	-0.1	0.147	204.03	0.177	1.02	0.1
E125 bi	425-500	0.55	0.0497	0.05	2.552	180.23	0.228	1.31	0.2
E125 bi	425-500	0.8	0.0496	-0.37	2.902	182.61	0.438	2.52	0.25
E125 bi	425-500	0.53	0.0482	0.61	1.346	594.49	0.361	2.07	0.09
E125 bi	425-500	0.54	0.0529	-0.15	1.456	329.57	0.364	2.09	0.11
E125 bi	425-500	0.65	0.0508	-0.42	1.905	283.43	0.412	2.37	0.14
E125 bi	500-2000	0.49	0.0491	-0.08	1.044	679.9	0.361	2.08	0.1
E125 bi	500-2000	0.29	0.0538	-0.29	-0.313	191.48	0.326	1.87	0.11
E125 bi	500-2000	0.44	0.0526	0.52	0.992	332.57	0.314	1.81	0.06
E125 bi	500-2000	0.32	0.0547	0.69	0.543	73.68	0.254	1.46	0.28
E125 bi	500-2000	0.8	0.0557	-0.1	2.017	352.01	0.551	3.16	0.09
E125 bi	500-2000	0.94	0.0564	-0.17	2.468	194.49	0.631	3.62	0.16
E125 bi	500-2000	1.04	0.053	0	3.524	337.68	0.604	3.47	0.11
E125 bi	500-2000	0.66	0.055	0.12	0.99	141.35	0.538	3.09	0.13
E125 bi	500-2000	0.54	0.0532	-0.16	1.467	517.97	0.353	2.03	0.07
E125 bi	500-2000	0.65	0.0534	0.02	2.338	560.36	0.362	2.08	0.08
E125 bi	500-2000	0.47	0.0509	-0.13	1.213	956.31	0.318	1.83	0.04
E125 bi	500-2000	1.37	0.0527	-0.36	6.061	305.22	0.613	3.52	0.15
E125 bi	500-2000	0.66	0.0511	0.2	2.433	653.55	0.358	2.06	0.1
E125 bi	500-2000	0.35	0.0497	0.95	1.277	31.33	0.187	1.08	0.82
E125 bi	500-2000	0.77	0.0525	-0.03	2.628	258.78	0.447	2.57	0.15
E125 bi	500-2000	0.67	0.052	1.82	2.251	319.9	0.392	2.25	0.12
E125 bi	500-2000	0.34	0.0527	0.17	0.702	128.24	0.252	1.45	0.24
E125 bi	500-2000	0.39	0.0526	1.48	0.469	149.13	0.331	1.9	0.18
E127 bi	250-425	2.33	0.0325	27.31	11.531	65.04	0.898	5.16	0.65
E127 bi	425-500	4.12	0.0184	20.77	12.2	148.36	2.609	14.94	0.51
E129 bi	425-500	1.93	0.0383	1.86	3.316	241.26	1.52	8.72	0.19
E129 bi	425-500	0.52	0.0406	3.57	0.316	190.01	0.483	2.77	0.14
E129 bi	425-500	0.45	0.0403	0.17	0.301	365.66	0.412	2.37	0.09
E129 bi	425-500	0.56	0.0409	-0.22	0.788	355.21	0.462	2.65	0.09
E129 bi	425-500	0.45	0.0419	0.98	0.7	199.98	0.365	2.1	0.13
E132 bi	425-500	8.6	0.0472	-0.39	1.84	21.74	8.366	47.47	0.72
E132 bi	425-500	8	0.0614	0.43	1.764	107.72	7.779	44.18	0.72
E132 bi	425-500	41.48	0.049	2.62	2.744	14.58	41.136	222.25	3.52
E132 bi	425-500	8.11	0.0581	0.07	0.971	61.82	7.984	45.33	0.75
E132 bi	425-500	16.08	0.0585	1.86	1.619	43.23	15.88	89.07	1.33
E132 bi	425-500	7.54	0.056	1.08	-0.509	19.63	7.6	43.18	0.98
E132 bi	425-500	7.81	0.0628	7.16	2.111	85.26	7.551	42.9	0.39
E138 bi	425-500	0.55	0.0359	3.02	0.422	165.88	0.494	2.84	0.16
E138 bi	425-500	0.76	0.0369	1.5	0.919	282.77	0.641	3.68	0.1
E138 bi	425-500	0.9	0.0278	0.89	1.024	224.69	0.772	4.43	0.1
E138 bi	425-500	0.9	0.0356	7.08	0.566	105.98	0.831	4.77	0.25

Sample	Grain size	40/39	38/39	37/39 (1)	36/39 (2)	39Ar (3)	40*/39	Age (Ma)	error (4)
E139 bi	425-500	3.27	0.0353	4.74	14.751	19.66	1.435	8.23	1.31
E139 bi	425-500	2.57	0.0352	2.34	13.512	32.56	0.893	5.13	1.18
E139 bi	425-500	0.85	0.032	1.17	2.328	94.5	0.562	3.23	0.28
E139 bi	425-500	1.46	0.0351	1.54	7.073	302.55	0.577	3.32	0.15
E139 bi	425-500	0.36	0.0349	2.36	-0.265	37.79	0.391	2.25	0.68
E145 bi	250-425	0.39	0.0519	1.17	0	68.6	0.391	2.25	0.46
E145 bi	250-425	0.47	0.046	1.35	0	44.02	0.469	2.69	0.46
E145 bi	425-500	0.43	0.0499	0.12	1.004	477.95	0.305	1.75	0.05
E145 bi	425-500	0.46	0.0485	0.21	0.866	323.19	0.355	2.04	0.07
E145 bi	425-500	0.3	0.0506	1.55	0.516	232.37	0.24	1.38	0.07
E145 bi	425-500	0.37	0.0494	0.45	0.602	66.43	0.294	1.69	0.24
Liachar Shear Zone samples (Fig. 6.10)									
L2 bi	250-425	26.29	0.0501	21.4	162.396	28.23	16.691	1.5	0.04
L2 mu	250-425	50.77	0.1669	99.75	279.669	3.99	34.238	3.09	0.29
E22 bi	250-425	1.39	0.0059	-0.77	3.658	116.35	0.936	0.71	0.12
E22 bi	425-500	5.37	0.0164	1.06	36.609	40.7	0.825	0.62	0.16
E22 bi	500-2000	8.81	0.0169	-0.8	48.871	83.08	2.745	2.08	0.1
E27 bi	425-500	2.64	0.0019	-0.28	2.34	113.53	2.349	1.78	0.1
E27 mu	425-500	1.48	0.0045	-4.23	6.114	22.19	0.716	0.54	0.49
E27 mu	425-500	5.96	0.0154	-0.04	38.785	103.13	1.149	0.87	0.04
E28 bi	425-500	7.41	0.0141	-0.15	17.967	52.88	5.18	3.92	0.13
E28 bi	425-500	6.01	0.0015	-0.7	3.653	56.3	5.558	4.21	0.19
E28 bi	425-500	3.66	0.0132	-0.81	9.999	34	2.421	1.83	0.12
E33 bi	250-425	12.45	0.0156	-1.15	19.092	40.86	10.083	7.62	0.15
E82 bi	425-500	32.13	0.1116	-3.7	138.017	12.68	14.998	11.33	0.75
E82 mu	425-500	12.37	0.0139	-4.57	3.901	10.25	11.886	8.98	0.47
E83 bi	425-500	7.7	0.0015	0.22	4.89	31.83	7.094	5.37	0.36
E154 bi	425-500	0.7	0.028	4.95	0.743	134.55	0.604	3.47	0.12
E154 bi	425-500	0.57	0.0286	3.85	0.051	195.09	0.563	3.23	0.12
E154 bi	425-500	0.73	0.0289	9.47	0	54.62	0.732	4.2	0.3
E156 bi	250-425	0.52	0.0466	-0.25	0.697	200.76	0.434	2.49	0.13
E156 bi	425-500	7.1	0.0507	-18.6	-21.941	2.28	9.818	55.58	4.37
E157 mu	250-425	2.32	0.0158	0.86	0.758	118.67	2.222	12.73	0.23
E157 mu	250-425	2.26	0.0149	0.51	1.491	67.09	2.078	11.91	0.31

(1) to get 37/39 ratio, divide the number shown by 1000
(2) to get 36/39 ratio, divide the number shown by 1,000,000
(3) x10-12 cc STP
(4) 1 sigma error

6.3.1 Rupal Valley

The Rupal valley provides an east-west cross-section through the massif, and one aim of this sampling was to compare the age pattern in this transect with published ages from the Indus Valley (Zeitler, 1985; Zeitler et al., 1989; Treloar et al., 1989c; George et al., 1995). Outcrop is restricted to the sides of the valley, and dated samples were collected from 4 locations between the village of Nahake in the east, and Mazeno base camp in the west (Fig. 6.4). Biotite and muscovite are both stable fabric-forming minerals in the schists, and so provide an opportunity to check on the reliability of biotite ages which may reflect excess argon in other parts of the massif.

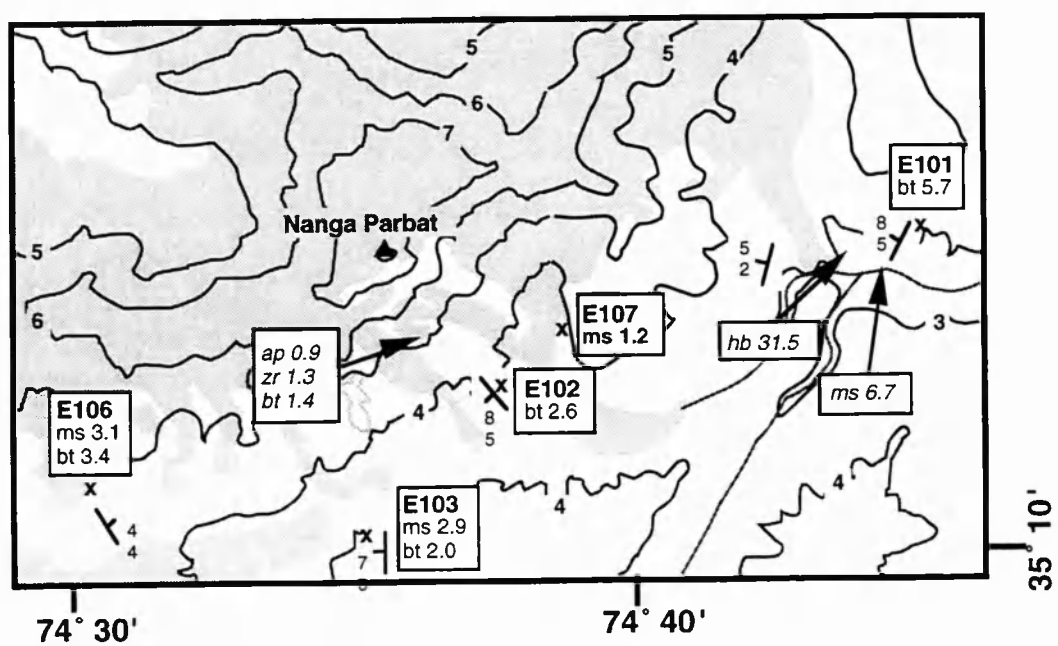

Fig. 6.4. Sample location map for the Rupal valley. Age data (in Ma) from this study (Table 6.2) shown as plain text, except for igneous samples in bold type, are best estimates as discussed in section 6.3; data from previous studies shown in italics, ap = apatite fission track, zr = zircon fission track, ksp = Ar-Ar on K-feldspar, bt = Ar-Ar on biotite, ms = Ar-Ar on muscovite, mon = U-Pb on monazite. Underlined samples are K-Ar ages. Shaded areas are glaciers.

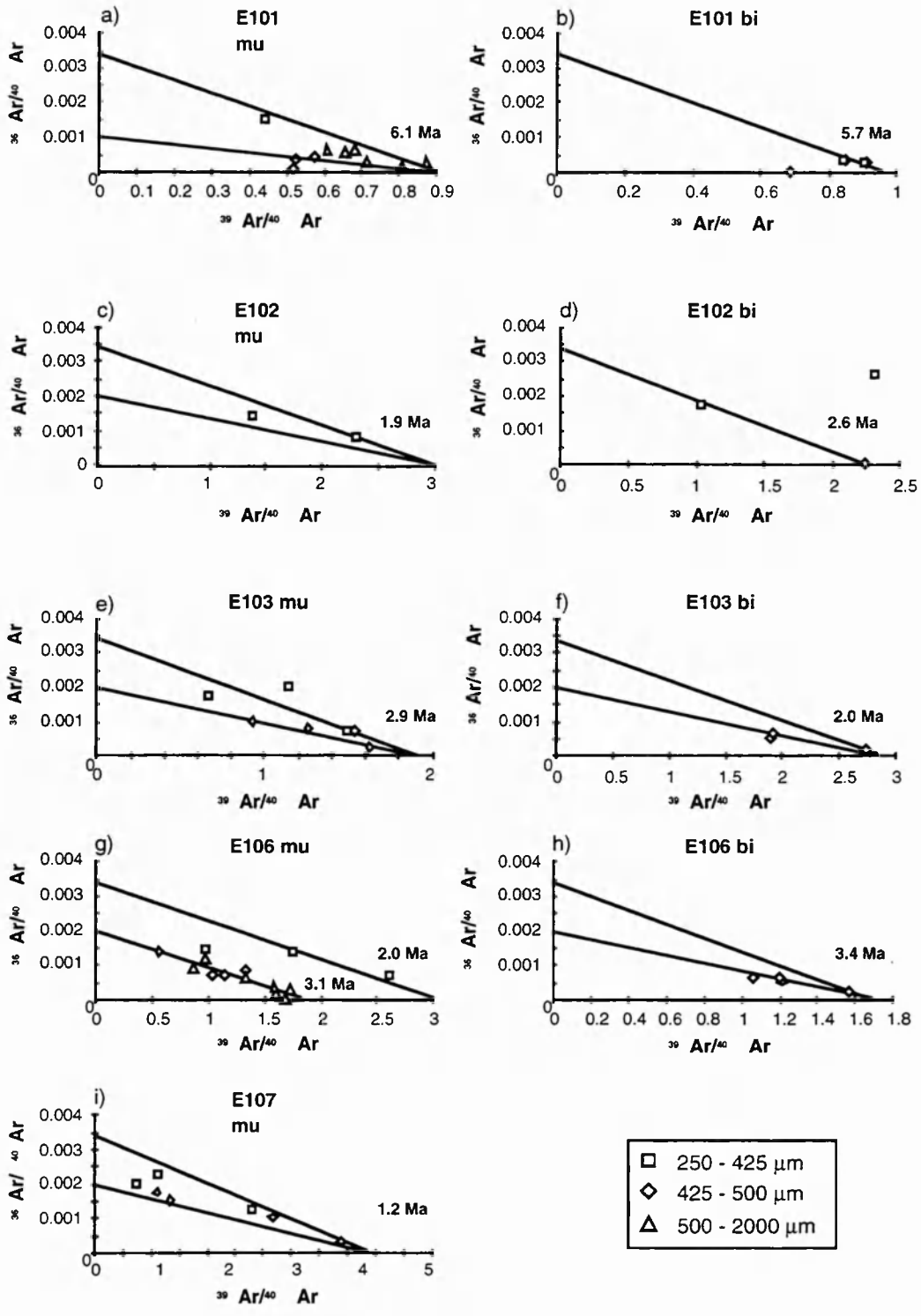
a)
E101
mu
6.1 Ma
b)
E101 bi
5.7 Ma
c)
E102
mu
1.9 Ma
d)
E102 bi
2.6 Ma
e)
E103 mu
2.9 Ma
f)
E103 bi
2.0 Ma
g)
E106 mu
2.0 Ma
3.1 Ma
h)
E106 bi
3.4 Ma
i)
E107
mu
1.2 Ma
36 Ar/40 Ar
39 Ar/40 Ar
250 - 425 µm
425 - 500 µm
500 - 2000 µm

Fig. 6.5. Argon correlation diagrams for Rupal valley samples. Sample locations in Fig. 6.4, data in Table 6.2. Squares = 250-425 μm fraction, diamonds = 425-500 μm fraction, triangles = 500-2000 μm fraction. Lines through the atmospheric $^{36}Ar/^{40}Ar$ intercept of 0.00338 are shown in each case, and reference lines with excess intercepts are shown where deemed appropriate (see text for discussion). Ages shown correspond to the marked ($^{39}Ar/^{40}Ar$) intercept, and are maximum constraints (see text for discussion).

Sample E101 is a mica schist from the village of Nahake, 2 km east of Tarshing. Ten analyses of muscovite (Fig. 6.5a) yield ages between 6.1 and 10.8 Ma. The 425-500 μm fraction yields older ages than the other fractions, and the data are indicative of an excess argon component, probably with a ($^{36}Ar/^{40}Ar$) ratio of about 0.001, in contrast to the atmospheric ($^{36}Ar/^{40}Ar$) ratio of 0.003384. Biotites from the same samples (Fig. 6.5b) yield four ages of 5.7 to 6.1 Ma, and one age of 8.4 Ma which probably also results from incorporation of excess argon. Muscovite ages are older than the biotite ages, as expected from closure temperature calculations.

Further west, E102 is a mica schist from Tup Meadow, 1 km west of the Bazhin glacier. Two muscovite ages of 1.9 and 2.5 Ma lie within 2σ error using an atmospheric ($^{36}Ar/^{40}Ar$) ratio (Fig. 6.5c). Two biotite analyses (Fig. 6.5d) give an age of about 2.6 Ma with an atmospheric ($^{36}Ar/^{40}Ar$) intercept, while one gives an age of 0.50 Ma, although the errors on this analysis are large due to the small amount of gas collected.

E103 is a mica schist from the south side of the Rupal valley at Shaigiri. Seven muscovite analyses give ages ranging from 1.9 to 4.3 Ma, with one analysis of 5.2 Ma with large errors (Fig. 6.5e). Some evidence for an excess argon component is clear when the data are plotted on a correlation diagram, with a ($^{36}Ar/^{40}Ar$) intercept of approximately 0.002, so that the true age could be even younger than

1.9 Ma. Three biotite analyses give ages between 2.0 and 2.6 Ma, with the older ages providing further evidence for an excess component (Fig. 6.5f).

E106 is the furthest west of any sample collected, from 1 km east of the Mazeno pass base camp. This sample provides an interesting example of excess argon , with 14 muscovite analyses yielding ages between 1.8 and 6.4 Ma. On a correlation diagram (Fig. 6.5g), these fall into two trends, with the majority of analyses forming a trend with a ($^{39}Ar/^{40}Ar$) intercept of 2, and a ($^{36}Ar/^{40}Ar$) intercept of 0.002. Two of the three fine-grained samples fall on a line with a ($^{39}Ar/^{40}Ar$) intercept of about 3, corresponding to ages of 1.8 and 2.0 Ma, and an atmospheric ($^{36}Ar/^{40}Ar$) intercept.

Five biotite analyses from E106 (Fig. 6.5h) give ages between 3.4 and 4.4 Ma, and on a correlation diagram there is again evidence for the excess component interpreted in muscovite from this sample, and in other samples. Hence the true age of biotite closure is likely to be less than 3.4 Ma, and if muscovite closure occurred at about 2.0 Ma, then biotite ages are expected to be even younger.

E107 is a leucogranitic sheet from the Polish base camp immediately east of the Bazhin glacier, showing an internal foliation interpreted to indicate multiple magma injection episodes (Chapter 2). Seven muscovite analyses give ages between 1.2 and 3.1 Ma (Fig. 6.5i). On a correlation diagram, the younger analyses define a trend with an atmospheric ($^{36}Ar/^{40}Ar$) intercept, while the older analyses fall below this line, suggesting an excess argon component. The real cooling age is interpreted to be about 1.2 Ma, since both atmospheric and excess argon trends intercept the ($^{39}Ar/^{40}Ar$) axis at a value corresponding to this age. Biotite in this sheet was too scarce to be analysed.

To summarise results from the Rupal valley, muscovite cooling ages are between 2 and 3 Ma, except to the east of Tarshing where ages increase to over 6 Ma. A leucogranite sheet has a younger cooling age of 1.2 Ma, indicating that the sheet

was probably emplaced subsequent to cooling of the country rock through the muscovite closure temperature. Excess argon can be detected in the majority of samples, giving rise to trends which have a ($^{36}Ar/^{40}Ar$) intercept of about 0.002 in many cases.

6.3.2 Fairy Meadows and the Tato Pluton

Samples were systematically collected along both sides of the Tato valley, with the aim of obtaining a traverse southwards towards the core of the massif (Fig. 6.6). At the same time, these data will test for differential cooling rates on either side of the valley, as predicted by Zeitler et al. (1993) across the "Tato Fault", inferred to lie beneath the glacier. In addition, mica separates from several samples of the Tato pluton itself were dated, with the combined aims of constraining the cooling path followed by the pluton after initial emplacement and crystallisation, and to determine whether the pluton was emplaced into country rocks above or below the closure temperature for argon diffusion in biotite.

The pluton contains both muscovite and biotite, and samples of each have been analysed. The country rocks are generally biotite orthogneisses, and do not contain muscovite. The identification of excess argon has been discussed in section 6.2.2, and its effect on ages from the pluton can be assessed by comparison with coexisting muscovite fractions, and using argon correlation diagrams.

One muscovite analysis from the pluton yields a well-constrained age of 0.50 ± 0.07 Ma for muscovite (E5A, Table 6.2), while biotite ages range between 0.82 and 3.78 Ma (E5B, E70B, E70C, Figs. 6.7a, b, c). Another muscovite separate (E5B, Table 6.2) gives a negative age with large relative errors, due to the small amount of gas released by this sample (0.05 V of ^{40}Ar), and has been discarded for the

purpose of discussion. In fact, using the full 2 sigma uncertainty, it is within error of the 0.50 Ma age recorded by E5A, collected from the same outcrop.

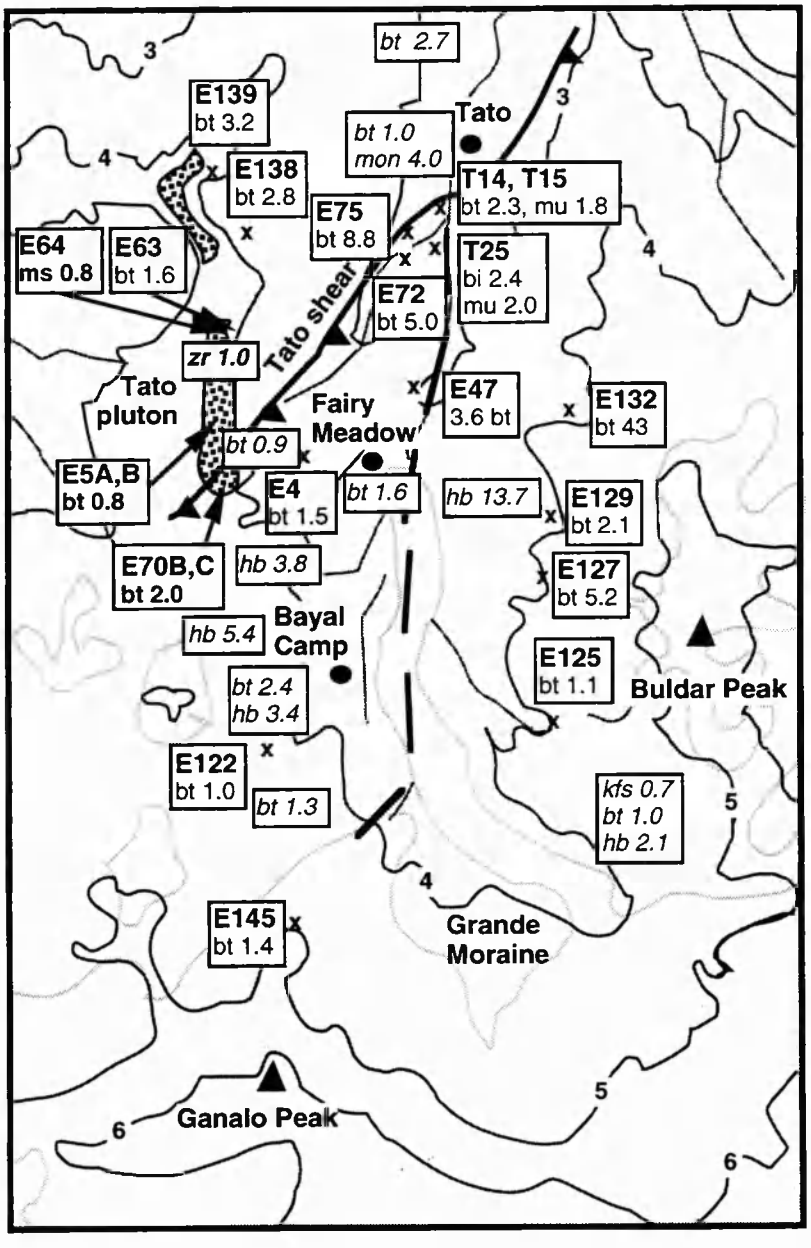

Fig. 6.6. Sample location map for the Tato pluton (stippled) and Fairy Meadows. with traces of the Tato Fault (heavy line) from Winslow et al. (1993) and Winslow et al. (1996), dashed where inferred. Other symbols as for Fig. 6.4.

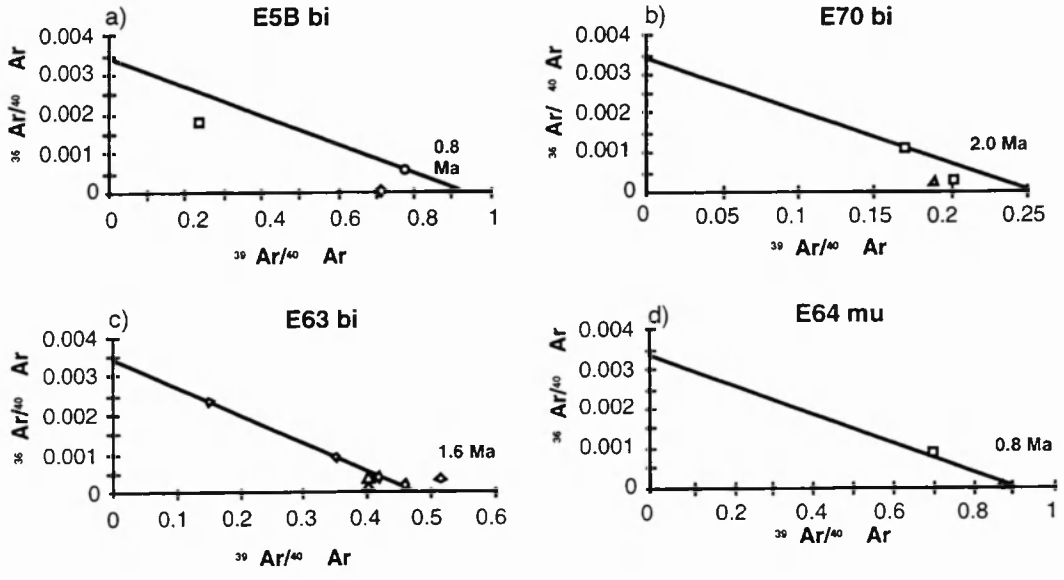

Fig. 6.7. Argon correlation diagrams for Tato pluton samples. Sample locations in Fig. 6.6. Symbols as for Fig. 6.5. Circle on plot (c) is a fine-grained sample (125-250 μm fraction).

Within individual samples from the pluton, biotite shows a wide spread in ages from both E5B and E70, from 0.8 to 1.5 (Fig. 6.7a) and from 2.0 to 3.8 Ma (Fig. 6.7b) respectively. In addition, there is a consistent pattern of biotite recording older ages than muscovite from the same samples (e.g. E5A muscovite and E5B biotite, Table 6.2). This appears to be due to incorporation of excess argon (Fig. 6.7), and so even the youngest of these ages places only a maximum constraint on the true age of biotite closure.

Two coexisting muscovite fractions of different grain sizes from E64, a feeder dyke at the lower margin of the pluton, record very similar ages of 0.84 ± 0.15 Ma and 0.88 ± 0.12 Ma (Fig. 6.7d). One biotite analysis gives an older age of 3.3 Ma, interpreted to be an artificially old age due to excess argon. Seven biotite fractions from E63, wall rock to this feeder dyke, record a narrow range of ages between 1.3 and 1.8 Ma, giving a mean age of 1.6 ± 0.2 Ma (Fig. 6.7c).

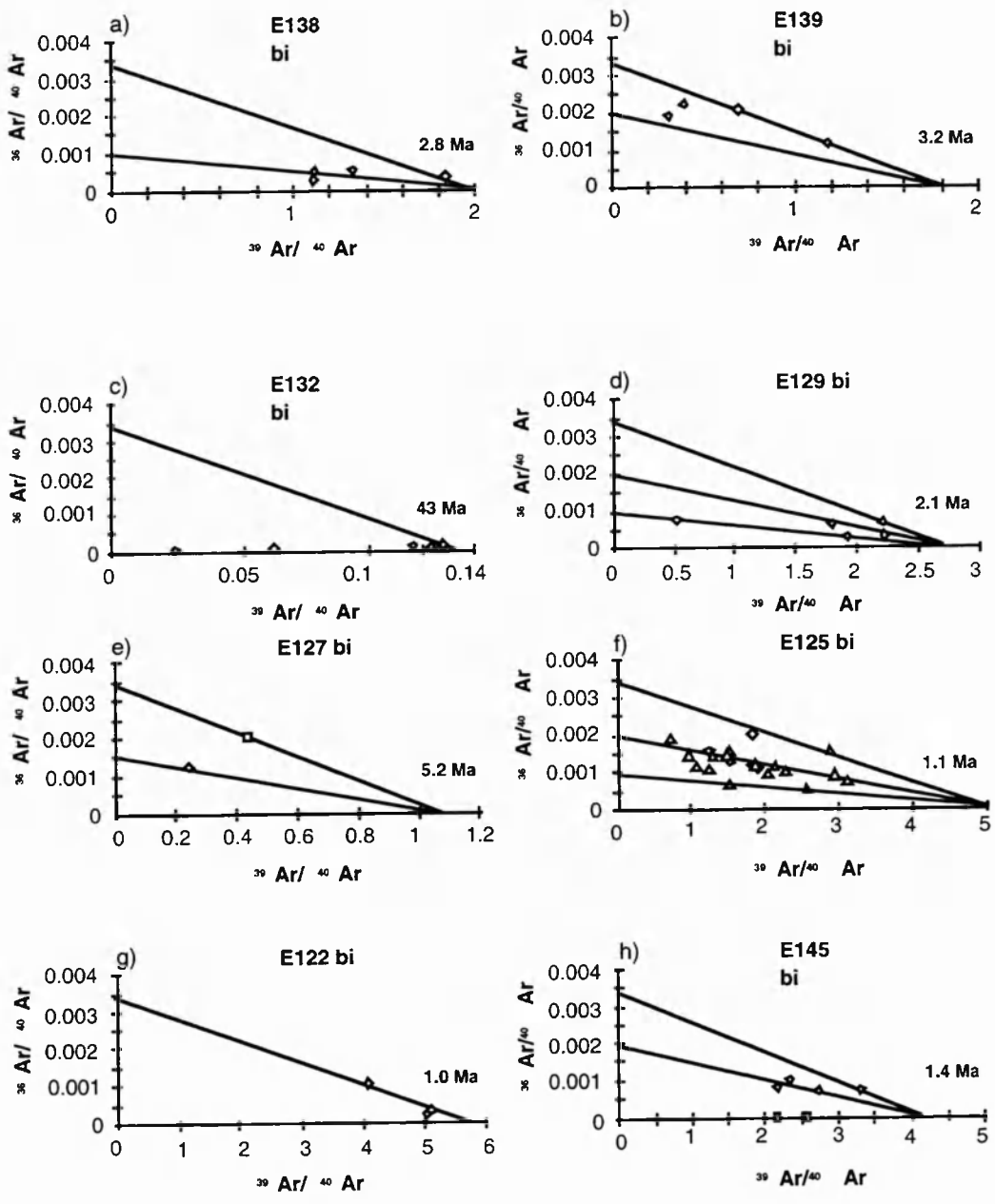

Fig. 6.8. Argon correlation diagrams for Fairy Meadows samples. Sample locations in Fig. 6.6. Symbols as for Fig. 6.5.

There are two possible explanations for this difference between muscovite and biotite from the same outcrop: either E63 biotite records a cooling age affected by excess argon, or E64 muscovite records a crystallisation age and E63 biotite records

cooling of the country rock prior to emplacement of the dyke, and may show evidence for partial resetting. The latter explanation is preferred, since on an argon correlation diagram there is no indication of a significant excess radiogenic ^{40}Ar component in E63 biotite (Fig. 6.7). The two slightly older ages, of 1.69 and 1.82 Ma are both within two standard deviations of the mean, and are also both slightly larger grain size fractions (500 to 2000 μm diameter) than the others (425 to 500 μm diameter), and would hence be expected to have a slightly higher closure temperature (see section 6.2.1), and therefore record a slightly older age. The younger age of 1.33 Ma is within error of the mean age (Table 6.2), and may indicate partial resetting due to heating near the closure temperature.

A single biotite analysis from E4 (Table 6.2), a pelitic rock from about 500m below the pluton and 1 km to the east, gives an age of 1.5 ± 0.3 Ma, in broad agreement with E63 from immediately below the pluton.

Further north, E138 and E139 are biotite schists from below the Tato pluton at Bezar Gali. Four analyses of E138 yield ages between 2.8 and 4.8 Ma (Fig. 6.8a), and five analyses of E139 yield ages between 2.2 and 8.2 Ma (Fig. 6.8b). Both samples show evidence for an excess argon component on correlation diagrams, and the youngest ages of about 2 Ma must be regarded as maximum cooling ages.

On the eastern side of the Raikhot valley, samples E132, E129, E127 and E125 also show the presence of excess argon (Fig. 6.8). Five biotite analyses from E132 yield a bizarre series of old ages from about 50 Ma to over 200 Ma (Fig. 6.8c), and these analyses must be interpreted as due to severe contamination, possibly due to poor hand-picking resulting in incorporation of chlorite or other alteration products resulting from infiltration of a fluid containing excess argon. Five biotite analyses from E129 yield a cluster of ages between 2.1 and 2.8 Ma (Fig. 6.8d), with one significantly older age of 8.7 Ma possibly indicating incorporation of an excess component with a ($^{36}Ar/^{40}Ar$) ratio of 0.001. Two analyses from E127 (Fig. 6.8e)

yield ages of 5.2 Ma (250-425 μm fraction) and 14.9 Ma (425-500μm fraction). None of these analyses yields much chronological information, except that cooling ages are probably no older than 2 Ma, and excess argon is very prevalent in these rocks.

Twenty-three analyses of biotite from E125 yield a widely scattered dataset (Fig. 6.8f). The predominant trend is towards an ($^{36}Ar/^{40}Ar$) intercept of 0.002 or less, as observed in rocks from the Rupal valley. There is no difference in ages recorded by different grain size fractions, but the spread in ages recorded is quite substantial (1.0 to 3.5 Ma). Since excess argon will move samples to lower values of both ($^{36}Ar/^{40}Ar$) and ($^{39}Ar/^{40}Ar$), it may be that the real closure age is 1.0 Ma, the youngest calculated age from this rock assuming an atmospheric ($^{36}Ar/^{40}Ar$) intercept, and that the older ages are due to variable inheritance of excess ^{40}Ar. There is another interpretation, since a trend with an ($^{36}Ar/^{40}Ar$) intercept of 0.002 will yield approximately the same ($^{39}Ar/^{40}Ar$) intercept, at about 5.0. The same age is obtained, but this interpretation suggests a well-constrained excess argon effect with a narrow range of calculated ages. The two points which lie above the line could then be interpreted as being due to argon loss.

South of the pluton, three samples of biotite from orthogneiss sample E122 yield ages of between 1.0 and 1.2 Ma with an atmospheric ($^{36}Ar/^{40}Ar$) intercept (Fig. 6.8g). Orthogneiss sample E145 was collected from the foot of Ganalo Peak, in the core of the massif. Six analyses of biotite from this rock yield ages between 1.4 and 2.7 Ma. On a correlation diagram (Fig. 6.8h), the two finer-grained analyses show the oldest ages and very little ^{36}Ar. Little gas was collected for these analyses, so they are poorly constrained. The four analyses from the larger grain size fraction show an excess argon trend with a ($^{36}Ar/^{40}Ar$) intercept of about 0.002 or less, and with a ($^{39}Ar/^{40}Ar$) intercept of about 5, corresponding to a well constrained age of 1.0 Ma that would not have been detected without the use of the correlation diagram.

6.3.3 Liachar Shear Zone

Several samples were collected from the Liachar Shear Zone, in order to assess the effects of excess argon within lithologies which have experienced fluid flux (Chamberlain et al., 1995; Butler et al., 1997), and to constrain cooling patterns across the massif margin (Fig. 6.9).

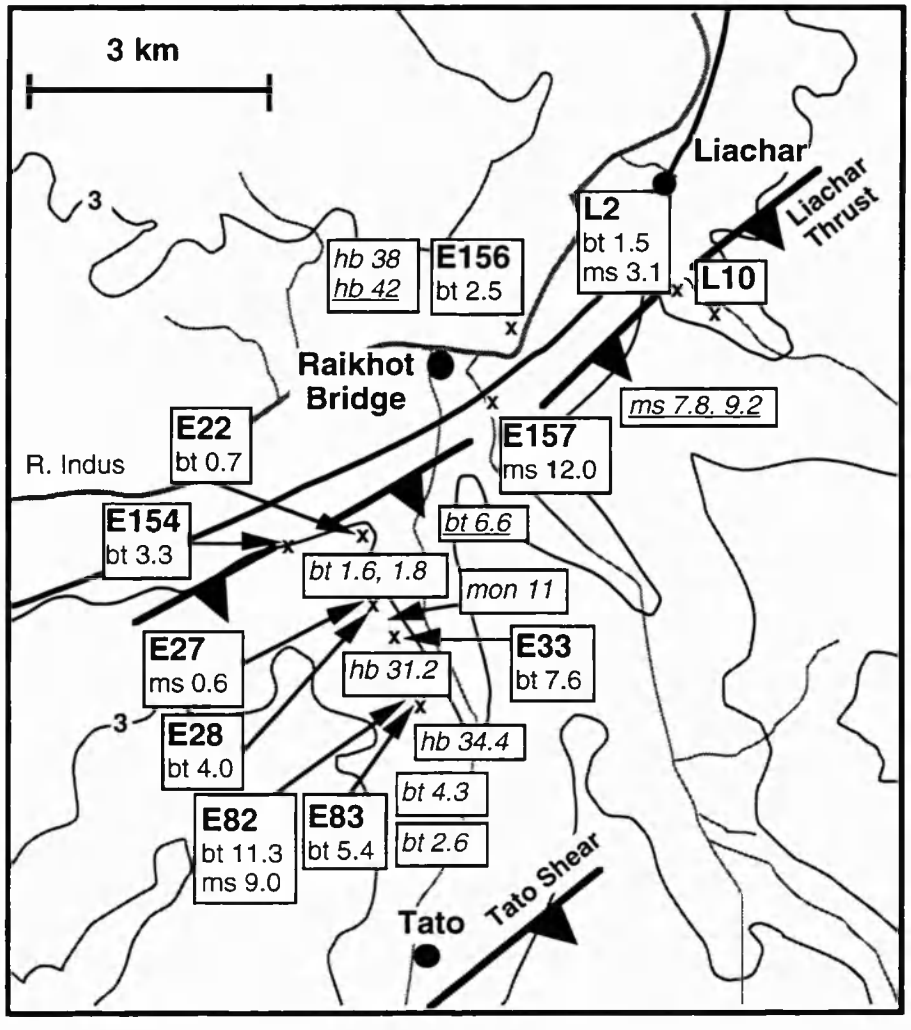

Fig. 6.9. Sample location map for the Liachar Shear Zone, including E157 (MMT zone) and E156 (Kohistan). Symbols as for Fig. 6.4.

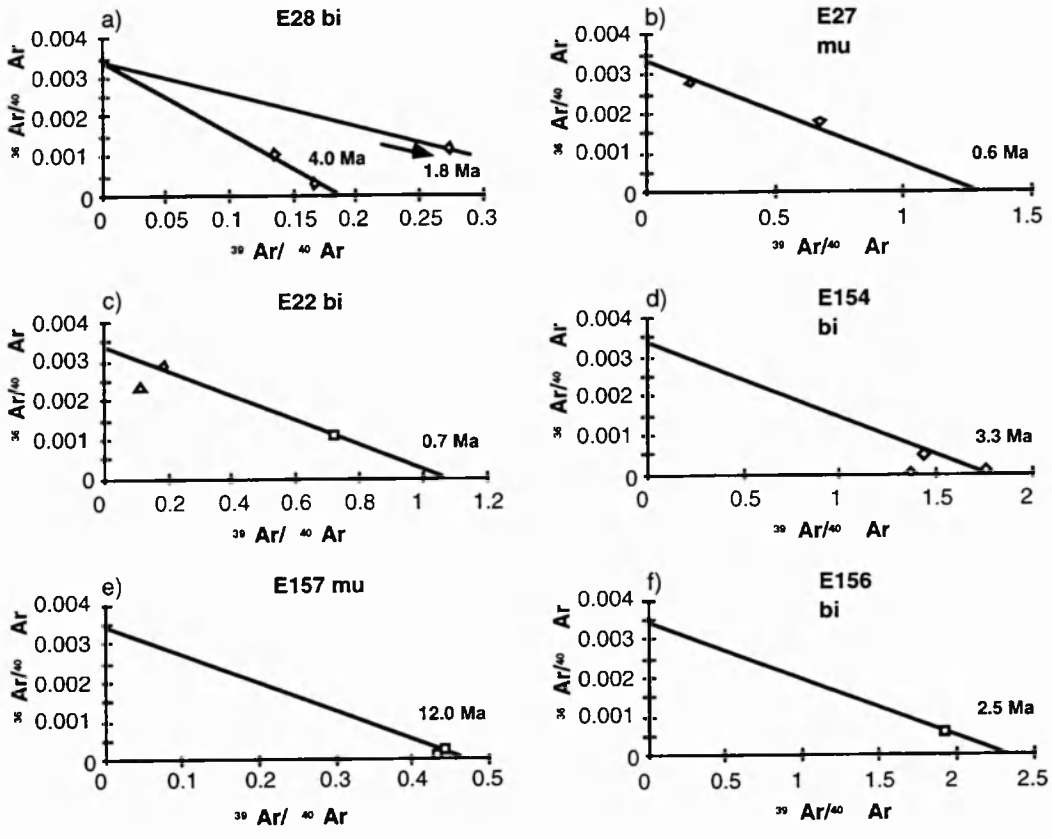

Fig. 6.10. Argon correlation diagrams for Liachar Shear Zone samples. Sample locations in Fig. 6.9. Symbols as for Fig. 6.5.

Single analyses from mica schist E82 yield coexisting muscovite and biotite ages of 9.0 and 11.3 Ma respectively (Table 6.2). A few metres away, E83 yielded a single biotite age of 5.4 Ma (Table 6.2). This variability and the older biotite age suggest the presence of excess argon, although more analyses are needed to confirm this on a correlation diagram.

One km further north, schists E27 and E28 yield variable biotite ages of 1.8 to 4.2 Ma (Figs. 6.10a, b), which are all older than ages obtained from coexisting muscovite (0.9 Ma; Table 6.2). A single biotite analysis from nearby E33 yields an even older age of 7.6 Ma (Table 6.2), which must be attributed to excess argon rather than any real deviation in cooling history over such short distances.

Just above the outcrop of the Liachar thrust, E22 and E154 are coarse-grained biotite-feldspar augen gneisses showing a strong foliation and top to the north-west shear sense (Chapter 2). Three analyses on different grain size fractions from E22 yielded young ages of 0.6, 0.7 and 2.1 Ma (Fig. 6.10c). The older age from the coarsest fraction is attributed to excess argon, although smaller grain sizes would normally be expected to incorporate excess argon more easily. Three analyses of one size fraction of E154 yield ages between 3.2 and 4.2 Ma (Fig. 6.10d). This is probably also due to excess argon, although the cooling effect of the footwall to the Liachar Thrust may also lead to older closure ages near the fault.

Five km north-west at Liachar village, the type locality for the Liachar Thrust, single muscovite and biotite analyses from the pelitic gneiss L2 (George, 1993) gave ages of 3.1 and 1.5 Ma respectively. These samples are discussed further in Chapter 7. A single muscovite analysis for L10 yielded no chronological information.

One sample was collected from the footwall to the Liachar Shear Zone, in the Main Mantle Thrust. E157 is a garnet-bearing mylonite with recrystallised muscovite and biotite, and quartz ribbons indicating ductile deformation associated with early syntaxial formation. Thus we may expect to obtain a deformation age if this last recrystallisation post-dated cooling through muscovite closure. Two analyses of fine-grained muscovite yielded ages of 12.7 and 11.9 Ma (Fig. 6.10e), within 2 σ error of each other, comparable with other ages from the western margin of 8.0 Ma in biotite from Sassi (Reddy et al., 1997) and 8 to 12 Ma in muscovite from Darchan (George and Bartlett, 1996).

On the north side of the Indus, E156 is a sample of Kohistan gabbro containing rare biotite. Two analyses of fine-grained biotite yielded ages of 55.6 Ma and 2.5 Ma (Fig. 6.10f). The older age may be due to excess argon, or may represent an early event. These rocks have experienced amphibolite facies metamorphism

(Jan, 1988), and further west other rocks of the Kamila amphibolite belt record hornblende Ar-Ar cooling ages of c. 80 Ma (Treloar et al., 1989c; Wartho et al., 1996), but near to the NPHM cooling ages decrease markedly in all lithologies and isotopic systems. Treloar et al. (1989c) sampled nearby outcrops and obtained hornblende ages of 28 and 38 Ma, although these are probably excess ages. The biotite age of 56 Ma is attributed to an incorporated excess argon component, and the younger age is interpreted to be a regional cooling age in the absence of any deformational features which could have led to recrystallisation.

6.4 Discussion

6.4.1 Implications for leucogranite emplacement

The cooling history of the Tato pluton is best constrained by muscovite, with an age of 0.50 ± 0.07 Ma from sample E5A, collected near the centre of the pluton. This is only slightly younger than a U-Pb SHRIMP age on zircon rims from the pluton of 1.0 Ma (Zeitler et al., 1993), and combining these ages indicates rapid cooling from crystallisation at about 700 °C to the muscovite closure temperature in about 0.5 Ma. An alternative interpretation is that the zircon rims are hydrothermal rather than magmatic in origin (Zeitler, 1989), since they show exceptionally high U concentrations of over 20,000 ppm (Zeitler and Chamberlain, 1991). This may also lead to unpredictable closure behaviour, although this effect will probably be minor on such a young age.

Since the young muscovite sample is from a higher altitude, it would be expected to cross the muscovite closure temperature isotherm earlier than the feeder dyke sample from the base of the pluton, which records an older age. This apparent contradiction may be reconciled by considering the thermal structure of a hot

pluton emplaced into cooler country rocks. In addition to the vertical thermal gradient (geotherm) present in the country rock, an additional gradient between the centre and margins of the pluton will be superimposed. The margins will cool first, insulating the interior of the pluton and leading to slower cooling, and hence a younger age. In contrast, although the country rocks at the base of the pluton will actually be hotter than those at the level of the middle of the pluton, feeder dykes will crystallise and cool quickly after emplacement due to their narrow width (typically 0.5 to 5 metres, Chapter 2).

The heat contribution from the pluton and feeder dykes to country rocks immediately below the pluton may be investigated using biotite gneiss sample E63, collected from the same outcrop as feeder dyke E64. This shows a well constrained age of about 1.6 ± 0.2 Ma with an atmospheric intercept, with one slightly younger analysis which may indicate partial resetting at 1.3 Ma. Other country rocks around the pluton also record older ages than the pluton, although many of these are poorly constrained and may contain excess argon.

Winslow et al. (1996) obtained two step-heated biotite ages of 0.9 ± 0.2 and 0.99 ± 0.03 Ma from rocks below and east of the pluton. While these are younger than ages obtained by this study, they are still older than muscovites from the pluton. Hence despite being emplaced into rocks which had cooled below the closure temperature of biotite (about 350 ± 30°C, section 6.2.2), the pluton apparently did not transfer sufficient heat to increase the temperature of rocks less than 100 m below the pluton above this closure temperature. Additionally, country rock biotites within a metre of a feeder dyke which crystallised and cooled below the closure temperature of muscovite (420 ± 30°C) at 0.85 Ma were not significantly reset, and therefore were not heated to this temperature.

Although the roof of the pluton was not sampled, lateral variation is documented by samples contrasting E4, about 500 m below the centre of the pluton, and E138

and E139 from about 200 m below the northern extremity of the pluton at Bezar Gali. Both of these are affected by excess argon, but E139 appears to record an age of 3.3 ± 0.3 Ma in contrast to the single age of 1.5 ± 0.3 Ma obtained from E4. This again suggests that the pluton did not significantly reset rocks which had already cooled through the biotite closure temperature, although the potential pitfalls of interpreting ages from samples known to contain excess argon should not be ignored.

Simple thermal modelling may be employed to investigate this insulating effect quantitatively, but the additional problems of rapid exhumation, and particularly the poorly known geothermal gradient render such calculations rather speculative.

Winslow et al. (1996) presented step-heating data in a traverse away from the margin of a leucogranite, although it is not specified whether this is a sheet or the pluton. They obtained an older age from the contact itself than from a sample 10 m away, and the oldest age was 2 m from the contact. They recognised the presence of excess argon in these samples from isotope correlation diagrams, which explains the observed variation in apparent age of over 1 Ma over a space of 10 m. Was this excess argon associated with the leucogranite? If so, then the leucogranites may apparently be younger than country rocks simply because of magmatic fluids containing excess argon. In this scenario, the pluton actually records a regional cooling age, rather than a crystallisation age. This model is not favoured, in part due to the 1.6 Ma age recorded by E63 from less than 100 m directly below the pluton, and also because other leucogranite sheets are certainly younger than their country rocks (Zeitler and Chamberlain, 1991; Zeitler et al., 1993). Examples include E64 from below the Tato pluton, E107 from the Rupal valley, and a duplicated muscovite Rb-Sr age from a leucogranite sheet in the Indus valley of 2.8 to 3.3 Ma (George et al., 1995). This age is also younger than the majority of metamorphic K-Ar and Ar-Ar samples from the Indus valley, indicating that this is likely to be a crystallisation age. In contrast, Ar-Ar ages of

5.6 ± 0.1 and 5.3 ± 0.4 Ma for the Jutial pluton are within error of ages from adjacent gneisses (George et al., 1995).

It is concluded that at least some leucogranite sheets, and probably the Tato pluton, were emplaced into country rocks which had already cooled below the closure temperature of Ar diffusion in micas. Hence Ar-Ar ages from these sheets should be near to crystallisation ages. A muscovite age from the pluton indicates that cooling from crystallisation at 1.0 Ma (Zeitler et al., 1993) to muscovite closure at about 450 °C occurred over a period of about 0.5 Ma.

If the pluton was emplaced without resetting country rocks below it, then magma ascent through dykes rather than diapirs is favoured, since diapiric ascent would carry hot rocks from below the pluton along with it, and these would necessarily record younger cooling ages than the pluton itself.

6.4.2 Implications for exhumation of the NPHM

In the absence of extensional tectonics, exhumation of the NPHM has been attributed to rapid erosion acting on crust which has been uplifted rapidly on reverse shear zones (Butler and Prior, 1988a, b; Butler et al., 1989) and by large scale antiformal folding (Coward et al., 1986; Treloar et al., 1991). Movement on the MMT last occurred at between 8 and 12 Ma (George et al., 1995; George and Bartlett, 1996; Reddy et al., 1997; this study) and deformation was transferred to a combination of oblique dextral-reverse movement on the Sassi-Darchan shear zone further north, and reverse movement on the ductile Liachar Shear Zone overprinted by brittle reverse movement on the Liachar Thrust.

This concentration of deformation on the western margin is evident in the cooling age profiles across the massif (Fig. 6.1b). Other recently active faults would also be expected to result in an abrupt change in cooling age between the hangingwall

and footwall, provided that movement on the fault post-dated closure in rocks currently exposed.

The "Tato Fault" of Zeitler et al. (1993) was drawn along the Raikhot Valley, with a south-over-north reverse shear sense. Chamberlain et al. (1995) have described the Tato Shear Zone as a group of 1- to 3-km wide shear zones mapped just south of Tato. Winslow et al. (1994) presented Ar-Ar ages from total fusion analyses of biotite in a traverse across the Tato Fault, and found older ages between the western margin of the NPHM and the Tato Fault than to the south of the Tato Fault. Four total fusion ages were checked by step-heating, revealing some excess argon in every case, but the pattern was similar. They interpreted this pattern as evidence for recent movement on the Tato Fault, although this conclusion is not clear from their data (Winslow et al., 1994, Fig. 2), especially since adjacent analyses gave ages of 2.7 and 4.3 Ma even when step-heated (Winslow et al., 1996, Fig. 7).

Winslow et al. (1996) presented data from either side of the Tato Shear, which they mapped as continuing southwest from Tato through the Tato pluton, rather than southwards to the Raikhot Face as previously described. Samples from either side of the fault again showed no clear evidence for recent movement on the shear zone. Although amphibole ages are older in the Liachar Shear Zone (31 and 34 Ma) than to the south of Tato (2 to 14 Ma, Winslow et al., 1996, Fig. 3), this pattern would also be anticipated from passive doming with more rapid erosion in the interior of the massif. The amphibole data also requires particularly careful interpretation due to excess argon, so that the old ages from the LSZ are only maximum estimates, and indeed are considerably older than U-Pb ages on monazite from this zone of 4 to 11 Ma (Smith et al., 1992).

Biotite data presented by Winslow et al. (1996, Fig. 6) is also interpreted as showing younger ages from the hangingwall of the Tato shear zone, although this

is not the case. Two samples from adjacent to their fault, on the footwall side, give ages of 0.9 and 1.0 Ma. Two closely-spaced samples from north of Tato give ages of 2.6 and 4.3 Ma, perhaps indicating the presence of excess argon, and two samples from the LSZ near to the MMT give ages of 1.8 and 1.6 Ma.

The data presented in this study provides a further test for the existence of the Tato Fault. The existence of north-verging high strain zones is not disputed, but no evidence was found in this study for a discrete zone of recent movement, and no structure was found to offset of the Tato pluton. Ages presented in this study from both sides of the fault traces drawn by Winslow et al. (1994) and Winslow et al. (1996) can test for differential exhumation (Fig. 6.11). These are compared with previous reported ages which have used atmospheric ($^{36}Ar/^{40}Ar$) argon intercepts in age calculations.

E122 and E145 (Fig. 6.6) are from opposite sides of the fault trace shown in Winslow et al. (1994, Fig. 1). The best estimate ages are about 1.0 Ma for both samples, while Winslow et al. (1996) present data from two samples near to E122 with ages of 2.44 ± 0.03 and 1.30 ± 0.02 Ma. Excess argon is clearly present on the correlation diagrams presented by Winslow et al. (1996), so that the reported ages are maximum estimates, and geological scatter is much greater than analytical precision. E4 and E47 (Table 6.2) lie approximately on the trace of the Tato Fault presented by Winslow et al. (1996), but single analyses give poorly constrained and unreliable ages.

A strong contrast with ages on the eastern side of the Raikhot valley would be expected if the Tato fault was a recently active structure. E132, E129, E127 and E125 all show evidence of excess argon, with a best estimate age of biotite from E125 of 1.1 Ma (Fig. 6.8f), while E129 records a maximum age of about 2.1 Ma. The maximum age of biotite from E127 is 5.2 Ma, and is probably considerably younger. Given the uncertainties due to excess argon, these ages are not

significantly different to those reported on the western side of the Raikhot valley, and provide no clear evidence for differential erosion across the Tato Fault.

In general it is concluded that all data from this region needs careful interpretation with regard to excess argon, and that differences in the apparent age of samples are not necessarily real. When differences between nearby samples are often in excess of 1 Ma (e.g. Pk/75-90, Pk/71-90 and Pk/17-90 and Pk/29-90, Winslow et al., 1996; Fig. 6.6), it seems unwise to attribute similar apparent age differences between samples to differential erosion across structures which are largely hidden by glaciers and moraine, and hence largely unmapped. By careful interpretation of correlation diagrams, it has been shown in this study that these differences in apparent age are largely artefacts resulting from excess argon.

An alternative interpretation of the age pattern revealed by the north-south traverse of Winslow et al. (1994, Fig. 2) is that the younger ages recorded within 4 km of the massif margin are recrystallisation ages rather than regional cooling ages. What is clear from their data is that single total fusion ages are unreliable, and careful interpretation of either step-heating or multiple total fusion analyses is required in this area.

The pattern of older ages outside the massif and on the massif flanks, and younger ages in the core of the massif, is clear from a number of geochronological systems. However, an interpretation of the syntaxial development of the NPHM based on contouring of biotite cooling ages (Winslow et al., 1996, Fig. 13) is not justified given the perils of excess argon detailed in this study. While cooling ages in the Indus valley are youngest in the cores of antiforms (Treloar et al., 1991), suggesting that the cooling age pattern is in part the result of folding, another explanation must be found for the exceptionally young ages found throughout the Raikhot valley which does not rely on differential exhumation across the Tato shear zone.

The difference in cooling age patterns between the southern and northern areas of the NPHM may be explained simply in terms of exhumation on the Liachar Shear Zone, since the northern margins of the massif are mainly strike-slip (Sassi-Darchan shear zone, Butler et al., 1989) or extensional (northern and eastern margins, Butler et al., 1993; Pognante et al., 1993). Movement on the Liachar Thrust, the discrete brittle equivalent of the distributed ductile Liachar Shear Zone, is ongoing, as indicated by superposition of basement gneiss over Quaternary gravels at Liachar (e.g. Butler et al., 1988a). Hence there is no need to invoke movement on the Tato Fault to explain recent denudation, and young ages from the Liachar Shear Zone may indicate recrystallisation rather than closure to volume diffusion.

6.4.3 Implications for fluid movement within the NPHM

Excess argon is widespread in the NPHM and has been documented by several workers (Zeitler, 1985; Treloar et al., 1989c; George et al., 1995; Winslow et al., 1996; Reddy et al., 1997; this chapter), although many have not taken sufficient account of this feature when interpreting their data. We may use argon as an isotopic tracer to extract information regarding the sources and timing of fluids within the NPHM, in a similar way to the treatment of oxygen isotope data by Chamberlain et al. (1995). This study has presented a wealth of data from across the southern NPHM, and the results will now be assessed to discern temporal and spatial patterns of fluids with different argon signatures.

In muscovite gneisses from the Rupal Valley, several samples show clear effects of excess argon. In some cases the data are delimited by a triangular field between trends with atmospheric intercepts, and trends with an excess argon intercept of about 0.002 (E103 mu, E103 bi, E106 bi, E107 mu, Fig. 6.5) which is the pattern predicted by Roddick et al. (1980), illustrated in Fig. 6.3. The data from E101 may

be explained by excess argon with a very low ($^{36}Ar/^{40}Ar$) ratio of less than 0.001 (Fig. 6.5a). In most cases, the ($^{39}Ar/^{40}Ar$) intercepts for both atmospheric and excess trends are similar, and so give the same age, which is the best estimate of the true cooling age (Fig. 6.3).

E106 mu (Fig. 6.5g) appears to have two trends, one well-defined excess trend with a ($^{36}Ar/^{40}Ar$) intercept of about 0.002, giving an age of about 3.5 Ma, while two finer-grained samples apparently have a near-atmospheric ($^{36}Ar/^{40}Ar$) intercept, and give an age of 1.9 ± 0.2 Ma. This is the reverse of the expected pattern, because smaller grains should incorporate excess argon more easily. The younger ages could be explained by radiogenic argon loss, which would be expected to affect smaller grains more than larger grains. The preferred interpretation attributes this pattern to excess argon rather than argon loss, since there is good evidence for excess argon in other NPHM samples. In this case, the analyses of smaller grains may reflect incorporation of atmospheric argon in late-closing grains but an excess component in larger grains which would effectively close earlier.

In biotite gneisses from the Fairy Meadows area, the presence of excess argon is irrefutable in all samples except for E122, which records the youngest age of 1.0 ± 0.1 Ma. The excess component appears to have a ($^{36}Ar/^{40}Ar$) ratio of 0.001 or less in many cases, and is particularly evident in the 23 analyses of biotite from E125.

The preferred interpretation of the pattern seen in E125 bi (Fig. 6.8f) is that the true cooling age of this sample is about 1.0 Ma, and that most grains have incorporated an older component of excess ^{40}Ar with a ($^{36}Ar/^{40}Ar$) ratio of about 0.002, although at least two grains appear to be free of this excess component. Without the use of the correlation diagram, the data would be interpreted as a wide spread in ages rather than having a well-constrained excess effect, although in both cases the estimated age of closure would fortuitously be the same. The two grains lying

on a line with an atmospheric intercept could be interpreted as having equilibrated with a (later?) meteoric fluid carrying argon with an atmospheric ratio (Fig. 6.8).

In samples from the Liachar Shear Zone, a minor excess argon component is apparent in E22 bi (Fig. 6.10c) and E154 bi (Fig. 6.10d). In E28 bi, two analyses point towards an atmospheric intercept, while a third appears to have an older age. While more data is required to interpret this pattern, it could have one of three origins: the younger age may result from argon loss, recrystallisation, or the older samples may reflect excess argon and spuriously suggest an atmospheric intercept (Arnaud and Kelley, 1995). The latter explanation is most likely because the older ages of 3.9 and 4.2 Ma are anomalously old within the LSZ, for example muscovite from nearby E27 records two ages of less than 1 Ma.

The mylonite from the MMT zone below the Liachar Thrust (E157, Fig. 6.10e) records two ages of 11.9 and 12.7 Ma which, although much older than samples from a few km to the south, is similar in age to other samples from shear zones on the massif margin (George et al., 1995; George and Bartlett, 1996; Reddy et al., 1997).

There are at least three different potential sources for argon-bearing fluids within the massif: metamorphic fluids from devolatilisation of basement rocks during Neogene high-temperature metamorphism, magmatic fluids associated with the crystallisation of the leucogranites and associated pegmatites, and meteoric fluids which may penetrate to significant depths in shear zones such as the LSZ (Chamberlain et al., 1995; Butler et al., 1997).

Data from the Tato pluton confirms that excess argon is associated with the leucogranites, as discussed in the previous section. Regional ages are apparently older than ages from the pluton, in which case excess argon in country rocks must have another source. The $\partial^{18}O$ values found in migmatites in the interior of the

NPHM, typically 10 to 13‰, were attributed by Chamberlain et al. (1995) to magmatic fluid infiltration from the leucogranites, which have lower $\partial^{18}O$ values of about 8‰. However, the range of values within migmatised gneisses in the massif interior and unmigmatised gneisses on the massif flanks is small (Fig. 3 of Chamberlain et al., 1995), and there is not significant evidence for pervasive movement of magmatic fluids. Furthermore, the leucogranites and currently exposed migmatites are not thought to be genetically related on the grounds of field relations (Butler et al., 1997; Whittington et al., 1997a), so that another source for excess argon-bearing fluids must be found.

The overall pattern is one of younger ages in the interior of the massif, characterised by excess argon, in many cases with an apparent ($^{36}Ar/^{40}Ar$) ratio of 0.002 or less, and ages on the margin of the massif which appear to be less affected by excess argon, although more data is required to substantiate this inference. A possible explanation for this is that all samples initially equilibrated with excess argon liberated by devolatilisation of old basement rocks during metamorphism. Samples in the LSZ, which was penetrated by meteoric fluids during metamorphism (Chamberlain et al., 1995; Butler et al., 1997; Reddy et al., 1997), were then reset during recrystallisation in equilibrium with meteoric fluids with an atmospheric ($^{36}Ar/^{40}Ar$) ratio. Tentative evidence for this process may be seen not only in the correlation diagram of E28 from the Liachar Shear Zone, but also in E106 from the upper Rupal valley, and E125 from near Fairy Meadows, where there are two apparent trends, one with an excess ($^{36}Ar/^{40}Ar$) intercept, and one with an atmospheric ($^{36}Ar/^{40}Ar$) intercept.

Reddy et al. (1997) conducted a detailed study of one sample from the western margin of the NPHM at Sassi, and found that excess argon was incorporated in both hornblendes and K-feldspars, at opposite ends of the range of closure temperatures found in common minerals. Biotite, chlorite and scapolite formed in retrograde greenschist facies shear zones contained limited excess argon, and the

age of biotite of 8 Ma was interpreted to be approximately the true age, placing a minimum constraint on timing of syntaxial development. The observed pattern was best fitted by a model of excess argon with a $^{36}Ar/^{40}Ar$ ratio of about 0.002 to 0.0025, although some samples showed $^{36}Ar/^{40}Ar$ ratios as low as 0.0004. Excess argon was incorporated at depth and retained through the closure of hornblende. A later fluid, of approximately atmospheric composition and hence probably meteoric, then percolated through discrete fault zones associated with retrograde metamorphism, so that minerals grown in these zones equilibrated with an atmospheric $^{36}Ar/^{40}Ar$ ratio. K-feldspar retained the excess signature by not being able to exchange with the later meteoric fluid.

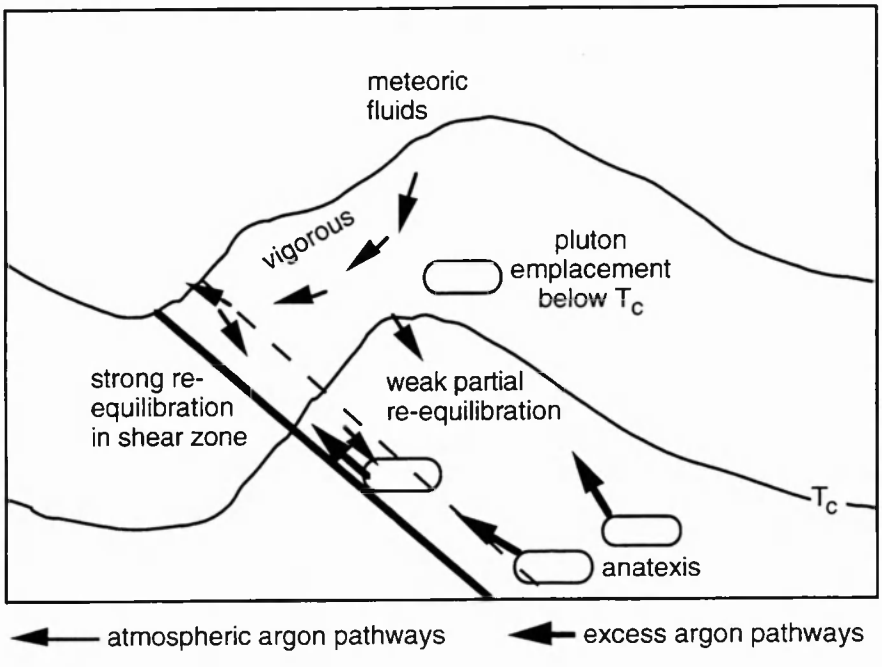

Fig. 6.11. Schematic diagram showing argon-bearing fluid fluxes within the NPHM, modified after Butler et al. (1997).

Hence the overall pattern of ages across the massif may be explained by initial equilibration with excess argon liberated by devolatilisation of old basement rocks during high grade metamorphism, followed by partial re-equilibration with meteoric fluids within shear zones (Fig. 6.11). The Tato pluton was associated with magmatic fluids containing excess argon, but this interacted little with country rocks which had already cooled below the closure temperature for argon diffusion in biotite.

6.5 Summary

$^{40}Ar/^{39}Ar$ data from three important regions have been presented from the southern part of the NPHM. In general, cooling ages are exceptionally young, with excess argon effects commonplace. The youngest reliable ages, of about 1.5 Ma, are found in the interior of the massif, around Fairy Meadows. These are older than the age of the Tato pluton, dated at 0.5 Ma by muscovite, and older than feeder dykes, dated at 0.8 to 0.9 Ma by muscovite. Ages in the Rupal valley are about 3 Ma for muscovite schists, increasing to over 6 Ma towards the eastern margin of the massif. Muscovite from a feeder dyke in the Rupal valley has been dated at 1.2 Ma, again suggesting that leucogranite emplacement occurred after regional cooling below the muscovite closure temperature. Ages recorded by samples from the Liachar Shear Zone are very variable, with differences of several Ma recorded over a few metres. Many of these ages may be affected by excess argon, fluid interaction, and recrystallisation during deformation. Ages from the MMT zone are older, as found by other studies, indicating movement on the MMT last occurred at between 8 and 12 Ma.

The effect of excess argon is particularly pronounced in the Rupal valley and Fairy Meadows regions, where correlation diagrams often suggest an excess ($^{36}Ar/^{40}Ar$) intercept of is more appropriate than an atmospheric intercept for calculating ($^{39}Ar/^{40}Ar$) ages. Care must be taken in the interpretation of data where excess argon is detected, since in general the youngest age calculated using an atmospheric intercept will only be a maximum cooling age. Where little ^{36}Ar is detected, this effect will be relatively unimportant as it will not significantly change the calculated ($^{39}Ar/^{40}Ar$) intercept or the calculated age.

This excess ^{40}Ar must come from an old source, probably devolatilisation of old basement rocks since magmatic fluids associated with leucogranites were available only after regional cooling of country rocks to below the closure temperature. Samples from the Liachar Shear Zone, an active conduit for hydrothermal fluid circulation (Chamberlain et al., 1995; Butler et al., 1997) show less evidence for excess argon. This may be because these hydrothermal fluids are meteoric in origin, and hence would be more likely to contain argon with an atmospheric signature, or it may be that not enough analyses were undertaken to show this pattern.

If the former explanation is correct, this confirms that fluids of predominantly meteoric origin, rather than metamorphic or magmatic fluids, were circulating at depths where the temperatures enabled argon exchange with micas. Exchange would be enhanced even at low temperatures in shear zones because deformation would reduce the effective diffusion radius, and may also promote fracturing and defects in grains which may provide faster argon transport mechanisms than volume diffusion.

CHAPTER 7 - THERMAL MODELLING

Author's note: This manuscript was published in a special volume of Tectonophysics, the proceedings of the 10th Himalaya-Karakorum-Tibet workshop in Ascona, Switzerland.

"Exhumation Overrated at Nanga Parbat, northern Pakistan"

by Alan Whittington, Tectonophysics, vol. 260, p. 216-226, 1996.

7.1 Abstract

New $^{40}Ar/^{39}Ar$ laserprobe and thermobarometric data from the Nanga Parbat - Haramosh Massif (NPHM) in northern Pakistan provide important constraints on thermal models of the evolving geotherm of the massif. Simple thermal models indicate that the unusually young cooling ages from this area do not necessarily imply extreme exhumation rates of about 7 mm/y, because the advection of heat resulting from rapid exhumation leads to a steepened near-surface geotherm. The most important control on the present-day thermal structure of the NPHM appears to be the thermal structure resulting from obduction of the Kohistan Arc some 50 million years ago. Transient geotherms calculated for the past 10 Ma can only be reconciled with published geochronological and thermobarometric studies if exhumation rates lay in the range of 3 to 4 mm/y, still considerably greater than exhumation rates determined from the main Himalayan orogen.

7.2 Introduction

The Nanga Parbat Syntaxis, or Nanga Parbat-Haramosh Massif (NPHM), forms a northward kink in the suture between the Indian Plate and Kohistan Island Arc at the western end of the Himalaya (Fig. 7.1). A combination of thrust and transpressive strike-slip faulting has resulted in unusually young cooling rates on the western margin of the massif over the past 5 Ma (Zeitler, 1985). Recent compressional structures related to this rapid exhumation can be observed

overprinting older Main Mantle Thrust (MMT) structures associated with collision and initial crustal thickening (Butler and Prior, 1988a, b).

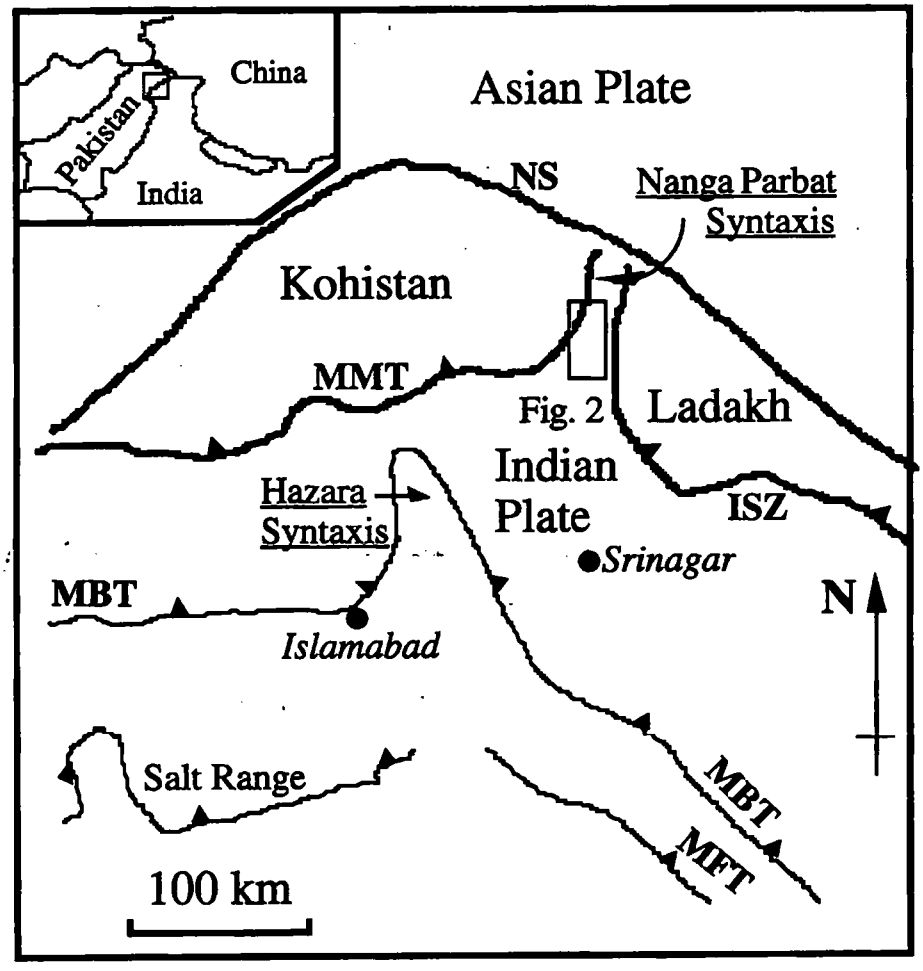

Fig. 7.1. Tectonic sketch map of the western Himalaya. ISZ = Indus Suture Zone, MMT = Main Mantle Thrust, MBT = Main Boundary Thrust, MFT = Main Frontal Thrust.

The Tato Valley which runs south from the peak of Nanga Parbat to the Indus valley at Raikhot Bridge (Fig. 7.2) is particularly problematic for geochronological and thermal modelling studies due to (i) its exceptionally high cooling rates, interpreted to indicate rapid and increasing exhumation rates of 7 mm/y (Zeitler et al., 1982a) and (ii) its unparalleled topography of 7 km vertical relief within a 21

km horizontal distance. New argon ages for biotite and muscovite from this valley are presented and evaluated in this study, and the difficulties of modelling the thermal structure of the region are discussed. In particular simple thermal modelling suggests that in active orogenic belts cooling rates cannot necessarily be used to directly calculate exhumation rates.

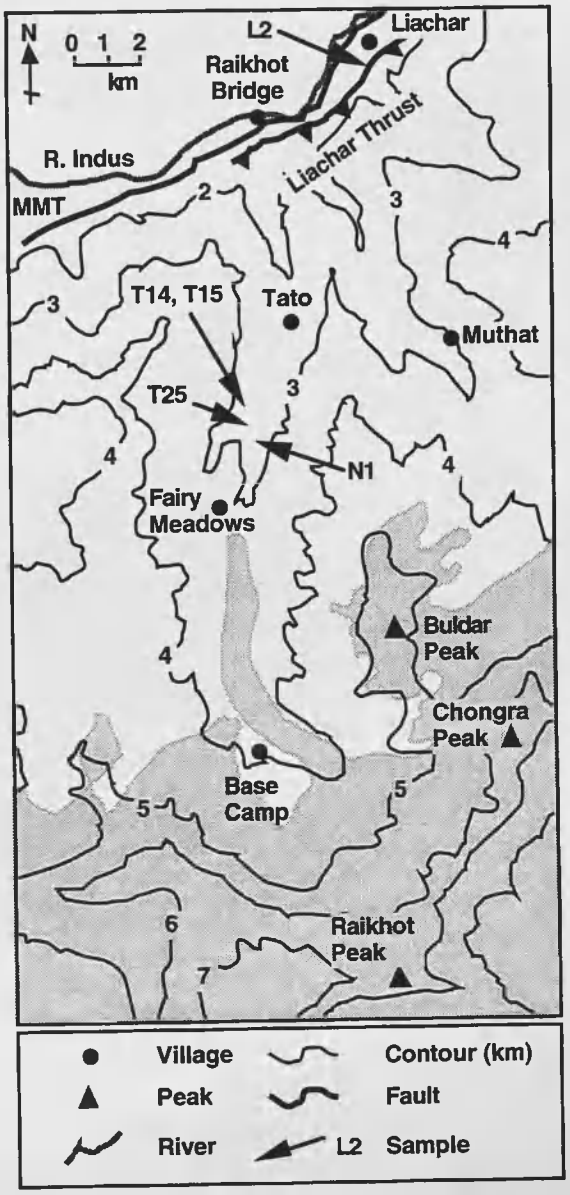

Fig. 7.2. Sample locations from the Tato Valley, Nanga Parbat.

7.3 Cooling ages and their interpretation

Four muscovite-biotite-plagioclase-quartz metapelites were selected for analysis, three from between Tato and Fairy Meadows and one from the lower Liachar Valley, just above the Liachar Thrust. These sample rocks were crushed and sieved, and both muscovite and biotite fractions were analysed with an infra-red laser using the technique of Kelley (1995). When possible, multiple analyses were undertaken on mineral separates, and in one case (T15 biotite), two different size fractions were analysed (Table 7.1).

Argon isotopic ratios of mica fractions were determined on a MAP 215-50 noble gas mass spectrometer at the Open University, and ages calculated from the measured isotopic ratios (Table 7.1). ^{39}Ar and ^{36}Ar blanks were calculated by correlation with the ^{41}Ar peak, and all blanks were averaged either side of each sample, but were found to lie within error of the daily average.

Results are plotted on an Ar correlation diagram (Fig. 7.3), that in the absence of excess Ar should define a line with a y intercept of 0.003384, representing atmospheric argon, and with a negative gradient representing the age. The scatter in data from biotite fractions of sample T15 indicate the presence of excess argon which is heterogeneous on a millimetre scale, as reported from the Sassi shear zone on the western margin of the NPHM by Reddy et al. (1997). Other samples from Tato all show excess argon in biotite, since the biotite ages are apparently older than muscovite ages and muscovite has a higher closure temperature (Table 7.2). Excess argon is also indicated by fine-grained biotites giving a higher age than larger grains.

Name	40 Ar	±	39 Ar	±	38 Ar	±	37 Ar	±	36 Ar	±	40Ar*/39Ar	±	Age (Ma)	±
L2mu1	1.01346	0.01258	0.01996	0.00257	0.00333	0.0009	0.00199	0.00099	0.00112	0.0003	34.24	6.32	3.09	0.58
L2bi1	3.71088	0.03891	0.14116	0.00471	0.00707	0.0011	0.00302	0.00101	0.00458	0.00032	16.69	0.91	1.5	0.08
T14mu	5.34399	0.17923	0.1844	0.0127	0.01392	0.00287	0.00651	0.00247	0.00596	0.00102	19.43	2.32	1.75	0.22
T14bi	4.4172	0.05425	0.11248	0.00863	0.01054	0.00246	0.00517	0.00245	0.00512	0.00069	25.82	2.72	2.33	0.24
T15mu	5.86863	0.04793	0.17976	0.00525	0.01058	0.00232	0.00401	0.00245	0.00678	0.0007	21.51	1.33	1.94	0.12
T15bi	2.32131	0.02467	0.05359	0.00257	0.00291	0.00217	0.00053	0.00244	0.00158	0.00022	34.6	2.12	3.12	0.20
T15bifg	0.3029	0.01459	0.00881	0.0021	0.00216	0.0019	0.00167	0.00166	-0.00022	0.00035	41.88	15.6	3.77	1.40
T15bifg	1.05073	0.02793	0.02837	0.00302	0.00378	0.00192	0.00293	0.00174	0.00053	0.00047	31.5	6	2.84	0.54
T25mu	3.28056	0.03329	0.12781	0.00699	0.01106	0.00223	0.00741	0.00261	0.00162	0.00076	21.92	2.14	1.98	0.20
T25mu	0.83862	0.00868	0.00796	0.00175	0.00151	0.00216	0.00007	0.00243	0.00225	0.00021	21.81	9.33	1.97	0.84
T25bi	2.91071	0.04068	0.06767	0.00708	0.00826	0.0022	0.00394	0.00244	0.00378	0.00058	26.52	3.8	2.39	0.34

Table 7.1. Measured argon isotopic ratios with calculated age and 2 sigma errors for mica samples from the Nanga Parbat Massif. Samples were collected by Mark George.

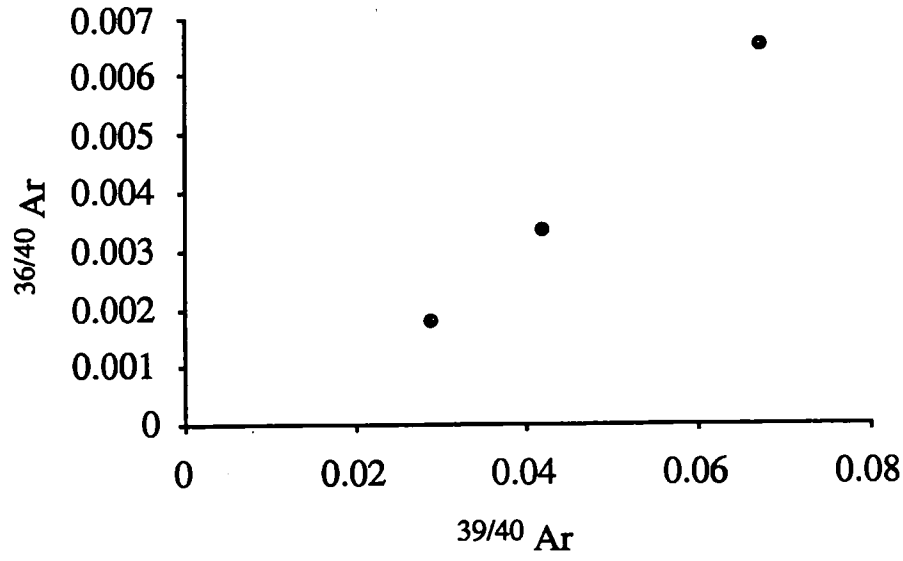

Fig. 7.3. Argon correlation diagram showing $^{36}Ar/^{40}Ar$ vs. $^{39}Ar/^{40}Ar$ for three biotite grains from sample T15. The positive slope on this plot indicates the presence of excess argon which is heterogeneous on a sub-grain size scale.

Closure temperatures have been calculated for the relevant grain sizes according to Harrison et al. (1985) for biotite, and Hamilton et al. (1989) for muscovite. The calculations are dependent on both cooling rate and grain size into account, so a range of temperatures was obtained for each sample (Table 6.1). Since the data suggest a cooling rate of about 200 °C / Ma, closure temperatures used below are calculated for this cooling rate. Note that the calculated cooling rate and calculated closure temperature are interdependent, so that closure temperature must be resolved by iteration.

Since smaller grains can maintain equilibrium with the rock at lower temperatures (as they have a smaller diffusive radius compared to larger grains), they have a lower closure temperature and hence would be expected to give younger ages. In this case their greater age indicates excess argon in the rock. If the muscovite ages are correct, these samples cooled through about 445 °C at between 1.8 and 2.0 Ma,

giving a cooling rate of between 250 and 220 °C / Ma (Fig. 7.4). The presence of excess argon means that the muscovite ages are maximum constraints, and cooling of the Tato rocks may have been even more rapid.

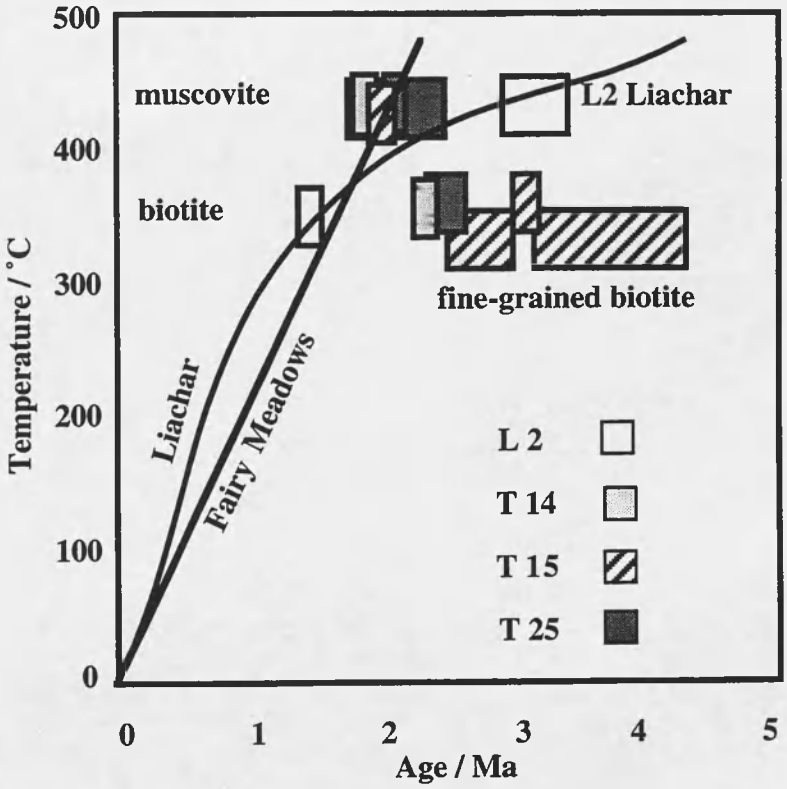

Fig. 7.4. Temperature-time curve for rocks from the Tato Valley, Nanga Parbat. Data from Table 7.1. Cooling curves for rocks immediately above the Liachar thrust and rocks near Fairy Meadows are shown. Note that biotite ages are older than muscovite ages, indicating excess argon in biotite from Fairy Meadows.

The hanging wall of the Liachar Thrust (L2) cooled through about 420 °C at 3.1 Ma, and through about 370 °C at 1.5 Ma, implying a cooling rate of 240 °C / Ma over the last 1.5 million years (Fig. 7.4). Excess argon in the biotite would lessen this rate but in any event the cooling must have been extremely rapid. Note that the 60 °C / Ma closure temperature for muscovite has been used, since average

cooling between muscovite and biotite closure was 40 °C / Ma. Note that all calculated cooling rates are average cooling rates over the time interval specified, and have uncertainties propagated by errors on both cooling ages and their assumed closure temperatures.

In summary, rocks from the edge of the massif (L2) and further south, between Tato and Fairy Meadows, all show rapid cooling from over 400 °C in the last 1.8 million years. In the case of Fairy Meadows cooling may have been even more rapid before this time, with a monazite age of 3.3 Ma reported from a migmatite (Zeitler et al. 1993). Extrapolating from cooling paths to exhumation requires a knowledge of the geotherm and its evolution through time. The limitations imposed by this requirement are discussed below.

7.4 Thermobarometric data and interpretation

Thermobarometric conditions for the last high-grade event in the massif are determined from a representative subsolidus metapelite with the equilibrium assemblage biotite-garnet-cordierite-sillimanite-K-feldspar-quartz (N1, Fig. 7.2). Analyses of solid-solution phases were obtained from a Cameca SX - 50 electron microprobe at the Department of Earth Sciences, Leeds University. Representative rim analyses, along with calculated endmember activities, are given in Table 7.2.

Thermobarometric constraints were calculated from the endmember activities using the Thermocalc program of Powell and Holland (1988). When run in average (PT) mode, for a water activity of 1, the best-fit calculation was 706 ± 50 °C at a pressure of 4.6 ± 0.5 kbar. For fluid-absent conditions, the best-fit calculation was 692 ± 50 °C at a pressure of 4.2 ± 0.5 kbar, indicating that the results are insensitive to assumptions regarding water activities during

metamorphism. Independent temperature and pressure estimates resulted in almost identical conditions, but with slightly smaller errors.

Mineral	Cordierite	Garnet	K-Feldspar	Biotite
Analysis number	cd.2/3	gt.2r2	ksp.1r2	bi.1/1
SiO_2	47.56	36.2	64.86	33.97
TiO_2	0	0.03		4.13
Al_2O_3	31.88	20.8	18.61	18.58
Cr_2O_3	-	0.02	-	-
Fe_2O_3	-	0.61	0.4	-
FeO	11.07	36.93	-	22.54
MnO	0.06	1.85	0.06	0.1
MgO	6.43	2.02	0	6.64
CaO	0	1.39	0.08	0
Na_2O	0.22	-	2.95	0.28
K_2O	0	-	12.38	9.28
H_2O	-	-	-	3.76
F	-	-	-	0.2
Cl	-	-	-	0.06
Total	97.22	99.83	99.34	99.53
O = F	-	-	-	0.09
O = Cl	-	-	-	0.01
Total weight %	97.22	99.83	99.34	99.43
Si	5.018	2.958	2.983	5.262
Ti	0	0.002	-	0.481
Al	0.977	2.003	1.009	3.393
Cr	-	0.001	-	-
Fe^{3+}	-	0.038	0.014	-
Fe^{2+}	0.977	2.524	-	2.921
Mn	0.006	0.128	0.002	0.013
Mg	1.012	0.246	0	1.533
Ca	0	0.122	0.004	0
Na	0.045	-	0.263	0.083
K	0	-	0.727	1.835
OH	-	-	-	3.885
F	-	-	-	0.099
Cl	-	-	-	0.015
Total cations	11.022	8.020	5.001	19.520

Table 7.2a. Electron microprobe analyses of representative rim compositions from sample N1.

Endmember activities	
Mg-cordierite	0.276714
Fe-cordierite	0.222005
Almandine	0.589284
Pyrope	0.000613
Grossular *	0.000084
Spessartine *	0.000077
Orthoclase	0.780124
Albite	0.739128
Phlogopite	0.013260
Annite	0.091659
Eastonite	0.019195
Na-phlogopite	0.003787

Table 7.2b. Activities of endmembers calculated from microprobe analyses (Table 7.2a). Endmembers marked with * were not used in the thermo-barometric calculations.

For the purposes of constraining thermal models of the NPHM, values of 700 ± 60 °C and 4.4 ± 0.6 kbar will be used. These may be combined with a metamorphic monazite U-Pb age of 4.0 ± 0.1 Ma reported by Smith et al. (1992) from near this locality, to determine the temperature-time curve for the massif. Taken together, these results imply an average exhumation rate over the last 4 Ma of between 3.5 and 4 mm/y. Previous P-T calculations by Zeitler et al. (1993) report two different P-T fields within the NPHM of 650 ± 50 °C and 6 ± 1 kbar, and about 600 °C and 4.1 ± 1 kbar, suggesting a retrograde path of isothermal decompression.

7.5 Problems of modelling an active orogen

There are numerous potential problems associated with attempting thermal modelling of an active orogen, five of which are briefly described here.

7.5.1 Active faults

Active faults typically move at more rapid rates than the maximum reported exhumation rates when averaged over geological time, and so faults provide a major control on thermal structure. In the case of crustal scale thrusting, the near surface geotherm will certainly be steepened if there is considerable frictional heating (England and Thompson, 1984; Grasemann, 1993), and increased erosional exhumation rates may also compress near surface isotherms. Regional scale studies often show sudden changes in cooling age across faults, as indicated by traverses across the margins of the NPHM (Zeitler et al. 1985, George et al., 1993).

At Nanga Parbat the Liachar Thrust has juxtaposed basement gneiss of the massif over quaternary gravels (Butler and Prior, 1988a) and remains active. Models of the thermal evolution of the massif margin should therefore take this fault into account, although this is not the case for the Fairy Meadows region that lies within the massif core where exhumation is thought to result from erosion of an antiformal dome structure rather than a faulted structure (Butler and Prior, 1988b).

7.5.2 Exhumation

Exhumation rates and surface uplift rates are distinct concepts, and are related by the equation

Surface uplift = Uplift of rocks - Exhumation of rocks

as discussed by England and Molnar (1990). Surface uplift and uplift of rocks are relative to the geoid, while exhumation of rocks is relative to the exposed surface. Rapid cooling rates can lead to an overestimation of exhumation rate due to a steepened near-surface geotherm, and the effect of exhumation on thermal structure is discussed below.

7.5.3 Topography

The effect of topography on isotherms will generally be minor, depending on the isotherms of interest, the amplitude and wavelength of topography, and the compression of near-surface geotherms due to advection during exhumation (Stüwe et al. 1994). Near surface isotherms, for example the 100 °C isotherm representing the closure temperature for fission track annealing in apatite, will be perturbed much more readily than a deeper isotherm, for example the 300 °C isotherm representing the closure temperature of argon in biotite.

The topography encountered at Nanga Parbat is characterised by a vertical distance of 6 km between valleys and peaks, and a horizontal wavelength of about 40 km (approximately the width of the massif). A two-dimensional analytical model of the steady-state isotherms for such topography , taken from Turcotte and

Schubert (1982, equation 4-66), has been calculated for a geotherm of about 40°C / km (Fig. 7.5).

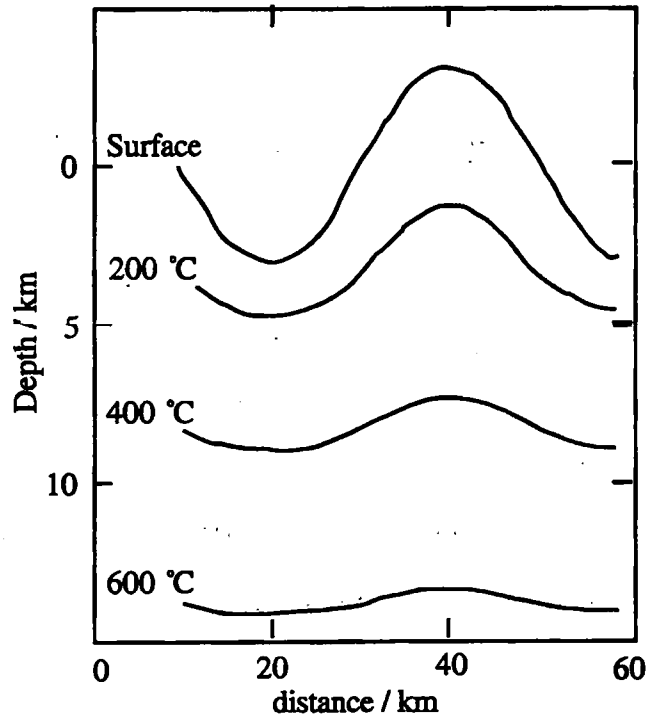

Fig. 7.5. The effect of topography on isotherms. This topography, shown with vertical exaggeration, is an approximation of a cross-section of the NPHM, with peak to valley distance of 6 km and wavelength of 40 km. This model is calculated for the steady state in the absence of exhumation, using equation (4-66) from Turcotte and Schubert (1982), with an average geothermal gradient of about 40 °C / km.

Isotherms are more compressed underneath valleys than they are underneath peaks, even though this model does not take account of exhumation and erosion. While the steady-state assumption is not valid for the vertical transport of heat in this area, the lateral variation of isotherms will be less affected unless there is a marked lateral anisotropy such as an active fault. The Liachar Thrust is such a fault, so that the findings of this section may be generally applicable to the NPHM

and other areas of extreme topography, but not to the margins of the massif, such as at Liachar.

When combined with the findings of the one-dimensional thermal model, it appears that there may be considerable perturbation of isotherms relevant to geochronology within the NPHM, since exhumation has led to a steepened near-surface geotherm. The 400 °C isotherm would probably lie at a mean depth of about 5 km in the absence of topography, so that by comparison with figure 7.5, we may expect it to be perturbed by up to 3 km underneath Nanga Parbat itself. This is in agreement with the two-dimensional model of Nanga Parbat presented in Craw et al. (1994, Fig. 5).

This perturbation of isotherms implies that differences in fission track and argon-argon cooling ages across the massif may depend partly on topographic effects as well as variable exhumation rates. Hence regional variation in cooling ages cannot be interpreted simply as implying regional variations in exhumation rate.

While variation in cooling temperatures for a single system is often applied to regional cooling patterns, enabling the identification of anomalous areas, it should not be used to estimate regional exhumation rate over time, as the following argument shows.

The average exhumation rate can be expresses as $\Delta z/\Delta t$, and average cooling rate as $\Delta T/\Delta t$, where Δt is the closure age recorded by the system, Δz is the depth from closure to the surface, and ΔT is the closure temperature.

$$\Delta z/\Delta t = (\Delta T/\Delta t) / (\Delta T/\Delta z)$$

average exhumation rate = cooling rate / geotherm

If the average geotherm ($\Delta T/\Delta z$) is assumed to be constant, then exhumation rate will be inversely proportional to age. On a graph of exhumation rate against time, exhumation will appear to be increasing towards the present day.

The apparent inverse relationship between exhumation rate and age is a necessary consequence of the false assumption of a constant geothermal gradient, since the geotherm in a rapidly exhuming region will evolve through time, and may not reach steady-state. Nonetheless a regional pattern of differences in cooling age is likely to be a useful indicator of anomalous areas and may even identify the structures accommodating anomalously rapid exhumation.

7.5.4 Heat advection by magma transport

The initial distribution of heat producing elements is also complicated by the presence of Miocene and Pliocene leucogranites in both Kohistan and the NPHM (George et al., 1993), which have transported heat producing elements upwards through the crust. Many such granites have probably now been eroded.

These leucogranites may also have advected significant heat during their ascent through the crust. The pluton near Fairy Meadows is at least 3 km^3 in volume, and there may be others as yet unmapped, hidden just below exposure level, or which have already been eroded. There are also numerous deformed dykes in the Liachar Shear zone, none of which is large enough to have advected significant heat on its own since they are generally no more than two metres wide. The total effect of a dyke swarm may be significant however, and there has certainly been widespread meteoric and metamorphic fluid activity in the area (Winslow et al., 1994) that may have contributed to thermal advection.

7.5.5 Differential erosion

Differential erosion can result in errors in thermal modelling if exhumation rates are calculated from sample elevations. Also note that in the Himalayas such differential erosion is thought to have contributed to some 20 to 30 % of the present elevation of Himalayan peaks due to isostatic compensation (Montgomery, 1994). This has implications for regional exhumation, as it affects both surface uplift (of mountain peaks only) and uplift of rocks (regionally, as isostatic compensation).

In the Nanga Parbat Massif there are at least two rivers antecedent to recent exhumation, the Indus and the Astor rivers. The NPHM is only about 40 km wide, so it is likely that isostatic compensation alone is not the only mechanism responsible for uplift of the massif, and similar thermal models may therefore be in error.

7.6 Thermal effects of exhumation - modelling Nanga Parbat

7.6.1 One-dimensional thermal models

Transient geotherms may be modelled using 1D or 2D solutions, with increasing complexity as exhumation, faulting and other features are incorporated. Although a 1D solution eliminates the possibility of incorporating topography in the model, Koons (1987) found that a thermal anomaly modelled in two dimensions approached the solution of a one-dimensional model for a high uplift zone of width greater than 15 km. For narrower zones of high uplift, the cooling effect of lateral heat conduction into adjacent non-uplifted material becomes significant. The NPHM is over 40 km in width, and so, while only the core is

being modelled, a one-dimensional solution is a reasonable approximation. In addition, surface topography is less relevant to a crustal scale model of exhumation following continental collision, where the dominant processes in shaping thermal evolution will be deep-seated and not affected by topography.

The "exhumeit" model used for this work is a one-dimensional model which allows exhumation rate to vary over time. The initial steady-state geotherm in stable Indian Plate crust must first be estimated. It is then assumed this was overthrust by a 25 km thick Kohistan Island Arc obducted "instantaneously" at 50 Ma. Between 50 Ma and 10 Ma the transient geotherm is allowed to relax towards the steady state, during erosional exhumation. From 10 Ma to the present, exhumation was rapidly increased, assuming that total exhumation for the core of the massif between 50 and 0 Ma had to lie between 30 and 35 km. This constraint follows from the cross section of Butler et al. (1988b, Fig. 9) which implied that the entire Kohistan Arc and between 5 and 10 km of Nanga Parbat material was eroded.

For all runs a 100 km thick lithosphere was used, with a constant basal heat flow of 38 mW m^{-2}. This is based on a value of heat flow into the base of Indian shield crust of 0.92 Heat Flow Units, where 1 HFU = 1 μcal / cm^2 s, taken from Rao et al. (1976).

7.6.2 Initial conditions

In order to test the significance of assumptions regarding the distribution of heat-producing elements, two different distributions were used; an exponential model with internal heat production 4 mW m^{-3} at the surface and a characteristic length-scale of 10 km, and a uniform model where the top 25 km of Nanga Parbat crust were assigned a constant value of 1.2 mW m^{-3}. Both models result in the same

overall quantity of internal heat-production in the crust. To find an equilibrium geotherm, these parameters were assigned to a model with an arbitrary initial geotherm of 15 °C / km over the entire lithosphere and allowed to equilibrate for 100 Ma with no exhumation.

7.6.3 Thermal relaxation after collision

The equilibrium models for heat flow within the Nanga Parbat crust were subjected to "instantaneous" obduction of the Kohistan Arc terrane at 50 Ma. George (1993) calculated the internal heat-production of an amphibolite sheet of Kohistan origin at 0.6 $mW\,m^{-2}$, and this value was adopted as uniform throughout Kohistan. The Kohistan arc was also assigned an initial geotherm of 15 °C / km throughout its 25 km thickness.

During thermal relaxation following obduction, erosional exhumation was allowed to occur at three different rates, which were held constant over the 40 Ma period. These were 0.025 mm/y, 0.1 mm/y and 0.25 mm/y, resulting in total unroofing of 1 km, 4 km and 10 km respectively. A background exhumation rate during this period of 0.1 mm/y is suggested from the regional geochronological datasets of Zeitler (1985) and George (1993).

Geotherms at 10 Ma for these three exhumation rates for each model of heat-production distribution are shown in figure 7.6. The important results are that the shape of the final geotherm is largely insensitive both to assumptions regarding the distribution of heat-producing elements, and to realistic variations of exhumation rates. However, runs which use an exponential distribution of heat-producing elements generally result in temperature about 50 °C greater at depth

than models using the uniform distribution, and faster exhumation rates over the period 50 to 10 Ma also result in greater temperatures at depth.

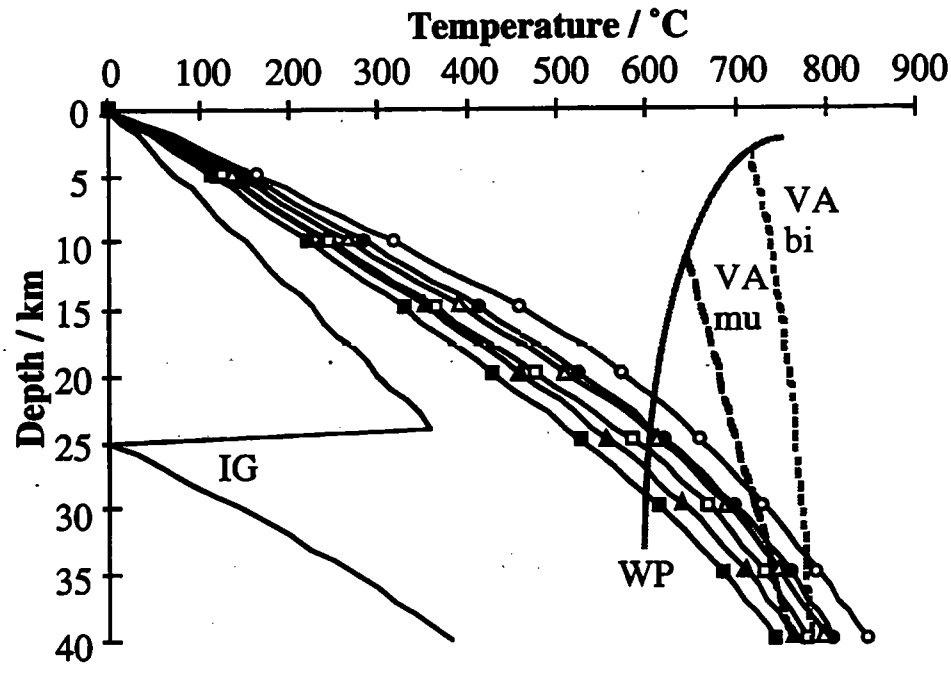

Fig. 7.6. Crustal geotherms at 10 Ma. IG is the initial geotherm at 50 Ma, with Kohistan emplaced "instantaneously" above the NPHM. Squares are for exhumation at 0.025 mm/y, triangles are for 0.1 mm/y, and circles are for 0.25 mm/y, resulting in total exhumation over the run of 1 km, 4 km and 10 km respectively. Open symbols are for the exponential decrease of heat-producing elements with depth, and black symbols are for the uniform model. WP is the wet metapelite solidus taken from Thompson (1982), VA mu is the vapour absent muscovite solidus taken from Petö (1976) and VA bi is the vapour absent biotite solidus taken from Le Breton and Thompson (1988).

7.6.4 Rapid recent exhumation

Output from the first stage of modelling provided the initial conditions for the second stage of modelling, between 10 Ma and the present day. Exhumation was increased at 10 Ma, with a range of exhumation patterns tested, within the constraint that the total exhumation experienced during both stages lay between 30 and 35 km. Patterns ranged from a constant rate of 3 mm/y, to a gentle 1 mm/y for the first 5 Ma and a rapid increase to 5 mm/y for the last 5 Ma.

Pressure - temperature paths and temperature - time paths derived from these models using the uniform model of internal heat-production are shown in figures 7.7 and 7.8. In every run assuming the exponential model of internal heat-production, temperatures at depth were about 50 °C greater compared with similar runs for which a uniform distribution is assumed.

These theoretical models are constrained by two sets of isotopic data; (i) monazite age of 4.0 ± 0.1 Ma (Smith et al., 1992) indicates either cooling through the monazite closure temperature of about 700 ± 50 °C (Copeland et al., 1988; Parrish, 1990), or the end of peak metamorphism and monazite growth, and (ii) an average muscovite age of 1.82 ± 0.16 Ma, determined from Ar-Ar data (Table 7.1) with the calculated 445 ± 30 °C closure temperature.

In addition peak P-T conditions must occur at 4.4 ± 0.6 kbar at 700 ± 60 °C, determined from phase equilibria (Table 7.3). Moreover, the absence of large volumes of granite currently exposed in the NPHM imply that pelitic lithologies never exceeded the vapour-absent biotite melting reaction. Such fertile rocks generally characterise the upper crust (Patiño Douce et al., 1990), and so it is assumed that the upper 20 km of Nanga Parbat crust are considered to be such

"fertile" rocks, and must not cross the vapour-absent biotite solidus during exhumation.

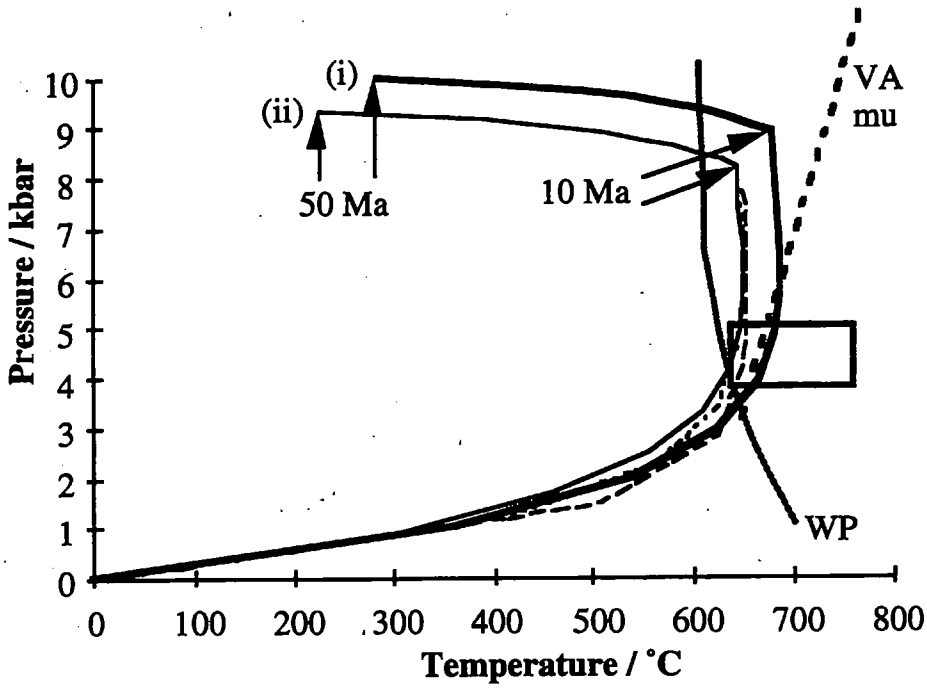

Fig. 7.7. Pressure - Temperature diagram showing the modelled P-T path of rocks exposed at the surface today. Positions at 50 Ma, immediately after emplacement of Kohistan over the NPHM, and 10 Ma, at the start of rapid exhumation, are indicated. All runs shown use the uniform distribution of heat-producing elements, and were exhumed at 0.1 mm/y between 50 and 10 Ma. Curve (i), marked by a thick solid line, is for exhumation at 3.0 mm/y between 10 and 5 Ma, and for 3.5 mm/y between 5 Ma and 0 Ma. Curve (ii), marked by a thin solid line, is for constant exhumation at 3 mm/y between 10 and 0 Ma. The dotted line is for exhumation at 2 mm/y between 10 and 5 Ma, followed by exhumation at 4 mm/y between 5 and 0 Ma. The dashed line is for exhumation at 1 mm/y between 10 and 5 Ma, followed by exhumation at 5 mm/y between 5 and 0 Ma. WP is the wet metapelite solidus taken from Thompson (1982), and VA mu is the vapour absent muscovite solidus taken from Petö (1976). The black rectangle indicates the P-T constraint of 4.4 ± 0.6 kbar at 700 ± 60 °C determined in this paper.

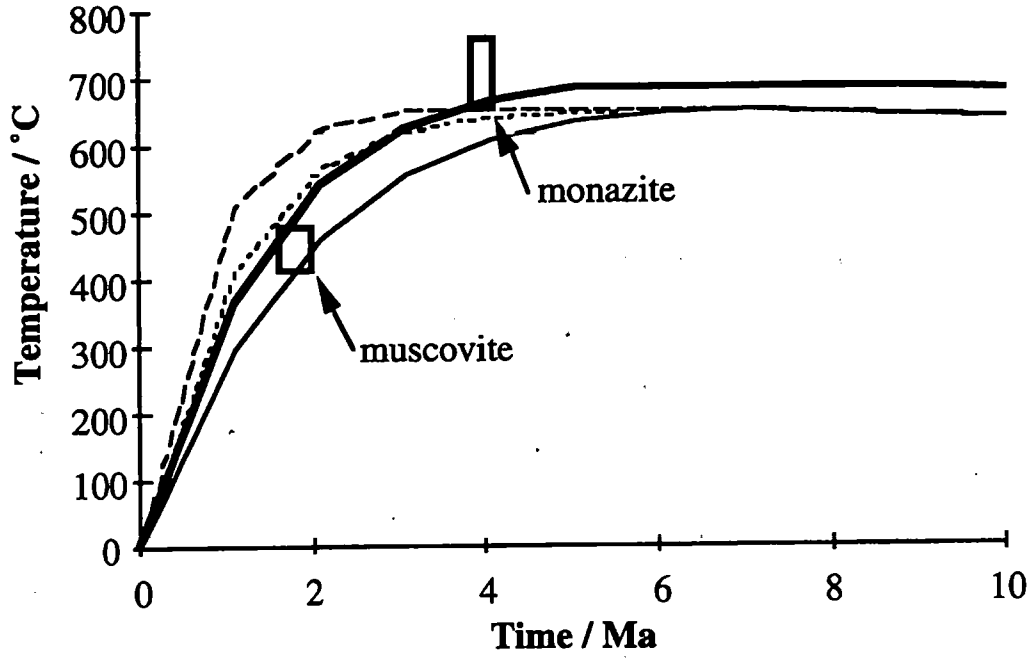

Fig. 7.8. Temperature - time curve showing the final cooling paths of rocks exhumed to the surface. The metamorphic monazite age is from Smith et al. (1992), and the muscovite cooling age is from this study. The thick solid line is for exhumation at 3.0 mm/y between 10 and 5 Ma, and for 3.5 mm/y between 5 Ma and 0 Ma. The thin solid line is for constant exhumation at 3 mm/y between 10 and 0 Ma. The dotted line is for exhumation at 2 mm/y between 10 and 5 Ma, followed by exhumation at 4 mm/y between 5 and 0 Ma. The dashed line is for exhumation at 1 mm/y between 10 and 5 Ma, followed by exhumation at 5 mm/y between 5 and 0 Ma.

Runs which assume an exponential distribution of heat-producing elements fail this criterion, since they generally result in higher temperatures at depth than models using the uniform distribution. Hence we shall assume a uniform distribution of heat-producing elements for subsequent discussion.

Runs which use an exhumation rate of 0.25 mm/y throughout the period 50 to 10 Ma do not allow rocks currently exposed at the surface to reach temperatures above 600 °C at any point during their Cenozoic history, and hence can be discounted. This is because at 10 Ma, rocks currently exposed at the surface

would be lying at a shallower depth than for runs where early exhumation was at a slower rate.

Results of this modelling preclude very high increase in exhumation rates at 5 Ma since this results in temperature excess of the muscovite closure temperature at 1.9 Ma (Fig. 7.8). Even if the muscovite age is considered unreliable, these models require that cooling of rocks now exposed below 700 °C occurred more recently than 4.0 Ma, inconsistent with the published monazite age. Note that the more rapid the recent exhumation, the larger the inconsistency between thermal modelling and geochronological constraints. For example, exhuming initially at 1 mm/y followed by 5 mm/y gives a significantly worse fit than 2 mm/y followed by 4 mm/y (Fig. 7.8).

The best fit cooling paths are obtained for exhumation rates of either 25 or 100 mm/y over the period 50 to 10 Ma, followed by exhumation at a 3.0 mm/y over the period 10 to 5 Ma, followed by an increase to 3.5 mm/y at 5 Ma (Fig. 7.8). This model implies a total of 32.5 km of exhumation since 10 Ma. The P-T paths corresponding to this range of acceptable runs indicates that some "fertile" NPHM rocks may cross the vapour absent solidus for muscovite breakdown, during the rapid recent exhumation. This fits with the observation of tourmaline-bearing leucogranites formed by vapour absent muscovite breakdown during decompression in this area (Whittington et al., 1995). Magmatic zircons from these leucogranites have yielded ages of between 2.3 Ma and 7 Ma (Zeitler and Chamberlain, 1991), confirming that the leucogranites were formed in the last 10 Ma. The results are also consistent with the isothermal decompression path derived from published P-T data (Zeitler et al., 1993).

Winslow et al. (1994) have attempted to measure the present near-surface geotherm at Nanga Parbat using fluid inclusions, and arrived at a figure of 350 °C at 6 km depth, although this estimate has considerable uncertainties. The final

near-surface geotherm for exhumation at 3 to 3.5 mm/y is 450 °C at 5 km, in agreement with this measured figure within error. Cooling paths from this model fits the measured ages, suggesting that it makes reasonable predictions of the exhumation path of exposed rocks. While the model is certainly a simplification, it is reassuring that the broad pattern of constant exhumation in the last 10 Ma is consistent with both thermobarometric estimates and geochronological constraints, while the alternative hypothesis of very rapid exhumation during the last 5 Ma appears to be inconsistent with both field and laboratory observations.

In summary, the exhumation rate at Nanga Parbat cannot be as high as 7 mm/y or recorded geochronological ages from the area would be much younger. Of the various models tested in this study, available geochronological and thermobarometric data is consistent with a path of slow exhumation following obduction of Kohistan at 50 Ma, followed by more rapid exhumation at a roughly constant rate of between 3 and 4 mm/y over the past 10 Ma. Nonetheless, this is still considerably greater than exhumation rates of about 1.2 mm/y determined from the main Himalayan orogen (Hubbard et al., 1991).

7.7 Conclusions

New ^{40}Ar-^{39}Ar geochronological data have been presented from the Tato Valley in the Nanga Parbat Haramosh Massif in northern Pakistan. The presence of excess argon has rendered biotite ages unreliable, but because the effect of excess argon is to increase the apparent cooling age, these provide a minimum constraint on the cooling rate. Muscovite ages suggest a cooling rate of at least 200 °C / m.y.

Thermobarometric data from equilibrium pelitic assemblages suggest peak metamorphic conditions were about 700 °C and 4.4 kbar. The combination of

geochronologic and thermobarometric results give strong constraints on thermal models of the evolution of the NPHM between 50 Ma and the present day. Further constraints include structural arguments, bracketing total exhumation since 50 Ma as between about 30 and 35 km, and the absence of large melt volumes exposed at the surface, indicating that fertile levels of NPHM crust did not cross the vapour-absent biotite solidus for pelitic assemblages.

Rather than assuming a geothermal gradient, which would necessarily change rapidly from the advection of heat by rapidly exhumed rocks, this study has applied one-dimensional thermal modelling to show that the available cooling ages fit a path of roughly constant exhumation at a rate of between 3 and 4 mm/y over the last 10 Ma after slow exhumation over the period 50 to 10 Ma. This is in sharp contrast to previous estimates of a rapidly increasing exhumation rate of 7 mm/y. The predicted near-surface geotherm resulting from this model lie within error of that calculated by Winslow et al. (1994) from fluid inclusion data. It should be emphasised that an increasing cooling rate through time does not necessarily imply increasing exhumation rates.

CHAPTER 8 - SUMMARY

This thesis has investigated the relations between magmatism, metamorphism, exhumation and tectonic controls in an active collisional orogen. The NPHM is a rapidly eroding, thrust-related antiform that is distinct from other regions of the Himalayan orogen in being both intruded by Late Miocene-Pliocene anatectic granites and permeated by a vigorous hydrothermal system. Exhumation is achieved by erosion during thrusting along the Liachar Thrust, in the apparent absence of extensional tectonics.

The NPHM has formed in response to rotation of Indian Plate about an "pinning point" to a major Himalayan Thrust, possibly the MCT. Rapid erosion of the antiformal structure has resulted in both exhumation of deeper structural levels than are exposed elsewhere in the Himalayan orogen, and the development of 7 km vertical topography across 20 km horizontal distance. Rapid exhumation has in turn led to an extreme near-surface geothermal gradient, and the combination of this geotherm with the topography has resulted in a vigorous fluid flux, making the NPHM an ideal place to study interactions between deformation, magmatism and hydrothermal activity during active crustal thickening (Butler et al., 1997).

A tacit assumption that underpins many Himalayan studies is that all structures relate to the youngest orogenic episode. However, the NPHM is a poly-metamorphic terrain, and it is imperative to establish a basement stratigraphy to discern between pre-Himalayan and more recent events. The metabasic sheets described in Chapter 5 provide an ideal marker to separate the two.

The precise ages of basement migmatisation, isotopic homogenisation, and intrusion by basic magmas, remain unresolved, and these processes may even

represent three unrelated events, separated by hundreds of millions of years. However, the isotopic data presented in Chapter 5 are tentatively interpreted to imply early Proterozoic intrusion of basic sheets at about 2 to 2.5 Ga, within error of the timing of basement isotopic homogenisation as recorded by errorchrons from both Rb-Sr and Sm-Nd systems. Field relations indicate that the intrusion of basic sheets post-dated granulite facies metamorphism and migmatisation of the basement.

The Neogene deviation of the NPHM from the patterns observed in the main Himalayan orogen is exemplified by the recognition of two melting events within the last 10 Ma. At depths in excess of 20 km, small batches of leucogranitic melt have been generated by fluid-absent breakdown of muscovite from metapelitic lithologies by vapour-absent muscovite "decompression" melting. Melt extraction at the relatively low melt fractions generated by this reaction was probably enhanced by deformation. Melt migration through the crust was aided by low water activities in the melt, and a shallow geothermal gradient at depth, contrasting with the steep near-surface geotherm.

These leucogranites are geochemically similar to the Miocene High Himalayan Leucogranites, but generated at least 10 million years later than the Miocene melts. Decompression and melting in the main orogen were pene-contemporaneous at circa 20 to 24 Ma, when the extensional STDS was active. Decompression at Nanga Parbat appears to have been achieved solely by erosion, and this may explain the longer duration of magmatism at Nanga Parbat, spanning at least the period 8 Ma to 1 Ma (Zeitler and Chamberlain, 1991; Zeitler et al., 1993).

At intermediate depths (~15 km), limited fluid infiltration is restricted to shear zones, resulting in a second localised anatectic event. The cordierite seams are interpreted to be restitic assemblages resulting from this event, although their variable geochemistry suggests that the melt may have been trapped and

recrystallised *in situ* in many cases. These seams are unknown from any other part of the Himalayan chain, are made possible by the elevated near-surface geothermal gradient, which allows fluid infiltration to depths at anatectic temperatures.

Nanga Parbat provides an ideal field laboratory to investigate interactions between fluid activity (including magmas) and deformation. Within the upper 8 km of crust, magmatic and meteoric fluid fluxes are channelised by active structures providing a feedback mechanism for focussing deformation. Leucogranite sheets show a range of pre-full crystallisation and high-temperature crystal-plastic textures indicative of strain localisation onto these sheets and away from the country rocks. At subsolidus temperatures, meteoric fluids promote strain localisation and may trigger cataclastic deformation. Since near-surface geothermal gradients are unusually steep, the macroscopic transition between distributed shearing and substantial, but localised, cataclastic deformation occurred at amphibolite-facies conditions (~600 °C).

The timing and conditions of metamorphism also differ between the NPHM and both the main orogen, and elsewhere in northern Pakistan. In the southern NPHM, sillimanite is the stable aluminosilicate phase and temperatures were high enough for spinel-cordierite intergrowths to form by very localised vapour-absent biotite breakdown in lithologies of suitable composition. Recorded pressures vary from 10 to 3 kbar, at temperatures restricted to the range 600 to 750 °C, providing further evidence for rapid near-isothermal decompression. U-Pb studies on metamorphic monazite (Smith et al., 1992, 1994; Zeitler et al., 1993) indicate that metamorphism occurred synchronously with anatexis, in the last 10 Ma.

On the eastern margin, kyanite is the stable aluminosilicate phase (Pognante et al., 1993), and P-T studies indicate that the same pressure range was traversed in both areas, but that temperatures were lower in the east. This observation is consistent

with slower exhumation acting on passive folding rather than active thrusting on the western margin.

Much future work remains to be done in the NPHM, which has recently become the focus for several research projects. Perhaps of most interest is the missing geochronological record between collision (circa 60 Ma) and Neogene activity (since about 10 Ma). Studies of the timing of garnet growth may reveal more about this period, which involved crustal thickening, obduction of the Kohistan arc, and thermal relaxation. Because Nanga Parbat has experienced much more rapid exhumation than surrounding areas, rocks currently exposed in this area have probably experienced a greater depth of burial than those from surrounding regions. Assuming that the anomalous exhumation is restricted to the last few millions of years, detailed work on these rocks should reveal features of the P-T-t path experienced by the lower crust which remain hidden to workers in other parts of the Himalaya.

Syntaxial formation is occurring elsewhere, at both ends of the Himalayan orogen. In northern Pakistan, the Hazara syntaxis was formed by rotation of principal thrusting direction in the opposite sense to that which generated the NPHM, and the Besham antiform may be a proto-syntaxis developing in a similar style to the NPHM as thrusting migrates southwards.

At the eastern end of the orogen, in south-east Tibet, the Namche Barwa syntaxis has revealed similarly young ages of metamorphism, and rapid cooling from high temperatures (Burg et al., 1997). The lack of post-tectonic leucogranites at Namche Barwa may be due to the P-T path of currently exposed lithologies, which may be considered analogous to that followed by NPHM in the past. If rapid exhumation continues, rocks presently at mid-crustal levels may stay at elevated temperatures long enough to cross vapour-absent melting reactions. This process may already be occurring at depth, but several kilometres of exhumation will be required to

expose the granitic products of these reactions at the surface. The specific tectonic setting of the Namche Barwa syntaxis is also different, since the overlying material is the Transhimalayan batholith on the southern margin of Asia, and there has been no island arc obduction such as occurred between Kohistan and Nanga Parbat in the west.

Syntaxial development in older orogenic belts may be more common than is currently recognised. One problem with recognising such regions is that the differences in timing of metamorphism, anatexis and cooling may currently be beyond geochronological resolution. Ancient syntaxial regions may be identified by anomalous P-T results (higher T, lower P) compared with other parts of the orogen, different ages of granite production, although not necessarily different geochemical signatures, and younger cooling ages. The causes of syntaxial development in northern Pakistan suggest that this feature will be more common at the "corners" of orogenic belts.

Several more general findings have also emerged from this work, particularly with regard to the various techniques employed. The use of internally consistent datasets enable useful comparison of the P-T conditions recorded by different samples in different areas, so that uncertainties introduced by different calibrations of thermobarometers can be eliminated. The use of computer programs such as Thermocalc reduces the problems of different closure temperatures associated with elemental exchange and net transfer reactions, although the rapid cooling of rocks at Nanga Parbat from temperatures in excess of 700 °C has resulted in rapid closure of thermobarometers, reducing this problem.

The assumption of an atmospheric ^{36}Ar component when interpreting $^{40}Ar/^{39}Ar$ data has also been challenged. At Nanga Parbat, excess argon is associated with magmatic and metamorphic fluid evolution, whereas samples recrystallised in the

Liachar Shear Zone in the presence of meteoric fluids record atmospheric $^{40}Ar/^{36}Ar$ intercepts. The use of argon correlation diagrams is highly recommended, and the interpretation of scattered results in terms of varying degrees of excess argon contamination enables maximum constraints to be placed on the minimum age of closure.

The patterns of excess argon revealed across the massif may be interpreted in terms of fluid flow. Atmospheric $^{40}Ar/^{36}Ar$ intercepts are restricted almost exclusively to samples which have been deformed near the brittle-ductile transition in the Liachar Shear Zone, confirming the conclusion made by Butler et al. (1997) that despite extreme surface topography, the meteoric fluid flux at Nanga Parbat is restricted to the upper ~8 km of the crust.

Although no other geochronological techniques were employed in this study, many references have been made to the U-Pb accessory phase data reported by Zeitler and co-workers (Zeitler et al., 1982, 1989, 1993; Zeitler, 1985, 1989; Zeitler and Chamberlain, 1991). Old zircon cores reported by this group record inherited ages of ~2500 Ma, ~1850 Ma, and ~500 Ma, which indicate the extended history of the NPHM. These ages are usually interpreted to be protolith ages, but the presence of retrogressed granulites in the Indus valley (Wheeler et al., 1995) raises the question of whether the closure temperature of U-Pb in zircon was exceeded during Precambrian metamorphism, in which case zircon ages may record this event rather than protolith formation.

While fabric-forming phases such as micas may be dated using the ^{40}Ar-^{39}Ar and Rb-Sr techniques, these techniques will record ages of regional cooling rather than peak metamorphism in high grade terranes such as the NPHM. Accessory phases such as zircon, which have high closure temperatures, may be dated precisely using the SHRIMP or a similar microprobe with good spatial, temporal and mass resolution (Zeitler, 1989). However, the interpretation of these dates may be

problematic without petrofabric information to relate the age to particular events. Garnet may be dated by a range of isotopic systems, has high closure temperatures to isotopic diffusion, and is a fabric-forming mineral in metapelitic lithologies over a wide range of P-T conditions. Combined with metamorphic and structural studies, isotopic dating of garnet may shed further light on the early Cenozoic prograde history of the NPHM, as this technique is already doing for the main Himalayan orogen (e.g. Prince et al., 1997; Vance et al., 1997).

A further implication of zircon inheritance in the leucogranites is that temperatures calculated from the zircon thermometer of Watson and Harrison (1983) should be overestimates. However, the narrow range of calculated temperatures, and the coincidence of temperatures calculated by both zircon and monazite thermometers, would be unlikely to result from variably inherited zirconium contents. The most reasonable explanation is that the inherited component is volumetrically small, although further work on the application of this extremely useful technique may shed further light on this conundrum.

Recent workers (e.g. Jamieson, 1991; Batt and Braun, 1997) have emphasised the importance of the second and third dimensions when considering orogenesis. The simpler one-dimensional modelling presented in this thesis identifies first-order implications, and the main conclusions from Chapter 7 that a steady-state geotherm can rarely be assumed, and that an increasing cooling rate does not necessarily imply an increasing exhumation rate, are perhaps best illustrated by simpler models which are valid assuming that lateral heat flow is negligible and exhumation is controlled by erosion rather than tectonics. While neither if these assumptions is strictly valid for the case of Nanga Parbat, the first-order control on thermal structure is rapid exhumation, and hence a one-dimensional model predicts the metamorphic and magmatic behaviour of the crust perfectly adequately. However, the presence of major discontinuities such as the MCT require at least two-dimensional modelling even for relatively linear orogenic belts

such as the main Himalayan range, if the spatial pattern of recorded P-T paths and anatectic behaviour is to be successfully interpreted.

Finally, it is interesting to note that nearly every facet of the plate tectonic cycle is represented within a few kilometres of Nanga Parbat. Admittedly, the old mid-ocean ridge which gave birth to the Tethys is now a few kilometres below the surface, but basaltic dykes associated with continental rifting are still to be found. The Kohistan island arc represents the early consumption of oceanic crust, while the collision and movement on the MMT buried the remainder, but blueschists and ophiolites remain exposed along the suture zone. Metamorphism and anatectic recycling of old crust are clearly in evidence, and these rocks are now being eroded, either redeposited immediately as moraine, or transported down the Indus and eventually finding their way to the Arabian Sea.

REFERENCES

Ahmad, T., and Bhat, M.I., 1987. Geochemistry and petrogenesis of the Mandi-Darla volcanics, northwestern Himalayas. Precambrian Research, v. 37, p. 231-256.

Ahmad, T., and Tarney, J., 1991. Geochemistry and petrogenesis of Garwhal volcanics: implications for evolution of the north Indian lithosphere. Precambrian Research, v. 50, p. 69-88.

Allègre, C.J., and 34 others, 1984. Structure and evolution of the Himalaya-Tibet orogenic belt. Nature, v. 307, p. 17-22.

Allen, T., and Chamberlain, C.P., 1991. Metamorphic evidence for an inverted crustal section, with constraints on the main Karakorum thrust, Baltistan, Pakistan. Journal of Metamorphic Geology, v. 9, p. 403-418.

Arnaud, N.O., and Kelley, S.P., 1995. Evidence for excess argon during high pressure metamorphism in the Dora Maira Massif (western Alps, Italy), using an ulra-violet laser ablation microprobe ^{40}Ar-^{39}Ar technique, Contributions to Mineralogy, v. 121, p. 1-11.

Atherton, M.P., 1968. The variation in garnet, biotite and chlorite composition in medium grade pelitic rocks from the Dalradian, Scotland, with particular reference to the zonation of garnet. Contributions to Mineralogy and Petrology, v. 18, p. 347-371.

Ayres, M.W., 1997. Trace element behaviour during high-grade metamorphism and anatexis of the Himalayas [unpublished PhD thesis]: the Open University, Milton Keynes, 400 pp.

Ayres, M.W., Harris, N.B.W., and Vance, D., 1997. Possible constraints on anatectic melt residence times from accessory mineral dissolution rates: an example from Himalayan leucogranites. Mineralogical Magazine, v. 61, p. 29-36.

Ayres, M.W., and Vance, D., 1997. A comparative study of diffusion profiles in Himalayan and Dalradian garnets: Constraints on diffusion data and the relative duration of the metamorphic events. Contributions to Mineralogy and Petrology, in press.

Baldwin, S.L., Harrison, T.M., and Fitzgerald, J.D., 1990. Diffusion of ^{40}Ar in metamorphic hornblende. Contributions to Mineralogy and Petrology, v. 105 p. 691-703.

Bard , J.P., Maluski, H., Matte, P., and Proust, F., 1980. The Kohistan sequence: crust and mantle of an obducted island arc. Special Issue of the Geological Bulletin of the University of Peshawar, v. 13, p. 87-94.

Bard, J.P., 1983. Metamorphism of an obducted island arc: Example of the Kohistan Sequence (Pakistan) in the Himalayan collided range. Earth and Planetary Science Letters, v. 65, p. 133-144.

Batt, G.E. and Braun, J., 1997. On the thermomechanical evolution of compressional orogens. Geophysical Journal International, v. 128, p. 364-382.

Bau, M., 1991. Rare-earth element mobility during hydrothermal and metamorphic fluid-rock interaction and the significance of the oxidation state of europium. Chemical Geology, v. 93, p. 219-230.

Beck, R.A., and 13 others, 1995. Stratigraphic evidence for an early collision between northwest India and Asia. Nature, v. 373, p. 55-58.

Becke, F., 1908. Über myrmekit. Min. Pet. Mitt., v. 27, p. 377-390.

Bell, T.H., 1985. Deformation partitioning and porphyroblast rotation in metamorphic rocks: a radical reinterpretation. Journal of Metamorphic Petrology, v. 3, p. 109-118.

Bell, T.H., and Rubenach, M.J., 1980. Crenulation cleavage development; evidence for progressive bulk inhomogeneous shortening from "millipede" microstructures in the Robertson River Metamorphics. Tectonophysics, v. 68, p. 9-15.

Bertrand, J.M., Kienast, J.R., and Pinardon, J.L., 1988. Structure and metamorphism of the Karakorum gneisses in the Braldu-Baltoro Valley (north Pakistan). Geodinimica Acta, v. 2, p. 135-150.

Besse, J., Courtillot, V., Pozzi, J.P., Westphal, M., and Zhou, Y.X., 1984. Palaeomagnetic estimates of crustal shortening in the Himalayan Thrusts and Zangbo suture. Nature, v. 311, p. 621-626.

Bhat, M.I., Zainuddin, S.M., and Rais, A., 1981. Panjal Trap chemistry and birth of Tethys. Geological Magazine, v. 118 (4), p. 367-375.

Bhat, M.I., 1984. Abor volcanics: further evidence for the birth of the Tethys Ocean in the Himalayan segment. Journal of the Geological Society, London, v. 141, p. 763 - 775.

Bhat, M.I., 1987. Spasmodic rift reactivation and its role in the pre-orogenic evolution of the Himalayan region. Tectonophysics, v. 134, p. 103-127.

Bhat, M.I., and Ahmad, T., 1990. Petrogenesis and the mantle source characteristics of the Abor volcanic rocks, Eastern Himalayas. Journal of the Geological Society of India, v. 36, p. 227-246.

Bhat, M.I., and Le Fort, P., 1992. Sm-Nd age and petrogenesis of Rampur metavolcanic rocks, NW Himalayas: Late Archaean relics in the Himalaya belt. Precambrian Research, v. 56, p. 191-210.

Bhat, M.I., Le Fort, P., and Ahmad, T., 1994. Bafliaz volcanics, NW Himalaya: origin of a bimodal, tholeiite and alkali basalt suite. Chemical Geology, v. 114, p. 217-234.

Bird, P., 1978. Initiation of intracontinental subduction in the Himalayas. Journal of Geophysical Research, v. 83, p. 4975-4987.

Blanckenburg, F. von, Villa, I.M., Baur, H., Morteani, G., and Steiger, R.H., 1989. Time calibration of a P-T path from the Western Tauern Window, Eastern Alps: the problem of closure temperatures. Contributions to Mineralogy and Petrology, v. 101, p. 1-11.

Blundy, J.D., and Holland, T.J.B., 1990. Calcic amphibole equilibria and a new amphibole-plagioclase geothermometer. Contributions to Mineralogy and Petrology, v. 104, p. 208-224.

Blundy, J.D., and Wood, B.J., 1991. Crystal-chemical controls on the partitioning of Sr and Ba between plagioclase feldspar, silicate melts, and hydrothermal solutions. Geochimica et Cosmochimica Acta, v. 55, p. 193-209.

Bossart, P., Dietrich, D., Greco, A., Ottiger, R., and Ramsay, J.G., 1988. The tectonic structure of the Hazara-Kashmir Syntaxis, southern Himalayas, Pakistan. Tectonics, v. 7., p. 273-297.

Brookfield, M.E., and Reynolds, P.H., 1981. Late Cretaceous emplacement of the Indus suture zone ophiolitic melanges and an Eocene-Oligocene magmatic arc on the northern edge of the Indian Plate. Earth and Planetary Science Letters, v. 55, p. 157-162.

Brouand, M., Banzet, G., and Barbey, P., 1990. Zircon behaviour during crustal anatexis. Evidence from the Tibetan Slab migmatites (Nepal). Journal of Volcanology and Geothermal Research, v. 44, p. 143-161.

Brunel, M., and Kienast, J.R., 1986. Étude petro-structurale des chevauchements ductiles himalayans sur la transversale de l'Everest-Makalu (Nepal oriental): Canadian Journal of Earth Sciences, v. 23, p. 1117-1137.

Burbank, D.W., Leland, J., Fielding, E., Anderson, R.S., Brozovic, N., Reid, M.R., and Duncan, C., 1996. Bedrock incision, rock uplift and threshold hil,lslopes in the northwestern Himalayas. Nature, v. 379, p. 505-510.

Burchfiel, B.C., and Royden, L.H., 1985. North-south extension within the convergent Himalayan region. Geology, v. 13, p. 679-682.

Burchfiel, B.C., Zhiliang, C., Hodges, K.V., Yuping, L., Royden, L.H., Changrong, D., and Jiene, X., 1992. The South Tibetan Detachment System, Himalayan Orogen: Extension contemporaneous with and parallel to shortening in a collisional mountain belt. Geological Society of America Special Paper, v. 269, p. 1-41.

Burg, J.P., Brunel, M., Gapais, D., Chen, G.M., and Liu, G.H., 1984. Deformation of leucogranites of the crystalline Main Central Thrust Sheet in southern Tibet (China). Journal of Structural Geology, v. 6, p. 535-542.

Burg, J.-P., Maurin, J.-C., Nievergelt, P., Oberli, F., Seward, D., Dhao Zhizhong, Davy, P., and Meier, M., 1997. The Namche Barwa syntaxis (SE Tibet): A deeply eroded crustal antiform. In: Abstract volume for the 12th Himalaya-

Karakorum-Tibet international workshop, p. 15-16. Academia Nazionale dei Lincei, Roma, Italy, 240 pp.

Butler, R.W.H., and Prior, D.J., 1988a, Tectonic controls on the uplift of the Nanga Parbat Massif, Pakistan Himalayas: Nature, v. 333., p. 247-250.

Butler, R.W.H. and Prior, D.J., 1988b. Anatomy of a continental subduction zone: the Main Mantle Thrust in Northern Pakistan. Geologische Rundschau, v. 77, p. 239-255.

Butler, R.W.H., Owen, W. and Prior, D.J., 1988. Flashfloods, earthquakes and uplift in the Pakistan Himalayas. Geology Today, v. 4, p. 197 - 201.

Butler, R.W.H., Prior, D.J., and Knipe, R.J., 1989, Neotectonics of the Nanga Parbat syntaxis, Pakistan, and crustal stacking in the northwest Himalayas: Earth and Planetary Science Letters, v. 94, p. 329-343.

Butler, R.W.H., George, M., Harris, N.B.W., Jones, C., Prior, D.J., Treloar, P.J., and Wheeler, J., 1992, Geology of the northern part of the Nanga Parbat massif, northern Pakistan, and its implications for Himalayan tectonics: Journal of the Geological Society, London, v. 149, p. 557-567.

Butler, R.W.H., 1995. When did India hit Asia? Nature, v. 373, p. 20-21.

Butler, R.W.H., Harris, N.B.W. and Whittington, A.G., 1997. Interactions between deformation, magmatism and hydrothermal activity during active crustal thickening: a field example from Nanga Parbat, Pakistan Himalayas. Mineralogical Magazine, v. 61, p. 37-51.

Carrington, D.P. and Harley, S.H., 1995. Partial melting and phase relations in metapelites: an experimental petrogenetic grid in the KFMASH system. Contributions to Mineralogy and Petrology, v. 120, p. 270-291.

Carrington, D.P. and Watt, G.R., 1995. A geochemical and experimental study of the role of K-feldspar during water-undersaturated melting of metapelites. Chemical Geology, v. 122, p. 59-76.

Cavallini, M., Vielzeuf, D., Bottazzi, P., Mazzuchelli, M., Martin, H., and Ottolini, L., 1995. Direct measurements of rare-earth contents in partial melts from metapelites. European Union of Geosciences, 8th meeting, Strasbourg, Terra Abstracts, abstract supplement no. 1 to Terra Nova, v. 7, p.143.

Chakraborty, S., and Ganguly, J., 1990. Compositional zoning and cation diffusion in garnets. In: Ganguly, J., (ed.), Diffusion, atomic ordering, and mass transport. Selected topics in geochemistry, 8. Springer-Verlag, p. 120-175.

Chalaron, E., and Mugnier, J.L., 1993. Séquence de propagation des failles dans un prisme d'accrétion: une modélisation numérique. Bull. Geol. Soc. France, v. 164, p. 113-121.

Chalaron, E., Mugnier, J.L., and Mascle, G., 1995. Control of thrust tectonics in the Himalayan foothills: a view from a numerical model. Tectonophysics, v. 248, p. 139-163.

Chamberlain, C.P., Jan, Q., and Zeitler, P.K., 1989. A Petrologic record of the collision between the Kohistan Island arc and the Indian Plate, northwestern Himalaya. In: Malinconico, L.L., and Lillie, R.J. (eds.), "Tectonics of the western Himalayas". Geological Society of America Special Paper 232, p. 23-32.

Chamberlain, C.P., Zeitler, P.K., and Erickson, E., 1991. Constraints on the tectonic evolution of the northwestern Himalaya from geochronologic and petrologic studies of the Babusar Pass, Pakistan. Journal of Geology, v. 99, p. 829-849.

Chamberlain, C.P., Zeitler, P.K., Barnett, D.E., Winslow, D.M., Poulson, S.R., Leahy, T., and Hammer, J.E., 1995. Active hydrothermal systems during the recent uplift of Nanga Parbat, Pakistan Himalaya. Journal of Geophysical Research, v. 100, p. 439-453.

Clarke, D.B., 1995. Cordierite in felsic igneous rocks: a synthesis: Mineralogical Magazine, v. 59, p. 311-325.

Clemens, J.D., and Mawer, C.K., 1992, Granitic magma transport by fracture propagation. Tectonophysics, v. 204, p. 339-360.

Condie, K.C., and Sinha, A.K., 1996. Rare earth and other trace element mobility during mylonitisation; a comparison of the Brevard and Hope Valley shear zones in the Appalachian Mountains, USA. Journal of Metamorphic Geology, v. 14, p. 213-226.

Copeland, P., Parrish, R.R., and Harrison, T.M., 1988. Identification of inherited radiogenic Pb in monazite and its implications for U-b systematics. Nature, v. 333, p. 760-763.

Copeland, P., Harrison, T.M., Hodges, K.V., Maruejol, P., Le Fort, P., and Pecher, A., 1991. An early Pliocene thermal disturbance of the Main Central Thrust, Central Nepal: Implications for Himalayan Tectnics. Journal of Geophysical Research, v. 96, p. 8475-8500.

Courtillot, V., Besse, J., Vandamme, D., Montigny, R., Jaeger, J.J., and Cappetta, H., 1986. Deccan flood basalts at the Cretaceous/Tertiary boundary? Earth and Planetary Science Letters, v. 80, p. 361-374.

Coward, M.P., Jan, M.Q., Rex, D., Tarney, J., Thirwall, M., and Windley, B.F., 1982. Geo-tectonic framework of the Himalaya of N. Pakistan. Journal of the Geological Society, London., v. 139. p. 299-308.

Coward, M.P., and Butler, R.W.H., 1985. Thrust tectonics and the deep structure of the Pakistan Himalaya. Geology, v. 13, p. 417-420.

Coward, M.P., Windley, B.F., Broughton, R.D., Luff, I.W., Petterson. M.G., Pudsey, C.J., Rex. D.C., and Asif Khan, M., 1986. Collision Tectonics in the NW Himalayas. In: Coward, M.P., and Ries, A., (eds.), "Collision Tectonics", Geological Society Special Publication 19, p. 203-219.

Coward, M.P., Butler, R.W.H., Asif Khan, M., and Knipe, R.J., 1987. The tectonic history of Kohistan and its implications for Himalayan structure. Journal of the Geological Society, London, v. 144, p. 377-391.

Coward, M.P., Butler, R.W.H., Chambers, A.F., Graham, R.H., Izatt, C.N., Asif Khan, M., Knipe, R.J., Prior,D.J., Treloar, P.J., and Williams, M.P., 1988. Folding and imbrication of the Indian crust during Himalayan collision. Philosophical Transactions of the Royal Society, London, v. 326, p. 89-116.

Craw, D., Koons, P.O., Winslow, D., Chamberlain, C.P. and Zeitler, P.K., 1994. Boiling fluids in a region of rapid uplift, Nanga Parbat Massif, Pakistan. Earth and Planetary Science Letters, v. 128, p. 169-182.

Crawford, M.B., and Windley, B.F., 1990. Leucogranites of the Himalaya / Karakorum: implications for magmatic evolution within collisional belts and

the study of collisional-related leucogranite petrogenesis. Journal of Volcanology and Geothermal Research, v. 44, p. 1-19.

Crawford, M.B., and Searle, M.P., 1992. Field relationships and geochemistry of pre-collisional (India-Asia) granitoid magmatism in the central Karakorum, northern Pakistan. Tectonophysics, v. 206, p. 171-192.

Cronin, V.S., Schurter, G.J., Sverdrup K.A., 1993. Preliminary Landsat lineament analysis of the northern Nanga Parbat-Haramosh massif, northwest Himalaya. In: Treloar, P.J., and Searle, M.P., (eds.), Himalayan Tectonics. Geological Society Special Publication 74, p. 193-206.

Dahl, P.S., 1996. The crystal-chemical basis for Ar retention in micas; inferences from interlayer partitioning and implications for geochronology. Contributions to Mineralogy and Petrology, v. 123, p. 22-39.

Dasgupta, S., Sengupta, P., Ehl, J., Raith, M. and Bardhan, S., 1995. Reaction textures in a suite of spinel granulites from the Eastern Ghats Belt, India: Evidence for polymetamorphism, a partial petrogenetic grid in the system KFMASH and the roles of ZnO and Fe_2O_3. Journal of Petrology, v. 36, p. 345-461.

Debon, F., Le Fort, P., Sheppard, S.M.F., and Sonet, J., 1986. The four plutonic belts of the Transhimalaya-Himalaya: a chemical, mineralogical, isotopic and chronological synthesis along aTibet-Nepal section. Journal of Petrology, v. 27, p. 219-250.

Debon, F., Le Fort, P., Dautel, D., Sonet, J., and Zimmerman, J.L., 1987. Granites of W. Karakorum and northern Kohistan (Pakistan): A composite mid-Cretaceous to upper Cenozoic magmatism. Lithos, v. 20, p. 19-40.

Deer, W.A., Howie, R.A., and Zussman, J., 1992. An introduction to the rock-forming minerals, 2nd edition. Longman, England, 696pp.

Dempster, T.J., 1985. Garnet zoning and metamorphism of the Barrovian Type area, Scotland. Contributions to Mineralogy and Petrology, v. 89, p. 30-38.

DePaolo, D.J., and Wasserburg, G.J., 1976. Nd isotopic variations and petrogenetic models. Geophysical Research Letters, v. 3, p. 249-252.

Desio, A., Tongiorgi, E., and Ferrara, G., 1964. On the geological age of somegranites of the Karakorum, Hindu Kush and Badakhstan, central Asia. Proc. 22nd Intern. Geol. Congr., New Delhi, v. 11, p. 479-496.

Desio, A., 1976. Some geotectonic problems of the Kashmir Himalaya-Karakorum-Hindu Kush-Pamir area. In: Geotettonica delle zone orogeniche del Kashmir Himalaya-Karakorum-Hindu Kush-Pamir, Atti dei convegni Lincei, v. 21, p. 115-129.

Desio, A., 1979. Geologic evolution of the Karakorum. In: Farah, A., and DeJong, K.A. (eds.), Geodynamics of Pakistan, Quetta, p. 111-124.

Dewey, J.F., Shackleton, R.M., Chengfa, C., and Yiyin, S., 1988. The tectonic evolution of the Tibetan Plateau. Philosophical Transactions of the Royal Society, London, v. 327, p. 379-413.

Dewey, J.F., Cande, S., and Pitman, W.C., 1989. Tectonic evolution of the India / Eurasia collision zone. Eclogae geologica Helvetiae, v. 82, p. 717-734.

Didier, J., and Dupraz, J., 1985. Magmatic and metasomatic cordierites in the Velay granitic massif (French Massif Central), in "The Crust - The Significance of Granites Gneisses in the Lithosphere". Theophrastus Publications, SA, Athens, p. 35-77.

Dietrich, V.J., Wolfgang, F., and Honegger, K., 1983. A Jurassic-Cretaceous island arc in the Ladakh Himalayas. Journal of Volcanology and Geothermal Research, v. 18, p. 405-433.

Dodson, M.H., 1973. Closure temperature in cooling geochronological and petrological systems. Contributions to Mineralogy and Petrology, v. 40, p. 259-274.

Duncan, A.R., 1987. The Karoo igneous province - a problem area for inferring tectonic setting from basalt geochemistry. Journal of Volcanology and Geothermal Research, v. 32, p. 13-34.

England, P.C. and Thompson, A., 1984. Pressure-temperature-time paths of regional metamorphism I. Heat transfer during the evolution of regions of thickened continental crust. Journal of Petrology, v. 25, p. 894-928.

England, P.C., and Houseman, G.A., 1988. The mechanics of the Tibetan Plateau. Philosophical Transactions of the Royal Society, London, v. A326, p. 310-319.

England, P.C. and Molnar, P., 1990. Surface uplift, uplift of rocks, and exhumation of rocks. Geology, v. 18, p. 1173-1177.

England, P., Le Fort, P., Molnar, P., and Pecher, A., 1992. Heat sources for Tertiary metamorphism and anatexis in the Annapurna-Manaslu region, central Nepal: Journal of Geophysical Research, v. 97 B2, p. 2107-2128.

Fitzsimons, I.C.W., 1996. Metapelitic Migmatites from Brattstrand Bluffs, East Antarctica - Metamorphism, melting and exhumation of the mid crust. Journal of Petrology, v. 37, p. 395-414.

Florence, F.P., and Spear, F.S., 1993. Influences of reaction history and chemical diffusion on P-T calculations for staurolite schists from the Littleton Formation, northwest New Hampshire. Am erican Mineralogist, v. 78, p. 345-359.

Foland, K.A., 1983. $^{40}Ar/^{39}Ar$ incremental heating plateaus for biotites with excess argon. Chemical Geology, v. 41, p. 3-21.

France-Lanord, C. and Le Fort, P., 1988. Crustal melting and granite genesis during the Himalayan collision orogenesis: Transactions of the Royal Society of Edinburgh: Earth Sciences, v. 79, p. 183-195.

Frank, W., Gansser, A., and Trommsdorff, V., 1977. Geological observations in the Ladakh area (Himalayas). A preliminary report. Schweiz. mineral. petrogr. Mitt., v. 57, p. 89-113.

Gaetani, M., and Garzanti, E., 1991. Multicyclic history of the northern India continental margin (Northwestern Himalaya). American Association of Petroleum Geologists Bulletin, v. 75, p. 1427-1446.

Gansser, A., 1964. Geology of the Himalayas. Interscience publishers, London, 289 pp.

Gansser, A., 1980. The significance of the Himalayan suture zone. Tectonophysics, v. 62, p. 37-52.

Gardien, V., Thompson, A.B., Grujic, D. and Ulmer, P., 1995. Experimental melting of biotite + plagioclase + quartz ± muscovite assemblages and

implications for crustal melting. Journal of Geophysical Research, v. 100 B8, p. 15,581 - 15, 591.

Garzanti, E., Baud, A., and Mascle, G., 1987. Sedimentary record of the northward flight of India and its collision with Eurasia (Ladakh Himalaya, India). Geodinimica Acta, v. 1, p. 297-312.

Gelinas, L., Mellinger, M., and Trudel, P., 1982. Archaean mafic metavolcanics from the Rouyn-Noranda district, Abitibi greenstone belt, Quebec. 1. Mobility of the major elements. Canadian Journal of Earth Sciences, v. 19, p. 2258-2275.

George, M.T., 1993. The magmatic, thermal and exhumation history of the Nanga Parbat-Haramosh Massif, western Himalaya [unpublished PhD thesis]: the Open University, Milton Keynes, 402 pp.

George, M.T., Harris, N.B.W., and Butler, R.W.H., 1993. The tectonic implications of contrasting granite magmatism between the Kohistan island arc and the Nanga Parbat-Haramosh Massif, Pakistan Himalaya. In: Treloar, P.J., and Searle, M.P., (eds.), Himalayan Tectonics. Geological Society Special Publication 74, p. 173-192.

George , M.T., Reddy, S.M., and Harris, N.B.W., 1995. Constraints on the cooling history of the Nanga Parbat-Haramosh Masif and Kohistan Arc, western Himalaya. Tectonics, v. 14., p. 237-252.

George, M.T., and Bartlett, J.M., 1996. Rejuvenation of Rb-Sr mica ages during shearing on the northwestern margin of the Nanga Parbat-Haramosh Massif. Tectonophysics, v. 260, p. 167-187.

Giletti, B.J., 1991. Rb and Sr diffusion in alkali feldspars with implications for the cooling histories of rocks. Geochimica et Cosmochimica Acta, v. 55, p. 1331-1343.

Gnos, E., 1992. The metamorphic rocks associated with the Semail ophiolite (Sultanate of Oman and United Arab Emirates) [PhD thesis]. University of Bern.

Grasemann, B., 1993. Numerical modelling of the thermal history of the NW Himalayas, Kullu Valley, India. In: P.J. Treloar and M.P.Searle (Eds.), Himalayan Tectonics. Geological Society Special Publication, 74, p. 475-484.

Guillot, S., and Le Fort, P., 1995, Geochemical constraints on the bimodal origin of High Himalayan leucogranites. Lithos, v. 35, p. 221-234.

Guillot, S., Lardeaux, J.M., Mascle, G., and Colchen, M., 1995. A new record of high-pressure metamorphism in the Himalayan Range - The retrogressed eclogites of the Tso Morari dome (East Ladakh). C.R. Acad. Sci. Ser. II, v. 320 (10 part 2), p. 931-936.

Hamilton, P.J., Kelley, S.P. and Fallick, A.E., 1989. K-Ar dating of illite in hydrocarbon reservoirs. Clay minerals, v. 24, p. 215-231.

Hammarstrom, J.M., and Zen, E-an, 1986. Aluminium in hornblende; an empirical igneous geobarometer. American Mineralogist, v. 71, p. 1297-1313.

Hanson, G.N., and Gast, P.W., 1967. Kinetic studies in contact metamorphic zones. Geochimica et Cosmochimica Acta, v. 31, p. 1119-1153.

Hanson, G.N., Simmons, K.R., and Bence, A.E., 1975. $^{40}Ar/^{39}Ar$ spectrum ages for biotite, hornblende and muscovite in a contact metamorphic zone. Geochimica et Cosmochimica Acta, v. 39, p. 1269-1277.

Hanson, C.R., 1989. The Northern Suture in the Shigar Valley, Baltistan, northern Pakistan. In: Malinconico, L.L., and Lillie, R.J. (eds.), Tectonics of the Western Himalayas. Geological Society of America Special Paper 232, p. 203-215.

Harris, N.B.W., Xu, R., Lewis, C.L., and Chengwei, J., 1988. Plutonic rocks of the 1985 Tibet Geotraverse, Lhasa to Golmud. Philosophical Transactions of the Royal Society, London, v. 327, p. 145-168., 1988

Harris, N.B.W., and Inger, S., 1992. Trace element modelling of pelite-derived granites. Contributions to Mineralogy and Petrology, v. 110, p. 46-56.

Harris, N.B.W., Inger, S., and Massey, J.A., 1993, The role of fluids in the formation of High Himalayan leucogranites, in Treloar, P.J. and Searle, M.P., eds., Himalayan Tectonics. Geological Society Special Publication 74, p. 391-400.

Harris, N.B.W., and Massey, J.A., 1994. Decompression and anatexis of Himalayan metapelites. Tectonics, v.13, p. 1537-1546.

Harris, N.B.W., 1995. Significance of weathering Himalayan metasedimentary rocks and leucogranites for the Sr isotope evolution of seawater during the early Miocene. Geology, v. 23, p. 795-798.

Harris, N.B.W., Ayres, M.W. and Massey, J., 1995. Geochemistry of granitic melts produced during the incongruent melting of muscovite; implications for the extraction of Himalayan leucogranite magmas. Journal of Geophysical Research, v. 100 B8, p. 15,767-15,777.

Harrison, T.M., Duncan, I. and McDougall, I., 1985. Diffusion of ^{40}Ar in biotite. Temperature, pressure and compositional effects. Geochimica et Cosmochimica Acta, v. 49, p. 2461-2468.

Harrison, T.M., and Fitzgerald, J.G., 1986. Exsolution in hornblende and its consequences for $^{40}Ar/^{39}Ar$ age spectra and closure temperatures. Geochimica et Cosmochimica Acta, v. 50, p. 247-253.

Harrison, T.M., Copeland, P., Kidd, W.S.F., and An, Y., 1992. Raising Tibet. Science, v. 255, p. 1663-1670.

Harrison, T.M., Copeland, P., Hall, S.A., Quade, J., Burner, S., Ojha, T., and Kidd, W.S.F., 1993. Isotopic preservation of Himalaya/Tibetan uplift, denudation and climAtic histories of two molasse deposits. Journal of Geology, v. 101, p. 157-175.

Harrison, T.M., McKeegan, K.D., and Le Fort, P., 1995. Detection of inherited monazite in the Manaslu leucogranite by $^{208}Pb/^{232}Th$ ion microprobe dating; crystallisation age and tectonic implications. Earth and Planetary Science Letters, v. 133, p. 271-282.

Harrison, T.M., Lovera, O.M., and Grove, M., 1997. New insights into the origin of two contrasting Himalayan granite belts. In: Abstract volume for the 12th Himalaya-Karakorum-Tibet international workshop, p. 43-45. Academia Nazionale dei Lincei, Roma, Italy, 240 pp.

Heizler, M.T., and Harrison, T.M., 1988. Multiple trapped argon isotope components revealed by $^{40}Ar/^{39}Ar$ isochron analysis. Geochimica et Cosmochimica Acta, v. 52, p. 1295-1303.

Henderson, P., 1982, Inorganic Geochemistry, Pergamon Press, Oxford.

Hensen, B.J., 1971. Theoretical phase relations involving cordierite and garnet in the system MgO-FeO-Al_2O_3-SiO_2. Contributions to Mineralogy and Petrology, v. 33, p. 191-214.

Hensen, B.J., and Green, D.H., 1973. Experimental study of the stability of cordierite and garnet in pelitic compositions at high pressures and temperatures; III, synthesis of available experimental data and geological applications. Contributions to Mineralogy and Petrology, v. 38, p. 151-166.

Hensen, B.J., and Harley, S.L., 1990. Graphical analysis of P-T-X relations in granulite facies metapelites. In: Ashworth, J.R., and Brown, M., (eds.), High temperature metamorphism and crustal anatexis. Mineralogical Society Series 2, Unwin Hyman, London, p. 19-56.

Herren, E., 1987. Zanskar shear zone: northeast-southwest extension within the Higher Himalayas (Ladakh, India). Geology, v. 15, p. 409-413.

Hodges, K.V., Parrish, R., Housch, T., Lux, D., Burchfiel, B.C., Royden, L., and Z. Chen, 1992. Simultaneous Miocene extension and shortening in the Himalayan Orogen. Science, v. 258, p. 1466-1470.

Hodges, K.V., Burchfiel, B.C., Royden, L.H., Chen, Z., and Lieu, Y., 1993. The metamorphic signature of contemporaneous extension and shortening in the central Himalayan orogen: data from the Nyalam transect, southern Tibet: Journal of Metamorphic Geology, v. 11, p. 721-737.

Holdaway, M.J., 1971. Stability of andalusite and the aluminosilicate phase diagram. American Journal of Science, v. 271, p. 97-131.

Holland, T.J.B., and Powell, R., 1990. An enlarged and updated internally consistent thermodynamic dataset with uncertainties and correlations: the system K_2O-Na_2O-CaO-MgO-MnO-FeO-Fe_2O_3-Al_2O_3-TiO_2-SiO_2-C-H_2-O_2 Journal of Metamorphic Geology, v. 8, p. 89-124.

Holland, T.J.B., and Blundy, J.D., 1994. Non-ideal interactions in calcic amphiboles and their bearing on amphibole-plagioclase thermometry. Contributions to Mineralogy and Petrology, v. 116, p. 443-449.

Holland, T.J.B., Babu, E.V.S.S.K. and Waters, D.J., 1996. Phase-relations of osumilite and dehydration melting in pelitic rocks - a simple thermodynamic

model for the KFMASH system. Contributions to Mineralogy and Petrology, v. 124, p. 383-394.

Hollister, L.S., 1966. Garnet zoning: an interpretation based on the Rayleigh fractionation model. Science, v. 154, p. 1647-1651.

Holm, P.E., 1982. Non-recognition of continental tholeiites using the Ti-Y-Zr diagram. Contributions to Mineralogy and Petrology, v. 79, p. 308-310.

Holtz, F. and Johannes, W., 1991. Genesis of peraluminous granites 1. Experimental investigation of melt compositions at 3 and 5 kb and various H_2O activities. Journal of Petrology, v. 32, p. 935-958.

Honegger, K., Dietrich, V., Frank, W., Gansser, A., Thoni, M., and Trommsdorff, V., 1982. Magmatism and metamorphism in the Ladakh Himalaya (the Indus-Tsangpo suture zone). Earth and Planetary Science Letters, v. 60, p. 253-292.

Honegger K., Le Fort, P., Mascle, G., and Van Haver, T., 1985. Presence de Schistes Bleus a Glaucophane dans la zone de suture de l'Indus au Ladakh (abstract). Terra Cognita, v. 5, p. 257.

Hubbard, M., Royden, L. and Hodges, K., 1991. Constraints on unroofing rates in the High Himalaya, eastern Nepal. Tectonics, v. 10, p. 287-298.

Inger, S and Harris, N.B.W., 1992. Tectonothermal evolution of the High Himalayan Crystalline sequence, Langtang valley, northern Nepal: Journal of Metamorphic Geology, v. 10, p. 439-452.

Inger, S. and Harris, N.B.W., 1993. Geochemical constraints on leucogranite magmatism in the Langtang valley, Nepal Himalaya. Journal of Petrology, v. 34, p.345-368.

Irving, A.J., and Frey, F.A., 1978. Distribution of trace elements between garnet megacrysts and host volcanic liquids of kimberlitic to rhyolitic composition. Geochimica et Cosmochimica Acta, v. 42, p. 771-787.

Jackson, J., and Yielding, G., 1983. The seismicity of Kohistan, Pakistan: source studies of the Hamran (1972.9.3), Darel (1981.9.12), and Patan (1974.12.28) earthquakes. Tectonophysics, v. 91, p. 15-28.

Jaeger, J.-J., Courtillot, V., and Taponnier, P., 1989. Palaeontological view of the ages of the Deccan Traps, the Cretaceous/Tertiary boundary, and the India-Asia collision: Geology, v. 17, p. 316-319.

Jagoutz, E., Palme, H., Baddenhausen, H., Blum, K., Cendales, M., Dreibus, G., Spottel, B., Lorenz, V., and Wanke, H., 1979. The abundances of major, minor and trace elements in the earth's mantle as derived from primitive ultramafic nodules. Proc. Lunar and Planet. Sci. Conf. No. 10, Geochimica et Cosmochimica Acta, Supplement 11, p. 2031-2050.

Jamieson, R.A., 1991. P-T-t paths of collisional orogens. Geologische Rundschau, v. 80, p. 321-332.

Jan, M.Q., and Howie, R.A., 1980. Ortho- and clinopyroxenes from the pyroxene granulites of Swat Kohistan, northern Pakistan. Mineralogical Magazine, v. 43, p. 715-726.

Jan, M.Q., and Howie, R.A., 1981. The mineralogy and geochemistry of the metamorphosed basic and ultrabasic rocks of the Jijal complex, Kohistan, NW Pakistan. Journal of Petrology, v. 22, p. 85-126.

Jan , M.Q., 1988. Geochemistry of amphibolites from the southern part of the Kohistan Arc, N. Pakistan. Mineralogical Magazine, v. 52, p. 147-159.

Jiang, J., and Lasaga, A.C., 1990. The effect of post-growth thermal events on growth-zoned garnet: implication for metamorphic P-T history calculations. Contributions to Mineralogy and Petrology, v. 105, p. 454-459.

Johannes, W. and Holtz, F., 1990. Formation and composition of H_2O-undersaturated granitic melts., in Ashworth, J.R. and Brown, M., eds., High-temperature metamorphism and crustal anatexis: Unwin Hyman, London, p. 87-101.

Johnson , B.D., Powell, McA., Veevers, J.J., 1976. Spreading history of the eastern Indian ocean, and greater India's northward flight from Antarctica and Australia. Geological Society of America Bulletin, v. 87, p. 1560-1566.,

Johnson N.M., Opdyke, N.D., Johnson, G.D., Lindsay, E.H., and Tahirkheli, R.A.K., 1982. Magnetic polarity, stratigraphy and ages of Siwalik group rocks of the Potwar plateau, Pakistan. Palaeogeogr. Palaeoclimatol. Palaeoecol., v. 37, p. 17-42.

Kazmi, A.H., Lawrence, R.D., Dawood, H., Snee, L.W., and Hussain, S.S., 1984. Geology of the Indus suture zone in the Mingora-Shangla area of Swat, N. Pakistan. Geological Bulletin of the University of Peshawar, v. 17, p. 127-144.

Kelley, S.P., 1995. Ar-Ar dating by laser microprobe. In: P.J. Potts, J.F.W. Bowles, S.J.B. Reed, and M.R. Cave (Editors), Microprobe Techniques in the Earth Sciences. Chapman and Hall, 420 pp.

Khan, M.A., Jan, M.Q., and Weaver, B.L., 1993. Evolution of the lower arc crust in Kohistan, N.Pakistan: temporal arc magmatism through early, mature and intra-arc rift stages. In: Treloar, P.J., and Searle, M.P. (eds.), Himalayan Tectonics, Geological Society Special Publication 74, p. 123-138.

Kleemann, U., and Reinhardt, J., 1994. Garnet-biotite thermometry revisited, I. The effect of Al^{VI} and Ti in biotite. European Journal of Mineralogy, v. 6, p. 925-942.

Klootwijk, C.T., 1984. A review of Indian Phanerozoic palaeomagnetism: implications for the India-Asia collision. In: H.K. Gupta (Ed.), Lithosphere: Structure, Dynamics and Evolution. Tectonophysics, v. 105, p. 331-353.

Klootwijk, C.T., Sharma, M.L., Gerga, J., Shah, S.K., and Tirkey, B., 1984. The Indus-Tsangpo suture zone in Ladakh, northwest Himalaya: further palaeomagnetic data and implications. Tectonophysics, v. 106, p. 215-238.

Klootwijk, C.T., Conaghan, P.J., and Powell, C. McA., 1985. The Himalayan Arc: Large-scale continental subduction, oroclinal bending and back-arc spreading. Earth and PLanetary Science Letters, v. 75, p. 167-183.

Klootwijk, C.T., Gee, J.S., Peirce, J.W., Smith, G.W., and McFadden, P.L., 1992. An early Indian-Asian contact: palaeomagnetic constraints from Ninetyeast ridge, ODP Leg 121. Geology, v.20, p.395-398.

Koons, P.O., 1987. Some thermal and mechanical consequences of rapid uplift. an example from the Southern Alps, New Zealand. Earth and Planetary Science Letters, v. 86, p. 307-319.

Kretz, R., 1983. Symbols for rock-forming minerals. American Mineralogist, v. 68, p. 277-279.

Langmuir, C.H., Bender, J.F., Bence, A.E., Hanson, G.N., and Hart, S.R., 1977. Petrogenesis of basalts from the FAMOUS area: mid-Atlantic ridge. Earth and Planetary Science Letters, v. 36, p. 133-156.

Lawrence, R.D., and Ghauri, A.A.K.,1983. Observations on the structure of the Main Mantle Thrust at Jijal, Kohistan, Pakistan. Geological Bulletin of the University of Peshawar, v. 16, p. 1-10.

Le Breton, N. and Thompson, A.B., 1988. Fluid-absent (dehydration) melting of biotite in metapelites in the early stages of crustal anatexis. Contributions to Mineralogy and Petrology, v. 99, p. 226-237.

Le Fort, P., 1975. Himalaya: the collided range. Present knowledge of the continental arc: American Journal of Science, v. 275, p. 1-44.

Le Fort, P., Debon, F., and Sonet, J., 1980. The lesser Himalayan cordierite granite belt. Typology and age of the pluton of Mansehra (Pakistan). Special Issue of the Geological Bulletin of the Iniversity of Peshawar, v. 13, p. 51-61.

Le Fort, P., 1981. Manaslu leucogranite: A collision signature of the Himalaya. A model for its genesis and emplacement. Journal of Geophysical Research, v. 86, p. 10545-10568.

Le Fort, P., Michard, A., Sonet, J., and Zimmermann, J.L., 1983. Petrography, geochemistry and geochronology of some samples from the Karakorum axial batholith (northern Pakistan). In: Shams, F.A. (ed.), "Granites of the Himalayas, Karakorum and Hindu Kush", Institute of Geology, Punjab University, Lahore, Pakistan, p. 377-387.

Le Fort, P., 1986. Metamorphism and magmatism during the Himalayan Collision. In: Coward, M.P., and Ries, A.C., (eds.), Collision Tectonics. Geological Society Special Publication 19, p. 159-172.

Le Fort, P., Cuney, M., Deniel, C., France-Lanord, C., Sheppard, S.M.F., Upreti, B.N., and Vidal, P., 1987, Crustal generation of the Himalayan leucogranites: Tectonophysics, v. 134, p. 39-57.

Le Fort, P., 1988. Granites in the tectoinic evolution of the Himalaya, Karakorum, and southern Tibet. Philosophical Transactions of the Royal Society, London, v. 326, p. 281-299.

Le Fort, P., 1989. The Himalayan Orogenic Segment. In: Sengor, A.M.C., (ed.), Tectonic Evolution of the Tethyan Region. NATO ASI Series C, v. 259, p. 289-386.

Le Fort, P., Guillot, S., and Pêcher, A., 1997. Discovery of retrogressed eclogites in the Indus suture, east of Nanga Parbat-Haramosh massif (northern Pakistan), the HP belt of NW Himalaya. Abstract volume, 12th Himalaya-Karakorum-Tibet international workshop, p. 57-58. Academia Nazionale dei Lincei, Roma, Italy, 240pp.

Le Maitre, R.W., and 10 others, 1989. A classification of igneous rocks and glossary of terms. Blackwell, Oxford.

Le Pichon, X., Fournier, M., and Joliat, L., 1992. Kinematics, topography, shortening and extrusion in the India-Asia collision. Tectonics, v. 11, p. 1085-1098.

Lee, J.K.W., 1993. The argon release mechanisms of hornblende in vacuo. Chemical Geology, v. 106, p. 133-170.

Lee, J.K.W., 1995. Multipath diffusion in geochronology. Contributions to Mineralogy and Petrology, v. 120, p. 60-82.

Lemennicier, Y., Le Fort, P., Lombardo, B., Pecher, A., and Rolfo, F., 1996. Tectonometamorphic evolution of the central Karakorum (Baltistan, northern Pakistan). Tectonophysics, v. 260, p. 119-145.

Lydekker, R., 1878. Geology of Kashmir, Kisthwar and Panghi. Records of the Geological Survey of India, v. 11, p. 31-64.

Lydekker, R., 1883. The geology of Kashmir and Chamba territories and the British districts of Khagan. Memoirs of the Geological Survey of India, v. 22, p. 31-34.

MacDonald, G.A., 1968. Composition and origin of Hawaiian lavas. In: Coats, R.R., Hay, R.L., and Anderson, C.A., (eds.), Studies in volcanology: a memoir in honour of Howel Williams. Geological Society of America Memoir 116, p. 477-522.

Macfarlane, A.M., 1993. Chronology of tectonic events in the crystalline core of the Himalaya, Langtang National Park, Central Nepal. Tectonics, v. 12, p. 1004-1025.

Madin, I.P., Lawrence, R.D., and Ur-Rehman, S., 1989. The northwestern Nanga Parbat-Haramosh Massif; evidence for crustal uplift of the northwestern corner of the Indian craton. In: Malinconico, L.L., and Lillie, R.J., (eds.), Tectonics of the Western Himalayas. Geological Society of America Special Paper 232, p. 169-182.

Malinconico, L.L., 1986. The structure of the Kohistan-Arc terrane in northern Pakistan as inferred from gravity data. Tectonophysics, v. 124, p. 297-307.

Maluski, H., Proust, F., and Xiao, X.C., 1982. $^{40}Ar/^{39}Ar$ dating of the Transhimalayan calcalkaline magmatism of southern Tibet. Nature, v. 298, p. 152-154.

Maluski, H., and Matte, P., 1984. Ages of Alpine Tectonometamorphic events in the NW Himalaya by $^{40}Ar/^{39}Ar$ method. Tectonics, v. 3., p. 1-18.

Massey, J.A., 1994. Metamorphism, melting and fluids in the High Himalayan Crystallines, Langtang Valley, Nepal. [unpublished Ph.D. thesis]: Open University, Milton Keynes, United Kingdom, 398 pp.

Mawer, C.K., 1987. Shear criteria in the Grenville Province, Ontario, Canada. In: Cobbold, P.R., Gapais, D., Means, W.D., and Treagus, S.H., (eds.), Shear Criteria in rocks. Journal of Structural Geology, v. 9, p. 531-539.

McDougall, I. and Harrison, T.M., 1988. Geochronology and Thermochronology by the $^{40}Ar/^{39}Ar$ method, Oxford University Press.

Misch, P., 1949. Metasomatic granitisation of batholithic dimensions. American Journal of Science, v. 247, p. 209-245.

Misch, P., 1964. Stable association of wollastonite-anorthite and other calc-silicate assemblages in amphibolite-facies crystalline schists of Nanga Parbat, Northwest Himalayas. Contributions to Mineralogy and Petrology, v. 10, p. 315-356.

Molnar, P., and Taponnier, P., 1975. Cenozoic Tectonics of Asia: Effects of a continental collision. Science, v. 189, p. 419-426.

Molnar, P., and England, P., 1990. Late Cenozoic uplift of mountain ranges and global climate change: chicken or egg? Nature, v. 346, p. 29-34.

Montel, J.M., 1993, A model for monazite/melt equilibrium and applications to the generation of granitic magmas. Chemical Geology, v. 110, p. 127-146.

Montgomery, D.R., 1994. Valley incision and uplift of mountain peaks. Journal of Geophysical Research, v. 99 B7, p. 13913-13921.

Nakamura, N., 1974. Determination of REE, Ba, Fe, Mg, Na and K in carbonaceous and ordinary chondrites. Geochimica Cosmochimica Acta, v. 38, p. 757-775.

Nash, W.P., and Crecraft, H.R., 1985, Partition coefficients for trace elements in silicic magmas, Geochimica Cosmochimica Acta, v. 49, p. 2309-2322.

Ni, J., and Rawazangi, M., 1984. Seismotectonics of the Himalayan Collision zone: geometry of the underthrusting Indian Plate beneath the Himalaya. Journal of Geophysical Research, v. 89, p. 1147-1163.

Nichols, G.T., Berry, R.F. and Green, D.H., 1992. Internally consistent gahnitic spinel-cordierite-garnet equilibria in the FMASHZn system; geothermobarometry and applications. Contributions to Mineralogy and Petrology, v. 111, p. 362-377.

Noble, S.R., and Searle, M.P., 1995. Age of crustal melting and leucogranite formation from U-Pb zircon and monazite dating in the western Himalaya, Zanskar, India. Geology, v. 23, p. 1135-1138.

Owen, L.A., 1989. Neotectonics and glacial deformation in the Karakorum Mountains and Nanga Parbat Himalaya. Tectonophysics, v. 163, p. 227-265.

Palmer, M.R., and Elderfield, H., 1985. Strontium isotope composition of seawater over the past 75 Myr. Nature, v. 314, p. 526-528.

Parrish, R., and Tirrul, R., 1989. U-Pb age of the Baltoro granite, northwest Himalaya, and implications for monazite U-Pb systematics. Geology, v. 17, p. 1076-1079.

Parrish, R.R., 1990. U-Pb dating of monazite and its application to geological problems. Canadian Journal of Earth Science, v. 27, p. 1431-1450.

Passchier, C.W., and Simpson, C., 1986. Porphyroblast systems as kinematic indicators. Journal of Structural Geology, v. 8, p. 831-843.

Patiño Douce, A.E., Humphreys, E.D. and Johnston, A.D., 1990. Anatexis and metamorphism in tectonically thickened continental crust exemplified by the Sevier hinterland, western North America. Earth and Planetary Science Letters, v. 97, p. 290-315.

Patiño Douce, A.E. and Johnston, A.D., 1991. Phase equilibria and melt productivity in the pelitic system: implications for the origin of peraluminous granitoids and aluminous granulites. Contributions to Mineralogy and Petrology, v. 107, p. 202-218.

Patriat, P., and Achache, J., 1984. India-Eurasia collision chronology has implications for crustal shortening anf driving mechanism of plates. Nature, v. 311, p. 615-621.

Patzelt, A., Huamei Li, Junda Wang, and Appel, E., 1996. Palaeomagnetism of Cretaceous to Tertiary sediments from southern Tibet: evidence for the extent of the northern margin of India prior to the collision with Eurasia. Tectonophysics, v. 259, p. 259-284.

Pearce, J.A., and Cann, J.R., 1973. Tectonic setting of basic volcanic rocks determined using trace element analyses. Earth and Planetary Science Letters, v. 19, p. 290-300.

Pearce, J.A., 1976. Statistical analysis of major element patterns in basalts. Journal of Petrology, v. 17, p. 15-43.

Pearce, J.A., and Gale, G.H., 1977. Identification of ore-deposition environment from trace element geochemistry of associated igneous host rocks. Geological Society Special Publication 7, p. 14-24.

Pearce, J.A., and Norry, M.J., 1979. Petrogenetic implications of Ti, Zr, Y, and Nb variations in volcanic rocks. Contributions to Mineralogy and Petrology, v. 69, p. 33-47.

Pearce, J.A., 1982. Trace element characteristics of lavas from destructive plate boundaries. In: Thorpe, R.S., (ed.), Andesites. Wiley, Chichester, p. 525-548.

Pearce, J.A., Harris, N.B.W., and Tindle, A.G., 1984, Trace element discrimination diagrams for the tectonic interpretation of granitic rocks. Journal of Petrology, v. 25, p. 956-983.

Peltzer, G., and Taponnier, P., 1988. Formation and evolution of strike-slip faults, rifts and basins during the India Asia collision: An experimental approach. Journal of Geophysical Research, v. 93., p. 15,085-15,117.

Petford, N., Lister, J.R., and Kerr, R.C., 1993, Dike transport of granitoid magmas: Geology, v. 21, p. 845-848.

Petö, P., 1976, An experimental investigation of melting relations involving muscovite and paragonite in the silica-saturated portion of the system K2O-Na2O-Al2O3-SiO2-H2O: Progress in Experimental Petrol.ogy, v.3 , p. 41-45.

Petterson, M.G., 1984. The structure, petrology and geochemistry of the Kohistan batholith, Gilgit, Kashmir, N. Pakistam. [unpublished Ph.D. thesis], University of Leicester, Leicester, United Kingdom.

Petterson, M.G., and Windley, B.F., 1985. Rb-Sr dating of the Kohistan arc-batholith in the Trans-Himalaya of north Pakistan, and tectonic implications. Earth and Planetary Science Letters, v. 74, p. 45-57.

Petterson, M.G., and Windley, B.F., 1991. Changing source regions of magmas and crustal growth in the trans-Himalayas: evidence from the Chalt batholith, Kohistan, northern Pakistan. Earth and Planetary Science Letters, v. 102, p. 326-341.

Pinet, C., and Jaupart, C., 1987, A thermal model for the distribution in space and time of the Himalayan granites: Earth and Planetary Science Letters, v. 84, p. 87-99.

Pognante, U., and Spencer, D.A., 1991. First report of eclogites from the Himalayan belt, Kaghan valley (northern Pakistan). European Journal of Mineralogy, v. 3, p. 613-618.

Pognante, U., 1992. Different P-T-t paths and leucogranite occurrences along the High Himalayan Crystallines: implications for subduction and collision along the northern Indian margin. Geodinimica Acta, v. 6, p. 5-17.

Pognante, U., Benna, P., and Le Fort, P., 1993. High-pressure metamorphism in the High Himalayan Crystallines of the Stak Valley, northeastern Nanga Parbat-Haramosh syntaxis, Pakistan Himalaya. In: Treloar, P.J., and Searle, M.P. (eds.), Himalayan Tectonics. Geological Society Special Publication 74, p. 161-172.

Potts, P.J., Williams Thorpe, O., Isaacs, M.C., and Wright, D.W., 1985, High precision instrumental neutron activation analysis of geological samples employing simultaneous counting with both planar and coaxial detectors: Chemical Geology, v. 48, p. 145-155.

Powell, C.McA., and Conaghan, P.J., 1973. Plate tectonics and the Himalaya. Earth and Planetary Science Letters, v. 20, p. 1-12.

Powell, C.McA., 1986. Continental underplating model for the rise of the Tibetan plateau. Earth and Planetary Science Letters, v. 81, p. 79-94.

Powell, R. and Holland, T.J.B., 1988. An internally consistent dataset with uncertainties and correlations: 3. Applications to geobarometry, worked examples and a computer program. Journal of Metamorphic Geology, v. 6, p. 173-204.

Powell, R. and Downes, J., 1990. Garnet porphyroblast-bearing leucosomes in metapelites: mechanisms, phase diagrams, and an example from Broken Hill, Australia. In: Ashworth, J.R. and Brown, M. (eds.) High Temperature Metamorphism and crustal anatexis.

Prince, C.I., Vance, D., and Harris, N., 1997. Timing of metamorphism in the Garwhal Himalaya, India. Abstract volume, 12th Himalaya-Karakorum-Tibet international workshop, p. 73. Academia Nazionale dei Lincei, Roma, Italy, 240pp.

Pudsey, C.J., Schroeder, R., and Skelton, P.W., 1985. Cretaceous (Aptian/Albian) age for island arc volcanics, Kohistan, N. Pakistan. In: Gupta, V.J. (ed.), Geology of the western Himalayas. Contributions to Himalayan Geology, v. 3, p. 150-168.

Pudsey, C.J., 1986. The northern suture, Pakistan: margin of a Cretaceous island arc. Geological Magazine, v. 123, p. 405-423.

Purdy, J.W., and Jäger, E., 1976. K-Ar ages on rock-forming minerals from the central Alps. Memorie degli Instituti di Geologia e Mineralogia dell'Universita di Padova, v. 30, p. 1-31.

Rao, R.U.M., Rao, G.V. and Narain, H., 1976. Radioactive heat generation and heat flow in the Indian Shield. Earth and Planetary Science Letters, v. 30, p. 57-64.

Raymo, M.E., Ruddiman, W.F., and Froelich, P.N., 1988. Influence of late Cenozoic mountain building on ocean geochemical cycles. Geology, v. 16, p. 649-653.

Raymo, M.E., and Ruddiman, W.F., 1992. Tectonic forcing of late Cenozoic climate. Nature, v. 359, p. 117-124.

Reddy, S.M., Searle, M.P. and Massey, J.A., 1993, Structural evolution of the High Himalayan Gneiss sequence, Langtang valley, Nepal, in Treloar, P.J., and Searle, M.P., (eds.), Himalayan Tectonics, Geological Society Special Publication 74, p. 375-390.

Reddy, S.M., Kelley, S.P., and Wheeler, J., 1996. A $^{40}Ar/^{39}Ar$ laser probe study of micas from the Sesia Zone, Italian Alps: implications for metamorphic and deformation histories. Journal of Metamorphic Geology, v. 14, p. 493-508.

Reddy, S.M., Kelley, S.P. and Magenniss, L., 1997. A microprobe and argon laserprobe study of shear zone development at the western margin of the Nanga Parbat-Haramosh Massif, western Himalayas. Contributions to Mineralogy and Petrology, in press.

Rex, A.J., Searle, M.P., Tirrul, R., Crawford, M.B., Prior, D.J., Rex, D.C., and Barnicoat, A., 1988. The geochemical and tectonic evolution of the central Karakorum, northern Pakistan. Philosophical Transactions of the Royal Society, London, v. 326, p. 229-255.

Rex, D.C., and Guise, P. G., 1995. Evaluation of argon standards with special emphasis on time scale measurements. In Odin, G.S., (ed.), Phanerozoic time scale. Bull. Liais. Inform. IUGS Subcom. Geochronol., 13, Offset Paris.

Reynolds, P.H., Brookfield, M.E., and McNutt, R.H., 1983. The age and nature of Mesozoic-Tertiary magmatism across the Indus suture zone in Kashmir and Ladakh (NW India and Pakistan). Geologische Rundschau, v. 72, p. 981-1004.

Robertson, A.H.F., and Degnan, P.J., 1993. Sedimentology and tectonic implications of the Lamayuru complex: deep-water facies of the Indian passive margin, Indus Suture Zone, Ladakh Himalaya. In: Treloar, P.J., and Searle, M.P., (eds.), Himalayan Tectonics. Geological Society Special Publication 74, p. 299-322.

Roddick, J.C., 1978. The application of isochron diagrams in ^{40}Ar-^{39}Ar dating: a discussion. Earth and Planetary Science Letters, v. 41, p. 233-244.

Roddick, J.C., Cliff, R.A., and Rex, D.C., 1980. The evolution of excess argon in Alpine biotites - a ^{40}Ar-^{39}Ar analysis.

Rollinson, H.R., 1983. The geochemistry of mafic and ultramafic rocks from the Archaean greenstone belts of Sierra Leone. Minerlogical Magazine, v. 47, p. 267-280.

Rollinson, H.R., 1993. Using geochemical data: evaluation, presentation, interpretation. Longman, England, 352 pp.

Rowley, D.B., 1996. Age of initiation of collision between India and Asia: A review of stratigraphic data. Earth and Planetary Science Letters, v. 145, p., 1-13.

Royden, L.H., 1993. The steady state thermal structure of eroding orogenic belts and accretionary prisms. Journal of Geophysical Research, v. 98, p. 4487-4507.

Ruddiman, W.F., and Kutzbach, J.E., 1989. Forcing of the late Cenozoic northern hemisphere climate by plateau uplift in southeast Asia and the American southwest. Journal of Geophysical Research, v. 94, p. 18409-18427.

Rutter, E.H., and Neumann, D.H.K., 1995, Experimental deformation of partially molten Westerly granite under fluid-absent conditions with implications for the extraction of granitic magmas: Journal of Geophysical Research, v. 100, p. 15697-15715.

Sarwar, G., and DeJong, K.A., 1979. Arcs, oroclines, syntaxes: the curvatures of mountain belts in Pakistan. In: Farah, A., and DeJong, A. (eds.), Geodynamics of Pakistan. Geological Survey of Pakistan, Quetta, 1979.

Saxena, M.N., and Miller, J.A., 1972. Metamorphism, magmatism and orogeny in the light of radiometric dates in the north-western Himalayas. Bulletin of the Indian Geological Association, v. 5., p. 63-69.

Schärer, U., Xu, R.H., and Allègre, C.J., 1984a. U-Pb geochronology of Gangdese (Transhimalayan) plutonism in the Lhasa-Xigase region, Tibet. Earth and Planetary Science Letters, v. 69, p. 311-320.

Schärer, U., Hamet, J., and Allègre, C.J., 1984b. The Transhimalayan (Gangdese) plutonism in the Ladakh region: a U-Pb and Rb-Sr study. Earth and Planetary Science Letters, v. 67, p. 327-339.

Schärer, U., Xu, R.H., and Allègre, C.J., 1986. U-(Th)-Pb systematics and ages of Himalayan leucogranites, south Tibet. Earth and Planetary Science Letters, v. 77, p. 35-48.

Schärer, U., Copeland, P., Harrison, T.M., and Searle, M.P., 1990. Badrinath-Gangotri plutons (Garwhal, India): Petrological and geochemical evidence for fractionation processes in a High Himalayan leucogranite. Journal of Volcanology and Geothermal Research, v. 44, p. 163-188.

Schneider, D.A., Edwards, M.A., Zeitler, P.K., and Kidd, W.S.F., 1997. Ion microprobe U-(Th)-Pb and Ar/Ar geochronology of Nanga Parbat-Haramosh Massif (part 1). Rupal valley, southern Nanga Parbat, and Jutial granite, Haramosh area. In: Abstract volume for the 12th Himalaya-Karakorum-Tibet international workshop, p. 205-206. Academia Nazionale dei Lincei, Roma, Italy, 240 pp.

Searle, M.P., 1983. Stratigraphy, structure and evolution of the Tibetan-Tethys zone in Zanskar and the Indus suture zone in the Ladakh Himalaya. Transactions of the Royal Society of Edinburgh, v. 73, p. 205-219.

Searle, M.P., 1986. Structural evolution and sequence of thrusting in the High Himalayan, Tibetan-Tethys and Indus suture zones of Zanskar and Ladakh, western Himalaya. Journal of Structural Geology, v. 8, p. 923-936.

Searle, M.P., Rex, A.J., Tirrul, R., Windley, B.F., St. Onge, M., and Hoffman, P., 1986. A geological profile across the Baltoro Karakorum range, N. Pakistan. Geological Bulletin of the University of Peshawar, v. 19, p. 1-12.

Searle , M.P., Windley, B.F., Coward, M.P., Cooper, D.J.W., Rex, A.J., Rex, D.C., Li Tingdong, Xiao Xuchang, Jan, M.Q., Thakur, V.C., and Kumar, S., 1987. The closing of Tethys and the tectonics of the Himalayas. Geological Society of America Bulletin, v. 98, 678-701.

Searle, M.P., Rex, A.J., Tirrul, R., Rex, D.C., Barnicoat, A., and Windley, B.F., 1989. Metamorphic, magmatic and tectonic evolution of the central Karakorum in the Biafo-Baltoro-Hushe regions of northern Pakistan. In: Malinconico, L.L., and Lillie, R.J. (eds.), Tectonics of the western Himalayas. Geological Society of America Special Paper 232, p. 47-73.

Searle, M.P., Parrish, R.R., Tirrul, R., and Rex, D.C., 1990. Age of crystallisation and cooling of the K2 gneiss in the Baltoro Karakorum. Journal of the Geological Society, London, v. 147, p. 603-606.

Searle, M.P., and Tirrul, R., 1991. Structural and thermal evolution of the Karakorum crust. Journal of the Geological Society, London, v. 148, p. 65-82.

Searle, M.P., Crawford, M.B., and Rex, A.J., 1992a. Field relations, geochemistry, origin and emplacement of the Baltoro granite, Central Karakorum. Transactions of the Royal Society of Edinburgh Earth Sciences, v. 83, p. 519-538.

Searle, M.P., Waters, D.J., Rex, D.C., and Wilson, R.N., 1992b. Pressure, temperature and time constraints on Himalayan metamorphism from eastern Kashmir and western Zanskar. Journal of the Geological Society, London, v. 149, p. 753-773.

Seeber, L., and Armbruster, J., 1979. Seismicity of the Hazara arc in northern Pakistan: decollement vs. basement faulting. In: Farah, A., and DeJong, K.A., (eds.), Geodynamics of Pakistan. Geological Survey of Pakistan, Quetta, p. 131-142.

Seeber, L., Armbruster, J.G., Quittmeyer, R.C., 1981. Seismicity and continental subduction in the Himalayan arc. American Geophysical Union, Geodynamical Series, vol. 5, 215-242.

Sengupta, S., Acharyya, S.K., and de Smeth, J.B., 1996. Geochemical characteristics of the Abor volcanic rocks, NE Himalaya, India: nature and early Eocene magmatism. Journal of the Geological Society, London, v. 153, p. 695-704.

Shah, S.K., Sharma, J.T., Gergan, J.T., and Tara, C.S., 1976. Stratigraphy and structure of the western part of the Indus suture belt, Ladakh, northwest India. Himalayan Geology, v. 6, p. 543-556.

Shams, F.A., 1972. Glaucophane-bearing rocks from near Topsin, Swat - first record from Pakistan. Pakistan Journal Scientific Research, vol. 24, p. 343-345.

Shelley, D., 1993. Igneous and metamorphic rocks under the microscope. 445pp, Chapman and Hall, London.

Shervais, J.W., 1982. Ti-V plots and the petrogenesis of modern and ophiolitic lavas. Earth and Planetary Science Letters, v. 59, p. 101-118.

Shroder, J.F., 1993. Himalaya to the sea: geomorphology and the Quaternary of Pakistan in the regional context. In: Shroder, J.F., (ed.), Himalaya to the sea: Geology, geomorphology and the Quaternary. Routledge, London, 429 pp.

Simpson, C., and Wintsch, R.P., 1989. Evidence for deformation-induced K-feldspar replacement by myrmekite. Journal of Metamorphic Geology, v. 7, p. 261-275.

Smith, H.A., Chamberlain, C.P. and Zeitler, P.K., 1992. Documentation of Neogene regional metamorphism in the Himalayas of Pakistan using U-Pb in monazite. Earth and Planetary Science Letters, v. 113, p. 93-105.

Smith, H.A., Chamberlain, C.P., and Zeitler, P.K., 1994. Timing and duration of Himalayan metamorphism within the Indian Plate, northwest Himalaya, Pakistan. Journal of Geology, v. 102, p. 493-508.

Snee, L.W., Lund, K., and Verplanck, P.L., 1988. Comparison of the Salmon River suture, Idaho, with the Indus suture, Pakistan. In: Geological Society of America, Rocky Mountain Section, 41st Annual meeting. Geological Society of America abstracts with programs, v. 20, p. 470.

Spear, F.S., and Selverstone, J., 1983. Quantitative P-T paths from zoned minerals: theory and tectonic applications. Contributions to Mineralogy and Petrology, v. 83, p. 348-357.

Spear, F.S., and Peacock, S.M., 1989. Metamorphic Pressure-Temperature-Time paths. Short course in Geology, v. 7. American Geophysical Union, Washington D.C., 102pp.

Spencer, D.A., Tonarini, S., and Pognante, U., 1995. Geochemical and Sr-Nd isotopic characterisation of Higher Himalayan eclogites (and associated metabasites). European Journal of Mineralogy, v. 7, p. 89-102.

Srimal, N., 1986. India-Asia collision: implications from the geology of the eastern Karakorum. Geology, v. 14, p. 523-527.

Srogi, L., Wagner, M.E. and Lutz, T.M., 1993. Dehydration partial melting and disequilibrium in the granulite-facies Wilmington complex, Pennsylvania-Delaware piedmont. American Journal of Science, v. 293, p. 405-462.

Stoddard, E.F., 1979. Zinc-rich hercynite in high-grade metamorphic rocks: a product of the dehydration of staurolite. American Mineralogist, v. 64, p. 736-741.

Stüwe, K., White, L. and Brown, R., 1994. The influence of eroding topography on steady-state isotherms. Application to fission track analysis. Earth and Planetary Science Letters, v. 124, p. 63-74.

Sullivan, M.A., Windley, B.F., Saunders, A.D., Haynes, J.R., and Rex, D.C., 1993. A palaeographic reconstruction of the Dir group: evidence for magmatic arc migration within Kohistan, N. Pakistan. In: Treloar, P.J., and Searle, M.P., (eds.), Himalayan Tectonics. Geological Society Special Publication 74, p. 139-160.

Sun, S.S., and McDonough, W.F., 1989, Chemical and isotopic systematics of oceanic basalts: implications for mantle composition and processes. In: Saunders, A.D., and Norry, M.J., (eds.), Magmatism in ocean basins. Geological Society Special Publication 42, p. 313-345.

Swapp and Hollister, L.S., 1991, Inverted metamorphism within the Tibetan Slab of Bhutan: Evidence for a tectonically transported heat source: Canadian Mineralogist, v. 29, p. 1019-1041.

Tahirkheli, R.A.K., Mattauer, M., Proust, F., and Tapponnier, P., 1977. Donnees nouvelles sur la suture Inde-Eurasie au Pakistan. In: Jest, C., (ed.), Himalaya;

sciences de la terre. Colloques Internationaux du Centre National de la Recherche Scientifique, 268, v. 2, p. 209-212.

Tahirkheli, R.A.K., 1979a. Geology of Kohistan, Karakorum Himalaya, northern Pakistan. Special Issue of the Geological Bulletin, University of Peshawar, v. 11, p. 1-30.

Tahirkheli, R.A.K., 1979b. Geotectonic evolution of Kohistan. Special Issue of the Geological Bulletin, University of Peshawar, v. 11, p. 113-130.

Tahirkheli, R.A.K., Mattauer, M., Proust, F., and Taponnier, P., 1979. The India-Eurasia suture zone in northern Pakistan: synthesis and interpretation of recent data at a plate scale. In: Farah, A., and DeJong, K.A., (eds.), Geodynamics of Pakistan. Geological Survey of Pakistan, Quetta, p. 125-130.

Taponnier, P., and Molnar, P., 1976. Slip-line field theory and large-scale continental tectonics. Nature, v. 264, p. 319-324.

Taponnier, P., Mattauer, M., Proust, F., and Cassaignea, C., 1981. Mesozoic ophiolites, sutures, and large-scale tectonic movements in Afghanistan. Earth and Planetary Science Letters, v. 52, p. 355-371.

Taponnier, P., Peltzer, G., Le Dain, A., and Armijo, R., 1982. Propagating extrusion tectonics in Asia: New insights from simple experiments with plasticene. Geology, v. 10, p. 611-616.

Taponnier, P., Peltzer, G., and Armijo, R., 1986. On the mechanics of the collision between India and Asia. In: Coward,M.P., and Ries, A.C., (eds.), Collision Tectonics. Geological Society Special Publication 19, p. 115-157.

Thompson, A.B., 1982. Dehydration melting of pelitic rocks and the generation of H_2O-undersaturated granitic liquids. American Journal of Science, v. 276, p. 425-454.

Tonarini, S., Villa, I.M., Oberli, F., Meier, M., Spencer, D.A., Pognante, U., and Ramsay, J.G., 1993. Eocene age of eclogite metamorphism in Pakistan Himalaya: implications for India-Eurasia collision. Terra Nova, v. 5., p. 13-20.

Treloar, P.J., Rex, D.C., Guise, P.G., Coward, M.P., Searle, M.P., Windley, B.F., Petterson, M.G., Jan, M.Q., and Luff, I.W., 1989a. K-Ar and Ar-Ar

geochronology of the Himalayan collision in NW Pakistan: Constraints on the timing of suturing, deformation, meatamorphism and uplift. Tectonics, v. 8, p. 881-809.

Treloar, P.J., Broughton, R.D., Williams, M.P., Coward, M.P., and Windley, B.F., 1989b. Deformation, metamorphism and imbrication of the Indian plate, south of the Main Mantle Thrust, north Pakistan. Journal of Metamorphic Geology, v. 7, p. 111-125.

Treloar, P.J., Williams, M.P., and Coward, M.P., 1989c. Metamorphism and crustal stacking in the north Indian Plate, north Pakistan. Tectonophysics, v. 165, p. 167-184.

Treloar and Rex, 1990. Cooling and uplift histories of the crystalline thrust stack of the Indian Plate internal zones west of Nanga Parbat, Pakistan Himalaya. Tectonophysics, v. 180 p. 323-349.

Treloar, P.J., Brodie, K.H., Coward, M.P., Jan, M.Q., Khan, M.A., Knipe, R.J., Rex, D.C., and Williams, M.P., 1990. The evolution of the Kamila shear zone, Kohistan, Pakistan. In: Salisbury, M.H., and Fountain, D.M. (eds.), Exposed cross-sections of the continental crust. Kluwer Academic Press, Amsterdam, p. 175-214.

Treloar, P.J., Potts, G.J., Wheeler, J., and Rex, D.C., 1991. Structural evolution and asymmetric uplift of the Nanga Parbat syntaxis, Pakistan Himalaya. Geologische Rundschau, v. 80, p. 411-428.

Treloar, P.J., and Izatt, C.N., 1993. Tectonics of the Himalayan collision between the Indian Pate and the Afghan block: a synthesis. In: Treloar, P.J., and Searle, M.P. (eds.), Himalayan Tectonics. Geological Society Special Publication 74, p. 69-88.

Treloar, P.J., 1995. Pressure-temperature-time paths and the relationship between collision, deformation and metamorphism in the north-west Himalaya. Geological Journal, v. 30, p. 333-348.

Turcotte, D.L. and Schubert, G., 1982. Geodynamics. Application of Continuum Physics to Geological Problems. J. Wiley and Sons, N.Y., 450pp.

Turner, G., 1971. Argon 40-Argon 39 dating: the optimisation of irradiation parameters. Earth and Planetary Science Letters, v. 10, p. 227-234.

Turner, S., Arnaud, N., Liu, J., Rogers, N., Hawkesworth, C.J., Harris, N., Kelley, S., van Calsteren, P., and Deng, W., 1996. Post-collision, shoshonitic volcanism on the Tibetan Plateau: Implications for convective thinning of the lithosphere and the source of ocean island basalts. Journal of Petrology, v. 37, p. 45-71.

Vance, D., and O'Nions, R.K., 1990. Isotopic chronometry of zoned garnets: growth kinematics and metamorphic histories. Earth and Planetary Science Letters, v. 97, p. 227-240.

Vance, D., Prince, C.I., Anckiewicz, R., and Harris, N., 1997. The timing and rate of prograde metamorphism in the Himalayan orogen. European Union of Geosciences, 9th meeting, Strasbourg. Terra Abstracts, abstract supplement no. 1 to Terra Nova, v. 9, p. 64.

Vannay, J.C., and Spring, L., 1993. Geochemistry of the continental basalts within the Tethyan Himalaya of Lahul-Spiti and SE Zanskar, northwest India. In: Treloar, P.J., and Searle, M.P. (eds.), Himalayan Tectonics, Geological Society Special Publication 74, p. 237-249.

Vernon, R.H., 1996. Problems with inferring P-T-t paths in low-P granulite facies rocks. Journal of Metamorphic Geology, v. 14, p. 143-153.

Verplanck, P.L., Snee, L.W., and Lund, K., 1985. The boundary between the Nanga Parbat massif and the Ladakh island arc terrane, northern Pakistan: a cross fault on the main mantle thrust (abstract). EOS, v. 66, p. 1074.

Vielzeuf, D. and Holloway, J.R., 1988. Experimental determination of the fluid-absent melting relations in the pelitic system. Consequences for crustal differentiation. Contributions to Mineralogy and Petrology, v. 98, p. 257-276.

Villa, I.M., and Puxeddu, M., 1994. Geochronology of the Larderello geothermal field: new data and the "closure temperature" issue. Contributions to Mineralogy and Petrology, v. 115, p. 415-426.

Villa, I.M., Lemennicier, Y., and Le Fort, P., 1996. Late Miocene to Early Pliocene tectonometamorphism and cooling in south-central Karakorum and Indus-Tsangpo suture, Chogo Lungma area (NE Pakistan). Tectonophysics, v. 260, p. 201-215.

Vince, K.J., and Treloar, P.J., 1996. Miocene, north-vergent extensional displacements along the Main Mantle Thrust, NW Himalaya, Pakistan. Journal of the Geological Society, London, v. 153, p. 677-680.

Wadia, D.N., 1932. Note on the geology of Nanga Parbat (Mt. Diamir) and adjoining portions of Chilas, Gilgit district, Kashmir. Records of the Geological Survey of India, v. 66, p. 212-235.

Wadia, D.N., 1961. Geology of India: Macmillan, New York, 536 pp.

Wartho, J.-A., Rex, D.C., and Guise, P.G., 1996. Excess argon in amphiboles linked to greenschist facies alteration in the Kamila amphibolite belt, Kohistan Island Arc system, northern Pakistan: insights from $^{40}Ar/^{39}Ar$ step-heating and acid leaching experiments. Geological Magazine, v. 133, p. 595-609.

Waters, D.J., 1991. Hercynite-quartz granulites: phase relations, and implications for crustal processes. European Journal of Mineralogy, v. 3, p. 367-386.

Watson, E.B., and Harrison, T.M., 1983, Zircon saturation revisited: temperature and composition effects in a variety of crustal magma types: Earth and Planetary Science Letters, v. 64, p. 295-304.

Watt, G.R., and Harley, S.L., 1993, Accessory phase controls on the geochemistry of crustal melts and restites produced during water-undersaturated partial melting: Contributions to Mineralogy and Petrology, v. 114, p. 550-556.

Wheeler, J,. Treloar, P.J. and Potts, G.J., 1995, Structural and metamorphic evolution of the Nanga Parbat syntaxis, Pakistan Himalayas, on the Indus gorge transect: the importance of early events: Geological Journal, v. 30, p. 349-371.

Whittington, A.G., Harris, N.B.W. and Butler, R.W.H., 1995. Metamorphism and anatexis during rapid exhumation of the Western Himalaya, Northern Pakistan. European Union of Geosciences, 8th meeting, Strasbourg. Terra Abstracts, abstract supplement no. 1 to Terra Nova, v. 7, p. 113.

Whittington, A.G., 1996. Exhumation overrated at Nanga Parbat, northern Pakistan. Tectonophysics, v. 260, p. 215-226.

Whittington, A.G., Harris, N.B.W., and Butler, R.W.H., 1997a. Contrasting anatectic styles at Nanga Parbat, northern Pakistan. Geological Society of America Special Publication, (in press).

Whittington, A.G., Harris, N.B.W., and Baker, J., 1997b. Low-pressure crustal anatexis: the significance of spinel and cordierite from metapelitic assemblages at Nanga Parbat, northern Pakistan. In: Treloar, P.J., and O'Brien, P. (eds.), Geological Society Special Publication (in press).

Winchester, J.A., and Floyd, P.A., 1977. Geochemical discrimination of different magma series and their differentiation products using immobile elements. Chemical Geology, v. 20, p. 325-343.

Winslow, D.M., Zeitler, P.K., Chamberlain, C.P., and Hollister, L.S., 1994. Direct evidence for a steep geotherm under conditions of rapid denudation, Western Himalaya, Pakistan. Geology, v. 22, p. 1075-1078.

Winslow, D.M., Chamberlain, C.P., and Zeitler, P.K., 1995, Metamorphism and melting of the lithosphere due to rapid denudation, Nanga Parbat Massif Himalaya: Journal of Geology, v. 103, p. 395-409.

Winslow, D.M., Zeitler, P.K., Chamberlain, C.P., and Williams, I.S., 1996. Geochronological constraints on syntaxial development in the Nanga Parbat region, Pakistan. Tectonics, v.15 no. 6, p. 1292-1308.

Wood, D.A., Joron, J-L., and Treuil, M., 1979. A re-appraisal of the use of trace elements to classify and discriminate between magma series erupted in different tectronic settings. Earth and Planetary Science Letters, v. 45, p. 326-336.

Wright, N., Layer, P.W., and York, D., 1991. New insights into thermal history from single grain $^{40}Ar/^{39}Ar$ analysis of biotite. Earth and Planetary Science Letters, v. 104, p. 70-79.

Wyllie, P.J., 1977, Crustal anatexis: An experimental review: Tectonophysics, v. 43, p. 41-71.

Xu, R.H., Scharer, U., and Allegre, C.J., 1985. Magmatism and metamorphism in the Lhasa block (Tibet): a geochronological study. Journal of Geology, v. 93, p. 41-57.

Yamamoto, H., and Nakamura, E., 1996. Sm-Nd dating of garnet granulites from the Kohistan complex, northern Pakistan. Journal of the Geological Society, London, v. 153, p. 965-969.

Yamamoto, H., 1993. Contrasting metamorphic P-T time paths of the Kohistan granulites and tectonics of the western Himalayas. Journal of the Geological Society, London, v. 150, p. 843-856.

Yeats, R.S., and Hussain, A., 1987. Timing of structural events in the Himalayan foothills of northwestern Pakistan. Geological Society of America Bulletin, v. 99, p. 161-176.

Yielding, G., Ahmad, S., Davison, I., Jackson, J.A., Khattak, R., Khurshid, A., King, G.C.P., and Lin Ban Zuo, 1984. A microearthquake survey in the Karakorum. In: Miller, K.J. (ed.), Proceedings of the International Karakorum Project. Royal Geographical Society, London, vol. 2, p. 150-169.

Zeitler, P.K., Johnson, N.M., Naeser, C.M. and Tahirkheli, R.A.K., 1982a. Fission-track evidence for Quaternary uplift of the Nanga Parbat region, Pakistan. Nature, v. 298, p. 255-257.

Zeitler, P.K., Tahirkheli, R.A.K., Naeser C.W., and Johnson, N.M., 1982b. Unroofing history of a suture zone in the Himalaya of Pakistan by means of fission-track annealing ages: Earth and Planetary Science Letters, v. 57, p. 227-240.

Zeitler, P.K., 1985. Cooling history of the NW Himalaya, Pakistan: Tectonics, v. 4, p. 127-151.

Zeitler, P.K., 1989, The geochronology of metamorphic processes. In: Daly, J.S., Cliff, R.A., and Yardley, B.W.D., (eds.), Evolution of metamorphic belts. Geological Society Special Publication 43, p. 131-147.

Zeitler, P.K., Sutter, J.F., Williams, I.S., Zartman, R., and Tahirkheli, R.A.K., 1989. Geochronology and temperature history of the Nanga Parbat-Haramosh Massif, Pakistan. In: "Malincnico, L.L., and Lillie, R.J. (eds.), "Tectonics of the western Himalayas". Geological Society of America Special Paper 232, p. 1-22.

Zeitler, P.K. and Chamberlain, C.P., 1991, Petrogenetic and tectonic significance of young leucogranites from the northwestern Himalaya, Pakistan: Tectonics, v. 10, p. 729-741.

Zeitler, P.K., Chamberlain, C.P., and Smith, H.A., 1993, Synchronous anatexis, metamorphism, and rapid denudation at Nanga Parbat (Pakistan Himalaya): Geology, v. 21, p. 347-350.

APPENDIX 1 - ANALYTICAL TECHNIQUES

A 1.1 Sample powder and mineral separate preparation

Whole-rock samples were cut into 5cm blocks and weathered surfaces were removed. Blocks were then crushed in a hardened steel jaw crusher, and a representative 100g portion of the crushate was then powdered in an agate tema mill for approximately 12 minutes to produce a powder of less than 200 mesh grain size.

Mineral separates were obtained by sieving a portion of the crushate from the jaw crusher, followed by hand-picking under a binocular microscope. The separates were then rinsed twice with distilled water in an ultrasonic bath.

A 1.2 XRF sample preparation and analysis

Rock powders were dried overnight to eliminate moisture. Glass discs for major element analysis were made by mixing lithium metaborate/tetraborate flux (Spectroflux 100B) to rock powders in the ratio 5:1. The resulting mixtures were fused in Pt - 5% Au crucibles in a muffle furnace at 1100 °C for 20 minutes. The fused mixtures were poured into heated, 3.6 cm diameter moulds to produce 1.5 mm thick discs. Loss on Ignition (LOI) for each sample was calculated by igniting the sample at 1000 °C for 30 minutes and measuring the percentage mass loss.

Powder pellets for trace element analysis were prepared by mixing 10 g of rock powder and 0.6 ml of polyvinylpyrollidone (PVP)-methyl cellulose binder. The mixtures were pressed into 3.8 cm diameter pellets in a hydraulic press at a pressure of 105 Pa. The pellets were then dried for 12 hours at 90 °C before analysis.

Major and trace element analyses were carried out by wavelength dispersive XRF spectrometry at the Open University. X-rays were generated using a 3 kW Rh anode end-window X-ray tube, and the diffracting crystals used were AX06, PET, Ge111, LiF200 and LiF220. Elemental intensities were corrected for background and known peak overlap interferences. Instrumental intensity drift was taken into account using a drift monitor. Count times for most trace elements were selected to achieve 2 sigma precision better than 2 ppm or 2 % relative at concentrations > 100 ppm. Major element matrix corrections employed the empirical Traill-Lachance procedure; trace element matrix corrections usually involved ratioing with the Compton scattered tube lines.

A 1.3 Instrumental neutron activation analysis (INAA)

Instrumental neutron activation analysis (INAA) was used to determine the concentrations of the rare earth elements La, Ce, Nd, Sm, Eu, Tb, Yb and Lu together with Th, U, Co, Ta and Hf. 0.3g of pre-dried rock powder was weighed into a polythene capsule and sealed. Nine samples and two standards were stacked into a cylinder, with weighed lacquered iron foil between each capsule to monitor the neutron flux variation along the length of the cylinder. The two standards used in each cylinder were an irradiation standard AC-2 (Ailsa Craig

microgranite) and a sample from the Whin Sill which was used as an internal standard.

Samples were irradiated in the core tube at the Imperial College Reactor Centre, Ascot, in a thermal neutron flux of 1 x 10^{12} ncm^2 sec^{-1} for 8 hours. The samples were left for a week before analysis to allow short lived radioactive isotopes to decay; details of counting conditions, peak fitting, calibration and corrections are described in Potts et al. (1985).

A 1.4 Microprobe analysis

Mineral compositions were determined by wavelength dispersive microprobe analysis on a Cameca SX 100 at the Open University. Analyses were undertaken using a 20 nA beam current, 20 kV accelerating potential, and a typical spot size of 20 μm. For spinel analyses, a reduced beam size of 1μm was used due to the small size of the crystals.

The SX100 has four spectrometers, and major elements were analysed using the PET, LiF and TAP diffracting crystals, calibrated using the following standards:

Si, Al, K	fspr-In5	Fe	hematite-ast3
Ti	rutile-BM4	Mg	forsterite-BM4
Mn, Ca	bustamite-ast3	Na	jadeite-BM4
P	apatite-BM4	Cr	crocoite-ast3
Cl	sylvite-BM4	F	LiF-4

Some analyses were peformed by energy dispersive analysis on the Cameca SX-50 at Cambridge (November to December 1995), and some on the Cameca SX-50 at Leeds (1994). Others were performed by wavelength dispersive analysis on the Cambridge Mark 9 microprobe at the Open University in 1994, with calibration to the basaltic glass standard ABG.

A 1.5 Radiogenic isotope analysis

A 1.5.1 Sample dissolution

Sr and Nd isotopic analyses and preparations were carried out in a clean-air laboratory in which a positive air pressure was maintained. All solutions used in the dissolutions were made up with teflon-distilled Milli-Q reverse osmosis (RO) purified water. Prior to use, beakers were rinsed in RO water, soaked in hot 15M HNO3 (aq) for at least 24 hours, rinsed and soaked in RO water overnight, and finally rinsed in hot 6M HCl.

Between 150 and 200 mg of rock powder was subjected to digestion with HF and HNO_3, and repeatedly treated with hot 15M HNO_3 and 6M HCl until complete dissolution was achieved. All solutions were evaporated to dryness and the residues redissolved in 1ml 2.5M HCl. Sr was separated using carefully calibrated ion-exchange columns of 10 ml preconditioned Bio-rad AG50W X8 200-400 mesh resin. For the separation of Nd, the MREE fraction was collected in 3M HNO_3 and evaporated to dryness. This residue was dissolved in 0.5 ml 0.25M HCl, and Nd separated using preconditioned reverse ion-exchange columns composed of 1g teflon powder (Voltalef 300LD PL micro) and 100g DEP (di(2-ethylhexyl)phosphate).

A 1.5.2 Mass spectrometry

Samples for $^{87}Sr/^{86}Sr$ and $^{143}Nd/^{144}Nd$ ratio measurements were carried out on a Finnegan M80 262 solid source, multi-collector mass spectrometer, interfaced with a HP 9836 computer using software designed by D.W Wright and P.W.C. van Calsteren. Filaments were outgassed before loading for 5 minutes at 4.5A in a vacuum better than 10-6 torr. Sr was loaded in phosphoric acid on single Ta filaments, and the measured $^{87}Sr/^{86}Sr$ ratios were exponentially fractionation corrected within each run to $^{87}Sr/^{88}Sr = 0.1194$. Machine standard NBS 987 was run with each batch of samples, and reported analyses have been corrected to a value of NBS 987 of 0.710220. 13 measurements of NBS 987 gave an average $^{87}Sr/^{86}Sr$ ratio of 0.710223 ± 17 (1 sigma), and the rock standard NBS 607 gave an $^{87}Sr/^{86}Sr$ ratio of 1.200872 ± 16 (1 sigma). Total procedural strontium blanks were less than 3 ng.

Neodymium was loaded on Ta filaments (a Re ionisation filament was used) and run as metal ions. $^{143}Nd/^{144}Nd$ ratios were exponentially fraction corrected to $^{146}Nd/^{144}Nd = 0.72190$. Eight analyses of an internal J&M Nd standard over the period of analysis had a mean value of 0.511753 ± 10 (1 sigma), and reported ratios have been corrected to a value for J&M of 0.511836, corresponding to a value for BCR-1 of 0.512638. Total procedural neodymium blanks were less than 1 ng.

A 1.5.3 Age corrections and constants

$^{87}Rb/^{86}Sr$ and $^{147}Sm/^{144}Nd$ ratios were calculated for each sample from the elemental ratios measured by XRF and INAA:

$$^{87}Rb/^{86}Sr = 2.891\ Rb/Sr$$

$$^{147}Sm/^{144}Nd = 0.602\ Sm/Nd$$

All initial isotope ratios have been calculated using the age equations:

$$(^{87}Sr/^{86}Sr)_{measured} = (^{87}Sr/^{86}Sr)_{initial} + {}^{87}Rb/^{86}Sr\ (e^{i1t}-1)$$

$$(^{143}Nd/^{144}Nd)_{measured} = (^{143}Nd/^{144}Nd)_{initial} + {}^{147}Sm/^{144}Nd(e^{i2t}-1)$$

where i1 = 1.42 x 10-11 y^{-1} and i2 = 6.54 x 10-12 y^{-1}.

Epsilon notation follows the definitions of De Paolo and Wasserburg (1976), and model Sr and Nd ages are reported relative to depleted mantle. The following constants have been used:

$^{87}Rb/^{86}Sr_{bulk\ earth} = 0.0847$ $^{147}Sm/^{144}Nd_{CHUR} = 0.1967$

$^{87}Sr/^{86}Sr_{bulk\ earth} = 0.7047$ $^{143}Nd/^{144}Nd_{CHUR} = 0.51264$

$^{87}Rb/^{86}Sr_{DM} = 0.0487$ $^{147}Sm/^{144}Nd_{DM} = 0.2238$

$^{87}Sr/^{86}Sr_{DM} = 0.70306$ $^{143}Nd/^{144}Nd_{DM} = 0.51310$

A 1.6 $^{40}Ar/^{39}Ar$ mass spectrometry

Pure, hand-picked mineral separates for $^{40}Ar/^{39}Ar$ analysis were packed in aluminium foil and loaded into known positions within a foil cylinder. The flux monitors MMHb1, GA1550 biotite (McDougall and Harrison, 1988) and Tinto felsite biotite (Rex and Guise, 1995) were included in the cylinder as standards to monitor neutron flux during irradiation. The samples were irradiated in three

batches, at different reactors with different J values, calculated using the flux monitors.

Batch 1 (1994) was irradiated at the Imperial College reactor, Ascot, U.K., with a J value of 5.0×10^{-5}.

Batch 2 (1995) was irradiated at the Oregon State University reactor, U.S.A., with a J value of 4.0×10^{-4}.

Batch 3 (1996) was irradiated at the Risø reactor, Copenhagen, with a J value of 3.3×10^{-3}.

The samples were loaded into an ultra high vacuum laser port and heated overnight to reduce atmospheric blank levels. Argon was extracted from individual mineral grains by firing short pulses of a continuous Spectron SL902CW Nd-YAG laser beam (TEMoo, wavelength 1064nm) through a customised petrological microscope. The beam was focused using a CCD camera, coaxial with the laser beam, to a spot size of about 20μm on the sample surface. The power of the beam was increased gradually on individual mineral grains until they began to melt. This method prevents grains jumping around the sample chamber when the laser beam impinges. Typical powers of 10 to 17 W were used, and pulse lengths of between 5 and 20 s.

The argon was purified using a SAES GP10 getter at 400°C for 5 minutes, and then allowed into a Mass Analyser Products 215-50 noble gas mass spectrometer via automated valves. Seven masses were analysed; 35, 36, 37, 38, 39, 40 and 41. Peaks between 35 and 41 were scanned 7 times and amounts extrapolated back to the inlet time. This overcomes the problem of argon either being released from or being adsorbed onto the mass spectrometer walls. A blank run was made after every sample run and blank corrections to the sample analysis were made by averaging the blank before and after the analysis. The mass spectrometer was run

in high resolution mode during the analysis of batches 2 and 3, with a 0.33 mm slit enabling distinction between argon and hydrocarbon peaks at similar masses, which resulted in improved blanks. Blank levels were found to be very constant throughout all the analysis periods. Mean blank levels, $x10^{-12}$ cc STP, are tabulated below:

Mass	Batch 1 (1994)	Batches 2 (1995) and 3 (1996)
Resolution	Low	High
^{40}Ar	6.4 ± 1.4	3.92 ± 0.06
^{39}Ar	7.8 ± 0.3	0.066 ± 0.008
^{38}Ar	0.9 ± 0.3	0.076 ± 0.006
^{37}Ar	1.2 ± 0.4	0.67± 0.02
^{36}Ar	1.4 ± 0.1	0.146 ± 0.009

These values are significantly smaller than blanks obtained from furnace step-heating argon machines where the walls of the furnace are also outgassed during heating.

The data were corrected for interfering nuclear reactions involving Ca and K; the correction factors used were:

Reactor	$(^{39}Ar/^{37}Ar)_{Ca}$	$(^{36}Ar/^{37}Ar)_{Ca}$	$(^{40}Ar/^{39}Ar)_{K}$
Ascot, 1994	0.000781	0.000205	0.031
OSU, 1995	0.000673	0.000260	0.00080
Risø, 1996	0.000670	0.000255	0.030

Corrections were also applied for mass spectrometer fractionation, ^{37}Ar decay since the time of irradiation, and background levels of Ar (monitored from analysis of blanks).

APPENDIX 2 - WHOLE-ROCK GEOCHEMICAL DATA

This appendix contains X-ray fluorescence, Instrumental Neutron Activation Analysis, and Rb-Sr and Sm-Nd isotopic analyses for whole-rock samples from the southern Nanga Parbat-Haramosh Massif. Rock names which are denoted alphanumerical subdivision, e.g. E5A, E5B, and Z13/i, Z13/ii are different pieces taken from the same hand specimen. Rocks with two identifiers (e.g. Z46C/i, Z46C/ii) were usually chosen to separate different lithologies from the same hand specimen, for example Z130a/i and Z130a/ii are a cordierite seam and biotite gneiss from the same hand specimen.

Isotopic results are normalised according to the procedures described in Appendix 1, but not age-corrected. Errors were less than ± 20 on $^{87}Sr/^{86}Sr$, and less than ± 10 on $^{143}Nd/^{144}Nd$, but only reflect the analytical accuracy claimed by the computer which processed the data output from the mass spectrometer.

In addition to pelite and marble, abbreviations used for rock type are:

amph = metabasaltic sheet

bi gneiss = muscovite-absent orthogneiss

calc-sil = calc-silicate

crd seam = cordierite seam

Koh = Kohistan

(def) lcg = (deformed) leucogranite sheet

MMT = MMT zone

mu gneiss = muscovite-bearing orthogneiss

peg = pegmatite

Tato = Tato pluton

	Basic sheets					
SAMPLE	E104A	E104B	E104C	E104D	E104E	E119A
TYPE	amph	amph	amph	amph	amph	amph
SiO2	46.81	48.45	46.14	46.49	47.08	51.6
TiO2	0.689	0.628	0.632	0.665	0.642	1.597
Al2O3	15.23	14.43	14.87	15.15	14.99	14.31
Fe2O3	12.64	11.76	12.03	12.48	12.09	12.78
MnO	0.183	0.182	0.189	0.181	0.185	0.217
MgO	8.56	8.61	8.4	8.46	8.6	6.35
CaO	11.05	10.98	11.62	11.26	10.92	8.85
Na2O	2.08	2.31	2.09	2.08	2.25	2.07
K2O	1.1	0.85	1.22	1.15	1.02	1.01
P2O5	0.07	0.07	0.065	0.07	0.066	0.139
LOI	1.22	1.65	2.49	1.68	1.89	1.01
TOTAL	99.63	99.92	99.75	99.67	99.73	99.93
Rb	68.3	56.7	91.7	72.7	72.1	47.6
Sr	160	154.2	157.6	160.7	158	381.4
Ba	161	132	127	122	162	229
Y	20.5	19.3	18.2	19.4	18.6	24.2
Zr	66	64	64	65	62	120
Nb	2.4	3.7	2.4	3.1	3.4	7.1
Pb	15	9	12	15	13	23
Th	5	5	6	7	3	4
U	0	1	0	1	0	0
Sc	36	36	32	38	37	37
V	276	255	261	262	266	300
Cr	462	406	460	477	467	213
Co	62	56	58	59	59	49
Ni	157	150	157	155	161	56
Cu	104	9	130	123	69	80
Zn	94	102	104	94	104	114
Ga	18	17	18	16	17	22
La	9.945	9.3	10.2	10.3	9.4	15.5
Ce	19.3	18.5	18.3	19.65	18.3	31.2
Nd	10.3	10.3	10.2	10.9	9.7	17.5
Sm	2.5	2.468	2.48	2.565	2.44	4.24
Eu	0.76	0.784	0.76	0.8	0.77	1.41
Tb	0.58	0.564	0.52	0.576	0.544	0.78
Yb	1.66	1.59	1.6	1.63	1.6	2.01
Lu	0.24	0.24	0.23	0.25	0.24	0.29
Th	3.26	3.09	3.175	3.41	3.06	3.229
U	0.6	0.69	0.95	0.63	0.5	1.15
Ta	0.22	0.21	0.22	0.23	0.23	0.53
Hf	1.81	1.71	1.84	1.79	1.84	3.216
87Sr/86Sr	0.749876	0.751775	0.750259	0.752296	0.750550	0.757660
143Nd/144Nd	0.511907	0.511887	0.511893		0.511874	0.511979

SAMPLE TYPE	E119B amph	E119C amph	E119D amph	E119E amph	E155 amph	Kohistan E156 Kohistan
SiO2	51.46	50.96	51.04	53.95	43.87	60.45
TiO2	1.579	1.634	1.518	1.421	0.324	0.763
Al2O3	14.47	14.18	13.78	14.9	6.13	16.45
Fe2O3	12.72	12.99	13.68	11.88	14.01	7.46
MnO	0.217	0.226	0.228	0.182	0.189	0.138
MgO	6.3	6.41	7.17	6.08	28.31	3.14
CaO	8.93	8.93	7.98	6.41	5.29	6.46
Na2O	2.12	1.92	1.63	1.93	0.22	3.17
K2O	0.94	1.04	1.69	2.05	0.11	1.74
P2O5	0.137	0.142	0.138	0.139	0.044	0.164
LOI	1.08	1.03	1.11	0.59	0.34	0.36
TOTAL	99.95	99.46	99.96	99.53	98.837	100.3
Rb	40.4	54.6	143	139.9	6.8	49.5
Sr	391.7	344	225.6	211.8	13.3	392.5
Ba	202	230	411	362	13	463
Y	24.1	25.4	22.1	24.2	9.1	23.2
Zr	114	125	115	144	31	128
Nb	7.4	7.9	6.8	11.9	1.2	2.9
Pb	24	24	17	36	2	19
Th	4	4	6	7	3	4
U	0	1	3	0	1	0
Sc	33	32	31	30	24	20
V	307	306	296	254	151	176
Cr	209	211	197	162	3969	23
Co	49	50	54	44	136	20
Ni	57	55	55	44	1589	12
Cu	94	78	63	52	183	46
Zn	113	115	131	265	86	76
Ga	21	23	20	21	9	18
La					4.1	18.2
Ce					8.4	37
Nd					4.4	18.2
Sm					1.07	3.98
Eu					0.31	1
Tb					0.25	0.64
Yb					0.82	2.21
Lu					0.13	0.36
Th					1.24	2.847
U					0.5	0.8
Ta					0.12	0.21
Hf					0.81	3.9
87Sr/86Sr	0.757680	0.760182	0.761970	0.770687	0.736207	0.705394
143Nd/144Nd		0.512013	0.511982	0.511810	0.512002	0.512639

	Metamorphic rocks					
SAMPLE	E160	Z69	Z71/i	Z71/ii	E110	E125
TYPE	Kohistan	bi gneiss	bi gneiss	bi gneiss	bi gneiss	bi gneiss
SiO2	55.58	73.21	73.7	72.76	66.65	71.81
TiO2	0.801	0.124	0.203	0.339	0.776	0.586
Al2O3	16.79	14.86	13.86	13.47	14.56	13.36
Fe2O3	8.11	1.21	1.59	2.36	5.62	4.78
MnO	0.133	0.023	0.02	0.026	0.068	0.057
MgO	5.02	0.22	0.51	0.79	1.53	1.04
CaO	8.18	0.55	1.03	1.17	1.77	1.73
Na2O	3.19	2.98	2.69	2.7	2.62	3.49
K2O	0.42	6.25	6.39	5.52	4.98	2.67
P2O5	0.165	0.232	0.069	0.064	0.182	0.15
LOI	1.97	0.41	0.32	0.37	0.49	0.41
TOTAL	100.36	100.07	100.38	99.57	99.25	100.08
Rb	7	238	211	214	296.8	317.9
Sr	372.8	167	149	138	144	106.2
Ba	121	686	922	787	720	543
Y	18.3	38.6	19.9	34.3	34.3	31.9
Zr	59	214	56	89	232	265
Nb	2.4	15.1	6	9	16	14.4
Pb	8	33	64	54	44	26
Th	1	25	10	17	37	28
U	1	5	3	5	5	5
Sc	23	17	2	5	10	10
V	210	51	14	19	48	28
Cr	103	54	48	35	54	41
Co	32	11	3	4	12	8
Ni	42	14	11	14	14	12
Cu	51	10	2	4	19	13
Zn	80	112	26	41	87	105
Ga	16	20	13	14	19	17
La		72.3				
Ce		147				
Nd		62.8				
Sm		11				
Eu		1.55				
Tb		1.54				
Yb		4.957				
Lu		0.71				
Th		30.3				
U		6.37				
Ta		1.63				
Hf		8.63				
87Sr/86Sr						
143Nd/144Nd						

SAMPLE	E154	E115	Z124	E127	Z150	Z151
TYPE	bi gneiss	calc-sil	calc-sil	calc-sil	marble	marble
SiO2	67.91	65.22	50.48	53.59	17.63	12.24
TiO2	0.856	0.263	0.507	0.774	0.162	0.108
Al2O3	14.25	7.88	17.56	14.41	3.87	2.59
Fe2O3	5.74	6.13	7.49	10.88	4.77	0.86
MnO	0.063	0.282	0.204	0.165	0.461	0.04
MgO	1.21	4.65	3.38	6.51	17.48	2.03
CaO	2.58	14.82	18.37	9.66	29.15	45.8
Na2O	2.51	0.18	0.28	2.4	0.25	1.36
K2O	4.21	0.16	0.55	1.15	0.72	0.45
P2O5	0.176	0.079	0.098	0.085	0.063	0.024
LOI	0.53	0.48	1.06	0.52	24.75	34.36
TOTAL	100.04	100.144	99.98	100.14	99.31	99.86
Rb	270.9	8.1	59.1	84.9	47.9	21.6
Sr	130.5	101.9	186.9	160.6	30.9	148.9
Ba	564	297	24	144	30	178
Y	34.3	20.9	35.8	20.4	16.7	6.4
Zr	258	174	86	78	56	27
Nb	15.8	6.6	15.9	4.6	3.2	3.4
Pb	34	16	19	11	6	26
Th	48	14	21	7	3	4
U	7	3	8	3	2	0
Sc	14	13	18	31	16	25
V	42	28	72	229	29	14
Cr	46	40	107	194	29	19
Co	9	24	14	45	5	6
Ni	13	45	38	51	13	8
Cu	10	14	8	19	7	6
Zn	92	161	83	80	17	20
Ga	21	10	28	18	5	4
La						
Ce						
Nd						
Sm						
Eu						
Tb						
Yb						
Lu						
Th						
U						
Ta						
Hf						
87Sr/86Sr						
143Nd/144Nd						

SAMPLE	E158	E157	E159	E101	E102	E103
TYPE	MMT amph	MMT pelite	MMT pelite	mu gneiss	mu gneiss	mu gneiss
SiO2	48.12	69.67	52.7	69.24	71.85	70.85
TiO2	0.713	0.614	0.993	0.657	0.467	0.527
Al2O3	13.01	15.04	13.02	14.28	14.02	14.28
Fe2O3	6.28	4.36	7.38	4.58	2.92	3.19
MnO	0.105	0.074	0.172	0.057	0.026	0.027
MgO	1.91	1.17	2.73	1.24	0.55	0.67
CaO	15.33	1.68	13.72	1.49	0.91	1.05
Na2O	1.11	2.62	0.67	3.26	2.68	2.62
K2O	1.85	3.59	1.25	4.64	5.82	5.76
P2O5	0.143	0.133	0.217	0.105	0.25	0.253
LOI	8.79	0.88	1.32	0.74	0.53	0.5
TOTAL	97.361	99.83	94.172	100.29	100.02	99.73
Rb	92.3	159.2	64.5	240	334	320
Sr	1060.5	100.5	669.9	155	72	68.3
Ba	218	397	170	608	361	396
Y	24.5	27.6	28	35.1	24.2	29.3
Zr	119	190	137	211	216	334
Nb	12.9	13.2	17.5	13	16.4	19.2
Pb	22	31	45	37	47	37
Th	17	26	15	36	41	69
U	2	2	2	7	4	5
Sc	17	8	19	11	1	4
V	175	57	114	45	18	20
Cr	131	43	105	50	16	14
Co	13	10	16	8	3	3
Ni	43	15	36	10	5	5
Cu	30	12	50	6	8	10
Zn	85	73	88	82	65	55
Ga	19	19	15	20	20	20
La				66	62	
Ce				143	145	
Nd				62.9	67.7	
Sm				11.5	12.4	
Eu				1.02	0.59	
Tb				1.23	1.08	
Yb				4.67	2.09	
Lu				0.69	0.3	
Th				37.2	50.4	
U				7.1	6.8	
Ta				1.52	1.69	
Hf				6.65	7.31	
87Sr/86Sr				0.834933	1.154826	1.063079
143Nd/144Nd				0.511230	0.511277	0.511320

SAMPLE TYPE	E106 mu gneiss	N1 pelite	E4 pelite	X4 pelite	X8 pelite	X8(ii) pelite
SiO2	70.96	51.06	67.89	57.61	66.35	66.61
TiO2	0.414	0.745	0.812	0.768	0.571	0.578
Al2O3	15.03	25.78	14.15	20.16	15.42	15.56
Fe2O3	3.23	10.99	6.02	9.02	7.42	7.41
MnO	0.031	0.064	0.065	0.092	0.15	0.148
MgO	1.08	4.43	1.74	3.12	2.3	2.3
CaO	1	0.24	1.28	1	1.66	1.68
Na2O	2.95	0.52	3.16	1.55	1.99	2.02
K2O	4.37	3.96	4.07	4.77	2.53	2.55
P2O5	0.21	0.045	0.19	0.09	0.108	0.112
LOI	1.02	2.25	0.33	1.75	1.17	1.17
TOTAL	100.3	100.08	99.71	99.93	99.67	100.14
Rb	335.7	233	214	264	170	170
Sr	114.9	46.1	128	155	205	205
Ba	329	568	614	1041	407	407
Y	13.5	17.5	20.7	36.2	32.5	32.5
Zr	163	108	233	148	194	194
Nb	17	13.5	15.9	14.3	15.3	15.3
Pb	27	14	36	27	17	17
Th	34	18	26	22	16	16
U	7	4	7	3	3	3
Sc	6	25	13	20	18	18
V	32	159	41	137	91	91
Cr	39	216	52	213	137	137
Co	8	29	12	28	20	20
Ni	18	66	13	72	50	50
Cu	14	11	10	43	85	85
Zn	73	173	86	124	82	82
Ga	23	35	24	26	20	20
La	43.1	54.4			45.6	
Ce	98.1	104			90	
Nd	45	41.2			36.87	
Sm	8.71	7.03			6.17	
Eu	0.61	1.59			1.21	
Tb	0.68	0.7966			0.84	
Yb	1.37	1.976			4.19	
Lu	0.22	0.3			0.61	
Th	36.5	18.1			17.6	
U	8	1.898			2.8	
Ta	1.84	0.91			1.46	
Hf	4.86	3.1			5.73	
87Sr/86Sr	0.906128	0.887004				
143Nd/144Nd	0.511353	0.511147				

SAMPLE TYPE	Z9/i pelite	Z9/ii pelite	Z13/i pelite	Z13/ii pelite	Z13/iii pelite	Z17A pelite
SiO2	74	73.84	74	73.46	73.65	63.01
TiO2	0.214	0.224	0.227	0.251	0.228	0.771
Al2O3	13.88	13.85	13.69	13.64	13.64	16.92
Fe2O3	2.01	1.96	2	2.18	2.02	7.34
MnO	0.021	0.017	0.017	0.018	0.017	0.074
MgO	0.36	0.37	0.4	0.44	0.39	2.96
CaO	0.68	0.69	0.64	0.62	0.64	1.41
Na2O	3.16	3.46	3.26	3.14	3.24	2.6
K2O	4.95	4.95	5.37	5.61	5.34	3.37
P2O5	0.212	0.193	0.215	0.229	0.214	0.09
LOI	0.67	0.54	0.37	0.58	0.78	0.51
TOTAL	100.16	100.09	100.19	100.17	100.16	99.06
Rb	355	346	363	389	373	228
Sr	58.9	59.8	58.2	60.5	57.1	248
Ba	184	187	185	192	183	640
Y	10.8	10.5	12.6	14.4	13.1	25.5
Zr	102	104	105	112	107	179
Nb	15.1	15.6	16.6	18.1	15.9	13.9
Pb	30	33	34	35	33	18
Th	17	14	20	19	19	14
U	12	11	9	9	8	3
Sc	4	3	4	2	5	16
V	8	9	9	10	9	117
Cr	17	16	19	45	15	166
Co	3	3	3	3	2	23
Ni	5	7	6	7	7	60
Cu	1	2	4	2	3	17
Zn	59	60	60	64	62	95
Ga	19	19	21	19	19	20
La	21.04		22			43.82
Ce	48.3		48.3			93.4
Nd	22.8		24.2			36.8
Sm	4.44		5.09			6.69
Eu	0.31		0.3			1.38
Th	0.59		0.69			0.868
Yb	1.06		0.82			2.56
Lu	0.11		0.12			0.38
Th	16.6		19.378			16.07
U	11.89		12.1			3.16
Ta	1.62		1.61			1.1
Hf	3.33		3.71			4.95
87Sr/86Sr	1.261778		1.275856			
143Nd/144Nd	0.511607		0.511704			

SAMPLE TYPE	E116 pelite	E126 pelite	E129 pelite	Z130a/ii pelite	Z130b/ii pelite	E132 pelite
SiO2	64.37	71.39	70.22	73.41	68.94	69.39
TiO2	0.626	0.506	0.462	0.054	0.522	0.479
Al2O3	15.99	13.63	14.53	14.72	14.91	14.37
Fe2O3	5.64	4.42	4.23	0.67	4.53	4.03
MnO	0.197	0.05	0.026	0.016	0.045	0.04
MgO	1.56	1.01	1.1	0.12	1.04	0.97
CaO	9.83	1.52	1.4	0.99	1.97	1.78
Na2O	0.47	2.51	2.66	2.53	2.98	3.48
K2O	0.5	4.29	4.91	6.94	4.25	4.68
P2O5	0.218	0.205	0.143	0.119	0.193	0.176
LOI	0.51	0.83	0.34	0.68	0.75	0.39
TOTAL	99.91	100.36	100.02	100.25	100.13	99.79
Rb	53.9	268.6	321	257.5	272.6	272.9
Sr	61.4	116.7	133.8	142.8	155.2	151.8
Ba	49	413	445	434	463	498
Y	44.5	27.4	15.9	24.2	24	30.6
Zr	358	207	177	207	199	251
Nb	23.3	15.4	18.2	21.7	23.5	13.5
Pb	6	29	38	28	31	34
Th	23	24	28	25	24	39
U	5	5	9	6	5	6
Sc	14	8	8	8	7	8
V	77	32	34	29	36	38
Cr	105	43	49	37	42	47
Co	10	8	6	8	9	9
Ni	25	19	11	12	14	16
Cu	2	17	8	22	17	25
Zn	56	87	77	61	76	74
Ga	30	20	24	22	23	20
La	55.3	45.5	56	53.8	46.3	
Ce	116	98.6	118	112	107	
Nd	48.1	42	47.5	47.9	46	
Sm	8.75	8.52	8.86	10.2	9.45	
Eu	1.44	0.9	1.43	0.95	1.05	
Tb	1.22	1.09	1.21	1.21	1.16	
Yb	4.53	2.8	4.48	1.85	1.75	
Lu	0.68	0.43	0.68	0.25	0.23	
Th	20.8	25.49	22.7	28.8	26.7	
U	5.3	5.8	5.5	8.87	6.3	
Ta	3.07	1.69	3.01	4.177	3.89	
Hf	10.2	6.495	10.4	6	6.42	
87Sr/86Sr		0.859012		0.849484	0.853127	
143Nd/144Nd				0.511521	0.511492	

SAMPLE TYPE	E138 pelite	E139 pelite	E145 pelite	E149 pelite	Z134 pelite	Z147 pelite
SiO2	71.71	74.38	69.7	75.14	69.46	60.4
TiO2	0.51	0.516	0.653	0.075	0.57	0.673
Al2O3	13.81	11.92	14.42	13.8	14.15	19.72
Fe2O3	3.22	4.18	3.88	2.26	5.16	8.3
MnO	0.023	0.062	0.032	0.086	0.108	0.09
MgO	0.81	1.59	0.89	0.45	1.76	3.09
CaO	0.91	1.8	1.77	1.75	6.2	0.57
Na2O	2.57	2.87	2.47	4.74	0.73	0.57
K2O	5.84	1.56	5.22	1.41	1.09	3.54
P2O5	0.17	0.049	0.218	0.063	0.141	0.11
LOI	0.32	1.03	0.46	0.36	0.67	2.84
TOTAL	99.89	99.96	99.713	100.13	100.04	99.9
Rb	357.2	62.7	335.6	105.2	72.3	227.9
Sr	74	346.4	117.5	33.1	215.6	31.2
Ba	362	725	535	14	229	422
Y	30	10.3	23.6	75.4	30.4	29.1
Zr	339	335	288	59	286	117
Nb	20.5	8.1	16.3	6.2	10.4	12.4
Pb	50	24	45	22	12	8
Th	104	6	73	19	20	20
U	17	3	5	10	4	3
Sc	4	9	8	6	12	21
V	11	67	22	6	74	111
Cr	14	118	29	31	104	152
Co	2	13	6	4	13	23
Ni	4	37	7	4	33	51
Cu	5	18	7	3	5	74
Zn	64	57	92	18	62	79
Ga	21	12	23	17	17	25
La						62.4
Ce						125
Nd						50
Sm						8.84
Eu						1.12
Tb						1.11
Yb						3.51
Lu						0.53
Th						23
U						2.5
Ta						1.08
Hf						3.48
87Sr/86Sr						
143Nd/144Nd						

	Granitic rocks					
SAMPLE	E5a/i	E5a/ii	E5B	E64	Z66A	Z66B
TYPE	Tato	Tato	Tato	Tato	Tato	Tato
SiO2	73.7	73.36	74.11	74.84	74.74	74.44
TiO2	0.074	0.089	0.082	0.063	0.078	0.078
Al2O3	14.33	14.3	14.21	14.09	14.02	13.97
Fe2O3	1.08	1.15	1.08	0.9	1.04	1.06
MnO	0.033	0.035	0.036	0.046	0.032	0.032
MgO	0.09	0.11	0.1	0.07	0.06	0.07
CaO	1.21	1.24	1.25	0.87	1.18	1.17
Na2O	3.43	3.61	3.65	3.87	3.44	3.5
K2O	4.8	4.8	4.81	4.55	4.92	4.91
P2O5	0.087	0.09	0.082	0.067	0.046	0.048
LOI	0.52	0.6	0.67	0.49	0.14	0.62
TOTAL	99.35	99.38	100.08	99.86	99.7	99.9
Rb	453	458	471	497	444	444
Sr	58.5	60	59.9	35.7	57.6	56.7
Ba	164	166	172	94	147	146
Y	38.8	41.2	41.6	40.5	46.7	46.4
Zr	60	62	64	44	70	72
Nb	11.2	12.1	12	13.4	11.2	11.7
Pb	77	77	76	65	90	89
Th	19	17	18	16	21	20
U	27	27	30	18	24	24
Sc	2	3	4	4	3	3
V	6	7	3	2	0	2
Cr	7	10	9	5	5	13
Co	1	1	1	1	1	1
Ni	3	2	2	3	4	3
Cu	8	3	3	0	2	2
Zn	30	31	31	28	29	28
Ga	22	23	22	22	21	23
La	18.5	17.9	16.5	15.7	19.3	
Ce	38	36	39.6	31.8	44	
Nd	21.7	20.68	21.9	17.4	21.5	
Sm	3.465	3.47	3.37	3.12	3.93	
Eu	0.36	0.38	0.39	0.24	0.36	
Tb	0.83	0.83	0.8569	0.82	0.95	
Yb	5.009	5.11	5.18	5.65	5.48	
Lu	0.756	0.74	0.75	0.82	0.85	
Th	16.423	16.056	16.7	16	20.7	
U	43.7	40.46	40.8	27	33	
Ta	3.8	4.02	3.88	5.5	3.4	
Hf	2.6	2.58	2.896	2.1	3.1	
87Sr/86Sr	0.877334	0.873815	0.874108	0.898255	0.880225	
143Nd/144Nd	0.877334	0.873815	0.511461	0.511449	0.511428	

SAMPLE TYPE	E70A Tato	E70B Tato	E70C Tato	E111 Tato	E112(1) Tato	E112(2) Tato
SiO2	73.95	73.33	74.08	73.83	74.11	73.79
TiO2	0.092	0.093	0.089	0.084	0.072	0.071
Al2O3	14.11	14.39	14.31	14.23	14.38	14.33
Fe2O3	1.18	1.2	1.19	1.14	1.09	1.08
MnO	0.03	0.031	0.031	0.035	0.036	0.036
MgO	0.11	0.09	0.09	0.13	0.11	0.09
CaO	1.41	1.43	1.42	1.37	1.17	1.16
Na2O	3.48	3.51	3.5	3.47	3.52	3.5
K2O	4.91	5.04	4.96	4.77	4.78	4.76
P2O5	0.057	0.062	0.059	0.056	0.07	0.067
LOI	0.42	0.43	0.39	0.52	0.63	0.63
TOTAL	99.75	99.61	100.12	99.64	99.97	99.51
Rb	395	397	395	474	467.4	467.4
Sr	71.7	71.1	71.7	67.5	54	54
Ba	195	194	204	182	134	134
Y	44.6	45.1	45.3	41.5	45.8	45.8
Zr	74	73	73	76	66	66
Nb	11.1	9.5	10.1	11.7	12.1	12.1
Pb	89	89	88	91	74	74
Th	21	21	21	18	17	17
U	30	28	30	27	33	33
Sc	3	3	4	4	2	2
V	3	4	2	7	5	5
Cr	9	9	11	11	7	7
Co	1	1	2	2	1	1
Ni	2	3	1	2	4	4
Cu	2	2	2	3	2	2
Zn	30	30	29	32	32	32
Ga	22	22	21	24	24	24
La	22.2	21.7	21.5	18.85	20.6	20.6
Ce	44	46.9	44	38.1	38.5	38.5
Nd	24.4	23.9	23.8	20.6	20.7	20.7
Sm	3.72	4.02	3.65	3.298	3.33	3.33
Eu	0.45	0.46	0.46	0.38	0.33	0.33
Tb	0.9	0.95	0.94	0.87	0.89	0.89
Yb	5.29	5.66	5.59	4.76	5.54	5.54
Lu	0.77	0.86	0.85	0.7	0.8	0.8
Th	20.91	20.6	20.2	17.2	17.3	17.3
U	39.35	44.5	48.5	33.8	34.2	34.2
Ta	2.47	2.21	2.277	2.86	3.8	3.8
Hf	3.29	3.33	3.4	3.16	2.81	2.81
87Sr/86Sr	0.885430	0.885913	0.874108	0.873002		
143Nd/144Nd	0.511418	0.511451	0.511429	0.511459	0.511489	

SAMPLE TYPE	Z140 Tato	Z141 Tato	Z142 Tato	Z143 Tato	E81 def lcg	E68 lcg
SiO2	73.48	73.52	73	73.69	74.8	73.03
TiO2	0.114	0.104	0.107	0.085	0.053	0.085
Al2O3	14.43	14.29	14.25	14.37	13.72	14.49
Fe2O3	1.4	1.33	1.32	1.1	0.61	1.12
MnO	0.037	0.037	0.037	0.038	0.021	0.031
MgO	0.23	0.24	0.22	0.11	0.1	0.09
CaO	1.51	1.44	1.42	1.19	0.98	1.43
Na2O	3.51	3.36	3.39	3.53	2.79	3.59
K2O	4.77	4.8	4.77	4.84	6.65	4.85
P2O5	0.06	0.057	0.065	0.073	0.068	0.052
LOI	0.55	0.6	0.51	0.7	0.24	0.4
TOTAL	100.09	99.778	99.09	99.73	100.03	99.17
Rb	436	468	471.5	481.8	267	387
Sr	78	70.1	68.8	60.5	46.5	68.7
Ba	193	173	173	159	79	172
Y	34.3	40.6	41.3	40	5.4	49.5
Zr	81	66	71	64	25	64
Nb	10.9	11.1	10.7	12.4	5.4	10.5
Pb	90	90	90	82	30	87
Th	19	19	19	19	3	21
U	25	26	25	28	2	26
Sc	3	1	2	1	3	1
V	7	11	9	3	2	2
Cr	12	11	20	8	6	9
Co	3	2	3	2	1	2
Ni	6	6	5	4	4	3
Cu	4	4	5	2	4	2
Zn	35	35	34	33	14	30
Ga	22	24	23	24	12	22
La	24.8	22.2			6.6	20.2
Ce	42.9	35.4			11.7	46
Nd	21.8	21.4			5.1	22.3
Sm	3.45	3.2			0.92	4.09
Eu	0.43	0.37			0.3	0.44
Tb	0.78	0.85			0.18	1.01
Yb	4.3	4.88			1.07	6.0097
Lu	0.67	0.71			0.17	0.96
Th	19.1	16.89			1.64	19.7
U	33.1	29.5			3.3	27.9
Ta	3.335	4.24			0.7	2.25
Hf	3.05	3.01			1	2.896
87Sr/86Sr	0.863560	0.860572			0.838086	
143Nd/144Nd	0.511476	0.511466			0.511277	

SAMPLE TYPE	Z105 lcg	E107(1) lcg	E107(2) lcg	E109 lcg	E114 lcg	E117 lcg
SiO2	75.45	75.67	75.63	74.08	74.59	74.23
TiO2	0.039	0.053	0.053	0.062	0.058	0.032
Al2O3	14.32	14.2	14.15	14.28	13.69	14.65
Fe2O3	0.82	0.83	0.83	1.05	0.93	0.27
MnO	0.061	0.019	0.02	0.027	0.034	0.013
MgO	0.09	0.1	0.11	0.09	0.06	0.08
CaO	0.78	0.9	0.9	1.17	0.94	0.76
Na2O	3.91	4.73	4.71	3.29	3.45	5.17
K2O	4.02	2.86	2.88	4.76	4.83	4.24
P2O5	0.064	0.177	0.177	0.063	0.06	0.09
LOI	0.55	0.34	0.34	0.42	0.57	0.3
TOTAL	100.1	99.88	99.8	99.292	99.21	99.84
Rb	506.2	214	214	396	470.2	641.6
Sr	21.5	16.6	16.6	56	37.1	17.4
Ba	29	14	14	139	94	52
Y	30.3	12.1	12.1	48.9	52.3	14.9
Zr	31	21	21	60	60	26
Nb	11.9	4.1	4.1	7.9	12.2	32.5
Pb	53	28	28	80	75	35
Th	10	7	7	16	19	10
U	12	14	14	28	29	13
Sc	5	2	2	2	1	1
V	2	3	3	4	4	5
Cr	17	15	15	8	5	7
Co	1	2	2	2	2	1
Ni	3	0	0	0	2	4
Cu	4	2	2	1	2	2
Zn	33	21	21	29	30	8
Ga	24	19	19	22	22	27
La	16.1	10.3	10.3		19.7	9.3
Ce	25	18.2	18.2		37.3	13.7
Nd	13.5	10.4	10.4		20.4	8
Sm	2.45	1.3	1.3		3.42	1.81
Eu	0.13	0.09	0.09		0.25	0.04
Tb	0.63	0.3	0.3		0.98	0.39
Yb	4.62	1.96	1.96		6.37	2.52
Lu	0.69	0.28	0.28		0.95	0.38
Th	9.75	6.06	6.06		17.4	10.9
U	23.2	24.1	24.1		30	16.5
Ta	5.15	1.5	1.5		4.54	14.1
Hf	1.77	0.95	0.95		2.53	2
87Sr/86Sr	0.862453	0.953764	0.953757	0.888461	0.887014	
143Nd/144Nd	0.511391	0.511428		0.511429	0.511480	

SAMPLE TYPE	E118 lcg	E120 lcg	E128 lcg	E133 lcg	E85A aplite	E85B aplite
SiO2	76.36	74.88	75.57	74.41	78.41	73.63
TiO2	0.05	0.039	0.034	0.057	0.084	0.066
Al2O3	14.36	14.25	14.01	14.4	12.8	14.47
Fe2O3	0.53	0.84	0.92	1	1.22	0.74
MnO	0.011	0.036	0.024	0.039	0.01	0.022
MgO	0.18	0.11	0.07	0.09	0.29	0.14
CaO	1.68	0.9	0.68	0.7	0.6	0.72
Na2O	5.25	4.06	3.58	3.27	2.79	3.47
K2O	0.8	4.13	4.54	5.25	3.28	6.05
P2O5	0.064	0.074	0.049	0.136	0.27	0.173
LOI	0.41	0.58	0.53	0.56	0.44	0.46
TOTAL	99.7	99.9	100.01	99.91	100.19	99.94
Rb	15.9	503	544.5	499.5	117	111
Sr	199.1	28.3	20.5	33	118	133
Ba	93	61	42	95	279	332
Y	3	32.8	32.8	22.8	6.3	6.1
Zr	24	40	40	37	42	41
Nb	2.4	11.5	6.5	12.8	3.3	2.5
Pb	35	56	59	44	33	32
Th	2	14	15	11	3	4
U	1	19	19	23	6	5
Sc	0	1	2	3	1	0
V	4	3	3	4	3	4
Cr	5	12	7	9	11	7
Co	1	1	1	0	1	2
Ni	1	3	2	1	3	4
Cu	3	3	1	3	2	2
Zn	7	29	32	24	14	14
Ga	11	23	23	21	19	18
La	9.08	15				10.6
Ce	17.9	26.8				21.2
Nd	8	14.9				9.8
Sm	1.58	2.52				2.31
Eu	0.74	0.17				0.43
Tb	0.18	0.68				0.28
Yb	0.27	4.69				0.57
Lu	0.04	0.63				0.08
Th	3.51	14.2				3.65
U	1.2	22.4				8.46
Ta	0.48	7.89				0.18
Hf	0.95	2.07				1.77
87Sr/86Sr			0.881003	0.891824		
143Nd/144Nd			0.511448	0.511457		

SAMPLE TYPE	Z6A(1) peg	Z6B(A) peg	Z6C/L1 peg	Z6C/L2 peg	Z6C/L3 peg	Z50 peg
SiO2	75.94	82.43	73.55	73.94	75.54	72.06
TiO2	0.086	0.211	0.087	0.078	0.09	0.025
Al2O3	14.34	9.19	14.56	14.46	13.82	14.89
Fe2O3	0.47	1.19	0.51	0.43	0.52	0.39
MnO	0.006	0.011	0.006	0.006	0.007	0.069
MgO	0.23	0.65	0.25	0.21	0.26	0.03
CaO	0.71	0.72	0.87	0.82	0.78	1.24
Na2O	4.04	3.14	4.35	4.45	4.2	3.87
K2O	4.13	2.14	4.62	4.83	4.68	6.17
P2O5	0.186	0.079	0.176	0.165	0.182	0.32
LOI	0.33	0.29	0.29	0.26	0.38	0.22
TOTAL	100.47	100.05	99.27	99.65	100.46	99.28
Rb	134	78.7	116	120	120	248
Sr	151	79.1	149	152	140	123
Ba	865	370	729	792	741	520
Y	14.5	18.8	14.7	14.5	18	15.2
Zr	40	142	52	50	46	27
Nb	2.6	4.1	3.3	2.7	2.8	1.1
Pb	42	19	40	39	38	56
Th	2	8	1	2	4	1
U	4	4	4	3	4	1
Sc	0	3	1	2	2	2
V	5	8	5	4	5	3
Cr	6	27	6	10	5	6
Co	1	3	2	1	2	1
Ni	6	8	3	3	2	1
Cu	2	0	2	2	3	2
Zn	7	11	8	5	6	4
Ga	10	9	12	11	10	13
La						
Ce						
Nd						
Sm						
Eu						
Tb						
Yb						
Lu						
Th						
U						
Ta						
Hf						
87Sr/86Sr						
143Nd/144Nd						

SAMPLE	Z51	Z52	Z58A	Z58B	Z58C	Z59A
TYPE	peg	peg	peg	peg	peg	peg
SiO2	70.75	71.54	75.94	77.72	76.3	69.48
TiO2	0.019	0.029	0.048	0.086	0.088	0.055
Al2O3	15.99	14.87	13.31	12.77	12.79	16.09
Fe2O3	0.54	0.67	0.52	1.21	1.21	0.75
MnO	0.106	0.11	0.009	0.01	0.01	0.072
MgO	0.05	0.07	0.1	0.29	0.28	0.17
CaO	2.28	1.12	0.68	0.59	0.53	3.18
Na2O	4.92	3.34	3.24	2.69	2.83	4.24
K2O	4.63	7.32	5.09	3.2	4.31	4.15
P2O5	0.637	0.506	0.347	0.266	0.242	1.189
LOI	0.22	0.15	0.77	0.5	0.46	0.37
TOTAL	100.14	99.73	100.05	99.33	99.05	99.75
Rb	177	285	401	314	333	242
Sr	122	114	56.4	45.5	45.9	176
Ba	287	531	180	145	150	558
Y	33	15.7	10.8	9.4	6.4	84.5
Zr	22	26	16	25	24	65
Nb	1.9	5.9	4	4.7	4.3	3
Pb	48	62	26	19	20	56
Th	0	1	3	1	1	0
U	3	3	13	6	4	4
Sc	2	2	2	5	2	3
V	4	1	1	2	4	2
Cr	8	7	10	16	7	8
Co	1	2	2	1	1	2
Ni	3	4	3	4	2	4
Cu	4	10	2	3	2	2
Zn	4	5	18	41	38	10
Ga	17	17	17	19	18	15
La	7.4					
Ce	16.6					
Nd	8.3					
Sm	2.64					
Eu	0.5					
Tb	0.72					
Yb	2.53					
Lu	0.34					
Th	0.28					
U	3					
Ta	0.45					
Hf	1.11					
87Sr/86Sr				1.330997		
143Nd/144Nd				0.511777		

	Cordierite seams					
SAMPLE	E121	X1	X10	Z12	Z41	Z42/i
TYPE	crd peg	crd seam	crd seam	crd seam	crd seam	crd seam
SiO2	74.56	73.29	74.05	73.76	76.64	74.48
TiO2	0.055	0.249	0.102	0.213	0.044	0.038
Al2O3	13.42	13.79	13.92	13.86	13.95	14.13
Fe2O3	0.4	2.19	2.52	1.59	0.49	0.56
MnO	0.006	0.024	0.062	0.019	0.018	0.013
MgO	0.04	0.43	0.67	0.24	0.13	0.1
CaO	0.32	0.72	0.52	0.69	3.85	0.57
Na2O	2.21	3.24	2.3	3.32	3.95	2.64
K2O	8.39	5.58	4.08	5.26	0.78	6.82
P2O5	0.193	0.236	0.177	0.234	0.191	0.309
LOI	0.3	0.35	1.34	0.55	0.36	0.54
TOTAL	99.89	100.1	99.74	99.74	100.4	100.2
Rb	263.7	391	200	358	50	341
Sr	90.3	65.7	66.2	62.8	239	81.5
Ba	376	196	210	174	49	385
Y	7.8	14.8	10.1	11.8	6.2	1.8
Zr	16	133	41	113	71	7
Nb	1.5	15.1	4.4	14.4	1.1	1.1
Pb	27	30	23	31	16	36
Th	1	24	4	21	2	0
U	1	10	5	9	0	3
Sc	2	2	1	4	2	0
V	5	13	6	8	5	0
Cr	12	13	7	20	15	7
Co	2	2	2	2	1	0
Ni	4	5	2	6	2	3
Cu	4	2	3	2	0	4
Zn	6	51	31	48	8	15
Ga	9	17	19	19	15	19
La	3.3	26.9	7.9		4.59	3.7
Ce	5.7	62.4	17.5		8.9	7.2
Nd	3.1	30.1	7.7		4.3	3
Sm	0.88	6.66	1.44		0.72	0.6
Eu	0.54	0.35	0.2556		0.698	0.42
Tb	0.22	0.78	0.29		0.163	0.1
Yb	1.56	1.27	1.35		0.64	0.45
Lu	0.24	0.15	0.2		0.08	0.06
Th	0.94	25.4	4.6145		1.85	0.23
U	1.7	13.8	6.55		2.94	3.16
Ta	0.68	1.05	0.57		0.41	0.26
Hf	0.65	4.43	1.22		3.95	0.29
87Sr/86Sr		1.195304	1.034153			1.003039
143Nd/144Nd		0.511702	0.511598			0.511401

SAMPLE TYPE	Z42/ii crd seam	Z42/iii crd seam	Z42/iv crd seam	Z43b/i crd seam	Z43b/iii crd seam	Z43b/iiR crd seam
SiO2	77.49	74.04	74.34	75.3	76.05	75.18
TiO2	0.044	0.039	0.035	0.113	0.123	0.129
Al2O3	12.42	14.43	14.24	13.91	13.46	14.11
Fe2O3	0.51	0.38	0.33	0.55	0.91	0.89
MnO	0.01	0.006	0.005	0.014	0.018	0.02
MgO	0.09	0.06	0.06	0.08	0.18	0.15
CaO	0.5	0.58	0.6	0.68	0.68	0.74
Na2O	2.32	2.74	2.63	3.27	3.05	3.25
K2O	5.83	7.07	6.45	5.86	5.15	5.36
P2O5	0.236	0.309	0.284	0.226	0.204	0.214
LOI	0.43	0.34	0.39	0.46	1.39	0.55
TOTAL	99.88	99.99	99.36	100.46	101.215	100.59
Rb	292	345	316	237	213	217
Sr	71.1	82.8	78	44	41.1	42.8
Ba	331	392	359	108	93	105
Y	2.2	2.6	2.5	5.8	5.6	6.3
Zr	11	7	8	17	17	16
Nb	1.4	2.1	1.8	5	5.7	5.7
Pb	29	36	34	25	23	23
Th	1	0	1	4	4	3
U	2	2	2	5	3	5
Sc	1	1	0	2	1	2
V	5	0	2	5	4	3
Cr	8	8	13	7	8	23
Co	1	1	2	2	1	0
Ni	4	3	1	3	4	3
Cu	4	3	3	1	2	2
Zn	13	12	12	14	24	22
Ga	19	20	22	16	16	17
La	2.9	4	4.26		4.6	
Ce	5.12	7.6	8.77		9.7	
Nd	2.66	3.5	3.6		4.2	
Sm	0.57	0.56	0.69		0.73	
Eu	0.37	0.44	0.51		0.14	
Tb	0.1	0.11	0.137		0.17	
Yb	0.39	0.44	0.51		0.79	
Lu	0.06	0.0679	0.07		0.12	
Th	0.31	0.17	0.2		2.128	
U	2.2	3	3.25		4.56	
Ta	0.29	0.23	0.229		0.55	
Hf	0.39	0.19	0.35		0.62	
87Sr/86Sr	1.002639	1.004014	1.004527			
143Nd/144Nd	0.511404	0.511373				

SAMPLE TYPE	Z44A crd seam	Z44B crd seam	Z44B crd seam	Z44B(1) crd seam	Z44B(1) crd seam	Z45A/i crd seam
SiO2	74.8	74.05	74	74.14	74.26	72.98
TiO2	0.063	0.083	0.084	0.085	0.082	0.121
Al2O3	14.03	13.86	13.82	13.87	13.81	14.83
Fe2O3	1.04	0.97	0.87	0.86	0.96	1.2
MnO	0.032	0.02	0.015	0.014	0.02	0.023
MgO	0.14	0.19	0.17	0.17	0.17	0.23
CaO	0.87	0.71	0.65	0.65	0.72	0.55
Na2O	3.6	3.09	3.09	3.08	3.14	2.98
K2O	4.87	6.42	6.47	6.45	6.46	6.24
P2O5	0.246	0.357	0.325	0.327	0.355	0.231
LOI	0.53	0.48	0.48	0.35	0.35	0.74
TOTAL	100.22	100.23	99.97	100	100.33	100.13
Rb	240	314	314	322	322	266
Sr	51.5	54.4	54.4	55.4	55.4	44.3
Ba	112	154	154	156	156	118
Y	8.5	13.8	13.8	10.8	10.8	8.5
Zr	36	38	38	37	37	23
Nb	2.8	5.2	5.2	5.5	5.5	5.4
Pb	26	32	32	32	32	24
Th	3	3	3	1	1	4
U	5	5	5	4	4	6
Sc	2	0	0	1	1	3
V	1	1	1	2	2	5
Cr	8	10	10	7	7	8
Co	0	1	1	1	1	2
Ni	2	3	3	2	2	2
Cu	3	4	4	3	3	2
Zn	18	21	21	21	21	26
Ga	19	15	15	16	16	19
La		5.77	5.77	4.78	4.78	
Ce		13.5	13.5	10.1	10.1	
Nd		7.77	7.77	6.1	6.1	
Sm		1.85	1.85	1.48	1.48	
Eu		0.24	0.24	0.23	0.23	
Tb		0.41	0.41	0.32	0.32	
Yb		1.148	1.148	0.87	0.87	
Lu		0.15	0.15	0.12	0.12	
Th		2.38	2.38	1.67	1.67	
U		6.2	6.2	5.188	5.188	
Ta		0.4	0.4	0.49	0.49	
Hf		1.57	1.57	1.27	1.27	
87Sr/86Sr						
143Nd/144Nd						

SAMPLE TYPE	Z45a/ii crd seam	Z45A/iii crd seam	Z45B crd seam	Z46A crd seam	Z46B crd seam	Z46C/i crd seam
SiO2	73.68	73.78	74.54	75.57	74.08	75.26
TiO2	0.131	0.091	0.133	0.095	0.108	0.055
Al2O3	14.51	14.22	14.56	13.73	13.83	13.27
Fe2O3	0.86	1.55	0.9	0.77	0.95	2.28
MnO	0.019	0.03	0.019	0.024	0.021	0.059
MgO	0.13	0.33	0.13	0.1	0.17	0.59
CaO	0.48	0.59	0.79	0.66	0.69	0.53
Na2O	2.97	2.63	3.32	3.2	3.16	2.37
K2O	6.85	5.55	5.37	5.83	5.75	3.83
P2O5	0.281	0.277	0.209	0.196	0.21	0.154
LOI	0.58	0.26	0.59	0.52	0.59	1.4
TOTAL	100.49	99.31	100.56	100.69	99.56	99.8
Rb	286	241	222	253	249	185
Sr	45.2	40.3	44.4	90	88.9	62.7
Ba	128	105	109	267	267	198
Y	10.3	15.8	6.8	8.1	9	10.9
Zr	19	21	29	48	48	32
Nb	6.4	4.6	5.7	2.8	5.7	2.8
Pb	26	23	22	36	36	23
Th	3	5	4	4	4	2
U	6	8	6	6	9	6
Sc	1	1	0	3	4	1
V	4	2	2	7	5	0
Cr	9	7	8	9	18	8
Co	1	1	1	2	1	2
Ni	3	2	4	3	4	2
Cu	1	2	2	2	2	3
Zn	17	25	19	11	15	29
Ga	17	18	20	15	17	18
La		7.8	9.8			6.1
Ce		17.9	18.7			12.9
Nd		9.06	8.4			6.26
Sm		1.77	1.45			1.22
Eu		0.146	0.16			0.27
Tb		0.38	0.26			0.29
Yb		1.84	1.019			1.48
Lu		0.27	0.14			0.22
Th		3.63	5.3			3.33
U		7.76	6.84			6.4
Ta		0.53	0.61			0.44
Hf		0.66	1.0988			1.15
87Sr/86Sr						1.032676
143Nd/144Nd						0.511557

SAMPLE TYPE	Z46C/ii crd seam	Z46C/iii crd seam	Z46C/iv crd seam	Z46C/v crd seam	E122 crd seam	Z130a/i crd seam
SiO2	75.6	75.75	75.35	74.57	88.98	73.97
TiO2	0.103	0.069	0.091	0.089	0.192	0.037
Al2O3	13.77	13.75	13.84	13.73	5.57	14.27
Fe2O3	1.03	1.08	0.68	0.63	1.09	0.78
MnO	0.03	0.031	0.02	0.021	0.008	0.02
MgO	0.22	0.24	0.14	0.12	0.37	0.13
CaO	0.75	0.59	0.63	0.62	0.66	1.03
Na2O	3.15	2.76	3.08	3.03	1.36	2.48
K2O	4.79	5.1	5.75	5.67	1.5	6.68
P2O5	0.174	0.185	0.191	0.189	0.051	0.135
LOI	0.62	0.29	0.25	0.4	0.27	0.58
TOTAL	100.24	99.85	100.02	99.07	100.05	100.11
Rb	215	229	250	245	67.9	325.7
Sr	86.6	80	91.4	88.7	34.7	168.9
Ba	240	250	291	283	210	884
Y	6.8	11.3	9.8	9.8	7.5	24.5
Zr	53	49	52	53	256	18
Nb	4.3	2.9	3.6	4.2	4	0.1
Pb	33	32	37	35	8	48
Th	6	7	4	5	7	3
U	6	8	5	7	2	9
Sc	0	1	2	0	3	0
V	5	6	4	4	11	2
Cr	37	9	7	9	30	13
Co	0	1	1	1	2	2
Ni	4	4	3	2	3	4
Cu	3	3	3	3	1	17
Zn	14	17	12	10	19	10
Ga	15	17	15	16	5	14
La	8.6	8	7.4	9.9		9.5
Ce	15.7	17.1	16.8	21.7		17.1
Nd	7.1	7.5	7.5	9.47		8.5
Sm	1.09	1.27	1.29	1.5		1.92
Eu	0.34	0.32	0.36	0.38		1.13
Tb	0.21	0.26	0.25	0.23		0.54
Yb	1	1.34	1.39	1.068		2.86
Lu	0.15	0.21	0.2	0.13		0.42
Th	4.63	4.82	4.42	5.969		4.36
U	7.42	6.58	7.4	9.5		9.5
Ta	0.6899	0.49	0.53	0.63		0.53
Hf	1.81	1.69	1.79	1.95		1.22
87Sr/86Sr	1.037582	1.046682	1.046016			0.846662
143Nd/144Nd	0.511616	0.511602	0.511597	0.511659		0.511586

SAMPLE TYPE	Z130b/i crd seam	Z130C crd seam	Z130d crd seam
SiO2	73.45	72.35	73.57
TiO2	0.053	0.051	0.043
Al2O3	14.71	15.03	14.51
Fe2O3	0.66	0.91	0.44
MnO	0.016	0.025	0.013
MgO	0.09	0.16	0.05
CaO	0.98	0.82	0.88
Na2O	2.39	2.33	2.4
K2O	6.86	7.36	7.71
P2O5	0.12	0.118	0.177
LOI	0.65	0.66	0.37
TOTAL	99.979	99.81	100.16
Rb	314.9	352	346.1
Sr	176.7	172	186.7
Ba	881	909	1020
Y	21.4	10.8	20.5
Zr	26	14	18
Nb	1	0.9	0.5
Pb	48	50	54
Th	4	4	5
U	3	6	7
Sc	1	0	0
V	6	6	5
Cr	8	8	12
Co	1	2	2
Ni	5	2	5
Cu	11	12	11
Zn	10	13	7
Ga	14	15	12
La	8.8	7.4	9.6
Ce	15.7	12.6	16.3
Nd	7.5	6.5	8.6
Sm	1.65	1.19	1.857
Eu	1.14	1.17	1.265
Tb	0.45	0.3	0.51
Yb	2.29	1.39	2.27
Lu	0.32	0.21	0.31
Th	3.93	3.03	3.97
U	5.05	8	8.4
Ta	0.6	0.74	0.51
Hf	1.27	0.95	1.336
87Sr/86Sr	0.847359	0.847050	0.846453
143Nd/144Nd	0.511557	0.511591	0.511587

APPENDIX 3 - MICROPROBE DATA

A 3.1 Mineral endmember abbreviations and formulae

Mineral abbreviations follow Kretz (1983) throughout, and endmember abbreviations used by Thermocalc are listed below.,

Mineral	Endmember name	Abbreviation	Formula
Biotite	phlogopite	phl	$KMg_3Si_3AlO_{10}(OH)_2$
	annite	ann	$KFe_3Si_3AlO_{10}(OH)_2$
	eastonite	east	$KMg_2Al_3Si_2O_{10}(OH)_2$
	Na-phlogopite	naph	$NaMg_3Si_3AlO_{10}(OH)_2$
Garnet	pyrope	py	$Mg_3Al_2Si_3O_{12}$
	almandine	alm	$Fe_3Al_2Si_3O_{12}$
	spessartine	spss	$Mn_3Al_2Si_3O_{12}$
	grossular	gr	$Ca_3Al_2Si_3O_{12}$
	andradite	andr	$Ca_3Fe_2Si_3O_{12}$
Cordierite	cordierite	crd	$Mg_2Si_5Al_4O_{18}$
	Fe-cordierite	fcrd	$Fe_2Si_5Al_4O_{18}$
	Mn-cordierite	mncd	$Mn_2Si_5Al_4O_{18}$
Spinel	spinel	sp	$MgAl_2O_4$
	hercynite	herc	$FeAl_2O_4$
	magnetite	mt	Fe_3O_4
	gahnite	-	$ZnAl_2O_4$
Ilmenite	ilmenite	ilm	$FeTiO_3$
Muscovite	muscovite	mu	$KAl_3Si_3O_{10}(OH)_2$
	paragonite	pa	$NaAl_3Si_3O_{10}(OH)_2$
	celadonite	cel	$KMgAlSi_4O_{10}(OH)_2$
Feldspar	anorthite	an	$CaAl_2Si_2O_8$
	albite	ab	$NaAlSi_3O_8$
	orthoclase	ksp	$KAlSi_3O_8$
Sillimanite	sillimanite	sill	Al_2SiO_5
Quartz	quartz	q	SiO_2

Mineral	Endmember name	Abbreviation	Formula
Amphibole	tremolite	tr	$Ca_2Mg_5Si_8O_{22}(OH)_2$
	ferro-tremolite	ftr	$Ca_2Fe_5Si_8O_{22}(OH)_2$
	tschermakite	ts	$Ca_2Mg_3Al_4Si_6O_{22}(OH)_2$
	pargasite	parg	$NaCa_2Mg_4Al_3Si_6O_{22}(OH)_2$
	glaucophane	gl	$Na_2Mg_3Al_2Si_8O_{22}(OH)_2$
	Fe-glaucophane	fgl	$Na_2Fe_3Al_2Si_8O_{22}(OH)_2$
	Mg-riebeckite	mrb	$Na_2Mg_3Fe_2Si_8O_{22}(OH)_2$
	riebeckite	rieb	$Na_2Mg_5Si_8O_{22}(OH)_2$
	anthophyllite	anth	$Mg_7Si_8O_{22}(OH)_2$
	Fe-anthophyllite	fath	$Fe_7Si_8O_{22}(OH)_2$
	cummingtonite	cumm	$Mg_7Si_8O_{22}(OH)_2$
	grunerite	grun	$Fe_7Si_8O_{22}(OH)_2$
	gedrite	ged	$Fe_4Mg_5Si_6O_{22}(OH)_2$
Pyroxene	diopside	di	$CaMgSi_2O_6$
	hedenbergite	hed	$CaFeSi_2O_6$
	jadeite	jd	$NaAlSi_2O_6$
	acmite	acm	$NaFeSi_2O_6$
	Ca-tschermakite	cats	$CaAl_2SiO_6$
Olivine	forsterite	fo	Mg_2SiO_4
	fayalite	fa	Fe_2SiO_4
Epidote	clinozoisite	cz	$Ca_2Al_3Si_3O_{12}(OH)$
	epidote	ep	$Ca_2Al_2FeSi_3O_{12}(OH)$
		ps	$Ca_2AlFe_2Si_3O_{12}(OH)$
Carbonate	calcite	cc	$CaCO_3$
	dolomite	dol	$CaMg(CO_3)_2$
	ferro-dolomite	fdol	$CaFe(CO_3)_2$
Wollastonite	wollastonite	wo	$CaSiO_3$
Fluid	water		H_2O
	Carbon dioxide		CO_2

A 3.2 Mineral analyses

The next 12 pages contain representative microprobe analyses from Nanga Parbat pelites, calc-silicates, cordierite seam Z130, amphibolite sheet E104, and the Tato pluton sample E5A. All analyses are from phase rims except where indicated by "core". Garnet core assemblages are denoted "gnt core" after the sample name. Where more than one domain was anlysed within a sample, different domains are denoted by the suffix "R1", "R2", etc. These correpsond to the domains mentioned in the detailed sample description in Chapter 3.

Cations per formula unit were calculated using the "ax96" program written by Tim Holland, except for spinel analyses where zinc was analysed, for which a spreadsheet was written to incorporate zinc and allow for Fe^{3+}, with the constraint that the cation sum must be 4.

	MMT ZONE PELITE									PELITE				PELITE		
	E157 R1				E157 R2				E157 R3	N1				E126 R1		
oxides	gnt	bt	pl	ms	gnt	bt	pl	ms	gnt	bt	crd	gnt rim	ksp	bt	pl	ksp
(wt.%)	3	32	25	35	69	53	72	79	162	155	2.3	2r2	1r2	1.1	123	174
SiO2	37.56	35.17	61.54	45.17	36.9	36.78	61.81	42.56	37.03	36.36	47.56	36.2	64.86	33.97	61.11	63.27
TiO2	0.04	1.61	0	1.48	0.03	0.69	0.01	0.07	0.03	1.96	0	0.03	0	4.13	0.04	0.08
Al2O3	21.04	18.04	22.76	31.23	20.93	20.12	22.86	29.55	20.83	18.03	31.88	20.8	18.61	18.58	22.73	18.07
Cr2O3	0.02	0.1	0.1	0.1	0.04	0.1	0.02	0	0.08	0.05	0	0.02	0	0	0.08	0.01
Fe2O3	2.22	0	0.1	0.47	3.9	0	0.15	4.33	2.3	0	0	0.61	0.4	0	0.29	0
FeO	29.3	22.36	0	2.66	28.18	19.8	0	3.9	31.93	22.61	11.07	36.93	0	22.54	0	0
MnO	0.5	0.27	0	0	1	0.17	0.05	0.07	1.23	0.23	0.06	1.85	0.06	0.1	0.04	0
MgO	5.06	7.54	0	1.56	5.33	7.42	0	2.69	5.63	7.3	6.43	2.02	0	6.64	0	0
CaO	4.48	0	4.9	0.05	3.28	0	4.61	0.02	0.85	0	0	1.39	0.08	0	4.9	0
Na2O	0.04	0.35	8.62	0.1	0.27	0.2	8.73	0.34	0	0.1	0.22	0	2.95	0.28	8.47	1.88
K2O	0.07	9.95	0.25	11	0	9.97	0.16	10.62	0	9.94	0	0	12.38	9.28	0.68	14.17
Total	100.34	95.41	98.27	93.83	99.86	95.25	98.4	94.17	99.91	96.59	97.22	99.83	99.34	95.52	98.34	97.5
cations																
Si	2.96	2.731	2.776	3.102	2.924	2.798	2.781	2.985	2.949	2.777	5.018	2.958	2.983	5.262	2.765	2.986
Ti	0.003	0.094	0	0.077	0.002	0.039	0	0.004	0.002	0.112	0	0.002	0	0.481	0.001	0.003
Al	1.955	1.652	1.21	2.529	1.955	1.804	1.213	2.443	1.956	1.623	0.977	2.003	1.009	3.393	1.212	1.006
Cr	0.002	0.006	0.004	0.005	0.002	0.006	0.001	0	0.005	0.003	0	0.001	0	0	0.003	0
Fe3	0.132	0	0.003	0.025	0.232	0	0.005	0.229	0.138	0	0	0.038	0.014	0	0.01	0
Fe2	1.931	1.453	0	0.153	1.868	1.259	0	0.229	2.127	1.444	0.977	2.524	0	2.921	0	0
Mn	0.033	0.018	0	0	0.067	0.011	0.002	0.004	0.083	0.015	0.006	0.128	0.002	0.013	0.001	0
Mg	0.594	0.872	0	0.16	0.63	0.841	0	0.281	0.668	0.831	1.012	0.246	0	1.533	0	0
Ca	0.378	0	0.237	0.003	0.278	0	0.222	0.001	0.072	0	0	0.122	0.004	0	0.237	0
Na	0.006	0.053	0.754	0.014	0.042	0.029	0.762	0.046	0	0.015	0.045	0	0.263	0.083	0.743	0.172
K	0.007	0.987	0.015	0.965	0	0.969	0.009	0.951	0	0.969	0	0	0.727	1.835	0.039	0.854
total	8.000	7.866	4.999	7.031	8.000	7.756	4.995	7.174	8.000	7.790	11.022	8.02	5.001	19.52	5.013	5.021

					PELITE							PELITE				
	E126 R1		E126 R2		Z137II R1				Z137II R2		E139 R1					
oxides	bt	gnt	bt	gnt	pl	gnt	bt	ksp	pl	pl	gnt	pl rim	pl core	gnt rim	gnt core	bt
(wt.%)	146	157	203	199	211	1	31	44	52	106	112	150	158	139	140	154
SiO2	33.06	36.51	33.67	35.97	61.68	36.59	34.21	65.54	65.6	64.52	36.62	59.87	61.84	36.73	36.75	34.08
TiO2	2.39	0.01	3.58	0	0	0	2.61	0	0.03	0	0	0	0.06	0.04	0.09	3.41
Al2O3	17.95	20.37	18.59	20.04	23.2	20.43	17.83	18.43	20.74	21.65	20.61	24.53	22.57	20.54	20.46	17.54
Cr2O3	0	0.05	0.07	0.02	0	0	0.04	0.03	0	0	0.02	0.02	0.04	0	0.02	0.12
Fe2O3	1.77	2.58	0	2.21	0.05	2.74	0	0.08	0	0.18	1.82	0.19	0	1.97	1.38	0
FeO	24.12	33.6	23.99	33.69	0	35.76	26	0	0	0	36.88	0	0	30.36	30.87	20.16
MnO	0.28	5.17	0.17	5.12	0.02	2.84	0.2	0	0	0	2.82	0	0	5.48	4.87	0.23
MgO	6.19	1.68	5.98	1.68	0.03	1.75	5.42	0	0	0	1.64	0.03	0.07	3.47	3.86	8.67
CaO	0.02	1.05	0	0.9	4.8	0.73	0	0.08	2.04	2.64	0.83	6.33	4.25	1.23	1.05	0
Na2O	0.32	0.11	0.51	0	8.26	0.22	0.36	4.05	10.19	9.78	0.02	8.04	8.63	0.06	0	0.35
K2O	8.25	0	9.66	0	0.67	0.01	9.11	11.31	0.74	0.83	0	0.36	0.79	0	0	9.06
Total	94.36	101.12	96.22	99.64	98.71	101.08	95.79	99.54	99.34	99.6	101.25	99.38	98.25	99.89	99.36	93.63
cations																
Si	2.622	2.956	2.618	2.959	2.771	2.96	2.687	2.996	2.908	2.862	2.962	2.688	2.791	2.965	2.975	2.667
Ti	0.143	0	0.209	0	0	0	0.154	0	0.001	0	0	0	0.002	0.003	0.006	0.201
Al	1.679	1.944	1.704	1.943	1.229	1.948	1.651	0.993	1.084	1.132	1.965	1.298	1.201	1.955	1.953	1.618
Cr	0	0.003	0.004	0.001	0	0	0.003	0.001	0	0	0.001	0.001	0.002	0	0.001	0.007
Fe3	0.106	0.157	0	0.137	0.002	0.167	0	0.003	0	0.006	0.111	0.006	0	0.12	0.084	0
Fe2	1.6	2.275	1.56	2.317	0	2.42	1.708	0	0	0	2.495	0	0	2.05	2.09	1.32
Mn	0.019	0.354	0.012	0.357	0.001	0.195	0.013	0	0	0	0.193	0	0	0.375	0.334	0.015
Mg	0.732	0.203	0.693	0.206	0.002	0.211	0.634	0	0	0	0.198	0.002	0.005	0.417	0.466	1.011
Ca	0.001	0.091	0	0.079	0.231	0.063	0	0.004	0.097	0.125	0.072	0.305	0.205	0.107	0.091	0
Na	0.049	0.017	0.076	0	0.719	0.035	0.054	0.359	0.876	0.841	0.003	0.699	0.756	0.01	0	0.052
K	0.835	0	0.959	0	0.038	0.001	0.914	0.66	0.042	0.047	0	0.021	0.046	0	0	0.905
total	7.786	8.000	7.836	8.000	4.993	8.000	7.817	5.015	5.007	5.013	8.000	5.020	5.006	8.000	8.000	7.798

	PELITE											SPINEL-BEARING PELITE				
	E139 R1	E139 R2			Z153II R1			Z153II R2				X8 spl		X8 gnt core		
oxides	bt	bt	pl core	pl rim	bt	gnt	crd	bt	bt	pl	ksp	spl	spl	bt	bt	gnt core
(wt.%)	209	210	133	159	141	6	98	109	207	225	198	210	#53	#4/1	#6/3	5c3
SiO2	32.97	33.12	62.15	60.75	34.53	36.84	46.31	33.27	35.35	63.39	64.83	3.76	0.4	33.59	34.8	37.81
TiO2	5.45	5.69	0.01	0	4.07	0.02	0	2.85	3.87	0.02	0.05	0.24	0.1	4.45	4.27	0
Al2O3	17.11	17.4	22.59	23.54	17.35	20.72	31.63	17.19	17.96	21.72	18.2	50.02	55.43	18.54	18.73	21.42
Cr2O3	0.12	0.16	0.08	0	0.14	0	0	0.11	0.03	0.03	0.12	0	0.26	0	0	0
Fe2O3	0	0	0.01	0.05	0	2.37	2.87	0	0	0.06	0.01	0	4.24	0	0	0
FeO	22.31	22.54	0	0	19.95	33.09	10.33	25.9	23.56	0	0	38.77	35	23.43	21.21	34.02
MnO	0.28	0.15	0.01	0	0.16	3.45	0.27	0.2	0.11	0.06	0.01	0.33	0.37	0.13	0.05	2.44
MgO	6.26	6.46	0	0	8.9	3.31	5.42	5.67	5.2	0	0	1.67	2.58	6.49	7.92	3.69
CaO	0	0	4.49	5.39	0	0.54	0	0	0.24	3.29	0.08	0.07	0.01	0	0.05	1.69
Na2O	0.12	0.1	8.38	7.89	0.35	0.19	0.49	0.32	0.92	9.15	2.92	0.16	0.04	0.2	0.26	n/a
K2O	9.5	9.64	0.83	0.62	9.3	0	0.05	9.15	8.74	0.65	12.1	0.41	0.05	9.37	8.87	n/a
ZnO													1.5			
Total	94.12	95.27	98.56	98.25	94.75	100.53	97.39	94.66	95.99	98.38	98.32	95.43	99.96	96.2	96.16	101.09
cations																
Si	2.61	2.591	2.796	2.746	2.668	2.961	4.925	2.656	2.727	2.846	3.003	0.114	0.012	2.599	2.646	2.999
Ti	0.324	0.335	0	0	0.236	0.001	0	0.171	0.225	0.001	0.002	0.005	0.002	0.259	0.244	0
Al	1.597	1.605	1.198	1.254	1.58	1.963	3.966	1.618	1.633	1.15	0.994	1.787	1.885	1.69	1.679	2.002
Cr	0.008	0.01	0.003	0	0.008	0	0	0.007	0.002	0.001	0.004	0	0.006	0	0	0
Fe3	0	0	0	0.002	0	0.143	0.23	0	0	0.002	0	0	0.092	0	0	0
Fe2	1.477	1.475	0	0	1.289	2.224	0.919	1.729	1.52	0	0	0.982	0.844	1.516	1.349	2.256
Mn	0.019	0.01	0	0	0.01	0.235	0.024	0.014	0.007	0.002	0	0.008	0.009	0.009	0.004	0.164
Mg	0.738	0.753	0	0	1.025	0.397	0.86	0.675	0.598	0	0	0.075	0.111	0.749	0.898	0.436
Ca	0	0	0.216	0.261	0	0.047	0	0	0.02	0.158	0.004	0.002	0	0	0.004	0.144
Na	0.019	0.015	0.731	0.692	0.053	0.03	0.102	0.05	0.138	0.797	0.262	0.009	0.002	0.03	0.038	0
K	0.961	0.963	0.048	0.036	0.917	0	0.007	0.933	0.861	0.037	0.716	0.016	0.002	0.926	0.861	0
													0.032			
total	7.753	7.756	4.993	4.990	7.787	8.000	11.032	7.852	7.731	4.994	4.985	3.000	2.997	7.775	7.721	8.001

	SPINEL-BEARING PELITE											SPINEL-BEARING PELITE				
	X8 core	X8 gnt rim		X2 spl					X2 gnt rim			X7 gnt rim				
oxides	plag	bt	gnt rim	plag	crd	bt	bt	spl	ksp	gnt rim	bt	pl	ksp	pl	gnt rim	bt
(wt.%)	#2/2	#8/3	#3r4	#1/2	#53	#28	#30	#36	#6	#9	#7	#23	4r1	1r1	2.2	2:1
SiO2	60.99	34.77	37.38	60.39	47.24	34.17	38.29	0.88	65.37	37.11	34.14	60.15	65.1	61.08	37.01	33.97
TiO2	0	0.96	0.06	0	0	3.16	3.06	0.12	0	0.07	2.98	0	0	0	0	2.06
Al2O3	23.99	18.69	20.99	25.18	32.25	20.12	21.82	56.57	18.34	20.98	17.75	24.48	18.75	24.25	20.74	17.5
Cr2O3	0	0	0.09	0	0	0.12	0.12	0.1	0	0.02	0	0	0	0	0.11	0
Fe2O3	0.29	0	0.54	0.17	2.1	3.17	0	2	0	0.49	0	0.19	0.07	0	0.41	2.85
FeO	0	25.31	35.22	0	8.59	19.77	20.08	35.75	0	33.97	23.71	0	0	0	33.6	22.17
MnO	0.06	0.12	1.91	0	0.32	0.22	0.12	0.36	0	3.64	0.18	0.04	0.03	0.02	4.21	0.31
MgO	0	7.11	3.2	0	6.98	7.75	6.21	3.17	0	3.16	7.52	0	0	0	2.63	7.75
CaO	6.28	0	1.69	7.36	0.04	0.06	0.1	0.01	0.1	1.17	0	6.98	0.11	6.02	1.46	0.03
Na2O	7.93	0.26	0	7.35	0.17	0.19	0.22	0.03	1.81	0	0.2	7.66	1.77	7.71	0	0.23
K2O	0.66	8.92	0	0.54	0.01	6.56	8.24	0.01	14.53	0	9.47	0.51	13.77	0.63	0	8.64
ZnO								1.17								
Total	100.21	96.14	101.08	101.01	97.7	95.3	98.26	100.16	100.16	100.61	95.96	100.01	99.61	99.71	100.17	95.51
cations																
Si	2.717	2.696	2.984	2.671	4.945	2.591	2.778	0.025	3	2.98	2.652	2.687	2.992	2.724	2.992	2.644
Ti	0	0.057	0.003	0	0	0.18	0.167	0.003	0	0.004	0.174	0	0	0	0	0.121
Al	1.259	1.708	1.975	1.313	3.98	1.798	1.866	1.903	0.992	1.986	1.626	1.289	1.016	1.275	1.977	1.606
Cr	0	0	0.006	0	0	0.007	0.007	0.002	0	0.001	0	0	0	0	0.007	0
Fe3	0.01	0	0.033	0.006	0.165	0.181	0	0.043	0	0.03	0	0.006	0.002	0	0.025	0.167
Fe2	0	1.642	2.351	0	0.752	1.254	1.218	0.853	0	2.281	1.541	0	0	0	2.272	1.443
Mn	0.002	0.008	0.129	0	0.028	0.014	0.007	0.009	0	0.248	0.012	0.002	0.001	0.001	0.288	0.02
Mg	0	0.822	0.381	0	1.09	0.876	0.671	0.135	0	0.378	0.871	0	0	0	0.317	0.899
Ca	0.3	0	0.144	0.349	0.005	0.005	0.008	0	0.005	0.101	0	0.334	0.005	0.288	0.127	0.003
Na	0.685	0.04	0	0.63	0.035	0.027	0.031	0.002	0.161	0	0.03	0.664	0.158	0.667	0	0.035
K	0.038	0.883	0	0.03	0.001	0.635	0.763	0	0.852	0	0.94	0.029	0.808	0.036	0	0.859
Zn								0.025								
total	5.01	7.855	8.006	5	11	7.568	7.516	2.999	5.01	8.008	7.846	5.011	4.982	4.99	8.004	7.796

	SPINEL-BEARING PELITE				SPINEL-BEARING PELITE								SPINEL-BEARING PELITE			
	X7 spl		Z135 spl				Z147 gnt rim				Z147 spl		PAK4A R1		R2	
oxides	spl	fsp	bt	crd	spl	bt	ksp	gnt	plag	bt	ksp	bt	spl	gnt	ksp	crd
(wt.%)	#198	#222	#175	#42	#31	#135	#119	#136	#141	#144	#166	#108	#47	162	173	211
SiO2	0.07	52.31	34.09	48.03	0.25	33.99	64.13	37.24	60.51	34.28	63.82	34.26	0.08	36.51	64.72	46.5
TiO2	0.09	0.07	5.38	0	0.06	3.4	0.18	0	0.08	1.81	0	5.63	0.09	0.03	0	0.05
Al2O3	56.95	35.16	18.77	32.44	57.19	17.37	18.48	20.79	24.46	18.67	18.16	18.8	57.77	20.1	18.84	32.33
Cr2O3	0.13	0	0.27	0	0.18	0.07	0	0.05	0.03	0.07	0.04	0.05	0.18	0	0	0
Fe2O3	3.72	1.81	0	1.62	2.73	0	0.26	1.73	0.03	0	0.13	0	1.6	1.64	0.07	2.74
FeO	34.54	0	22.37	9.57	34.3	23.54	0	32.65	0	20.21	0	22.29	36.29	37.18	0	12.39
MnO	0.3	0.01	0.09	0.29	0.31	0.26	0	2.06	0	0.21	0	0.06	0.18	2.48	0	0.21
MgO	3.49	0.72	6.78	6.58	2.83	6.92	0	4.21	0	9.07	0	6.38	2.42	1.77	0	4.15
CaO	0	0.03	0	0.01	0	0	0.08	1.73	6.29	0	0.1	0	0	0.66	0.07	0.01
Na2O	0.01	0.31	0.18	0.26	0.07	0.13	2.76	0	7.74	0.42	1.95	0.17	0.02	0	3.06	0.35
K2O	0.01	8.79	9.23	0	0	9.33	12.93	0.02	0.47	9.37	14.02	9.23	0.03	0	12.98	0.03
ZnO	0.69				2.28								0.9			
Total	100.02	99.22	97.17	98.8	100.2	95.01	98.83	100.48	99.58	94.11	98.24	96.87	99.55	100.37	99.75	98.74
cations																
Si	0.002	2.378	2.591	4.98	0.007	2.667	2.974	2.97	2.705	2.667	2.987	2.607	0.002	2.981	2.973	4.911
Ti	0.002	0.002	0.307	0	0.001	0.201	0.006	0	0.002	0.106	0	0.322	0.002	0.002	0	0.004
Al	1.915	1.884	1.682	3.966	1.927	1.607	1.01	1.955	1.289	1.712	1.002	1.687	1.956	1.934	1.02	4.025
Cr	0.003	0	0.016	0	0.004	0.004	0	0.003	0.001	0.004	0.001	0.003	0.004	0	0	0
Fe3	0.08	0.062	0	0.126	0.059	0	0.009	0.104	0.001	0	0.004	0	0.034	0.101	0.002	0.218
Fe2	0.824	0	1.422	0.83	0.82	1.545	0	2.178	0	1.315	0	1.419	0.872	2.538	0	1.095
Mn	0.007	0	0.006	0.026	0.008	0.017	0	0.139	0	0.014	0	0.004	0.004	0.172	0	0.018
Mg	0.148	0.049	0.768	1.017	0.121	0.809	0	0.5	0	1.052	0	0.724	0.104	0.215	0	0.653
Ca	0	0.001	0	0.002	0	0	0.004	0.148	0.301	0	0.005	0	0	0.058	0.003	0.001
Na	0.001	0.027	0.027	0.053	0.004	0.02	0.248	0	0.67	0.064	0.177	0.024	0.001	0	0.272	0.071
K	0	0.51	0.896	0	0	0.935	0.766	0.002	0.027	0.931	0.838	0.897	0.001	0	0.762	0.004
Zn	0.015				0.048								0.019			
total	2.998	4.915	7.715	11	2.999	7.804	5.017	8	4.996	7.866	5.016	7.687	3	8.000	5.033	11.000

	SPINEL-BEARING PELITE						SPINEL-BEARING PELITE									
	PAK4B R1				PAK4B R2		PAK4C R1				PAK4C R2			PAK4C R3		
oxides	gnt	bt	ksp	pl	gnt	bt	pl	bt	pl	ksp	gnt	gnt	bt	ksp	bt	spl
(wt.%)	13	64	49	58	160	106	102	18	26	28	37	116	119	108	61	69
SiO2	36.48	33.22	63.99	64.05	36.22	32.93	63.81	33.24	63.24	64.79	36.3	36.53	32.64	63.96	33.34	1.94
TiO2	0	3.72	0.02	0.01	0	2.79	0.01	3.88	0	0	0	0.07	5.64	0.07	3.83	0.18
Al2O3	20.53	17.74	18.54	20.93	20.35	17.82	21.93	17.77	21.72	18.55	20.44	20.3	15.77	18.76	18.67	53.57
Cr2O3	0.02	0.09	0	0.06	0.06	0.01	0.01	0	0.03	0.07	0	0	0.06	0.04	0.07	0.1
Fe2O3	3.47	0	0.03	0.01	2.71	0	0.29	0	0.25	0.03	3.07	2.55	0	0.11	0	7.1
FeO	34.94	25.45	0	0	35.3	24.57	0	24.55	0	0	35.44	36.49	29.08	0	25	30
MnO	3.21	0.14	0.06	0	3.38	0.08	0	0.06	0	0	2.33	2.32	0.09	0	0.13	0.18
MgO	2.25	5.35	0	0	2.02	5.74	0	5.45	0	0.01	2.62	2.22	3.05	0	5.57	2.63
CaO	0.46	0	0.06	2.31	0.43	0	3.1	0	3.07	0.1	0.56	0.59	0.01	0.09	0	0.03
Na2O	0.18	0.35	2.42	9.7	0.09	0.28	9.39	0.31	9.35	3.84	0.05	0.04	0.48	3.78	0.4	1.65
K2O	0	9.4	12.94	0.86	0	9.47	0.67	9.37	0.62	11.67	0	0	9.26	11.39	9.35	0.39
Total	101.54	95.47	98.08	97.92	100.57	93.7	99.21	94.64	98.28	99.07	100.81	101.1	96.1	98.21	96.38	97.76
cations																
Si	2.934	2.625	2.984	2.885	2.947	2.643	2.842	2.636	2.843	2.982	2.936	2.954	2.619	2.968	2.597	0.056
Ti	0	0.221	0.001	0	0	0.168	0	0.231	0	0	0	0.005	0.341	0.002	0.224	0.004
Al	1.947	1.652	1.019	1.111	1.952	1.686	1.152	1.661	1.151	1.007	1.949	1.935	1.492	1.026	1.715	1.83
Cr	0.001	0.006	0	0.002	0.004	0.001	0	0	0.001	0.003	0	0	0.004	0.001	0.004	0.002
Fe3	0.21	0	0.001	0	0.166	0	0.01	0	0.009	0.001	0.187	0.155	0	0.004	0	0.155
Fe2	2.351	1.681	0	0	2.402	1.649	0	1.628	0	0	2.397	2.468	1.952	0	1.629	0.727
Mn	0.219	0.009	0.002	0	0.233	0.005	0	0.004	0	0	0.16	0.159	0.006	0	0.008	0.004
Mg	0.27	0.63	0	0	0.245	0.687	0	0.644	0	0	0.316	0.267	0.365	0	0.647	0.114
Ca	0.039	0	0.003	0.111	0.037	0	0.148	0	0.148	0.005	0.048	0.051	0.001	0.005	0	0.001
Na	0.028	0.054	0.219	0.847	0.015	0.043	0.811	0.048	0.815	0.343	0.007	0.007	0.074	0.34	0.061	0.093
K	0	0.949	0.771	0.049	0	0.97	0.038	0.949	0.036	0.686	0	0	0.949	0.675	0.93	0.014
total	8.000	7.827	5.000	5.006	8.006	7.853	5.001	7.801	5.002	5.027	8.000	8.000	7.804	5.021	7.815	3.000

	CORDIERITE SEAM						CALC-SILICATE								
	PAK4C R3	Z130					E115(1) R1	E115(1) R2			E115(1) R3				
oxides	pl	ksp	crd	gnt	ksp	bt	cpx	pl	cpx	gnt	pl	cpx	pl	cc	wo
(wt.%)	75	86	134	64	41	106	15	39	96	88	60	133	147	188	193
SiO2	63.81	64.61	47.03	36.38	64.82	35.41	50.82	43.71	51.95	36.82	45.52	51.8	43.15	0.2	50.62
TiO2	0.08	0	0.01	0	0	4.31	0.05	0.07	0.13	1.09	0.04	0.05	0	0	0.02
Al2O3	21.25	18.66	32.5	20.97	18.77	17.54	1.16	34.58	1.14	10.68	33.57	0.35	34.86	0	0
Cr2O3	0.04	0.03	0	0.04	0	0	0.08	0.05	0.03	0.07	0.02	0.16	0.07	0.03	0.17
Fe2O3	0.06	0	0.59	0.39	0.02	0	3.1	0.31	1.65	16.32	0.25	2.23	0.22	0	0.56
FeO	0	0	14.45	37.58	0	26.47	9.83	0	8.32	1.35	0	9.3	0	0.01	0.03
MnO	0	0	0.31	2.37	0	0.11	0.62	0.03	0.55	0.66	0	0.64	0	0.06	0.45
MgO	0	0	3.47	1.51	0	3.72	9.69	0	11.24	0.2	0	10.54	0	0.01	0.58
CaO	2.61	0.07	0.02	0.65	0.15	0	24.52	19.5	24.85	33.26	18.86	24.66	19.6	54.95	46.62
Na2O	9.41	3.65	0.28	0	3.29	0.23	0.34	0.52	0.32	0	0.25	0.34	0.4	0	0
K2O	0.86	11.9	0.02	0	11.14	8.53	0.08	0.08	0	0.01	0.07	0.03	0.08	0	0.05
Total	98.13	98.93	98.68	99.9	98.2	97.56	100.26	98.85	100.19	100.44	98.59	100.09	98.38	55.32	99.09
cations															
Si	2.869	2.98	4.979	2.975	2.992	5.427	1.94	2.05	1.959	2.94	2.126	1.97	2.034	0.007	1.98
Ti	0.003	0	0	0	0	0.497	0.001	0.002	0.004	0.065	0.002	0.001	0	0	0.001
Al	1.126	1.015	4.056	2.022	1.021	3.168	0.052	1.912	0.051	1.006	1.848	0.016	1.937	0	0
Cr	0.002	0.001	0	0.003	0	0	0.002	0.002	0.001	0.004	0.001	0.005	0.003	0.001	0.005
Fe3	0.002	0	0.047	0.024	0.001	0	0.089	0.011	0.047	0.981	0.009	0.064	0.008	0	0.016
Fe2	0	0	1.279	2.571	0	3.393	0.314	0	0.262	0.09	0	0.296	0	0	0.001
Mn	0	0	0.028	0.164	0	0.014	0.02	0.001	0.018	0.045	0	0.021	0	0.002	0.015
Mg	0	0	0.547	0.184	0	0.85	0.551	0	0.632	0.023	0	0.598	0	0	0.034
Ca	0.126	0.004	0.002	0.057	0.007	0	1.003	0.98	1.004	2.846	0.944	1.005	0.99	1.99	1.954
Na	0.821	0.327	0.058	0	0.294	0.069	0.025	0.047	0.023	0	0.023	0.025	0.037	0	0
K	0.05	0.701	0.003	0	0.657	1.668	0.002	0.005	0	0.001	0.004	0.001	0.005	0	0.002
total	4.998	5.026	11.000	8.000	4.973	14.616	4.000	5.011	4.000	8.000	4.957	4.000	5.013	2.000	4.009

	CALC-SILICATE															
	E116(1) R1		E116(1) R2			E116(1) R3			E116(2) R1			E116(2) R2				
oxides	bt	pl	gnt	amph	cpx	pl	hbl	pl	cpx	gnt	pl	bt	hbl	gnt	cpx	pl
(wt.%)	214	245	221	91	96	71	295	261	273	212	177	180	289	263	281	270
SiO2	34.75	50.11	36.95	42.83	50.78	44.66	41.6	43.92	50.37	37.48	45.61	36.14	40.86	37.53	50.98	43.66
TiO2	3.15	0.15	0.09	0.91	0.21	0	0.92	0	0.07	0.04	0	3.36	0.92	0.09	0.1	0
Al2O3	14.63	30.14	20.24	9.57	1.77	34.89	10.07	34.38	1.33	20.69	33.83	14.32	11.19	20.42	1.16	35.07
Cr2O3	0.1	0.01	0	0.15	0.14	0	0.07	0.04	0.04	0.04	0.07	0	0.04	0.06	0.1	0.05
Fe2O3	0.18	0.59	2.9	3.5	2.64	0.28	4.13	0.33	2.96	2.27	0.26	0	4.85	1.56	0.67	0.33
FeO	22.99	0	26.37	19.43	11.95	0	19.13	0	11.99	26.63	0	22.96	18.87	21.64	13.56	0
MnO	0.2	0	2.29	0.38	0.51	0.02	0.68	0.05	0.59	2.6	0.03	0.17	0.8	3.64	0.57	0
MgO	9.02	0.03	2.47	7.07	9.98	0.02	6.99	0	9.63	2.68	0	9.24	5.99	1.12	9.64	0
CaO	0	16.17	8.67	11.66	22.76	18.97	11.59	18.96	22.55	8.12	17.63	0	11.44	13.73	22.8	19.43
Na2O	0.25	1.36	0	0.91	0.32	0.95	1.5	0.88	0.36	0.08	1.53	0.07	0.99	0	0.11	0.58
K2O	9.18	0.32	0.02	0.95	0	0.03	1.03	0	0	0.02	0.04	9.3	1.12	0.01	0	0.03
Total	94.46	98.88	100.01	97.36	101.07	99.82	97.72	98.56	99.9	100.63	99	95.57	97.07	99.8	99.68	99.16
cations																
Si	2.742	2.313	2.954	6.604	1.926	2.069	6.436	2.063	1.938	2.969	2.123	2.804	6.362	2.988	1.964	2.04
Ti	0.187	0.005	0.005	0.106	0.006	0	0.107	0	0.002	0.002	0	0.196	0.107	0.005	0.003	0
Al	1.361	1.64	1.908	1.74	0.079	1.906	1.837	1.905	0.061	1.933	1.857	1.31	2.055	1.917	0.053	1.932
Cr	0.007	0	0	0.019	0.004	0	0.008	0.002	0.001	0.003	0.003	0	0.005	0.004	0.003	0.002
Fe3	0.011	0.02	0.175	0.406	0.075	0.01	0.48	0.012	0.086	0.135	0.009	0	0.568	0.094	0.019	0.012
Fe2	1.518	0	1.763	2.506	0.379	0	2.475	0	0.386	1.764	0	1.49	2.457	1.441	0.437	0
Mn	0.013	0	0.155	0.049	0.016	0.001	0.089	0.002	0.019	0.174	0.001	0.012	0.105	0.246	0.019	0
Mg	1.061	0.002	0.294	1.624	0.564	0.001	1.612	0	0.552	0.316	0	1.068	1.389	0.133	0.553	0
Ca	0	0.8	0.743	1.926	0.925	0.942	1.922	0.954	0.929	0.689	0.879	0	1.909	1.172	0.941	0.973
Na	0.038	0.122	0	0.273	0.024	0.086	0.451	0.08	0.027	0.012	0.138	0.011	0.3	0	0.008	0.053
K	0.925	0.019	0.002	0.187	0	0.002	0.204	0	0	0.002	0.003	0.921	0.223	0.001	0	0.002
total	7.863	4.922	8.000	15.439	4.000	5.016	15.622	5.018	4.000	8.000	5.013	7.811	15.479	8.000	4.000	5.014

	CALC-SILICATE															
	Z124 R1					Z124 R2				Z124 R3					Z124 R4	
oxides	cpx cor	cpx rim	pl	gnt core	gnt rim	hbl	cpx rim	cpx cor	ep	cpx rim	cpx cor	gnt	gnt	pl	cpx cor	cpx rim
(wt.%)	3	4	11	24	26	44	66	70	79	1	4	10	11	14	38	42
SiO2	51.72	50.55	42.97	35.91	36.06	48.64	52.3	52.38	37.55	49.12	50.86	36.08	36.34	42.76	51.11	49.35
TiO2	0.11	0.07	0.03	0.69	0.43	0.6	0.09	0.12	0.19	0.21	0.09	0.85	0.49	0	0.05	0.13
Al2O3	1.55	1.6	35.45	4.99	5.25	5.37	1.49	0.98	23.63	1.7	1.4	5.08	6.64	35.11	1.32	2.58
Cr2O3	0.07	0.14	0.13	0.15	0.15	0.03	0.08	0.04	0.05	0.16	0.09	0.04	0.16	0	0.09	0.1
Fe2O3	3.29	2.14	0.45	25.44	24.23	3.54	1.44	2.65	10.62	2.34	1.78	23.94	22.02	0.44	2.66	2.95
FeO	7.33	11.35	0	2.88	2.85	12.08	7.08	7.95	1.93	15	11.42	1.42	3.11	0	9.57	11.99
MnO	0.55	0.39	0.02	0.36	0.59	0.42	0.56	0.51	0.38	0.5	0.68	0.42	0.37	0	0.72	0.54
MgO	11.54	9.75	0	0.08	0	13.27	12.69	11.98	0.02	7.18	9.56	0.1	0.15	0	10.35	8.62
CaO	24.55	24.26	19.95	30.67	31.21	12.07	24.37	24.86	23.37	23.9	23.92	32.19	31.32	19.82	24.11	23.39
Na2O	0.42	0.07	0.27	0.18	0	0.65	0.25	0.33	0.06	0	0.24	0.14	0	0.26	0.28	0.25
K2O	0.03	0	0.04	0.01	0.02	0.39	0	0.06	0.01	0	0	0	0	0	0.07	0.03
Total	101.15	100.31	99.3	101.36	100.8	97.05	100.35	101.36	97.8	100.13	100.03	100.27	100.61	98.39	100.34	99.92
cations																
Si	1.931	1.932	2.01	2.942	2.965	7.183	1.952	1.951	3.003	1.918	1.948	2.969	2.968	2.017	1.942	1.904
Ti	0.003	0.002	0.001	0.042	0.027	0.066	0.003	0.003	0.011	0.006	0.003	0.053	0.03	0	0.001	0.004
Al	0.068	0.072	1.955	0.482	0.509	0.934	0.065	0.043	2.228	0.078	0.063	0.492	0.64	1.952	0.059	0.117
Cr	0.002	0.004	0.005	0.01	0.01	0.004	0.002	0.001	0.003	0.005	0.003	0.003	0.01	0	0.003	0.003
Fe3	0.093	0.062	0.016	1.568	1.5	0.394	0.041	0.074	0.639	0.069	0.051	1.483	1.354	0.016	0.076	0.086
Fe2	0.229	0.363	0	0.198	0.196	1.492	0.221	0.248	0.129	0.49	0.366	0.098	0.212	0	0.304	0.387
Mn	0.017	0.012	0.001	0.025	0.041	0.052	0.018	0.016	0.025	0.016	0.022	0.029	0.026	0	0.023	0.018
Mg	0.642	0.555	0	0.01	0	2.921	0.706	0.665	0.002	0.418	0.545	0.013	0.019	0	0.586	0.495
Ca	0.982	0.993	1	2.693	2.75	1.909	0.975	0.972	2.003	1.001	0.981	2.838	2.741	1.002	0.981	0.967
Na	0.03	0.005	0.024	0.029	0	0.186	0.018	0.024	0.009	0	0.018	0.022	0	0.024	0.021	0.019
K	0.001	0	0.002	0.001	0.002	0.074	0	0.003	0.001	0	0	0	0	0	0.004	0.002
total	4.000	4.000	5.014	8.000	8.000	15.215	4.000	4.000	8.055	4.000	4.000	8.000	8.000	5.011	4.000	4.000

	CALC-SILICATE													CALC-SILICATE		
	Z124 R4	Z148 R1					Z148 R2							Z150 R1		
oxides	pl	gnt	ep	gnt	pl core	pl rim	ksp	hbl rim	hbl core	pl rim	pl core	cpx rim	cpx cor	cc	spl	bt
(wt.%)	45	52	53	16	23	28	50	62	68	85	83	95	92	1	2	47
SiO2	42.62	35.81	36.94	35.95	42.3	42.9	64.5	42.27	40.54	43.78	43.5	50.53	50.16	0.18	0.05	38.36
TiO2	0	0.7	0.12	0.52	0.04	0	0	0.83	0.87	0.05	0	0.12	0.27	0.09	0.03	1
Al2O3	34.94	5.09	22.59	5.92	35.39	34.71	18.07	10.19	11.8	34.47	34.73	1.72	2.42	0	65.1	15.51
Cr2O3	0.01	0.22	0.1	0.1	0	0.04	0.05	0.11	0.12	0	0.04	0.1	0.09	0	0	0.07
Fe2O3	0.28	23.79	11.08	22.82	0.38	0.38	0	4.42	4.44	0.17	0.24	3.95	2.92	0	2.57	0.82
FeO	0	2.75	2.46	2.64	0	0	0	15.38	15.89	0	0	8.17	9.13	0.19	11.49	4.2
MnO	0.04	0.68	0.18	0.54	0.04	0	0	0.38	0.31	0	0	0.62	0.62	0.31	0.78	0.15
MgO	0.02	0.07	0.09	0	0	0	0	9.36	8.36	0	0	10.85	10.6	0.75	19.16	23.08
CaO	19.72	31.13	23.44	31.39	20.06	19.62	0	11.77	11.88	18.9	19.32	23.2	23.09	53.07	0.04	0
Na2O	0.22	0	0	0	0.17	0.41	0.48	1.1	1.04	0.85	0.54	0.58	0.42	0.07	0.09	0.68
K2O	0.03	0	0	0.01	0.01	0.05	15.47	1.4	1.68	0.01	0.09	0	0.01	0.07	0.05	9.88
Total	97.88	100.25	97.02	99.91	98.39	98.1	99.58	97.22	96.95	98.24	98.45	99.84	99.73	54.73	99.36	93.76
cations																
Si	2.02	2.961	2.996	2.968	1.998	2.029	3	6.453	6.248	2.062	2.047	1.921	1.911	0.006	0.001	2.782
Ti	0	0.044	0.007	0.032	0.001	0	0	0.095	0.101	0.002	0	0.003	0.008	0.002	0.001	0.055
Al	1.952	0.496	2.16	0.577	1.971	1.936	0.991	1.834	2.144	1.914	1.927	0.077	0.108	0	1.953	1.326
Cr	0	0.015	0.007	0.006	0	0.001	0.002	0.013	0.015	0	0.001	0.003	0.003	0	0	0.004
Fe3	0.01	1.48	0.676	1.418	0.013	0.014	0	0.508	0.515	0.006	0.008	0.113	0.084	0	0.049	0.045
Fe2	0	0.19	0.167	0.183	0	0	0	1.964	2.048	0	0	0.26	0.291	0.005	0.245	0.254
Mn	0.002	0.048	0.012	0.038	0.002	0	0	0.049	0.041	0	0	0.02	0.02	0.009	0.017	0.009
Mg	0.001	0.009	0.011	0	0	0	0	2.13	1.921	0	0	0.615	0.602	0.038	0.727	2.494
Ca	1.002	2.757	2.039	2.777	1.015	0.995	0	1.926	1.962	0.954	0.974	0.945	0.942	1.931	0.001	0
Na	0.021	0	0	0	0.015	0.038	0.043	0.326	0.31	0.078	0.05	0.043	0.031	0.005	0.004	0.096
K	0.002	0	0	0.001	0	0.003	0.978	0.274	0.331	0.001	0.005	0	0.001	0.003	0.002	0.915
total	5.010	8.000	8.076	8.000	5.016	5.015	5.014	15.573	15.635	5.016	5.012	4.000	4.000	2.000	3.000	7.981

										METABASALTIC SHEET						
	Z150R1	Z150 R2				Z150 R3				E104						
oxides	cpx	spl	ol	cc	bt	cc	dol	ol	spl	hbl	hbl	hbl	hbl	bt	bt	pl
(wt.%)	74	57	83	70	91	112	52	22	91	avge	#10	#126	#4.3	avge	#117	avge
SiO2	53.49	0.03	40.17	0.1	37.85	0.11	0.12	40.33	0	45.33	45.03	43.17	50.88	35.73	36.87	56.76
TiO2	0.26	0.13	0.02	0.04	1.29	0	0	0.03	0.14	0.63	0.67	0.6	0.29	2.52	2.54	0
Al2O3	1.53	64.28	0	0	17.01	0	0.06	0.02	62.67	11.41	11.37	14.4	5.07	16.01	15.59	26.95
Cr2O3	0.05	0.18	0	0	0	0.03	0.04	0.12	0	0.11	0.02	0.01	0.19	0.05	0.05	0
Fe2O3	0.94	3.75	0.71	0	0.59	0	0	0.31	6.37	1.3	1.68	1.53	0.9	1.66	0.53	0.13
FeO	2.41	8.21	11.19	0.25	3.01	0.22	1.76	10.71	6.8	13.26	13.19	13.37	14.68	16.27	16.87	0
MnO	0.21	0.59	0.84	0.29	0.14	0.46	0.5	0.62	0.41	0.24	0.23	0.25	0.26	0.15	0.14	0
MgO	16.35	21.18	46.9	1.66	23.72	3.1	19.56	47.48	21.59	11.35	11.32	10.03	12.69	13.1	12.89	0.01
CaO	24.73	0.14	0.02	51.62	0	50.11	29.82	0	0.1	11.95	11.98	11.73	12.13	0.31	0.02	9.07
Na2O	0.16	0.1	0.13	0	1.11	0	0.03	0.12	0.24	1.1	1.08	1.24	0.49	0.14	0.15	6.34
K2O	0	0.02	0	0.08	9.76	0.04	0.03	0.01	0.02	0.85	0.9	1.11	0.19	8.08	8.99	0.36
Total	100.13	98.62	99.98	54.25	94.49	54.06	51.94	99.75	98.36	97.54	97.49	97.43	97.77	94.03	94.65	99.62
cations																
Si	1.952	0.001	0.996	0.003	2.709	0.004	0.004	0.998	0	6.681	6.653	6.395	7.434	2.722	2.794	2.558
Ti	0.007	0.003	0	0.001	0.07	0	0	0.001	0.003	0.07	0.074	0.067	0.032	0.145	0.145	0
Al	0.066	1.924	0	0	1.435	0	0.002	0.001	1.885	1.985	1.981	2.515	0.873	1.439	1.393	1.434
Cr	0.001	0.004	0	0	0	0.001	0.001	0.002	0	0.013	0.002	0.002	0.021	0.003	0.003	0
Fe3	0.026	0.072	0.013	0	0.032	0	0	0.006	0.122	0.145	0.187	0.17	0.099	0.095	0.03	0.004
Fe2	0.074	0.174	0.232	0.007	0.18	0.006	0.047	0.222	0.145	1.635	1.629	1.657	1.794	1.037	1.069	0
Mn	0.006	0.013	0.018	0.008	0.009	0.013	0.013	0.013	0.009	0.03	0.029	0.031	0.032	0.01	0.009	0
Mg	0.889	0.801	1.733	0.094	2.53	0.156	0.921	1.751	0.821	2.493	2.494	2.214	2.763	1.487	1.456	0.001
Ca	0.967	0.004	0.001	1.882	0	1.818	1.009	0	0.003	1.887	1.897	1.862	1.899	0.026	0.002	0.439
Na	0.011	0.005	0.006	0	0.154	0	0.002	0.006	0.012	0.316	0.31	0.357	0.14	0.02	0.022	0.553
K	0	0.001	0	0.004	0.892	0.002	0.001	0	0.001	0.16	0.17	0.209	0.036	0.785	0.87	0.021
total	4.000	3.000	3.000	2.000	8.011	2.000	2.000	3.000	3.000		15.427	15.478	15.124		7.794	

	TATO PLUTON															
	E104				E5A											
oxides	pl	pl	pl	pl	ksp	ksp	ksp	ksp	pl	pl	pl	bt	bt	tur	tur	tur
(wt.%)	#157	#237	#36	#169	#88	5	6	3	25	26	31	1	2	1	2	3
SiO2	56.93	50.92	63.01	67.25	64.56	65.45	65.65	65.34	62.55	58.79	65.34	38.29	43.89	33.88	34.78	34.48
TiO2	0	0	0	0	0.01	0.02	0.02	0.02	0	0.02	0.02	1.66	0.75	0.63	0.22	0.41
Al2O3	26.84	30.79	23.4	20.3	18.05	18.09	18.22	18.01	22.82	25.51	21.04	21.09	26.72	32.83	35.28	34.65
Cr2O3	0	0	0.01	0	0	0	0	0	0	0	0	0	0	0	0	0
Fe2O3	0.19	0.16	0.29	0.16	0.27	0.03	0.03	0.14	0.04	0.12	0.03	0	0	0	0	0
FeO	0	0	0	0	0	0	0	0	0	0	0	19.46	9.84	14.08	12.16	12.78
MnO	0	0	0.01	0.01	0	0	0	0.03	0	0	0	0.78	0.42	0.15	0.08	0.11
MgO	0.01	0.01	0	0	0	0	0	0	0	0	0	1.55	1.11	1.54	1.56	1.8
CaO	9.05	13.5	4.58	1.02	0.02	0.03	0.19	0.02	4.51	7.78	2.41	0.01	0.01	0.35	0.21	0.45
Na2O	6.54	3.9	9.14	11.16	0.38	2.19	2.99	1.29	8.87	6.96	10.08	0.09	0.26	2.2	1.67	1.83
K2O	0.12	0.08	0.24	0.18	15.98	14.11	11.99	15.4	0.27	0.2	0.28	8.87	10.64	0.04	0.02	0.04
Total	99.68	99.36	100.68	100.08	99.28	99.94	99.11	100.27	99.06	99.38	99.2	91.81	93.65	85.76	86.03	86.6
cations																
Si	2.563	2.331	2.775	2.946	3.004	3.007	3.012	3.007	2.794	2.641	2.896	2.979	3.146			
Ti	0	0	0	0	0	0.001	0.001	0.001	0	0.001	0.001	0.097	0.04			
Al	1.425	1.662	1.215	1.048	0.99	0.98	0.986	0.977	1.202	1.351	1.099	1.935	2.258			
Cr	0	0	0	0	0	0	0	0	0	0	0	0	0			
Fe3	0.006	0.005	0.01	0.005	0.009	0.001	0.001	0.005	0.001	0.004	0.001	0	0			
Fe2	0	0	0	0	0	0	0	0	0	0	0	1.266	0.59			
Mn	0	0	0	0	0	0	0	0.001	0	0	0	0.051	0.026			
Mg	0.001	0	0	0	0	0	0	0	0	0	0	0.18	0.119			
Ca	0.436	0.662	0.216	0.048	0.001	0.001	0.009	0.001	0.216	0.375	0.114	0.001	0.001			
Na	0.571	0.346	0.781	0.948	0.034	0.195	0.266	0.115	0.768	0.606	0.866	0.014	0.036			
K	0.007	0.005	0.013	0.01	0.95	0.828	0.703	0.905	0.015	0.011	0.016	0.881	0.974			
total	5.01	5.011	5.01	5.006	4.988	5.013	4.978	5.012	4.996	4.989	4.994	7.404	7.19			

APPENDIX 4 - SAMPLE THERMOCALC OUTPUT

A 4.1 Sample Thermocalc output

The first step is to convert a set of mineral analyses into an input file. Taking the analyses for cordierite seam presented in Appendix 3.2, endmember activities are calculated using the "ax96" program, written by Tim Holland, and the following datafile is constructed:

%th dZ130
phl 2.33 x 10^{-3}
ann 1.48 x 10^{-1}
east 4.93 x 10^{-3}
naph 9.65 x 10^{-5}
crd 9.92 x 10^{-2}
fcrd 4.49 x 10^{-1}
mncd 2.18 x 10^{-4}
py 2.30 x 10^{-4}
gr 6.80 x 10^{-6}
alm 6.29 x 10^{-1}
spss 1.65 x 10^{-4}
ksp 6.85 x 10^{-1}
ab 3.07 x 10^{-1}
sill
q
H_2O
CO_2
*

Unspecified activities for sillimanite and quartz indicate that they are in excess. H_2O and CO_2 activities are variable, and are specified for each Thermocalc run. Activity models are listed in Appendix 4.2

The next step is to run Thermocalc. The output below is annotated (linmes beginning with >).

```
THERMOCALC v2.4, © Roger Powell and Tim Holland running at
13.14 on Tue 3 Jun,1997

(thermodynamic dataset produced at 13.35 on Wed 31 May, 1995)

an independent set of reactions has been calculated

rock
```

> List of input endmembers and their activities. sd (a)/a indicates uncertainty in activity divided by the acitivity. Realistic uncertainties are assigned by Thermocalc unless input in the data file. Note user specified X(H2O) = 1.0, i.e. aqueous fluid present.

```
                phl      ann     east     naph      crd     fcrd
mncd      ksp
a           0.00233    0.148 0.00493 9.65e-5   0.0992
0.4490.000218    0.685
sd(a)/a     0.54347 0.19969 0.51870103.62694 0.24343
0.1000045.87156 0.05000
                 ab       py      alm     spss     sill        q
H2O
a              0.3070.000230    0.6290.000165     1.00     1.00
1.00
sd(a)/a     0.14407 0.79309 0.15000 0.80398        0        0
```

> List of independent set of reactions used for average (PT) calculation

```
reactions
1)   5phl + py + 12sill = 5east + 4crd
2)   east + py + 3q = phl + crd
3)   10phl + 21sill = 9east + 6crd + ksp + H2O
4)   2naph + 6sill + 9q = 3crd + 2ab + 2H2O
5)   6phl + alm + 12sill = ann + 5east + 4crd
6)   3crd + 2alm = 3fcrd + 2py
7)   20phl + 10ann + 6spss + 72sill = 30east + 15fcrd + 9mncd
```

> List of thermodynamic data for the reactions listed above

```
calculations (for x(H2O) = 1.0)
        P(T)   sd(P)       a   sd(a)         b         c
ln_K sd(ln_K)
1        5.9    1.75   42.26   13.38  -0.20081   19.884
2.882    3.961
2        1.8    1.84  -27.22    2.70  -0.03478    5.123
5.317    1.119
3        6.3    2.16  187.48   24.07  -0.38743   29.519
-1.435    7.312
4        2.1  117.79  146.90    5.43  -0.27971   14.234
9.198  207.255
5        5.5    1.84   88.17   13.40  -0.21320   20.176
-0.880    4.286
6        1.4   18.41   88.64    2.06   0.00170    0.798
-11.298    1.797
7        4.2   27.00  768.14   84.44  -0.95845  123.863
-54.662  413.316
```

> The answer. sd indicates 1 sigma errors, cor = correlation (for error ellipse), f = "fit" parameter (within 95% confidence in this case).

```
rock : average PT (for x(H2O) = 1.0)


T = 681°C, sd = 41,
P = 3.6 kbars, sd = 0.4, cor = 0.865, f = 0.86

****************************************
```

> This time, average (T) calculations are performed for a range of specified pressures, using the same input data as before.

```
an independent set of reactions has been calculated

rock

                phl      ann     east     naph      crd     fcrd
mncd      ksp
a           0.00233    0.148 0.00493 9.65e-5   0.0992
0.4490.000218    0.685
sd(a)/a     0.54347 0.19969 0.51870103.62694 0.24343
0.1000045.87156 0.05000

                 ab       py      alm     spss     sill        q
H2O
a             0.3070.000230    0.6290.000165     1.00     1.00
1.00
sd(a)/a     0.14407 0.79309 0.15000 0.80398        0        0
```

```
reactions
1)  5phl + 4crd = east + 4ksp + 7py + 4H2O
2)  2east + crd + q = 2phl + 4sill
3)  10phl + 21sill = 9east + 6crd + ksp + H2O
4)  5naph + 6crd = 5ab + 9py + 3sill + 5H2O
5)  2ann + 6sill + 9q = 3fcrd + 2ksp + 2H2O
6)  ann + sill + 2q = ksp + alm + H2O
7)  2ann + 3crd + 2spss = 2phl + 3mncd + 2alm


calculations  at P = 4.5 kbar(for x(H2O) = 1.0)
        T(P)   sd(T)       a   sd(a)         b         c
ln_K sd(ln_K)
1        671     286  466.38    7.72  -0.19783  -18.907
-25.916    6.282
2        421     309  -21.96    5.30   0.04722   -4.972
0.812    1.522
3        549     202  182.42   24.07  -0.34353   30.311
-1.435    7.312
4        743   21549  526.24   12.98  -0.21453  -29.900
-21.208  518.186
5        742      25  163.95    3.80  -0.23548   16.077
0.662    0.509
6        651      42   55.58    1.82  -0.06920    0.046
1.069    0.255
7       1290   30877   86.24    9.40   0.03977    0.582
-10.172  137.631

average temperatures (for x(H2O) = 1.0)
```

> This time, the fit parameter was not statistically acceptable within 95% confidence limits. The information below enables the user to identify specific endmembers which are either influential in the calculations (hat parameter), or which have suspect activities. In this case, fcrd is the most influential endmember, and east is particularly suspect. East will not be input for the next run.

```
Single end-member diagnostic information

av, sd, fit are result of doubling the uncertainty on ln a :
a ln a is suspect if any are v different from lsq values.
e* are ln a residuals normalised to ln a uncertainties :
large absolute values, say >2.5, point to suspect info.
hat are the diagonal elements of the hat matrix :
large values, say >0.47, point to influential data.
For 95% confidence, fit (= sd(fit)) < 1.45;
however a larger value may be OK - look at the diagnostics!
```

```
          av    sd   fit
lsq      832    58  2.53

              T     sd    fit     e*   hat
     phl    827     58   2.50    1.0  0.04
     ann    874     54   2.10   -2.7  0.17
    east    827     49   2.16    3.2  0.00
    naph    832     58   2.53    0.0  0.00
     crd    821     51   2.21   -2.6  0.02
    fcrd    819     75   2.52   -0.5  0.36
    mncd    832     58   2.53   -0.1  0.00
     ksp    834     59   2.52    0.3  0.02
      ab    832     58   2.53   -0.0  0.00
      py    832     57   2.51    0.9  0.00
     alm    811     54   2.26    2.5  0.08
    spss    832     58   2.53    0.0  0.00
    sill    832     58   2.53      0     0
       q    832     58   2.53      0     0
     H2O    832     58   2.53      0     0


P       1.0   2.0   3.0   4.0   5.0   6.0   7.0   8.0
av T    507   588   664   747   832   914   996  1078
sd       52    50    44    50    58    66    78    91
f       2.5   2.2   2.0   2.2   2.5   2.9   3.4   4.0

****************************************
```

> This time, both east and ann have been deleted from the input file (an intermediate run containing ann also failed to achieve a statistically acceptable fit value). Conditions are still fluid present.

```
an independent set of reactions has been calculated

rock

                phl     naph      crd     fcrd     mncd      ksp
a           0.00233 9.65e-5   0.0992   0.4490.000218    0.685
sd(a)/a   0.54347103.62694 0.24343 0.1000045.87156 0.05000

                 ab       py      alm     spss     sill        q
H2O
a             0.3070.000230   0.6290.000165     1.00     1.00
1.00
sd(a)/a     0.14407 0.79309 0.15000 0.80398        0        0

reactions
1)   5phl + 6crd = 5ksp + 9py + 3sill + 5H2O
2)   4phl + 3crd + 3q = 4ksp + 6py + 4H2O
3)   5naph + 6crd = 5ab + 9py + 3sill + 5H2O
4)   3crd + 2alm = 3fcrd + 2py
5)   4phl + 3mncd + 3q = 4ksp + 4py + 2spss + 4H2O
```

```
calculations  at P = 4.5 kbar(for x(H2O) = 1.0)
   T(P) sd(T)      a  sd(a)       b        c     ln_K sd(ln_K)
1  678   341  573.57  9.22 -0.20527  -28.639  -33.115    7.780
2  692   213  438.12  7.04 -0.22421  -13.803  -20.599    5.286
3  743 21549  526.24 12.9  -0.21453  -29.900  -21.208  518.186
4  727  5541   87.34  2.06  0.00292    0.805  -11.298    1.797
5  458  5112  261.26 11.67 -0.24029  -14.982   -2.902  137.678

average temperatures (for x(H2O) = 1.0)
```

> A statistically acceptable fit value has been achieved.

```
P       1.0   2.0   3.0   4.0   5.0   6.0   7.0   8.0
av T    501   597   683   750   798   828   840   838
sd       51    32    31    29    27    25    25    26
f       1.6   0.8   0.2   0.3   0.6   0.9   1.1   1.2
```

A 4.2 Activity models used by the "ax96" program

Name and abbreviation		Mixing model and ferric iron
Amphibole	amph	Ideal mixing-on-sites model from Holland and Powell (1990). Ferric from: Av from max and min constraints, Holland & Blundy (1994)
Biotite	bi	Holland and Powell (1990) site-mixing model with Eugster et al. (1972) gammas. Ferric from: Tet + Oct cation sum = 6.9 for 11 oxygens. Max Ratio = 0.15
Carbonate	carb	1-site ideal mixing , all iron ferrous
Clinopyroxene	cpx	Ideal 2-site mixing. Ferric from: Cation Sum = 4 for 6 oxygens
Cordierite	cd	2-site Mg-Fe-Mn mixing, anhydrous basis. Ferric from: Cation Sum = 11 for 18 oxygens. Max Ratio = 0.2 WFeMg=1.5, WMgMn=1.5, WFeMn=0 (kJ)
Feldspar	fsp	ksp - Waldbaum and Thompson (1969), all iron ferric plag - Holland & Powell (1992) model 1, all iron ferric
Garnet	g	2-site mixing with Newton and Haselton (1981) gammas. Ferric from: Cation Sum = 8 for 12 oxygens
Muscovite	mu	Holland and Powell (1990) site-mixing model with Eugster et al. (1972) gammas. Ferric from: Tet + Oct cation sum = 6.05 for 11 oxygens. Max Ratio = 0.5
Olivine	ol	Ferric from: Cation Sum = 3 for 4 oxygens. Max Ratio = 0.1 2-site mixing with reg solution W = 4 kJ per site

APPENDIX 5 - SAMPLE CATALOGUE

This appendix contains a comprehensive list of rocks samples collected from the southern NPHM. Some sample numbers are missing due to a rock fall which buried these rocks.

Key to sample catalogue:

No.	Sample number	
	Note X or Z prefix indicates float, E or N indicates in situ	
	X and N samples collected by Nigel Harris in 1994	
Sub	Subdivision	
Loc.	Location:	
	Koh	Kohistan
	MMT	MMT zone
	LSZ	Lichar S
	Tato	road between Tato village and Fairy Meadows
	FM	Fairy Meadows
	TP	Tato pluton
	Bul	Buldar (E Raikhot valley)
	BC	Bayal camp (W Raikhot valley)
	ABC	Advance Base (float from Raikhot face)
	Tar	Tarshing (lower Rupal valley)
	Rup	Rupal
	Sha	Shaigiri (upper Rupal valley)

Type	diorite	Kohistan diorite
	metabasalt	amphibolite dyke
	calcic gneiss	contains hornblende and biotite
	calc-silicate	contains hornblende and pyroxene
	marble	contains free calcite and dolomite
	bt orthogneiss	bt-qtz-ksp-plag orthogneiss
	mu orthogneiss	mu-bt-qtz-ksp-plag orthogneiss
	bt pelite	bt-sill-ksp-q pelitic gneiss
	gnt pelite	gnt-bt-sill-ksp-q pelite
	crd pelite	crd-gnt-bt-sill-ksp-q pelite
	spl pelite	spl-crd-gnt-bt-sill-ksp-q pelite
	crd seam	crd-ksp-q assemblage
	Tato pluton	Tato pluton leucogranite
	Tato dyke	undeformed leucogranite (feeder) dyke
	def dyke	deformed leucogranite dyke
	peg	pegmatite (tur = tourmaline, cd = cordierite, gnt = garnet)
TS	Thin section	
PS	Polished section	
XRF M	X-Ray Fluorescence analysis for major elements	
XRF T	X-Ray Fluorescence analysis for trace elements	
INA REE	Instrumental Neutron Activation Analysis (rare earth elements)	
Sr	87Sr-86Sr whole-rock analysis	
Nd	143Nd-144Nd whole-rock analysis	
Ar	40Ar-39Ar analysis: B = biotite, M = muscovite	
MA	Microprobe mineral analysis	

No.	Sub	Loc.	Type	TS	PS	XRF M	XRF T	INA REE	Sr	Nd	Ar	MA
Z1		Tato	crd pelite	√	√							
E1		Tato	bt pelite	√	√							
E2		Tato	calc-silicate	√	√							
E3		Tato	Tato dyke	√								
E4		FM	gnt pelite	√	√	√	√				B	
E5	E5A/i	TP	Tato pluton	√	√	√	√	√	√	√	M	√
	E5A/ii	TP	Tato pluton			√	√	√	√	√		
	E5B	TP	Tato pluton	√		√	√	√	√	√	BM	
Z6	Z6a	Tato	tur peg	√	√	√	√					
	Z6b	Tato	tur peg	√		√	√					
	Z6c/L1	Tato	tur peg	√		√	√					
	Z6c/L2	Tato	tur peg	√		√	√					
	Z6c/L3	Tato	tur peg	√		√	√					
	Z6d	Tato	tur peg	√								
Z7		Tato	gnt pelite	√	√							
Z8		Tato	crd seam	√								
Z9	Z9/i	Tato	crd pelite	√	√	√	√	√	√	√		
	Z9/ii	Tato	crd pelite			√	√					
Z10		Tato	crd seam	√								
Z11		Tato	crd seam	√								
Z12		Tato	crd seam	√	√	√	√					
Z13	Z13/i	Tato	crd pelite	√	√	√	√	√	√	√		
	Z13/ii	Tato	crd pelite			√	√					
	Z13/iii	Tato	crd pelite			√	√					
Z14		Tato	cd peg / bt pelite	√								
Z15	Z15a	Tato	gnt pelite	√	√							
	Z15b	Tato	gnt pelite	√	√							
	Z15c	Tato	gnt pelite	√	√							
	Z15d	Tato	gnt pelite	√	√							
Z16	Z16a	Tato	cd peg / bt pelite	√								
	Z16b	Tato	cd peg / bt pelite	√	√							
Z17	Z17a	Tato	gnt pelite	√	√	√	√	√				
	Z17b	Tato	gnt pelite	√	√							
	Z17c	Tato	gnt pelite	√	√							
Z18	Z18a	Tato	tur peg	√								
	Z18b	Tato	tur peg									
	Z18c	Tato	tur peg									
Z19		Tato	gnt pelite	√	√							
Z20	Z20a	Tato	tur-cd peg	√								
Z20	Z20b	Tato	tur-cd peg	√								
Z20	Z20c	Tato	tur-cd peg	√								
Z20	Z20d	Tato	tur-cd peg	√								
Z20	Z20e	Tato	tur-cd peg									
Z21		Tato	calc-silicate	√	√							
E22		LSZ	bt orthogneiss	√	√						B	
E27		LSZ	ms orthogneiss	√	√						M	
E28		LSZ	bt orthogneiss	√							B	

No.	Sub	Loc.	Type	TS	PS	XRF M	XRF T	INA REE	Sr	Nd	Ar	MA
E29		LSZ	bt orthogneiss	√	√							
E32		LSZ	calc-silicate	√	√							
E33		LSZ	def dyke / bt gneiss	√	√						B	
E34		LSZ	calc-silicate	√	√							
E35		LSZ	calc-silicate	√	√							
E36		LSZ	def dyke									
E37		Tato	crd seam / bt pelite	√	√							
E38		Tato	crd seam / bt pelite	√	√							
Z39		Tato	tur peg / calc-silicate	√								
Z40		Tato	gnt pelite	√	√							
Z41		Tato	crd seam	√	√	√	√	√				
Z42	Z42/i	Tato	crd seam	√		√	√	√	√	√		
	Z42/ii	Tato	crd seam	√		√	√	√	√	√		
	Z42/iii	Tato	crd seam	√		√	√	√	√	√		
	Z42/iv	Tato	crd seam	√		√	√		√			
Z43	Z43a	Tato	crd seam / gnt pelite	√								
	Z43b/i	Tato	crd seam	√	√	√	√					
	Z43b/ii	Tato	crd seam			√	√					
	Z43b/iii	Tato	crd seam			√	√	√				
Z44	Z44a	Tato	crd seam	√		√	√					
	Z44b(1)	Tato	crd seam	√	√	√	√	√				
Z45	Z45a/i	Tato	crd seam / gnt pelite	√	√	√	√					
	Z45A/ii	Tato	crd seam / gnt pelite			√	√					
	Z45A/iii	Tato	crd seam / gnt pelite			√	√	√				
	Z45b	Tato	crd seam / gnt pelite	√		√	√	√				
	Z45c	Tato	crd seam / gnt pelite	√								
Z46	Z46a	Tato	crd seam / gnt pelite	√	√	√	√					
	Z46b	Tato	crd seam / gnt pelite	√		√	√					
	Z46c/i	Tato	crd seam / gnt pelite	√		√	√	√	√	√		
	Z46c/ii	Tato	crd seam / gnt pelite	√		√	√	√	√	√		
	Z46c/iii	Tato	crd seam / gnt pelite	√		√	√	√	√	√		
	Z46c/iv	Tato	crd seam / gnt pelite	√		√	√	√	√	√		
	Z46c/v	Tato	crd seam / gnt pelite			√	√	√		√		
	Z46d	Tato	crd seam / gnt pelite	√								
E47		Tato	bt pelite	√							B	
Z48		Tato	calc-silicate	√								
Z49		Tato	bt pelite / gnt peg	√								
Z50		Tato	gnt peg	√	√	√	√					
Z51		Tato	gnt peg	√	√	√	√	√				
Z52		Tato	gnt peg	√	√	√	√					
Z53		Tato	bt pelite / tur peg	√								
Z54	Z54a	Tato	gnt pelite	√	√							
	Z54b	Tato	gnt pelite	√								
Z55		Tato	gnt pelite	√								
Z56		Tato	gnt pelite	√								
Z57		Tato	gnt pelite	√	√							
Z58	Z58a	Tato	def peg	√	√	√	√					

No.	Sub	Loc.	Type	TS	PS	XRF M	XRF T	INA REE	Sr	Nd	Ar	MA
	Z58b	Tato	def peg	√		√	√		√	√		
	Z58c	Tato	def peg	√		√	√					
	Z58d	Tato	def peg	√	√							
Z59	Z59a	Tato	def peg	√	√	√	√					
	Z59b	Tato	def peg	√								
	Z59c	Tato	def peg	√								
	Z59d	Tato	def peg	√								
	Z59e	Tato	def peg	√								
	Z59f	Tato	def peg	√								
E62		TP	Tato dyke / bt gneiss	√								
E63		TP	Tato dyke / bt gneiss	√							B	
E64		TP	Tato dyke	√		√	√	√	√	√	BM	
E65		TP	Tato pluton / bt gneiss	√								
Z66	Z66a	TP	Tato pluton	√	√	√	√	√	√	√		
	Z66b	TP	Tato pluton			√	√					
Z67		Tato	gnt pelite	√	√							
E68		TP	Tato dyke	√	√	√	√	√				
Z69		TP	bt orthogneiss	√	√	√	√	√				
E70	E70a	TP	ridge leucogranite	√	√	√	√	√	√	√		
	E70b	TP	ridge leucogranite	√		√	√	√	√	√	B	
	E70c	TP	ridge leucogranite	√		√	√	√	√	√	B	
Z71	Z71/i	Tato	bt pelite	√		√	√					
	Z71/ii	Tato	bt pelite			√	√					
E72		Tato	crd seam	√							B	
E73		Tato	bt pelite	√								
E74		Tato	crd seam / bt pelite	√								
E75		Tato	tur-crd peg / bt pelite	√							B	
Z76	Z76a	Tato	crd seam / bt pelite	√	√							
	Z76b	Tato	crd seam /gnt pelite	√								
Z77		Tato	crd seam / bt pelite	√								
E78		Tato	crd seam / bt pelite	√								
E79		LSZ	bt orthogneiss	√								
E80		LSZ	def dyke / gnt pelite	√								
E81		LSZ	def dyke	√	√	√	√	√	√	√		
E82		LSZ	ms-bt pelite	√							BM	
E83		LSZ	bt pelite	√							B	
E84		LSZ	bt orthogneiss	√								
E85	E85a	LSZ	undef aplite dyke	√	√	√	√					
	E85b	LSZ	undef aplite dyke	√		√	√	√				
N1		Tato	crd pelite	√	√	√	√	√	√	√	B	√
X1		Tato	crd seam	√	√	√	√	√	√	√		
X2		Tato	spl pelite	√	√							√
X4		Tato	crd pelite	√	√	√	√					
X7		Tato	spl pelite	√	√							√
X8	X8/i	Tato	spl pelite	√	√	√	√	√				√
	X8/ii	Tato	spl pelite			√	√					
X10		Tato	crd seam	√	√	√	√	√	√	√		

No.	Sub	Loc.	Type	TS	PS	XRF M	XRF T	INA REE	Sr	Nd	Ar	MA
E100		Tar	gnt pelite		√							
E101		Tar	mu orthogneiss		√	√	√	√	√	√	BM	
E102		Rup	mu orthogneiss		√	√	√	√	√	√	BM	
E103		Sha	mu orthogneiss		√	√	√		√	√	BM	
E104	E104A	Sha	metabasalt	√	√	√	√	√	√	√		√
	E104B	Sha	metabasalt	√		√	√	√	√	√		
	E104C	Sha	metabasalt	√		√	√	√	√	√		
	E104D	Sha	metabasalt	√		√	√	√	√			
	E104E	Sha	metabasalt	√		√	√	√	√	√		
Z105		Sha	Tato dyke		√	√	√	√	√	√		
E106		Sha	mu orthogneiss	√		√	√	√	√	√	BM	
E107	E107(1)	Rup	Tato dyke		√	√	√	√	√	√	M	
	E107(2)	Rup	Tato dyke			√	√	√	√			
E108		Rup	mu gneiss / Tato dyke	√								
E109		BC	Tato dyke	√		√	√		√	√		
E110		BC	bt gneiss / Tato dyke		√	√	√					
E111		TP	Tato pluton	√		√	√	√	√	√		
E112	E112(1)	TP	Tato pluton		√	√	√	√		√		
	E112(2)	TP	Tato pluton	√		√	√	√				
E113		Tato	crd seam / bt pelite									
E114		BC	Tato dyke			√	√	√	√	√		
E115		BC	calcic gneiss		√	√	√					√
E116		BC	calcic gneiss		√	√	√	√				√
E117		BC	Tato dyke	√		√	√	√				
E118		BC	Tato dyke	√		√	√	√				
E119	E119A	BC	amphibolite	√	√	√	√	√	√	√		
	E119B	BC	amphibolite	√		√	√		√			
	E119C	BC	amphibolite	√		√	√		√	√		
	E119D	BC	amphibolite	√		√	√		√	√		
	E119E	BC	amphibolite	√		√	√		√	√		
E120		BC	Tato dyke	√		√	√	√				
E121		BC	cd-tur peg	√		√	√	√				
E122		BC	cd seam	√		√	√				B	
Z123		BC	calc-silicate		√							
Z124		BC	calc-silicate		√	√	√					√
E125		Bul	bt orthogneiss	√		√	√				B	
E126		Bul	gnt pelite		√	√	√	√	√			√
E127		Bul	bt orthogneiss	√		√	√				B	
E128		Bul	Tato dyke	√		√	√		√	√		
E129		Bul	bt orthogneiss	√		√	√	√			B	
Z130	Z130a/i	Bul	cd seam		√	√	√	√	√	√		√
	Z130a/ii	Bul	crd pelite		√	√	√	√	√	√		√
	Z130b/i	Bul	cd seam		√	√	√	√	√	√		
	Z130b/ii	Bul	crd pelite		√	√	√	√	√	√		
	Z130c	Bul	cd seam		√	√	√	√	√	√		
	Z130d	Bul	cd seam		√	√	√	√	√	√		
E131	E131a	Bul	calc-silicate	√								

No.	Sub	Loc.	Type	TS	PS	XRF M	XRF T	INA REE	Sr	Nd	Ar	MA
	E131b	Bul	calc-silicate	√								
E132		Bul	bt orthogneiss		√	√	√				B	
E133		Bul	Tato dyke			√	√		√	√		
Z134		Bul	spl pelite	√		√	√					
Z135		Bul	spl pelite	√	√							√
Z136	Z136a	Bul	crd seam	√								
	Z136b	Bul	crd pelite	√								
Z137	Z137a	Bul	crd seam									
	Z137b	Bul	crd pelite									√
E138		TP	gnt pelite		√	√	√				B	
E139		TP	gnt pelite		√	√	√				B	√
Z140		TP	Tato pluton		√	√	√	√	√	√		
Z141		TP	Tato pluton		√	√	√	√	√	√		
Z142		TP	Tato pluton		√	√	√					
Z143		TP	Tato pluton		√	√	√					
Z144		ABC	crd pelite		√							
E145		ABC	bt orthogneiss		√	√	√				B	
Z146		ABC	crd seam		√							
Z147		ABC	spl pelite		√	√	√	√				√
Z148		ABC	calc-silicate		√							√
Z149		ABC	gnt pelite		√	√	√					
Z150		ABC	marble		√	√	√					√
Z151		ABC	marble		√	√	√					
Z152		ABC	crd seam		√							
Z153	Z153/i	ABC	crd seam		√							
	Z153/ii	ABC	spl pelite		√							√
E154		LSZ	augen gneiss	√		√	√				B	
E155		BC	metabasalt		√	√	√	√	√	√		
E156		Koh	Kohistan diorite		√	√	√	√	√	√	B	
E157		MMT	mu-gnt pelite		√	√	√				M	√
E158		MMT	altered pelite		√	√	√					
E159		MMT	altered pelite		√	√	√					
E160		MMT	Kohistan diorite		√	√	√					

BACKWORD

"Of course, as a Cambridge graduate, he had imbibed, at least by osmosis. something of modern skeptical scholarship, and he knew all this might be mere infatuation with a wonderful myth."

(from "Masks of the Illuminati", by Robert Anton Wilson, 1981, Dell Publishing, New York)